Colorado State University

A Short Course on
Flood Hazard Simulation

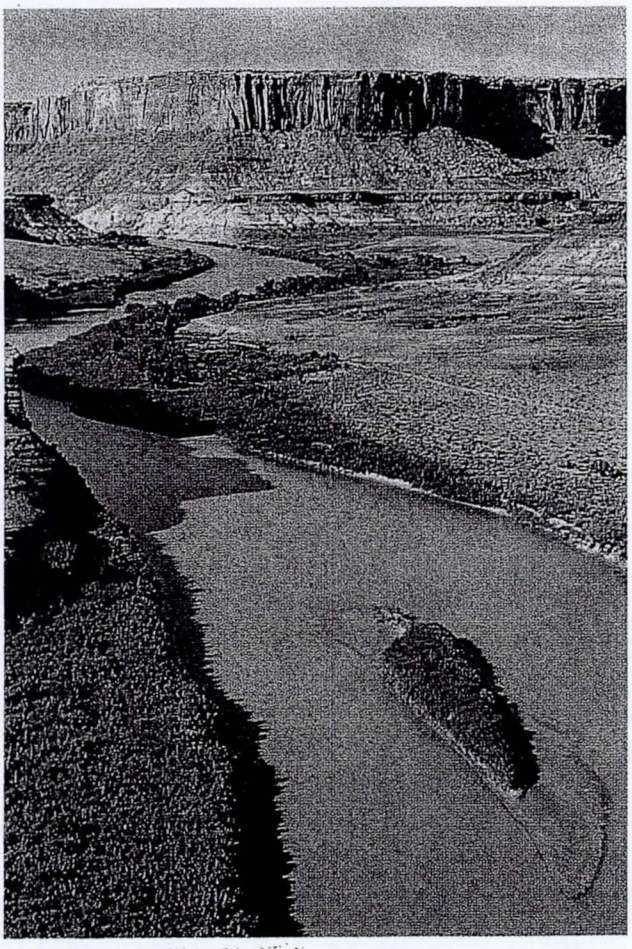

October 5-7, 1998
Cliff Lodge, Snowbird Resort
Snowbird, Utah

FLO ENGINEERING INC

Colorado State University

A Short Course on
Flood Hazard Simulation

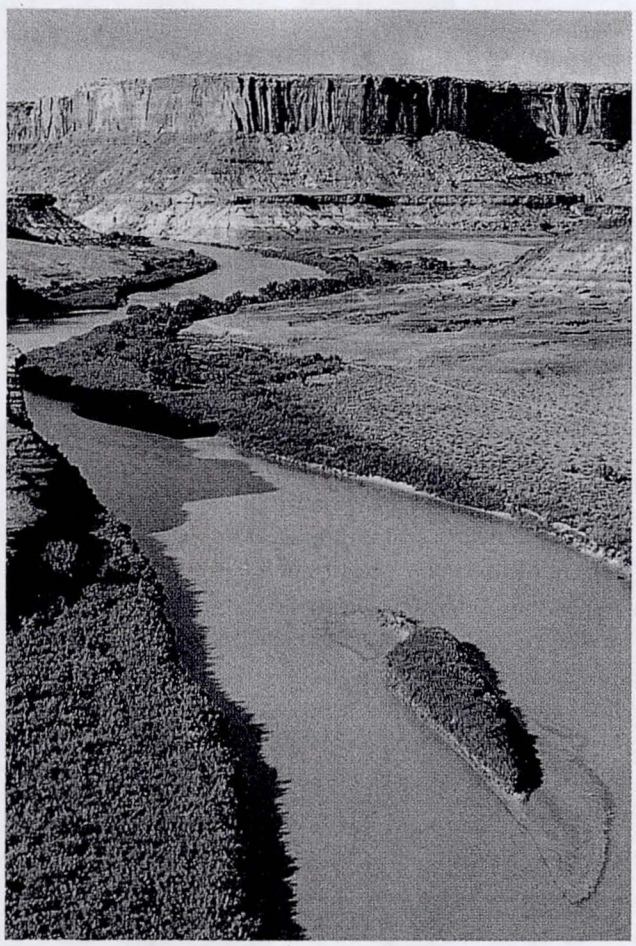

October 5-7, 1998
Cliff Lodge, Snowbird Resort
Snowbird, Utah

FLO ENGINEERING INC

PHYSICAL PROPERTIES AND MECHANICS OF HYPERCONCENTRATED SEDIMENT FLOWS

by J. S. O'Brien and P. Y. Julien

ABSTRACT

The authors advance a better understanding of hyperconcentrated sediment flows, commonly referred to as debris flows or mudflows, with a fundamental investigation of the nature of fluid motion. In these flows of large concentrations of sediment, the predominant processes of energy dissipation are related to the viscous, turbulent, dispersive and yield stresses. The relative magnitude of these components largely depend on the fluid properties and whether the flow matrix consists of cohesive or noncohesive sediment. Based on experimental data, the following relationships are provided: 1) stress versus rate of strain, 2) viscosity versus sediment concentration, and 3) yield strength versus sediment concentration. These results expand our knowledge of the physical properties of hyperconcentrated flows.

The authors also review the application of fluid principles to these flows. The fundamentals of fluid mechanics are outlined for the case of hyperconcentrated flows on steep slopes with emphasis on the physical properties of non-Newtonian fluids. A theoretically sound and simplified methodology prescribe the engineering analysis for these hazard flows.

INTRODUCTION

Hyperconcentrated sediment flows are commonly referred to as mud flows or debris flows. The term hyperconcentrated, however, depicts a broader spectrum of sediment transport ranging from large concentrations of suspended sediment in streams to landslides. Sharp and Nobles (1953) refer to hyperconcentrated flows as debris flows instead of mud flows when fifty percent or more of the sediment in the flow matrix is coarser than sand. Debris flows have also been described as granular flows which are identified by the absence of fine material (silts and clays).

Hyperconcentrated flows originate in basins which can be delineated into three zones. The sediment source area is located in the uppermost region of the watershed and may be in a landslide area. The zone of sediment transport is a steep channel system in which erosion and deposition are generally in equilibrium. Finally, the alluvial fan is a depositional zone often identified by a break in the bed slope of the main channel.

Jim S. O'Brien, P.E., is Research Associate at the Civil Engineering Department, Colorado State University, Fort Collins, Colorado.
Pierre Y. Julien, Ph.D., is faculty Affiliate at the Civil Engineering Department, Colorado State University, Fort Collins, Colorado.

PHYSICAL PROPERTIES AND MECHANICS OF HYPERCONCENTRATED SEDIMENT FLOWS

by J. S. O'Brien and P. Y. Julien

ABSTRACT

The authors advance a better understanding of hyperconcentrated sediment flows, commonly referred to as debris flows or mudflows, with a fundamental investigation of the nature of fluid motion. In these flows of large concentrations of sediment, the predominant processes of energy dissipation are related to the viscous, turbulent, dispersive and yield stresses. The relative magnitude of these components largely depend on the fluid properties and whether the flow matrix consists of cohesive or noncohesive sediment. Based on experimental data, the following relationships are provided: 1) stress versus rate of strain, 2) viscosity versus sediment concentration, and 3) yield strength versus sediment concentration. These results expand our knowledge of the physical properties of hyperconcentrated flows.

The authors also review the application of fluid principles to these flows. The fundamentals of fluid mechanics are outlined for the case of hyperconcentrated flows on steep slopes with emphasis on the physical properties of non-Newtonian fluids. A theoretically sound and simplified methodology prescribe the engineering analysis for these hazard flows.

INTRODUCTION

Hyperconcentrated sediment flows are commonly referred to as mud flows or debris flows. The term hyperconcentrated, however, depicts a broader spectrum of sediment transport ranging from large concentrations of suspended sediment in streams to landslides. Sharp and Nobles (1953) refer to hyperconcentrated flows as debris flows instead of mud flows when fifty percent or more of the sediment in the flow matrix is coarser than sand. Debris flows have also been described as granular flows which are identified by the absence of fine material (silts and clays).

Hyperconcentrated flows originate in basins which can be delineated into three zones. The sediment source area is located in the uppermost region of the watershed and may be in a landslide area. The zone of sediment transport is a steep channel system in which erosion and deposition are generally in equilibrium. Finally, the alluvial fan is a depositional zone often identified by a break in the bed slope of the main channel.

Jim S. O'Brien, P.E., is Research Associate at the Civil Engineering Department, Colorado State University, Fort Collins, Colorado.
Pierre Y. Julien, Ph.D., is faculty Affiliate at the Civil Engineering Department, Colorado State University, Fort Collins, Colorado.

analyzed for size fraction and silt and clay content, and the properties of the mixture were described for various water and sediment concentrations. The results were incorporated into the definitions promulgated by the NRC committee and are shown in Table 1.

In nature, there exist a continuum of flow conditions and one hydrologic event may consist of several flow processes. Flow deposits, scour characteristics, and fan patterns are helpful tools in identifying the flow regimes and processes. Although the transition between the different types of flow are difficult to distinguish, mass wasting processes can be divided in four main categories: water floods, mud floods, mud flows, and landslides.

Conventional water flooding is defined as water inundation by overbank discharge. Sediment is transported through the mechanisms of suspension and rolling and saltation along the bed which depend largely on water velocity and turbulence. For water floods, standard hydrologic and sediment transport capacity methods and formulas are applicable. Water floods are not a phenomena analyzed in this paper.

Mud floods define a range of concentration from 20 to 45 percent by volume (Table 1). This concentration refers to the fluid matrix and should be assumed to consist of silts, clays and fine sands only. Water floods and mud floods display inherent fluid properties, both are unable to resist shear stress without motion or exhibit any appreciable yield strength. Conventional analysis using momentum, energy and continuity equations are applicable. Sediment transport capacity equations such as Einstein and Meyer-Peter and Müller are inappropriate because higher viscosities of the mixture and lower fall velocities of solid particles invalidate the empirical constants which are based on clear water as the fluid medium. Water floods and mud floods are classified under the National Flood Insurance Program (NFIP) definition of floods by the NCR (see Figure 1).

In mud flows the sediment concentration is sufficient to support large clastic material in a quiescent condition without settling. The flow matrix exhibits a distinct resistance to motion (high yield strength). This resistance to shear stress is a pseudo-plastic flow property corresponding to high viscosities. The National Research Council (NRC, 1982) report states, "The key characteristic in differentiating between mud floods and mud flows is that a mud flow displays a combination of density and strength that will support inclusions of higher density than water, such as boulders, both during transport and when the mass comes to rest". Throughout the flow process the combination of fluid matrix density and small settling velocities keep the boulders near the surface in the absence of turbulence. In steep basins, mud flows are generated under certain conditions of rainfall and sediment availability. When unlimited supplies of sediment become available, the probability of producing a mud flow is very high for intense rainfall events. Debris flows are acknowledged as having more than fifty percent of the sediment sizes coarser than sand. Debris flows without fine materials (silts and clays) are referred to as granular flows.

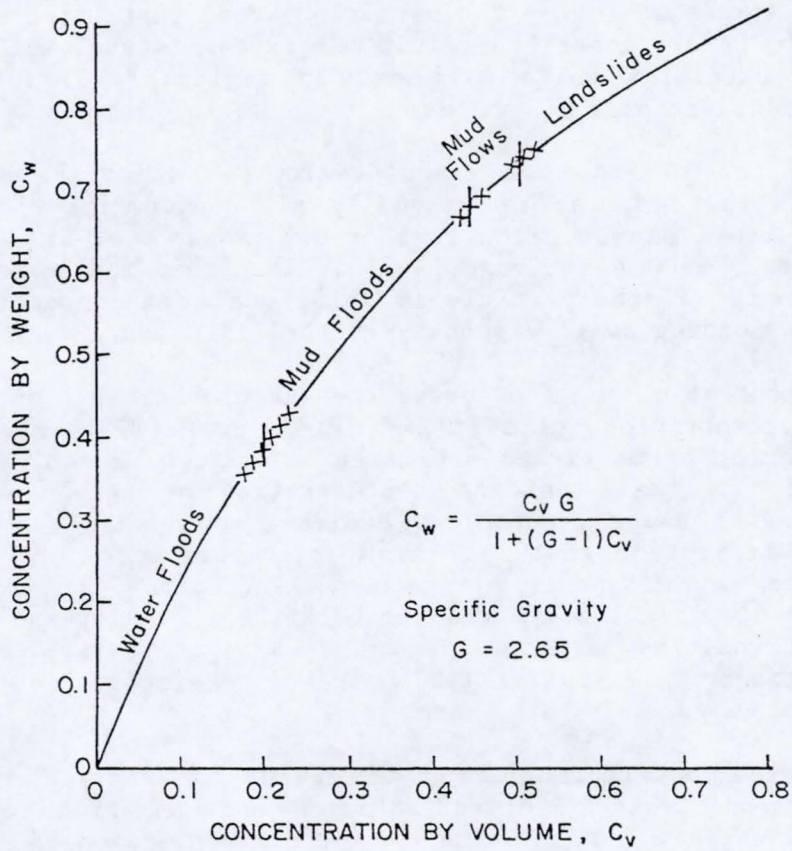

FIGURE 1. HYPERCONCENTRATED SEDIMENT FLOWS CLASSIFICATION

Landslides consist of downslope movement of earth by mechanisms of falling, toppling, sliding and spreading. Such earth movements may be either wet or dry. Landslides and bank slumps are an integral part of generating mud flows and mud floods in steep basins. This mechanism delivers source material to channel in brief singular events that often perturbate the channel flow hydraulics.

PHYSICAL PROPERTIES OF THE FLUID MATRIX

The presence of large concentrations of sediment induces complex processes of energy dissipation in the fluid matrix. Besides the viscous and turbulent stresses existing in clear water flows, the interaction of water and sediment, the exchange of sediment particles with the channel boundary, and the collisions of suspended particles (dispersive stress) all contribute to the dissipation of energy from the fluid matrix. Moreover, the presence of clay particles whose cohesive forces arise from hydrophilic bonding, modifies the physical processes governing the fluid flows. Hyperconcentrated sediment flows, therefore, are a function of complex interrelationships between water and sediments which require further investigation.

properties of viscosity and density and, therefore, the lift, drag and buoyancy forces acting on the particle exceed that which would have been exerted by water alone. The fluid matrix consists of the fluid plus the sediment particles which will have a negligible fall velocity in a quiescent condition.

Consider the case of granular flows in which the fluid matrix is water and the sediment is virtually all noncohesive clastic material. Granular flows may be either wet or dry (Passman et al., 1980, Nunziato and Passman, 1980 and Savage, 1979). The fluid medium is water and the fall velocity of the particle is large due to the absence of fines and the corresponding small viscosity of the fluid matrix.

Concentration and flow properties should be expected to change with larger concentrations of silt and clay. Graf (1971) reported that the fall velocity of particles decreases with the addition of fine sediment to water. A small percent concentration by weight of sediment in flowing water dampens turbulent eddies (Vanoni, 1941). Bagnold (1956) further indicated that at high concentrations of sediment, the turbulence may disappear altogether. Increasing the concentration of fines has the effect of increasing both the viscosity and density of the flow. Viscosities of actual debris flow deposits have been measured in the laboratory in excess of 1000 poises (the viscosity of water is about 0.01 poises).

The sediment concentration determines the physical characteristics of hyperconcentrated sediment flows. Concentration can be measured either by weight C_w or by volume C_v with a conversion of

$$C_w = \frac{C_v G}{1 + (G-1)C_v} \qquad (1)$$

where G is the specific gravity of dry sediment. A concentration of 50% by volume corresponds to 73% concentration by weight using 2.65 as the specific gravity for the sediment. Referring to Table 1, 50% concentration by volume represents a perceived limit to a mud flow with some fluid properties as determined through laboratory experiments.

It is noteworthy that Bagnold (1954), in his paper on dispersive stress theory, described flows of uniform grains with a concentration by volume of 57% as a granular paste and 52% concentration by volume as the Newtonian fluid limit. In his calculations he correctly reported that the maximum concentration for spheres is 74% by volume with a lower value of 65% for natural, reasonably rounded uniform grains. Using some data from Lamb and Whitman (1969) and Das (1983) the concentrations in Table 2 were computed. The loosest stable arrangement for uniform spheres is a simple cubic structure with a concentration of 53% by volume. The average minimum volumetric concentration of several soil types shown in this table is 54%. For impending fluid motion of the sediment, the concentrations must decrease from these minimum values given in Table 2; otherwise the sediment would move as a block. This evidence supports the delineation of flow definitions indicated in Table 1.

In the field, higher concentrations may be possible with larger quantities of silt and clay in the flow matrix. Written accounts of mud flows describe a wide range of concentrations with maximum concentrations by weight as high as 79 to 85% (Sharp and Nobles, 1953), 60 to 78% (Pierson, 1981) 59 to 86% (Pierson, 1980), 60 to 90% (Johnson, 1970) and 91% (Curry, 1966). Any loss of water during the sampling process, however, could result in significantly higher concentrations than actually occurred during the flow events. Surges and nonuniformity in the flow concentrations also distort the measured estimates of the flow properties. It is suggested that attempts at reporting mud and debris flow events should focus on a description of the mean flow properties which will assist in developing future predictive methods.

MECHANICS OF HYPERCONCENTRATED SEDIMENT FLOWS

The predominant processes of energy dissipation and resistance to motion are a function of the viscous, turbulent, dispersive and yield shear stresses. The relative magnitude of these stresses largely depend on the fluid properties, the concentration of sediment and whether the flow matrix includes cohesive sediment. Although the initiation of motion through landslides and creeping soil failures are more properly examined through a soil mechanics approach, the hyperconcentrated flows should be analyzed in a continuum approach to describe a wide range of concentrations ranging from clear water to very viscous mud flows.

Newton's second law is applied to describe the one-dimensional motion of an incompressible water-sediment mixture. The force equilibrium per unit mass may be written as

$$\frac{\partial u}{\partial t} + u \frac{\partial u}{\partial x} = g \sin\theta - \frac{1}{\rho_m} \frac{\partial p}{\partial x} + \frac{1}{\rho_m} \frac{\partial \tau}{\partial y} \qquad (2)$$

where ρ_m is the density of the fluid mixture, u is the velocity in the downstream x-direction, p is the internal pressure, τ is the shear stress, g is the gravitational acceleration, $\sin\theta$ is the channel slope and y is the upward distance above the channel bed perpendicular to the flow. The left side of the equation represents the local and convective acceleration of the fluid. These terms depict the unsteadiness and nonuniformity of the flow. The right side of the equation represents the gravity, pressure, and resistive shear stress terms. In the original Navier-Stokes equation valid for Newtonian fluids, the pressure distribution can be assumed to be hydrostatic and the shear stress is a function of the viscosity μ and of the rate of deformation

$$\tau = \mu \frac{\partial u}{\partial y} \qquad (3)$$

In mud flows, however, the shear stress is a complex function of the water and sediment properties comprising the fluid matrix which limits its direct application for predictive modeling. A general equation postulated for the resistive shear stress in a water sediment mixture is

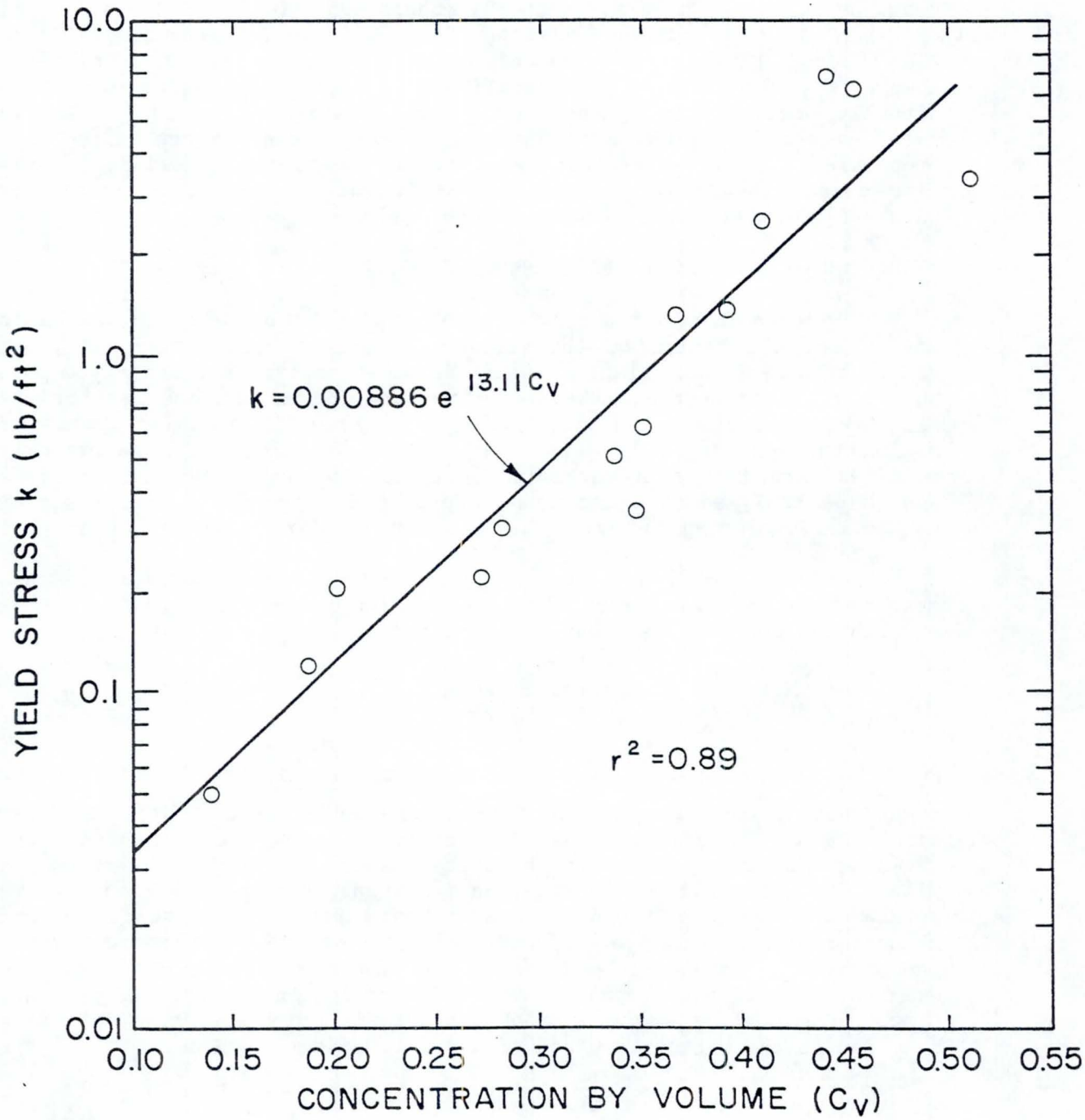

FIGURE 3. YIELD STRESS vs. CONCENTRATION BY VOLUME

the eddies in a cumulative manner dissipating the smaller eddies first or hampering their formation altogether. Sharp and Nobles (1953) noted this phenomena in their descriptive paper. In this fashion, the energy is sapped from the main body of the flow and expended to increase the sediment particle velocity and the height of suspension. This energy is distributed throughout the various levels of the flow and is eventually lost in the fluid mixture through viscous heat.

The turbulence and dispersive stresses lose their separate identities in a hyperconcentrated sediment flow and both stresses can be combined in the last term of Eq. 4. The stress-strain relationship given by Eq. 4 is promoted as correctly representing the behaviour of hyperconcentrated sediment mixtures. This relationship is theoretically sound since it is derived from fundamental principles in fluid mechanics, and the parameters of this function represent physical quantities. The relative magnitude of these parameters depends on the composition of the water-sediment mixture which can be described by (the concentration by weight C_w or the concentration by volume C_v and the concentration of fine material C_f.

Equation 4 was tested in laboratory analysis using a rotating viscometer to measure the stress-strain relationship of a fluid matrix from a mud flow deposit. The results are shown in Figure 5. The physical properties defined by the relationship are the yield stress ($k = 0.0108$ lb/ft^2), the viscosity of the fluid matrix ($\mu_m = 0.00065$ lb-s/ft^2 = 0.31 poises) and $C_1 = 0.0065$ lb-s^2/ft^2. The viscosity of the mixture is about thirty times larger than that of clear water. The parabolic relationship defined by regression analysis generates a better fitting curve ($r^2 = 0.98$) than a linear relationship between stress and strain rate ($r^2 = 0.95$). The Bingham model erroneously predicts a viscosity (9.43 poises) thirty times larger than the Eq. 4.

The ratio R of the inertial stress term to the viscous stress, the last two terms on the right side of Eq. 4, is

$$R = \frac{C_1}{\mu_m} \frac{\partial u}{\partial y} \tag{8}$$

This non-dimensional ratio defines the relative magnitude of the inertial to viscous stresses in a form similar to the Rouse number for clear water turbulent flows. This ratio supercedes the use of any critical Reynolds number which is not applicable to delineate non-Newtonian flow regimes. A small value of R indicates the predominance of viscous stresses and suggest the use of a Bingham model rather than the complete solution of Eq. 4. The value of C_1 is determined through laboratory analysis from Figure 3 and is a function of the sediment concentration, particle diameter, flow depth and clay concentration.

Similarly the Bingham number can be written as the ratio of the yield stress to the viscous stress

$$B = \frac{k}{\mu_m} \frac{\partial y}{\partial u} \tag{9}$$

This ratio indicates the relative magnitude of the yield and viscous terms. As R becomes small and B reduces to zero, the fluid will behave as a Newtonian fluid. These two ratios R and B are valid at every point along a velocity profile since they are both a function of $\frac{\partial u}{\partial y}$. In order to describe the mean flow characteristics, however, the partial derivative $\frac{\partial u}{\partial y}$ can be replaced by the ratio of average velocity $\bar{u}$ to the flow depth d in Eqs. 8 and 9. Both ratios must be defined by laboratory investigation.

APPLICATIONS

The physical processes encountered in mud flows are extremely complex. Valuable insight into the real nature of these non-Newtonian flows was gained through theoretical work, laboratory analysis and field investigations. Simplified methodologies based on the dominant physical processes have been applied to 16 small steep watersheds generating mud flows near Glenwood Springs, Colorado. One objective was to determine the relative magnitude of the losses attributed to internal viscous dissipation as compared to the losses due to channel boundary roughness. This analysis is based on the force balance equation (Eq. 2). The pressure term is written as a function of flow depth d and the shear stress τ in the channel is subdivided in two components. The first component τ_b is due to the large boundary roughness elements written as a function of the boundary energy loss gradient S_b and the second accounts for the internal stress τ_i. Assuming an hydrostatic pressure distribution in a one-dimensional flow over rough boundaries, Eq. 2 can be rewritten as

$$\frac{\partial u}{\partial t} + u \frac{\partial u}{\partial x} + g \frac{\partial d}{\partial x} - g \sin\theta + g S_b + \frac{1}{\mu_m} \frac{\partial \tau_i}{\partial y} = 0 \tag{10}$$

The solution to this equation when combined with the continuity equation gives a complete one-dimensional dynamic description of the motion of hyperconcentrated sediment flows. Steady uniform flow conditions can be assumed which eliminates the first three terms of Eq. 10, the internal energy gradient S_i is then defined as

$$S_i = \frac{1}{\rho_m g} \frac{\partial \tau_i}{\partial y} = S_o - S_b \tag{11}$$

where the bed slope ($\sin\theta$) is written as S_o. The boundary friction slope term S_b is important because the large boundary roughness elements force the fluid mixture to flow around boulders, trees and other channel obstacles, thus creating additional losses which enhance the C_1 term in Eq. 4. In this manner, energy is first transformed into turbulence and

TABLE 3. RATIO OF INTERNAL TO BOUNDARY ROUGHNESS STRESSES R_s

	Flood Event Return Period in Years		
C_v	100	25	10
.36	2.2*	2.3	2.7
.38	3.3	4.0	4.9
.40	5.3	6.6	8.2
.42	9.5	11.9	14.6
.44	17.0	20.8	24.9
.46	30.0	36.4	42.3
.49	48.2	57.0	63.5
.51	71.5	78.1	82.7
.54	88.3	92.3	94.2

*R_s values in percent, Standard Error ranged from 0.3 to 3.9%

This simplified analysis reveals the importance of the physical properties of the fluid matrix and prescribes the need for more fundamental research on mud flows. Ignoring either the viscous or friction slope term in the analysis would result in the overprediction of the velocity of the flow. There are inaccuracies in this analysis. First, the Manning's equation is only applicable for fully developed rough turbulent flows. Second, the Bingham model is not applicable for high velocity, rough turbulent flow. Mud flows and debris are inherently unsteady, nonuniform flows. On steep slopes, using the kinematic wave analogy, equation (15) should be solved using the three terms of Eq. 4 and this requires the use of C_1. More experimental analysis is required for the evaluation of C_1 and its variability with concentration, sediment size and boundary roughness. A stainless steel viscometer has been designed for this purpose.

CONCLUSION

The devastating effects of hyperconcentrated sediment flows in the past demonstrate an urgent need for a predictive methodology to define the hazard levels and to aid in the design of adequate mitigations measures and structures. Such a methodology would rely on an accurate knowledge of the physical properties of the water-sediment mixture. Research efforts must be focused on fundamental investigations involving both theoretical and experimental analysis.

This paper emphasizes the physical properties of hyperconcentrated sediment flows. Flow descriptions have been classified as a function of the concentration of sediments. Various experimental, theoretical and field data show that the maximum concentration by volume for mud flows is unlikely to be in excess of 0.50.

Basic fluid mechanics principles are recommended to describe the broad continuum of hyperconcentrated flows. A simple quadratic model (Eq. 4) is postulated, in which each term represents a well-defined physical property of the fluid. The last term of this equation

G specific gravity of sediments

k yield stress

p internal pressure

r^2 coefficient of determination

R ratio of inertial stress to viscous stress

R_s ratio of internal stress to boundary roughness stress

S_b boundary energy gradient

S_i internal energy gradient

S_o bed slope

t time

u velocity

$\bar{u}$ mean velocity

x longitudinal coordinate (positive downstream)

y upward distance above the channel bed

κ von Karman constant

θ angle of the channel with the horizontal

λ linear concentration

μ_m dynamic viscosity of the mixture

ρ density of clear water

ρ_m density of the fluid mixture

τ shear stress

τ_b shear stress from the boundary roughness

τ_D dispersive stress

τ_i internal stress

τ_R turbulence stress

REFERENCES

Bagnold, R. A. 1954. Experiments on a gravity-free dispersion of large solid spheres in a Newtonian fluid under shear. Proceedings Royal Society of London, Series A, V. 225, pp. 49-63.

Bagnold, R. A. 1956. Flow of cohension grains in fluids. Philosophical Transactions of the Royal Society of London, Series A, V. 249, pp. 234-297.

Curry, R. R. 1966. Observations of alpine mudflows in the Ten Mile Range, central Colorado. Geol. Soc. Am. Bull., V. 77, pp. 771-776.

Das, B. M. 1983. Advanced Soil Mechanics, McGraw-Hill, New York, 511 p.

Hydrological Sciences – Journal – des Sciences Hydrologiques, 32, 3, 9/1987

Macroscale analysis of upland erosion

PIERRE Y. JULIEN
Department of Civil Engineering, Colorado State University, Fort Collins, Colorado 80523, USA
MARCEL FRENETTE
Department of Civil Engineering, Laval University, Quebec, Canada G1K 7P4

ABSTRACT Scale effects in computing sheet and rill erosion losses from large basins have been studied for grid sizes ranging from 0.03 to 4 km^2 over drainage areas up to 3000 km^2. As a result of the analysis conducted on the Chaudière basin (5830 km^2), the mean characteristics of the basin can be used to estimate the mean annual upland erosion losses after a correction factor for the influence of grid size is introduced into the calculation. The use of fine-meshed grids can be justified when information on the areal distribution of soil erosion is desired.

Analyse macroscopique de l'érosion superficielles
RESUME Une méthode de prédétermination d'érosion superficielle sur les grands bassins versants a été mise au point à partir d'une étude détaillée du bassin de la rivière Chaudière (A = 5830 km^2). Plusieurs grilles dont la taille varie de 0.03 à 4 km^2 ont été superposées au bassin pour calculer l'érosion pluviale sur des superficies atteignant 3000 km^2. Un facteur de correction fonction de la superficie drainée est introduit dans les équations. Il en résulte que l'érosion totale des grands bassins est estimée à partir des caractéristiques moyennes du bassin. L'utilisation de quadrillages devient justifiable pour définir la distribution spatiale de l'érosion superficielle.

NOTATION

A_o	drainage area of cells
A	drainage area
C	area-weighted value of the crop management factor
C_o	crop management factor
C_v	coefficient of variation for the sum of erosion losses from N independent units
e	estimate of the annual soil erosion loss per unit area
e_o	annual soil erosion loss per unit area
h_1	minimum elevation on an infinitesimal unit
h_2	maximum elevation on an infinitesimal unit
h_{max}	maximum elevation on one unit

Open for discussion until 1 March 1988.

h_{min}	minimum elevation on one unit
ℓ	size of a grid
N	number of units
Q_e	correction factor for the grid size
$\bar{Q}_e$	mean value of the correction factor
Q_e^*	relative correction factor
$\bar{Q}_{es}$	expected value of the correction factor for small grid sizes
$\bar{Q}_e^*$	mean value of the relative correction factor
Q_{e95}	confidence interval at 95 percent of the correction factor
S_o	slope on infinitesimal grids
S	slope estimator
β	exponent of slope in the soil loss equation
θ	angle between contour lines and the side of infinitesimal grid sizes
σ	standard deviation of log-transformed correction factors
σ_s	standard deviation of the sum of N independent log-transformed correction factors

INTRODUCTION

Rainfall-induced overland flow has the ability to detach and transport large amounts of sediment from upland areas. Sheet and rill erosion losses are complex processes related to landform geometry, surface slope, overland runoff length, rainfall intensity, soil infiltration rate, interception, storage, ground cover, canopy cover, evaporation, evapotranspiration, land use and conservation practices. The fundamentals of soil erosion and conservation are detailed in Hudson (1981), Zachar (1982), Jansson (1981), and Schwab *et al.* (1981). Methodologies to quantify erosion losses include the widely used Universal Soil-Loss Equation (USLE) which has been derived for data from small experimental plots.

Because soil-loss equations were developed for small upland areas (about one hectare), small basins are preferably discretized into small homogeneous areas to evaluate soil erosion losses from the drainage area. Square grids can be superimposed onto drainage basins with the mesh size conditioned by the applicability of the soil-loss equation. This method has been successfully applied to drainage areas up to 50 km^2 and soil erosion maps can be plotted with the aid of computers. The inherent limitations of this method are the data requirements which become prohibitive as the size of the drainage area increases beyond 100 km^2.

It seems interesting to examine whether larger grid sizes beyond the limit of applicability of soil-loss equations could provide sufficient accuracy in predicting upland erosion losses. The investigation reported here discusses the applicability of upland erosion equations to large drainage areas. Detailed information from the Chaudière basin in Canada is scrutinized to determine the scale effects associated with various grid sizes in the calculation of soil erosion losses. The development of simple methodologies to estimate on-site erosion losses over large basins with minimum data requirements also figures among the research objectives of foremost

importance.

FIELD SITE AND DATA SOURCES

The Chaudière basin shown in Fig.1 was selected for this study. This Appalachian basin covers an area of 5830 km^2 to St-Lambert-de-Lévis where the downstream gauging station is located.

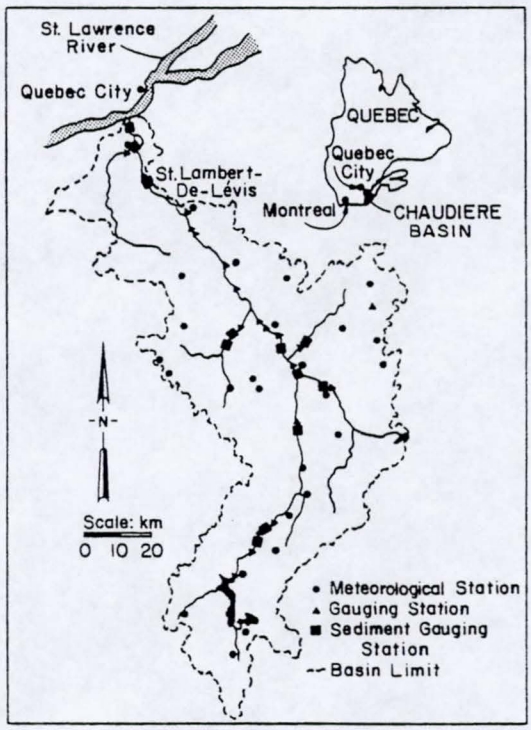

Fig. 1 Location of the Chaudière basin.

The basin geometry, vegetation and land use were accurately determined from topographical maps (1:50 000), land use and soil classification maps (1:200 000), forest maps (1:125 000), aerial photographs and Landsat imagery. Data from a network of 22 meteorological stations, 16 gauging stations and nine sediment gauging stations were available on a daily basis. Approximately 65% of the basin is still forested whereas 35% is used for agriculture and pasture lands. All the parameters related to soil erosion have been carefully documented (Julien, 1979, 1982; Frenette & Julien, 1986). Data analysis shows a relative uniformity of rainfall erosivity, soil erodibility and conservation practice on the drainage basin.

The annual soil erosion loss per unit area, e_o, in kt km^{-2} is a function of the slope, S_o, in m m^{-1} and the crop-management factor, C_o, of the USLE. For the Chaudière basin the following relationship is applicable for predicting rainfall erosion losses:

$$e_o = 226\ S_o^{\beta}\ C_o \qquad (1)$$

Detailed investigations (Julien, 1979; Julien & Frenette, 1986a) showed that the results obtained with Kilinc and Richardson's method ($\beta = 1.46$) are in close agreement with those of the USLE. Julien & Simons (1985) showed similarities between several sediment transport relationships for overland flow, including the USLE, and the values of the exponent, β, using different methods are given.

GRID SIZE ANALYSIS

When an infinitesimal square grid is superimposed onto the drainage basin, the slope and crop-management factors become uniform for each unit. The actual slope, S_o, in m m^{-1} on the unit is calculated from the minimum and maximum elevations h_1 and h_2, located on opposite corners of a square unit of size, ℓ, and angle, θ, sketched in Fig.2:

$$S_o = \frac{h_2 - h_1}{\ell(\cos\theta + \sin\theta)} \tag{2}$$

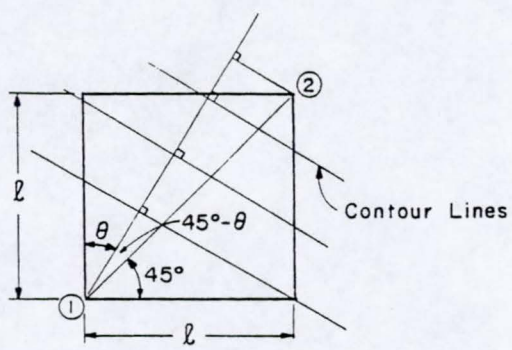

Fig. 2 Infinitesimal grid.

With increasing grid size, the slope varies within each unit and the extreme elevations are not found on opposite corners. The following estimate of slope, S, in m m^{-1} is defined as a function of the maximum elevation h_{max}, in m, the minimum elevation, h_{min}, in m, and the drainage area, A, in m^2:

$$S = \frac{h_{max} - h_{min}}{\sqrt{A}} \tag{3}$$

Similarly, the area-weighted value of the crop management factor, C, is employed for large areas. Substituting S and C for S_o and C_o in equation (1) yields the soil loss estimator, e. The ratio, e/e_o, defines the correction factor, Q_e, which is to be used with the soil loss estimator, e, to determine the actual erosion losses, e_o.

For infinitesimal grids, equations (1), (2) and (3) yield the following relationship for Q_e as a function of θ and β, given that $C = C_o$, and $A = \ell^2$:

$$Q_e = (\cos\theta + \sin\theta)^{\beta} \tag{4}$$

The gradual increase in Q_e with θ and β is illustrated in Fig.3(a). Obviously Q_e reduces to unity when $\beta = 0$, or when $\theta = 0$.

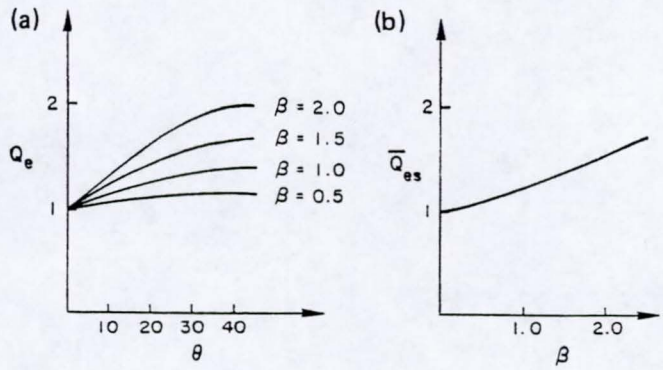

Fig. 3 (a) Variation of Q_e with θ and β for infinitesimal grids; (b) expected value of the correction factor, $\bar{Q}_{es}$, for infinitesimal grids.

When the angle, θ, is unknown, the following procedure has been developed. Considering the random variability of the angle θ, the analytical expression of the expected value of the correction factor, $\bar{Q}_{es}$, is:

$$\frac{1}{\bar{Q}_{es}} = \frac{4}{\pi} \int_0^{\pi/4} \frac{d\theta}{(\cos\theta + \sin\theta)^{\beta}} \tag{5}$$

The results of the numerical integration of equation (5), plotted in Fig.3(b), indicate a gradual increase in $\bar{Q}_{es}$ with β.

For larger drainage areas, the following grid size analysis has been conducted. Square areas were randomly selected from the Chaudière basin as shown in Fig.4. The square areas were subdivided into matrices of 12 x 12 cells and classified in Table 1 into three sets according to the area of the cells. The surface area of cells in Data Sets A, B and C is respectively 2.8 ha, 25 ha and 4 km^2. In addition, Data Set D combines 4 km^2 cells into large square matrices with surface areas ranging from 4 to 3000 km^2 over the entire basin.

For each of the areas of the four Data Sets, a relative correction factor, Q_e^* (an asterisk is used to denote relative correction factors), has been defined as the ratio of soil erosion from the total area, A, over the sum of individual losses from each cell; this is schematized in Fig.5 for a small 2 x 2 matrix. The calculation procedure is repeated for larger matrices (3 x 3; 4 x 4; 6 x 6...) and details of the computerized data analysis are presented in Julien (1979).

Several thousand values of the relative correction factor were computed; Q_e^* depends on the number of cells, N, and the size A_o, of the cells. For given values of A_o and N, the first three moments

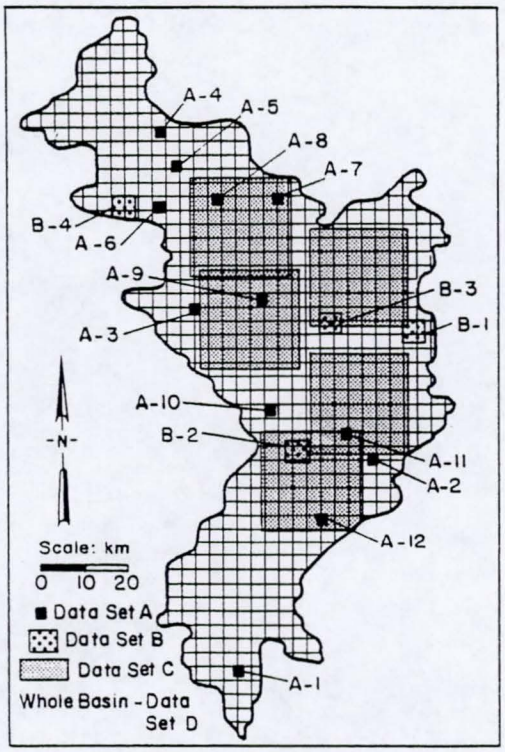

Fig. 4 Random selection of square areas for the grid size analysis.

Table 1 Scope of grid size analysis

Data Set	Cell area (km^2)	Matrix size	Matrix area (km^2)	Number of matrices
A	0.028	144 (12 x 12)	4	12
B	0.25	144 (12 x 12)	36	4
C	4.0	144 (12 x 12)	576	5
D	4.0	up to 1600	3000	N/A

N/A Not Applicable.

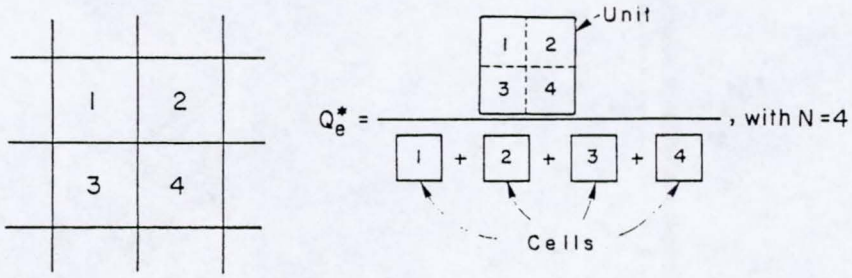

Fig. 5 Definition sketch for the relative correction factor, Q_e^*.

of the distribution of log Q_e^* give very low values of the skewness coefficient. Therefore, it was hypothesized and verified that Q_e^* is lognormally distributed; the results of the analysis for Data Set B are shown in Fig.6 as an example. The mean value and the confidence intervals at 95% are obtained from the following analysis of the first two moments.

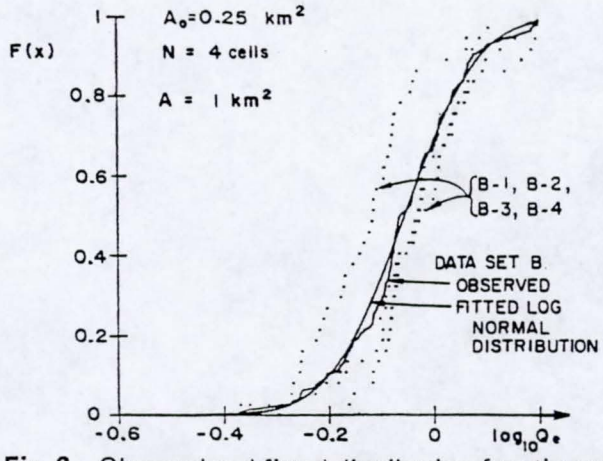

Fig. 6 Observed and fitted distribution function of Q_e for the Data Set B.

Mean value of the correction factor

The mean value of the log-transformed relative correction factor, $\bar{Q}_e^*$, shown in Fig.7 gradually decreases as N increases for all sets. The only exception to this general trend is that values of $\bar{Q}_e^*$ remain constant for N < 9 on the smallest drainage areas (Data Set A). Interestingly, this corresponds to the expected correction factor, $\bar{Q}_{es}$, discussed previously (Fig.3(b)). The value of $\bar{Q}_{es}$ = 1.13 has been obtained for drainage areas smaller than 0.125 km^2 on the Chaudière basin when the USLE was used for the calculation of soil erosion. For larger areas, regression analysis gives the following relative correction factor, $\bar{Q}_e^*$, as a function of $\bar{Q}_{es}$, A and A_o:

$$\log \bar{Q}_e^* = +0.0061 - 0.137 \log A + 0.083 \log A_o \qquad (6)$$

A correction factor, $\bar{Q}_e$, is defined by the following change of variables:

$$\log \bar{Q}_e = \log \bar{Q}_e^* - 0.083 \log A_o - 0.129 + \log \bar{Q}_{es} \qquad (7)$$

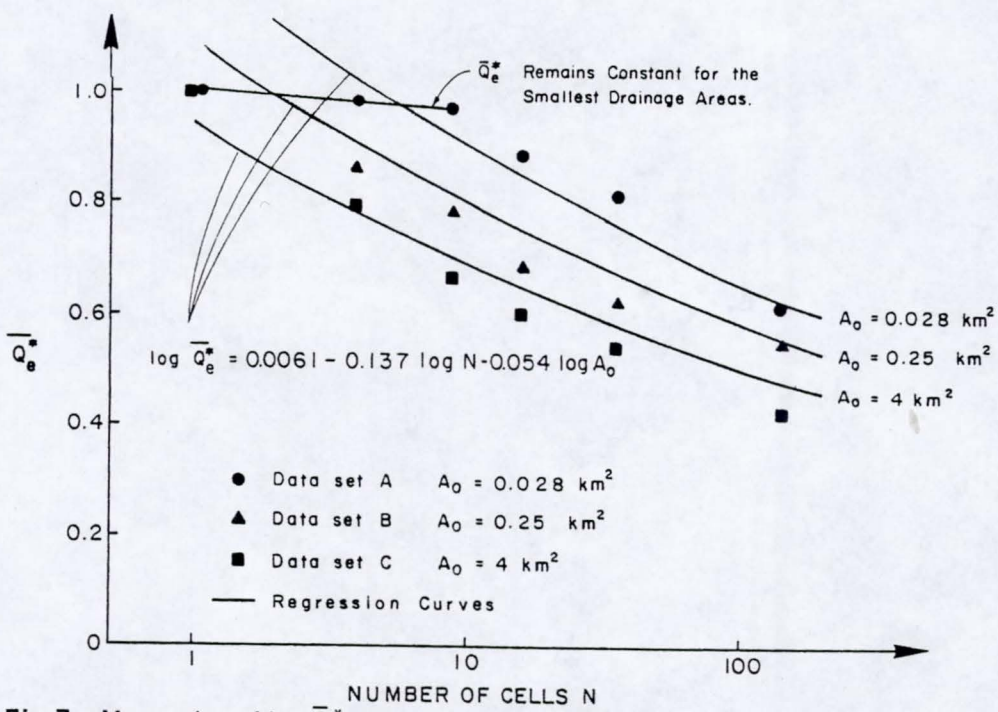

Fig. 7 Mean value of log $\bar{Q}_e^*$ *vs.* the number of cells, N.

Thus substituting equation (7) into equation (6), the correction factor, $\bar{Q}_e$, becomes independent of A_o with the following relationship:

$$\bar{Q}_e = 0.75\ \bar{Q}_{es} A^{-0.137} \qquad A > 0.125\ km^2 \tag{8}$$

As a result, with $\bar{Q}_{es} = 1.13$, a correction factor, $\bar{Q}_e$, which is a function of the drainage area only is obtained and all the data from Fig.6 collapse onto a single curve shown in Fig.8. Two governing laws for the correction factor, $\bar{Q}_e$, are identified. First, for $A < 0.125\ km^2$, the correction factor, $\bar{Q}_e$, remains constant ($\bar{Q}_e = \bar{Q}_{es}$) which indicates that the soil loss equation can be applied to these areas without bias. As the drainage area increases beyond the threshold value $A > 0.125\ km^2$, the correction factor, $\bar{Q}_e$, decreases gradually as shown in Fig.8.

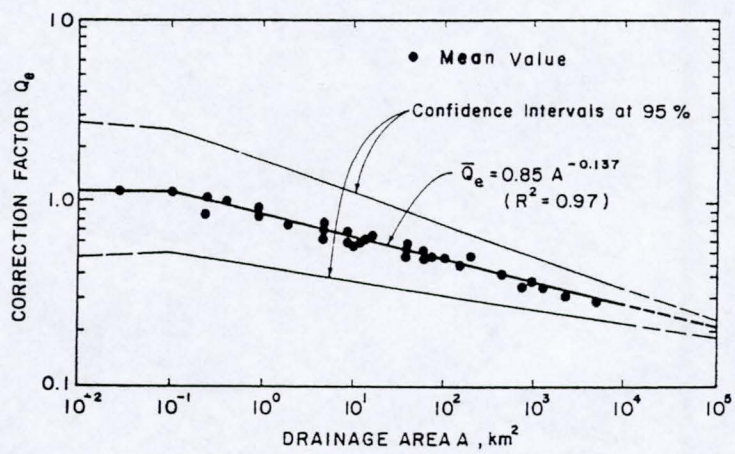

Fig. 8 Mean value and confidence intervals at 95% of the correction factor, Q_e, *vs.* drainage area, A.

Confidence intervals of the correction factor

The standard deviations, σ, of the log-transformed relative correction factor, Q_e^*, for Data Sets A, B and C are shown in Fig.9. All three Data Sets have similar shapes with an increase in σ for $N < 9$, a peak around $9 < N < 36$ and then a gradual decrease for $N > 36$. As a second interesting feature, the magnitude of the peak decreases as A_o increases. Regression analysis provides a quantitative relationship for the standard deviation, σ. After substituting A_o with A/N, the following regression relationship has been obtained.

$$\sigma = 0.00235 + \left[\frac{N - 1}{N}\right] (0.148 - 0.0226 \log A) \tag{9}$$

Note that under this form the standard deviation, σ, depends on the drainage area, A, and the number of cells, N. The standard deviation decreases to zero as N approaches unity. As N increases, the term in brackets reduces to unity and σ becomes solely a function of A.

The confidence intervals of the correction factor, Q_e, are

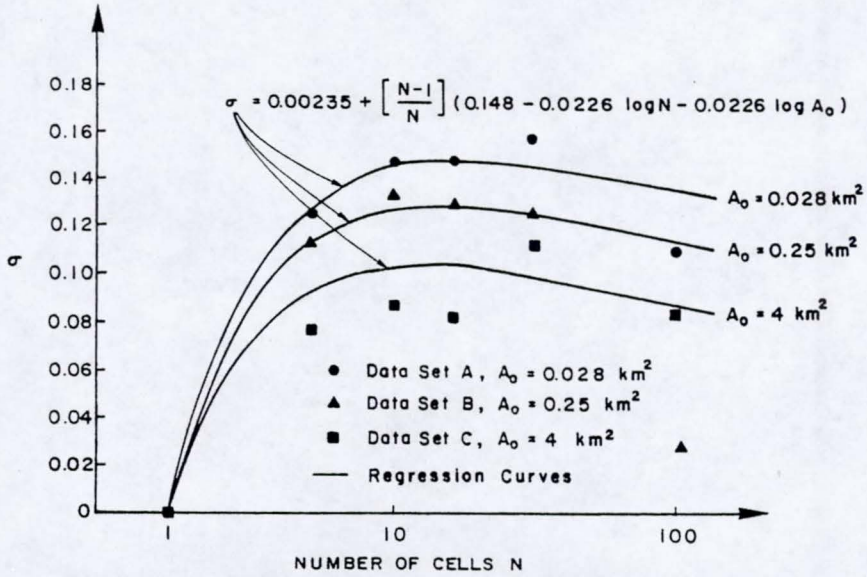

Fig. 9 Standard deviation, σ, of log $\bar{Q}_e^*$ *vs.* the number of cells, N.

obtained after combining equations (8) and (9) using the properties of lognormal distributions for Q_e. The confidence interval at 95% can be written:

$$Q_{e95} = \bar{Q}_e \times 10^{\pm 1.96\sigma} \tag{10}$$

Agreement between equation (10) and the Data Set D is shown in Fig.10. Confidence intervals at 66% are given after replacing 1.96 in equation (10) with unity. As N becomes large, the expression for the confidence intervals reduces to a function of Q_e and A which has been plotted in Fig.8. These results can be used for design purposes as discussed below.

The foremost conclusion of this analysis is drawn from the

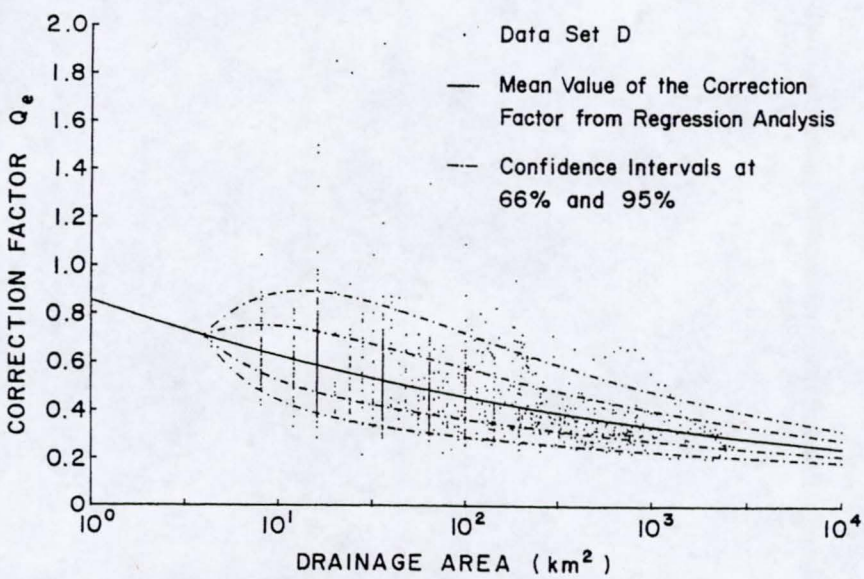

Fig. 10 Mean value and confidence intervals at 66% and 95% of the correction factor, Q_e, for Data Set D.

gradual decrease of the standard deviation with increase in drainage area. This property enables the development of a reasonably accurate method to estimate the total upland erosion losses for large drainage basins. Indeed the results shown in Fig.8 indicate that for drainage basins as large as 1000 km^2, the variability of the correction factor ranged from 0.17 to 0.49 (from equation (10)) with a mean value of 0.33 (from equation (8)). Therefore, a first estimate of the total annual upland erosion losses can be obtained from the soil loss estimator, e, and the average correction factor, $\bar{Q}_e$. Examples are given in Frenette & Julien (1980) and Julien & Frenette (1986b).

When the erosion loss from a large basin is calculated from the sum of N independent calculation units, the standard deviation of the sum, σ_s, is obtained after considering the lognormal distribution of the log-transformed correction factors, thus:

$$\sigma_s = \frac{\sigma}{\sqrt{N}} \tag{11}$$

As could be expected, σ_s decreases as the number of calculation units, N, increases. The coefficient of variation, C_v, of the sum is therefore given by:

$$C_v = 10^{\sigma_s} - 1 \tag{12}$$

After combining equations (9), (11), and (12), the coefficient of variation is illustrated in Fig.11 as a function of A and N. For example, when a drainage basin covering an area of 1000 km^2 is subdivided into N = 1000 units for the calculation of soil erosion, the coefficient of variation of the sum (Fig.11) is less than 1%, as compared to C_v = 6% when the same drainage area is subdivided into N = 10 units.

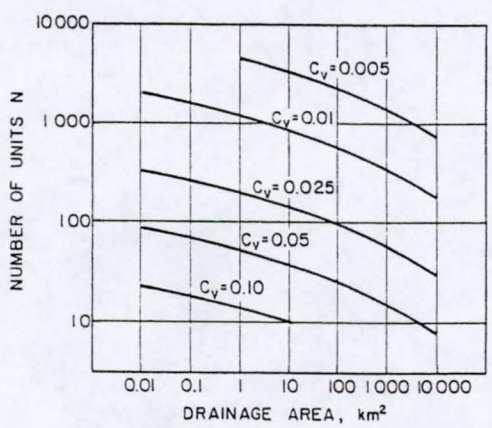

Fig. 11 Coefficient of variation of the sum of N independent upland erosion losses.

This conclusion remains valid when a large number of independent units from the same population is considered. The validity of the

method depends mostly on the applicability of the sediment transport relationship, equation (1). The method should preferably be used on morphologically homogeneous basins since the same soil loss equation is applied to the entire watershed.

CONCLUSION

A substantial analysis of the influence of grid size in calculating sheet and rill erosion losses from upland areas has been presented. Using grid sizes ranging from 0.03 to 3000 km^2 in the Chaudière basin, a correction factor, Q_e, which is a function of the grid size, has been defined and shown in Fig.8. The mean value of Q_e and the confidence intervals at 95% decrease gradually when $A > 0.125$ km^2. A simplified method has been developed to provide estimates of the total soil erosion losses from the mean characteristics of a large drainage basin. Fine-meshed grids are best used to define the spatial distribution of soil erosion, and for better accuracy in predicting the total upland erosion losses from large basins. Quantitative evaluation can be made from Fig.11 as a function of drainage area and number of units.

ACKNOWLEDGEMENTS This study has been carried out at Laval University, Canada. The support from the Civil Engineering Department and the CTI at Laval University for conducting computerized research is gratefully acknowledged.

REFERENCES

Frenette, M. & Julien, P.Y. (1980) Méthode simplifiée de prédiction d'érosion de bassin versant et d'apport solide en suspension dans les cours d'eau nordiques. *Proc. Second Hydrotechnical Conference* (CSCE-Quebec, Sherbrooke, Canada).

Frenette, M. & Julien, P.Y. (1986) LAVSED I - Un modèle pour prédire l'érosion des bassins et le transfert des sédiments fins dans les cours d'eau nordiques. *Can. J. Civ. Engng,* CSCE 13(2), 150-161.

Hudson, N. (1981) *Soil Conservation.* Cornell Univ., Ithaca, New York, USA.

Jansson, M. (1981) Land erosion by water in different climates. *UNGI Report 57, Uppsala Univ.*

Julien, P. (1979) Erosion de bassin et apport solide en suspension dans les cours d'eau nordiques. MS Thesis, Laval Univ., Québec, Canada.

Julien, P. (1982) Prédiction d'apport solide pluvial et nival dans les cours d'eau nordiques à partir du ruissellement superficiel. PhD Dissertation, Laval Univ., Québec, Canada.

Julien, P.Y. & Frenette, M. (1986a) LAVSEDII - A model for predicting soil erosion and washload in streams. *Can. J. Civ. Engng,* CSCE 13(2), 162-170.

Julien, P.Y. & Frenette, M. (1986b) Scale effects in predicting soil erosion. In: *Drainage Basin Sediment Delivery* (Proc.

Albuquerque Symp., August 1986), 253-259. IAHS Publ.no.159.
Julien, P.Y. & Simons, D.B. (1985) Sediment transport capacity of overland flow. *Trans Am. Soc. Agric. Engrs* 28(3), 755-762.
Kilinc, M. & Richardson, E.V. (1973) Mechanics of Soil Erosion from Overland Flow Generated by Simulated Rainfall. *Hydrol. Pap. 63, Colorado State University, Fort Collins, Colorado.*
Schwab, G.O., Frevert, R.K., Edminster, T.W. & Barnes, K.K. (1981) *Soil and Water Conservation Engineering.* Wiley, Chichester, UK.
Zachar, D. (1982) *Soil Erosion.* Developments in Soil Science 10, Elsevier.

Received 1 October 1986; accepted 25 February 1987.

Pergamon

Computers & Geosciences Vol. 24, No. 2, pp. 183–192, 1998
© 1998 Elsevier Science Ltd. All rights reserved
Printed in Great Britain
0098-3004/98 $19.00 + 0.00

PII: S0098-3004(97)00100-3

ESTIMATION OF UPLAND EROSION USING GIS

DARCY K. MOLNÁR and PIERRE Y. JULIEN

Department of Civil Engineering, Engineering Research Center, Colorado State University, Fort Collins, CO 80523

(*e-mail*: dkm@riverside.com)

(Received 18 June 1996; revised 28 May 1997)

Abstract—The Universal Soil-Loss Equation (USLE) is a widely used method for calculating annual soil erosion losses, based on rainfall, runoff, slope, runoff length, soil type, and landuse parameters. The equation was originally developed on small agricultural plots, but has since been adopted for evaluating erosion from large watersheds under a wide range of landuses. This study was designed to compare USLE calculations in a GIS environment at grid sizes ranging from 30 × 30 m up to 6 × 6 km. The analysis of two watersheds in Mississippi shows that large grid sizes tend to underestimate soil losses. At grid sizes exceeding 100 × 100 m, a correction factor must be included in the calculations. With the use of the correction factor, the USLE can be applied directly at macroscales, providing an important tool for studies of basin-wide upland erosion rates. The proposed method is shown to be applicable for large watersheds under different climates. © 1998 Elsevier Science Ltd. All rights reserved.

Key Words: Soil erosion, Geographic information system, Upland erosion, Sediment source, Sediment yield.

INTRODUCTION

Soil erosion from upland areas is a large source of sediment transported in rivers (Meyer, 1971). The extent of sheet and rill erosion is controlled by factors such as climate, topography, soil type, and landuse. Erosion rates in upland areas depend on erosive forces from raindrop impact and runoff, and on soil resistance to detachment and transport. Numerous physical processes are involved in the detachment of soil and its subsequent transport downslope, and this complexity makes it difficult to evaluate upland erosion.

A study by Musgrave (1947) gave rise to a first approximation of the relationship between major causal factors and the resulting rate of erosion. Musgrave determined that the primary factors influencing the rate of erosion are rainfall, flow characteristics of surface runoff, soil characteristics, and vegetation. Work by Wischmeier and Smith (1965, 1978) led to the definition of the Universal Soil Loss Equation (USLE) as a relationship to calculate the long-term average soil loss as the product of the parameters R, K, L, S, C and P, where average long-term soil losses are calculated in annual tons acre^{-1}, R is a rainfall erosivity factor, K is a soil-erodibility factor, L is a slope-length factor, S is a slope-steepness factor, C is a cropping-management factor, and P is a conservation practice factor. The determination of sediment yield from upland sediment sources is summarized in Shen and Julien (1993).

The USLE is used by soil conservationists around the world in predicting the average annual soil loss due to sheet and rill erosion. Yet the equation was derived on small agricultural plots, and is thus only valid up to 1 ha (0.01 km^2). In the 1980s, Julien and Frenette (1987) performed studies on the Chaudière basin in Canada, in order to examine the applicability of the USLE on large areas. They were able to extend the applicability of the USLE to large watersheds by applying a correction factor. This method can be used for simple and straightforward calculations of upland erosion losses on large watersheds, based on average watershed characteristics. The method has also been applied in Spain by Julien and Gonzalez del Tanago (1991).

Today, the data required for USLE calculations are readily available in a Geographic Information Systems (GIS) format. GIS has the unique capability of representing watershed characteristics within a grid cell environment at fine resolutions. The USLE is theoretically applicable only at grid sizes less than 100 × 100 m (0.01 km^2). The accuracy of USLE calculations using larger grid sizes can be studied within the GIS environment by applying the equation at a wide range of cell sizes. Increasing grid size leads to a loss of information that must be accounted for if the equation is to be applied at grid sizes larger than 100 × 100 m.

The purpose of this study is to use GIS in calculating soil loss rates at various grid sizes, and thus to be able to draw conclusions regarding the appli-

cability of the USLE at macroscales. The following objectives are defined: (1) erosion mapping at a 30-m resolution and evaluation of mean annual soil loss; and (2) application of the USLE at grid sizes ranging from 30×30 m to 6×6 km and determination of grid-size correction factors.

EROSION MAPPING IN THE GIS GRASS ENVIRONMENT

USLE calculations at a 30-m resolution

The analysis was performed using GRASS (Geographic Resources Analysis Support System) capabilities for the display and manipulation of GIS data. GRASS is a tool that can be used in aggregating GIS data and in performing calculations on raster values of individual cells. The Goodwin Creek watershed in Mississippi was used in the analysis because it has been extensively monitored by the United States Department of Agriculture. Over 10 years of runoff and sediment transport measurements are available (Blackmarr, 1995; Shields, Knight and Cooper, 1995; Alonso, 1996). Goodwin Creek covers an area of 21.6 km^2 and is located in north-western Mississippi.

The USLE determines soil loss as the product of the factors R, K, L, S, C and P. The original GIS raster maps used in establishing the required parameters were: (1) a digital elevation map (DEM) generated by the United States Geological Survey; (2) a soil map generated by the Soil Conservation Service; and (3) a landuse map developed by the Agricultural Research Service in Oxford, Mississippi. The DEM at a 30-m resolution is shown in Figure 1, with the channel network overlaid on the elevation map.

The average annual value of the rainfall erosivity factor, R, was estimated from an iso-erodent map of R factors for the United States (Wischmeier and Smith, 1965). The factor R indirectly accounts for variations in rainfall intensity-duration-frequency, specific to different geographic locations. A uniform value of 330 was selected as representative of the Goodwin Creek basin.

The soil-erodibility factor, K, is a measure of the intrinsic ability of a soil to erode, and thus varies as a function of soil type. A table from Schwab *et al.* (1981) was used in determining the K factor, in tons $acre^{-1}$, corresponding to each soil type. The GRASS command *r.reclass* was then used to reclassify the raster soil map into a map representing the spatial distribution of K (Fig. 2), based on a soil survey performed by Galberry (1960).

The slope-length factor, L, accounts for increases in runoff volume as downslope runoff lengths increase. The value corresponding to Goodwin Creek was assumed to be 100 m, as determined by the drainage density of the basin.

The slope-steepness factor, S, accounts for increased runoff velocity as slope steepens. The DEM (Fig. 1) was a key component in evaluating the S factor. Based on elevations in the DEM, the GRASS command *r.slope.aspect* was used to generate a raster map showing the spatial distribution of slopes at a 30-m resolution. Slopes in the Goodwin Creek watershed ranged from less than 1% to 23%, as shown in Figure 3.

For direct application of the USLE, a combined slope-length and slope-steepness (LS) factor was evaluated for each cell as (Wischmeier and Smith, 1965):

$$LS = l^{0.5}(0.0076 + 0.0053s + 0.00076s^2), \quad (1)$$

where l = runoff length in feet, and s = slope (per cent).

The cropping-management factor C is a function of landuse conditions such as vegetation type, before and after harvesting, crop residues, and crop sequence. Values of C range from zero to one. The Goodwin Creek landuse map was reclassified according to tables in Wischmeier and Smith (1965) and Meyer (1971). Cropping management factors corresponding to Goodwin Creek landuse categories are shown in Figure 4.

The conservation practice factor, P, is determined by the extent of conservation practices such as strip cropping, contouring, and terracing practices, which tend to decrease the erosive capabilities of rainfall and runoff. Values of P range from zero to one. Since such methods are not used in the Goodwin Creek basin, the value of P was assumed to be 1.

Having specified the values for all parameters, on a cell-by-cell basis, the USLE was applied using the GRASS command *r.mapcalc*. Soil loss for every 30×30 m cell was calculated as the product of the factors R, K, LS, C, and P corresponding to that particular cell. At the 30 m resolution, annual soil-loss rates in Goodwin Creek ranged from 200 tons $acre^{-1}$ to 0.0 tons $acre^{-1}$ as shown in Figure 5.

USLE calculations at grid sizes beyond 30 m

In evaluating soil erosion losses at grid sizes larger than the original 30-m resolution, it was first necessary to aggregate the 30-m input data. Matrix aggregation within GRASS can be performed for matrices of 3×3, 5×5, 7×7,... up to 23×23. The 30-m data were therefore aggregated into cell sizes ranging from 90×90 m to 690×690 m.

Since the rainfall erosivity factor, R, the slope-length factor, L, and conservation factor, P, were considered to be constant throughout the watershed, their values were not affected by increases in grid size. In contrast, the soil erodibility factor, K, the crop management factor, C, and slope-steepness factor, S, differed spatially throughout the watershed and therefore were affected by increased grid

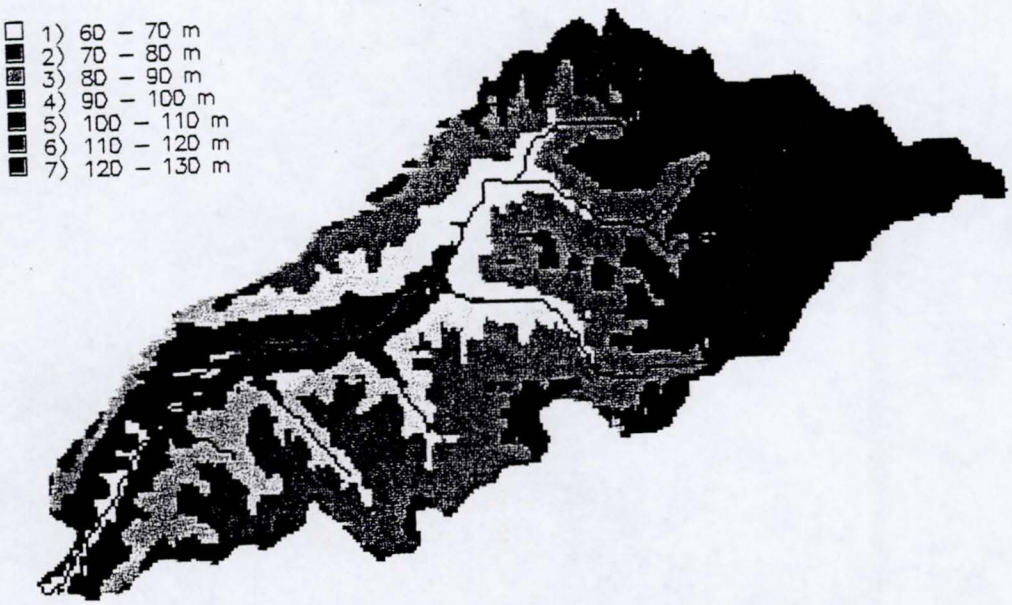

Figure 1. Goodwin Creek elevations.

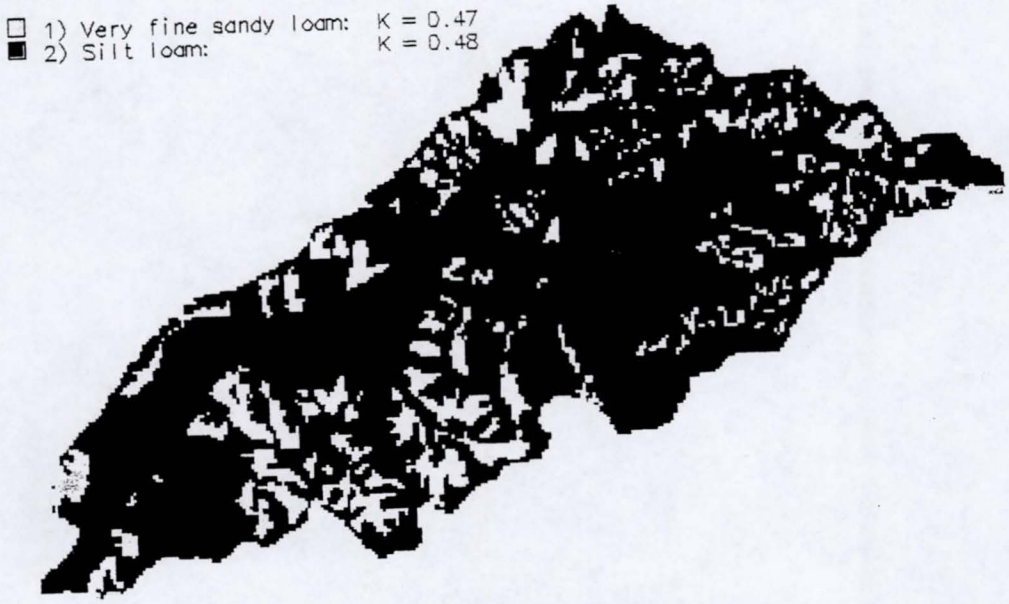

Figure 2. Goodwin Creek soil types and K values.

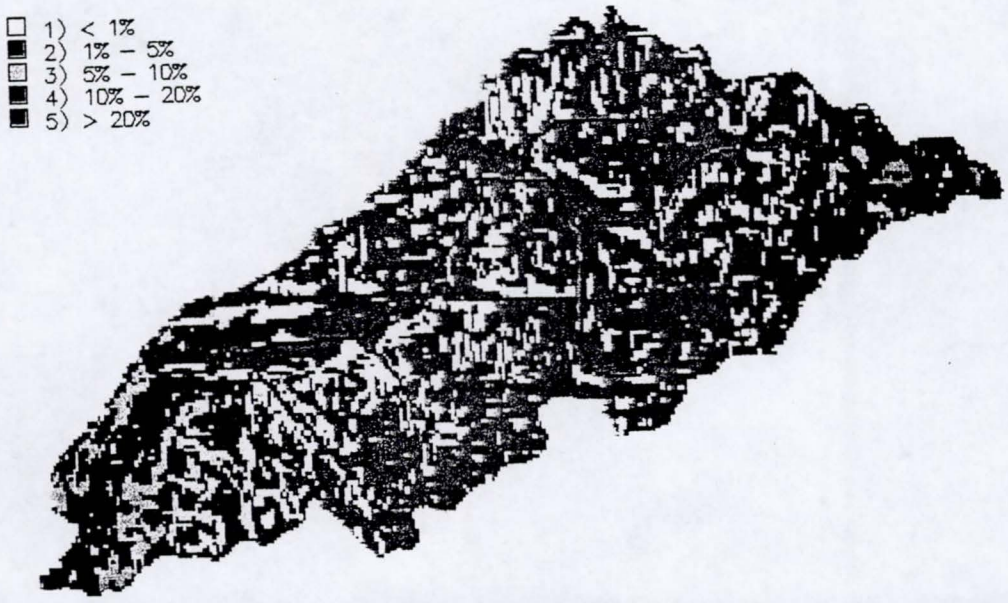

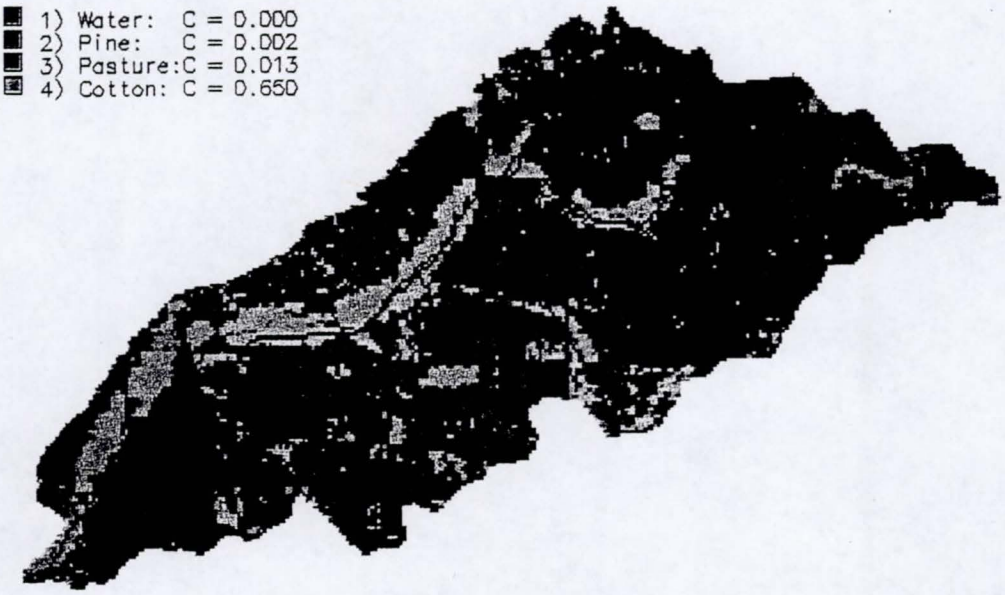

Figure 4. Goodwin Creek landuse and *C* values.

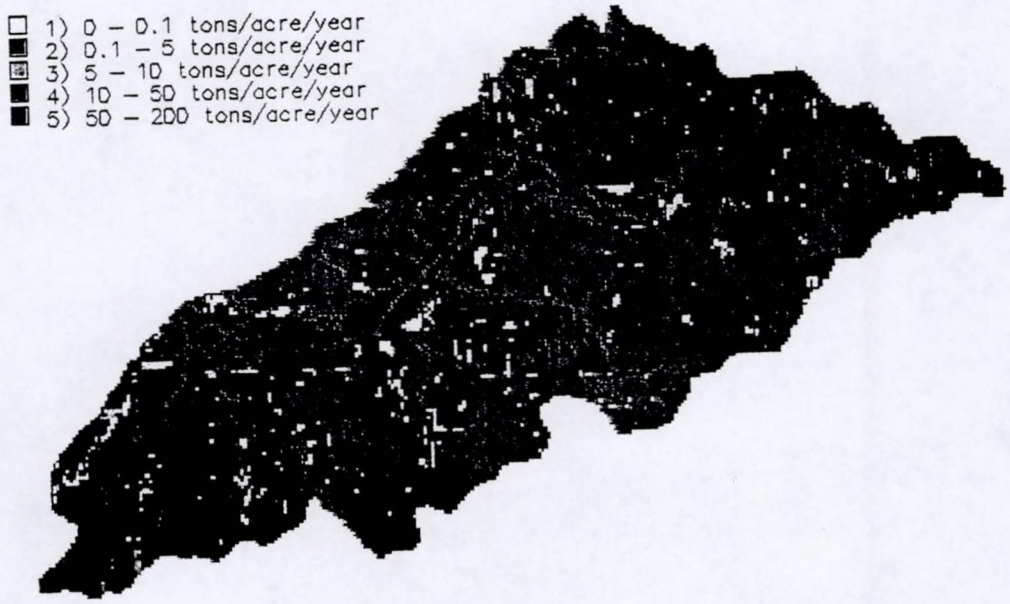

Figure 5. Goodwin Creek soil loss rates.

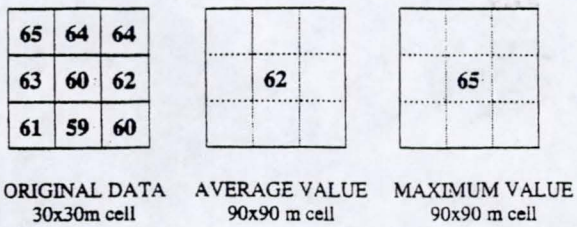

Figure 6. Matrix aggregation.

sizes. At coarser resolutions, the factors K, C and S were evaluated, based on matrix aggregation of the original 30-m input data.

Matrix aggregation was performed using the GRASS command *r.neighbors*, which allows the user to select the average, minimum, or maximum value of aggregated cells as the value corresponding to the larger grid size (Fig. 6). K and C values at grid sizes larger than 30×30 m were determined as the average value corresponding to the matrix of 30-m cells. For example, parameters corresponding to a 90×90-m cell were obtained by applying a 3×3 matrix to the original 30×30 m data, with the K and C values determined as averages of the nine 30×30 m cells contained within one 90×90 m cell.

The GRASS command *r.neighbors* was also used in evaluating the slopes corresponding to larger grid sizes. Maximum and minimum elevations were specified within each matrix aggregation, allowing for the calculation of grid slopes as:

$$s = \frac{Z_{\max} - Z_{\min}}{\sqrt{A}}, \qquad (2)$$

where s = slope, in m m^{-1}; $Z_{\max,\min}$ = maximum or minimum grid cell elevation, in m; and A = area of grid cell, in m^2. The combined slope-length and slope-steepness factor (LS) was then evaluated using Equation (1).

The LS factor is clearly affected by changes in scale. As cell size is increased from 30×30 m to 690×690 m, the distribution of slopes is smoothed out and tends toward a lower mean slope for the entire watershed. The cumulative distribution function corresponding to Goodwin Creek slopes, as affected by changes in grid size, is shown in Figure 7. At coarser grid resolutions, slopes decrease significantly. The maximum grid cell slope corresponding to a 30-m resolution is 23%, whereas the maximum slope corresponding to a 690-m resolution is only 16%.

Having defined the parameters R, K, LS, C and P corresponding to cell sizes greater than 30×30 m, the USLE was applied on a cell-by-cell basis. A wide range of grid sizes was used, based on aggregated cell matrices. Annual soil-loss rates were determined for every cell within the basin. The cumulative distribution function of estimated annual erosion rates is shown in Figure 8, for cell sizes ranging from 30 m to 690 m. Clearly, the distribution of slopes at increasing grid sizes has an important effect on the distribution of erosion rates as grid size is increased. At a 690-m resolution, the maximum erosion rate is approximately 30 tons acre^{-1}, in contrast to a maximum value of 200 tons acre^{-1} at a 30-m resolution. In addition, at

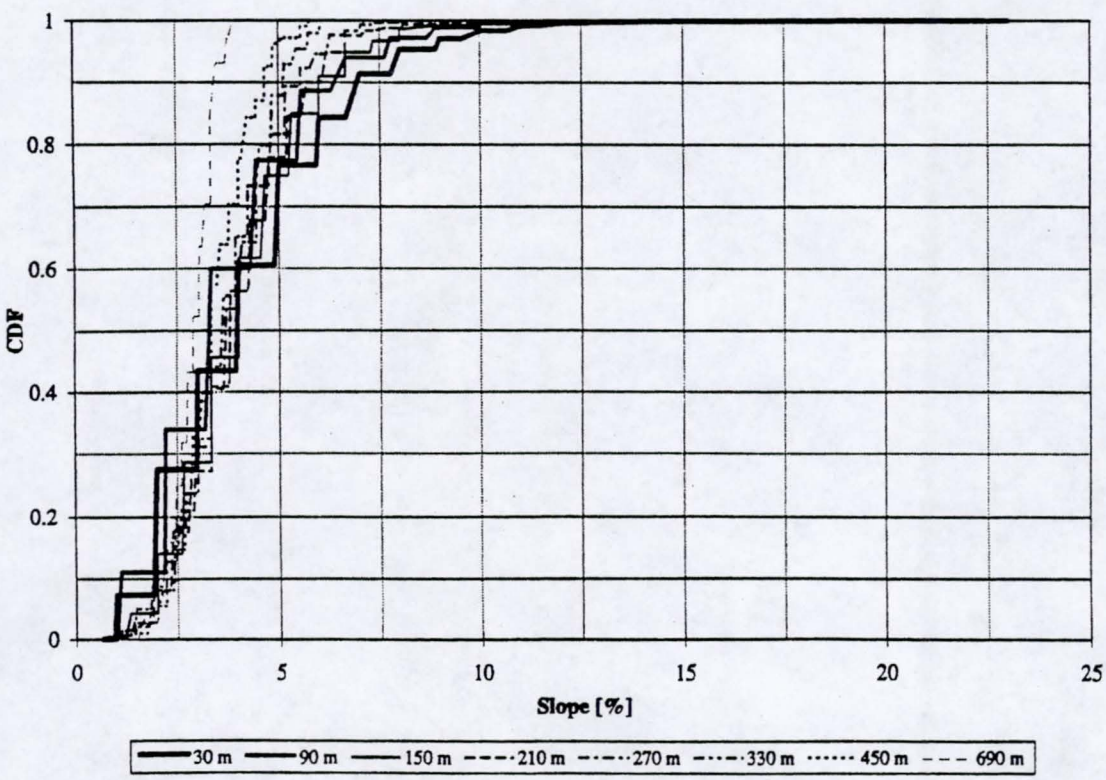

Figure 7. Goodwin Creek distribution of slopes with increasing grid size.

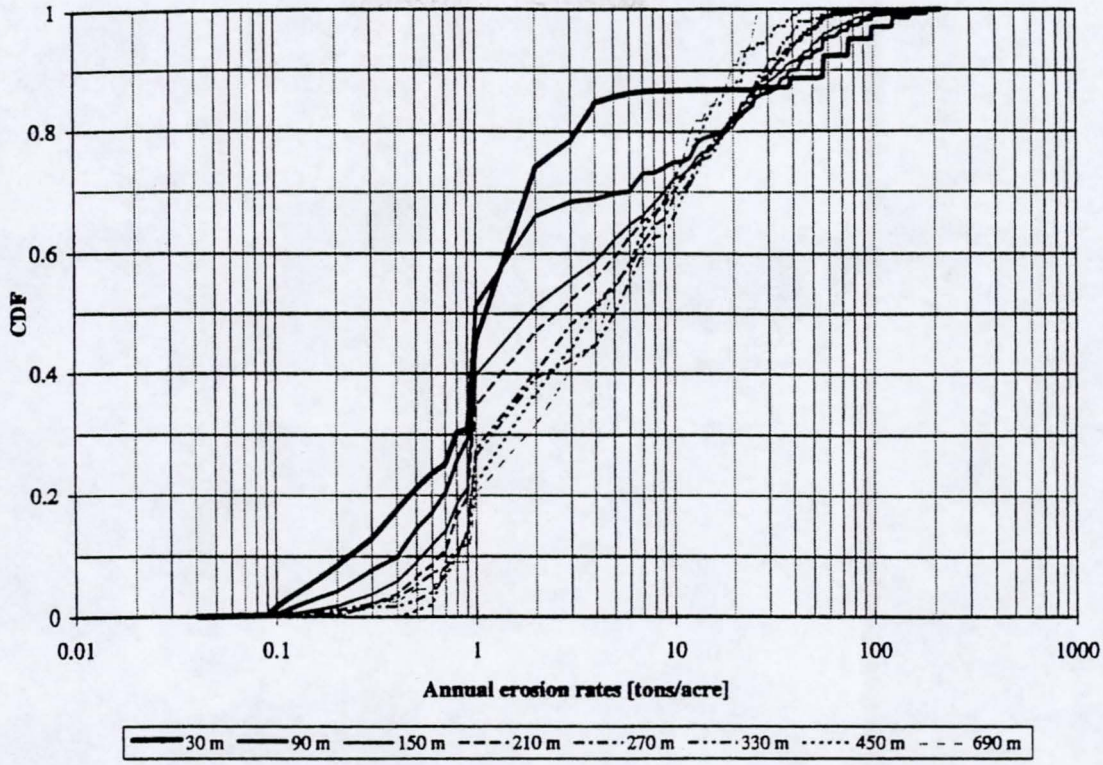

Figure 8. Goodwin Creek distribution of soil erosion rates with increasing grid size.

a 690-m resolution, 90% of the basin has erosion rates less than 20 tons acre^{-1}, whereas at a 30-m resolution, 90% of the basin has erosion rates less than 70 tons acre^{-1}. The coarser resolution will result in a reduced estimation of erosion losses for the entire basin.

GRID SIZE ANALYSIS

Selected range of grid sizes used in the study

The range of grid sizes used in the analysis was selected, based on GRASS capabilities for matrix aggregation. Using the original 30-m input data, the largest possible aggregation (23×23) resulted in a 690×690 m cell size. In order to extend the analysis beyond 690-m, it was therefore necessary to re-aggregate the 90-m and 150-m data. A 23×23 matrix applied to the 150-m Goodwin Creek data resulted in a maximum cell resolution of 3450×3450 m. At this point, due to the potential loss of information resulting from multiple aggregations of original input data, it was decided that a second watershed should be included in the analysis. A sub-basin of the Hickahala Basin, also located in north-western Mississippi, was selected. With an area of 304.5 km^2, this sub-basin allowed for the grid analysis to be extended to cell sizes up to 6×6 km.

The grid size analysis was performed using two categories of cells. The cells serving as original data for matrix aggregations were defined as cells with area A_o. The original 30-m grid size was defined as having an area of $A_o[1]$. The cell sizes resulting from matrix aggregations were defined as cells with area, A. Comparisons of erosion loss rates at different grid sizes depended on the relationships between areas A_o and A. As shown in Table 1A and B, the cells with area A_o were 30×30 m, 90×90 m, and 150×150 m for Goodwin Creek and 30×30 m, 92×92 m, and 274×274 m for Hickahala. The maximum grid size used on Goodwin Creek was a 3450×3450 m cell, corresponding to an area A of 11.90 km^2. The maximum grid size used on Hickahala was 6310×6310 m, with an area, A, of 39.80 km^2. N was defined as the ratio of A/A_o, serving as an indicator of the number of cells A_o within any matrix aggregation.

Determination of the grid size correction factor Q_e

In order to understand the effect of grid size on USLE calculations, a relationship relating soil loss estimates calculated at various grid sizes was established. The relative correction factor Q_e^* was thus defined as:

$$Q_e^* = \frac{\text{total loss calculated for the watershed subdivided into grid size A}}{\text{total loss calculated for the watershed subdivided into grid size A}_o}. \quad (3)$$

The values of Q_e^* resulting from USLE calculations are shown for Goodwin Creek and Hickahala in Table 1A and B, respectively. The relative correction

Table 1. Relative correction factor Q_e^* for (A) Goodwin Creek and (B) Hickahala sub-basin

Grid area A_o (km^2)	Grid area A (km^2)	N (A/A_o)	Number of cells	Total area (km^2)	Total loss (tons)	Average soil loss (tons acre^{-1})	Q_e^*
			(A) Goodwin Creek				
0.0009 (30 m × 30 m)	0.0009	1	23 770	21.39	65 986	12.48	1.00
	0.0081	9	2672	21.64	58 966	11.03	0.89
	0.0225	25	966	21.74	63 060	11.74	0.96
	0.0441	49	490	21.61	56 011	10.49	0.85
	0.0729	81	299	21.80	57 846	10.74	0.88
	0.1089	121	198	21.56	56 385	10.58	0.85
	0.2025	225	108	21.87	45 399	8.40	0.69
	0.4761	529	44	20.95	39 908	7.71	0.60
0.0081 (90 m × 90 m)	0.0081	1	2672	21.64	58 966	11.03	1.00
	0.0729	9	299	21.80	27 728	5.15	0.47
	0.2025	25	108	21.87	24 995	4.63	0.42
	0.9801	121	23	22.54	23 022	4.13	0.39
	2.3409	289	9	21.07	25 362	4.87	0.43
	4.2849	529	4	17.14	18 663	4.41	0.32
0.0225 (150 m × 150 m)	0.0225	1	966	21.74	63 060	11.74	1.00
	0.2025	9	108	21.87	24 983	4.62	0.40
	0.5625	25	39	21.94	27 687	5.11	0.44
	2.7225	121	9	24.50	20 933	3.46	0.33
	6.5025	289	4	26.01	33 351	15.19	0.53
	9.9225	441	3	29.77	12 335	1.68	0.20
	11.9025	529	2	23.81	16 035	2.73	0.25
			(B) Hickahala sub-basin				
0.0009 (30 m × 30 m)	0.0009	1	322 894	299.98	1 017 102	13.72	1.00
	0.0084	9	30 031	251.10	838 189	13.51	0.82
	0.0753	81	3903	293.71	825 739	11.38	0.81
	0.2090	225	1438	300.59	707 878	9.53	0.70
	0.4097	441	740	303.18	620 780	8.29	0.61
	0.4915	529	618	303.72	608 037	8.10	0.60
0.0084 (92 m × 92 m)	0.0084	1	30 031	251.10	838 189	13.51	1.00
	0.0753	9	3200	240.80	482 375	8.11	0.58
	0.2090	25	1169	244.36	414 965	6.87	0.50
	0.4097	49	616	252.38	375 181	6.02	0.45
	0.6773	81	396	268.20	359 801	5.43	0.43
	1.8813	225	155	291.60	295 418	4.10	0.35
	4.4231	529	69	305.19	276 764	3.67	0.33
0.0753 (150 m × 150 m)	0.0753	1	3903	293.71	825 739	11.38	1.00
	0.6773	9	396	268.20	360 303	5.44	0.44
	1.8813	25	155	291.60	262 274	3.64	0.32
	9.1054	121	33	300.48	168 542	2.27	0.20
	16.9316	225	17	287.84	133 294	1.87	0.16
	39.8080	529	7	278.66	156 006	2.27	0.19

factor Q_e^* is plotted as a function of N in Figure 9, with three series corresponding to Goodwin Creek and three series corresponding to Hickahala. As grid size increases, values of Q_e^* decrease significantly, indicating that the USLE tends to underestimate soil loss rates when large cell sizes are used. Demonstrated trends in Q_e^* can be traced back to effects of increasing grid size on the cumulative distribution function of slopes and erosion losses. The loss of information at larger grid sizes can be generalized by considering the effects of A and A_o on the relative correction factor Q_e^*. The following relationship is defined:

$$\log Q_e^* = a + b \log A + c \log \frac{A_o}{A_o[1]}, \qquad (4)$$

where a, b and c = constants, $A_o[1]$ = area of original raster map data cell (30 × 30 m), A_o = cell area before aggregation; and A = cell area after aggregation.

Based on calculated values of Q_e^*, the constants a, b and c were evaluated using a multiple linear regression analysis. The correction factor, Q_e, was then determined using the procedure of Julien and Frenette (1987), whereby Q_e is defined as:

$$Q_e = \tilde{a} A^{\tilde{b}} \qquad (5)$$

where $\tilde{a}$, $\tilde{b}$ = constants, and A = cell area.

The maximum value of Q_e is defined as $Q_{e_{max}}$. The values of the parameters a, b and c in Equation (4), and parameters $\tilde{a}$ and $\tilde{b}$ in Equation (5) are listed in Table 2 for Goodwin Creek, Hickahala, and the Chaudière basin. The analysis was performed separately for Goodwin Creek and Hickahala, yielding similar results. The correction factor equation shown in Table 2 must be used whenever grid sizes are larger than 100 × 100 m (0.01 km^2). When grid sizes are smaller than 100 × 100 m, Q_e is constant and is equal to $Q_{e_{max}}$.

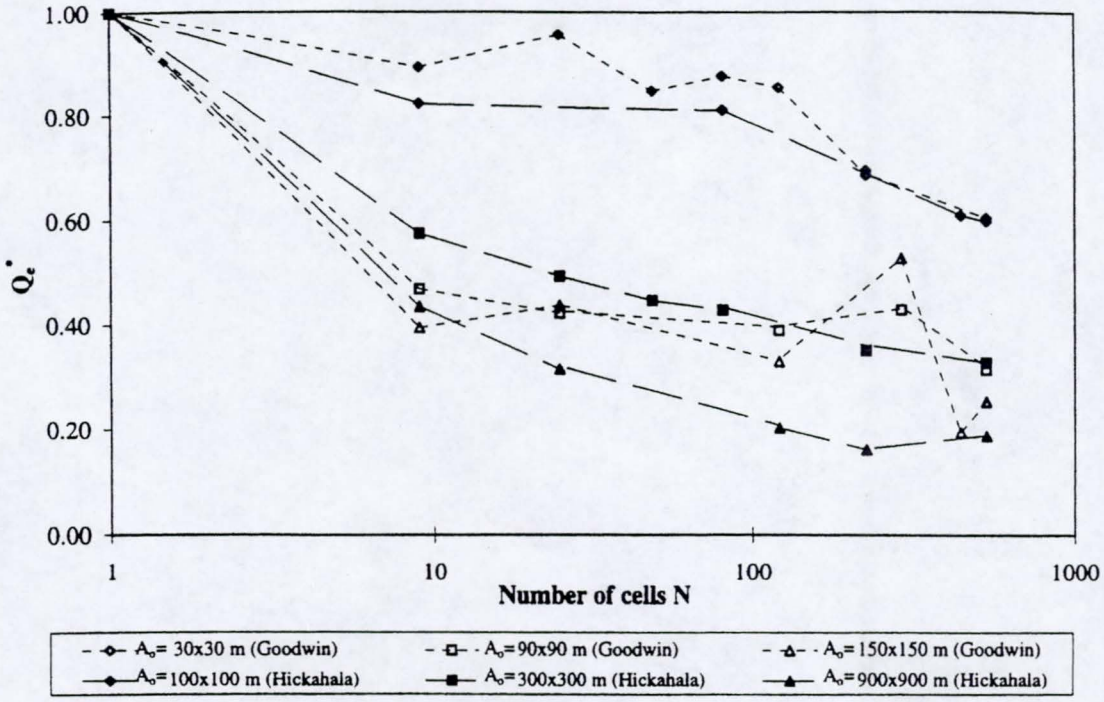

Figure 9. Relative correction factor Q_e^* as function of N.

As shown in Figure 10, by evaluating the correction factor in terms of the relative effects of A_o and A_o[1], points plotted in Figure 9 now collapse more or less along a single line. The correction factor equations for Goodwin Creek and Hickahala, located in Mississippi, are similar to that of the Chaudière basin, which is located in Canada.

Total upland erosion losses using the correction factor method

The advantage of the correction factor method is that it allows for soil loss calculations to be made, assuming that a watershed can be represented by a single grid cell. According to the correction factor method, actual soil loss can be estimated as:

$$\text{Soil loss} = \frac{\bar{R}\,\bar{K}\,\bar{L}\,\bar{S}\,\bar{C}\,\bar{P}}{Q_e}, \qquad (6)$$

where $\bar{R}\,\bar{K}\,\bar{L}\,\bar{S}\,\bar{C}\,\bar{P}$ = estimated soil loss using average watershed characteristics, and Q_e = correction factor corresponding to the watershed area.

The method is applied to Goodwin Creek and Hickahala. An estimated value of annual soil loss is first calculated using average watershed characteristics, assuming the watershed is represented by a single cell. The correction factor Q_e corresponding to each watershed is then determined as a function of the total basin area, using the equations shown in Table 2. Finally, actual soil loss is calculated according to Equation (6). Table 3 summarizes the calculations made in applying the correction factor method to Goodwin Creek and to Hickahala.

As shown in Table 3, the average annual basin soil-loss rates calculated using the correction-factor method are similar to the values estimated using individual grid cell calculations. Yet, at a 30-m resolution, the application of the USLE on Goodwin Creek required calculations for 24 000 individual cells, whereas on Hickahala, calculations for 300 000 cells were required. When the correction factor method is used, calculations are needed for only one cell.

Comparison with field measurements of sediment yield lends itself to the following analysis. The dominant source of sediment on Goodwin Creek has been observed to be supplied from channel ero-

Table 2. Correction factor values for three watersheds

	Goodwin Creek	Hickahala	Chaudière Basin
Parameter a	−0.278	−0.353	−0.123
Parameter b	−0.135	−0.174	−0.137
Parameter c	−0.092	−0.043	+0.083
Parameter $\bar{a}$	0.665	0.577	0.853
Parameter $\bar{b}$	−0.135	−0.174	−0.137
Correction factor equation	$Q_e = 0.665 \times A^{-0.135}$	$Q_e = 0.577 \times A^{-0.174}$	$Q_e = 0.853 \times A^{-0.137}$
Maximum correction factor	$Q_{e_max} = 1.26$	$Q_{e_max} = 1.30$	$Q_{e_max} = 1.13$

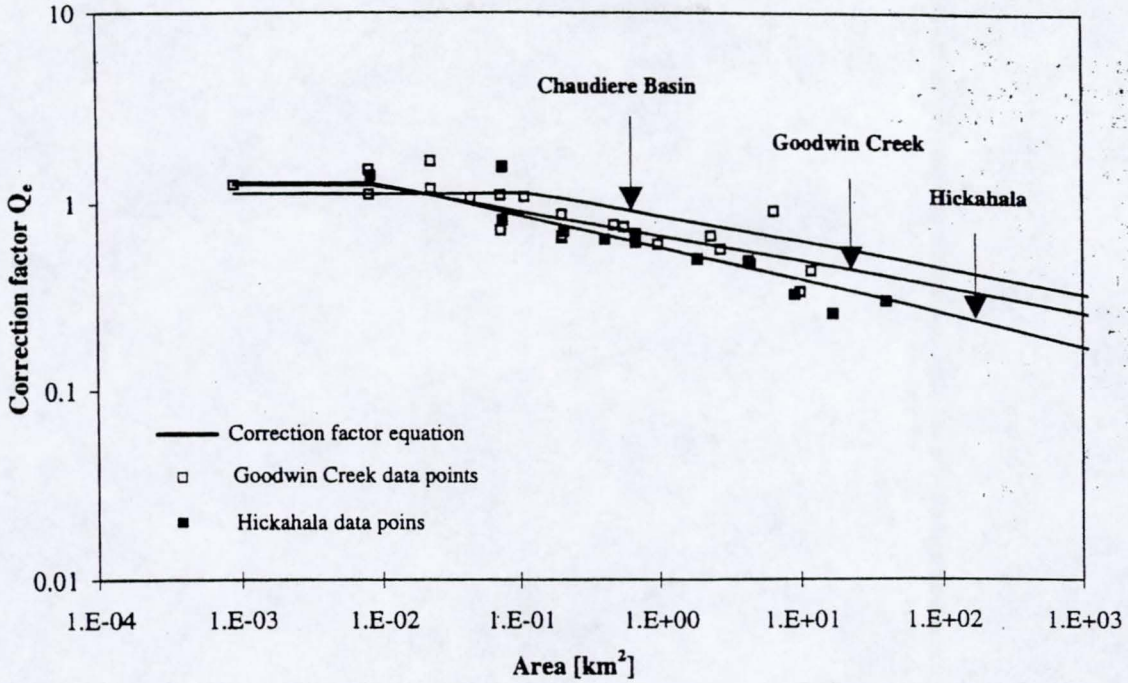

Figure 10. Correction factor Q_e as function of grid area A.

Table 3. Annual soil loss rates

Parameter	Description of parameter	Goodwin Creek	Hickahala
A	Area of basin	21.6 km^2	304.5 km^2
Q_e	Correction factor	0.439	0.213
$\bar{R}$	Rainfall-erosivity factor	330	320
$\bar{K}$	Soil-erodibility factor	0.48 tons acre^{-1}	0.45 tons acre^{-1}
$\bar{L}$	Slope length factor	100 m	100 m
$\bar{S}$	Slope steepness factor	0.014	0.005
$\bar{C}$	Cropping-management factor	0.098	0.101
$\bar{P}$	Conservation practice factor	1.0	1.0
$\bar{R}\,\bar{K}\,\bar{L}\,\bar{S}\,\bar{C}\,\bar{P}$	Soil loss using average values	4.62 tons acre^{-1}	2.77 tons acre^{-1}
Soil loss	Assuming one grid cell	10.53 tons acre^{-1}	12.97 tons acre^{-1}
Soil loss	Assuming 24 000 grid cells	12.48 tons acre^{-1}	
(30-m resolution)	Assuming 300 000 grid cells		13.72 tons acre^{-1}

sion (Alonso, 1996; Kuhnle and others, 1996). Approximately 30% of the total gross erosion comes from upland sources. With a measured sediment yield averaging 5 tons acre-year^{-1} and a sediment delivery ratio of about 0.16, the mean annual upland erosion loss from the measured sediment yield can be estimated at about $5 \times 0.3/0.16 =$ 9.4 tons acre-year^{-1}. This value compares well with the calculated values, i.e. 10–12 tons acre-year^{-1}, for Goodwin Creek in Table 3.

CONCLUSIONS

The usefulness of GIS for the analysis of physical processes in large watersheds is demonstrated in this study of upland erosion. Large databases describing watershed characteristics were analyzed for Goodwin Creek (21.6 km^2) and the Hickahala sub-basin (304.5 km^2) within the GIS GRASS environment.

Analysis led to an increased understanding of the effect of grid size on soil-loss calculations. It is determined that the effect of grid resolution on the slope-steepness factor, S, plays a major role. As grid size increases, slope values for individual cells decrease, which ultimately leads to an underestimation of soil loss. By comparing annual soil-loss rates for Goodwin Creek and Hickahala at a range of grid sizes, a correction factor was determined to compensate for the underestimation of soil loss at larger grid sizes. The correction factor method is a simple technique that can be used in estimating erosion losses from large basins with minimal input data.

Acknowledgments—We gratefully acknowledge the helpful discussions and encouragements of C. V. Alonso, R. Bingner, R. Kuhnle, and W. Blackmarr at the USDA National Sedimentation Laboratory in Oxford, Mississippi. We also acknowledge collaboration with W. Doe at CEMML in Fort Collins, Colorado, and B. E. Johnson and J. Jorgeson at the USACE Waterways Experiment Station in Vicksburg, Mississippi. This study has been made possible under the support of the Army Research Office to the Center for Geosciences at Colorado State University (ARO/DAAH 04-94-G-0420).

REFERENCES

Alonso, C. V. (1996) Hydrologic Research on the USDA Goodwin Creek Experimental Watershed, Northern Mississippi. Proceedings Hydrology Days, 15–18 April, Colorado State University, Fort Collins, 25–36.

Blackmarr, W. A., ed. (1995) Documentation of hydrologic, geomorphic, and sediment transport measurements on the Goodwin Creek experimental watershed, northern Mississippi, for the period of 1982–1993. USDA Agricultural Research Service, Research Report 3, National Sedimentation Laboratory, Oxford, Mississippi, 41 pp.

Galberry, H. S. (1960) Soil Survey of Panola County, Mississippi. *Soil Survey Series* **1960**(10), 1–33.

Julien, P. Y. and Frenette, M. (1987) Macroscale analysis of upland erosion. *Hydrological Sciences Journal* **32**(3), 347–358.

Julien, P. Y. and Gonzalez del Tanago, M. (1991) Spatially varied soil erosion under different climates. *Hydrological Sciences Journal* **36**(6), 511–523.

Kuhnle, R. A., Bingner, R. L., Foster, G. R. and Grissinger, E. H. (1996) Effect of landuse changes on sediment transport in Goodwin Creek. *Water Resources Research* **32**(10), 3189–3196.

Meyer, C. D. (1971) Soil erosion by water on upland areas. In *River Mechanics Vol. II*, ed. H. W. Shen, pp. 27.1–27.5. Privately published, Fort Collins, Colorado.

Musgrave, G. W. (1947) The quantitative evaluation of factors in water erosion—a first approximation. *Journal of Soil and Water Conservation* **0**, 133–138.

Schwab, G. O., Frevert, R. K., Edminster, T. W. and Barnes, K. K. (1981) *Soil and Water Conservation Engineering*, 3rd edn. Wiley, New York, 683 pp.

Shen, H. W. and Julien, P. Y. (1993) Erosion and sediment transport. In *Handbook of Hydrology*, ed. D. R. Maidment, pp. 12.45–12.54.

Shields, F. D., Knight, S. S. and Cooper, C. M. (1995) Rehabilitation of watersheds with incising channels. *Water Resources Bulletin, AWRA* **31**(6), 971–981.

Wischmeier, W. H. and Smith, D. D. (1965) Predicting Rainfall-Erosion Losses from Cropland East of the Rocky Mountains. U.S. Department of Agriculture, Agricultural Handbook **282**, U.S. Government Printing Office, Washington, DC, 47 pp.

Wischmeier, W. H. and Smith, D. D. (1978) Predicting rainfall erosion losses—A guide to conservation planning. U.S. Department of Agriculture. Agricultural Handbook **537**, U.S. Government Printing Office, Washington, DC, 55 pp.

Transforms for Runoff and Sediment Transport

By Pierre Y. Julien,[1] Member, ASCE

Abstract: Transforms reduce the distributions of surface-runoff and sediment-transport variables to near-exponential distributions typical of rainfall duration and intensity. Two transform parameters are determined from field measurements using either a graphical method or the method of moments. The transforms were tested on both small experimental plots and very large watersheds for the distributions of rainfall depth, runoff volume and discharge, sediment concentration and sediment discharge, as well as concentration and transport of chemicals from surface runoff. As expected from deterministic relationships, the inverse transform exponent $\hat{b}$ for point rainfall is close to unity, increases to about 1.5 for runoff discharge, and varies between 1.5 and 3 for sediment and chemical transport. Several examples show that the transforms are useful to determine exceedance probability, flow and sediment duration curves, expected sediment load, and sediment-rating curves for poorly correlated concentration and discharge measurements.

INTRODUCTION

Soil detachment and chemical transport in upland areas is related to excess rainfall and surface runoff. The complexity of the physical processes between rainfall, surface runoff, sediment and chemical transport, not to mention the perturbations induced by human activities, contribute to make the problem of transport of sediment and chemicals a very difficult one to quantify. In general, the relationship between surface runoff and sediment or chemical transport is conducive to site-specific empirical formulas. The transport of fine sediments in terms of wash load and the transport of chemicals from surface runoff usually exhibit poor correlations with surface-runoff parameters such as flow depth, flow velocity, shear stress, or discharge. Coefficients of determination not exceeding 0.5 are commonly encountered, this causes difficulties in the determination of rainfall-sediment relationships from regression analysis. The need for correction factors [e.g., Ferguson (1986)] has been proposed to account for the large scatter of field measurements around the mean of log-transformed surface-runoff and transport variables.

There is extensive literature on extreme events and flood-frequency distributions that is to some extent germane to the foregoing analysis. Starting with Gumbel (1958), the contributions of Schaake et al. (1967), Todorovic (1968), Todorovic and Rousselle (1971), and Eagleson (1972, 1978) have been followed by Ashkar and Rousselle (1981), Hebson and Wood (1982), Diaz-Granados et al. (1984), Wood and Hebson (1986), Moughamian et al. (1987), Fontaine and Potter (1989), and Foufoula-Georgiou (1989). Most recent contributions include those of Shen et al. (1990), Cadavid et al. (1991), Kavvas and Govindaraju (1991), Govindaraju and Kavvas (1991), Hjelmfelt (1991), Hawkins (1993), and Raines and Valdes (1993).

This study is, however, not limited to extreme events and considers the entire database. In doing so, information will be quantified for the mean value, duration curves, and exceedance probability. Conceptually, this study stems from the probabilistic nature of rainfall parameters, which has been shown to compare very well with exponential probability density functions (EPDFs). Because runoff results from rainfall duration and intensity, an analysis based on the probability density function (PDF) of rainfall, runoff, and transport variables may be preferable. The foregoing analysis expands upon the hypothesis that a power relationship exists between rainfall, runoff, and sediment variables (e.g., rainfall intensity and runoff discharge). This study attempts to determine the power relationship from an analysis of the PDFs of both variables.

The objective is to examine the properties of power transforms and their use in defining sediment-duration curves, the exceedance probability, and nonlinearities of rainfall-runoff-transport relationships from the plot size to large watersheds. This paper describes the transforms and tests the proposed procedure with field measurements of surface runoff and sediment and chemical transport at small and large scales. The method is summarized in terms of properties of rainfall characteristics, followed by the transform procedure and parameter evaluation. The findings from several applications to the PDF of runoff and transport variables lead to a discussion of the nonlinearity of rainfall-runoff-transport relationships.

RAINFALL CHARACTERISTICS

Rainfall characteristics are important because they generate surface runoff and transport of sediment and chemicals. Point-rainfall precipitation can be described as a random time series of discrete storm events, each event having finite duration and constant intensity. Several stochastic models have been develped since Todorovic (1968) and Todorovic and Woolhiser (1974). In these models, rainfall precipitation has been described as a Poisson arrival process of rainfall events of duration t_r and average rainfall intensity i.

The storm duration t_r has been found to be exponentially distributed. Considering a period where the average rainfall duration $\bar{t}_r$ remains constant, the PDF of the storm duration $p(t_r)$ is given by

$$p(t_r) = \lambda_1 e^{-\lambda_1 t_r} \tag{1}$$

in which the rainfall duration parameter $\lambda_1 = 1/\bar{t}_r$ is the reciprocal of the average storm duration $\bar{t}_r$.

The rainstorm intensity i has also been shown to be exponentially distributed. The probability density function, $p(i)$, is

$$p(i) = \lambda_2 e^{-\lambda_2 i} \tag{2}$$

in which the rainfall intensity parameter $\lambda_2 = 1/\bar{i}$ is the reciprocal of the average rainstorm intensity $\bar{i}$. Good agreement between the EPDF for both rainfall duration and intensity were reported in the literature by Eagleson (1978), and on a monthly basis by Nguyen and Rousselle (1981) and Julien (1982). Julien and Frenette (1985) examined the monthly variability in expected rainfall erosion from the monthly variability in average rainfall duration and intensity.

[1]Prof. of Civ. Engrg., Engrg. Res. Ctr., Colorado State Univ., Fort Collins, CO 80523.

Note. Discussion open until December 1, 1996. To extend the closing date one month, a written request must be filed with the ASCE Manager of Journals. The manuscript for this paper was submitted for review and possible publication on September 11, 1995. This paper is part of the *Journal of Hydrologic Engineering*, Vol. 1, No. 3, July, 1996. ©ASCE, ISSN 1084-0699/96/0003-0114–0122/$4.00 + $.50 per page. Paper No. 11601.

TRANSFORMS

The details of the proposed transforms are presented with emphasis on the procedure and on the evaluation of the transform parameters. Properties of an EPDF of variable y are such that after dividing the variable y by the mean value $\bar{y}$, a reduced variable ϕ is defined as $\phi = y/\bar{y}$. The properties of the EPDF $p(\phi)$ and the exceedance probability $P(\phi)$ defined as $P(\phi) = \int_\phi^\infty p(\phi)\, d\phi$ are such that

$$P(\phi) = p(\phi) = e^{-\phi} \tag{3}$$

The identity between both the EPDF and the exceedance probability will yield useful applications.

The purpose of the transform is to determine whether the PDF of a runoff or sediment variable x reduces to an EPDF of variable ϕ after the following transform:

$$\phi = ax^b \tag{4}$$

where a and b = transform coefficient and exponent, respectively, hereby referred to as transform parameters. If successful, this would transform the unknown exceedance probability of variable x into a simple EPDF of the reduced variable ϕ.

The inverse transform is simply defined from (4) as

$$x = (1/a)^{1/b}\phi^{1/b} = \hat{a}\phi^{\hat{b}} \tag{5}$$

where $\hat{a}$ and $\hat{b}$ = inverse transform parameters simply calculated from a and b as $\hat{a} = (1/a)^{1/b}$ and $\hat{b} = 1/b$. Conversely, one finds $a = \hat{a}^{-1/\hat{b}} = \hat{a}^{-b}$ and $b = 1/\hat{b}$. The inverse transform exponent $\hat{b}$ is most important to determine the degree of nonlinearity of the variable x and can be related to deterministic relationships.

The properties of the transform are such that once the transform parameters a and b are known, the exceedance probability of variable x is calculated directly from (3) and (4). The PDF $p(x)$ is a Weibull distribution

$$p(x) = abx^{b-1}e^{-ax^b} = ab(\phi/a)^{(b-1)/b}e^{-\phi} \tag{6}$$

One can also demonstrate that $p(x)\, dx = p(\phi)\, d\phi$ and $P(x) = P(\phi)$. Stedinger et al. (1993) cites relationships between the Weibull, Gumbel, and generalized extreme value distributions. For instance, if x has a Weibull distribution, $y = -\ln x$ has a Gumbel distribution and the goodness-of-fit tests available for the Gumbel can be applied to the Weibull distribution. The emphasis of this study is to define the transform parameters a and b in order to take advantage of the properties of the exponential distribution for ϕ.

TRANSFORM PARAMETER EVALUATION

Two procedures are examined for the transform parameter evaluation: a graphical method; and the method of mements. A detailed example of the evaluation procedure follows. It may be noted that Gumbel (1958) approached a similar problem with the maximum-likelihood method but needed successive approximations for the solution.

Graphical Method

The graphical method capitalizes on the properties of the EPDF and exceedance probability in (3). The natural logarithm of (3) is combined with (4) to give

$$-\ln P(\phi) = \phi = ax^b \tag{7}$$

The transform parameters a and b will be evaluated graphically after taking the natural logarithm of (7) in the form

$$\Pi = \ln(-\ln P) = \ln[-\ln P(\phi)] = \ln \phi = \ln a + b \ln x \tag{8}$$

where the shorthand exceedance probability Π designates the double logarithm of the exceedance probability P. Of course, this transform requires all values of x to be positive.

A straight line is fitted on the graphical presentation of Π as a function of $\ln x$ to yield estimates for a and b. It becomes clear from (8) that $\ln a$ corresponds to the value of Π when $x = 1$. Likewise, if the points on the graph Π versus $\ln x$ assemble on a straight line, the slope of the line gives directly the transform exponent b. The graphical method is subjective but provides a qualitative appreciation of the goodness of fit. Ideally, all points should plot on a straight line for the power transform in (4) to be exactly applicable.

Method of Moments

Parameter estimation from the method of moments takes advantage of the information contained in the first and second moments of the sample. The transform parameters a and b can be evaluated after equating with the first and second moments of the transformed variables. Specifically, the first moment, or mean value, of the sample $\bar{x}$ is equated to the first moment M_1 of the transformed distribution, given $x = (\phi/a)^{1/b}$ and $p(x)\, dx = p(\phi)\, d\phi$

$$M_1 = \int_0^\infty xp(x)\, dx$$

$$= \left(\frac{1}{a}\right)^{1/b} \int_0^\infty \phi^{1/b}e^{-\phi}\, d\phi = \left(\frac{1}{a}\right)^{1/b} \Gamma\left(1 + \frac{1}{b}\right) = \hat{a}!\hat{b} = \bar{x} \tag{9}$$

TABLE 1. Useful Values of Transform Parameter *b*

b (1)	$\overline{x^2}/\bar{x}^2$ (2)	$\Gamma(b)$ (3)	$!(b)$ (4)
0.1	184,756	9.51	0.951
0.15	2,213	6.22	0.933
0.2	252	4.59	0.918
0.25	70	3.62	0.906
0.3	30.243	2.99	0.897
0.35	16.777	2.54	0.891
0.4	10.864	2.21	0.887
0.45	7.793	1.97	0.886
0.5	6	1.77	0.886
0.55	4.861	1.61	0.888
0.6	4.090	1.49	0.893
0.65	3.543	1.38	0.900
0.7	3.138	1.30	0.908
0.75	2.830	1.22	0.919
0.8	2.588	1.16	0.931
0.85	2.395	1.11	0.945
0.9	2.238	1.07	0.962
0.95	2.108	1.02	0.980
1	2	1.00	1.00
1.05	1.907	0.973	1.02
1.1	1.828	0.951	1.046
1.2	1.700	0.918	1.10
1.3	1.601	0.897	1.17
1.4	1.523	0.887	1.24
1.5	1.460	0.886	1.33
1.6	1.409	0.893	1.43
1.7	1.366	0.909	1.54
1.8	1.330	0.931	1.68
1.9	1.299	0.962	1.83
2	1.273	1.00	2.0
2.5	1.183	1.33	3.32
3	1.132	2.0	6.0
3.5	1.100	3.32	11.6
4	1.078	6.0	24.0
4.5	1.063	11.6	52.3
5	1.052	24	120
6	1.037	120	720
7	1.028	720	5,040
8	1.022	5,040	40,320
9	1.017	40,320	362,880
10	1.014	362,880	3,628,800

Accordingly, the expected value $\bar{x}$ can be simply evaluated from a simple gamma function of the inverse transform parameters as $\bar{x} = \hat{a}!\hat{b}$, where ! designates the factorial function of the argument $\hat{b}$.

Likewise, the second moment of the sample $\overline{x^2}$ is equated to the second moment M_2 of the transformed distribution

$$M_2 = \int_0^\infty x^2 p(x)\, dx = \left(\frac{1}{a}\right)^{2/b} \int_0^\infty \phi^{2/b} e^{-\phi}\, d\phi$$

$$= \left(\frac{1}{a}\right)^{2/b} \Gamma\left(1 + \frac{2}{b}\right) = \hat{a}^2!(2\hat{b}) = \overline{x^2} \tag{10}$$

The evaluation of the transform parameters a and b follows after the transform coefficient a is eliminated from the ratio (10) to the square of (9), thus

$$\frac{\overline{x^2}}{\bar{x}^2} = \frac{\Gamma\left(1 + \frac{2}{b}\right)}{\left[\Gamma\left(1 + \frac{1}{b}\right)\right]^2} = \frac{!(2\hat{b})}{[!\hat{b}]^2} \tag{11}$$

From the calculated values of $\bar{x}$ and $\overline{x^2}$ of the sample, the value of b on the right-hand side of (11) can best be evaluated numerically. For instance, an interpolation procedure based on the numerical values given in Table 1 proves to be sufficiently accurate. The value of the transform coefficient a then follows from $\hat{a}!\hat{b} = \bar{x}$ in (9) as

$$a = \left[\frac{\Gamma\left(1 + \frac{1}{b}\right)}{\bar{x}}\right]^b = \left[\frac{!\hat{b}}{\bar{x}}\right]^{1/\hat{b}} \tag{12}$$

Parameter estimation from the method of moments is direct and not subjective but lacks the visual information inherent to the graphical method. The evaluation of the transform parameters using both the graphical method and the method of moments is illustrated with the following example.

PARAMETER-EVALUATION EXAMPLE

Consider the following sample of an unknown variable $\bar{x}$ = 4.5, 1.0, 7.0, 2.0, 9.0, 0.5, 6.0, 11.0, and 3.5. The first step consists of ranking the $n = 9$ numbers in decreasing order of x as shown in Table 2, column 2; the values of x are squared in column 3. The second step consists of calculating the exceedance probability using the Weibull plotting position. Accordingly, the numbers in decreasing order are ranked from 1 to n as shown in column 4; 1 being the largest and n being the smallest number. After dividing the rank by $1 + n$, the plotting position corresponds to the exceedance probability $P(\phi)$ or $P(x)$ in column 5. The values of $\ln x$ and $\Pi = \ln[-\ln P(\phi)]$ are tabulated in columns 6 and 7, respectively, for the plot shown in Fig. 1. Graphically, the parameter estimation gives $a \approx 0.1$ and $b \approx 1.3$. The line is usually fit through the higher values of $\ln x$ because for sediment-transport parameters the large values of x are usually those contributing to most of the sediment load.

Using the method of moments, the average value, $\bar{x} = 4.94$ is calculated at the bottom of Table 2, column 2. The average value of $\overline{x^2} = 36.1$ is compiled at the bottom of column 3. From Table 1, the ratio $\overline{x^2}/\bar{x}^2 = 36.1/(4.94)^2 = 1.479$ in column 2 corresponds to a value of $b \approx 1.45$ from interpolation with the values given in Table 1, column 1. The value of $a \approx 0.085$ is thereafter calculated from (12). We note that the gamma function can be approximated by Stirling's asymptotic series

TABLE 2. Example of Transformation Procedure

Sample $\bar{x}$ (1)	Ranked x (2)	x^2 (3)	Rank (4)	$P(x)$ (5)	$\ln(x)$ (6)	$\ln[-\ln P(x)]$ (7)
4.5	11.0	121.00	1	0.1	2.3979	0.8340
1.0	9.0	81.00	2	0.2	2.1972	0.4759
7.0	7.0	49.00	3	0.3	1.9459	0.1856
2.0	6.0	36.00	4	0.4	1.7918	−0.0874
9.0	4.5	20.25	5	0.5	1.5041	−0.3665
0.5	3.5	12.25	6	0.6	1.2528	−0.6717
6.0	2.0	4.00	7	0.7	0.6931	−1.0309
11.0	1.0	1.00	8	0.8	0.0000	−1.4999
3.5	0.5	0.25	9	0.9	−0.6931	−2.2504
Average	$\bar{x} = 4.94$	$\overline{x^2} = 36.1$	—	—	—	—

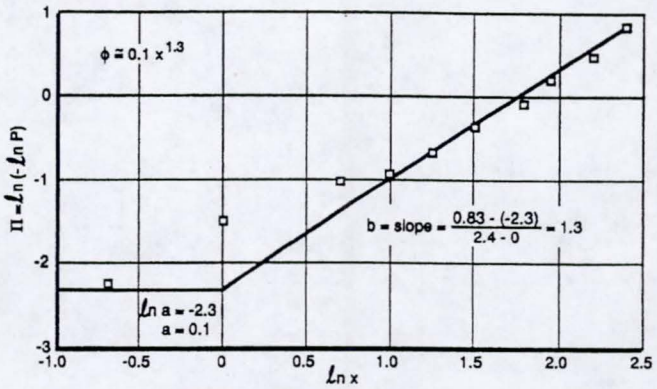

FIG. 1. Example of Transform Parameter Evaluation

$$!(x) = \Gamma(x + 1)$$

$$= \sqrt{2\pi x}\, x^x e^{-x} \left\{1 + \frac{1}{12x} + \frac{1}{288x^2} - \frac{139}{51840x^3} \cdots\right\} \tag{13}$$

which is sufficiently accurate when $x > 0.25$.

TRANSFORMS FOR SURFACE RUNOFF AND SEDIMENT TRANSPORT

Excess rainfall generates surface runoff as overland flow and channel flow. To capture the essential features of the rainfall-runoff relationship, a rectangular hyetograph of constant excess rainfall intensity i and duration t_r is considered. An important parameter in surface-runoff modeling is the resistance relationship, which can be written as $q = \alpha h^\beta$, where the unit discharge q = a power function of flow depth h. The resistance coefficients are found in Table 3 in terms of Darcy-Weisbach friction factor f, Chézy coefficient C, Manning n, or laminar resistance coefficient K for various overland flow conditions including friction slope S, runoff length L, gravitational acceleration g, and kinematic fluid viscosity ν. Woolhiser (1975) presented a method to evaluate resistance coefficients in overland flow.

The time to equilibrium t_e is defined as the time at which the surface runoff reaches an equilibrium state. On a rectangular plane, it is calculated when flow depth $h = it_e$ is sufficiently large to convey the equilibrium discharge $q = \alpha h^\beta = iL$. The general solution for t_e is a function of the flow-resistance relationship and excess rainfall intensity i

$$t_e = \left[\frac{L}{\alpha i^{\beta - 1}}\right]^{1/\beta} \tag{14}$$

Values of t_e for different resistance relationships are presented in Table 3. Surface runoff from the dimensional equations of Woolhiser (1977) over a rectangular plane of length L can be written in dimensionless form $\psi = q/(iL)$ as a function of the dimensionless time $\theta = (t - t_r)/t_e$, where t_e = time to equilib-

TABLE 3. Resistance Relationships $q = \alpha h^{\beta}$

Flow type (1)	Resistance coefficient (2)	α (3)	β (4)	t_e (5)
Laminar	K = constant	$8gS/K\nu$	3	$(K\nu L/8gSi^2)^{1/3}$
Turbulent				
Darcy-Weisbach	f = constant	$\sqrt{8gS/f}$	1.5	$(fL^2/8gSi)^{1/3}$
Chézy	C = constant	$CS^{1/2}$	1.5	$(L^2/C^2Si)^{1/3}$
Manning (S.I.)	n = constant	$S^{1/2}/n$	1.67	$(nL/S^{1/2}i^{0.667})^{0.6}$

rium. Fig. 2 illustrates the shape of dimensionless surface-runoff hydrographs on rectangular planes. The general dimensionless relationships for the rising and falling limbs in the ψ-θ plane are valid for any resistance equation.

In the case of small watersheds, surface runoff is essentially described by complete equilibrium hydrographs. Complete equilibrium hydrographs are those for which the rainfall duration t_r exceeds the time to equilibrium t_e, hence the dimensionless ratio $\lambda = t_r/t_e$ is greater than unity. The surface runoff hydrograph can be subdivided into three parts: rising limb, equilibrium, and falling limb. The rising limb of the complete equilibrium hydrograph is given by $\psi = (\theta + \lambda)^{\beta}$. The equilibrium discharge simply equals $\psi = 1$, and the falling limb is given by $\theta = (1 - \psi)/\beta\psi^{(\beta-1)/\beta}$, as shown in Fig. 2. Given constant excess rainfall intensity, Julien and Moglen (1990), Ogden and Julien (1993), Saghafian et al. (1995), and Ogden et al. (1995) highlighted similarities in surface-runoff characteristics between one-dimensional planes and two-dimensional surface-runoff hydrographs. Essentially, small watersheds are characterized with values of $\lambda = t_r/t_e > 1$ for which the dimensionless discharge during the equilibrium portion of the hydrograph is close to unity. Accordingly, the magnitude of the maximum discharge varies linearly with the rainfall intensity, $\psi = iL$. Consequently, the PDF of surface runoff and the PDF of discharge measurements should closely approximate the PDF of rainfall intensity. For near impervious small watersheds, one therefore expects the exponent b of the transforms to remain close to unity, resulting in a near EPDF for runoff discharge.

Sediment transport from small watersheds is known to vary with rainfall intensity but also depends largely on infiltration (e.g., there is little sediment transport when the infiltration rate exceeds the rainfall intensity). Surface runoff is usually a better parameter to correlate with sediment transport than rainfall. For instance, the power relationship $q_s \sim q^d$ for surface runoff gives empirical values of the exponent $1.4 < d < 2.4$ [e.g., Julien (1995), p. 223]. Accordingly, the inverse transform parameter for sediment and perhaps chemical transport from small watersheds is expected to be $1.5 < \hat{b} < 2.5$ if the rainfall-runoff relationship is nearly linear.

Large watersheds are hereby referred to those with time to equilibrium t_e exceeding the duration of rainfall t_r, or $\lambda = t_r/t_e < 1$. With reference to Fig. 2, the hydrograph is said to reach partial equilibrium characterized with low peak discharge at an amplitude corresponding to $\psi = \lambda^{\beta} < 1$, or $q < iL$. From this relationship, one infers that the maximum discharge under partial equilibrium is $q \cong iL(t_r/t_e)^{\beta}$. In statistical terms, on a watershed with given topography in constant α and constant L, considering t_e from (14), the PDF of maximum unit discharge depends on the PDF of $i^{2-(1/\beta)}t_r^{\beta}$. As opposed to the results from small watersheds, the PDF of surface-runoff discharge on large watersheds should therefore reflect the resistance equation through β, which should be somewhat comparable to the inverse transform exponent $\hat{b}$, or approximately $1 < \hat{b} < \beta$ when i and t_r are independent.

Sediment transport from large watersheds should become difficult to quantify because of the nonlinearity of the rainfall-runoff relationship. However, one may expect a higher inverse transform parameter, $\hat{b} > 1.5$, for sediment discharge in large rivers.

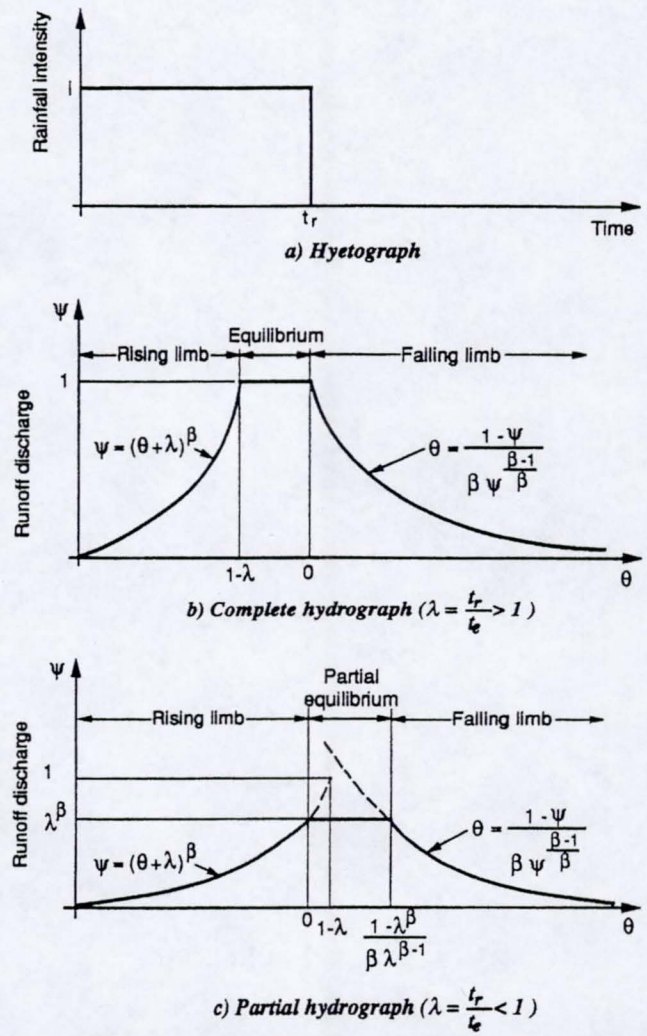

FIG. 2. Hyetograph, Complete, and Partial Equilibrium Hydrographs for Rectangular Planes

APPLICATIONS TO SMALL WATERSHEDS

Point Rainfall

The analysis of natural point-rainfall processes serves as the generating function for the surface-runoff and sediment-transport processes. As previously explained, the PDF of rainfall duration and rainfall intensity have been demonstrated to be near-exponentially distributed and independent. The meteorological data from the agronomic station at Laval University, near Québec City, Canada, has been used for the analysis of the PDF of rainfall duration. Measurements with an accuracy of ±5 min were available (Villeneuve 1968) during the months of June–November from 1966 to 1970. The values of the transform parameters are given in Table 4 as calculated from both the graphical method and the method of moments. The results of both methods confirm that the transform exponent b remains close to unity. The linearity of the transformed distribution is very good as shown in Fig. 3.

The PDF of rainfall depth from individual rainstorms has been examined with the Laval University data collected during June–November 1966–1970 with an accuracy of ±0.01 in. The transform for rainfall depth is given in Table 4 for comparison with other processes. The inverse transform exponent, $\hat{b} \cong 1.2$, differs slightly from unity but the transformed distributions of rainfall depth fits a straight line as shown in Fig.

TABLE 4. Typical Values of Transform Parameters

Variable (1)	Unit (2)	Watershed size (3)	Location (4)	Number of points (5)	INVERSE TRANSFORMS $x = \hat{a}\phi^{\hat{b}}$ Graphical $\hat{a}$ (6)	Graphical $\hat{b}$ (7)	Moments $\hat{a}$ (8)	Moments $\hat{b}$ (9)	TRANSFORMS $\phi = ax^b$ Graphical a (10)	Graphical b (11)	Moments a (12)	Moments b (13)
(*a*) Rainfall												
Duration (t_r)	min.	point	Quebec	327	263	1.08	257	1.02	5.87×10^{-3}	0.92	4.32×10^{-3}	0.98
Depth (it_r)	in.	point	Quebec	327	0.29	1.28	0.29	1.21	2.63	0.78	2.77	0.82
Depth (it_r)	in.	plot 1	Missouri	402	1.10	1.03	1.27	0.90	0.87	0.97	0.77	1.10
Depth (it_r)	in.	plot 3	Missouri	410	1.18	0.94	1.31	0.85	0.84	1.06	0.73	1.18
(*b*) Snowmelt												
Discharge	mL/s	plot	Quebec	389	8.46	1.37	9.92	1.15	0.21	0.73	0.14	0.87
(*c*) Runoff												
Volume/area	in.	plot 1	Missouri	404	0.32	1.52	0.31	1.62	2.11	0.66	2.06	0.62
Volume/area	in.	plot 33	Missouri	438	0.34	1.46	0.35	1.47	2.08	0.68	2.06	0.68
Discharge	m^3/s	5,830 km^2	Quebec	3,285	82.8	1.77	98.4	1.52	0.083	0.56	0.048	0.66
Discharge	ft^3/sec	279,460 km^2	Colorado River	1,826	9,557	1.62	12,931	1.25	3.5×10^{-3}	0.62	5.25×10^{-4}	0.80
(*d*) Chemical Concentration												
Ammonia	ppm	50 km^2	Iowa	1,005	0.26	1.34	0.27	1.41	2.67	0.75	2.51	0.71
Nitrate	ppm	50 km^2	Iowa	1,094	8.91	0.46	7.56	0.67	8.8×10^{-3}	2.16	0.05	1.47
Orthophosphate	ppm	50 km^2	Iowa	1,104	0.05	1.48	0.057	1.40	7.5	0.67	7.6	0.71
(*e*) Chemical Yield												
Nitrate	lb/acre	plot 33	Missouri	187	0.11	1.63	0.08	2.22	3.77	0.61	3.05	0.45
Ammonia	lb/acre	plot 33	Missouri	185	0.027	2.33	0.032	2.25	4.72	0.43	4.61	0.44
Orthophosphate	lb/acre	plot 33	Missouri	165	0.014	1.81	0.017	1.48	10.5	0.55	15.4	0.67
Sediment nitrogen	lb/acre	plot 33	Missouri	159	0.93	2.13	1.08	2.09	1.04	0.47	0.96	0.47
Sediment phosphate	lb/acre	plot 33	Missouri	117	0.019	2.22	0.022	2.16	5.91	0.45	5.81	0.46
(*f*) Sediment												
Concentration	mg/L	5,830 km^2	Quebec	1,377	30.0	1.64	20.8	2.14	0.13	0.61	0.24	0.47
Concentration	mg/L	279,460 km^2	Colorado River	1,826	3,016	1.26	3,362	1.13	1.74×10^{-3}	0.79	7.5×10^{-4}	0.88
Yield	t/acre	plot 33	Missouri	284	0.23	2.35	0.25	2.20	1.86	0.42	1.89	0.45
Discharge (Q_s)	t/day	5,830 km^2	Quebec	1,375	392	2.84	493	2.56	0.12	0.35	0.089	0.39
Discharge (Q_s)	t/day	279,460 km^2	Colorado River	1,826	79,875	2.18	120,230	1.70	5.74×10^{-3}	0.46	1.04×10^{-3}	0.59

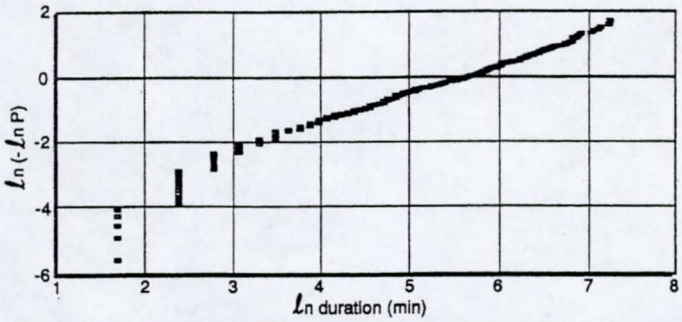

FIG. 3. Transform Diagram for Point Rainfall Duration

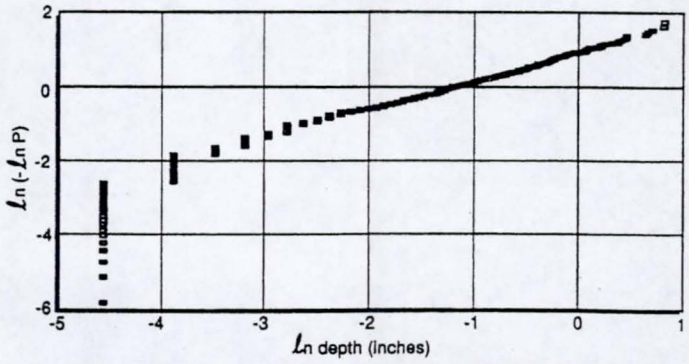

FIG. 4. Transform Diagram for Point Rainfall Depth

4. The rainfall precipitation measurements on claypan soils at Kingdom City, Missouri (R. B. Burwell, unpublished USDA ARS Watershed Research Unit report, 1982; Hjelmfelt and Burwell 1984; Jamison et al. 1968) were considered for comparison. The precipitation depth measurements give transform exponents close to unity for plots 1 and 33, as shown in Table 4.

Surface Runoff on Small Plots

The surface-runoff volume from a single event is usually expected to be less than the volume of rainfall. Indeed, in previous small watersheds, surface runoff is generated from the rainfall intensity in excess of the infiltration rate. The precipitation measurements of the claypan soils in Missouri (Burwell, unpublished report, 1982) were examined in terms of the relationship between rainfall depth and surface-runoff depth. At rainfall depths not exceeding 2.5 cm (1 in.), the surface-runoff depth is almost negligible. Conversely, as the rainfall precipitation depth approaches 25 cm (10 in.), the surface-runoff depth becomes asymptotically equal to the rainfall depth. The proposed transforms are used to reduce the runoff depth data into an EPDF as shown in Fig. 5. The transform parameters are compiled in Table 4 for comparison with other precipitation variables.

Finally, the PDF of snowmelt has been examined with the proposed transforms; specifically, the hourly snowmelt data of Rousseau (1979) has been processed for comparison with other precipitation variables. Although the time variability of hourly snowmelt data is highly nonlinear (Julien 1982), the

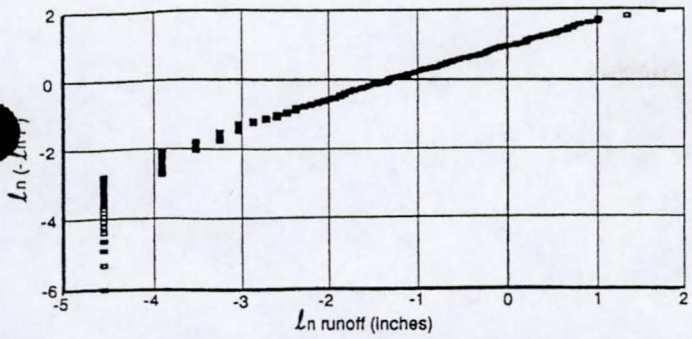

FIG. 5. Transform Diagram for Runoff Volume per Surface Area

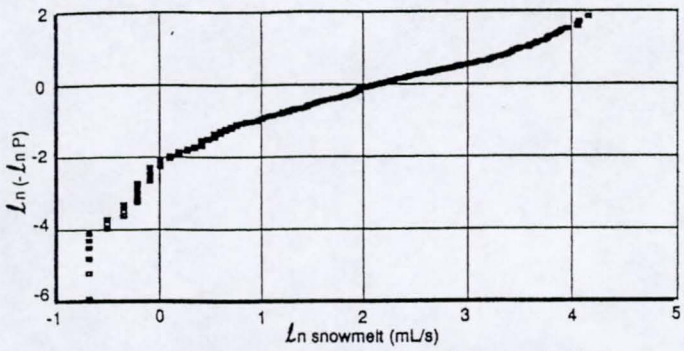

FIG. 6. Transform Diagram for Hourly Snowmelt Discharge

transforms of the data set covering an entire snowmelt season indicate a fairly linear fit of the reduced variable as shown in Fig. 6. The results in Table 4 are quite comparable to those for rainfall intensity.

Sediment and Chemical Transport

Sediment and chemical transport from small watersheds is intriguing given the poor correlation between sediment, or chemical concentration, with rainfall parameters. The use of the proposed transforms is first demonstrated in terms of concentration. The data collected at Four Mile Creek, Iowa, during the period 1976–78 (Johnson and Baker 1982) has been examined for this analysis. Similar results were obtained for the transport of agricultural chemicals from small upland watersheds near Watkinsville, Georgia (Smith et al. 1978). As shown in Table 4, the transforms yield reasonable agreement between the measured concentrations of ammonia and orthophosphate, while the values of the inverse transform exponents $\hat{b}$ range between 1.34 and 1.48. The concentration of nitrate yields ambiguous results because both surface and subsurface flows contribute to the concentration. Fig. 7 is quite typical of the PDF in chemical concentration yielded from agricultural plots as viewed from the proposed transforms.

In terms of sediment yield, the PDF of the sediment delivery from experimental plots is subjected to poor correlation with either rainfall depth or surface-runoff depth. Nevertheless, the proposed transforms reduce the sediment yield data from the claypan soils in Missouri into valuable results shown in Fig. 8. The inverse transform exponents are listed in Table 4, and, the sediment yield corresponds to a higher power of the rainfall or runoff parameter. As expected in sediment-transport studies, the sediment discharge varies with approximately the square of the water discharge. This is reflected in the inverse transform exponents $\hat{b} > 2$ for sediment yield in Table 4.

The delivery of chemicals from agricultural plots of the claypan soils in Missouri was examined to determine the transform parameters listed in Table 4, which are quite consistent for all five chemicals measured: nitrate, sediment nitrogen, ammonia, sediment phosphate, and orthophosphate. The yield of

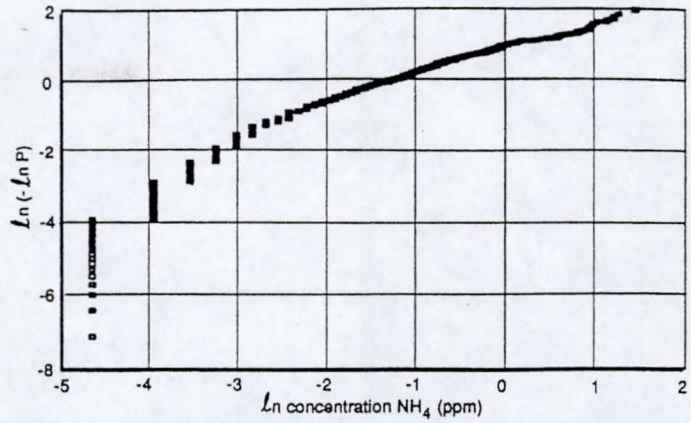

FIG. 7. Transform Diagram for Ammonium Concentration from Small Watershed

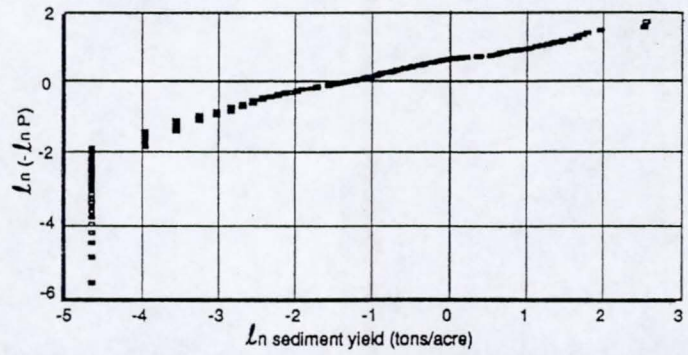

FIG. 8. Transform Diagram for Sediment Yield from Small Watershed

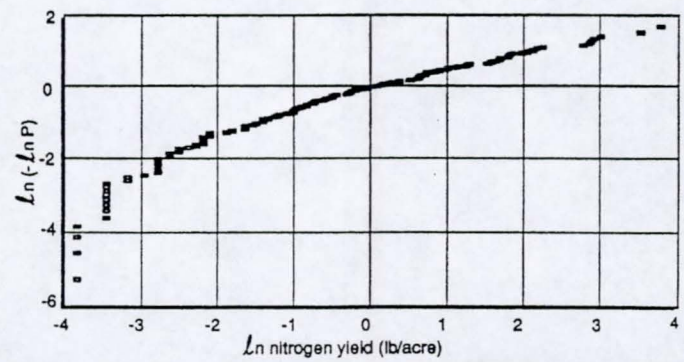

FIG. 9. Transform Diagram for Nitrogen Yield from Small Watershed

chemicals from agricultural plots varies roughly with the second power of the linear rainfall processes; Fig. 9 is quite typical of the results.

APPLICATIONS TO LARGE WATERSHEDS

The application to large watersheds focuses on the PDF of daily discharges, sediment concentration, and sediment discharge. Two large watersheds were considered: the Chaudière river in Canada covers 5,830 km^2 and was sampled during 1968–76; and the Colorado river at Lee's Ferry in Arizona covers 279,460 km^2 and was sampled daily from 1955 to 1959. Daily discharge measurements from the Chaudière river provide the flow-duration curve in terms of transform diagram in Fig. 10, which exhibits a nearly straight fit of the transformed distribution at higher discharges. The values of the inverse transform exponent $1.52 < \hat{b} < 1.77$ are quite comparable to the resistance exponent $1.5 < \beta < 1.67$ in Table 3 for turbulent flow.

As a first application example, the transforms provide useful

information in the analysis of exceedance probability and flow duration curves. Indeed, the exceedance probability of a discharge Q can be directly calculated from (3) and (4)

$$P(x) = e^{-ax^b} = e^{-(x/\hat{a})^{1/\hat{b}}} \tag{15}$$

given the transform parameters in Table 4. For instance, the flow discharge in the Chaudière river is given by $\phi = 0.048Q^{0.66}$ from Table 4. The exceedance probability $P(1{,}000\ \mathrm{m^3/s})$ of a daily discharge $Q = 1{,}000\ \mathrm{m^3/s}$ is approximately $P(1{,}000) \cong e^{[-0.048 \cdot 1{,}000^{0.66}]} = 0.01$, which compares well with the recorded value (0.008) on the flow-duration curve reported in Julien (1995, p. 234). Actually, the entire flow-duration curve for this river is in very good agreement with (15).

Sediment concentration was measured periodically with emphasis during the periods of high discharge. The upper portion of the concentration diagram (Fig. 11) is also quite amenable to the use of the proposed transforms, for which the exceedance probability of sediment concentration can be calculated from (15). From the relationship in Table 4 the inverse transform exponent $1 < \hat{b} < 2$ indicates that sediment concentration varies nonlinearly with the exponential rainfall characteristics.

As a second example, the sediment-rating curve during the period of sampling can also be examined with the use of the transforms. From the method of moments in Table 4, the transform of sediment concentration for the Chaudière river is $\phi = 0.24C_{\mathrm{mg/L}}^{0.47}$, and that of runoff discharge during the same period is $\phi = 0.048Q_{\mathrm{mcs}}^{0.66}$ (mcs = cubic meters per second). From the double identity $\phi = 0.24C_{\mathrm{mg/L}}^{0.47} = 0.048Q_{\mathrm{mcs}}^{0.66}$, the relationship between $C_{\mathrm{mg/L}}$ and Q can be written as $C_{\mathrm{mg/L}} = 0.032Q_{\mathrm{mcs}}^{1.40}$. This is remarkably close to the equation obtained by regression analysis, $C_{\mathrm{mg/L}} = 0.04Q_{\mathrm{mcs}}^{1.3}$, found in Julien (1995, p. 234). A similar relationship can be defined for the Colorado river at Lee's Ferry from $\phi = 7.5 \times 10^{-4}\ C_{\mathrm{mg/L}}^{0.88} = 5.25 \times 10^{-4}\ Q_{\mathrm{ft^3/s}}^{0.80}$, or $C_{\mathrm{mg/L}} = 0.67Q_{\mathrm{ft^3/s}}^{0.91}$.

The expected value of variable x can be directly estimated from (9), given the inverse transform parameters $\hat{a}$ and $\hat{b}$

$$\bar{x} = \left(\frac{1}{a}\right)^{1/b} \Gamma\left(1 + \frac{1}{b}\right) = \hat{a}\Gamma(1 + \hat{b}) = \hat{a}!\hat{b} \tag{16}$$

For instance, the mean daily flow of the Chaudière river is calculated directly from the inverse transform parameters by the method of moments in Table 4, thus $\bar{Q} = 98.4\Gamma 2.52 = 98.4!1.52 = 132\ \mathrm{m^3/s}$.

As a third practical example, the transforms enable very rapid calculations of the sediment discharge of a river once the inverse transform parameters $\hat{a}$ and $\hat{b}$ have been determined. The average sediment load in suspension in the Colorado river at Lee's Ferry (shown in Fig. 12) is estimated from the transform parameters $\hat{a}$ and $\hat{b}$ for Q_s in Table 4. The average daily sediment discharge $\bar{Q}_s = 120{,}230!1.70 = 185{,}700$ tons/day calculated from daily measurements over a period of five years (1955–59) is close to the average measurement of 140,000 tons/day for the period 1912–65 calculated by C. F. Nordin Jr. (personal communication, 1995). This approximation based on the transform parameters, circumvents the traditional sediment-load calculations using the combined flow-duration curve and sediment-rating curve method. It should prove particularly useful in rivers with significant washload where sediment concentration and discharge are uncorrelated and the sediment-rating curve is difficult to determine.

As a fourth practical example, the transforms also enable the user to estimate the daily sediment discharge that will be exceeded a certain fraction of the time from (15) after solving for x

$$x = [-\ln P(x)]^{1/b} \left(\frac{1}{a}\right)^{1/b} = \hat{a}[-\ln P(x)]^{\hat{b}} \tag{17}$$

For instance, the daily sediment discharge of the Colorado river at Lee's Ferry that is exceeded 1% of the time, or 3.65 days a year, is calculated with $\hat{a} = 120{,}230$ and $\hat{b} = 1.7$; $P(Q_s) = 0.01$, which gives $Q_s = 120{,}230(-\ln 0.01)^{1.7} = 1.6 \times 10^6$ tons/day. Conversely, one can estimate the percentage of the time where the daily sediment discharge exceeds a certain value. For instance, how many days a year can someone expect the daily sediment discharge to exceed 1 million tons per day. From (15), one obtains directly $P(Q_s) = e^{-aQ_s^b} = e^{-1.04\times 10^{-3}(1\times 10^6)^{0.59}} = 0.027$, or about 10 days per year (0.027×365 days).

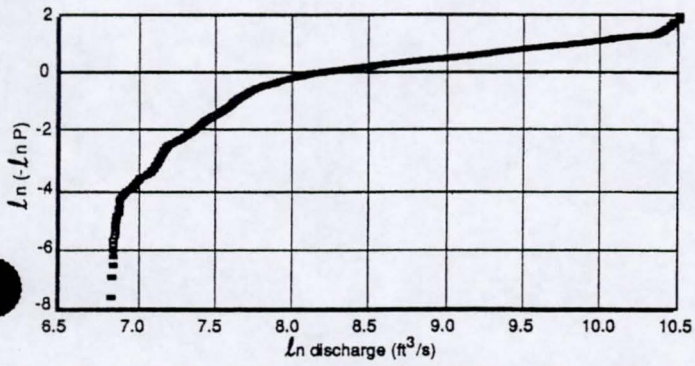

FIG. 10. Transform Diagram for Daily Discharge from Chaudiere River

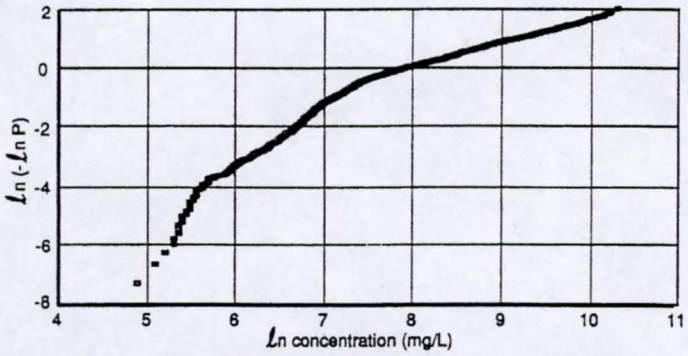

FIG. 11. Transform Diagram for Sediment Concentration in Chaudiere River

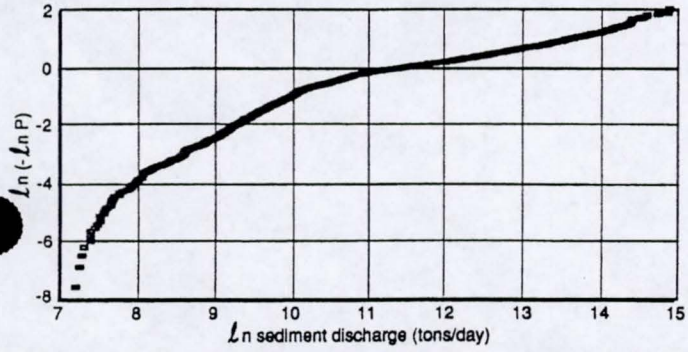

FIG. 12. Transform Diagram for Daily Sediment Discharge in Colorado River

NONLINEARITY

The inverse transform exponent $\hat{b}$ is viewed as a measure of nonlinearity between runoff, or sediment transport, and point rainfall. It can be seen from Table 4 that point rainfall is nearly linear with values of $0.85 < \hat{b} < 1.28$. There is a general increase in nonlinearity as depicted by the inverse transform exponent $\hat{b}$ in going from point rainfall to runoff to chemical/sediment transport. The range of values of $\hat{b}$ for various processes is summarized in Table 5. In increasing order

TABLE 5. Typical Values of $\hat{b}$ for Different Variables

Process (1)	$\hat{b}$ (2)
Point rainfall	0.85–1.28
Upland snowmelt	1.15–1.37
Upland chemical concentration	0.46–1.40
Upland runoff	1.46–1.62
River flow discharge	1.25–1.77
River sediment concentration	1.13–2.14
Upland chemical yield	1.48–2.33
Upland sediment yield	2.20–2.35
River sediment discharge	1.70–2.84

of nonlinearity, one finds point rainfall, surface runoff, chemical and sediment concentration, and chemical and sediment yield. The importance of $\hat{b}$ is illustrated with the following analysis and examples.

Once the magnitude x_1 and exceedance probability P_1 of an event are known, one can determine the unknown magnitude x_2 of another event of exceedance probability P_2 simply as a function of the inverse transform exponent $\hat{b}$. At a given $\hat{b}$, one defines $\xi = P_2/P_1$ to determine the unknown $\eta = x_2/x_1$. From (15), one obtains $P_1 = e^{-ax_1^{\hat{b}}}$ and $\xi P_1 = e^{-a(\eta x_1)^{\hat{b}}}$ to be solved for ξ as a function of η and b as

$$\xi = e^{-ax_1^{\hat{b}}(\eta^{\hat{b}}-1)} = P_1^{(\eta^{\hat{b}}-1)} \tag{18}$$

or conversely for η as a function of ξ and $\hat{b}$

$$\eta = \left[1 + \frac{\ln \xi}{\ln P_1}\right]^{\hat{b}} = \left[\frac{\ln P_2}{\ln P_1}\right]^{\hat{b}} \tag{19}$$

which shows that at any given value of ξ and P_1, the magnitude of η increases with the exponent $\hat{b}$.

As a fifth example, it is known that in the Colorado river ($\hat{b}$ = 1.7) the daily sediment discharge of $x_1 = 1 \times 10^6$ tons/day is exceeded 10 days a year ($P_1 = 0.0274$). Calculate the exceedance probability P_2 of a daily sediment discharge $x_2 = 2 \times 10^6$ tons/day. In this first case, ξ is calculated from (18), given $\eta = x_2/x_1 = 2$ and $b = 1/\hat{b} = 0.59$ for the Colorado river, thus $\xi = (0.0274)^{(2^{0.59}-1)} = 0.162$ or $P_2 = 0.162P_1 = 4.45 \times 10^{-3}$ or 1.62 days per year.

As a sixth example, the magnitude of infrequent events can be estimated from the mean value $\bar{x}$ and $\hat{b}$. For instance, given the mean daily sediment discharge of 185,700 tons/day in the Colorado river ($\hat{b}$ = 1.7), estimate the magnitude of the daily sediment discharge x_2 exceeded one day per year (P_2 = 0.00274). The exceedance probability of the mean daily sediment discharge of the Colorado river $\bar{Q}_s$ = 185,700 tons/day is first calculated from (15) given $a = 1.04 \times 10^{-3}$ and b = 0.59. This yields $P_1 = P(\bar{Q}_s) = e^{-1.04\times10^{-3}\times185{,}700^{0.59}} = 0.263$. The value of η is then calculated from (19), given $\xi = P_2/P_1$ = 0.0104 and $\hat{b}$ = 1.70 for the Colorado river, thus $\eta = [1 + (\ln 0.0104/\ln 0.263)]^{1.7} = 12.5$ or $x_2 = \eta x_1 = 12.5 \times 185{,}700 = 2.32 \times 10^6$ tons/day. This example shows that the higher the value of $\hat{b}$ associated with nonlinearity, the higher the value of η, and subsequently x_2.

As a final result, the transforms enable the user to calculate the magnitude of infrequent events from the mean value of a variable and the inverse transform parameter $\hat{b}$. Considering the previous example, one demonstrates from (9) and (15) that the exceedance probability of the mean value is only a function of $\hat{b}$ as

$$-\ln P(\bar{x}) = (!\hat{b})^{1/\hat{b}} \tag{20}$$

The value of x that has an exceedance probability $P(x)$ is then directly calculated from (19) as a function of $\bar{x}$ and $\hat{b}$

$$x = \left[\frac{\ln P(x)}{\ln P(\bar{x})}\right]^{\hat{b}} \bar{x} = \left[\frac{[-\ln P(x)]^{\hat{b}}}{!\hat{b}}\right] \bar{x} \tag{21}$$

This equation is quite simple and demonstrates the usefulness of the inverse transform parameter $\hat{b}$.

As a last practical example, the mean daily sediment concentration in a river is 250 mg/L. Estimate the value of concentration that is exceeded 5% of the time [$P(x) = 0.05$]. Without knowing the distribution of daily sediment-concentration measurements, one can nevertheless find rough estimates from $1.13 < \hat{b} < 2.14$ in Table 5. Hence, one can estimate x assuming $\hat{b} \cong 1.6$ to get from (21), $x = [(-\ln 0.05)^{1.6}/1.43] \times 250$ mg/L $\cong$ 1,000 mg/L. The brackets obtained from $\hat{b}$ = 1.13 and $\hat{b}$ = 2.14 are, respectively, $x \cong 800$ mg/L and $x \cong 1{,}150$ mg/L. One would thus expect the daily sediment concentration exceeded 5% of the time to range between 800 and 1,150 mg/L.

SUMMARY AND CONCLUSIONS

This study examines the information contained in rainfall-runoff-transport variables in terms of expected value, duration curves, and exceedance probability. Starting from exponential distribution of rainfall characteristics, the properties of power transforms and the practical implications of the nonlinearities of the transform are examined from point characteristics to runoff and sediment transport in large watersheds.

Transforms are proposed for the analysis of the probability density functions of rainfall, runoff, sediment, and chemical transport variables. Two transform parameters are evaluated either from a graphical method or from the method of moments. The results enable rapid estimates of expected values and exceedance probability at a given value of parameters such as rainfall intensity, duration, depth, flow discharge, chemical concentration, sediment concentration, sediment yield, and sediment discharge.

The transforms are particularly valuable in the analysis of flow and sediment duration curves, as wel as for the definition of poorly correlated and sediment-rating curves. In the determination of the mean annual sediment yield in a river, the method circumvents the tedious combined flow-duration curve and sediment-rating curve method. Moreover, the sediment-duration curves can be determined with an assessment of how frequently a daily sediment discharge, or sediment concentration level is exceeded.

The values of the inverse transform exponents $\hat{b}$ are quite representative of physical processes. Point rainfall duration, intensity and depth are nearly exponentially distributed and $\hat{b}$ remains close to unity. Surface runoff discharge and volume per unit area display values of $\hat{b}$ closer to the flow resistance exponent β. The concentration of chemicals in surface runoff varies with values of $0.7 < \hat{b} < 2.2$. Likewise, sediment yield, sediment concentration, and sediment discharge become highly nonlinear and $1.1 < \hat{b} < 2.6$. The value of $\hat{b}$ can be used to estimate the magnitude of infrequent events.

ACKNOWLEDGMENTS

The writer is grateful to C. F. Nordin Jr. for the informative discussion on the sediment load of the Colorado river, and to A. T. Hjelmfelt Jr. for the unpublished report of R. B. Burwell on the plot records from claypan soils in Missouri. Financial support from the Army Research Office (grant ARO/DAAH 04-94-G-0420) is gratefully acknowledged.

APPENDIX I. REFERENCES

Ashkar, F., and Rousselle, J. (1981). "Design discharge as a random variable: A risk study." *Water Resour. Res.*, 17(3), 577–591.

Cadavid, L., Obeysekera, J. T. B., and Shen, H. W. (1991). "Flood-frequency derivation from kinematic wave." *J. Hydr. Engrg.*, ASCE, 117(4), 489–509.

Diaz-Granados, M. A., Valdes, J. B., and Bras, R. L. (1984). "A physically based flood frequency distribution." *Water Resour. Res.*, 20(7), 995–1002.

Eagleson, P. S. (1972). "Dynamics of flood frequency." *Water Resour. Res.*, 18(2), 878–898.

Eagleson, P. S. (1978). "Climate, soil and vegetation, 2. The distribution of annual precipitation derived from observed storm sequence." *Water Resour. Res.*, 14(5), 713–721.

Ferguson, R. I. (1986). "River loads underestimated by rating curves." *Water Resour. Res.*, 22(1), 74–76.

Fontaine, T. A., and Potter, K. W. (1989). "Estimating probabilities of extreme rainfalls." *J. Hydr. Engrg.*, ASCE, 115(11), 1562–1575.

Foufoula-Georgiou, E. (1989). "A probabilistic storm transposition approach for estimating exceedance probabilities of extreme precipitation depths." *Water Resour. Res.*, 25(5), 799–815.

Govindaraju, R. S., and Kavvas, M. L. (1991). "Stochastic overland flows, Part 2: Numerical solutions evolutionary probability density functions." *Stochastic Hydro. and Hydr.*, 5, 105–124.

Gumbel, E. J. (1958). *Statistics of extremes*. Columbia University Press, New York, N.Y.

Hawkins, R. H. (1993). "A symptotic determination of runoff curve numbers from data." *J. Irrig. and Drain. Engrg.*, ASCE, 119(2), 334–345.

Hebson, C., and Wood, E. F. (1982). "A derived flood frequency distribution using Horton order ratios." *Water Resour. Res.*, 18(5), 1509–1518.

Hjelmfelt, A. T. (1991). "Investigation of curve number procedure." *J. Hydr. Engrg.*, ASCE, 117(6), 725–737.

Hjelmfelt, A. T., and Burwell, R. E. (1984). "Spatial variability of surface runoff." *J. Irrig. and Drain. Engrg.*, ASCE, 110(1), 46–54.

Jamison, V. C., Smith, D. D., and Thornton, J. F. (1968). "Soil and water research on a claypan soil." *USDA, ARS, Tech. Bull. No. 1379*, U.S. Govt. Printing Ofc., Washington, D.C.

Johnson, H. P., and Baker, J. L. (1982). "Field-to-stream transport of agricultural chemicals and sediment in an Iowa watershed part I: Data base for model testing (1976–1978)." *Rep. EPA-600/3-82-032*, Envir. Res. Lab., Envir. Protection Agency (EPA), Athens, Ga.

Julien, P. Y. (1982). "Prédiction d'apport solide pluvial et nival dans les cours d'eau nordiques à partir du ruissellement superficiel," PhD dissertation, Civ. Engrg. Dept., Laval Univ., Québec, Canada (in French).

Julien, P. Y. (1995). *Erosion and sedimentation*. Cambridge University Press, London, England.

Julien, P. Y., and Frenette, M. (1985). "Modeling of rainfall erosion." *J. Hydr. Engrg.*, ASCE, 111(10), 1344–1359.

Julien, P. Y., and Moglen, G. E. (1990). "Similarity and length scale for spatially-varied overland flow." *Water Resour. Res.*, 26(8), 1819–1832.

Kavvas, M. L., and Govindaraju, R. S. (1991). "Stochastic overland flows Part 1: Physics-based evolutionary probability distributions." *Stochastic Hydro. and Hydr.*, 5, 89–104.

Moughamian, M. S., McLaughlin, D. B., and Bras, R. L. (1987). "Estimation of flood frequency: an evaluation of two derived procedures." *Water Resour. Res.*, 23(7), 1309–1319.

Nguyen, V. T. V., and Rousselle, J. (1981). "A stochastic model for the time distribution of hourly rainfall depth." *Water Resour. Res.*, 17(2), 399–409.

Ogden, F. L., and Julien, P. Y. (1993). "Runoff sensitivity to temporal and spatial rainfall variability at runoff plan and small basin scale." *Water Resour. Res.*, 29(8), 2589–2597.

Ogden, F. L., Richardson, J. R., and Julien, P. Y. (1995). "Similarity in catchment response 2. moving rainstorms." *Water Resour. Res.*, 31(6), 1543–1547.

Raines, T., and Valdes, J. B. (1993). "Estimation of flood frequencies for ungaged catchments." *J. Hydr. Engrg.*, ASCE, 119(10), 1138–1154.

Rousseau, C. (1979). "Analyse des caracteristiques hydrologiques d'une couverture nivale," MS thesis, Civ. Engrg. Dept., Laval Univ., Québec, Canada (in French).

Saghafian, B., Julien, P. Y., and Ogden, F. (1995). "Similarity in catchment response 1. stationary rainstorms." *Water Resour. Res.*, 31(6), 1533–1541.

Schaake, J. C., Geyer, J. C., and Knapp, J. W. (1967). "Experimental examination of the rational method." *J. Hydr. Engrg.*, ASCE, 93(6), 353–370.

Shen, H. W., Koch, G. J., and Obeysekera, J. T. B. (1990). "Physically based flood features and frequencies." *J. Hydr. Engrg.*, ASCE, 116(4), 494–514.

Smith, C. N., Leonard, R. A., Langdale, G. W., and Bailey, G. W. (1978). "Transport of agricultural chemicals from small upland piedmont watersheds." *Rep. EPA-600/3-78-056*, U.S. Envir. Protection Agency (EPA), Athens, Ga.

Stedinger, J. R., Vogel, R. M., and Foufoula-Georgiou, E. (1993). "Chapter 18: Frequency analysis of extreme events." *Handbook of hydrology*,. McGraw-Hill, New York, N.Y.

Todorovic, P. (1968). "A mathematical study of precipitation phenomena." *Rep. CER67-68PT65*, Engrg. Res. Ctr., Colorado State Univ., Fort Collins, Colo.

Todorovic, P., and Rousselle, J. (1971). "Some problems of flood analysis." *Water Resour. Res.*, 7(5), 1144–1150.

Todorovic, P., and Woolhiser, D. A. (1974). "Stochastic model of daily rainfall." *Proc., Symp. on Statistical Hydro., Misc. Publ. No. 1275*, U.S. Dept. of Agric., Agric. Res. Service, 232–246.

Villeneuve, G. O. (1968). "Données météorologiques de la station agronomique de Laval." *Data Rep. Publ. MP-9, MP-17, MP-23, MP-33, and MP-52 for 1966, 1967, 1968, 1969, 1970, Publ. MP-9*, Ministère des Richesses Naturelles, Québec, Canada (in French).

Wood, E. F., and Hebson, C. S. (1986). "On hydrologic similarity. 1. Derivation of the dimensionless flood frequency curve." *Water Resour. Res.*, 21(11), 1549–1554.

Woolhiser, D. A. (1975). "Chapter 12: Simulation of unsteady overland flow." *Unsteady flow in open channels*, Water Resources Publications, Littleton, Colo., 485–508.

Woolhiser, D. A. (1977). "Unsteady free-surface flow problems." *Mathematical models for surface water hydrology*, John Wiley & Sons, New York, N.Y., 195–213.

APPENDIX II. NOTATION

The following symbols are used in this paper:

a, b = transform coefficient and exponent;
$\hat{a}$, $\hat{b}$ = inverse transform coefficient and exponent;
C = Chézy coefficient;
$C_{mg/L}$ = sediment concentration in mg/L;
f = Darcy-Weisbach friction factor;
g = gravitational acceleration;
h = flow depth;
i = rainfall intensity;
K = laminar resistance coefficient;
L = runoff length;
M_1, M_2 = first and second moments of distribution;
n = Manning resistance coefficient;
$P(\phi)$ = exceedance probability, $P(\phi) = \int_{\phi}^{\infty} p(\xi)\, d\xi$;
$p(\phi)$ = probability density function;
Q = total discharge;
Q_s = daily sediment discharge;
q = unit discharge;
S = friction slope;
t = time;
t_e = time to equilibrium;
t_r = rainfall duration;
x, $\tilde{x}$, y = variables;
$\bar{x}$ = average value of x;
α, β = coefficient and exponent of resistance relationship;
$\Gamma(x + 1)$ = gamma function, $\Gamma(x + 1) = !(x)$;
θ = dimensionless time, $\theta = (t - t_r)/t_e$;
λ = dimensionless time ratio, $\lambda = t_r/t_e$;
λ_1, λ_2 = reciprocal of average rainstorm duration and intensity;
ν = kinematic fluid viscosity;
Π = double natural logarithm of $P(\phi)$, $\Pi = \ln[-\ln P(\phi)]$;
ϕ = reduced variable;
ψ = dimensionless discharge, $\psi = q/iL$; and
$!(x)$ = factorial function of x, $!x = x(x - 1)(x - 2)\ldots$.

10

CATCHMENT ROUTING

Catchment routing refers to the calculation of flows in time and space within a catchment. The objective of catchment routing is to transform effective rainfall into streamflow. This is accomplished either in a lumped mode (e.g., time-area method) or in a distributed mode (e.g., kinematic wave method).

Methods for catchment routing are similar to those of reservoir and stream channel routing. In fact, many techniques used in reservoir and channel routing are also applicable to catchment routing. For instance, the concept of linear reservoir is used in both reservoir and catchment routing. Kinematic wave techniques were originally developed for river routing [9], but later were applied to catchment routing [19, 22].

Methods for catchment routing are of two types: (1) hydrologic and (2) hydraulic. Hydrologic methods are based on the storage concept and are spatially lumped to provide a runoff hydrograph at the catchment outlet. Examples of hydrologic catchment routing methods are the time-area method and the cascade of linear reservoirs. Hydraulic methods use kinematic or diffusion waves to simulate surface runoff within a catchment in a distributed context. Unlike hydrologic methods, hydraulic methods can provide runoff hydrographs inside the catchment.

Catchment routing models can use parametric, conceptual, and/or deterministic components. For instance, the hydrograph obtained by the time-area method can be routed through a linear reservoir using a storage constant derived by empirical (i.e., parametric) means. The cascade of linear reservoirs is a typical example of a conceptual model used in catchment routing. Kinematic and diffusion models are examples of deterministic methods used in catchment routing.

The concepts of *translation* and *storage* are central to the study of flow routing, whether in catchments, reservoirs, or stream channels. They are particularly important in catchment routing because they can be studied separately, unlike in reservoir and channel routing. Translation may be interpreted as the movement of water in a direction parallel to the channel bottom. Storage may be interpreted as the movement of water in a direction perpendicular to the channel bottom. Translation is synonymous with runoff concentration; storage is synonymous with runoff diffusion.

In reservoir routing, storage is the primary mechanism, with translation almost nonexistent. In stream channel routing, the situation is reversed, with translation being the predominant mechanism and storage playing only a minor role. This is the reason why kinematic and diffusion waves are useful models of stream channel routing. In catchment routing, translation and storage are about equally important, and, therefore, they are often accounted for separately. The translation effect can be related to runoff concentration, whereas the storage effect can be simulated with linear reservoirs.

This chapter is divided into six sections. Section 10.1 describes the time-area method of hydrologic catchment routing. Section 10.2 describes the Clark unit hydrograph, a procedure closely related to the time-area method. Section 10.3 deals with the cascade of linear reservoirs, a widely accepted method of hydrologic catchment routing. Sections 10.4 and 10.5 describe two hydraulic methods of catchment routing, based on kinematic and diffusion waves, respectively. Section 10.6 contains a discussion of the capabilities and limitations of catchment routing techniques.

10.1 TIME-AREA METHOD

The time-area method of hydrologic catchment routing transforms an effective storm hyetograph into a runoff hydrograph. The method accounts for translation only and does not include storage. Therefore, hydrographs calculated with the time-area method show a lack of diffusion, resulting in higher peaks than those that would have been obtained if storage had been taken into account. If necessary, the required amount of storage can be incorporated by routing the hydrograph obtained by the time-area method through a linear reservoir. The required amount of storage is determined by calibrating the linear reservoir storage constant K with measured data. Alternatively, suitable values of K can be estimated based on regionally derived formulas.

The time-area method is essentially an extension of the runoff concentration principle used in the rational method (Chapter 4). Unlike the rational method, however, the time-area method can account for the temporal variation of rainfall intensity. Therefore, the applicability of the time-area method is extended to midsize catchments.

The time-area method is based on the concept of *time-area histogram,* i.e., a histogram of contributing catchment subareas. To develop a time-area histogram, the catchment's time of concentration is divided into a number of equal time intervals. Cumulative time at the end of each time interval is used to divide the catchment into zones delimited by *isochrone lines,* i.e., the loci of points of equal travel time to the catchment outlet, as shown in Fig. 10-1(a). For any point inside the catchment, the travel time refers to the time that it would take a parcel of water to travel from that

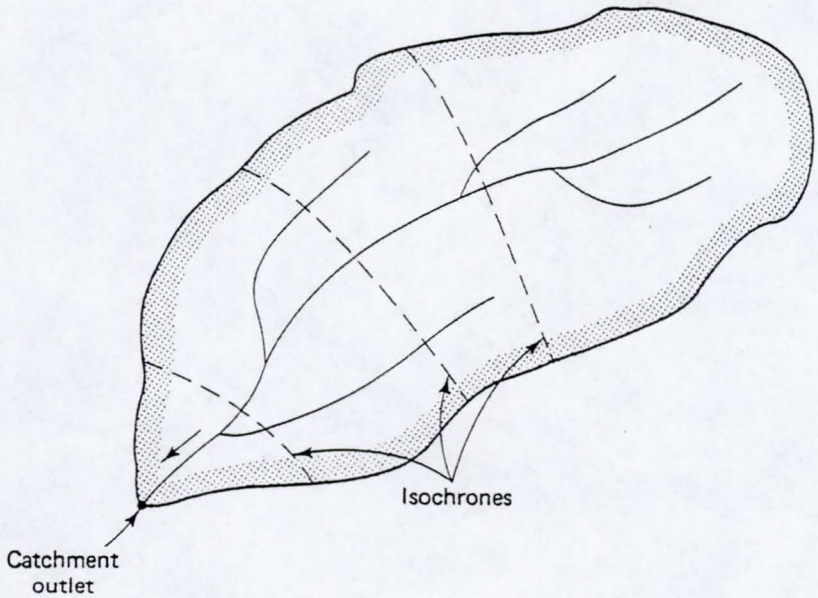

(a)

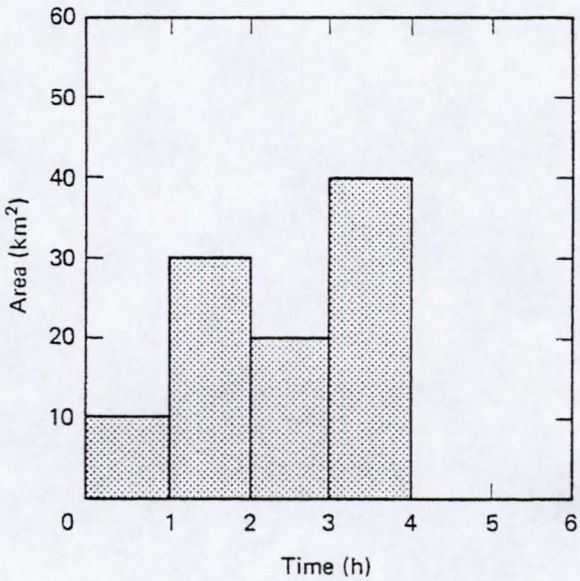

(b)

Figure 10-1 Time-area method: (a) isochrone delineation; (b) time-area histogram.

point to the outlet. The catchment subareas delimited by the isochrones are measured and plotted in histogram form as shown in Fig. 10-1(b).

The time interval of the effective rainfall hyetograph should be equal to the time interval of the time-area histogram. The rationale of the time-area method is that, according to the runoff concentration principle (Section 2.4), the partial flow at the end of each time interval is equal to the product of effective rainfall times contributing subarea. The lagging and summation of the partial flows results in a runoff hydrograph for the given effective rainfall hyetograph and time-area histogram. While the time-area method accounts for runoff concentration only, it has the advantage that the catchment shape is reflected in the time-area histogram and, therefore, in the runoff hydrograph. The procedure is illustrated by the following example.

Example 10-1.

A 100-km^2 catchment has a 4-h concentration time, with isochrones at 1-h intervals resulting in the time-area histogram shown in Fig. 10-1(b). A 6-h storm has the following effective rainfall hyetograph (Fig. 10-2):

Time (h)	0	1	2	3	4	5	6
Effective rainfall (cm/h)	0.5	1.0	2.0	1.5	1.0	0.5	

Use the time-area method to calculate the outflow hydrograph.

The routing is shown in Table 10-1. Column 1 shows time in hours. The flows shown in Cols. 2-7 were obtained by multiplying effective rainfall intensity times the contributing partial area. For instance, Col. 2 shows the contribution of the first effective rainfall interval (0.5 cm/h) on each of the subareas (10, 30, 20, and 40 km^2). At $t = 1$ h, the partial flow due to the first effective rainfall interval is 0.5 cm/h $\times$ 10 km^2 = 5 km^2-cm/h (i.e., the flow contributed by the subarea enclosed within the catchment outlet and the first isochrone takes 1 h to concentrate). Likewise, at $t = 2$ h, the partial flow due to the first effective rainfall interval is 0.5 cm/hr $\times$ 30 km^2 = 15 km^2-cm/h (i.e., the flow contributed by the subarea enclosed within the first and second isochrones takes 2 h to concentrate at the catchment outlet). The remaining values in Col. 2 (10 and 20) are calculated in a similar way. Finally, at $t = 5$ h, the flow is zero because it takes a full time interval (in the absence of runoff diffusion) for the last concentrated partial flow to recede back to zero. Columns 2 to 7 show the partial flows contributed by the six effective rainfall intervals, each appropriately lagged a time interval (because the contribution of the second rainfall interval starts at $t = 1$, the third rainfall interval at $t = 2$, and so on). The sum of these partial flows, shown in Col. 8, is the catchment outflow hydrograph. In Col. 9, the hydrograph of Col. 8 is expressed in cubic meters per second. The time base of the outflow hydrograph is 10 h, which is equal to the concentration time (4 h) plus the effective rainfall duration (6 h). To verify the accuracy of the computations, the sum of Col. 8 is 650 km^2-cm/h, which represents 6.5 cm of effective rainfall depth uniformly distributed over the entire catchment area (100 km^2). This value (6.5 cm) agrees with the total amount of effective rainfall.

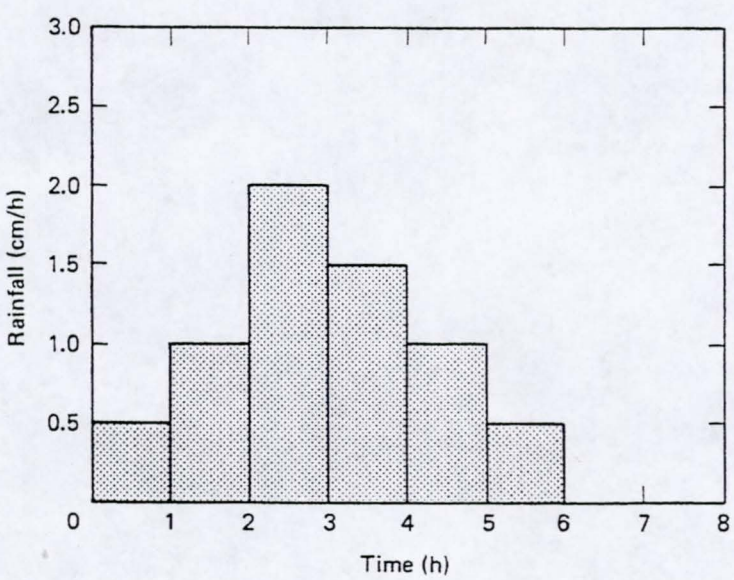

Figure 10-2 Effective rainfall hyetograph: Example 10-1.

TABLE 10-1 TIME-AREA METHOD OF CATCHMENT ROUTING: EXAMPLE 10-1

(1)	(2)	(3)	(4)	(5)	(6)	(7)	(8)	(9)
	Partial Flows and Sum (km^2-cm/h)							
Time (h)	0.5 cm/h	1.0 cm/h	2.0 cm/h	1.5 cm/h	1.0 cm/h	0.5 cm/h	Sum	Flow (m^3/s)
0	0						0	0.0
1	5	0					5	13.9
2	15	10	0				25	69.4
3	10	30	20	0			60	166.7
4	20	20	60	15	0		115	319.4
5	0	40	40	45	10	0	135	375.0
6		0	80	30	30	5	145	402.8
7			0	60	20	15	95	263.9
8				0	40	10	50	138.9
9					0	20	20	55.6
10						0	0	0.0
Total							650	

It is readily seen that the time-area method and the rational method share a common theoretical basis. However, since the time-area method uses effective rainfall and does not rely on runoff coefficients, it can account only for runoff concentration, with no provision for runoff diffusion. Diffusion can be provided by routing the hydrograph calculated by the time-area method through a linear reservoir with an appropriate storage constant.

The time-area method leads to an alternate way of calculating concentration time. Provided there is no runoff diffusion, as would be the case of a hydrograph calculated by the time-area method, concentration time can be calculated as the difference between hydrograph time base and effective rainfall duration. Intuitively, as rainfall ceases, the farthest parcels of water concentrate at the catchment outlet at a time equal to the concentration time. Therefore,

$$t_c = T_b - t_r \tag{10-1}$$

in which t_c = concentration time, T_b = time base of the translated-only hydrograph, and t_r = effective rainfall duration.

Equation 10-1 can also be expressed in a slightly different form. Assuming that the point of inflection (i.e., the point of zero curvature) on the receding limb of a measured (i.e., translated and diffused) hydrograph coincides with the end of the translated-only hydrograph, the time to point of inflection of the measured hydrograph can be used in Eq. 10-1 in lieu of time base. Therefore, concentration time can be defined as the difference between the time to point of inflection and the effective rainfall duration (see Fig. 10-3):

$$t_c = t_i - t_r \tag{10-2}$$

in which t_i = time to point of inflection on the receding limb of a measured hydrograph. The advantage of Eq. 10-2 over Eq. 10-1 is that, unlike the time base of the

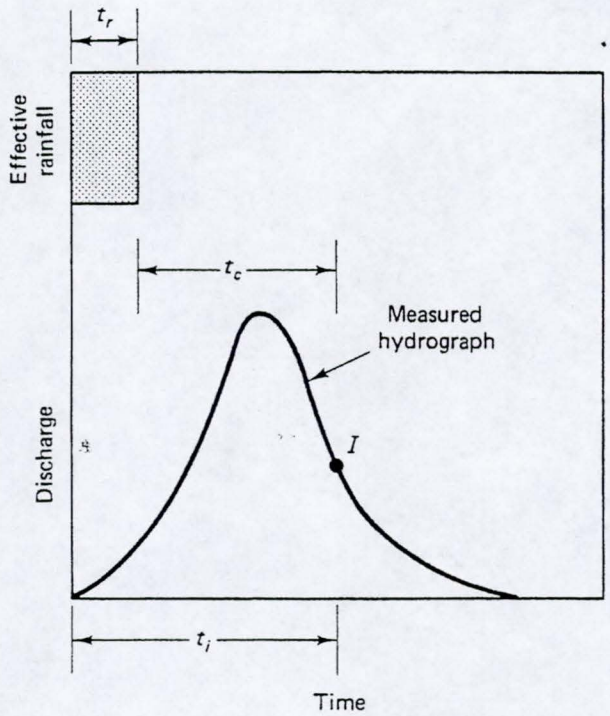

Figure 10-3 Alternate definition of concentration time.

translated-only hydrograph, the point of inflection on the receding limb of a measured hydrograph can be readily ascertained.

10.2 CLARK UNIT HYDROGRAPH

The procedure to derive a Clark unit hydrograph parallels that of the time-area method [2]. First, it is necessary to determine the catchment isochrones. In the Clark method, however, a *unit* effective rainfall is used in lieu of the effective storm hyetograph used in the time-area method. This leads to an outflow hydrograph corresponding to a unit runoff depth, that is, a unit hydrograph. Since the unit hydrograph calculated in this way lacks runoff diffusion, Clark suggested that it be routed through a linear reservoir. As with the time-area method, an estimate of the linear reservoir storage constant is required. This can be obtained either from the tail of a measured hydrograph or by using a regionally derived formula. In the latter case, the Clark unit hydrograph can be properly regarded as a synthetic unit hydrograph.

Like the time-area method, the Clark unit hydrograph method has the advantage that the catchment's properties (shape, hydraulic length, surface roughness, and so on) are reflected in the time-area histogram and, therefore, on the shape of the unit hydrograph. This feature has contributed to the popularity of the Clark unit hydrograph in engineering practice [7].

When using the Clark or time-area methods, the storage constant can be estimated from the tail of a measured hydrograph. For this purpose, the differential equation of storage (Eq. 8-4) is evaluated at a time for which inflow equals zero ($I = 0$), i.e., past the end of the translated-only hydrograph. Alternatively, it can be evaluated at the point of inflection on the receding limb of a measured hydrograph (Fig. 10-3). This leads to:

$$-O = \frac{dS}{dt} \tag{10-3}$$

and since $S = KO$, the following expression for K is obtained:

$$K = -\frac{O}{\frac{dO}{dt}} \tag{10-4}$$

in which O and dO/dt are evaluated past the end of the translated-only hydrograph or at (the time to) the point of inflection on the receding limb of a measured hydrograph.

The derivation of the Clark unit hydrograph is illustrated by the following example.

Example 10-2.

Use the Clark method to derive a 2-h unit hydrograph for the catchment of Example 10-1. To provide storage, route the translated-only hydrograph through a linear reservoir of storage constant $K = 2$ h. Use $\Delta t = 1$ h.

The 2-h unit hydrograph has an effective rainfall intensity of 0.5 cm/h (i.e., 1-cm depth over a 2-h duration). The calculations are shown in Table 10-2. Column 1 shows time in

TABLE 10-2 DERIVATION OF CLARK UNIT HYDROGRAPH: EXAMPLE 10-2

(1)	(2)	(3)	(4)	(5)	(6)	(7)	(8)	(9)
	Partial Flows and Sum (km^2-cm/h)							
Time (h)	0.5 cm/h	0.5 cm/h	Sum	C_0I_2	C_1I_1	C_2O_1	Sum	Flow (m^3/s)
0	0		0	—	—	—	0.00	0.00
1	5	0	5	1	0	0	1.00	2.78
2	15	5	20	4	1	0.60	5.60	15.55
3	10	15	25	5	4	3.36	12.36	34.33
4	20	10	30	6	5	7.42	18.42	51.17
5	0	20	20	4	6	11.05	21.05	58.47
6	0	0	0	0	4	12.63	16.63	46.19
7	0	0	0	0	0	9.98	9.98	27.72
8	0	0	0	0	0	5.99	5.99	16.64
9						3.59	3.59	9.97
10						2.15	2.15	5.97
11						1.29	1.29	3.58
12						0.78	0.78	2.17
13						0.46	0.46	1.28
14						0.28	0.28	0.78
15						0.17	0.17	0.47
16						0.10	0.10	0.28
17						0.06	0.06	0.17
18						0.04	0.04	0.11
19						0.02	0.02	0.06
20						0.01	0.01	0.03
Total			100				99.98	

hours. Column 2 shows the contribution of the first hour, with 0.5 cm/h of effective rainfall. The procedure is the same as in Table 10-1, Col. 2. Column 3 shows the contribution of the second hour, with 0.5 cm/h of effective rainfall. Again, the procedure is the same as in Table 10-1, Col. 2, but the partial flows are lagged 1 h. The translated-only unit hydrograph shown in Col. 4 is the sum of the partial flows (Cols. 2 and 3). The translated-only unit hydrograph (Col. 4) is the inflow to the linear reservoir. With $\Delta t/K = \frac{1}{2}$, the routing coefficients (Table 8-1) are $C_0 = \frac{1}{5}$, $C_1 = \frac{1}{5}$, and $C_2 = \frac{3}{5}$. The partial flows of the linear reservoir routing are shown in Cols. 5 to 7, and the translated-and-diffused unit hydrograph (in km^2-cm/h) shown in Col. 8 is the sum of Cols. 5 to 7 (See Example 8-1 for details of the linear reservoir-routing procedure). Column 9 shows the translated-and-diffused Clark unit hydrograph in cubic meters per second. The sum of the ordinates of the translated-only hydrograph (Col. 4) is 100, which amounts to 1 cm of effective rainfall depth uniformly distributed over 100 km^2 of catchment area. Likewise, the sum of the ordinates of the translated-and-diffused hydrograph (Col. 8) is 99.98, which verifies not only that the calculated hydrograph is a unit hydrograph but also that the calculation is mass (i.e., volume) conservative. Notice that the peak of the translated-only unit hydrograph (Col. 4) is 30 km^2-cm/h, whereas the peak of the translated-and-diffused unit hydrograph (Col. 8) is 21.05 km^2-cm/h. Also, notice that the time base of the translated-only unit hydrograph ends sharply at 6 h, whereas the time base of the translated and diffused unit hydrograph is much longer, with the receding limb of the unit hydrograph gradually approaching zero. This reveals the substantial amount of runoff diffusion provided by the linear reservoir.

By using Eq. 10-4, the linear reservoir storage constant can be calculated directly from the tail of a measured hydrograph. To illustrate the procedure, in Table 10-2, Col. 9, the two lines for $t = 6$ h and $t = 7$ h show zero outflow in the translated-only unit hydrograph (Col. 4), that is, *zero inflow* to the linear reservoir. Therefore, Eq. 10-4 can be applied between $t = 6$ h and $t = 7$ h. The average outflow (Col. 9) is $(46.19 + 27.72)/2 = 36.955$ m^3/s and the rate of change of outflow is $(27.72 - 46.19)/(1\text{ h}) = -18.47$ (m^3/s)/h. Therefore, the storage constant (Eq. 10-4) is: $K = -(36.955)/(-18.47) = 2$ h. Likewise, between $t = 7$ h and $t = 8$ h: $K = -[(27.72 + 16.64)/2]/[(16.64 - 27.72)/(1)] = 2$ h. In other words, Eq. 10-4 applies at the tail of the outflow hydrograph, after the translated-only (inflow) hydrograph has receded back to zero. When using the Clark (or time-area) method, the time base of the translated-only hydrograph is equal to the sum of concentration time plus the unit hydrograph (or effective storm) duration (See Eq. 10-1).

With the help of regional analysis (Chapter 7), the Clark parameters (concentration time and linear reservoir storage constant) can be estimated based on catchment characteristics. This effectively qualifies the Clark unit hydrograph as a synthetic unit hydrograph. The Eaton [4], O'Kelly [11], and Cordery [3] models are examples of this approach. See Singh [16] for a recent review.

10.3 CASCADE OF LINEAR RESERVOIRS

As seen in Section 8.2, a linear reservoir has a diffusion effect on the inflow hydrograph. If an inflow hydrograph is routed through a linear reservoir, the outflow hydrograph has a reduced peak and an increased time base. This increase in time base causes a difference in the relative timing of inflow and outflow hydrographs, referred

to as the *lag*. The amount of diffusion (and associated lag) is a function of the ratio $\Delta t/K$, a larger diffusion effect corresponding to smaller values of $\Delta t/K$.

The cascade of linear reservoirs is a widely used method of hydrologic catchment routing. As its name implies, the method is based on the connection of several linear reservoirs in series. For N such reservoirs, the outflow from the first would be taken as inflow to the second, the outflow from the second as inflow to the third, and so on, until the outflow from the $(N - 1)$th reservoir is taken as inflow to the Nth reservoir. The outflow from the Nth reservoir is taken as the outflow from the cascade of linear reservoirs. Admittedly, the cascade of reservoirs to simulate catchment response is an abstract concept. Nevertheless, it has proven to be quite useful in practice.

Each reservoir in the series provides a certain amount of diffusion and associated lag. For a given set of parameters $\Delta t/K$ and N, the outflow from the last reservoir is a function of the inflow to the first reservoir. In this way, a one-parameter linear reservoir method ($\Delta t/K$) is extended to a two-parameter catchment routing method. Moreover, the basic routing formula (Eq. 8-15) and routing coefficients (Eqs. 8-16 to 8-18) remain essentially the same.

The addition of the second parameter (N) provides considerable flexibility in simulating a wide range of diffusion and associated lag effects. However, the conceptual basis of the method restricts its general use, since no relation between either of the parameters to the physical problem can be readily envisaged. Notwithstanding this apparent limitation, the method has been widely used in catchment simulation, primarily in applications involving large gaged river basins. Rainfall-runoff data can be used to calibrate the method, i.e., to determine a set of parameters $\Delta t/K$ and N that produces the best fit to the measured data.

The analytical version of the cascade of linear reservoirs is referred to as the Nash model [10]. The numerical version is featured in several hydrologic simulation models developed in the United States and other countries. Notable among them is the SSARR model (Chapter 13), which uses it in its watershed and stream channel routing modules [18]. To derive the routing equation for the method of cascade of linear reservoirs, Eq. 8-15 is reproduced here in a slightly different form:

$$Q_{j+1}^{n+1} = C_0\, Q_j^{n+1} + C_1\, Q_j^n + C_2\, Q_{j+1}^n \tag{10-5}$$

in which Q represents discharge, whether inflow or outflow and j and n are space and time indexes, respectively (Fig. 10-4).

As with Eq. 8-15, the routing coefficients C_0, C_1 and C_2 are a function of the dimensionless ratio $\Delta t/K$. This ratio is properly a Courant number ($C = \Delta t/K$). In terms of Courant number, Eqs. 8-16 to 8-18 are expressed as follows:

$$C_0 = \frac{C}{2 + C} \tag{10-6}$$

$$C_1 = C_0 \tag{10-7}$$

$$C_2 = \frac{2 - C}{2 + C} \tag{10-8}$$

For application to catchment routing, it is convenient to define the average inflow as follows:

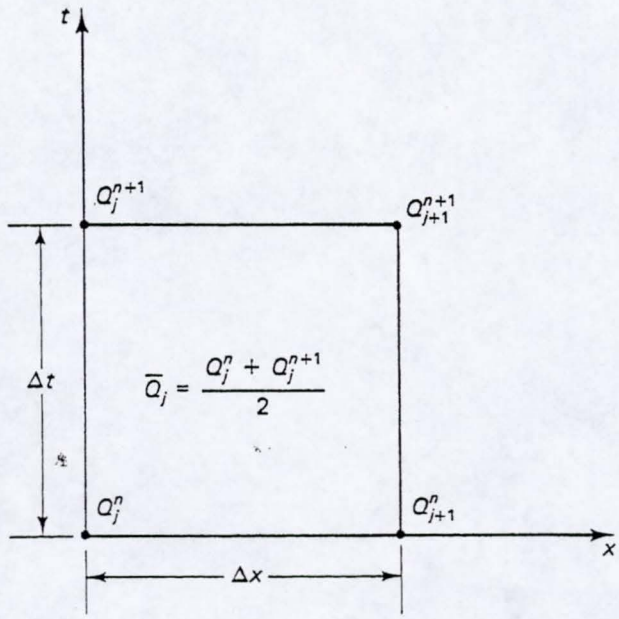

Figure 10-4 Space-time discretization in the method of cascade of linear reservoirs.

$$\bar{Q}_j = \frac{Q_j^n + Q_j^{n+1}}{2} \tag{10-9}$$

Substituting Eq. 10-6 to 10-9 into 10-5 gives

$$Q_{j+1}^{n+1} = 2C_1\bar{Q}_j + C_2Q_{j+1}^n \tag{10-10}$$

or, alternatively:

$$Q_{j+1}^{n+1} = \frac{2C}{2 + C}[\bar{Q}_j - Q_{j+1}^n] + Q_{j+1}^n \tag{10-11}$$

which is the routing equation used in the SSARR model [18]. Equations 10-10 and 10-11 are in a form convenient for catchment routing because the inflow is usually a rainfall hyetograph, that is, a constant average value per time interval.

Smaller values of C lead to greater amounts of runoff diffusion. For values of C greater than 2, the behavior of Eq. 10-10 (or Eq. 10-11) is highly dependent on the type of input. For instance, in the case of a unit impulse (rainfall duration equal to the time interval), Eq. 10-10 (or Eq. 10-11) results in negative outflow values (numerical instability). For this reason, Eq. 10-10 is restricted in practice to $C \leq 2$.

The method of cascade of linear reservoirs is illustrated by the following example.

Example 10-3.

Use the method of cascade of linear reservoirs to route the following effective storm hyetograph for a 1000 km^2 basin. Use $N = 3$, $\Delta t = 6$ h and $K = 12$ h.

Time (h)	0	6	12	18	24
Effective rainfall (cm/h)	0.2	1.0	0.8	0.4	
Effective rainfall (cm)	1.2	6.0	4.8	2.4	

The Courant number is $C = \Delta t/K = \frac{6}{12} = \frac{1}{2}$, which results in $2C_1 = \frac{2}{5}$, and $C_2 = \frac{3}{5}$. The computations are shown in Table 10-3. Column 1 shows time in hours. Column 2 shows the inflow to the first reservoir (in km^2-cm/h) calculated by multiplying each one of

TABLE 10-3 CASCADE OF LINEAR RESERVOIRS: EXAMPLE 10-3

(1)	(2)	(3)	(4)	(5)	(6)	(7)
	Flow (km^2-cm/h)					
	$N = 1$		$N = 2$		$N = 3$	
Time (h)	Inflow	Outflow	Inflow	Outflow	Inflow	Outflow
0	200	0.00	40.00	0.00	8.00	0.00
6	1000	80.00	264.00	16.00	65.60	3.20
12	800	448.00	518.40	115.20	195.84	28.16
18	400	588.80	551.04	276.48	331.39	95.23
24	0	513.28	411.62	386.30	391.36	189.69
30	0	309.97	247.38	396.43	366.62	270.36
36	0	184.78	147.83	336.81	299.01	308.86
42	0	110.87	88.69	261.22	226.71	304.92
48	0	66.52	53.21	192.21	164.41	273.64
54	0	39.91	31.93	136.61	115.68	229.95
60	0	23.95	19.16	94.74	79.63	184.24
66	0	14.37	11.50	64.51	53.91	142.40
72	0	8.62	6.89	43.31	36.02	107.00
78	0	5.17	4.14	28.74	23.82	78.61
84	0	3.10	2.48	18.90	15.62	56.69
90	0	1.86	1.49	12.33	10.16	40.26
96	0	1.12	0.89	7.99	6.57	28.22
102	0	0.67	0.53	5.15	4.22	19.56
108	0	0.40	0.32	3.30	2.70	13.42
114	0	0.24	0.19	2.11	1.73	9.30
120		0.14		1.34		6.17
	2400	2401.77		2399.68		2389.71

the effective rainfall intensities (0.2, 1.0, 0.8, and 0.4 cm/h) times the basin area (1000 km^2). Column 3 is the outflow from the first reservoir. Columns 4 and 5 are the inflow and outflow for the second reservoir. Columns 6 and 7 are the inflow and outflow for the third reservoir. (All values shown are in km^2-cm/h; to convert to m^3/s, multiply by 2.78). To illustrate the calculations for the first reservoir, following Eq. 10-10, $\frac{2}{5}$ of the average inflow for the first time interval [$(\frac{2}{5}) \times 200$ km^2-cm/h] plus $\frac{3}{5}$ of the outflow at time $t = 0$ h [$(\frac{3}{5}) \times 0$ km^2-cm/h] is equal to the outflow at 6 h: 80 km^2-cm/h. Likewise, $\frac{2}{5}$ of the average inflow for the second time interval [$(\frac{2}{5}) \times 1000$ km^2-cm/hr] plus $\frac{3}{5}$ of the outflow at time $t = 6$ h [$(\frac{3}{5}) \times 80$ km^2-cm/h] is equal to the outflow at 12 h: 448 km^2-cm/h, and so on. The (average) inflow to the second reservoir (Col. 4) is the average outflow from the first reservoir (Col. 3). For instance, for the first time interval, 40 km^2-cm/h is the average of 0 and 80 km^2-cm/h. The calculations proceed in a recursive fashion until the routing through the three linear reservoirs has been completed. Notice that the sum of Cols. 3, 5 and 7 is approximately the same: 2400 km^2-cm/hr. Since the time interval is 6 h, this is equivalent to $2400 \times 6/1000 = 14.4$ cm of effective rainfall depth uniformly distributed over 1000 km^2 of basin area. Also notice that the peak outflow from the first reservoir is 588.8 km^2-cm/h, and it occurs at 18 h; the peak outflow from the second reservoir is 396.43 km^2-cm/h, occurring at 30 h; and the peak outflow from the third reservoir is 308.86 km^2-cm/h, occurring at 36 h. This shows that the effect of the cascade is to produce a certain amount of runoff diffusion at every step, with a corresponding increase in the lag of catchment response.

The cascade of linear reservoirs provides a convenient mechanism for simulating a wide range of catchment routing problems. Furthermore, the method can be applied to each runoff component (surface runoff, subsurface runoff, and baseflow) separately, and the catchment response can be taken as the sum of the responses of the individual components. For instance, assume that a certain basin has 10 cm of runoff, of which 7 cm are surface runoff, 2 cm are subsurface runoff, and 1 cm is baseflow. Since surface runoff is the less diffused process, it can be simulated with a high Courant number, say $C = 1$, and a small number of reservoirs, say $N = 3$. Subsurface runoff is much more diffused than surface runoff; therefore, it can be simulated with $C = 0.4$ and $N = 5$. Baseflow, being very diffused, can be simulated with $C = 0.1$, and $N = 7$. In practice, the parameters C and N are determined by extensive calibration. In this sense, the cascade of linear reservoirs remains essentially a conceptual model [15].

10.4 CATCHMENT ROUTING WITH KINEMATIC WAVES

Hydraulic catchment routing using kinematic waves was introduced by Wooding in 1965 [19, 20, 21]. Since then, the kinematic wave approach has been widely used in deterministic catchment modeling. The approach can be either lumped or distributed, depending on whether the parameters are kept constant or allowed to vary in space. Analytical solutions are suited to lumped modeling, whereas numerical solutions are more appropriate for distributed modeling.

Wooding used an open-book geometric configuration (Fig. 4-15) to represent the catchment-stream problem physically. As its name implies, an open-book configuration consists of two rectangular catchments separated by a stream and draining laterally into it; in turn the streamflow drains out of the catchment outlet. Wooding used analytical solutions of kinematic waves and the method of characteristics to formulate his method. Since diffusion is absent from these solutions, the method is strictly applicable only to kinematic waves. Criteria for the applicability of kinematic waves have been developed by Woolhiser and Liggett [22] (Eq. 4-51) for overland flow, and by Ponce et al. [12] for stream channel flow (Eq. 9-44).

Kinematic catchment routing models can be approached in a variety of ways. Methods can be either (1) analytical or numerical, (2) lumped or distributed, (3) linear or nonlinear, or (4) single plane, two-plane, or a cascade of planes [7, 8]. Analytical models take advantage of the nondiffusive properties of kinematic waves, whereas numerical models are usually based on the method of finite differences or the method of characteristics. Linear models assume a constant wave celerity, but nonlinear models relax this restriction. The feature of variable wave celerity often renders the nonlinear models impractical because of wave steepening and associated *kinematic shock* development [8, 13]. Single- and two-plane models are used in hydrologic engineering practice [7].

The application of kinematic wave modeling to catchment routing is illustrated here with an example of a two-plane finite difference numerical model. The model could be either lumped or distributed, depending on whether the inputs and parameters are allowed to vary in space or not. For simplicity, this example considers constant

input (i.e., constant effective rainfall) and constant parameters (i.e., a linear mode of computation). In practice, a computer-aided solution may relax this restriction.

Two-Plane Linear Kinematic Catchment Routing Model

Assume a catchment configured as two rectangular planes adjacent to each other, draining laterally into a stream channel located between them. Each of the planes is 100 m long by 200 m wide, and the channel is 200 m long (Fig. 10-5). The bottom friction in the planes and channel is such that the average velocity in the planes is 0.0417 m/s and the average velocity in the channel is 0.3 m/s. It is desired to obtain the hydrograph at the catchment outlet resulting from an effective rainfall of 9 cm/h lasting 20 min.

Calculation of Flow Parameters. Since the model is linear, it is first necessary to calculate the flow parameters on which to base the calculation of the routing parameters and coefficients.

The flow per unit width in the midlength of each plane is equal to the effective rainfall intensity times the contributing area (50 m × 1 m):

$$q_p = \frac{9 \text{ cm/h} \times 50 \text{ m} \times 0.01 \text{ m/cm}}{3600 \text{ s/h}} = 0.00125 \text{ m}^2/\text{s} \tag{10-12}$$

Since the average velocity in the planes is $v_p = 0.0417$ m/s, the average flow depth in the planes is $d_p = q_p/v_p = 0.03$ m. Laminar flow in the planes is assumed, with discharge-depth rating exponent $\beta_p = 3$. Therefore, the wave celerity in the planes is $c_p = \beta_p v_p = 0.125$ m/s.

The flow in the midlength of the channel is equal to the effective rainfall intensity times the contributing area (2 planes × 100 m × 100 m):

$$Q_c = \frac{9 \text{ cm/h} \times 2 \times 100 \text{ m} \times 100 \text{ m} \times 0.01 \text{ m/cm}}{3600 \text{ s/h}} = 0.5 \text{ m}^3/\text{s} \tag{10-13}$$

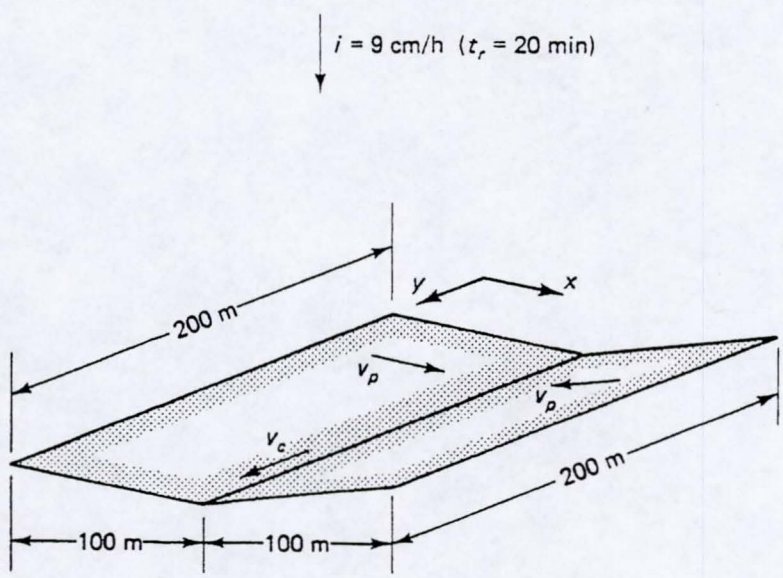

$v_p = 0.0417$ m/s
$v_c = 0.3$ m/s

Figure 10-5 Two-plane linear kinematic catchment routing model.

Assume a channel top width $T_c = 5$ m. Therefore, the flow per unit width in the channel is $q_c = Q_c/T_c = 0.1$ m^2/s. Since the average velocity in the channel is $v_c = 0.3$ m/s, the average flow depth in the channel (at midlength) is $d_c = q_c/v_c = 0.333$ m. A wide channel and turbulent Manning friction is assumed, with discharge-area rating exponent $\beta_c = 1.67$. Therefore, the wave celerity in the channel is $c_c = \beta_c v_c = 0.5$ m/s.

The concentration time is equal to the travel time in the planes plus the travel time in the channel. The travel time in the planes is (100 m)/(0.125 m/s) = 800 s. The travel time in the channel is (200 m)/(0.5 m/s) = 400 s. Therefore, the concentration time is 800 + 400 = 1200 s, which is equal to the effective rainfall duration. This assures concentrated flow at the catchment outlet.

The maximum possible (i.e., equilibrium) peak flow is equal to the product of rainfall intensity and catchment area:

$$Q_e = \frac{9 \text{ cm/h} \times 2 \times 100 \text{ m} \times 200 \text{ m} \times 0.01 \text{ m/cm}}{3600 \text{ s/h}} = 1 \text{ m}^3/\text{s} \qquad (10\text{-}14)$$

The total volume of runoff is

$$V_r = \frac{9 \text{ cm/h} \times 20 \text{ min} \times 2 \times 100 \text{ m} \times 200 \text{ m}}{100 \text{ cm/m} \times 60 \text{ min/h}} = 1200 \text{ m}^3 \qquad (10\text{-}15)$$

Selection of Discrete Intervals. For simplicity, a space interval $\Delta x = 100$ m is chosen for the planes. This amounts to one spatial increment in the planes. In an actual application using a computer, a smaller value of Δx would be indicated. The time interval is chosen as $\Delta t = 10$ min. This leads to a Courant number in the planes $C_p = c_p(\Delta t/\Delta x) = 0.75$. In the case of the channel, a space interval $\Delta y = 200$ m is chosen, that is, one spatial increment in the channel. This leads to a Courant number in the channel $C_c = c_c(\Delta t/\Delta y) = 1.5$.

Selection of Routing Scheme. There are many possible choices for routing scheme. Either first- or second-order schemes may be used (Section 9.2). In practice, first-order schemes are preferred because they are *more stable* than second-order schemes (compare the results of a first order scheme, Table 9-5, with those of a second order scheme, Table 9-4).

Two first-order schemes are chosen here: (1) Scheme I, forward-in-time, backward-in-space, stable for Courant numbers less than or equal to 1 (similar to the convex method, see Example 9-5), and (2) Scheme II, forward-in-space, backward-in-time, stable for Courant numbers greater than or equal to 1 (exact opposite of the convex method). The use of these two schemes guarantees that the solution will remain stable because scheme I is used for Courant numbers less than or equal to 1, whereas scheme II is used for Courant numbers greater than 1 [7]. In the present application, scheme I is used for routing in the planes ($C_p = 0.75$), and scheme II is used for routing in the channel ($C_c = 1.5$).

Lateral inflows are an integral part of catchment routing. For routing in the planes, lateral inflow is the effective rainfall; for channel routing, lateral inflow is the lateral contribution from the planes. Therefore, it is necessary to discretize the kinematic wave equation with lateral inflow, Eq. 9-43.

The discretization of Eq. 9-43 in a forward-in-time, backward-in-space linear scheme (Fig. 10-6(a)) leads to:

$$Q_{j+1}^{n+1} = C_1 Q_j^n + C_2 Q_{j+1}^n + C_3 Q_L \tag{10-16}$$

in which $C_1 = C$; $C_2 = 1 - C$; and $C_3 = C$, with C being the Courant number ($C = \beta v\ \Delta t/\Delta s$), with Δs either Δx (planes) or Δy (channel). The term Q_L is the lateral inflow in cubic meters per second. For routing in the planes, the lateral inflow is equal to the effective rainfall (centimeters per hour) times the applicable area (square meters). For channel routing, the lateral inflow is the average distributed lateral inflow (cubic meters per second per meter) multiplied by the channel length (meters).

The discretization of Eq. 9-43 in a forward-in-space, backward-in-time linear scheme (Fig. 10-6(b)) leads to:

$$Q_{j+1}^{n+1} = C_0 Q_j^{n+1} + C_1 Q_j^n + C_3 Q_L \tag{10-17}$$

in which $C_0 = (C - 1)/C$; $C_1 = 1/C$; and $C_3 = 1$.

The catchment routing is shown in Table 10-4. Column 1 shows time in minutes. Columns 2–4 show the plane routing, and Cols. 5–7 show the channel routing. Column 2 shows the lateral inflow to each plane:

$$Q_{Lp} = \frac{9\ \text{cm/h} \times 100\ \text{m} \times 200\ \text{m} \times 0.01\ \text{m/cm}}{3600\ \text{s/h}} = 0.5\ \text{m}^3/\text{s} \tag{10-18}$$

Notice that the lateral inflow is an average value for a time interval, and it lasts 20 min (i.e., the effective rainfall duration). Column 3 shows the upstream inflow to the plane, that is, zero (this example does not consider upstream inflow to the planes). Column 4 is obtained by routing with Eq. 10-16, with Courant number in the planes $C_p = 0.75$. Column 4 is the outflow hydrograph from each plane. The sum of Col. 2 is 1.0; likewise, the sum of Col. 4 is 0.9999, which confirms that the volume under the

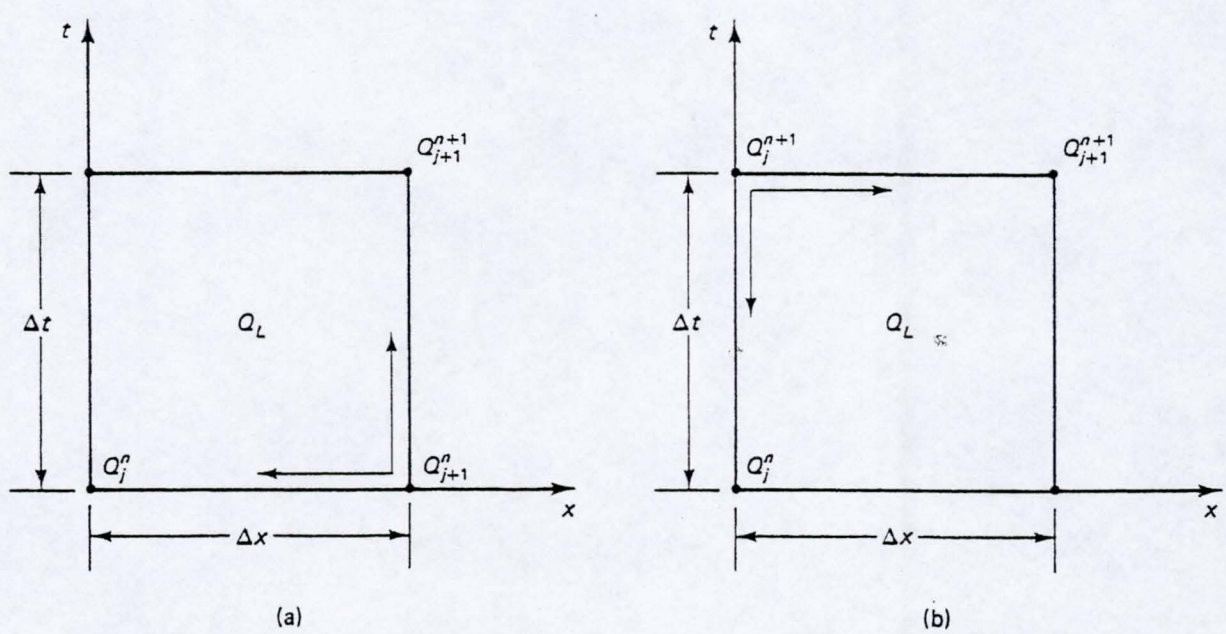

Figure 10-6 Space-time discretization of first-order schemes of kinematic wave equation with lateral inflow: (a) forward-in-time, backward-in-space; (b) forward-in-space, backward-in-time.

TABLE 10-4 TWO-PLANE CATCHMENT ROUTING WITH KINEMATIC WAVE TECHNIQUE

(1)	(2)	(3)	(4)	(5)	(6)	(7)
Time (min)	Flow (m^3/s)					
	Q_{Lp}	I_p	O_p	Q_{Lc}	I_c	O_c
0		0	0		0	0
	0.5			0.3750		
10		0	0.3750		0	0.3750
	0.5			0.8437		
20		0	0.4687		0	0.8437
	0			0.5859		
30		0	0.1172		0	0.5859
	0			0.1465		
40		0	0.0293		0	0.1465
	0			0.0366		
50		0	0.0073		0	0.0366
	0			0.0091		
60		0	0.0018		0	0.0091
	0			0.0023		
70		0	0.0005		0	0.0023
	0			0.0006		
80		0	0.0001		0	0.0006
	0			0.0001		
90		0	0		0	0.0001
Sum	1.00		0.9999			1.9998

outflow hydrograph from each plane is 1 $m^3/s \times 10$ min $\times$ 60 s/min = 600 m^3. Column 5 shows the average lateral inflow to the channel, obtained by multiplying by 2 the average lateral inflow from each plane (Col. 4) (to account for two planes of the same dimensions). Column 6 is the upstream inflow to the channel, that is, zero (this example does not consider upstream inflow to the channel). Column 7 is obtained by routing with Eq. 10-17, with Courant number in the channel $C_c = 1.5$. Column 7 is the outflow hydrograph from the catchment. The sum of Col. 7 is 1.9998, which confirms that the total runoff volume is 1.9998 $m^3/s \times 10$ min $\times$ 60 s/min = 1200 m^3.

Assessment of Kinematic Wave Method. The calculated outflow hydrograph peak is 0.8437 m^3/s, and it occurs at 20 min. This value is less than the maximum peak flow, Eq. 10-14: 1.0 m^3/s. Since the rainfall duration is equal to the concentration time, this implies that the hydrograph has undergone a certain amount of runoff diffusion. This diffusion is really numerical diffusion, due primarily to the coarse grid size and secondarily to the Courant numbers (of planes and channel) being different than 1.

To prove this assertion, it is necessary to reduce the grid size and test the *convergence* of the kinematic wave schemes, Eqs. 10-16 and 10-17. Convergence refers to the ability of the numerical scheme to approach the analytical solution as the grid is refined. Due to the large number of calculations involved, the procedure is better accomplished with the aid of a computer program. Table 10-5 shows the results obtained

TABLE 10-5 KINEMATIC WAVE CATCHMENT ROUTING: EFFECT OF GRID RESOLUTION

Number of Increments	Δx (m)	Δy (m)	Δt (s)	Peak Flow (m^3/s)
1	100	200	600	0.8437
2	50	100	300	0.9063
4	25	50	150	0.9490
8	12.5	25	75	0.9776
16	6.25	12.5	37.5	0.9899

by successive grid refinement, using program EH1000B included in Appendix D. It is seen that the results are a function of grid size and that the peak flow value converges to the maximum possible value (1.0 m^3s) as the grid is refined.

It is concluded that a kinematic wave numerical solution for catchment routing is grid dependent. If necessary, numerical diffusion can be eliminated by successive grid refinement (while keeping the Courant number as close to 1 as possible). However, in this case the calculated hydrograph would be translated-only, with no diffusion. This may be adequate for catchments with negligible runoff diffusion (e.g., small catchments with slopes on the order of 1%), but is generally not adequate for catchments showing substantial amounts of runoff diffusion (e.g., midsize catchments). For the latter, the diffusion wave technique may be used as a viable alternative to the kinematic wave.

10.5 CATCHMENT ROUTING WITH DIFFUSION WAVES

Catchment routing with diffusion waves is applicable to cases where both translation and diffusion are important, that is, for routing in midsize catchments where catchment slope is such that the kinematic wave criterion is not satisfied. Although the concept of diffusion waves and catchment routing dates back to the work of Dooge [1], actual numerical applications have only recently been attempted [6, 14]. Diffusion wave routing can provide grid-independent results, and is therefore regarded as an improvement over grid-dependent techniques.

The diffusion wave catchment routing approach is illustrated here by using the same example as in the previous section. The Muskingum-Cunge method (Chapter 9) is used as the routing scheme of the diffusion wave method [14].

Two-Plane Linear Diffusion Catchment Routing Model

This example is similar to that of the previous section. Assume a catchment configured as two rectangular planes adjacent to each other, draining laterally into a stream channel located between them. Each of the planes is 100 m long by 200 m wide, and the channel is 200 m long (Fig. 10-5). The slopes of planes and channel (in the direction of the flow) are $S_{op} = 0.01$; and $S_{oc} = 0.01$, respectively. The bottom friction in the planes and channel is such that the average velocity in the planes is 0.0417 m/s, and the average velocity in the channel is 0.3 m/s. It is desired to calculate the runoff

hydrograph at the catchment outlet resulting from an effective rainfall of 9 cm/h lasting 20 min.

Calculation of Flow Parameters. Since the model is linear, it is first necessary to calculate the flow parameters on which to base the calculation of the routing parameters and coefficients. As described in the preceding section, the flow per unit width in the midlength of each plane is equal to $q_p = 0.00125$ m^2/s. Since the average velocity in the planes is $v_p = 0.0417$ m/s, the average flow depth in the planes is $d_p = q_p/v_p = 0.03$ m. Laminar flow in the planes is assumed, with a discharge-depth rating exponent $\beta_p = 3$. Therefore, the wave celerity in the planes is $c_p = \beta_p v_p = 0.125$ m/s. The flow in the midlength of the channel is equal to 0.5 m^3/s. Assume a channel top width $T_c = 5$ m. Therefore, the flow per unit width in the channel is $q_c = Q_c/T_c = 0.1$ m^2/s. Since the average velocity in the channel is $v_c = 0.3$ m/s, the average flow depth in the channel (at midlength) is $d_c = q_c/v_c = 0.333$ m. A wide channel with turbulent Manning friction is assumed, with a discharge-area rating exponent $\beta_c = 1.67$. Therefore, the wave celerity in the channel is $c_c = \beta_c v_c = 0.5$ m/s. The concentration time is equal to 1200 s, which is equal to the rainfall duration. The maximum possible peak flow is 1.0 m^3/s. The total volume of runoff is 1200 m^3.

Selection of Discrete Intervals. For simplicity, a space interval of $\Delta x = 100$ m is chosen for the planes, and $\Delta y = 200$ m for the channel. This amounts to one spatial increment in planes and channel. The time interval is chosen as $\Delta t = 10$ minutes. In an actual computer application, a finer grid size would be indicated.

Selection of Routing Scheme. The chosen routing scheme is the Muskingum-Cunge method, Eq. 9-62, with the routing coefficients calculated by Eqs. 9-74 to 9-76 but modified with the addition of lateral inflow. For this purpose, Eq. 9-43 is discretized in the same way as Eq. 9-61, leading to

$$Q_{j+1}^{n+1} = C_0 Q_j^{n+1} + C_1 Q_j^n + C_2 Q_{j+1}^n + C_3 Q_L \tag{10-19}$$

which has the same meaning as Eq. 9-62 with Eqs. 9-74 to 9-76, except for the addition of the lateral inflow term, with routing coefficient:

$$C_3 = \frac{2C}{1 + C + D} \tag{10-20}$$

The term Q_L is the lateral inflow in cubic meters per second. For overland flow routing, the lateral inflow is equal to the effective rainfall (centimeters per hour) times the applicable area (square meters). For channel routing, the lateral inflow is the average distributed lateral inflow (cubic meters per second per meter) multiplied by the channel length (meters).

The grid size and physical parameters allow the calculation of the routing parameters. The Courant numbers in the planes and channel (Eq. 9-69) are $C_p = 0.75$ and $C_c = 1.5$, respectively. The cell Reynolds numbers in the planes and channel (Eq. 9-71) are $D_p = 0.01$ and $D_c = 0.1$, respectively.

With Eqs. 9-74 to 9-76 and 10-20, the routing coefficients in the planes are $C_0 = -0.136$, $C_1 = 0.988$, $C_2 = 0.148$, and $C_3 = 0.852$. Likewise, the routing coefficients in the channel are $C_0 = 0.231$, $C_1 = 0.923$, $C_2 = -0.154$, and $C_3 = 1.154$.

TABLE 10-6 TWO-PLANE CATCHMENT ROUTING WITH DIFFUSION WAVE TECHNIQUE

(1)	(2)	(3)	(4)	(5)	(6)	(7)
	Flow (m^3/s)					
Time (min)	Q_{Lp}	I_p	O_p	Q_{Lc}	I_c	O_c
0		0	0		0	0
	0.5			0.4260		
10		0	0.4260		0	0.4916
	0.5			0.9150		
20		0	0.4890		0	0.9802
	0			0.5614		
30		0	0.0724		0	0.4969
	0			0.0831		
40		0	0.0107		0	0.0194
	0			0.0123		
50		0	0.0016		0	0.0112
	0			0.0018		
60		0	0.0002		0	0.0004
	0			0.0002		
70		0	0		0	0.0002
Sum	1.00		0.9999			1.9999

The catchment routing is shown in Table 10-6. Column 1 shows time in hours. Columns 2–4 show the plane routing and Cols. 5–7 show the channel routing. As in the previous example, the lateral inflow to the plane is 0.5 m^3/s (Eq. 10-18). Column 3 shows the upstream inflow to each plane, that is, zero (this example does not consider upstream inflow to the planes). Column 4 is the outflow from each one of the planes, obtained by routing with Eq. 10-19. Column 5 shows the average lateral inflow to the channel, obtained by multipying by 2 the average inflow from each plane (Col. 4) (two planes, each of the same dimensions). Column 6 is the upstream inflow to the channel, that is, zero (this example does not consider upstream inflow to the channel). Column 7 is the outflow from the catchment, obtained by routing with Eq. 10-19. As in the previous example, the sums of Cols. 2, 4 and 7 confirm that the runoff volumes are appropriately conserved.

Assessment of the Diffusion Wave Method. The calculated outflow hydrograph peak is 0.9802 m^3/s, and it occurs at 20 min. This value is very close to the maximum possible peak flow (1.0 m^3/s), revealing that the amount of physical diffusion for this particular example is relatively small.

To study the effect of grid size on the hydrograph calculated by the diffusion wave method, a test similar to that of the previous section is performed with the aid of a computer program. Table 10-7 shows the results obtained by successive grid refinement, using program EH1000C included in Appendix D. It is shown that the results are essentially independent of grid size. A coarse grid (one increment in space and time) results in a peak flow of 0.9804, whereas a fine grid (16 increments in space and time) results in a value of 0.9845. However, it should be noted that the coarse-grid

TABLE 10-7 DIFFUSION WAVE CATCHMENT ROUTING: EFFECT OF GRID RESOLUTION

Number of Increments	Δx (m)	Δy (m)	Δt (s)	Peak Flow (m^3/s)
1	100	200	600	0.9804
2	50	100	300	0.9716
4	25	50	150	0.9766
8	12.5	25	75	0.9814
16	6.25	12.5	37.5	0.9845

solution (one increment in space and time) exhibits a small but perceptible amount of numerical dispersion, as demonstrated by its peak (0.9804) being somewhat greater than the peak obtained with two increments (0.9716). This is caused by the negative C_0 in the planes ($C_0 = -0.316$).

Unlike in the kinematic wave method, in the diffusion wave technique the numerical diffusion is matched to the physical problem. As in the case of stream channel routing (Section 10.4), this procedure works best when numerical dispersion is minimized, that is, when Courant numbers are kept reasonably close to 1. In practice, substantial deviations from this condition may lead to increased numerical dispersion and associated numerical instability. As with other finite difference schemes, a test of grid independence similar to that shown in Table 10-7 is necessary to verify the convergence of the numerical scheme.

10.6 ASSESSMENT OF CATCHMENT-ROUTING TECHNIQUES

Catchment-routing techniques have evolved from the simple time-area methods to the more elaborate physically based kinematic and diffusion wave techniques. The variety of existing methods and techniques reflects the fact that no one method is applicable to all cases. Surface runoff in catchments is a complex phenomenon, and research continues to unveil improved ways of solving the problem.

In nature, catchments can be either small, midsize, or large. Runoff processes are nonlinear and distributed—nonlinear in the sense that the parameters do not increase in the same proportion as the flow and distributed in the sense that the parameters vary within the catchment. Hydrographs originating in catchment runoff are generally concentrated, diffused, and dispersed. From the mathematical standpoint, concentration is a first-order process, diffusion a second-order process, and dispersion a third-order process [5]. Being a first-order process, runoff concentration is the primary mechanism; it is also referred to as translation or wave travel. For certain applications, diffusion also plays an important role—for instance, in the modeling of runoff response in catchments with mild slopes. Early description of the diffusion mechanism referred to it as storage. The usage is so widespread that it has been preserved in this book. In a routing context, diffusion and (longitudinal channel) storage have essentially the same meaning. Dispersion is a third order process; therefore, it is usually much smaller than runoff concentration and diffusion. Physical dispersion translates

into wave steepening, a concept similar to that of skewness, or the third moment of a statistical distribution (Chapter 6).

The time-area method can calculate concentration but it cannot account for diffusion or dispersion. Therefore, the time-area method should be limited to small and midsize catchments where translation is by far the predominant mechanism. When used indiscriminately, the time-area method always overestimates the peak of the outflow hydrograph. If necessary, diffusion can be added by routing the time-area hydrograph through a linear reservoir. However, the storage constant would have to be determined either from measured data or by synthetic means. While the time-area method is a lumped method, it can be used as a component of larger network models which have a distributed structure [17].

In principle, the method of cascade of linear reservoirs accounts for runoff diffusion only. However, the connection of several linear reservoirs in series provides enough diffusion so that translation is actually being simulated by means of diffusion. The method is linear insofar as the routing parameters are determined by calibration. Nevertheless, by successive calibrations at different flow levels, from low to high, the method can be made to reflect the nonlinearity actually existing in nature. The method is lumped, but it can be used as a component of larger network models that have a distributed structure. The method has been successfully applied to very large basins (in excess of 10,000 km^2), which exhibit substantial amounts of runoff diffusion. For such large basins, the distributed models of the kinematic and diffusion type would be impractical due to the prohibitive amount of data required to properly specify the spatial diversity.

The kinematic wave model provides translation and diffusion, the latter, however, due only to the finite grid size. The method can be linear or nonlinear, and lumped or distributed, depending on the numerical scheme and input data. The method is applicable to small catchments with steep slopes where diffusion is small and can be controlled by grid refinement. Theoretically, the method could also be applicable to midsize catchments, as long as physical diffusion remains small. In practice, the larger the catchment, the more unlikely it is that physical diffusion is negligible. The distributed nature of kinematic wave models results in substantial data needs; the use of average parameters would render the model lumped, with the consequent loss of detail. Another important consideration in kinematic wave models is the validity of the geometric configuration. For instance, two-plane descriptions are adequate as long as the catchment geometry fits the two-plane model configuration. Otherwise, a certain amount of lumping would be introduced by the model's inability to properly account for the physical detail. In practice, the larger the catchment, the more difficult it is to fit catchments within two-plane descriptions. Multiple-plane descriptions are possible but invariably lead to additional complexity [8].

The diffusion wave technique (Muskingum-Cunge scheme) provides translation and diffusion, and, unlike the kinematic wave model, its solution is generally independent of grid size. Therefore, it is applicable to catchments with substantial amounts of physical diffusion, either small catchments of mild slope or midsize catchments with average slopes. The method is linear or nonlinear and lumped or distributed, depending on the numerical scheme and input data. As with kinematic models, the validity of the geometric configuration is important in diffusion wave catchment models. Unless the model's geometric abstraction is a reasonable representation of the catchment's

actual geometry, the degree of lumping introduced would tend to mask the distributed nature of the model.

The preceding comments have referred specifically to catchment routing, i.e., the conversion of effective rainfall into runoff. In practice, comparative evaluations of the performance of catchment-routing methods are hampered by the fact that it is seldom possible to determine effective rainfall with any degree of certainty. Hydrologic abstractions are time-variant, distributed, and nonlinear. Therefore, a proper estimation of hydrologic abstractions is crucial to the performance evaluation of catchment-routing models.

From this discussion, it can be concluded that no one method or model is suitable for all applications. All have strengths and weaknesses; they are either simple or complex and suffer from lack of detail or require a substantial amount of data for their successful operation. In practice, the choice of catchment-routing method remains one of individual preference and experience.

QUESTIONS

1. What is the difference between hydrologic and hydraulic methods of catchment routing?
2. What are catchment isochrones? How are they determined?
3. How is concentration time defined when using hydrographs generated by the time-area method?
4. When can the Clark unit hydrograph be considered synthetic? Explain.
5. What is the difference between translation and diffusion? How are the time-area and rational methods related?
6. How can the linear reservoir storage coefficient be determined for runoff data?
7. What is the principle behind the method of cascade of linear reservoirs used in catchment routing?
8. Why is it necessary to use two schemes in catchment routing using first-order kinematic wave techniques?
9. Why is a kinematic wave solution using numerical techniques usually grid dependent? Why is the diffusion wave solution grid independent?

PROBLEMS

10-1. A 45-km^2 catchment has a 6-h concentration time with isochrones at 2-h intervals, resulting in the following time-area histogram:

Time (h)	0		2		4		6
Area (km^2)		9		21		15	

Use the time-area method to calculate the outflow hydrograph from the following effective storm pattern:

Time (h)	0		2		4		6		8		10		12
Effective rainfall (cm/h)		0.5		1.0		2.0		3.0		1.0		0.5	

WATER RESOURCES BULLETIN
VOL. 31, NO. 3 AMERICAN WATER RESOURCES ASSOCIATION JUNE 1995

RASTER-BASED HYDROLOGIC MODELING OF SPATIALLY-VARIED SURFACE RUNOFF[1]

Pierre Y. Julien, Bahram Saghafian, and Fred L. Ogden[2]

ABSTRACT: The proliferation of watershed databases in raster Geographic Information System (GIS) format and the availability of radar-estimated rainfall data foster rapid developments in raster-based surface runoff simulations. The two-dimensional physically-based rainfall-runoff model CASC2D simulates spatially-varied surface runoff while fully utilizing raster GIS and radar-rainfall data. The model uses the Green and Ampt infiltration method, and the diffusive wave formulation for overland and channel flow routing enables overbank flow storage and routing. CASC2D offers unique color capabilities to display the spatio-temporal variability of rainfall, cumulative infiltrated depth, and surface water depth as thunderstorms unfold. The model has been calibrated and independently verified to provide accurate simulations of catchment response to moving rainstorms on watersheds with spatially-varied infiltration. The model can accurately simulate surface runoff from flashfloods caused by intense thunderstorms moving across partial areas of a watershed.
(KEY TERMS: hydrologic model; surface runoff; GIS hydrology; radar hydrology; flashfloods; moving rainstorms.)

INTRODUCTION

Recent developments in Geographic Information System (GIS) and micro-computer technology enhance our capabilities to handle large databases describing the detailed spatial configuration of land-surface. As opposed to a vector-based format, a raster-based GIS offers a practical method for storing land-surface characteristics with digital values of a parameter on square grid elements. A watershed is divided into square cells of specified grid size, and a single value of a land-surface parameter is assigned to each cell. Land-surface characteristics such as elevation, soil type, and land-use are obtained by field sampling (in the case of soil classification) or remote sensing (photogrammetry for elevation, satellite imagery for land-use classification).

There is an extensive effort in many states to establish a raster database of soil classification with 200 m spatial resolution. The U.S. Geological Survey maintains an on-line Internet accessible Digital Elevation Model (DEM) of raster elevations for the entire U.S., primarily at a 90 m horizontal resolution and 1 m vertical resolution. Advances are also being made in the field of rainfall remote sensing, which allow widespread estimation of rainfall rates at spatial resolutions ranging from 1 to 4 km. The U.S. National Weather Service is presently updating its weather radar capabilities with the deployment of over 120 WSR-88D radars, known as NEXRAD (Klazura and Imy, 1993). The NEXRAD precipitation processing system produces hourly accumulated rainfall estimates on a 4 x 4 km grid. Furthermore, there are several regions covered by research weather radars which can provide rainfall rate estimates at spatial and temporal resolutions as fine as 1 km every 5 minutes.

Physically-based distributed hydrologic models typically employ field-measured or remotely-sensed values describing the spatially-varied nature of watershed topography, soils, vegetation, drainage networks, and rainfall. These variables are used as input to numerical algorithms based on the physics of infiltration and overland and channel flow to model the transient response of a watershed. Two-dimensional physically-based numerical models are gaining popularity among hydrologists concerned with simulating the non-linear response of watersheds to spatially-varied rainfall and infiltration. Models of this type

[1]Paper No. 94057 of the *Water Resources Bulletin*. **Discussions are open until February 1, 1996.**
[2]Respectively, Associate Professor of Civil Engineering, Engineering Research Center, Colorado State University, Fort Collins, Colorado 80523; formerly at the Civil Engineering Department, Engineering Research Center, Colorado State University, Fort Collins, Colorado; and Assistant Professor, Department of Civil Engineering, University of Connecticut, Storrs, Connecticut (formerly at Colorado State University).

incorporate a description of watershed and rainfall spatial variability at resolutions considerably finer than contemporary lumped parameter models.

Abbott *et al.* (1986) reported on the structure of a physically-based distributed modeling system named Système Hydrologique Européen (SHE), which uses modular construction for the addition of new components. Two-dimensional overland flow routing is performed using an explicit finite difference scheme, while one-dimensional channel flow routing is carried out by an implicit method. Other SHE components include interception, evapotranspiration, saturated and unsaturated zone flows, and snowmelt. Abbott *et al.* (1986) predicted that technological advances in remote sensing and radar measurement would enhance data handling for SHE.

More recent developments in two-dimensional hydrodynamic modeling of runoff routing include, among others, Zhang and Cundy (1989) and James and Kim (1990). The first model considers the spatial variation in hillslope physical characteristics and numerically solves the general hydrodynamic equations of continuity and motion using a finite difference scheme. The second model simulates uncoupled overland and channel flow routing for a single storm event. Excess rainfall calculated by the Green-Ampt infiltration equation is routed as overland flow using a two-dimensional diffusive wave implicit scheme.

Two-dimensional overland flow modeling using the finite element approach was reported by Goodrich *et al.* (1991). They developed a method using the kinematic wave equations approximated in space by finite elements on a topographic triangular irregular network (TIN). The resulting ordinary differential equations were then solved in time via finite differences. Goodrich *et al.* (1991) hinted at the need for further research to incorporate infiltration and refinement of their numerical techniques. Marcus (1991) developed a distributed finite element overland flow model to simulate moving rainstorms event on natural watersheds subdivided by quadrilateral elements. A two-dimensional kinematic wave approximation combined with the Manning resistance equation was formulated to compute the surface runoff. The model was linked to a one-dimensional full dynamic channel network model (Choi and Molinas, 1993) for the simulation of flashfloods in semi-arid watersheds.

While models exist which use a format consistent with recent developments in GIS and rainfall remote sensing technologies, none have been developed expressly for the purpose of fully utilizing raster-based GIS and radar capabilities. Additionally, none of the above-mentioned models include capabilities for visualizing the spatial variability of rainfall, surface water, or cumulative infiltrated depth during a simulation.

Data manipulation and visualization capabilities gained in GIS-hydrologic model linkage were demonstrated by Cline *et al.* (1989) and Vieux (1991), who linked distributed process-based models with GIS. Past efforts and trends in the application of GIS for hydrologic analysis, comparison and grid-, TIN-, and contour-based GIS, and the use of remotely sensed data in GIS and hydrologic modeling were extensively reviewed by DeVantier and Feldman (1993).

This paper describes the distributed watershed model CASC2D. CASC2D is fully compatible with a raster-based GIS and raster weather radar rainfall estimates, and it simulates Hortonian surface runoff from moving rainstorms in semi-arid and humid regions. The objectives for developing this model include the need for: (a) spatial data handling linked with raster-based GIS; (b) hydrologic modeling linked with remotely sensed rainfall data; (c) accurate flash-flood simulation for intense thunderstorms moving across partial areas of a watershed; and (d) graphical display capability for educational, scientific, and diagnostic applications which illustrate the spatio-temporal variability of rainfall, infiltration, and surface water depth.

This paper demonstrates the capabilities and limitations of CASC2D with emphasis on model formulation, features, calibration, verification, independent testing, and numerical stability. Two examples illustrate the capabilities: (a) the calibration run with rainfall data from a dense raingauge network, and (b) research results using dual-Doppler weather radar.

MODEL FORMULATION

CASC2D is designed to operate on watershed data discretized into square raster elements of desired spatial resolution. The selection of an appropriate grid size for simulations is not a trivial matter. In selecting a grid size, the user must balance between accuracy, data availability, and computational effort. The availability and accuracy of the data used for calibration and verification should also be considered. Values of model grid size used with CASC2D to date range from 30 m to 800 m, with typical values between 100 and 200 m. Small grid sizes are used when the spatial variability of relevant parameters is known in detail. Larger grid sizes may be preferred when the spatial variability of watershed characteristics is not significant or when computational efficiency is a concern, such as simulations of very large watersheds or large numbers of storms – e.g., Monte-Carlo simulations. A raster-based GIS proves to be extremely useful when data sets need to be rescaled to larger grid resolutions.

The geographic region which bounds the watershed is divided into raster cells of size W. Each grid cell is identified by its row and column numbers (j,k). A mask map is developed which describes whether or not a particular grid cell lies within the boundary of the watershed. The mask map resembles a matrix where 1 denotes a grid cell within the watershed, while a value of 0 indicates that the grid cell lies outside the watershed. Cells on the boundary are considered inside the watershed if more than 50 percent of their area is contained within the watershed boundary line.

The following sections contain algorithmic descriptions of the three main components of CASC2D. These main components include: infiltration, overland flow routing, and channel routing.

Infiltration

The Green and Ampt equation is used to determine infiltration rates, assuming the soils are homogeneous, deep, and well-drained within each grid cell (Rawls *et al.*, 1983):

$$f = K\left(1 + \frac{H_f M_d}{F}\right) \tag{1}$$

where f = infiltration rate; K = hydraulic conductivity; H_f = capillary pressure head at the wetting front; M_d = soil moisture deficit equal to $(\theta_e - \theta_i)$; θ_e = effective porosity equal to $(\phi - \theta_r)$; ϕ = total soil porosity; θ_r = residual saturation; θ_i = initial soil moisture content; and F = total infiltrated depth. The degree of initial soil saturation S in percent is given by $S = \theta_i/\theta_e$. The head due to surface depth is neglected because H_f is typically much greater than the overland flow depth. Based on soil textural classification, Rawls *et al.* (1983) provided average values for the Green and Ampt parameters.

Starting from an initial surface water depth, usually zero at the beginning of a storm, the rainfall depth during the time step Δt is first added to the surface water depth. The infiltration rate is then calculated for each grid cell from Equation (1). The actual infiltration rate is taken as the lesser of the infiltration capacity and the maximum available rate calculated by dividing the surface water depth by the time step. Solving Equation (1) for the middle of the time step yields:

$$f^{t+\Delta t/2} = \frac{1}{2\Delta t}\left\{\left(K\Delta t - 2F^t\right) + \left[\left(K\Delta t - 2F^t\right)^2 + 8\left(KF^t + KH_f M_d\right)\Delta t\right]^{1/2}\right\} \tag{2}$$

in which Δt = time step, and the superscripts correspond to time. This model essentially simulates the Hortonian surface runoff mechanism. There is no provision for the recovery of infiltration capacity between storms because of soil-moisture redistribution. This has little effect on single storm simulations but should be reset for multiple storm simulations. At this time, this formulation does not include provisions for sub-surface storage or routing. For this reason, the CASC2D simulates surface runoff from watersheds; baseflow contributions from subsurface flow should be added when appropriate.

The required input data for the infiltration routine includes raster maps of textural classification (Rawls *et al.* 1983) and initial soil moisture deficit. These data may be derived from field estimates or manually digitized county soil surveys at the desired spatial resolution or obtained from the Soil Conservation Service within a particular state in raster GIS format.

Overland Flow

A two-dimensional explicit finite difference formulation was selected to model overland flow. Topographical data from a DEM are assigned to each raster grid cell as conceptualized in Figure 1. This figure illustrates the description of topography within CASC2D and is consistent with raster GIS formulations. In general, each raster cell is assumed a homogeneous unit with one representative value of any hydraulic or hydrologic parameter (e.g., hydraulic conductivity, roughness coefficient, elevation, etc).

The Saint-Venant equations of continuity and momentum describe the physics of gradually-varied overland flow. The two-dimensional continuity equation in partial differential form is:

$$\frac{\partial h}{\partial t} + \frac{\partial q_x}{\partial x} + \frac{\partial q_y}{\partial y} = i_e \tag{3}$$

where h = surface flow depth; q_x = unit discharge in x-direction; q_y = unit discharge in y-direction; i_e = excess rainfall equal to (i-f); i = rainfall intensity; x and y = rectangular coordinates; and t = time.

Application of a first order approximation to the continuity equation for element (j,k) results in:

$$h^{t+\Delta t}(j,k) = h^{t}(j,k) + i_e \Delta t - \left[\frac{q_x{}^t(k \to k+1) - q_x{}^t(k-1 \to k)}{W} + \frac{q_y{}^t(j \to j+1) - q_y{}^t(j-1 \to j)}{W} \right] \Delta t \quad (4)$$

where $h^{t+\Delta t}(j,k)$ and $h^t(j,k)$ denote flow depths at element (j,k) at time t+ Δt and t, respectively; i_e is the average excess rainfall rate over one time step beginning from time t; $q_x{}^t(k \to k+1)$ and $q_x{}^t(k-1 \to k)$ describe unit flow rates in x-direction at time t, from (j,k) to (j,k+1), and from (j,k-1) to (j,k), consecutively; likewise $q_y{}^t(j \to j+1)$, $q_y{}^t(j-1 \to j)$ denote unit flow rates in y-direction at time t, from (j,k) to (j+1,k), and from (j-1,k) to (j,k), respectively; and W = grid size.

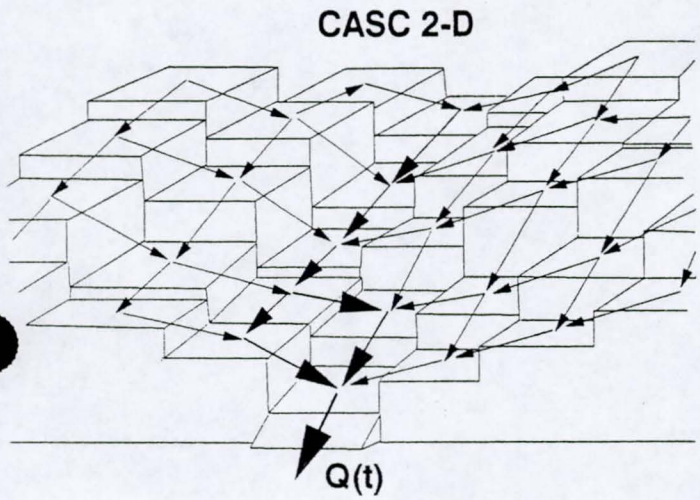

Figure 1. Topographical Representation in Overland Flow Routing Scheme.

The momentum equations in the x and y directions may be derived by relating the net forces per unit mass to flow acceleration. The diffusive wave approximation of the momentum equation in the x-direction is:

$$S_{fx} = S_{ox} - \frac{\partial h}{\partial x} \quad (5)$$

where S_{fx} = friction slope in the x-direction; and S_{ox} = land surface slope in the x-direction. With reference to Figure 1, the land surface slope in the x- and y-directions is calculated as the difference in elevation between two adjacent cells divided by the grid size, W.

The unit discharge at any position and any time depends primarily upon the flow direction, which is determined by the sign of the friction slope. For example, in the x-direction, first the friction slope based on the diffusive wave approximation is computed as:

$$S_{fx}{}^t(k-1 \to k) = S_{ox}(k-1 \to k) - \frac{h^t(j,k) - h^t(j,k-1)}{W} \quad (6)$$

in which the bed slope is given by:

$$S_{ox}(k-1 \to k) = \frac{E(j,k-1) - E(j,k)}{W} \quad (7)$$

where E represents the ground surface elevation of the element, and the arrows imply the computational direction. From the three equations of continuity and momentum, five hydraulic variables must be determined. Therefore, a resistance law in terms of depth-discharge relationship is required such as:

$$q_x = \alpha_x h^{\beta} \quad (8)$$

where α_x varies with the derivative of depth in diffusive formulation and β is a constant. Both α_x and β depend on flow regime – i.e., laminar or turbulent.

For turbulent flow over a rough boundary, the Manning resistance equation, in SI units, is used:

$$\alpha_x = \frac{S_{fx}{}^{1/2}}{n}; \quad \beta = \frac{5}{3} \quad (9)$$

where n=Manning roughness coefficient. Notice that the parameter β remains constant while the coefficient α_x varies during a rainstorm simulation according to S_{fx} from Equation (6).

The calculated unit discharge for turbulent flow is then given by:

$$q_x{}^t(k-1 \to k) = \frac{1}{n(j,k-1)} \left[h^t(j,k-1) \right]^{5/3} \left[S_{fx}{}^t(k-1 \to k) \right]^{1/2} \text{ if } S_{fx}{}^t(k-1 \to k) \geq 0 \quad (10)$$

$$q_x{}^t(k-1 \to k) = \frac{-1}{n(j,k)} \left[h^t(j,k) \right]^{5/3} \left[-S_{fx}{}^t(k-1 \to k) \right]^{1/2} \text{ if } S_{fx}{}^t(k-1 \to k) < 0 \quad (11)$$

Equation (11) corresponds to a negative friction slope and negative unit discharge and therefore implies that the flow direction is actually from (j,k) to (j,k-1).

The flow rates in the y-direction are calculated based on the sign of the friction slopes in the y-direction. Backwater effects are handled in Equations (10), (11), and (4) whenever the sign of bed slope S_o and friction slope S_f happen to be opposite. Wherever microscale topography within a cell prevents the surface water from flowing after soil saturation, a retention storage depth specified for each cell causes ponding of surface water without runoff until the specified retention depth is exceeded.

Data requirements for the overland flow portion of CASC2D include raster maps of topography, retention storage depth, and surface roughness coefficient. The land-surface slope map is derived from the topographical map. Each of these raster maps may be generated either manually or with a raster GIS.

This formulation has several unique features. Firstly, it enables the simulation of run on, which occurs when surface runoff from one cell flows onto an adjacent cell where it is infiltrated. Secondly, the diffusive wave formulation allows flow on adverse slopes due to backwater effects. The upstream boundary condition for overland flow allows no inflow into the watershed across its boundary. The coupling of overland flow and channel flow is addressed in the next section.

Channel Flow

The one-dimensional diffusive wave formulation is applied to the following one-dimensional continuity equation:

$$\frac{\partial A_X}{\partial t} + \frac{\partial Q}{\partial x} = q_1 \tag{12}$$

where A_x = channel flow cross section; Q = total discharge in the channel; and q_1 = lateral inflow rate per unit length, in (+) or out (–) of the channel. The application of the Manning resistance equation to the channel flow can be described as:

$$Q = \frac{1}{n} A_x R^{2/3} S_f^{1/2} \tag{13}$$

where R = channel hydraulic radius; and S_f = channel friction slope. The solution of Equation (12) using Equations (13) and (6) is similar to Equation (4), although only in one-dimension.

Grid cells which contain channel segments are referred to as "drainage cells." The connectivity between the overland flow and channel network is specified by the user in a raster map. Channels are assumed to flow between the center of two successive drainage cells. The length of the channel segment between two successive drainage cells may be specified as a length other than the grid size to account for channel sinuosity or flow along the diagonal (relative to the grid directions) lines.

At each time step, overland flow is calculated to determine the net surface runoff discharge flowing into the drainage cells. The entire incoming flow exceeding a specified retention depth in drainage cells is treated as lateral inflow to the channel segments within those cells. Figure 2 shows a typical drainage cell containing a channel segment of width WCH, bankfull depth DCH, and water depth HCH. If HCH is less than DCH, all overland inflow to a drainage cell from adjacent overland cells is passed to the channel. However, when HCH exceeds DCH, overbank flow occurs onto the adjacent floodplain. During periods of overbank flow, the volume of water within each drainage cell is distributed between in-channel and floodplain compartments each time step with the assumption of an equal water surface elevation in the channel and on the floodplain. Once water leaves the channel and moves onto the floodplain, it is treated as overland flow and accordingly may interact with other neighboring overland cells, or infiltrate. As the flood wave in the channel recedes, water on the flood plain is returned to the channel, with the exception of the specified retention depth.

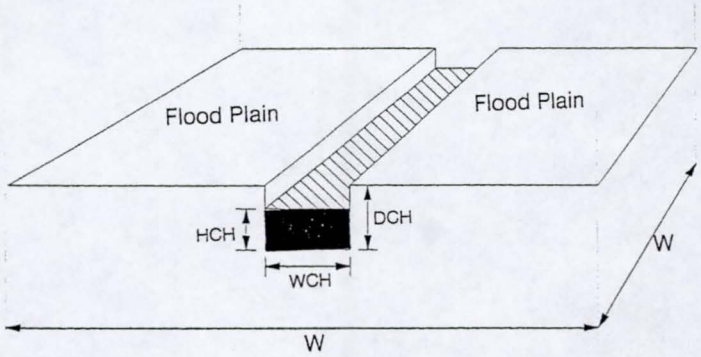

Figure 2. Typical Drainage Cell with Channel Cross Section.

The upstream boundary condition for first-order streams at the hillslope-channel interface is the overland flow rate entering the upstream drainage cells. The continuity equation and an equal water surface assumption serve as boundary conditions at channel junctions. At the watershed outlet the downstream boundary condition can be specified as: normal depth, weir or a stage vs. time relationship. Data requirements for the channel routing portion of CASC2D

include raster maps of drainage cell locations (connectivity), channel geometry (width, depth), and roughness coefficient (Manning n).

The diffusive wave channel routing formulation in CASC2D simulates backwater effects. This is particularly important in streams with very flat or adverse slopes. This formulation also allows flow over artificial barriers due to errors in DEM data or "digital dams" obstructing the flow in a wide cross-section. Surface water accumulates behind the barrier until the depth exceeds the barrier height and then spills over. Engineering judgement is required to remove, smooth, or filter errors in DEM data bases.

MODEL FEATURES

There are three specific features which enhance the applicability of CASC2D:

1. GIS Data Link – CASC2D operates on raster GIS-processed input data files (e.g., DEM, soil textural classification, land-use and land-cover data). To date, development has focused on the linkage of CASC2D with the public-domain Geographic Resources Analysis Support System (GRASS) GIS developed by the U.S. Army Construction Engineering Research Laboratories in Champaign, Illinois. The CASC2D-GRASS linkage was first demonstrated by Doe and Saghafian (1992), where GRASS capabilities were used to generate maps of land-surface disturbance at the Pinon Canyon Maneuver Site in Southern Colorado (Doe, 1992). CASC2D is ASCII-compatible with GRASS raster maps and conceptually compatible with any other raster-based GIS.

2. Moving Rainstorm Input Capability – There are three methods to input rainfall rates in CASC2D. These methods are spatially uniform rainfall rate of specified duration, rainfall time-series with constant temporal resolution at a number of rain gauges, or raster rainfall estimates with specified temporal resolution. Rainfall fields are interpolated from rainfall rates recorded by gauges located on or near the watershed using either Thiessen polygon or inverse distance squared techniques. Raster maps of rainfall rate from either weather radar (Ogden and Julien, 1994) or space-time rainfall model sources (Ogden and Julien, 1993) sources may be applied at a specified temporal resolution.

3. Graphical Display – One of the stated objectives for the development of CASC2D was the desire for visual interpretation of the rainfall-runoff process. GIS methods have allowed visual inspection of large geophysical, geological, and other datasets. The same display capability within a hydrologic modeling context is quite useful for educational, scientific, and diagnostic purposes. The graphical capabilities of CASC2D consist of a large window which is broken into several sub-windows. Each sub-window displays either a specified raster map, or a runoff hydrograph at a specified point in the watershed. Versions of the graphical display exist for both the MS-DOS and UNIX/X-Windows environments.

COMPONENT CALIBRATION/VERIFICATION

Several case studies to test the performance of CASC2D are reported in Julien and Saghafian (1991) and are summarized here. These test cases were used to assess the accuracy of individual components of CASC2D (i.e., overland flow routing, channel flow routing, and infiltration), as well as the combined performance of all components.

The overland flow routing component of CASC2D was tested against analytical solutions of the kinematic wave equation on the one-dimensional flow plane (Woolhiser, 1975) and converging plane (Woolhiser, 1969). Analytical solutions are available only for the kinematic wave situation, and despite the fact that CASC2D employs the diffusive wave formulation, the diffusive wave solution becomes identical to the kinematic wave on steeper slopes where backwater effects are negligible. In each of these two cases, the numerical solution provided by the CASC2D algorithm is identical to the analytical solution with the exception of slight numerical diffusion near the peak on the rising limb.

The CASC2D overland flow formulation was also compared with multiple experimental data sets reported by Dickinson *et al.* (1967) for an impervious butyl rubber converging plane, and by Schaake (1965) for the asphalt-covered Johns Hopkins University parking lot. The Manning roughness coefficient was used as the sole calibration parameter of the CASC2D overland flow algorithm. In this evaluation, one subset of each of the above data sets was used as a calibration data set, and the model was verified against the remaining data sets. CASC2D was calibrated on the magnitude of the peak discharge. Results from these calibrations/verifications are shown in Table 1, and they support the validity of the formulation. The average verification errors are 3 percent and –4.5 percent for the peak discharge and time to peak, while the average absolute values of the verification errors are 4.4 percent and 4.5 percent for the peak discharge and time to peak, respectively. The average calibration error on the runoff volume at the end of the

TABLE 1. Calibration/Verification of CASC2D Overland Flow Module with Experimental Datasets of Dickinson *et al.* (1967) and of Schaake (1965).

	Peak Discharge			Time to Peak			Runoff Volume (at end of observed data)		
	Observed m^3/s	Simulated m^3/s	Error %	Observed sec.	Simulated sec.	Error %	Observed m^3/s	Simulated m^3/s	Error %
Data Sets by Dickinson *et al.* (1967)									
Calibration Run	0.0035	0.0035	0.00	156	159	1.92	0.56	0.53	–5.36
Verification Run	0.0109	0.0116	6.42	121	112	–7.44	1.21	1.27	4.96
Data Sets by Schaake *et al.* (1965)									
Calibration Run (Storm #7)	0.0215	0.0215	0.00	426	438	2.82	14.4	13.3	–7.63
Verification Run (Storm #3)	0.0344	0.0351	1.97	1014	978	–3.55	18.8	19.9	5.85
Verification Run (Storm #13)	0.0654	0.0696	6.38	672	660	–1.79	37.6	43.7	16.22
Verification Run (Storm #18)	0.0277	0.0269	–2.85	702	666	–5.13	10.5	9.7	–7.62

observed data sets is –6.5 percent, while on the verification data sets it is 4.9 percent. Note that runoff volume was not considered a calibration requirement. The results in Table 1 indicate that there is a tendency to underestimate the time to peak by 4.5 percent. Otherwise, there are no obvious biases in the overland flow algorithm as evidenced by the signs on the error magnitudes with the peak discharge and runoff volume.

The channel routing algorithm was evaluated against the implicit full dynamic solution of the shallow water equations of motion developed by Choi and Molinas (1993). The explicit channel routine was found to be mass-conservative and accurate compared to the full-dynamic routing method. The performance of the Green and Ampt formulation used in CASC2D was compared with a numerical solution of Richards equation (Mein and Larson, 1971). The infiltration algorithm produced infiltration rate curves within a few percent of the Richards equation solution.

INDEPENDENT TESTING

Johnson *et al.* (1993) performed an independent calibration and verification of CASC2D on the Goodwin Creek experimental watershed in Mississippi. Calibration of CASC2D at the outlet of this basin was verified against stream flow gauging stations within the basin, for a total of five different runoff events. CASC2D was also compared with the Snyders Instantaneous Unit Hydrograph (SIUH) and SCS Curve Number (CN) approaches in HEC-1, using Muskingum-Cunge channel routing. These researchers concluded that CASC2D consistently performed as well or better than either the SIUH or CN HEC-1 approaches on the Goodwin Creek dataset. The primary calibration parameters used include initial soil moisture deficit, channel roughness coefficient, retention storage depth, and overland flow roughness coefficient. They also concluded that CASC2D always produced more accurate hydrographs on simulated ungauged basins (from the parametric values of Manning n and infiltration based on soil types without calibration).

STABILITY AND NUMERICAL ACCURACY

The stability of CASC2D was examined during the development (Saghafian, 1992; Julien and Saghafian, 1991). In summary, the explicit overland and channel flow algorithms require relatively small time steps for stability. The optimum time step depends upon the grid size, rainfall intensity, rainfall duration, both average and local bed slopes in the basin, surface roughness, and infiltration parameters. Specifically, the Courant condition evaluated under peak discharge conditions, which is the critical state with maximum flow velocity, provides a preliminary time

step value. The maximum time step for which the model is stable should be used because optimum solution convergence is achieved when the Courant number is near 1.0. Numerical stability is achieved on typical grid sizes with time steps between 5 and 60 seconds.

Situations which are particularly difficult to model with the CASC2D channel routing formulation include narrow channels with substantial changes in bed slope or channel cross-section. These can cause numerical instability in the transfer of water between the channel and floodplain during periods of over bank flow.

Surfaces with highly irregular microtopography at scales much smaller than the grid size do not pose a problem. Tayfur *et al.* (1993) found that replacing spatially varying microtopography with an average constant slope and appropriate retention storage causes no significant changes in the outflow hydrograph but does cause substantial deviations in local flow depths and velocities. Therefore, the user should be cautioned regarding the accuracy of flow velocity calculations within individual grid cells.

EXAMPLE APPLICATIONS OF CASC2D

The following two sections present example applications of CASC2D. The first section is an application of CASC2D with rainfall data from a dense raingauge network during a calibration run. The second section presents a brief discussion of contemporary weather radar rainfall rate estimation techniques and illustrates the applicability of weather radar estimated rainfall within CASC2D.

Modeling of Macks Creek Experimental Watershed with Raingauge Data

Macks Creek, a 32.2 km^2 sub-basin of the Reynolds Creek Experimental Watershed, is a steep semi-arid watershed located in southwest Idaho. A contour plot of Macks Creek is shown in Figure 3, with a 1 km grid overlay as a scale reference. The elevation drops from 1830m in the mountains along the western edge to 1130m at the outlet which is located in the northeast corner of the watershed. Two main channels, each

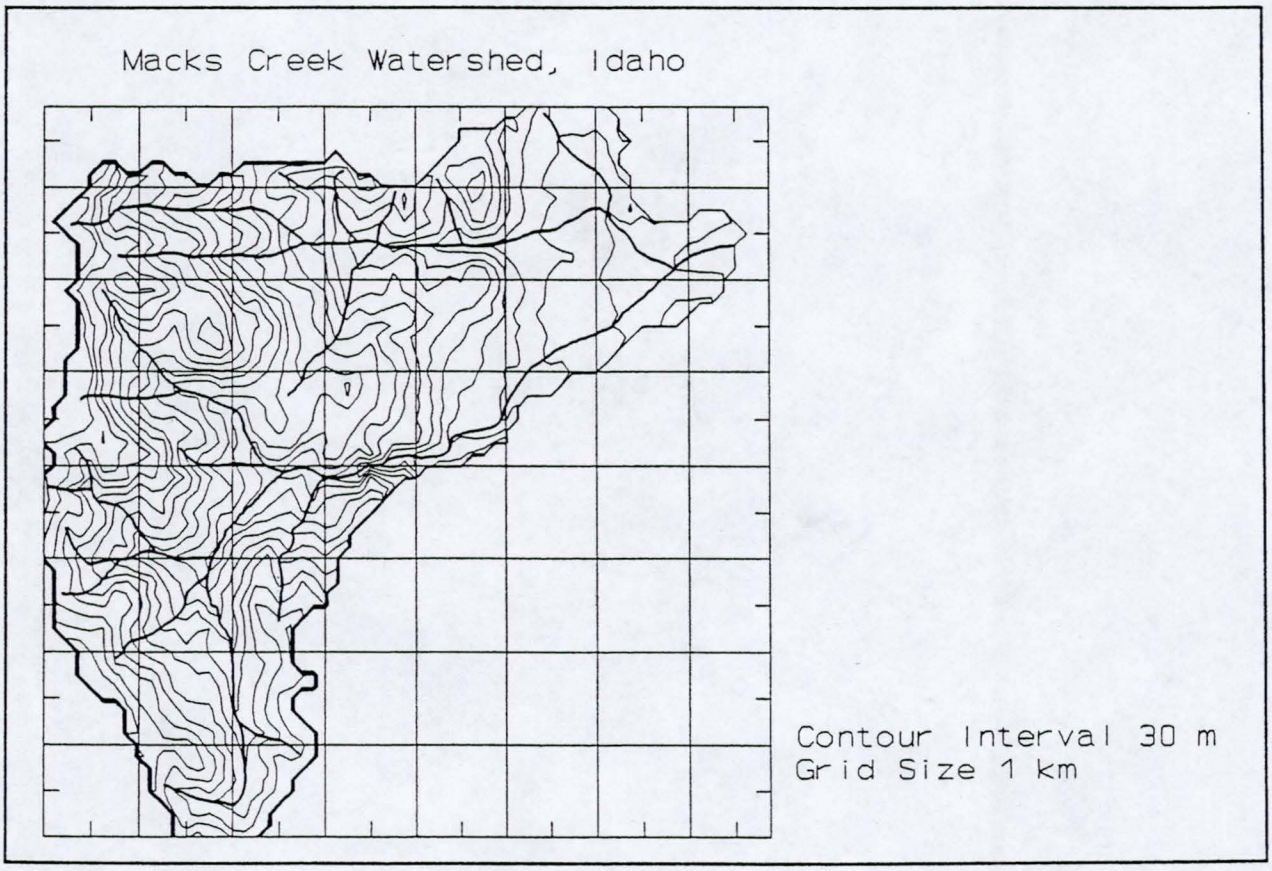

Figure 3. Macks Creek Watershed Topography and Channel Network.

with slopes averaging 5 percent and lengths near 10 km, collect surface runoff. The channel network is shown on Figure 3 with heavy lines. Note the longest continuous channel which drains the southern portion of the watershed and flows approximately from southwest to northeast. The second main channel drains the northern portion of the watershed, and flows in a roughly easterly direction.

For this particular calibration run the storm of August 23, 1965, was selected. Rainfall data with two-minute resolution was recorded by eight raingauges located on or near the watershed. The recorded accumulated rainfall depth over the two-hour storm reached 1.65 cm at one gauge, with a maximum rainfall rate over a two-minute period exceeding 20 cm/hr. Inverse distance squared weighting was applied to interpolate rainfall fields from the raingauge data. Outflows were recorded at a pre-calibrated 100 m^3/s capacity drop box weir at the watershed outlet on 15-minute intervals. A base flow of approximately 0.023 m^3/s at the outlet was neglected in the view of the 2.4 m^3/s measured peak discharge.

The geographical region containing the watershed was divided into a 53 x 53 grid, with a grid size of 152 m. The watershed mask contains 1390 grid cells. In this instance, the topography of Macks Creek was manually digitized to produce a raster DEM at a grid size of 152 m. The SCS soil classification map of Macks Creek was digitized by Cline (1988) at this same grid size. Both digitized maps were entered in the GRASS GIS for storage, editing, and export to CASC2D.

Values of hydraulic conductivity and capillary drive based on soil textural classification were used as recommended by Rawls *et al.* (1983). Antecedent soil moisture conditions were assumed near-dry owing to the semi-arid climate of the region, the absence of any substantial rainfall on the preceding day, and the negligible base flow at the weir. A spatially uniform value of Manning n for overland flow equal to 0.06 was used, which is within the range proposed by Woolhiser (1975) for sparse vegetation. The calibration parameters selected for this example are surface roughness and initial soil moisture deficit. Adequacy of this particular calibration was judged based on the timing and magnitude of the peak discharge, as well as the total runoff hydrograph volume.

Figure 4 shows the CASC2D visual display at 20, 35, 70, and 239.5 minutes during the model run. Each visual display is further broken down into sub-windows. The upper left sub-window shows the rainfall rate over the watershed, while the upper right sub-window depicts the surface water depth in each grid cell. The lower left and right sub-windows, respectively, display the cumulative infiltrated depth and the outflow hydrograph. The purple dots on the hydrograph sub-window represent observed discharge measurements at the weir.

With reference to the upper left quadrant of Figure 4, the storm is approaching the southeastern border of the watershed at t = 20 minutes. Note that at this point in the model run, the surface water depth is zero everywhere with the exception of a few rock outcrops along the western edge of the catchment. The classic "egg yolk" features in the interpolated rainfall field are the result of the inverse-distance squared rainfall interpolation scheme. Referring to the top right quadrant of Figure 4, at t = 35 minutes, the storm has moved to the northwest and intensified over the northeastern portion of the watershed. Accordingly, the cumulative infiltrated depth and surface water depth windows illustrate the partitioning of the rainfall into soil and surface water components. Note the partial areas of contribution in the surface water depth map.

As this particular storm unfolds, no surface runoff is generated from the southern third of the watershed. With reference to the lower left quadrant of Figure 4, at t = 70 minutes, there is no surface water in this portion of the watershed. At this time the hydrograph peak has just reached the catchment outlet. The short-duration high-intensity rainfall on the northern portion of the watershed is responsible for this sudden flashflood. In the lower right quadrant of Figure 4, at t = 239.5 minutes, all surface water is now limited to channel flow draining slowly toward the outlet. As evidenced by the hydrograph plot, fair agreement is observed between the computed hydrograph (solid red line) and the observed hydrograph (purple dots). Given the 15-minute temporal resolution of the recorded outflow hydrograph and the flashy response of Macks Creek, there is considerable uncertainty regarding the magnitude and timing of the measured hydrograph peak. Overall, this calibration run demonstrates that surface runoff is generated on partial areas of the watershed (northern part in this case). The model can accurately simulate surface runoff from flashfloods caused by intense thunderstorms moving across partial areas of a watershed.

Example Application of CASC2D with Weather Radar Estimated Rainfall

This section illustrates a CASC2D runoff simulation using real weather radar rainfall rates applied to a watershed at a different location. Weather radar observations of a convective storm over the plains of eastern Colorado are converted to rainfall rate estimates and used as input to CASC2D on the Macks Creek, Idaho, experimental watershed, which was discussed in the previous section. This simulation

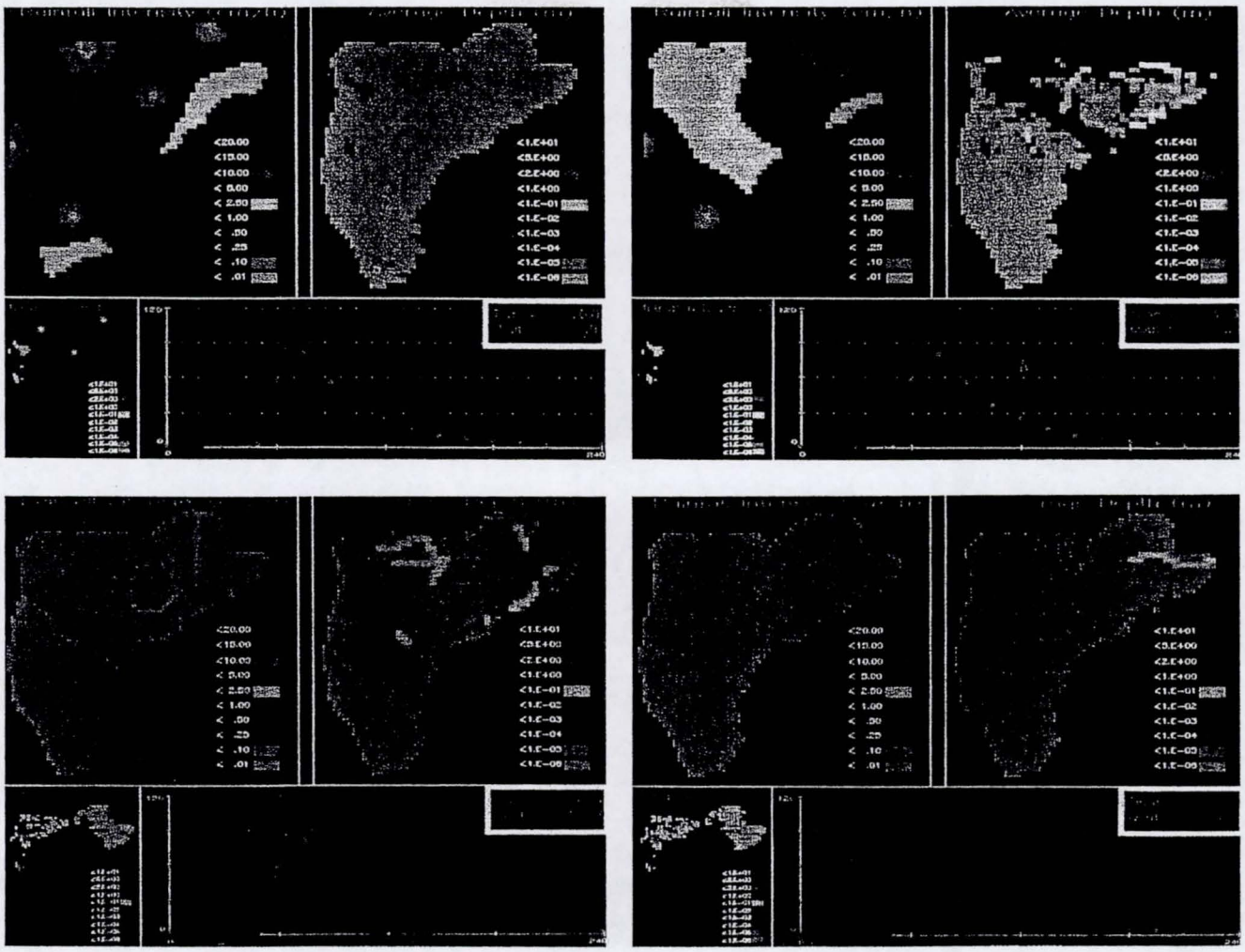

Figure 4. CASC2D Calibration on Macks Creek Using Raingauge Data at t = 20 Min. (upper left), 35 Min. (upper right), 70 Min. (lower left), and 239.5 Min. (lower right).

illustrates how CASC2D can interface with radar data, although, without comparison of the simulation results with an actual runoff hydrograph.

The raster formulation of CASC2D readily accepts raster estimates of rainfall rate at any spatial resolution. Raster rainfall estimates may be derived from interpolated raingauge data or isohyetal maps, weather radar or satellite observations, or space-time stochastic rainfall models. The only requirement is that the rainfall raster grid size must be evenly divisible by the runoff model grid size. For this reason, the elevation and soil classification maps of Macks Creek were re-digitized at a resolution of 125 m. Rainfall data grid size considerations and related scaling issues are discussed at length by Ogden and Julien (1994).

This example simulation relies upon CSU-CHILL weather radar observations of a convective rainstorm at five-minute intervals and 1 km spatial resolution. The CSU-CHILL radar is a research facility jointly funded by the National Science Foundation and Colorado State University. It operates at a non-attenuating wavelength of 10 cm (frequency = 2.95 GHz), has a 1 degree beam-width, and has dual-linear polarization and Doppler capabilities. For this example the radar measurements (Reflectivity, Differential Reflectivity, and Specific Differential Propagation Phase Shift) were converted into rainfall rate using the method detailed in Ogden and Julien (1994) and Ogden (1992). Readers interested in advanced radar-rainfall estimation techniques are referred to discussions by Zawadzki (1982), Sachidananda and Zrnic (1987), Chandrasekar *et al.* (1990, 1993), Gorgucci *et al.* (1994), and Aydin *et al.* (1995).

The CSU-CHILL radar monitored a convective storm on June 3, 1991. The radar measurements were

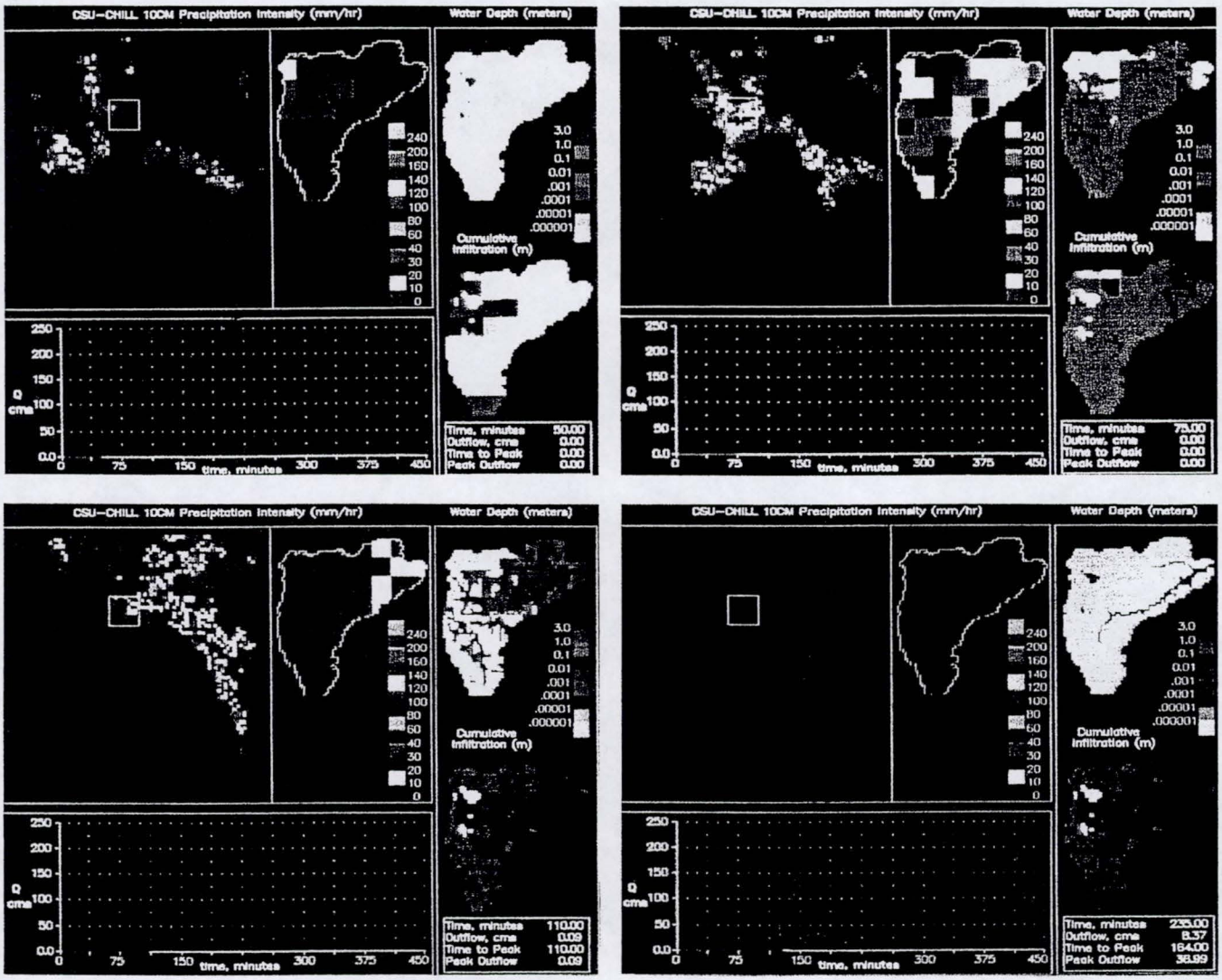

Figure 5. CASC2D Simulation on Macks Creek Using Weather Radar Estimated Rainfall at t = 50 Min. (upper left),75 Min. (upper right), 110 Min. (lower left), and 235 Min. (lower right).

recorded in spherical coordinates, with 300 m spatial resolution in the direction of the radar beam, and 1 degree resolution in the azimuthal and elevation angle directions. Radar scans at a beam elevation angle of 1 degree above the horizon were completed once per five minutes over the duration of the storm, which lasted about 150 minutes. After conversion to rainfall rates in spherical radar coordinates, the rainfall estimates were converted onto a 1 km x 1 km raster grid using a minimum-curvature spline technique.

Similar to Figure 4, Figure 5 shows a visual display of CASC2D with weather radar estimated rainfall at four different times during the simulation (50, 75, 110, and 235 minutes respectively). The CASC2D graphical display with radar-estimated rainfall is different from the display with raingauge rainfall. Specifically, the upper-left sub-window was added to illustrate the spatial variability of rainfall within a large radar domain around the watershed, which is 80 x 80 km in size. The location of the watershed within this sub-window is bounded by a white rectangle, and the radar is located near the center of the sub-window. For this illustrative example, the location of the watershed within the radar domain was chosen arbitrarily.

With reference to the visual display shown in the upper left quadrant of Figure 5, at simulation time t = 50 minutes after the beginning of simulation, the storm can be seen building west of the watershed location in the radar domain sub-window. The spatial variability of the 1 km raster rainfall field over the watershed is shown in the upper-middle sub-window. The light blue pixel in the watershed rainfall

sub-window indicates a rain rate between 30 and 40 mm/h on the very western edge of the basin. The upper-right and lower-right sub-windows detail the surface water and cumulative infiltrated depths, respectively, at this point in the simulation. Note the similarity with the graphical displays in Figure 4 with regard to the rocky outcrops along the western edge of the watershed. The surface depth map indicates ponded conditions on the rocky areas while the cumulative infiltrated depth map indicates no infiltration.

Referring to the upper right quadrant of Figure 5, at t = 75 minutes, the convective storm can be seen directly over the watershed in the upper left sub-window. The upper-middle sub-window shows one 1 km x 1 km region (yellow rainfall pixel) receiving an estimated rainfall rate between 120 and 140 mm/h. The upper right sub-window shows that the overland flow in the southwestern portion of the watershed is beginning to accumulate in the channel network, while the lower right sub-window shows a significant increase in infiltrated depth, particularly in the northeastern corner of the watershed, where it is now raining most heavily. The hydrograph display and simulation summary box in the lower portion of the video display indicate that runoff has not yet reached the outlet.

The video display in the lower-left quadrant of Figure 5 shows the state of the simulation at t = 110 minutes. As seen in the radar domain sub-window, the bulk of the storm has passed east of the watershed location. The upper-middle sub-window shows that rainfall rates less than 30 mm/h continue to fall in the extreme northeast corner of the watershed, while light rainfall less than 10 mm/h covers the central portion of the catchment. The surface depth map shows significant accumulations of water in the channel network with a flood wave moving toward the outlet in each of the two main channels. The cumulative infiltration map shows significant cumulative infiltration in the middle and eastern portions of the watershed, while the simulation status box in the extreme lower-right corner indicates the present outflow rate is 0.09 m^3/s.

The lower right quadrant of Figure 5 shows the CASC2D visual display at a simulation time of 235 minutes. The radar domain sub-window indicates no precipitation in the area or on the watershed. The surface water depth sub-window shows that all surface waters have infiltrated except in some channels, floodplains, and rocky regions. Furthermore, this window shows that the flood waves from both main channels have passed through to the outlet. The resulting hydrograph from this storm is shown in the lower-left sub-window, and the simulation summary sub-window indicates a peak discharge of 36.99 m^3/s passed the outlet at t = 184 minutes. Note the degree of spatial detail available at the end of the simulation regarding the location of flood waters, and spatial variability of cumulative infiltrated depth. This information could be most useful for the initiation of a new simulation if a second storm were to be headed toward the watershed.

SUMMARY AND CONCLUSIONS

Recent developments and increasing usage of GIS technology for the storage and retrieval of watershed characteristics in raster format enhance hydrological models that can fully access these data sources. GIS technology has also shown the educational, scientific, and diagnostic value of visual displays of large data sets. Furthermore, the increasing availability of weather radar rainfall estimates in raster format also necessitates the development of hydrological models capable of incorporating spatially-varied rainfall while preserving the spatial and temporal information provided by weather radars.

This paper outlines the details of the model formulation and list assumptions pertaining to the development and verification of the components. The calibration and accuracy of CASC2D are discussed together with numerical stability and model limitations. Two example applications which simulate the response of the 32.2 km^2 Macks Creek experimental watershed in southwestern Idaho are presented. The first application illustrates a CASC2D calibration run with rainfall rates interpolated from a dense network of raingauges. The second example illustrates the link between CASC2D and radar-estimated rainfall. In both examples, the utility of the graphical display in relating the state of a simulation to the user is discussed.

The accuracy of the overland flow, infiltration, and channel routing components of CASC2D has been assessed independently. CASC2D produces runoff hydrographs which are generally more accurate than either the SCS CN or Snyders Instantaneous Unit Hydrograph approaches with Muskingum Cunge channel routing in HEC-1. The unique visual display capability of CASC2D allows the user unprecedented access to the entire simulation while it is in progress. The visual display essentially provides CASC2D users access to the results of the simulation as it unfolds. This capability has potential for practical as well as research applications. The model is particularly well-suited to the simulation of flashfloods from intense thunderstorms moving across partial areas of a watershed.

In conclusion, the physically-based distributed nature of CASC2D makes it a suitable modeling tool to carry out fundamental research on spatially-varied systems. CASC2D features include GIS compatibility, direct link with remotely-sensed rainfall data, accuracy of simulation, and unique graphical interface. The paper presents innovative applications of recent advances in computational hydrology. As illustrated in Figure 4, the model can accurately simulate surface runoff from flashfloods caused by intense thunderstorms moving across partial areas of a watershed.

ACKNOWLEDGMENTS

This study was completed at the Engineering Research Center within the Center for Excellence in Geosciences at Colorado State University. Financial support by the U.S. Army Research Office (Grant ARO/DAAL 03-86-0175) is gratefully acknowledged. We appreciate the technical assistance of Drs. J. S. O'Brien, W. Doe III, O. R. Stein, Y. Q. Lan, K. Marcus, and G. Choi at the time the model was developed. Our gratitude is extended to Dr. W. Bach for his continuous support of this research program.

LITERATURE CITED

Abbott, M. B., J. C. Bathurst, J. A. Cunge, P. E. O'Connell, and J. Rasmussen, 1986. An Introduction to the European Hydrological System – Système Hydrologique Européen, "SHE." 2: Structure of a Physically-Based, Distributed Modelling System, Journal of Hydrology 87:61-77.

Aydin, K., V. N. Bringi, and L. Liu, 1995. Rain Rate Estimation in the Presence of Hail Using S-band Specific Differential Phase and Other Radar Parameters, Journal Appl. Meteorol. 34(2) (In Press).

Chandrasekar, V., V. N. Bringi, N. Balakrishnan, and D. S. Zrnic, 1990. Error Structure of Multiparameter Radar and Surface Measurements of Rainfall. Part III: Specific Differential Phase. Journal Atmos. Oceanic Technol. 7(5):621-629.

Chandrasekar, V., E. Gorgucci, and G. Scarchilli, 1993. Optimization of Multiparameter Radar Estimates of Rainfall. Journal Appl. Meteorol. 32(7):1288-1293.

Choi, G. W. and A. Molinas, 1993. Simultaneous Solution Algorithm for Channel Network Modeling. Water Resources Research 29(2):321-328.

Cline, T. J., 1988. Development of a Watershed Information System for HEC-1 with Application to Macks Creek, Idaho. M.S. Thesis, Civil Engineering Dept., Colorado State University, Fort Collins, Colorado, 238 pp.

Cline, T. J., A. Molinas, and P. Julien, 1989. An Auto-CAD-Based Watershed Information System for the Hydrologic Model HEC-1. Water Resources Bulletin, 25(3), pp. 641-652.

DeVantier, B. A. and A.D. Feldman, 1993. Review of GIS Applications in Hydrologic Modeling. Journal of Water Resources Planning and Management, ASCE, 119(2):246-261.

Dickinson, W. T., M. E. Holland, and G. L. Smith, 1967. An Experimental Rainfall-Runoff Facility. Hydrology Paper No. 25, Colorado State University, Fort Collins, Colorado.

Doe, W. W., 1992. Simulation of the Spatial and Temporal Effects of Army Maneuvers on Watershed Response. Ph.D. Dissertation, Civil Engineering Dept., Colorado State University, Fort Collins, Colorado, 301 pp.

Doe, W. W. and B. Saghafian, 1992. Spatial and Temporal Effects of Army Maneuvers on Watershed Response: The Integration of GRASS and a 2-D Hydrologic Model. Proc. 7th Annual GRASS Users Conference, National Park Service Technical Report NPS/NRG15D/NRTR-93/13, Lakewood, Colorado, pp. 91-165.

Goodrich, D. C., D. A. Woolhiser, and T. O. Keefer, 1991. Kinematic Routing Using Finite Elements on a Triangular Irregular Network. Water Resources Research 27(6):995-1003.

Gorgucci, E., G. Scharchilli, and V. Chandrasekar, 1994. A Robust Pointwise Estimator of Rainfall Rate Using Differential Reflectivity. Journal Atmos. Oceanic. Tech. 11(2):586-592

James, W. P. and K. W. Kim, 1990. A Distributed Dynamic Watershed Model. Water Resources Bulletin 26(4):587-596.

Johnson, B. E., N. K. Raphelt, and J. C. Willis, 1993. Verification of Hydrologic Modeling Systems. Proc. Federal Water Agency Workshop on Hydrologic Modeling Demands for the 90's, USGS Water Resources Investigations Report 93-4018, June 6-9, Sec. 8., pp. 9-20.

Julien, P. Y. and B. Saghafian, 1991. A Two-Dimensional Watershed Rainfall-Runoff Model. Civil Engr. Report, CER90-91PYJ-BS-12, Dept. of Civil Engineering, Colorado State University, Fort Collins, Colorado, 63 pp.

Klazura, G. E. and D. A. Imy, 1993. A Description of the Initial Set of Analysis Products Available from the NEXRAD WSR-88D System. Bull. Am. Meteor. Soc., 74(7):1293-1311.

Marcus, K. B., 1991. Two-Dimensional Finite Element Modeling of Surface Runoff from Moving Storms on Small Watersheds. Ph.D. Dissertation, Civil Engineering Dept., Colorado State University, Fort Collins, Colorado.

Mein, R. G. and C. L. Larson, 1971. Modeling the Infiltration Component of the Rainfall-Runoff Process. Bulletin 43, Water Resources Research Center, University of Minnesota, Minneapolis, Minnesota.

Ogden, F. L., 1992. Two-Dimensional Runoff Modeling with Weather Radar Data. Ph.D. Dissertation, Civil Engineering Dept., Colorado State University, Fort Collins, Colorado., 211 pp.

Ogden, F. L. and P. Y. Julien, 1993. Runoff Sensitivity to Temporal and Spatial Rainfall Variability at Runoff Plane and Small Basin Scales. Water Resources Research 29(8):2584-2597.

Ogden, F. L. and P. Y. Julien, 1994. Runoff Model Sensitivity to Radar-Rainfall Resolution. Journal of Hydrology 158:1-18.

Rawls, W. J., D. L. Brakensiek, and N. Miller, 1983. Green-Ampt Infiltration Parameters from Soils Data. Journal of Hydraulic Engineering, ASCE 109(1):62-70.

Sachidananda, M. and D. S. Zrnic , 1987. Rain Rate Estimates from Differential Polarization Measurements. Journal of Atmos. and Oceanic Tech 4:588-596.

Saghafian, B., 1992. Hydrologic Analysis of Watershed Response to Spatially Varied Infiltration. Ph.D. Dissertation, Department of Civil Engineering, Colorado State University, Fort Collins, Colorado.

Schaake, J. C., 1965. Synthesis of the Inlet Hydrograph. Ph.D. Dissertation, Dept. of Sanitary Engineering and Water Resources, The Johns Hopkins University, Baltimore, Maryland.

Tayfur, G., M. L. Kavvas, R. S. Govindaraju, and D. E. Storm, 1993. Applicability of St. Venant Equations for Two-Dimensional Overland Flows Over Rough Infiltrating Surfaces. Journal of Hydraulic Engineering, ASCE 119(1):51-63.

Vieux, B. E., 1991. Geographic Information Systems and Non-Point Source Water Quality and Quantity Modeling. Hydrological Processes 5:101-113.

Woolhiser, D. A., 1969. Overland Flow on a Converging Surface. Trans. of ASAE, 12(4):460-462.

Woolhiser, D. A., 1975. Simulation of Unsteady Overland Flow. *In:* Unsteady Flow in Open Channels, Vol. II, Chapter 12, K. Mahmood and V. Yevjevich (Editors). Water Resources Publications, Fort Collins, Colorado.

Zawadzki, I, 1982. The Quantitative Interpretation of Weather Radar Measurements. Atmos. Ocean 20:158-180.

Zhang, W. and T. W. Cundy, 1989. Modeling of Two-Dimensional Overland Flow. Water Resources Research 25(9):2019-2035.

NOTATIONS

E = ground elevation

f = infiltration rate

F = cumulative infiltration depth

g = gravitational acceleration

h = flow depth

H_f = capillary pressure head at the wetting front

i = rainfall intensity

i_e = excess rainfall intensity

j = row number of grid cell

k = column number of grid cell

L = total length along hydraulically longest kinematic flow path

M_d = soil moisture deficit

n = Manning roughness coefficient

q = unit discharge

q_1 = lateral inflow

q_x, q_y = unit discharge in the x,y directions

Q = total discharge

R = hydraulic radius

S = degree of initial soil saturation

S_o = bed slope

S_f = friction slope

t = time

V = flow velocity

W = overland plane width

x,y = Cartesian coordinates

α_x, β, γ = parameters of the resistance equations

θ_e = the effective soil porosity

θ_i = initial soil moisture content

θ_r = residual saturation

ϕ = total soil porosity

HYDROLOGICAL PROCESSES, VOL. 10, 1503–1511 (1996)

LAND-USE IMPACT ON WATERSHED RESPONSE: THE INTEGRATION OF TWO-DIMENSIONAL HYDROLOGICAL MODELLING AND GEOGRAPHICAL INFORMATION SYSTEMS

WILLIAM W. DOE III

Department of Geography and Environmental Engineering, US Military Academy, West Point, NY 10996, USA

BAHRAM SAGHAFIAN

US Army Construction Engineering Research Laboratories, Champaign, IL 61826, USA

AND

PIERRE Y. JULIEN

Department of Civil Engineering, Engineering Research Center, Colorado State University, Fort Collins, CO 80523, USA

ABSTRACT

The integration of a two-dimensional, raster-based rainfall–runoff model, CASC2D, with a raster geographical information system (GIS), GRASS, offers enhanced capabilities for analysing the hydrological impact under a variety of land management scenarios. The spatially varied components of the watershed, such as slope, soil texture, surface roughness and land-use disturbance, were characterized in GRASS at a user-specified grid cell resolution for input into the CASC2D model. CASC2D is a raster-based, single-event rainfall–runoff model that divides the watershed into grid cell elements and simulates the hydrological processes of infiltration, overland flow and channel flow in response to distributed rainfall precipitation. The five-step integration of CASC2D and GRASS demonstrates the potential for analysing spatially and temporally varied hydrological processes within a 50 square mile semi-arid watershed. By defining possible land-use disturbance scenarios for the watershed, a variety of rainfall–runoff events were simulated to determine the changes in watershed response under varying disturbance and rainfall conditions. Additionally, spatially distributed infiltration outputs derived from the simulations were analysed in GRASS to determine the variability of hydrological change within the watershed. Grid cell computational capabilities in GRASS allow the user to combine the scenario simulation outputs with other distributed watershed parameters to develop complex maps depicting potential areas of hydrological sensitivity. This GIS–hydrological model integration provides valuable spatial information to researchers and managers concerned with the study and effects of land-use on hydrological response.

KEY WORDS hydrology; rainfall–runoff models; watershed responses; geographical information systems

INTRODUCTON

The analysis of watershed response during rainfall–runoff events can be greatly enhanced by the integrated use of geographic information system (GIS) technology with physically based hydrological models. The advantages and disadvantages of using a GIS with hydrological modelling have been summarized by DeVantier and Feldman (1993). Successful applications of such integration were demonstrated by Ross and Tara (1993), who used this approach for the analysis of reclaimed mine site land use. An integrated GIS–modelling approach is particularly useful for land managers who are concerned with the range of effects caused by varying types and intensities of land-use within a watershed. The simulation of multiple

CCC 0885–6087/96/111503–09
© 1996 by John Wiley & Sons, Ltd.

Received 1 May 1994
Accepted 22 May 1995

land-use scenarios in the GIS–modelling environment can provide valuable spatial information to land managers and assist them with the implementation of sound land-use management practices.

In this study, the Geographic Resources Analysis Support System (GRASS), a raster-based GIS, is integrated with a two-dimensional, raster-based rainfall–runoff model, CASC2D, to investigate potential watershed impacts. The focus of this paper is to describe the general methodology used and to illustrate its utility for analysing spatially and temporally varied hydrological processes in a watershed during rainfall–runoff events. The emphasis is on the benefits brought by merging a raster-based GIS and hydrological model. In this respect, the substance of this analysis is not specific to GRASS and CASC2D; equivalent results should be obtained with comparable raster-based GISs and hydrological models. In a demonstration study, this integrated approach investigates land-use impacts on a 50-square mile, semi-arid watershed, the Taylor Arroyo, in south-eastern Colorado. The particular land-use impacts evaluated were disturbances caused by US Army tracked vehicle manoeuvers across the watershed.

WATERSHED DESCRIPTION AND RAINFALL CHARACTERISTICS

The Taylor Arroyo watershed encompasses a 50-square mile area of semi-arid grasslands and uplands in south-eastern Colorado. The baseline hydrology of the watershed has been studied and documented by von Guerard *et al.* (1987;1993). Their studies focused on the collection and analysis of rainfall and streamflow data as well as water quality parameters. The watershed is drained by a complex network of ephemeral streams or arroyos. Two principal arroyos drain the watershed and converge approximately 3 miles above the watershed outlet before entrenching into a deep rock canyon. Channel cross-sections vary greatly, but can be as deep as 3 m and as wide as 25 m. The arroyos are further characterized by steep banks of alluvium subject to downslope erosion. Rainfall events are infrequent and result primarily from intense convective thunderstorms in the summer. The dominant hydrological processes within the watershed are infiltration and channel flow. Infiltration is controlled primarily by the antecedent soil moisture conditions and the hydraulic properties of the surface layer. Subsurface flow from singular rainfall events is negligible. Channel flow is controlled primarily by the density of channel networks and surface runoff immediately adjacent to the channels.

A system of nine automated rain gauges and one stream gauge near the outlet is operated by the US Geological Survey (USGS). They provided distributed rainfall data and stream discharge data for this demonstration. These data were collected for a thunderstorm event occurring on 9 August 1987, which represented the largest recorded runoff event for the water year. The rainfall data used for the model calibration were recorded at 5 min intervals for a duration of 3 h. Simulations for the watershed were performed in CASC2D using this spatially distributed event as an undisturbed calibration example to determine how well the model represented the watershed and its hydrological response. Both the volumetric relationships for inflow–outflow and the peak discharge were simulated accurately (Doe, 1992).

Additional rainfall data were derived from historical precipitation–frequency maps for the south-eastern region of Colorado (Miller *et al.*, 1973). Rainfall data from these maps were used to determine representative storms of constant rainfall intensity for the 5 yr, 3 h event (2.0 equivalent inches of depth) and the 10 yr, 1 h event (1.9 equivalent inches of depth). These constant rainfall events provided standard storms to examine the effects of non-uniform surface characteristics on the spatial and temporal response's distribution of surface runoff on the watershed.

BRIEF DESCRIPTION OF CASC2D

CASC2D is a distributed, single-event, rainfall–runoff model. The model is fully documented in Julien and Saghafian (1991) and was initially developed as a research tool for analysing the spatial and temporal variations of watershed response. Since its development CASC2D has been applied to several watersheds for hydrological analysis. Saghafian (1992) calibrated and validated early versions of the model on a small, semi-arid watershed, Mack's Creek in Idaho, to examine the hydrological response due to spatially varied

infiltration. Ogden and Julien (1993; 1994) used weather radar data with the model to test runoff sensitivity on both Mack's Creek and the Taylor Arroyo watersheds to temporally and spatially varied rainfall precipitation. Johnson *et al.* (1993) independently calibrated and tested CASC2D with observed data from five rainfall events on a small watershed in Mississippi. They reported that CASC2D performed well for these storm events, particularly with regard to the shape of the runoff hydrograph and peak flow computations. In selecting the CASC2D model for application to the Taylor Arroyo watershed, several factors were considered: (a) its ability to replicate the dominant hydrological processes found in the watershed, particularly infiltration and surface runoff adjacent to channels; (b) the capability to handle spatial and temporal variability; and (c) its compatibility with spatial data and raster GISs.

The primary features of CASC2D include the Green and Ampt method for infiltration, a two-dimensional, explicit solution of the diffusive wave form of the de St. Venant equations for overland flow, and a one-dimensional, explicit solution of the diffusive wave formulation for channel routing. Three hydraulic parameters (saturated hydraulic conductivity, capillary pressure head at the wetting front and soil moisture deficit) are required to solve the Green and Ampt equation. These parameters were determined from infiltrometer tests in the field and compared with the classifications of Rawls *et al.* (1983). The model also contains provisions to account for interception and detention storage, but these were not used in the simulations. To calculate surface runoff the model solves the two-dimensional equations of continuity and momentum which describe gradually varied overland flow. Resistance to flow is described by Manning's equation. Finite-width channel flow routing is performed in a similar fashion, but in only one direction along the channel path. The overland flow and channel flow are fully coupled to allow lateral inflows and outflows along the channel lengths.

The physical watershed domain in CASC2D is characterized by square (raster) grid cells. Raster data files for elevation, soil texture and surface roughness must be prepared. Although spatial variability is allowed from one grid cell to the next, each cell is represented as a homogeneous unit. The channel network is delineated in a file indicating the network connectivity and the physical characteristics of the various channel segments. The size of the surface feature files and channel network file is largely dictated by the user-selected grid cell resolution. At the selected grid cell size the channels were at a sub-grid cell scale, with the immediate floodplain composing the remainder of each channel cell in the file. In such a case the surface water depth accumulated over the floodplain portion of the cell is routed into the incised sub-grid cell size channel via a weir-type equation.

Uniform or spatially distributed rainfall data may be input to the model. For spatially distributed rainfall data the inverse distance squared algorithm is used to distribute the rainfall across the entire watershed. Rainfall–runoff simulation is performed for each grid cell at a user specified time step. Firstly, the existing surface depth, including the rainfall depth added during the time step, is reduced by the infiltration capacity of the grid cell's occupying soil, based on the user-specified Green and Ampt parameters. Then the remaining surface depth, if any, is routed to adjacent cells according to the water surface slope. The overland flow is routed in two orthogonal directions within each grid cell. The model also enables simulation of run-on and subsequent reinfiltration, which occurs when surface runoff from upstream cells infiltrates into pervious downstream cells. Finally, the runoff from overland cells which reaches the channel cells is routed through the channel network to the watershed outlet.

CASC2D provides the user with a number of simulation options, including a visual colour display of both the static and dynamic characteristics of the watershed simulation. The static windows include colour-coded maps depicting categories of elevation, soil texture, surface roughness and land-use areas. The dynamic display has four windows that appear simultaneously when the simulation begins. Three of these windows depict the spatial distribution of rainfall intensity, infiltration depth and surface water depth. The fourth window provides a display of the outflow hydrograph as the simulation progresses.

BRIEF DESCRIPTION OF GRASS

GRASS is a fully documented, raster-based GIS that was initially developed by the US Army for natural resources and land management applications at federal installations (US Army, 1991). GRASS has been

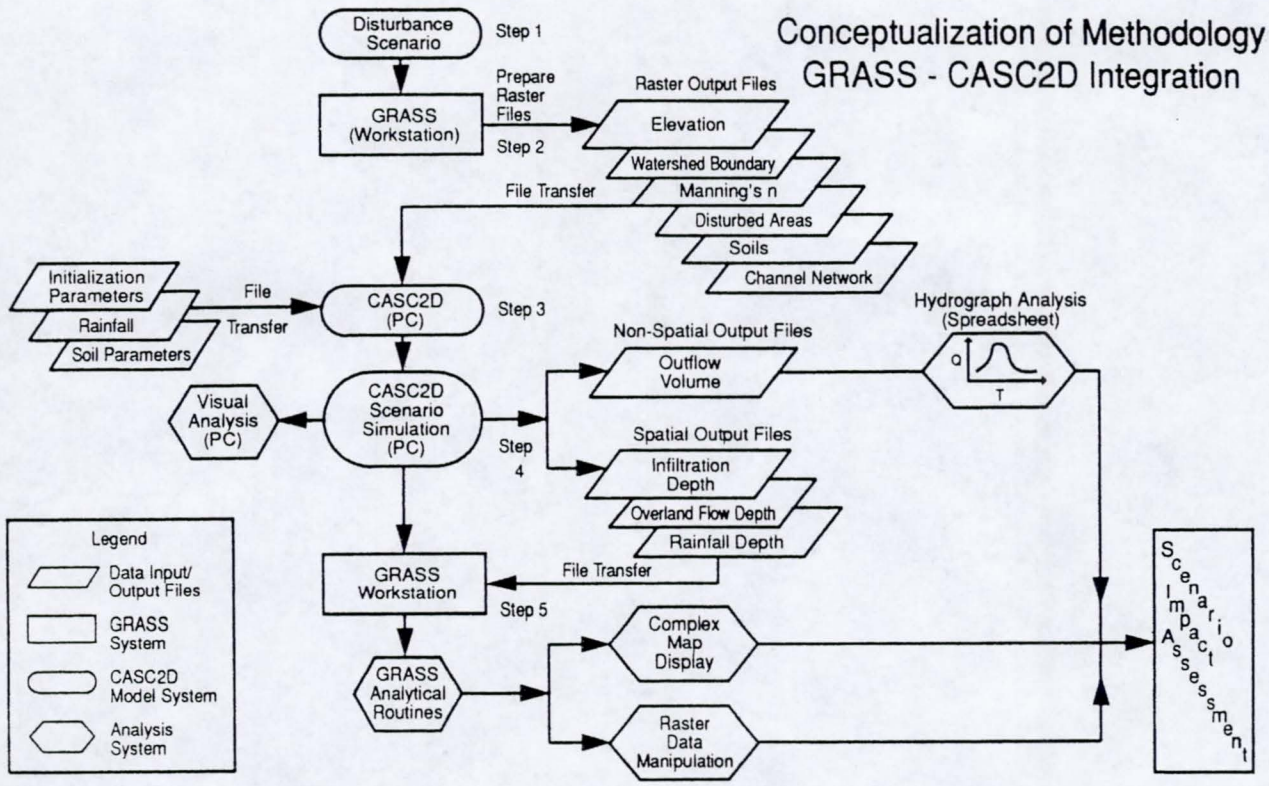

Figure 1. Five-step methodology for GRASS–CASC2D integration

coupled with a variety of hydrological models to examine environmental processes within watersheds. For example, Chen *et al.* (1994) integrated GRASS with a phosphorus transport model to study agricultural land-use and non-point source phosphorus loading in a small watershed in Oklahoma.

GRASS contains a number of advanced programs for hydrological analysis to include routines that delineate sub-watershed boundaries and channel networks from digital elevation model (DEM) data. These routines greatly simplify watershed delineation and characterization for hydrological modelling applications. As with most GIS–modelling applications, the time-consuming derivation of the digital information from primary sources is the critical first step. A GRASS data set for Taylor Arroyo was made available by the US Army, which greatly facilitated the CASC2D–GRASS integration process.

INTEGRATED CASC2D–GRASS METHODOLOGY

A five-step methodology, as shown in Figure 1, was used to assess the impacts of multiple land-use scenarios on the Taylor Arroyo watershed. The approach demonstrated, although specific to CASC2D and GRASS, more importantly provides a framework for similar analysis of land-use impacts on watersheds using other GISs and distributed hydrological models.

Step 1: scenario development

A wide range of potential scenarios can be developed and tested using the approach described. It is recommended that these scenarios are developed in concert with the land manager or other knowledgeable staff so that they represent a realistic spectrum of possible impacts. To illustrate the potential for this type of analysis, three land-use disturbance scenarios for the Taylor Arroyo watershed were developed from generalized land management concepts for the watershed. As described in the following and shown in Figure 2, each land-use scenario defines a different level of land-use impacts with regards to both the intensity and areal extent of use: (1) The increased protection scenario was defined as medium intensity usage over

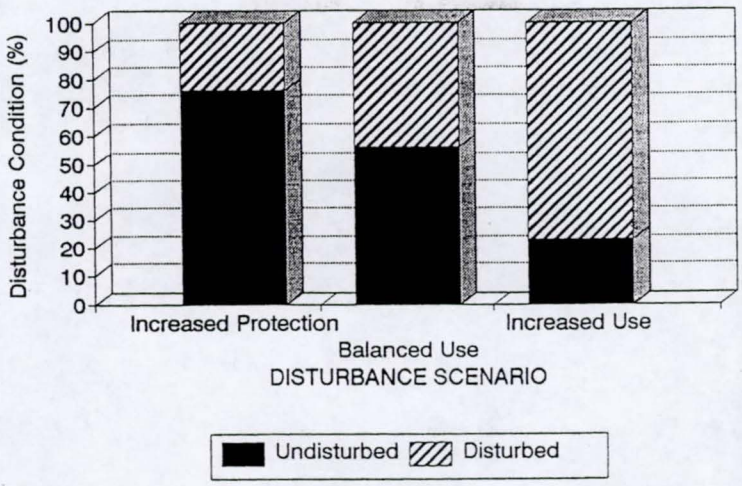

Figure 2. Percentage disturbed and undisturbed areas for generalized land-use scenarios

25% of the watershed area; (2) The balanced use scenario was defined as medium intensity usage over 50% of the watershed area; and (3) The increased use scenario was defined as high intensity usage over 75% of the watershed area.

The medium and high intensity disturbance levels were quantified as the percentage change in porosity due to compaction of the soil based on the results of *in situ* infiltrometer tests for natural conditions and after the passage of tracked vehicles (Doe, 1992). Texture-based values of the soil hydraulic properties for a 10 and 20% change in porosity were determined using the techniques described by Rawls and Brakensiek (1983). Based on the assigned soil texture, each grid cell with a disturbed soil was assigned new parameter values for the Green–Ampt infiltration equation, to include effective soil porosity, soil capillary pressure head (cm) and soil hydraulic conductivity (cm/h), to distinguish them from undisturbed grid cell values. The disturbed parameter values were distributed to the appropriate grid cells across the watershed according to the defined disturbance scenario.

Because of the variability of soils and other natural characteristics throughout the watershed, the spatial distribution of land-use impacts has a significant effect on the overall watershed response as well as on the internal watershed dynamics. The percentage of disturbed area for each scenario was allocated across the watershed in GRASS. Several contiguous areas of disturbance within the watershed were defined under the assumption that land-use tends to be concentrated in areas rather than distributed uniformly. The delineation of potentially disturbed areas in the watershed could be digitized directly from topographic maps or other sources into GRASS if that information is available to the land manager.

Step 2: spatial characterization of the watershed in GRASS

Before the prescribed rainfall events and land-use scenarios can be simulated in the CASC2D model, the physical dimensions and spatial attributes of the watershed had to be defined and input to the model as raster (grid cell) files. The raster data handling and manipulation capabilities of GRASS made this a convenient and efficient system for characterizing the watershed from digital data. The inherent spatial variability found within the watershed was characterized at grid cell resolution in GRASS. A grid cell resolution of 300 m was selected.

The basic raster map layers needed to characterize the watershed in the CASC2D model included (1) watershed boundary, (2) elevation, (3) soil texture classes, (4) Manning's n overland flow resistance classes and (5) channel network. In addition, for each scenario a soil map layer indicating the spatial coverage of disturbed areas had to be created because these soils would show different hydraulic properties. Each of these raster layers was produced, as illustrated through CASC2D graphics capability in Figure 3, using an array of standard GRASS routines for data import, conversion, manipulation and analysis.

Digital elevation model data at 30 m resolution were obtained from the USGS. The DEM data were

smoothed, filtered and regridded to 300 m resolution using the suite of DEM import routines and neighbourhood smoothing filters. Once a seamless and smoothed elevation map was created, the watershed routines in GRASS were used with the DEM elevation data to delineate the subwatershed boundaries. The channel network was digitized separately based on DEM data, topographic maps and field observations. The resultant output maps were reclassified to provide a mask of the watershed for grid cell analysis. The masked area inside the watershed boundary consisted of a 46 × 60 grid cell matrix.

A digital map of Soil Conservation Service undisturbed soil classifications was reclassified into five textural soil categories based on the available soil information and field samples. The five textural soil groups identified were (1) rock, (2) clay, (3) clay loam, (4) loam and (5) sandy loam. The values of the soil hydraulic properties for each soil texture category were derived from field sampling and published tabular values from Rawls *et al.* (1983).

A digital map of vegetation classes derived from 1:40 000 scale aerial photography was reclassified into four classes of Manning's n overland flow resistance categories based on observed field data and published reports. Each vegetation category was assigned a value of n based on published tables from Woolhiser (1975).

Finally, the channel delineation produced by the GRASS watershed routines was reclassified and thinned to a one cell wide network. As reported by Fairfield and Leymarie (1991), difficulties are associated with deriving drainage networks from DEM data. The data capture processes used to derive DEM data and the deterministic eight-neighbourhood method of determining flow direction in a raster GIS can often lead to data bias that is engendered by the sampling grid orientation. This bias is particularly evident in moderate terrain with fairly uniform slopes and can result in parallel flow lines that are unnatural. The channel network produced from the 30 m DEM data had a density comparable with that of the 1:24 000 scale topographic maps, although the directional bias was apparent and several tributary junctions were misrepresented. When the channel network was delineated from the 300 m resolution data, the results were more satisfactory, although the channel network was obviously less detailed. The network delineated at the 300 m resolution consisted of 176 grid cells or approximately 13% of the total number of elements inside the watershed.

Step 3: Linkage of GRASS spatial data with the CASC2D model

The standard data export and conversion routines in GRASS were used to convert the decribed raster map layers into ASCII text files that could be then be imported directly into the model on a desktop computer.

With the exception of the channel network file, all of the GRASS-produced raster map files were read directly into the appropriate CASC2D model file without modification. Static map displays of elevation, soil textural categories, surface roughness categories and disturbance categories can be displayed in the model if desired. The modified channel network was divided into channel segments indicating the location of each element in the segment as well as the physical characteristics of the segment (width, depth and Manning's n roughness value).

After the raster map data files were imported, the data initialization file was prepared in the model. This file contains information on gauge locations, number of channel segments, values of Manning overland flow roughness and values of soil hydraulic properties for each soil type. The file also contains essential information on model time step, rainfall descriptors and graphics visualization routines.

Step 4: Hydrological simulation of scenarios in CASC2D and hydrograph analysis

Once the watershed characterization was complete for all raster inputs and the non-distributed parameter values were initialized, selected land-use scenarios were simulated in the model. Typically each rainfall–runoff event was simulated for a 25 h period. Depending on the simulation time step chosen, the graphics routines used, and the computer speed, a simulation would run for 60–90 min for an average simulation/measured ratio of 1:20. If visualization of the rainfall and the watershed response is desired, the full graphics capability can be used to display windows depicting the dynamic changes in rainfall intensity, infiltration depth, overland and channel flow depth and outlet hydrograph. As illustrated in Figure 4, the visualization routines are particularly valuable for observing where and when water flows from various

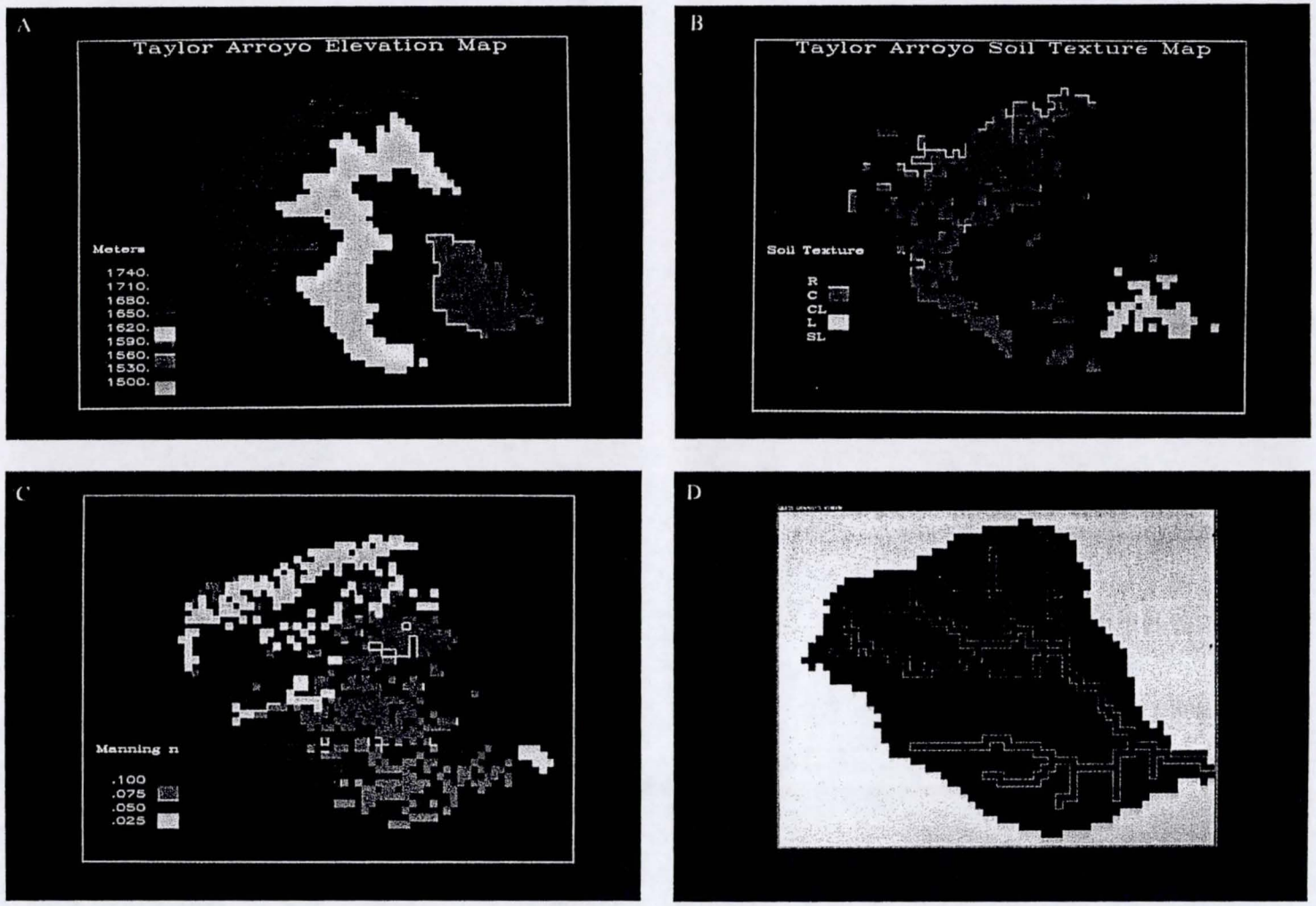

Figure 3. GRASS-generated raster maps for characterization of the Taylor Arroyo in CASC2D; (A) elevation (B) soil texture; (C) Manning's *n*; and (D) channel network

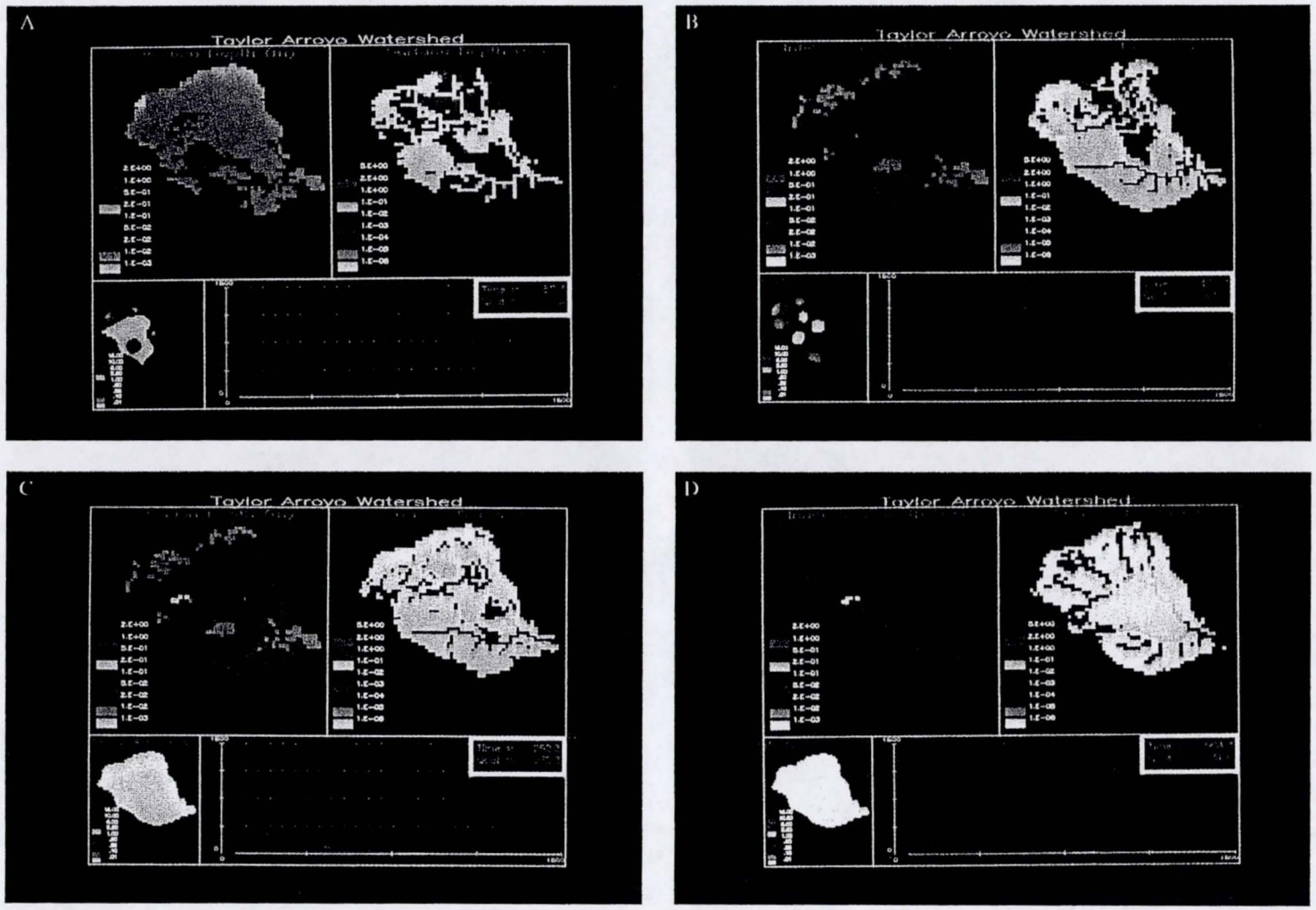

Figure 4. CASC2D simulation showing dynamic visualization graphics for a non-uniform rainfall case at; (A) 52; (B) 172; (C) 252; and (D) 904 min

portions of the watershed to the channel network and ultimately to the watershed outlet. The hydrograph for the increased use case is shown in Figure 5.

The model can be run without the visualization routines if the user is only interested in the model outputs from a scenario. In either instance the standard outputs from the model include (1) time-dependent discharge (hydrograph) in cubic feet per second (cfs) at the outlet, (2) mass balance computations for rainfall input, infiltration, surface storage and outflow and (3) final infiltration and overland flow depths (mm) at the end of simulation time for each grid cell. The model can be modified to provide the spatial outputs of infiltration and overland flow depths for any desired time step during the simulation. In this fashion a quantitative snapshot of these processes at any point during the simulation can be obtained.

The hydrograph data produced by the simulation can be easily imported into a computer spreadsheet for analysis and graphical plotting. Hydrograph envelopes, as shown in Figure 5, can be created to illustrate the watershed response under a variety of land-use scenarios. These hydrographs are useful for comparison with base case (undisturbed) scenarios. The percentage of rainfall that is infiltrated, stored or discharged from the watershed can be computed from the mass balance statistics and provides an additional quantitative assessment of how various scenarios affect the watershed.

Although the discussed data outputs provide useful quantitative information on the aggregated response of the watershed, they do not give information about the internal watershed dynamics. The model's raster outputs of infiltration depth and overland flow depth provide spatial information that can be analysed in a variety of ways. These data can be analysed by importing them into a spreadsheet and computing histograms of depth at various time intervals. These types of displays can reveal similarities or trends between scenarios that may provide useful information for management consideration. However, this type of analysis does not fully use the potential of the spatial information gained from the two-dimensional model simulation. Further analysis can be achieved by importing the simulation results back into GRASS for detailed spatial analysis and post-processing using the suite of analytical functions available.

Step 5: Linkage of CASC2D spatial outputs to GRASS for spatial analysis

The entire range of raster computational and analytical functions in GRASS can be used to manipulate and display the model outputs for further analysis. For example, the infiltration depth values can be correlated with other map layers, such as soils or vegetation, to explore significant spatial coincidences between infiltration and watershed surface characteristics. The infiltration data can be reclassified into more meaningful categories for management decision-making. Map calculations can be performed to compare the percentage differences in infiltration from various scenarios across each element of the watershed.

A raster map of the percentage difference in infiltration depth between the undisturbed and disturbed conditions for a representative scenario was derived in GRASS using the raster map calculation routines. This map is then reclassified into seven categories indicating the degree of increase or decrease in infiltration depth. This spatial data manipulation transforms the model outputs into more meaningful management information for the delineation of sensitive areas within the watershed. The model outputs can be further combined with other map layer categories using expert-derived inference rules to identify hydrologically sensitive areas. Such an approach can provide the land manager with spatially distributed information on the watershed response to various land-use scenarios that he or she contemplates.

USER CONSIDERATIONS FOR INTEGRATING HYDROLOGICAL MODELS WITH GISs

The integration of advanced hydrological models with GIS technology should not be viewed as a panacea for solving the complexities of watershed processes. However, there are several clear advantages of this integration which can be exploited, as shown by the CASC2D-GRASS approach. Maidment (1991) provides a comprehensive discussion of the advantages afforded by the modelling–GIS linkage. These advantages include the ability of a GIS to provide a digital database representing the land surface environment, without having to measure or planimeter the data from maps and other sources, and the capabilities of a GIS to act as a display environment for hydrological model outputs.

Despite the obvious advantages and capabilities of such integrated systems there remain serious concerns

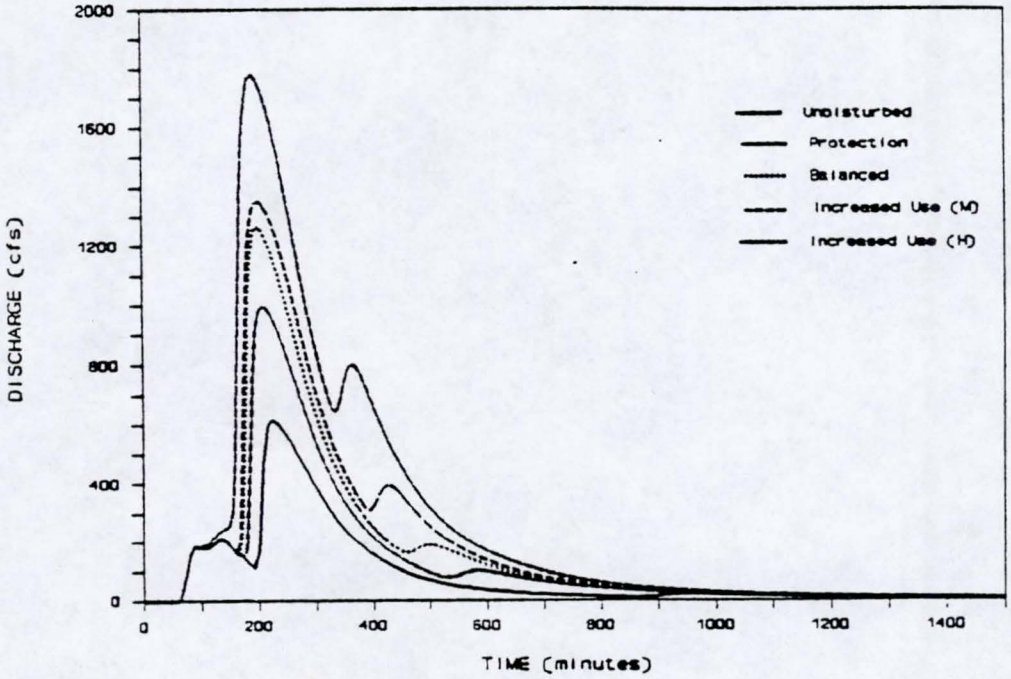

Figure 5. Envelope of scenario hydrographs for a uniform rainfall case

with regard to the quality of data, parameter estimation and grid cell scale and how these affect the representation of hydrological processes. Loague and Gander (1990) performed a comprehensive study of spatial variability of infiltration within a watershed and addressed the implications of this variability in attempting to model rainfall–runoff events, particularly when the simulation scale and parameter measurement scales are different. Field-based measurements of infiltration and hydraulic properties of the soil are suspect when extrapolated across large watersheds. The determination of grid cell scale for hydrological simulation is a major issue surrounding the use of distributed models, which is affected by a number of factors, including the original resolution of the spatial data, the governing equations and computational power of the system. In some respects, the capabilities and sophistication of hydrological models and GIS technology have exceeded our ability to provide the necessary input data given the natural variability inherent in the watershed system. Recognizing these limitations, the hydrological community should continue to foster the development and integration of spatial systems and explore the potential they provide for better understanding of land-use impacts on natural hydrological processes.

CONCLUSIONS

A series of land-use scenarios and rainfall events were simulated on a 50-square mile, semi-arid watershed, the Taylor Arroyo, using a five-step methodology that integrates the CASC2D hydrological model and the GRASS GIS. This integration was successful in depicting the temporally and spatially varied response of the watershed under different scenarios. Although CASC2D and GRASS were well suited for this specific application, the methodology illustrates the potential for other distributed modelling–GIS systems to analyse a variety of hydrological processes and associated land-use impacts. The technology and analytical methodology provided by this integration can provide otherwise unrecognized information and insights into the hydrological regime of a watershed. This added dimension can assist land managers in determining sensitive areas and future land management practices within a watershed.

ACKNOWLEDGEMENTS

This research was conducted at the Army Center for Geosciences, Colorado State University. Funding

support was provided by the US Army Research Office Grant No. ARO/DAAL 03-86K-0175 and ARO/DAAH04-94-G-0420, the US Army Construction Engineering Research Laboratories (USACERL), the US Army Cold Regions Research and Engineering Laboratory (USACRREL) and the Energy, Environment and Natural Resources Directorate, Fort Carson, Colorado. The authors thank Mr Paul von Guerard, US Geological Survey, formerly of the Water Resources Division, Pueblo, Colorado, for his technical assistance in providing rainfall and streamflow data for the Taylor Arroyo.

REFERENCES

Chen, Z. *et al.* 1994. Prioritizing nonpoint source phosphorus loading using a GRASS-modeling system,' *Wat. Resour. Bull.*, **30,** 589–594.

DeVantier, B. A. and Feldman, A. 1993. Review of GIS applications in hydrologic modeling,' *J. Wat. Resour. Planning Manag. ASCE*, **119,** 246–261.

Doe, W. W. 1992. 'Simulation of the spatial and temporal effects of army maneuvers on watershed response,' *PhD Dissertation*, Department of Civil Engineering, Colorado State University.

Doe, W. W. and Saghafian, B. 1992. Spatial and temporal effects of army maneuvers on watershed response: the integration of GRASS and a 2-D hydrologic model,' In *Proc. 7th Annual GRASS Users Conference, Lakewood, CO, National Park Service Tech. Rep. NPS/NRG15D/NRTR-93/13*, 91–105.

Fairfield, J. and Leymarie, P. 1991 'Drainage networks from grid digital elevation models,' *Wat. Resour. Res.*, **27,** 709–717.

Johnson, B. E., Raphelt, N. K. and J. C. Willis, N. K. 1991. 'Verification of hydrological modelling systems' In *Proc. Federal Water Agency Workshop on Hydrologic Modeling: Demands for the 90's, Fort Collins, CO, US Geol. Surv. Wat. Resour. Invest. Rep. 93–4018*, 9–20.

Julien, P. Y. and Saghafian B. 1991. 'A two-dimensional watershed rainfall–runoff model: CASC2D user's manual,' *Colorado State Univ. Rep. CER90-91PYJ-BS-12*, 66 pp.

Loague, K.M. and Gander, G.A. 1990. 'R-5 revisited: spatial variability of infiltration on a small rangeland catchment,' *Wat. Resour. Res.*, **26,** 957–971.

Maidment, D.R. 1991. 'GIS and hydrologic modeling,' *Proc. First Int. Symp./Workshop on GIS and Environmental Modeling, Boulder, CO.*

Miller, J., Frederick, R. and Tracey, R. 1973. *Precipitation-Frequency Atlas of the Western United States, Volume III-Colorado, NOAA Atlas 2.* National Oceanic and Atmospheric Administration.

Ogden, F. and Julien, P. Y. 1993. 'Runoff sensitivity to rainfall temporal and spatial variability at runoff plane and small basin scales,' *Wat. Resour. Res.*, **29,** 2589–2597.

Ogden, F. and Julien, P. Y. 1994. 'Runoff sensitivity to radar rainfall resolution,' *J. Hydrol.*, **158,** 1–18.

Rawls, W. J. and Brakensiek, D. L. 1983a. 'A procedure to predict Green and Ampt infiltration parameters,' *Proc. ASAE Conf. Advances in Infiltration, Chicago.* pp. 102–112.

Rawls, W. J. and Brakensiek, D. L. 1983b. 'Green–Ampt infiltration parameters from soils data,' *J. Hydr. Engin. ASCE*, **109,** 62–69.

Ross, M. A. and Tara, P. D. 1993. 'Integrated hydrologic modeling with geographic information systems,' *J. Wat. Resour. Planning Manage. ASCE*, **119,** 129–140.

Saghafian, B. 1992. 'Hydrologic analysis of watershed response to spatially varied infiltration,' *PhD Dissertation*, Colorado State University, Department of Civil Engineering.

US Army Corps of Engineers 1991. *GRASS 4.0 User's Reference Manual.* US Army Construction Engineering Research Laboratories, Champaign, IL. 513 pp.

von Guerard, P., Abbott, P. and Nickless, R. 1987. 'Hydrology of the US Army Pinon Canyon Maneuver Site, Las Animas County, CO,' *US Geol. Surv. Wat. Resour. Invest. Rep. 87-4227*, 117 pp.

von Guerard, P., Parker, R. S. and Dash, R. G. 1993.' Assessment of the effects of military maneuvers on the streamflow, water quality, and sediment yields at the US Army Pinon Canyon maneuver site, Las Animas County, CO,' *US Geol. Surv. Wat. Resour. Invest. Rep. 91-4095*, 84 pp.

Woolhiser, D. A. 1975. 'Simulation of unsteady overland flow' in Mahmood, K. and Yevjevich, V. (Eds), *Unsteady Flow in Open Channels.* Water Resources Publications, Fort Collins. pp. 485–508.

9

STREAM CHANNEL ROUTING

Stream channel routing uses mathematical relations to calculate outflow from a stream channel once inflow, lateral contributions, and channel characteristics are known.

Stream channel routing usually implies open channel flow conditions, although there are exceptions, such as storm sewer flow, for which mixed open channel-closed conduit flow conditions may prevail. In this chapter, stream channel routing refers to unsteady flow calculations in streams and rivers. Channel *reach* refers to a specific length of stream channel possessing certain translation and storage properties. The hydrograph at the upstream end of the reach is the inflow hydrograph; the hydrograph at the downstream end is the outflow hydrograph. Lateral contributions consist of point tributary inflows and/or distributed inflows (i.e. interflow and groundwater flow).

The terms stream channel routing and *flood routing* are often used interchangeably. This is attributed to the fact that most stream channel-routing applications are in flood flow analysis, flood control design, or flood forecasting.

Two general approaches to stream channel routing are recognized: (1) hydrologic and (2) hydraulic. As in the case of reservoir routing, hydrologic stream channel routing is based on the storage concept. Conversely, hydraulic channel routing is based on the principles of mass and momentum conservation. Hydraulic routing techniques are of three types: (1) kinematic wave, (2) diffusion wave, and (3) dynamic wave. The dynamic wave is the most complete model of unsteady open channel flow. Kinematic and diffusion waves are convenient and practical approximations to the dynamic wave.

An alternate approach to hydrologic and hydraulic routing has emerged in recent years. This approach is similar in nature to the hydrologic routing methods yet contains sufficient physical information to compare favorably with the more complex hydraulic routing techniques. This *hybrid* approach is the basis of the Muskingum-Cunge method of flood routing.

At the outset of the study of stream channel routing, it is necessary to introduce a few basic modeling concepts. A typical hydrologic model consists of system, input, and output. In surface water hydrology, the system is usually a catchment, a reservoir, or a stream channel. In the case of a catchment, the input is a storm hyetograph. For reservoirs and stream channels, the input is an inflow hydrograph. For all three cases, catchments, reservoirs, and channels, the output is an outflow hydrograph.

In general, modeling problems are classified into three types: (1) prediction, (2) calibration, and (3) inversion. In the prediction problem, input and system are known and described by properties or parameters, and the task is to calculate the output based on the knowledge of system and input. For instance, with known inflow hydrograph, lateral contributions, and channel reach parameters, the outflow hydrograph from a stream channel can be computed using routing techniques.

In the calibration problem, input and output are known, and the objective is to determine the properties or parameters describing the system. In the case of a stream channel, with known upstream inflow, lateral contributions, and outflow hydrograph, the routing parameters are calculated by a calibration procedure.

The inversion problem is the third type of modeling problem. In this case, system and output are known, and the task is to calculate the inflow or inflows. This is accomplished by reversing the routing process in a technique known as *inverse* channel routing. For instance, with known upstream inflow, outflow, and channel reach parameters, the lateral contributions can be calculated by inverse routing.

The prediction problem is the more common type of modeling application. However, a calibration is usually required in advance of the prediction. Model verification is the process of testing the model with actual data to establish its predictive accuracy. To calibrate and verify a model, it is usually necessary to assemble two different data sets. The first set is used in model calibration, and the second set is used in model verification. A close agreement between calculated and measured data is an indication that the model has been verified. A detailed discussion of these subjects is given in Chapter 13.

This chapter is divided into five sections. Section 9.1 describes the Muskingum method, the most widely used method of hydrologic stream channel routing. Sections 9.2 and 9.3 discuss simplified hydraulic routing techniques: kinematic and diffusion waves, respectively. Section 9.4 describes the Muskingum-Cunge method. Section 9.5 introduces the subject of dynamic wave routing, the most complete hydraulic routing technique.

9.1 MUSKINGUM METHOD

The Muskingum method of flood routing was developed in the 1930s in connection with the design of flood protection schemes in the Muskingum River Basin, Ohio [11].

It is the most widely used method of hydrologic stream channel routing, with numerous applications in the United States and throughout the world.

The Muskingum method is based on the differential equation of storage, Eq. 8-4, reproduced here:

$$I - O = \frac{dS}{dt} \tag{8-4}$$

In an ideal channel, storage is a function of inflow and outflow. This is in constrast with ideal reservoirs, in which storage is solely a function of outflow (see Eqs. 8-5 to 8-7). In the Muskingum method, storage is a linear function of inflow and outflow:

$$S = K[XI + (1 - X)O] \tag{9-1}$$

in which S = storage volume; I = inflow; O = outflow; K = a time constant or storage coefficient; and X = a dimensionless weighting factor. With inflow and outflow in cubic meters per second, K in hours, storage volume is in (cubic meters per second)-hour. Alternatively, K could be expressed in seconds, in which case storage volume is in cubic meters.

Equation 9-1 was developed in 1938 [11] and has been widely used since then. It is essentially a generalization of the linear reservoir concept (Eq. 8-7). In fact, for $X = 0$, Eq. 9-1 reduces to Eq. 8-7. In other words, linear reservoir routing is a special case of Muskingum channel routing for which $X = 0$.

To derive the Muskingum routing equation, Eq. 8-4 is discretized on the xt plane (Fig. 8-2), to yield Eq. 8-13, repeated here:

$$\frac{I_1 + I_2}{2} - \frac{O_1 + O_2}{2} = \frac{S_2 - S_1}{\Delta t} \tag{8-13}$$

Equation 9-1 is expressed at time levels 1 and 2:

$$S_1 = K[XI_1 + (1 - X)O_1] \tag{9-2}$$

$$S_2 = K[XI_2 + (1 - X)O_2] \tag{9-3}$$

Substituting Eqs. 9-2 to 9-3 into Eq. 8-13 and solving for O_2 yields Eq. 8-15, repeated here:

$$O_2 = C_0 I_2 + C_1 I_1 + C_2 O_1 \tag{8-15}$$

in which C_0, C_1 and C_2 are routing coefficients defined in terms of Δt, K, and X as follows:

$$C_0 = \frac{(\Delta t/K) - 2X}{2(1 - X) + (\Delta t/K)} \tag{9-4}$$

$$C_1 = \frac{(\Delta t/K) + 2X}{2(1 - X) + (\Delta t/K)} \tag{9-5}$$

$$C_2 = \frac{2(1 - X) - (\Delta t/K)}{2(1 - X) + (\Delta t/K)} \tag{9-6}$$

Since $(C_0 + C_1 + C_2) = 1$, the routing coefficients can be interpreted as weighting

coefficients. For $X = 0$, Eqs. 9-4, 9-5, and 9-6 reduce to Eqs. 8-16, 8-17, and 8-18, respectively.

Given an inflow hydrograph, an initial flow condition, a chosen time interval Δt, and routing parameters K and X, the routing coefficients can be calculated with Eqs. 9-4 to 9-6 and the outflow hydrograph, with Eq. 8-15. The routing parameters K and X are related to flow and channel characteristics, K being interpreted as the *travel time* of the flood wave from upstream end to downstream end of the channel reach. Therefore, K accounts for the translation (or concentration) portion of the routing (Fig. 9-1).

The parameter X accounts for the storage portion of the routing. For a given flood event, there is a value of X for which the storage in the calculated outflow hydrograph matches that of the measured outflow hydrograph. The effect of storage is to reduce the peak flow and spread the hydrograph in time (Fig. 9-1). Therefore, it is often used interchangeably with the terms *diffusion* and peak attenuation.

The routing parameter K is a function of channel reach length and flood wave speed; parameter X is a function of the flow and channel characteristics that cause runoff diffusion. In the Muskingum method, X is interpreted as a weighting factor and restricted in the range 0.0 to 0.5. Values of X greater than 0.5 produce hydrograph amplification (i.e., negative diffusion), which does not correspond with reality. With $K = \Delta t$ and $X = 0.5$, flow conditions are such that the outflow hydrograph retains the same shape as the inflow hydrograph, but it is translated downstream a time equal to K. For $X = 0$, Muskingum routing reduces to linear reservoir routing (Section 8.2).

In the Muskingum method, parameters K and X are determined by calibration using streamflow records. Simultaneous inflow-outflow discharge measurements for a given channel reach are coupled with a trial-and-error procedure, leading to the deter-

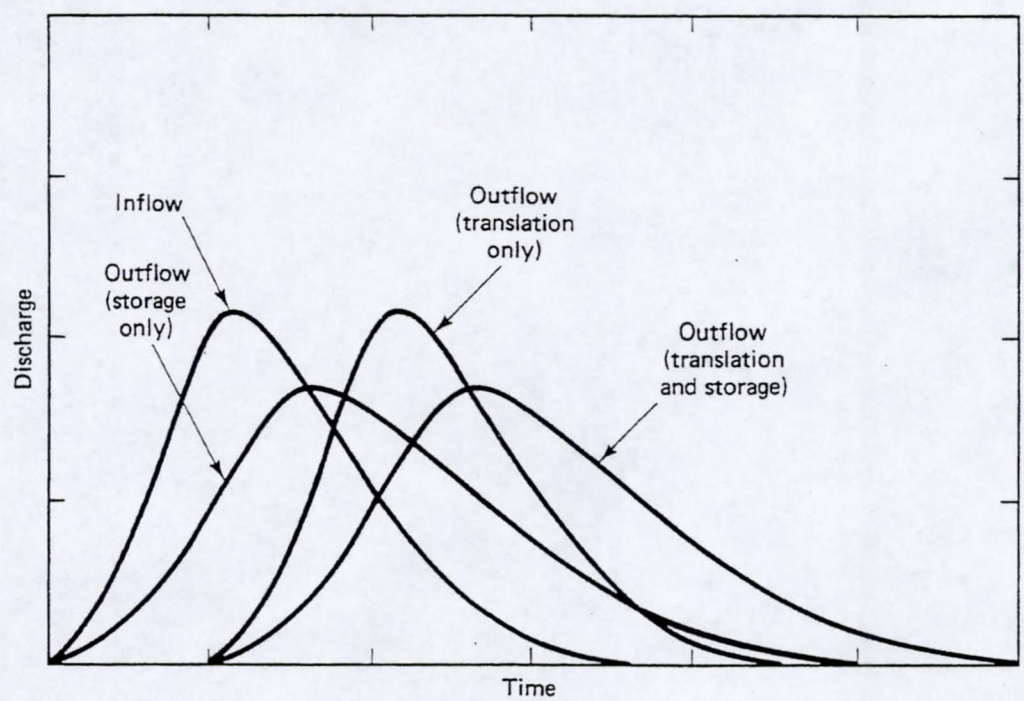

Figure 9-1 Translation and storage processes in stream channel routing.

mination of K and X (see Example 9-2). The procedure is time-consuming and lacks predictive capability. Values of K and X determined in this way are valid only for the given reach and flood event used in the calibration. Extrapolation to other reaches or to other flood events (of different magnitude) within the same reach is usually unwarranted.

When sufficient data are available, a calibration can be performed for several flood events, each of different magnitude, to cover a wide range of flood levels. In this way, the variation of K and X as a function of flood level can be ascertained. In practice, K is more sensitive to flood level than X. A sketch of the variation of K with stage and discharge is shown in Fig. 9-2.

Example 9-1.

An inflow hydrograph to a channel reach is shown in Col. 2 of Table 9-1. Assume baseflow is 352 m^3/s. Using the Muskingum method, route this hydrograph through a channel reach with $K = 2$ d and $X = 0.1$ to calculate an outflow hydrograph.

First, it is necessary to select a time interval Δt. In this case, it is convenient to choose $\Delta t = 1$ d. As with reservoir routing, the ratio of time-to-peak to time interval ($t_p/\Delta t$) should be greater than or equal to 5. In addition, the chosen time interval should be such that the routing coefficients remain positive. With $\Delta t = 1$ d, $K = 2$ d, and $X = 0.1$, the routing coefficients (Eqs. 9-4 to 9-6) are: $C_0 = 0.1304$; $C_1 = 0.3044$; and $C_2 = 0.5652$. It is verified that $C_0 + C_1 + C_2 = 1$. The routing calculations are shown in Table 9-1. Column 1 shows the time in days, and Col. 2 shows the inflow hydrograph ordinates in cubic meters per second. Columns 3–5 show the partial flows. Following Eq. 8-15, Cols. 3–5 are summed to obtain Col. 6, the outflow hydrograph ordinates in cubic meters per second. To explain the procedure briefly, the outflow at the start (day 0) is assumed to be equal to the inflow at the start: 352 m^3/s. The inflow at day 1 multiplied by C_0 is entered in Col. 3, day 1: 76.6 m^3/s. The inflow at day 0 multiplied by C_1 is entered in Col. 4, day

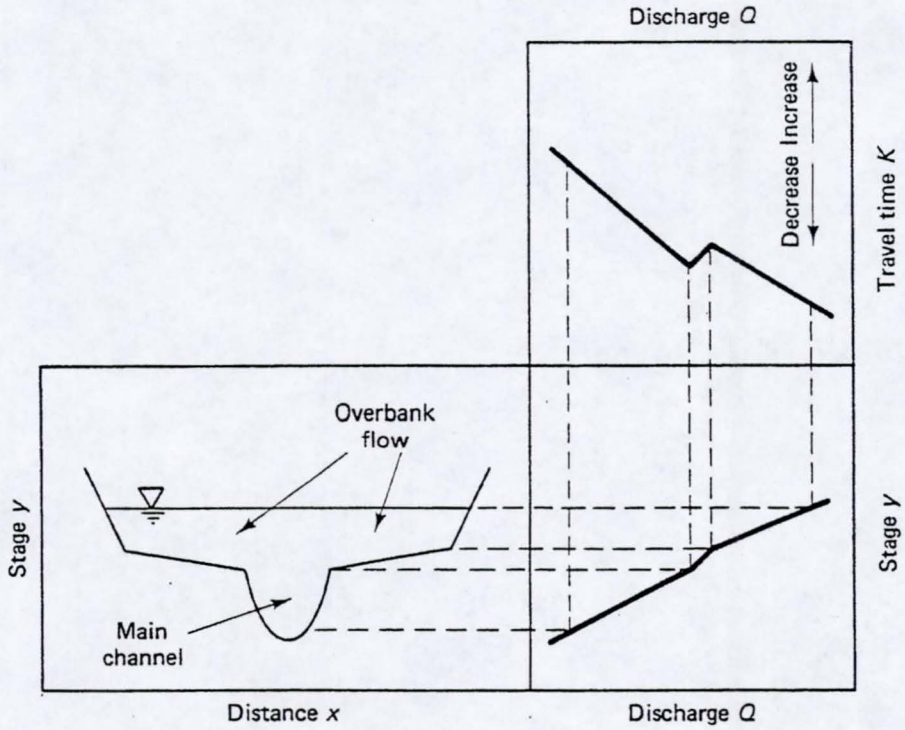

Figure 9-2 Sketch of travel time as a function of discharge and stage.

TABLE 9-1 CHANNEL ROUTING BY THE MUSKINGUM METHOD: EXAMPLE 9-1

(1)	(2)	(3)	(4)	(5)	(6)
		Partial Flows (m^3/s)			
Time (d)	Inflow (m^3/s)	C_0I_2	C_1I_1	C_2O_1	Outflow (m^3/s)
0	352.0	—	—	—	352.0
1	587.0	76.6	107.1	199.0	382.7
2	1353.0	176.5	178.6	216.3	571.4
3	2725.0	355.4	411.8	323.0	1090.2
4	4408.5	575.0	829.4	616.2	2020.6
5	5987.0	780.9	1341.7	1142.1	3264.7
6	6704.0	874.4	1822.1	1845.3	4541.8
7	6951.0	906.7	2040.3	2567.1	5514.1
8	6839.0	892.0	2115.5	3116.7	6124.2
9	6207.0	809.6	2081.5	3461.5	6352.6
10	5346.0	697.3	1889.1	3590.6	6177.0
11	4560.0	594.8	1627.0	3491.4	5713.2
12	3861.5	503.7	1387.8	3229.2	5120.7
13	3007.0	392.2	1175.2	2894.3	4461.7
14	2357.5	307.5	915.2	2521.8	3744.5
15	1779.0	232.0	717.5	2116.5	3066.0
16	1405.0	183.3	541.4	1733.0	2457.7
17	1123.0	146.5	427.6	1389.1	1963.2
18	952.5	124.2	341.8	1109.6	1575.6
19	730.0	95.2	289.9	890.6	1275.7
20	605.0	78.9	222.2	721.0	1022.1
21	514.0	67.1	184.1	577.7	828.9
22	422.0	55.1	156.4	468.5	680.0
23	352.0	45.9	128.4	384.4	558.7
24	352.0	45.9	107.1	315.8	468.8
25	352.0	45.9	107.1	265.0	418.0

1: 107.1 m^3/s. The outflow at day 0 multiplied by C_2 is entered in Col. 5, day 1: 199 m^3/s. Columns 3–5 of day 1 are summed to obtain Col. 6 of day 1: 76.6 + 107.1 + 199.0 = 382.7 m^3/s. The calculations proceed in a recursive manner until all outflows in Col. 6 have been calculated. Inflow and outflow hydrographs are plotted in Fig. 9-3. The outflow peak is 6352.6 m^3/s, which shows that the inflow peak, 6951 m^3/s, has attenuated to about 91% of its initial value. The peak outflow occurs at day 9, 2 d after the peak inflow, which occurs at day 7. The time elapsed between the occurrence of peak inflow and peak outflow is generally equal to K, the travel time.

Unlike reservoir routing, stream channel-routing calculations exhibit a definite (time) lag between inflow and outflow. Furthermore, in the general case ($X \neq 0$), maximum outflow does not occur at the time when inflow and outflow coincide.

Example 9-1 has illustrated the predictive stage of the Muskingum method, in which the routing parameters are known in advance of the routing. If the parameters are not known, it is first necessary to perform a calibration. The trial-and-error procedure to calibrate the routing parameters is illustrated by the following example.

Example 9-2.

Use the outflow hydrograph calculated in the previous example together with the given

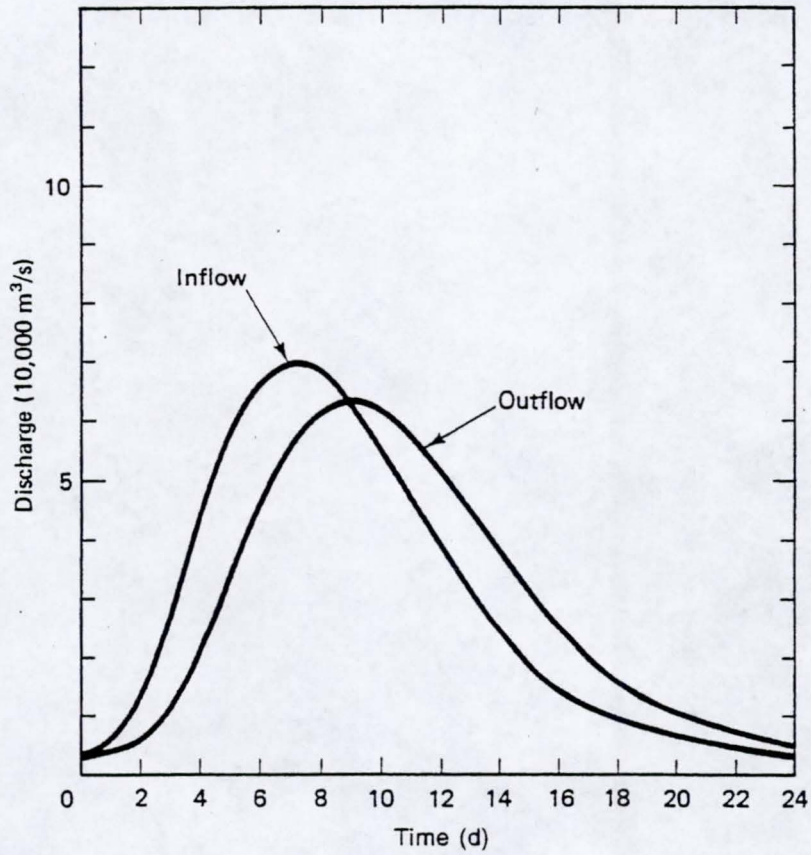

Figure 9-3 Stream channel routing by Muskingum method: Example 9-1.

inflow hydrograph to calibrate the Muskingum method, that is, to find the routing parameters K and X.

The procedure is summarized in Table 9-2. Column 1 shows the time in days. Cols. 2 shows the inflow hydrograph in cubic meters per second; Col. 3 shows the outflow hydrograph in cubic meters per second; Column 4 shows the channel storage in (cubic meters per second)-days. Channel storage at the start is assumed to be 0, and this value is entered in Col. 4, day 0. Channel storage is calculated by solving Eq. 8-13 for S_2:

$$S_2 = S_1 + (\Delta t/2)(I_1 + I_2 - O_1 - O_2) \tag{9-7}$$

Several values of X are tried, within the range 0.0 to 0.5, for example, 0.1, 0.2 and 0.3. For each trial value of X, the weighted flows $[XI + (1 - X)O]$ are calculated, as shown in Cols. 5–7. Each of the weighted flows is plotted against channel storage (Col. 4), as shown in Fig. 9-4. The value of X for which the storage versus weighted flow data plots closest to a line is taken as the correct value of X. In this case, Fig. 9-4(a): $X = 0.1$ is chosen. Following Eq. 9-1, the value of K is obtained from Fig. 9-4(a) by calculating the slope of the storage vs weighted outflow curve. In this case, the value of $K = [2000\ (\text{m}^3/\text{s})\text{-d}]/(1000\ \text{m}^3/\text{s}) = 2$ d. Thus, it is shown that $K = 2$ days and $X = 0.1$ are the Muskingum routing parameters for the given inflow and outflow hydrographs.

The estimation of routing parameters is crucial to the application of the Muskingum method. The parameters are not constant, tending to vary with flow rate. If the routing parameters can be related to flow and channel characteristics, the need for trial-and-error calibration would be eliminated. Parameter K could be related to

TABLE 9-2 CALIBRATION OF MUSKINGUM ROUTING PARAMETERS: EXAMPLE 9-2

(1)	(2)	(3)	(4)	(5)	(6)	(7)
				Weighted Flow (m^3/s)		
Time (d)	Inflow (m^3/s)	Outflow (m^3/s)	Storage (m^3/s)-d	$X = 0.1$	$X = 0.2$	$X = 0.3$
0	352.0	352.0	0	—	—	—
1	587.0	382.7	102.2	403.0	423.5	443.9
2	1,353.0	571.4	595.2	649.6	727.7	805.9
3	2,725.0	1,090.2	1,803.4	1,253.7	1,417.2	1,580.6
4	4,408.5	2,020.6	3,814.7	2,259.4	2,498.2	2,737.0
5	5,987.0	3,264.7	6,369.8	3,536.9	3,809.2	4,081.4
6	6,704.0	4,541.8	8,812.1	4,758.0	4,974.2	5,190.5
7	6,951.0	5,514.1	10,611.6	5,657.8	5,801.5	5,945.2
8	6,839.0	6,124.2	11,687.5	6,195.7	6,267.2	6,338.6
9	6,207.0	6,352.6	11,972.1	6,338.0	6.323.5	6,308.9
10	5,346.0	6,177.0	11,483.8	6,093.9	6,010.8	5,927.7
11	4,560.0	5,713.2	10,491.7	5,597.9	5,482.6	5,367.2
12	3,861.5	5,120.7	9,285.5	4,994.8	4,868.9	4,742.9
13	3,007.0	4,461.7	7,928.5	4,316.2	4,170.8	4,025.3
14	2,357.5	3,744.5	6,507.7	3,605.8	3,467.1	3,328.4
15	1,779.0	3,066.0	5,170.7	2,937.3	2,808.6	2,679.9
16	1,405.0	2,457.7	4,000.8	2,352.4	2,247.2	2,141.9
17	1,123.0	1,963.2	3,054.4	1,879.2	1,795.2	1,711.1
18	952.5	1,575.6	2,322.7	1,513.4	1,451.1	1,388.7
19	730.0	1,275.7	1,738.2	1,221.1	1,166.6	1,112.0
20	605.0	1,022.1	1,256.8	980.4	938.7	897.0
21	514.0	828.9	890.8	797.4	765.9	734.4
22	422.0	680.0	604.4	654.2	628.4	602.6
23	352.0	558.7	372.0	537.9	517.3	496.6
24	352.0	468.8	210.3	457.1	445.4	433.8
25	352.0	418.0	118.9	411.4	404.8	398.2

reach length and flood wave velocity, whereas X could be related to the diffusivity characteristics of flow and channel. These propositions are the basis of the Muskingum-Cunge method (Section 9.4).

9.2 KINEMATIC WAVES

Three types of unsteady open channel flow waves are commonly used in engineering hydrology: (1) kinematic, (2) diffusion, and (3) dynamic waves. Kinematic waves are the simplest type of wave, and dynamic waves are the most complex. Diffusion waves lie somewhere in between kinematic and dynamic waves. Kinematic waves are discussed in this section, and diffusion waves are discussed in Section 9.3. An introduction to dynamic waves is given in Section 9.5.

Kinematic Wave Equation

The derivation of the kinematic wave equation is based on the principle of mass conservation within a control volume. This principle states that the difference between

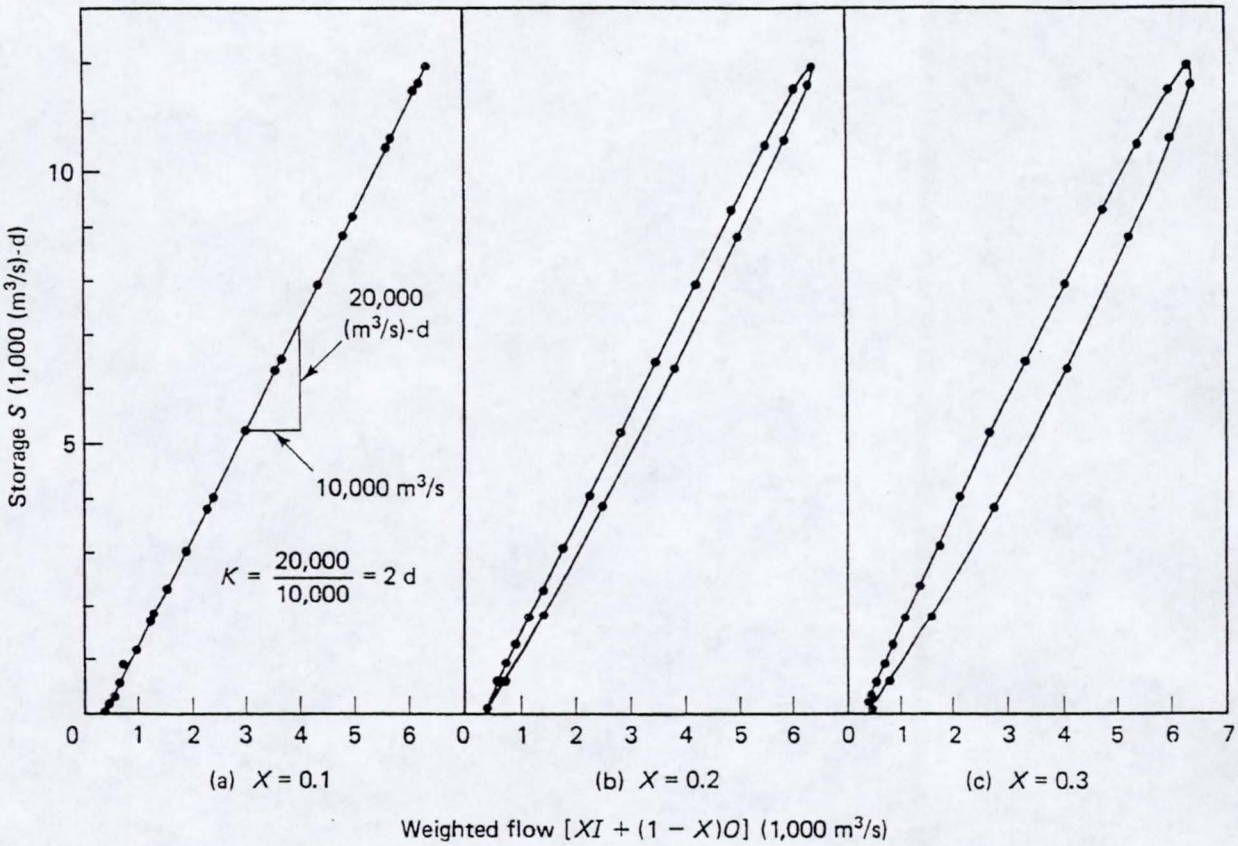

Figure 9-4 Calibration of Muskingum routing parameters: Example 9-2.

outflow and inflow within one time interval is balanced by a corresponding change in volume. In terms of finite intervals (i.e., finite differences) it is:

$$(Q_2 - Q_1)\Delta t + (A_2 - A_1)\Delta x = 0 \tag{9-8}$$

in which Q = flow; A = flow area; Δt = time interval; and Δx = space interval. In differential form, Eq. 9-8 can be written as:

$$\frac{\partial Q}{\partial x} + \frac{\partial A}{\partial t} = 0 \tag{9-9}$$

which is the equation of conservation of mass, or equation of continuity.

The equation of conservation of momentum (Eq. 4-22) contains local inertia, convective inertia, pressure gradient (due to flow depth gradient), friction (friction slope), gravity (bed slope), and a momentum source term (Section 4.2). In deriving the kinematic wave equation, a statement of uniform flow is used in lieu of conservation of momentum. Since uniform flow is strictly a balance of friction and gravity, it follows that local and convective inertia, pressure gradient, and momentum source terms are excluded from the formulation of kinematic waves. In other words, a kinematic wave is a simplified wave that does not include these terms or processes. As shown later in this section, this simplification imposes limits to the applicability of kinematic waves.

Uniform flow in open channels is described by the Manning or Chezy formulas (Section 2.4). The Manning equation is:

$$Q = \frac{1}{n} AR^{2/3} S_f^{1/2} \tag{9-10}$$

in which R is the hydraulic radius in meters, S_f is the friction slope in meters per meter, and n is the Manning friction coefficient.

The Chezy equation is:

$$Q = CAR^{1/2}S_f^{1/2} \tag{9-11}$$

in which C = Chezy coefficient. Notice that in unsteady flow, friction slope is used in Eqs. 9-10 and 9-11 in lieu of channel slope.

The hydraulic radius is $R = A/P$, in which P is the wetted perimeter. Substituting this into Eq. 9-10, leads to:

$$Q = \frac{1}{n}\frac{S_f^{1/2}}{P^{2/3}}A^{5/3} \tag{9-12}$$

Assume for the sake of simplicity that n, S_f, and P are constant. This may be the case of a wide channel in which P can be assumed to be essentially independent of A. Equation 9-12 can then be written as:

$$Q = \alpha A^{\beta} \tag{9-13}$$

in which α and β are parameters of the discharge-area rating (see rating curve, Section 2.4), defined as follows:

$$\alpha = \frac{1}{n}\frac{S_f^{1/2}}{P^{2/3}} \tag{9-14}$$

$$\beta = \frac{5}{3} \tag{9-15}$$

In Eq. 9-13, differentiating Q with respect to A leads to

$$\frac{dQ}{dA} = \beta\frac{Q}{A} = \beta V \tag{9-16}$$

in which V is the mean flow velocity.

Multiplying Eqs. 9-9 and 9-16 and applying the chain rule, the kinematic wave equation is obtained:

$$\frac{\partial Q}{\partial t} + \left(\frac{dQ}{dA}\right)\frac{\partial Q}{\partial x} = 0 \tag{9-17}$$

or, alternatively

$$\frac{\partial Q}{\partial t} + (\beta V)\frac{\partial Q}{\partial x} = 0 \tag{9-18}$$

Equation 9-17 (or 9-18) describes the movement of waves which are kinematic in nature. These are referred to as kinematic waves, i.e., waves for which inertia and pressure (flow depth) gradient have been neglected. Equation 9-17 is a first order partial differential equation. Therefore, kinematic waves travel with wave celerity dQ/dA (or βV) and do not attenuate. Wave attenuation can only be described by a second-order partial differential equation.

The absence of wave attenuation can be further explained by resorting to a

mathematical argument. Since dQ/dA is the celerity of the unsteady (i.e., wavelike) Q, it can be replaced by dx/dt. Therefore, in Eq. 9-17:

$$\frac{\partial Q}{\partial t} + \left(\frac{dx}{dt}\right)\frac{\partial Q}{\partial x} = 0 \tag{9-19}$$

which is equal to the total derivative dQ/dt. Since the right side of Eq. 9-19 is zero, it follows that Q remains constant in time for waves traveling with celerity dQ/dA.

Discretization of Kinematic Wave Equation

Equation 9-18 (or 9-17) is a nonlinear first-order partial differential equation describing the change of discharge Q in time and space. It is nonlinear because the wave celerity βV (or dQ/dA) varies with discharge. The nonlinearity, however, is usually mild, and therefore, Eq. 9-18 can also be solved in a linear mode by considering the wave celerity to be constant.

The solution of Eq. 9-18 can be obtained by analytical or numerical methods. The simplest kinematic wave solution is a linear numerical solution. For this purpose, it is necessary to select a numerical scheme with which to discretize Eq. 9-18 on the xt plane (Fig. 9-5). A review of basic concepts of numerical analysis is necessary before discussing numerical schemes.

Order of Accuracy of Numerical Schemes. The *order of accuracy* of a numerical scheme measures the ability of the scheme to reproduce (i.e., recreate) the terms of the differential equation. In general, the higher the order of accuracy of a scheme, the better it is able to reproduce the terms of the differential equation. *Forward* and *backward* finite differences have first-order accuracy, i.e., discretization errors of first order. *Central* differences have second-order accuracy, with discretization errors of second order. In connection with the numerical solution of Eq. 9-18,

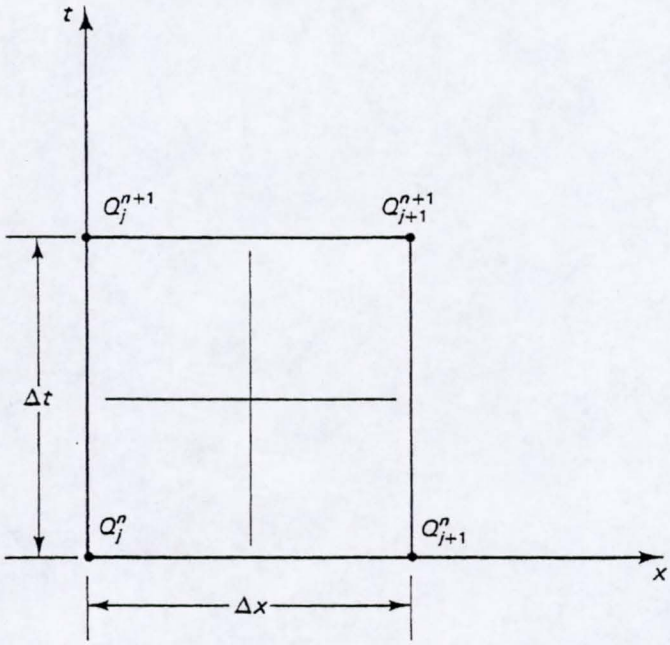

Figure 9-5 Space-time discretization of kinematic wave equation.

first-order schemes create *numerical diffusion* and *numerical dispersion,* while second-order schemes create only numerical dispersion. A third-order scheme creates neither numerical diffusion nor dispersion. Numerical diffusion and/or dispersion are caused by the finite grid size and are not necessarily related to the physical problem.

Second-order-accurate Numerical Scheme. The discretization of Eq. 9-18 following a linear second-order-accurate scheme (i.e., using central differences in space and time) leads to (Fig. 9-5):

$$\frac{\dfrac{Q_{j+1}^{n+1} + Q_j^{n+1}}{2} - \dfrac{Q_{j+1}^{n} + Q_j^{n}}{2}}{\Delta t} + \beta V \frac{\dfrac{Q_{j+1}^{n} + Q_{j+1}^{n+1}}{2} - \dfrac{Q_j^{n} + Q_j^{n+1}}{2}}{\Delta x} = 0 \quad (9\text{-}20)$$

in which βV has been held constant (linear mode), leading to:

$$Q_{j+1}^{n+1} = C_0 Q_j^{n+1} + C_1 Q_j^n + C_2 Q_{j+1}^n \quad (9\text{-}21)$$

in which

$$C_0 = \frac{C - 1}{1 + C} \quad (9\text{-}22)$$

$$C_1 = 1 \quad (9\text{-}23)$$

$$C_2 = \frac{1 - C}{1 + C} \quad (9\text{-}24)$$

and C is the Courant number, defined as follows:

$$C = \beta V \frac{\Delta t}{\Delta x} \quad (9\text{-}25)$$

Notice that Courant number is the ratio of physical wave celerity βV to *grid celerity* $\Delta x/\Delta t$. The Courant number is a fundamental concept in the numerical solution of *hyperbolic* partial differential equations.

Example 9-3.

Use Eq. 9-21 with the routing coefficients of Eqs. 9-22 to 9-24 (linear kinematic wave numerical solution using central differences in space and time) to route the following triangular flood wave. Consider the following three cases: (1) $V = 1.2$ m/s and $\Delta x = 7200$ m; (2) $V = 1.2$ m/s and $\Delta x = 4800$ m; and (3) $V = 0.8$ m/s and $\Delta x = 4800$ m. Use $\beta = 5/3$, and $\Delta t = 1$ h.

Time (h)	0	1	2	3	4	5	6	7	8	9	10
Inflow (m^3/s)	0	30	60	90	120	150	120	90	60	30	0

1. Using Eq. 9-25: C = 1. Using Eqs. 9-22 to 9-24: $C_0 = 0$; $C_1 = 1$; $C_2 = 0$. The routing by Eq. 9-21 shown in Table 9-3 depicts the pure translation of the hydrograph a time equal to Δt. In other words, for $\beta V = \Delta x/\Delta t$ (i.e., $C = 1$), the central difference scheme is of third order, and the numerical solution is exactly equal to the analytical solution.
2. Using Eq. 9-25: $C = 1.5$. Using Eqs. 9-22 to 9-24: $C_0 = 0.2$; $C_1 = 1.0$; $C_2 = -0.2$. The routing by Eq. 9-21 shown in Table 9-4 depicts the translation of the hydrograph a time approximately equal to Δt, but it also shows a small amount of numerical dispersion because βV is not equal to $\Delta x/\Delta t$. The dispersion, including the notorious negative out-

TABLE 9-3 KINEMATIC WAVE ROUTING: PURE TRANSLATION EXAMPLE 9-3, PART 1

(1)	(2)	(3)	(4)	(5)	(6)
		Partial Flows (m^3/s)			
Time (h)	Inflow (m^3/s)	C_0I_2	C_1I_1	C_2O_1	Outflow (m^3/s)
0	0	—	—	—	0
1	30	0	0	0	0
2	60	0	30	0	30
3	90	0	60	0	60
4	120	0	90	0	90
5	150	0	120	0	120
6	120	0	150	0	150
7	90	0	120	0	120
8	60	0	90	0	90
9	30	0	60	0	60
10	0	0	30	0	30
11	0	0	0	0	0

TABLE 9-4 KINEMATIC WAVE ROUTING: TRANSLATION AND DISPERSION EXAMPLE 9-3, PART 2

(1)	(2)	(3)	(4)	(5)	(6)
		Partial Flows (m^3/s)			
Time (h)	Inflow (m^3/s)	C_0I_2	C_1I_1	C_2O_1	Outflow (m^3/s)
0	0	—	—	—	0
1	30	6	0	0	6
2	60	12	30	−1.20	40.80
3	90	18	60	−8.16	69.84
4	120	24	90	−13.97	100.03
5	150	30	120	−20.91	129.99
6	120	24	150	−26.00	148.00
7	90	18	120	−29.60	108.40
8	60	12	90	−21.68	80.32
9	30	6	60	−16.06	49.94
10	0	0	30	−9.99	20.01
11	0	0	0	−4.00	−4.00
12	0	0	0	0.80	0.80
13	0	0	0	−0.16	−0.16

flows at the trailing end of the hydrograph, are caused by errors associated with the scheme's second-order accuracy.

3. Using Eq. 9-25, $C = 1$. Therefore, the solution is the same as in the first case, exhibiting pure hydrograph translation.

The three cases of Example 9-3 illustrate the properties of kinematic waves. The second-order-accurate scheme has no numerical diffusion. In addition, for Courant

number $C = 1$, i.e., the wave celerity βV equal to the grid celerity $\Delta x/\Delta t$, the scheme has no numerical dispersion, with the hydrograph being translated downstream without change in shape. In other words, the numerical solution by Eqs. 9-21 to 9-25 is exact only for Courant number $C = 1$. For any other value of C, the numerical solution exhibits a small but perceptible amount of numerical dispersion.

First-order-accurate Numerical Scheme. The numerical solution of Eq. 9-18 can also be attempted using a first-order-accurate scheme, i.e., one featuring forward or backward finite differences. The discretization of Eq. 9-18 in a linear mode, using backward differences in both space and time yields (Fig. 9-5):

$$\frac{Q_{j+1}^{n+1} - Q_{j+1}^{n}}{\Delta t} + \beta V \frac{Q_{j+1}^{n+1} - Q_{j}^{n+1}}{\Delta x} = 0 \tag{9-26}$$

from which

$$Q_{j+1}^{n+1} = C_0\, Q_j^{n+1} + C_2\, Q_{j+1}^{n} \tag{9-27}$$

in which

$$C_0 = \frac{C}{1 + C} \tag{9-28}$$

$$C_2 = \frac{1}{1 + C} \tag{9-29}$$

and C is the Courant number defined by Eq. 9-25.

Example 9-4.

Use Eq. 9-27 with the coefficients calculated by Eq. 9-28 and 9-29 to route the same inflow hydrograph as in the previous example. Use $V = 1.2$ m/s; $\Delta x = 7200$ m; $\beta = \frac{5}{3}$; and $\Delta t = 1$ h.

Using Eq. 9-25, $C = 1$. Therefore, $C_0 = 0.5$, and $C_2 = 0.5$. The routing using Eq. 9-27 is shown in Table 9-5. It is observed that off-centering the derivatives by using backward differences has caused a significant amount of numerical diffusion, with peak outflow of 120.93 m^3/s as compared to peak inflow of 150 m^3/s. The conclusion is that different schemes for solving Eq. 9-18 lead to different answers, depending on the time and space intervals, Courant number, order of accuracy of the scheme, and associated numerical diffusion and/or dispersion.

Convex Method. The convex method of stream channel routing belongs to the family of linear kinematic wave methods. Until recently (1982), it was part of the SCS TR-20 model for hydrologic simulation (Chapter 13). The routing equation for the convex method is obtained by discretizing Eq. 9-18 in a linear mode using a forward-in-time, backward-in-space finite difference scheme, to yield (Fig. 9-5):

$$\frac{Q_{j+1}^{n+1} - Q_{j+1}^{n}}{\Delta t} + \beta V \frac{Q_{j+1}^{n} - Q_{j}^{n}}{\Delta x} = 0 \tag{9-30}$$

from which

TABLE 9-5 KINEMATIC WAVE ROUTING: TRANSLATION AND DIFFUSION EXAMPLE 9-4

(1)	(2)	(3)	(4)	(5)	(6)
		Partial Flows (m^3/s)			
Time (h)	Inflow (m^3/s)	C_0I_2	C_1I_1	C_2O_1	Outflow (m^3/s)
0	0	—	—	—	0
1	30	15	—	0	15.00
2	60	30	—	7.5	37.50
3	90	45	—	18.75	63.75
4	120	60	—	31.87	91.87
5	150	75	—	45.93	120.93
6	120	60	—	60.46	120.46
7	90	45	—	60.23	105.23
8	60	30	—	52.62	82.62
9	30	15	—	41.31	56.31
10	0	0	—	28.15	28.15
11	0	0	—	14.08	14.08
12	0	0	—	7.04	7.04
13	0	0	—	3.52	3.52
14	0	0	—	1.76	1.76
15	0	0	—	0.88	0.88

$$Q_{j+1}^{n+1} = C_1\, Q_j^n + C_2\, Q_{j+1}^n \tag{9-31}$$

in which

$$C_1 = C \tag{9-32}$$

$$C_2 = 1 - C \tag{9-33}$$

and C is the Courant number (Eq. 9-25), restricted to values less than or equal to 1 for numerical stability reasons. In the convex method, C is regarded as an empirical routing coefficient. The following example illustrates the application of the convex method.

Example 9-5.

Use Eq. 9-31 (the convex method) to route the same inflow hydrograph as in Example 9-3. Assume $C = \frac{2}{3}$.

The routing coefficients are $C_1 = C = \frac{2}{3}$; and $C_2 = 1 - C = \frac{1}{3}$. The routing is shown in Table 9-6. The convex method leads to a significant amount of diffusion, with peak outflow of 135.06 m^3/s as compared to peak inflow of 150 m^3/s. The calculated diffusion amount is a function of C, with practical values of C being restricted in the range 0.5 to 0.9. For $C = 1$, the hydrograph is translated with no diffusion or dispersion, as in the first and third parts of Example 9-3. Values of C greater than 1 render the calculation unstable (large negative values of discharge) and are therefore not recommended. It should be noted that the instability of the convex method for C values greater than 1 has a parallel in the instability of the Muskingum method for X values greater than 0.5.

The convex method is relatively simple, but the solution is dependent on the routing parameter C. The latter could be interpreted as a Courant number and related

TABLE 9-6 KINEMATIC WAVE ROUTING: CONVEX METHOD
EXAMPLE 9-5

(1)	(2)	(3)	(4)	(5)	(6)
		Partial Flows (m^3/s)			
Time (h)	Inflow (m^3/s)	C_0I_2	C_1I_1	C_2O_1	Outflow (m^3/s)
0	0	—	—	—	0.00
1	30	—	0	0	0.00
2	60	—	20	0	20.00
3	90	—	40	6.67	46.67
4	120	—	60	15.56	75.56
5	150	—	80	25.19	105.19
6	120	—	100	35.06	135.06
7	90	—	80	45.02	125.02
8	60	—	60	41.67	101.67
9	30	—	40	33.89	73.89
10	0	—	20	24.63	44.63
11	0	—	0	14.88	14.88
12	0	—	0	4.96	4.96
13	0	—	0	1.65	1.65
14	0	—	0	0.55	0.55

to kinematic wave celerity and grid size, as in Eq. 9-25. However, for values of C other than 1, the amount of diffusion introduced in the numerical problem is unrelated to the true diffusion, if any, of the physical problem. Therefore, the convex method (as well as all kinematic wave methods featuring uncontrolled amounts of numerical diffusion) is regarded as a somewhat crude approach to stream channel routing.

Kinematic Wave Celerity

The kinematic wave celerity is dQ/dA, or βV. A value of $\beta = \frac{5}{3}$ was derived for the case of a wide channel (for which the wetted perimeter P is independent of flow area A) governed by Manning friction.

The kinematic wave celerity is also known as the Kleitz-Seddon or Seddon, law [8, 18]. In 1900, Seddon published a paper in which he studied the nature of unsteady flow movement in rivers and concluded that the celerity of long disturbances was equal to dQ/dA. In view of the fact that $dA = T\,dy$, in which T is the channel top width and y is the stage or water surface elevation, the Seddon law can be expressed in practical terms as follows:

$$c = \frac{1}{T}\frac{dQ}{dy} \tag{9-34}$$

in which c = kinematic wave celerity.

From Eq. 9-34 it is concluded that kinematic wave celerity is a function of the slope of the discharge-stage rating (Q versus y). This slope is likely to vary with stage; therefore, kinematic wave celerity is not constant but varies with stage and flow level. If $c = \beta V$ is a function of Q, then Eq. 9-18 is a nonlinear equation requiring an iterative solution. Nonlinear kinematic wave solutions account for the variation of

kinematic wave celerity with stage and flow level. The simpler linear solutions, as in Examples 9-3 and 9-4, assume a constant value of kinematic wave celerity βV. Notice that there is a striking similarity between the linear kinematic wave solutions and the Muskingum method. This subject is further examined in Section 9.4.

Theoretical β values other than $\frac{5}{3}$ can be obtained for other friction formulations and cross-sectional shapes. For turbulent flow governed by Manning friction, β has an upper limit of $\frac{5}{3}$ but is usually not less than 1. For laminar flow in wide channels, β is equal to 3; for mixed or transitional flow—between laminar and turbulent Manning—it ranges from $\frac{5}{3}$ to 3. For flow in a wide channel described by the Chezy formula, $\beta = \frac{3}{2}$ (Section 4.2). The calculation of β as a function of frictional type and cross-sectional shape is illustrated by the following example.

Example 9-6.

Calculate the β value for a triangular channel (see Fig. 9-6) with Manning friction.

Equation 9-10 is the Manning equation. Substituting $R = A/P$ leads to Eq. 9-12. Since P is a function of A, Eq. 9-12 can be written as follows:

$$Q = K_1 \frac{A^{5/3}}{P^{2/3}} \tag{9-35}$$

in which K_1 is a constant containing n and S_f. The latter have been assumed to be independent of either A or P. For the triangular-shaped channel of Fig. 9-6, the top width is proportional to the flow depth, say $T = Kd$, in which T is the top width, d is the flow depth, and K is a proportionality constant. The flow area is

$$A = K \frac{d^2}{2} \tag{9-36}$$

and the wetted perimeter is

$$P = 2d\left[1 + \frac{K^2}{4}\right]^{1/2} \tag{9-37}$$

Eliminating d from Eqs. 9-36 and 9-37:

$$P = \frac{2(2^{1/2})A^{1/2}}{K^{1/2}}\left[1 + \frac{K^2}{4}\right]^{1/2} \tag{9-38}$$

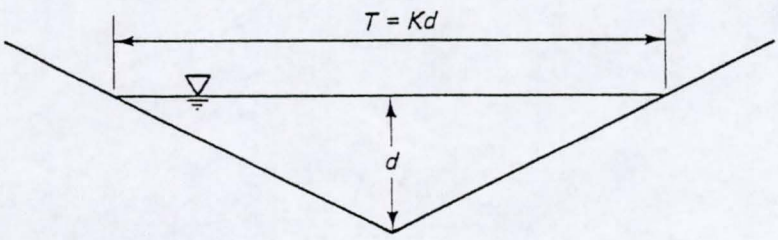

Flow area $A = \dfrac{Kd^2}{2}$

Wetted perimeter $P = 2d\left(1 + \dfrac{K^2}{4}\right)^{1/2}$

Figure 9-6 Properties of triangular channel cross section.

from which

$$P^{2/3} = K_2 A^{1/3} \tag{9-39}$$

in which K_2 is a constant containing K. Substituting Eq. 9-39 into Eq. 9-35 leads to:

$$Q = K_3 A^{4/3} \tag{9-40}$$

in which K_3 is a constant containing K_1 and K_2. From Eq. 9-40:

$$\frac{dQ}{dA} = \frac{4}{3}\frac{Q}{A} \tag{9-41}$$

and the value of β for a triangular channel with Manning friction is $\beta = \frac{4}{3}$.

Kinematic Waves with Lateral Inflow

Practical applications of stream channel routing often require the specification of lateral inflows. The latter could be either concentrated, as in the case of tributary inflow at a point along the channel reach, or distributed along the channel, as with groundwater exfiltration (for effluent streams) or infiltration (for influent streams). As with Eq. 9-9, a mass balance leads to:

$$\frac{\partial Q}{\partial x} + \frac{\partial A}{\partial t} = q_L \tag{9-42}$$

which, unlike Eq. 9-9, includes the source term q_L, the lateral flow per unit channel length. For Q given in cubic meters per second and x in meters, q_L is given in cubic meters per second per meter $[L^2T^{-1}]$. Multiplying Eq. 9-42 by dQ/dA (or βV), as with Eq. 9-17 (or Eq. 9-18), leads to:

$$\frac{\partial Q}{\partial t} + (\beta V)\frac{\partial Q}{\partial x} = (\beta V) q_L \tag{9-43}$$

which is the kinematic wave equation with lateral inflow (or outflow). For q_L positive, there is lateral inflow (e.g., tributary flow); for q_L negative, there is lateral outflow (e.g., channel transmission losses).

Applicability of Kinematic Waves

The kinematic wave celerity is a fundamental streamflow property. Flood waves which approximate kinematic waves travel with the kinematic wave celerity ($c = \beta\ V$) and are subject to very little or no attenuation.

In practice, flood waves are kinematic if they are of long duration or travel on a channel of steep slope. Criteria for the applicability of kinematic waves to overland flow [19] (Section 4.2) and stream channel flow [14] have been developed. The stream channel criterion states that in order for a wave to be kinematic, it should satisfy the following dimensionless inequality:

$$\frac{t_r S_o V_o}{d_o} \geq N \tag{9-44}$$

in which t_r is the time-of-rise of the inflow hydrograph, S_o is the bottom slope, V_o is

the average velocity, and d_o is the average flow depth. For 95 percent accuracy in one period of translation [14], a value of $N = 85$ is indicated.

Example 9-7.

Use the kinematic wave criterion (Eq. 9-44) to determine whether a flood wave with the following characteristics is a kinematic wave: time-of-rise $t_r = 12$ h; bottom slope $S_o = 0.001$; average velocity $V_o = 2$ m/s; average flow depth $d_o = 2$ m.

For the given channel and flow characteristics, the left side of Eq. 9-44 is equal to 43.2, which is less than 85. For values greater than 85, the wave would be kinematic—therefore, subject to negligible diffusion. Since the value is 43.2, this wave is not kinematic and is likely to experience a significant amount of diffusion. If this wave is routed as a kinematic wave with zero diffusion and dispersion, as in Example 9-3 (Part 1), the peak outflow would be much larger than in reality. If this wave is routed as a kinematic wave with diffusion or dispersion, as in Examples 9-3 (Part 2) and 9-4, it is likely that the amount of numerical diffusion and/or dispersion would be different from the actual amount of physical diffusion. It should be noted that had the bottom slope been $S_o = 0.01$, the left side of Eq. 9-44 would be 432, satisfying the kinematic wave criterion. Therefore, it is concluded that the steeper the channel slope, the more kinematic the flow is.

9.3 DIFFUSION WAVES

In Section 9.1, the Muskingum method was used to calculate unsteady flows in a hydrologic sense. In Section 9.2, the principle of mass conservation was coupled with a uniform flow formula to derive the kinematic wave equation. Solutions to this equation have been widely used in engineering hydrology, particularly for overland flow and other routing applications involving steep slopes or slow-rising hydrographs.

The Muskingum method and linear kinematic wave solutions show striking similarities. Both methods have the same type of routing equation. The Muskingum method, however, can calculate hydrograph diffusion, whereas the kinematic wave can do so only by the introduction of numerical diffusion. The latter is dependent on the grid size and type of numerical scheme.

Kinematic wave theory can be enhanced by allowing a small amount of physical diffusion in its formulation [10]. In this way, an improved type of kinematic wave can be formulated, a kinematic-with-diffusion wave, for short, a diffusion wave. A definite advantage of the diffusion wave is that it includes the diffusion which is present in most natural unsteady open channel flows.

Diffusion Wave Equation

In Section 9.2, the kinematic wave equation was derived by using a statement of steady uniform flow (i.e., friction slope is equal to bottom slope) in lieu of momentum conservation. In deriving the diffusion wave, a statement of steady *nonuniform* flow (i.e., friction slope is equal to water surface slope) is used instead (Fig. 9-7). This leads to

$$Q = \frac{1}{n} A R^{2/3} \left(S_o - \frac{dy}{dx} \right)^{1/2} \tag{9-45}$$

in which the term $S_o - (dy/dx)$ is the water surface slope. The difference between

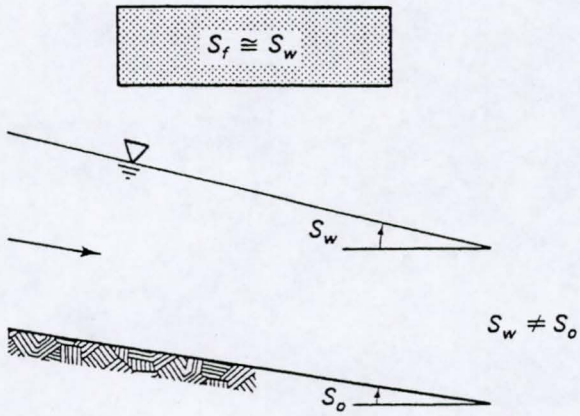

Figure 9-7 Diffusion wave assumption.

kinematic and diffusion waves is in the term dy/dx. From a physical standpoint, the term dy/dx accounts for the natural diffusion processes present in unsteady open channel flow phenomena.

To derive the diffusion wave equation, Eq. 9-45 is expressed in a slightly different form:

$$mQ^2 = S_o - \frac{dy}{dx} \tag{9-46}$$

in which m is the reciprocal of the square of the channel conveyance K, defined as

$$K = \frac{1}{n} AR^{2/3} \tag{9-47}$$

With $dA = T\,dy$, (T = top width), Eq. 9-46 changes to:

$$\left(\frac{1}{T}\right)\frac{dA}{dx} + mQ^2 - S_o = 0 \tag{9-48}$$

Equations 9-9 and 9-48 constitute a set of two partial differential equations describing diffusion waves. These equations can be combined into one equation with Q as dependent variable. However, it is first necessary to linearize the equations around *reference flow* values. For simplicity, a constant top width is assumed (i.e., a wide channel assumption).

The linearization of Eqs. 9-9 and 9-48 is accomplished by small perturbation theory [4]. This procedure, while heuristic, has seemed to work well in a number of applications. The variables Q, A, and m can be expressed in terms of the sum of a reference value (with subscript o) and a small perturbation to the reference value (with superscript $'$): $Q = Q_o + Q'$; $A = A_o + A'$; $m = m_o + m'$. Substituting these into Eqs. 9-9 and 9-48, neglecting squared perturbations, and subtracting the reference flow leads to:

$$\frac{\partial Q'}{\partial x} + \frac{\partial A'}{\partial t} = 0 \tag{9-49}$$

and

$$\frac{1}{T}\frac{\partial A'}{\partial x} + Q_o^2 m' + 2m_o Q_o Q' = 0 \tag{9-50}$$

Differentiating Eq. 9-49 with respect to x and Eq. 9-50 with respect to t gives

$$\frac{\partial^2 Q'}{\partial x^2} + \frac{\partial^2 A'}{\partial x\, \partial t} = 0 \tag{9-51}$$

$$\frac{1}{T}\frac{\partial^2 A'}{\partial x \partial t} + Q_o^2 \frac{\partial m'}{\partial t} + 2m_o Q_o \frac{\partial Q'}{\partial t} = 0 \tag{9-52}$$

Using the chain rule and Eq. 9-49 yields

$$\frac{\partial m'}{\partial t} = \frac{\partial m'}{\partial A'}\frac{\partial A'}{\partial t} = -\frac{\partial m'}{\partial A'}\frac{\partial Q'}{\partial x} \tag{9-53}$$

Combining Eq. 9-52 with Eq. 9-53,

$$\frac{1}{T}\frac{\partial^2 A'}{\partial x \partial t} - Q_o^2 \frac{\partial m'}{\partial A'}\frac{\partial Q'}{\partial x} + 2m_o Q_o \frac{\partial Q'}{\partial t} = 0 \tag{9-54}$$

Combining Eqs. 9-51 and 9-54 and rearranging gives

$$\frac{\partial Q'}{\partial t} - \left[\frac{Q_o}{2m_o}\right]\frac{\partial m'}{\partial A'}\frac{\partial Q'}{\partial x} = \left[\frac{1}{2Tm_o Q_o}\right]\frac{\partial^2 Q'}{\partial x^2} \tag{9-55}$$

Since by definition: $mQ^2 = S_f$, it follows that

$$\frac{\partial Q'}{\partial m'} = \frac{\partial Q}{\partial m} = -\frac{Q_o}{2m_o} \tag{9-56}$$

and also

$$m_o Q_o = \frac{S_o}{Q_o} \tag{9-57}$$

Substituting Eqs. 9-56 and 9-57 into Eq. 9-55, using the chain rule, and dropping the superscripts for simplicity, the following equation is obtained:

$$\frac{\partial Q}{\partial t} + \left[\frac{\partial Q}{\partial A}\right]\frac{\partial Q}{\partial x} = \left[\frac{Q_o}{2TS_o}\right]\frac{\partial^2 Q}{\partial x^2} \tag{9-58}$$

The left side of Eq. 9-58 is recognized as the kinematic wave equation, with $\partial Q/\partial A$ as the kinematic wave celerity. The right side is a second-order (partial differential) term that accounts for the physical diffusion effect. The coefficient of the second-order term has the units of diffusivity $[L^2T^{-1}]$, being referred to as the *hydraulic diffusivity,* or channel diffusivity.

The hydraulic diffusivity is a characteristic of the flow and channel, defined as:

$$\nu_h = \frac{Q_o}{2TS_o} = \frac{q_o}{2S_o} \tag{9-59}$$

in which $q_o = Q_o/T$ is the reference flow per unit of channel width. From Eq. 9-59, it is concluded that hydraulic diffusivity is small for steep bottom slopes (e.g., those of small mountain streams), and large for mild bottom slopes (e.g., tidal rivers).

Equation 9-58 describes the movement of flood waves in a better way than Eq. 9-

17 or 9-18. It falls short from describing the full momentum effects, but it does physically account for peak flow attenuation.

Equation 9-58 is a second-order *parabolic* partial differential equation. It can be solved analytically, leading to Hayami's *diffusion analogy* solution for flood waves [7], or numerically with the aid of a numerical scheme for parabolic equations such as the Crank-Nicolson scheme [3]. An alternate approach is to match the hydraulic diffusivity with the numerical diffusion coefficient of the Muskingum scheme. This approach is the basis of the Muskingum-Cunge method [4, 12] (Section 9.4).

Applicability of Diffusion Waves

Most flood waves have a small amount of physical diffusion; therefore, they are better approximated by the diffusion wave rather than by the kinematic wave. For this reason, diffusion waves apply to a much wider range of practical problems than kinematic waves. Where the diffusion wave fails, only the dynamic wave can properly describe the translation and diffusion of flood waves. The dynamic wave, however, is very strongly diffusive, especially for flows well in the subcritical regime [14]. In practice, most flood flows are only mildly diffusive, and therefore, are subject to modeling with the diffusion wave.

To determine if a wave is a diffusion wave, it should satisfy the following dimensionless inequality [14]:

$$t_r S_o \left[\frac{g}{d_o}\right]^{1/2} \geq M \tag{9-60}$$

in which t_r is the time-of-rise of the inflow hydrograph, S_o is the bottom slope, d_o is the average flow depth, and g is the gravitational acceleration. The greater the left side of this inequality, the more likely it is that the wave is a diffusion wave. In practice, a value of $M = 15$ is recommended for general use.

Example 9-8.

Use the criterion of Eq. 9-60 to determine whether the flood wave of Example 9-7 can be considered a diffusion wave.

For $t_r = 12$ h, $S_o = 0.001$, and $d_o = 2$ m, the left side of Eq. 9-60 is 95.7, which is greater than 15. In the previous example, this wave was shown not to satisfy the kinematic wave criterion. This example shows, however, that this wave is a diffusion wave. Had Eq. 9-60 not been satisfied, the flood wave would have been properly a dynamic wave, subject only to dynamic wave routing. Dynamic wave routing takes into account the complete momentum equation, including the inertia terms (local and convective) that were neglected in the formulation of kinematic and diffusion waves. Section 9.5 contains a brief introduction to dynamic waves.

9.4 MUSKINGUM-CUNGE METHOD

The Muskingum method can calculate runoff diffusion, ostensibly by varying the parameter X. A numerical solution of the linear kinematic wave equation using a third-order-accurate scheme ($C = 1$) leads to pure flood hydrograph translation (see Exam-

ple 9-3, Part 1). Other numerical solutions to the linear kinematic wave equation invariably produce a certain amount of numerical diffusion and/or dispersion (See Example 9-3, Part 2). The Muskingum and linear kinematic wave routing equations are strikingly similar. Furthermore, unlike the kinematic wave equation, the diffusion wave equation does have the capability to describe physical diffusion.

From these propositions, Cunge [4] concluded that the Muskingum method is a linear kinematic wave solution and that the flood wave attenuation shown by the calculation is due to the numerical diffusion of the scheme itself. To prove this assertion, the kinematic wave equation (Eq. 9-18) is discretized on the xt plane (Fig. 9-8) in a way that parallels the Muskingum method, centering the spatial derivative and off-centering the temporal derivative by means of a weighting factor X:

$$\frac{X(Q_j^{n+1} - Q_j^n) + (1 - X)(Q_{j+1}^{n+1} - Q_{j+1}^n)}{\Delta t} + c\frac{(Q_{j+1}^n - Q_j^n) + (Q_{j+1}^{n+1} - Q_j^{n+1})}{2\Delta x} = 0 \tag{9-61}$$

in which $c = \beta V$ is the kinematic wave celerity.

Solving Eq. 9-61 for the unknown discharge leads to the following routing equation:

$$Q_{j+1}^{n+1} = C_0 Q_j^{n+1} + C_1 Q_j^n + C_2 Q_{j+1}^n \tag{9-62}$$

The routing coefficients are

$$C_0 = \frac{c\,(\Delta t/\Delta x) - 2X}{2(1 - X) + c\,(\Delta t/\Delta x)} \tag{9-63}$$

$$C_1 = \frac{c\,(\Delta t/\Delta x) + 2X}{2(1 - X) + c\,(\Delta t/\Delta x)} \tag{9-64}$$

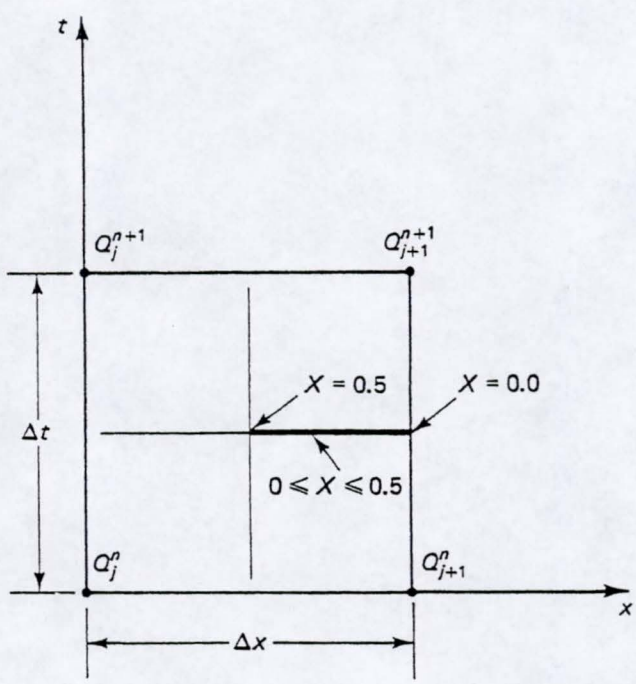

Figure 9-8 Space-time discretization of kinematic wave equation paralleling Muskingum method.

$$C_2 = \frac{2(1 - X) - c\,(\Delta t/\Delta x)}{2(1 - X) + c\,(\Delta t/\Delta x)} \tag{9-65}$$

By defining

$$K = \frac{\Delta x}{c} \tag{9-66}$$

it is seen that the two sets of Eqs. 9-63 to 9-65 and Eqs. 9-4 to 9-6 are the same.

Equation 9-66 confirms that K is in fact the flood-wave travel time, i.e., the time it takes a given discharge to travel the reach length Δx with the kinematic wave celerity c. In a linear mode, c is constant and equal to a reference value; in a nonlinear mode, it varies with discharge.

It can be seen that for $X = 0.5$, Eqs. 9-63 to 9-65 reduce to the routing coefficients of the linear second-order-accurate kinematic wave solution, Eqs. 9-22 to 9-24. For $X = 0.5$ and $C = 1$ ($C = c\,\Delta t/\Delta x = \beta V \Delta t/\Delta x$, the Courant number, Eq. 9-25) the routing equation is third-order accurate, i.e., the numerical solution is equal to the analytical solution of the kinematic wave equation. For $X = 0.5$ and $C \neq 1$, it is second-order accurate, exhibiting only numerical dispersion. For $X < 0.5$ and $C \neq 1$, it is first-order accurate, exhibiting both numerical diffusion and dispersion. For $X < 0.5$ and $C = 1$, it is first-order accurate, exhibiting only numerical diffusion. These relations are summarized in Table 9-7.

In practice, the numerical diffusion can be used to simulate the physical diffusion of the actual flood wave. By expanding the discrete function $Q(j\Delta x,\ n\Delta t)$ in Taylor series about grid point $(j\Delta x,\ n\Delta t)$, the numerical diffusion coefficient of the Muskingum scheme is derived (see Appendix B):

$$\nu_n = c\,\Delta x\left(\frac{1}{2} - X\right) \tag{9-67}$$

in which ν_n is the numerical diffusion coefficient of the Muskingum scheme. This equation reveals the following: (1) for $X = 0.5$ there is no numerical diffusion, although there is numerical dispersion for $C \neq 1$; (2) for $X > 0.5$, the numerical diffusion coefficient is negative, i.e., numerical amplification, which explains the behavior of the Muskingum method for this range of X values; (3) for $\Delta x = 0$, the numerical diffusion coefficient is zero, clearly the trivial case.

A predictive equation for X can be obtained by matching the hydraulic diffusivity ν_h (Eq. 9-59) with the numerical diffusion coefficient of the Muskingum scheme ν_n (Eq. 9-67). This leads to the following expression for X:

TABLE 9-7 NUMERICAL PROPERTIES OF MUSKINGUM-CUNGE METHOD

Parameter X	Parameter C	Order of Accuracy	Numerical Diffusion	Numerical Dispersion
0.5	1	Third	No	No
0.5	$\neq 1$	Second	No	Yes
< 0.5	$\neq 1$	First	Yes	Yes
< 0.5	1	First	Yes	No

$$X = \frac{1}{2}\left(1 - \frac{q_o}{S_o\, c\, \Delta x}\right) \tag{9-68}$$

With X calculated by Eq. 9-68, the Muskingum method is referred to as Muskingum-Cunge method [12]. Using Eq. 9-68, the routing parameter X can be calculated as a function of the following numerical and physical properties: (1) reach length Δx, (2) reference discharge per unit width q_o, (3) kinematic wave celerity c, and (4) bottom slope S_o.

It should be noted that Eq. 9-68 was derived by matching physical and numerical diffusion (i.e., second-order processes), and does not account for dispersion (a third-order process). Therefore, in order to simulate wave diffusion properly with the Muskingum-Cunge method, it is necessary to optimize numerical diffusion (with Eq. 9-68) while minimizing numerical dispersion (by keeping the value of C as close to 1 as practicable).

A unique feature of the Muskingum-Cunge method is the grid independence of the calculated outflow hydrograph, which sets it apart from other linear kinematic wave solutions featuring uncontrolled numerical diffusion and dispersion (e.g., the convex method). If numerical dispersion is minimized, the calculated outflow at the downstream end of a channel reach will be essentially the same, regardless of how many subreaches are used in the computation. This is because X is a function of Δx, and the routing coefficients C_0, C_1, and C_2 vary with reach length.

An improved version of the Muskingum-Cunge method is due to Ponce and Yevjevich [15]. The C value is the Courant number, i.e., the ratio of wave celerity c to grid celerity $\Delta x/\Delta t$:

$$C = c\,\frac{\Delta t}{\Delta x} \tag{9-69}$$

The grid diffusivity is defined as the numerical diffusivity for the case of $X = 0$. From Eq. 9-67, the grid diffusivity is

$$\nu_g = \frac{c\,\Delta x}{2} \tag{9-70}$$

The cell Reynolds number [17] is defined as the ratio of hydraulic diffusivity (Eq. 9-59) to grid diffusivity (Eq. 9-70). This leads to

$$D = \frac{q_o}{S_o\, c\, \Delta x} \tag{9-71}$$

in which D = cell Reynolds number. Therefore

$$X = \tfrac{1}{2}\,(1 - D) \tag{9-72}$$

Equations 9-71 and 9-72 imply that for very small values of Δx, D may be greater than 1, leading to negative values of X. In fact, for the *characteristic reach length*

$$\Delta x_c = \frac{q_o}{S_o c} \tag{9-73}$$

the cell Reynolds number is $D = 1$, and $X = 0$. Therefore, in the Muskingum-Cunge

method, reach lengths shorter than the characteristic reach length result in negative values of X. This should be contrasted with the classical Muskingum method (Section 9.1), in which X is restricted in the range 0.0–0.5. In the classical Muskingum, X is interpreted as a weighting factor. As shown by Eqs. 9-71 and 9-72, nonnegative values of X are associated with long reaches, typical of the manual computation used in the development and early application of the Muskingum method.

In the Muskingum-Cunge method, however, X is interpreted in a moment-matching sense [2] or diffusion-matching factor. Therefore, negative values of X are entirely possible. This feature allows the use of shorter reaches than would otherwise be possible if X were restricted to nonnegative values.

The substitution of Eqs. 9-69 and 9-72 into Eqs. 9-63 to 9-65 leads to routing coefficients expressed in terms of Courant and cell Reynolds numbers:

$$C_0 = \frac{-1 + C + D}{1 + C + D} \tag{9-74}$$

$$C_1 = \frac{1 + C - D}{1 + C + D} \tag{9-75}$$

$$C_2 = \frac{1 - C + D}{1 + C + D} \tag{9-76}$$

The calculation of routing parameters C and D, Eqs. 9-69 and 9-71, can be performed in several ways. The wave celerity can be calculated with either Eq. 9-16 or Eq. 9-34. With Eq. 9-16, $c = \beta V$; with Eq. 9-34, $c = (1/T)\ dQ/dy$. Theoretically, these two equations are the same. For practical applications, if a stage-discharge rating and cross-sectional geometry are available (i.e., stage-discharge-top width tables), Eq. 9-34 is preferred over Eq. 9-16 because it accounts directly for cross-sectional shape. In the absence of a stage-discharge rating and cross-sectional data, Eq. 9-16 can be used to estimate flood wave celerity.

With the aid of Eqs. 9-69 and 9-71, the routing parameters can be based on flow characteristics. The calculations can proceed in a linear or nonlinear mode. In the linear mode, the routing parameters are based on reference flow values and kept constant throughout the computation in time. The choice of reference flow has a bearing on the calculated results [2, 15], although the overall effect is likely to be small. For practical applications, either an average or peak flow value can be used as reference flow. The peak flow value has the advantage that it can be readily ascertained, although a better approximation may be obtained by using an average value [15]. The linear mode of computation is referred to as the constant-parameter Muskingum-Cunge method to distinguish it from the variable-parameter Muskingum-Cunge method, in which the routing parameters are allowed to vary with the flow. The constant-parameter method resembles the Muskingum method, with the difference that the routing parameters are based on measurable flow and channel characteristics instead of historical streamflow data.

Example 9-9.

Use the constant-parameter Muskingum-Cunge method to route a flood wave with the following flood and channel characteristics: peak flow $Q_p = 1000\ \mathrm{m^3/s}$; baseflow $Q_b = 0$

m^3/s; channel bottom slope $S_o = 0.000868$; flow area at peak discharge $A_p = 400\ m^2$; top width at peak discharge $T_p = 100$ m; rating exponent $\beta = 1.6$; reach length $\Delta x =$ 14.4 km; time interval $\Delta t = 1$ h.

Time (h)	0	1	2	3	4	5	6	7	8	9	10
Flow (m^3/s)	0	200	400	600	800	1000	800	600	400	200	0

The mean velocity (based on the peak discharge) is $V = Q_p/A_p = 2.5$ m/s. The wave celerity is $c = \beta V = 4$ m/s. The flow per unit width (based on the peak discharge) is $q_o = Q_p/T_p = 10\ m^2/s$. The Courant number (Eq. 9-69) is $C = 1$. The cell Reynolds number (Eq. 9-71) is $D = 0.2$. The routing coefficients (Eqs. 9-74 to 9-76) are $C_0 = 0.091$; $C_1 = 0.818$; and $C_2 = 0.091$. It is confirmed that the sum of routing coefficients is equal to 1. The routing calculations are shown in Table 9-8.

Resolution Requirements

When using the Muskingum-Cunge method, care should be taken to ensure that the values of Δx and Δt are sufficiently small to approximate closely the actual shape of the hydrograph. For smoothly rising hydrographs, a minimum value of $t_p/\Delta t = 5$ is recommended. This requirement usually results in the hydrograph time base being resolved into at least 15 to 25 discrete points, considered adequate for Muskingum routing.

Unlike temporal resolution, there is no definite criteria for spatial resolution. A criterion borne out by experience is based on the fact that Courant and cell Reynolds numbers are inversely related to reach length Δx. Therefore, to keep Δx sufficiently small, Courant and cell Reynolds numbers should be kept sufficiently large. This leads to the practical criterion [16]:

TABLE 9-8 CHANNEL ROUTING BY MUSKINGUM-CUNGE METHOD: EXAMPLE 9-9

(1)	(2)	(3)	(4)	(5)	(6)
		Partial Flows			
Time (h)	Inflow (m^3/s)	C_0I_2	C_1I_1	C_2O_1	Outflow (m^3/s)
0	0	—	—	—	0.0
1	200	18.2	0.0	0.0	18.20
2	400	36.4	163.6	1.66	201.66
3	600	54.6	327.2	18.35	400.15
4	800	72.8	490.8	36.41	600.01
5	1000	91.0	654.4	54.60	800.00
6	800	72.8	818.0	72.80	963.60
7	600	54.6	654.4	87.69	796.69
8	400	36.4	490.8	72.50	599.70
9	200	18.2	327.2	54.57	399.97
10	0	0.0	163.6	36.40	200.00
11	0	0.0	0.0	18.20	18.20
12	0	0.0	0.0	1.66	1.66
13	0	0.0	0.0	0.16	0.16

$$C + D \geq 1 \tag{9-77}$$

which can be written as: $-1 + C + D \geq 0$. This confirms the necessity of avoiding negative values of C_0 in Muskingum-Cunge routing (See Eq. 9-74). Experience has shown that negative values of either C_1 or C_2 do not adversely affect the method's overall accuracy [16].

Notwithstanding Eq. 9-77, the Muskingum-Cunge method works best when the numerical dispersion is minimized, that is, when C is kept close to 1. Values of C substantially different from 1 are likely to cause the notorious dips, or negative outflows, in portions of the calculated hydrograph. This computational anomaly is attributed to excessive numerical dispersion and should be avoided.

Nonlinear Muskingum-Cunge Method

The kinematic wave equation, Eq. 9-18, is nonlinear because the kinematic wave celerity varies with discharge. The nonlinearity is mild, among other things because the wave celerity variation is usually restricted within a narrow range. However, in certain cases it may be necessary to account for this nonlinearity. This can be done in two ways: (1) during the discretization, by allowing the wave celerity to vary, resulting in a nonlinear numerical scheme to be solved by iterative means; and (2) after the discretization, by varying the routing parameters, as in the variable-parameter Muskingum-Cunge method [15]. The latter appproach is particularly useful if the overall nonlinear effect is small, which is often the case.

In the variable-parameter method, the routing parameters are allowed to vary with the flow. The values of C and D are based on local q_o and c values instead of peak flow or other reference value as in the constant-parameter method. To vary the routing parameters, the most expedient way is to obtain an average value of q_o and c for each computational cell. This can be achieved with a direct three-point average of the values at the known grid points (See Fig. 9-8), or by an iterative four-point average, which includes the unknown grid point. To improve the convergence of the iterative four-point procedure, the three-point average can be used as the first guess of the iteration. Once q_o and c have been determined for each computational cell, the Courant and cell Reynolds numbers are calculated by Eqs. 9-69 and 9-71. The value of bottom slope S_o remains unchanged within each computational cell.

The variable parameter Muskingum-Cunge method represents a small yet sometimes perceptible improvement over the constant parameter method. The differences are likely to be more marked for very long reaches and/or wide variations in flow levels. Flood hydrographs calculated with variable parameters show a certain amount of distortion, either wave steepening in the case of flows contained inbank or wave attenuation in the case of typical overbank flows. This is a physical manifestation of the nonlinear effect, i.e., different flow levels traveling with different celerities. On the other hand, flood hydrographs calculated using constant parameters do not show such wave distortion.

Assessment of Muskingum-Cunge Method

The Muskingum-Cunge method is a physically based alternative to the Muskingum method. Unlike the Muskingum method where the parameters are calibrated using

streamflow data, in the Muskingum-Cunge method the parameters are calculated based on flow and channel characteristics. This makes possible channel routing without the need for time-consuming and cumbersome parameter calibration. More importantly, it makes possible extensive channel routing in ungaged streams with a reasonable expectation of accuracy. With the variable-parameter feature, nonlinear properties of flood waves (which could otherwise only be obtained by more elaborate numerical procedures) can be described within the context of the Muskingum formulation.

Like the Muskingum method, the Muskingum-Cunge method is limited to diffusion waves. Furthermore, the Muskingum-Cunge method is based on a single-valued rating and does not take into account strong flow nonuniformity or unsteady flows exhibiting substantial loops in discharge-stage rating (i.e., dynamic waves). Thus, the Muskingum-Cunge method is suited for channel routing in natural streams without significant backwater effects and for unsteady flows that classify under the diffusion wave criterion (Eq. 9-60).

An important difference between the Muskingum and Muskingum-Cunge methods should be noted. The Muskingum method is based on the storage concept (Chapter 4) and, therefore, the parameters K and X are reach averages. The Muskingum-Cunge method, however, is kinematic in nature, with the parameters C and D being based on values evaluated at channel cross sections rather than being reach averages. Therefore, for the Muskingum-Cunge method to improve on the Muskingum method, it is necessary that the routing parameters evaluated at channel cross sections be representative of the channel reach under consideration.

Historically, the Muskingum method has been calibrated using streamflow data. On the contrary, the Muskingum-Cunge method relies on physical characteristics such as rating curves, cross-sectional data and channel slope. The different data requirements reflect the different theoretical bases of the methods, i.e., storage concept in the Muskingum method, and kinematic wave theory in the Muskingum-Cunge method.

9.5 INTRODUCTION TO DYNAMIC WAVES

In Section 9.2, kinematic waves were formulated by simplifying the momentum conservation principle to a statement of steady uniform flow. In Section 9.3, diffusion waves were formulated by simplifying the momentum principle to a statement of steady nonuniform flow. These two waves, in particular the diffusion wave, have been extensively used in stream channel routing applications. The Muskingum and Muskingum-Cunge methods are examples of calculations using the concept of diffusion wave.

A third type of open channel flow wave, the dynamic wave, is formulated by taking into account the complete momentum principle, including its inertial components. As such, the dynamic wave contains more physical information than either kinematic or diffusion waves. Dynamic wave solutions, however, are more complicated than either kinematic or diffusion wave solutions.

In a dynamic wave solution, the equations of mass and momentum conservation are solved by a numerical procedure, either the method of finite differences, the

method of characteristics, or the finite element method. In the method of finite differences, the partial differential equations are discretized following a chosen numerical scheme [9]. The method of characteristics is based on the conversion of the set of partial differential equations into a related set of ordinary differential equations, and the solution along a *characteristic grid,* i.e. a grid that follows characteristic directions. The method of finite elements solves a set of integral equations over a chosen grid of finite elements.

In the past two decades, the method of finite differences has come to be regarded as the most expedient way of obtaining a dynamic wave solution for practical applications [6, 9]. Among several numerical schemes that have been used in connection with the dynamic wave, the Preissmann scheme is perhaps the most popular. This is a four-point scheme, centered in the temporal derivatives and slightly off-centered in the spatial derivatives. The off-centering in the spatial derivatives introduces a small amount of numerical diffusion necessary to control the numerical stability of the nonlinear scheme. This produces a workable yet sufficiently accurate scheme.

The stream channel is divided into several reaches for computational purposes. The application of the Preissmann scheme to the governing equations for the various reaches results in a matrix solution requiring a *double sweep* algorithm, i.e., one that accounts only for the nonzero entries of the coefficient matrix, which are located within a narrow band surrounding the main diagonal. This technique leads to a considerable savings in storage and execution time. With the appropriate upstream and downstream boundary conditions, the solution of the set of hyperbolic equations marches in time until a specified number of time intervals is completed.

In practice, a dynamic wave solution represents an order of magnitude increase in complexity and associated data requirements when compared to either kinematic or diffusion wave solutions. Its use is recommended in situations where neither kinematic or diffusion wave solutions are likely to represent adequately the physical phenomena. In particular, dynamic wave solutions are applicable to flow over very flat slopes, flow into large reservoirs, strong backwater conditions and flow reversals. In general, the dynamic wave is recommended for cases warranting a precise determination of the unsteady variation of river stages.

Relevance of Dynamic Waves to Engineering Hydrology

Dynamic wave solutions are often referred to as *hydraulic river routing* . As such, they have the capability to calculate unsteady discharges and stages when presented with the appropriate geometric channel data and initial and boundary conditions. Their relevance to engineering hydrology is examined here by comparing them to kinematic and diffusion wave solutions.

Kinematic waves calculate unsteady discharges; the corresponding stages are subsequently obtained from the appropriate rating curves. Usually, equilibrium (steady, uniform) rating curves are used for this purpose. Diffusion waves may or may not use equilibrium rating curves to calculate stages. Some methods, e.g., Muskingum-Cunge, use equilibrium ratings, but more elaborate diffusion wave solutions may not.

Dynamic waves rely on the physics of the phenomena as built into the governing equations to generate their own unsteady rating. A looped rating curve is produced at

every cross section, as shown in Fig. 9-9. For any given stage, the discharge is higher in the rising limb of the hydrograph and lower in the receding limb. This loop is due to hydrodynamic reasons and should not be confused with other loops, which may be due to erosion, sedimentation, or changes in bed configuration (Chapter 15).

The width of the loop is a measure of the flow unsteadiness, with wider loops corresponding to highly unsteady flow, i.e, dynamic wave flow. If the loop is narrow, it implies that the flow is mildly unsteady, perhaps a diffusion wave. If the loop is practically nonexistent, the flow can be approximated as kinematic flow. In fact, the basic assumption of kinematic flow is that momentum can be simulated as steady uniform flow, i.e., that the rating curve is single-valued.

The preceding observations lead to the conclusion that the relevance of dynamic waves in engineering hydrology is directly related to the flow unsteadiness and the associated loop in the rating curve. For highly unsteady flows such as dam-break flood waves, it may well be the only way to account properly for the looped rating. For other less unsteady flows, kinematic and diffusion waves are a viable alternative, provided their applicability can be clearly demonstrated (Eqs. 9-44 and 9-60).

Diffusion Wave Solution with Dynamic Component

A simplified approach to dynamic wave routing is that of the diffusion wave with dynamic component [2]. In this approach, the complete governing equations, including inertia terms, are linearized in a similar way as with diffusion waves. This leads to a diffusion equation similar to Eq. 9-58, but with a modified hydraulic diffusivity. The equation is [5]:

$$\frac{\partial Q}{\partial t} + \left[\frac{\partial Q}{\partial A}\right]\frac{\partial Q}{\partial x} = \left[\frac{Q_o}{2TS_o}\right][1 - (\beta - 1)^2 F_o^2]\frac{\partial^2 Q}{\partial x^2} \tag{9-78}$$

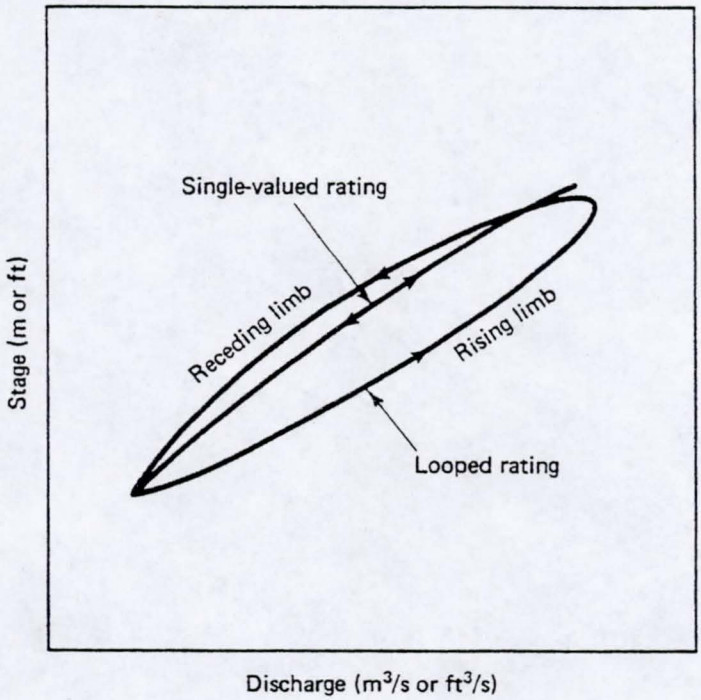

Figure 9-9 Sketch of the looped rating of dynamic waves.

in which the hydraulic diffusivity is also a function of the rating curve parameter β and the Froude number, defined as:

$$F_o = \frac{V_o}{(gd_o)^{1/2}} \tag{9-79}$$

with g = gravitational acceleration and d_o = reference flow depth.

Equation 9-78 provides an enhanced predictive capability for the simulation of diffusion waves including a dynamic component. For instance, for $\beta = 1.5$ (i.e., Chezy friction in wide channels) and $F_o = 2$, the hydraulic diffusivity in Eq. 9-78 vanishes, which is in agreement with physical reality [10, 13]. On the other hand, the hydraulic diffusivity of the diffusion wave (Eq. 9-58) is independent of the Froude number. Therefore, Eq. 9-78 is a somewhat better model than Eq. 9-58, especially for Froude numbers in the supercritical regime. Most natural flows, however, are in the range well below critical, with Eq. 9-58 remaining a practical model of unsteady open channel flow phenomena.

QUESTIONS

1. What is routing? What types of waves are used in describing unsteady open channel flow processes?
2. What is model calibration? What is model verification?
3. In the Muskingum method, what does the parameter K represent? What does the parameter X represent?
4. How does channel routing differ from reservoir routing? What differences are to be noted in the routed hydrographs?
5. What is the kinematic wave celerity? What is the practical range of turbulent flow values of β, the rating constant used in the kinematic wave celerity?
6. What is the order of accuracy of a numerical scheme? What is the difference between numerical diffusion and numerical dispersion in connection with kinematic wave solutions?
7. What is a linear model in the context of kinematic wave routing? What is a nonlinear model?
8. Why are the results of convex routing dependent on the grid size?
9. What is a diffusion wave? How does it differ from a kinematic wave?
10. What is hydraulic diffusivity? Why is it important in flood routing?
11. What values of parameters X and C optimize numerical diffusion and minimize numerical dispersion in the Muskingum-Cunge method?
12. Why are negative values of X entirely possible in Muskingum-Cunge routing? Why are values of X in excess of 0.5 unfeasible?
13. What is the Courant number? What is the cell Reynolds number?
14. Describe the difference between linear and nonlinear solutions to channel routing problems.
15. What is a dynamic wave? How does it differ from the diffusion and kinematic waves?
16. How does the method of finite differences differs from the method of characteristics? What is a double sweep algorithm?

Laboratory Analysis of Mudflow Properties

By Jim S. O'Brien[1] and Pierre Y. Julien,[2] Member, ASCE

Abstract: A rotational viscometer has been designed for laboratory measurements of the rheological properties of natural mudflow deposits in Colorado. The mudflow matrices comprised of silt and clay particles are sheared under temperature-controlled conditions at volumetric sediment concentrations ranging from 0.10–0.45. This study stresses the importance of conducting rheological measurements at low rates of shear because: 1) Those are the conditions found in natural channels; and 2) they avoid the slippage problems observed at large sediment concentrations. At low rates of shear, the Bingham model is fitted to the measured rheograms, and both the viscosity and yield stress increase exponentially with the sediment concentration of the fluid matrix. Both the yield stress and the viscosity increase by three orders of magnitude as the volumetric concentration of sediments in the fluid matrix changes from 0.10 to 0.40. The addition of sand particles does not significantly alter the rheological properties of the matrix unless the volumetric concentration of sands exceeds 0.20.

Introduction

In the United States, losses from landslides, subsidence, and other ground failures exceed the losses from all other natural hazards combined. Indeed, the Committee on Ground Failure Hazards (NRC 1982) reported that landsliding in the U.S. causes $1–$2 billion in economic losses and 25–50 deaths each year. Individual landslides can be widely scattered in space and time, but a substantial portion of the annual landslide loss is associated with a few major catastrophic events such as the mudflows in the San Francisco Bay area and along the Wasatch Front in Utah. Semiarid alpine mudflows and debris flows are triggered by the slumping or slipping of unconsolidated material on steep slopes (Higgins et al. 1983). Such movement usually occurs following soil saturation due to fairly intense and short-duration rainfall events, or as a consequence of rapid snowmelt. Mud and debris flows originate on steep slopes or landslide areas. The zone of sediment transport typically has a steep channel system, at the end of which a sudden break in slope on the valley floor induces deposition to form a conical debris fan.

Several investigations have promulgated various classifications of mudflows and hyperconcentrated flows [e.g., Blackwelder (1928), Sharp and Nobles (1953), Johnson (1965), and O'Brien and Julien (1985)]. An attempt to delineate hyperconcentrated flows and mass wasting processes was initiated by the National Research Council Committee on Methodologies for Predicting Mud Flows (NRC 1982). The committee proposed four main categories: water floods, mud floods, mudflows, and landslides. The

[1]Res. Assoc., Dept. of Civ. Engrg., Colorado State Univ., Ft. Collins, CO 80523.
[2]Asst. Prof., Dept. of Civ. Engrg., Colorado State Univ., Ft. Collins, CO 80523.

Note. Discussion open until January 1, 1989. To extend the closing date one month, a written request must be filed with the ASCE Manager of Journals. The manuscript for this paper was submitted for review and possible publication on May 6, 1987. This paper is part of the *Journal of Hydraulic Engineering*, Vol. 114, No. 8, August, 1988. ©ASCE, ISSN 0733-9420/88/0008-0877/$1.00 + $.15 per page. Paper No. 22680.

Laboratory Analysis of Mudflow Properties

By Jim S. O'Brien[1] and Pierre Y. Julien,[2] Member, ASCE

Abstract: A rotational viscometer has been designed for laboratory measurements of the rheological properties of natural mudflow deposits in Colorado. The mudflow matrices comprised of silt and clay particles are sheared under temperature-controlled conditions at volumetric sediment concentrations ranging from 0.10–0.45. This study stresses the importance of conducting rheological measurements at low rates of shear because: 1) Those are the conditions found in natural channels; and 2) they avoid the slippage problems observed at large sediment concentrations. At low rates of shear, the Bingham model is fitted to the measured rheograms, and both the viscosity and yield stress increase exponentially with the sediment concentration of the fluid matrix. Both the yield stress and the viscosity increase by three orders of magnitude as the volumetric concentration of sediments in the fluid matrix changes from 0.10 to 0.40. The addition of sand particles does not significantly alter the rheological properties of the matrix unless the volumetric concentration of sands exceeds 0.20.

Introduction

In the United States, losses from landslides, subsidence, and other ground failures exceed the losses from all other natural hazards combined. Indeed, the Committee on Ground Failure Hazards (NRC 1982) reported that landsliding in the U.S. causes $1–$2 billion in economic losses and 25–50 deaths each year. Individual landslides can be widely scattered in space and time, but a substantial portion of the annual landslide loss is associated with a few major catastrophic events such as the mudflows in the San Francisco Bay area and along the Wasatch Front in Utah. Semiarid alpine mudflows and debris flows are triggered by the slumping or slipping of unconsolidated material on steep slopes (Higgins et al. 1983). Such movement usually occurs following soil saturation due to fairly intense and short-duration rainfall events, or as a consequence of rapid snowmelt. Mud and debris flows originate on steep slopes or landslide areas. The zone of sediment transport typically has a steep channel system, at the end of which a sudden break in slope on the valley floor induces deposition to form a conical debris fan.

Several investigations have promulgated various classifications of mudflows and hyperconcentrated flows [e.g., Blackwelder (1928), Sharp and Nobles (1953), Johnson (1965), and O'Brien and Julien (1985)]. An attempt to delineate hyperconcentrated flows and mass wasting processes was initiated by the National Research Council Committee on Methodologies for Predicting Mud Flows (NRC 1982). The committee proposed four main categories: water floods, mud floods, mudflows, and landslides. The

[1]Res. Assoc., Dept. of Civ. Engrg., Colorado State Univ., Ft. Collins, CO 80523.
[2]Asst. Prof., Dept. of Civ. Engrg., Colorado State Univ., Ft. Collins, CO 80523.

Note. Discussion open until January 1, 1989. To extend the closing date one month, a written request must be filed with the ASCE Manager of Journals. The manuscript for this paper was submitted for review and possible publication on May 6, 1987. This paper is part of the *Journal of Hydraulic Engineering*, Vol. 114, No. 8, August, 1988. ©ASCE, ISSN 0733-9420/88/0008-0877/$1.00 + $.15 per page. Paper No. 22680.

shows convexity to the shear stress, and this behavior is referred to as yield-pseudoplastic. There is no theoretically based equation for yield-pseudoplastics, but any empirical equation such as the power-law equation can be used:

$$\tau = \tau_y + a\left(\frac{du}{dy}\right)^n \quad \text{(2)}$$

in which a and n = empirical parameters. This model, first proposed by Herschel and Bulkley (1926), describes the behavior of clay-water suspensions reasonably well at high rates of shear (Govier and Aziz 1982).

Although several investigators have applied the Bingham model to water-sediment mixtures, most available data were collected for dilute mixtures of bentonite and kaolin clays under very high shear rates, well in excess of 100 s^{-1} (Thomas 1963; Plessis and Ansley 1967; Valentik and Whitmore 1965; Mills et al. 1983). When compared to measurements under low rates of shear, these analyses led to larger values of yield stress and lower values of viscosity. It must be considered that typical shear rates for hyperconcentrated sediment flows in the field are on the order of 5–50 s^{-1}. Data from Johnson (1970) show this value to be of a magnitude of 10 s^{-1} or less. Yano and Daido (1965) report shear rates less than 10 s^{-1} for open-channel mudflows with concentrations up to 35% by weight. Therefore, rates of shear in excess of 50 s^{-1} appear to be uncommon in open-channel mudflows. This corroborates the findings of Qian and Wan (1986) in that the rate of shear in hyperconcentrated flows rarely exceeds 100 s^{-1}. Thus, not only must the viscometer experiments be conducted at low shear rates, but the fluid properties must be evaluated at lower shear rates as well.

Measurement of Mudflow Properties

The measurement and interpretation of the physical properties of mudflow mixtures is more complex than the viscosity measurements of Newtonian fluids. Three different types of apparatus are in common use for measuring the rheological properties of non-Newtonian fluids; (1) The capillary viscometer; (2) the rotational viscometer; and (3) the cone-and-plate viscometer.

A capillary viscometer measures the rate of flow of a fluid in a capillary tube under a given pressure gradient. The rate of shear varies across the capillary section; this viscometer is not suitable for time-dependent fluids. Due to its simplicity, this viscometer can be invaluable at large rates of shear.

In rotational viscometers, the fluid is sheared at a nearly constant rate between a stationary and a rotating cylinder. The shear stress is obtained from the torque measured on the stationary cylinder. Precautions must be taken to ensure laminar flow and constant temperature; end-effect corrections may also be required. Its suitability to a wide range of shear stresses makes it a versatile and useful instrument to analyze non-Newtonian fluids.

The cone-and-plate viscometer shears the fluid in the narrow space between the flat circular rotating plate and an inverted cone. This viscometer is ideal to study the properties of non-Newtonian fluids at low and

shows convexity to the shear stress, and this behavior is referred to as yield-pseudoplastic. There is no theoretically based equation for yield-pseudoplastics, but any empirical equation such as the power-law equation can be used:

$$\tau = \tau_y + a\left(\frac{du}{dy}\right)^n \quad \text{(2)}$$

in which a and n = empirical parameters. This model, first proposed by Herschel and Bulkley (1926), describes the behavior of clay-water suspensions reasonably well at high rates of shear (Govier and Aziz 1982).

Although several investigators have applied the Bingham model to water-sediment mixtures, most available data were collected for dilute mixtures of bentonite and kaolin clays under very high shear rates, well in excess of 100 s^{-1} (Thomas 1963; Plessis and Ansley 1967; Valentik and Whitmore 1965; Mills et al. 1983). When compared to measurements under low rates of shear, these analyses led to larger values of yield stress and lower values of viscosity. It must be considered that typical shear rates for hyperconcentrated sediment flows in the field are on the order of 5–50 s^{-1}. Data from Johnson (1970) show this value to be of a magnitude of 10 s^{-1} or less. Yano and Daido (1965) report shear rates less than 10 s^{-1} for open-channel mudflows with concentrations up to 35% by weight. Therefore, rates of shear in excess of 50 s^{-1} appear to be uncommon in open-channel mudflows. This corroborates the findings of Qian and Wan (1986) in that the rate of shear in hyperconcentrated flows rarely exceeds 100 s^{-1}. Thus, not only must the viscometer experiments be conducted at low shear rates, but the fluid properties must be evaluated at lower shear rates as well.

Measurement of Mudflow Properties

The measurement and interpretation of the physical properties of mudflow mixtures is more complex than the viscosity measurements of Newtonian fluids. Three different types of apparatus are in common use for measuring the rheological properties of non-Newtonian fluids; (1) The capillary viscometer; (2) the rotational viscometer; and (3) the cone-and-plate viscometer.

A capillary viscometer measures the rate of flow of a fluid in a capillary tube under a given pressure gradient. The rate of shear varies across the capillary section; this viscometer is not suitable for time-dependent fluids. Due to its simplicity, this viscometer can be invaluable at large rates of shear.

In rotational viscometers, the fluid is sheared at a nearly constant rate between a stationary and a rotating cylinder. The shear stress is obtained from the torque measured on the stationary cylinder. Precautions must be taken to ensure laminar flow and constant temperature; end-effect corrections may also be required. Its suitability to a wide range of shear stresses makes it a versatile and useful instrument to analyze non-Newtonian fluids.

The cone-and-plate viscometer shears the fluid in the narrow space between the flat circular rotating plate and an inverted cone. This viscometer is ideal to study the properties of non-Newtonian fluids at low and

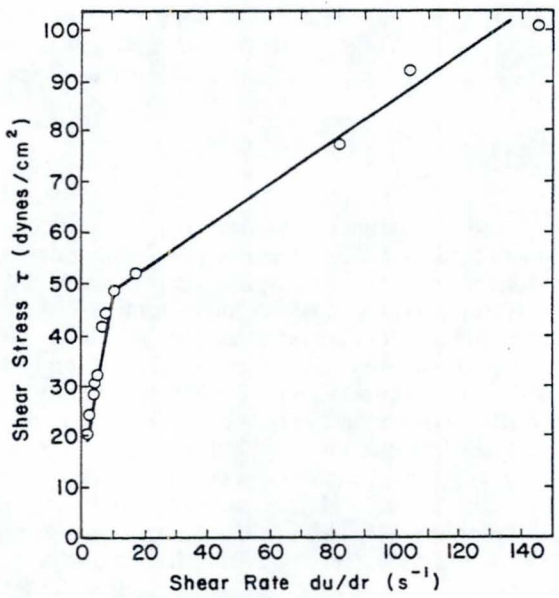

FIG. 1. Aspen Natural Soil Rheogram (C_v = 34.2%; Silts and Clays)

$10\ s^{-1}$, as shown in Fig.1. For this reason, the evaluation of viscosity and yield stress from the Bingham plastic model was based on the measurements taken at lower shear rates. Of course, when compared to measurements at high rates of shear, this analysis gives slightly lower values of yield stress and larger viscosity measurements.

In hyperconcentrated flows, the Bingham plastic model (Eq. 1) has been used by many researchers, e.g., Cao et al. (1983), Hou and Yang (1983), Higgins et al. (1983), Street (1958), Thomas (1963), Qian et al. (1980), Govier and Aziz (1982), and Dai et al. (1980). It has been generally accepted that both the viscosity η and the yield stress τ_y increase exponentially with the volumetric concentration of fine sediments C_v:

$$\eta = \alpha_1 e^{\beta_1 C_v} \quad (3)$$

and

$$\tau_y = \alpha_2 e^{\beta_2 C_v} \quad (4)$$

The values of the four empirical coefficients α_1, α_2, β_1, and β_2 obtained by regression analysis for each mudflow sample are presented in Table 2; the results are in reasonable agreement with those found in the literature. Particularly, the experimental values of the yield stress fall within the range of values defined by Fei (1981). The dispersion of the points at a given concentration certainly calls for more fundamental research to examine possible effects of thixotropy and clay mineralogy. Nevertheless, the open points (Glenwood) indicating lower percentages of clay in Fig. 2 have lower values of yield stress when compared with the samples with larger clay contents (Aspen). This trend is not quite apparent when

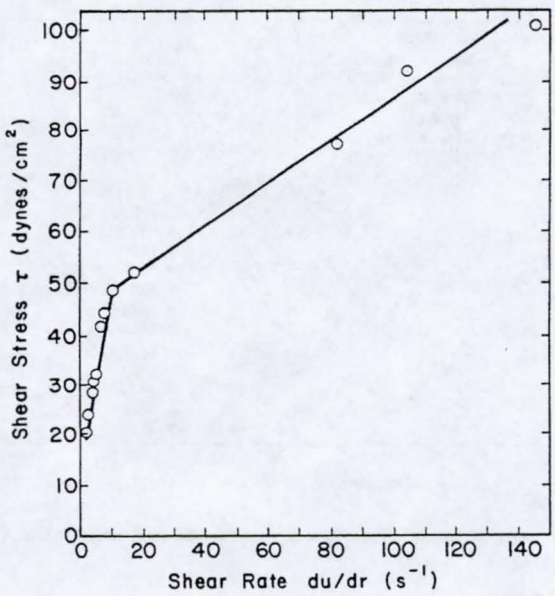

FIG. 1. Aspen Natural Soil Rheogram (C_v = 34.2%; Silts and Clays)

$10\ s^{-1}$, as shown in Fig.1. For this reason, the evaluation of viscosity and yield stress from the Bingham plastic model was based on the measurements taken at lower shear rates. Of course, when compared to measurements at high rates of shear, this analysis gives slightly lower values of yield stress and larger viscosity measurements.

In hyperconcentrated flows, the Bingham plastic model (Eq. 1) has been used by many researchers, e.g., Cao et al. (1983), Hou and Yang (1983), Higgins et al. (1983), Street (1958), Thomas (1963), Qian et al. (1980), Govier and Aziz (1982), and Dai et al. (1980). It has been generally accepted that both the viscosity η and the yield stress τ_y increase exponentially with the volumetric concentration of fine sediments C_v:

$$\eta = \alpha_1 e^{\beta_1 C_v} \quad (3)$$

and

$$\tau_y = \alpha_2 e^{\beta_2 C_v} \quad (4)$$

The values of the four empirical coefficients α_1, α_2, β_1, and β_2 obtained by regression analysis for each mudflow sample are presented in Table 2; the results are in reasonable agreement with those found in the literature. Particularly, the experimental values of the yield stress fall within the range of values defined by Fei (1981). The dispersion of the points at a given concentration certainly calls for more fundamental research to examine possible effects of thixotropy and clay mineralogy. Nevertheless, the open points (Glenwood) indicating lower percentages of clay in Fig. 2 have lower values of yield stress when compared with the samples with larger clay contents (Aspen). This trend is not quite apparent when

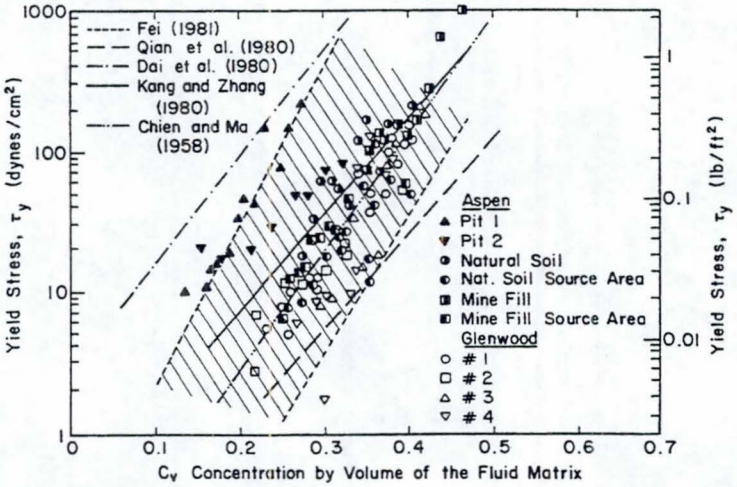

FIG. 2. Yield Stress of Mudflow Samples versus Volumetric Concentration

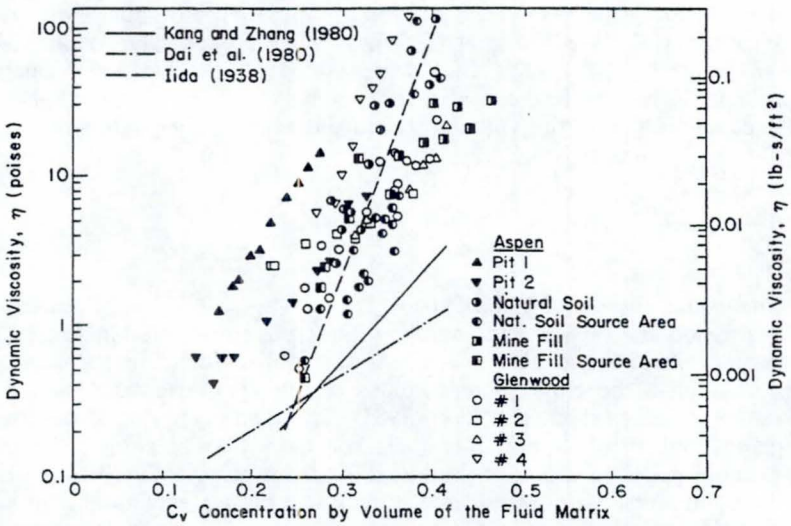

FIG. 3. Dynamic Viscosity of Mudflow Samples versus Volumetric Concentration

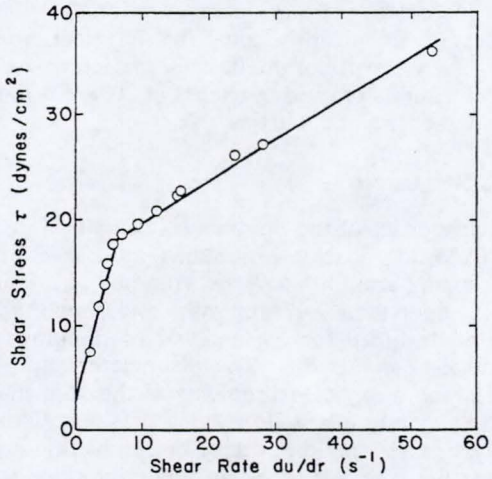

FIG. 4. Rheogram for Aspen Natural Soil (C_v = 30% Silts and Clays) with Added Sand Concentration C_v = 14%; C_{total} = 44%)

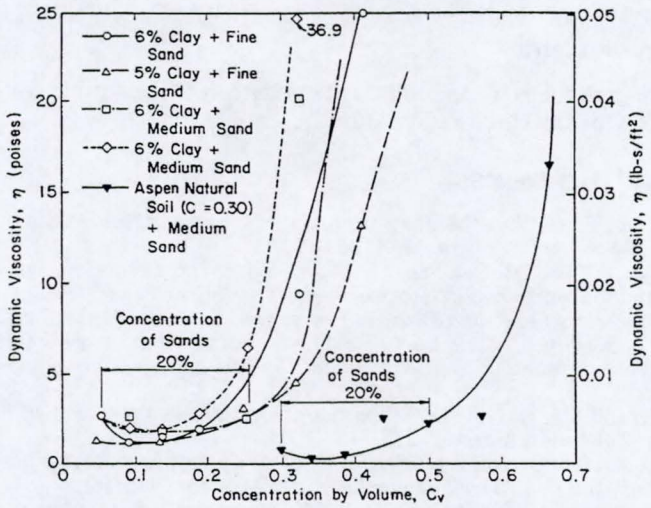

FIG. 5. Dynamic Viscosity of Mixtures with Added Sand Particles versus Total Volumetric Concentration

obtained, which indicates that large concentrations of sand particles are required in order to significantly alter the physical properties of the mudflow matrix. The viscosity of the fluid matrix increases very rapidly at volumetric concentrations of sand in excess of 20%. Further investigation is needed with coarser grained slurries.

Summary and Conclusion

Two physical properties of the fluid matrix of natural mudflow deposits in the central Colorado Rocky Mountains have been investigated at concentrations ranging from 10–45% by volume. The fluid matrix comprised of particles finer than 0.07 mm (silts and clays) was sheared in a special viscometer designed for the analysis of mudflow samples under temperature-controlled conditions. The viscometer gap size was determined to provide laboratory measurements of the fluid matrix properties under laminar flow conditions at low rates of shear without secondary flows. This study stresses the importance of conducting measurements at low rates of shear because: (1) those are the conditions found in natural channels; and (2) they avoid the slippage problems observed at large sediment concentrations. The Bingham rheological model was applied to the measured rheograms at low rates of shear. Both the yield stress and viscosity are shown in Figs. 2 and 3 to increase by three orders of magnitude as the volumetric concentration of sediments in the fluid matrix changes from 10–40%. The effect of adding sand particles to either a bentonite clay suspension or natural mudflow matrix of silts and clays is negligible, provided that the sand concentration remains less than 20% by volume. The viscosity of mudflow material with volumetric sand concentrations less than 20% simply corresponds to the viscosity of the silt-clay mixture. The viscosity of the mixture, however, increases rapidly with volumetric sand concentrations beyond 20%.

Acknowledgments

We are grateful to Y. Lan, Ph.D. candidate at CSU, for his comprehensive review of the Chinese literature.

Appendix I. References

Blackwelder, E. (1928). "Mudflow as a geologic agent in semiarid mountains." *Geologic Soc. Am., Bulletin* 39(1), 465–484.

Bradley, J. B., and McCutcheon, S. C. (1985). "The effects of high sediment concentration on transport processes and flow phenomena." *Proc., Conf. on Erosion, Debris Flow, and Disaster Prevention*, Tsukuba, Japan, 219–225.

Cao, R., et al. (1983). "The Law of hydraulic resistance in density current with hyperconcentration." *Proc., Second Int. Symposium on River Sedimentation*, 65–79.

Chien, N., and Ma, H. (1958). "Properties of slurry flow." *J. Sediment Res.*, 3(3), Beijing, China (in Chinese).

Dai, J., et al. (1980). "An experimental study of slurry transport in pipes." *Proc., Int. Symposium on River Sedimentation*, 195–204 (in Chinese).

Fei, X. J. (1981). "Bingham yield stress of sediment water mixtures with hyperconcentration." *J. Sediment Res.*, 3, Beijing, China, 19–28 (in Chinese).

Govier, G. W., and Aziz, K. (1982). *The flow of complex mixtures in pipes*. Krieger Publishing Co., Melbourne, Fla.

obtained, which indicates that large concentrations of sand particles are required in order to significantly alter the physical properties of the mudflow matrix. The viscosity of the fluid matrix increases very rapidly at volumetric concentrations of sand in excess of 20%. Further investigation is needed with coarser grained slurries.

Summary and Conclusion

Two physical properties of the fluid matrix of natural mudflow deposits in the central Colorado Rocky Mountains have been investigated at concentrations ranging from 10–45% by volume. The fluid matrix comprised of particles finer than 0.07 mm (silts and clays) was sheared in a special viscometer designed for the analysis of mudflow samples under temperature-controlled conditions. The viscometer gap size was determined to provide laboratory measurements of the fluid matrix properties under laminar flow conditions at low rates of shear without secondary flows. This study stresses the importance of conducting measurements at low rates of shear because: (1) those are the conditions found in natural channels; and (2) they avoid the slippage problems observed at large sediment concentrations. The Bingham rheological model was applied to the measured rheograms at low rates of shear. Both the yield stress and viscosity are shown in Figs. 2 and 3 to increase by three orders of magnitude as the volumetric concentration of sediments in the fluid matrix changes from 10–40%. The effect of adding sand particles to either a bentonite clay suspension or natural mudflow matrix of silts and clays is negligible, provided that the sand concentration remains less than 20% by volume. The viscosity of mudflow material with volumetric sand concentrations less than 20% simply corresponds to the viscosity of the silt-clay mixture. The viscosity of the mixture, however, increases rapidly with volumetric sand concentrations beyond 20%.

Acknowledgments

We are grateful to Y. Lan, Ph.D. candidate at CSU, for his comprehensive review of the Chinese literature.

Appendix I. References

Blackwelder, E. (1928). "Mudflow as a geologic agent in semiarid mountains." *Geologic Soc. Am., Bulletin* 39(1), 465–484.

Bradley, J. B., and McCutcheon, S. C. (1985). "The effects of high sediment concentration on transport processes and flow phenomena." *Proc., Conf. on Erosion, Debris Flow, and Disaster Prevention*, Tsukuba, Japan, 219–225.

Cao, R., et al. (1983). "The Law of hydraulic resistance in density current with hyperconcentration." *Proc., Second Int. Symposium on River Sedimentation*, 65–79.

Chien, N., and Ma, H. (1958). "Properties of slurry flow." *J. Sediment Res.*, 3(3), Beijing, China (in Chinese).

Dai, J., et al. (1980). "An experimental study of slurry transport in pipes." *Proc., Int. Symposium on River Sedimentation*, 195–204 (in Chinese).

Fei, X. J. (1981). "Bingham yield stress of sediment water mixtures with hyperconcentration." *J. Sediment Res.*, 3, Beijing, China, 19–28 (in Chinese).

Govier, G. W., and Aziz, K. (1982). *The flow of complex mixtures in pipes*. Krieger Publishing Co., Melbourne, Fla.

Disaster Prevention Research Institute, Kyoto University, Kyoto, Japan, 7, 340–347.

Appendix II. Notation

The following symbols are used in this paper:

a, n = empirical parameters for pseudo-plastic fluids;
C_v = volumetric concentration of fluid matrix;
D = sediment size;
du/dy = velocity gradient;
$\alpha_1, \alpha_2, \beta_1, \beta_2$ = coefficients;
η = dynamic viscosity of fluid matrix;
τ = total shear stress; and
τ_y = yield stress.

Rheology of Hyperconcentrations

By Pierre Y. Julien[1] and Yongqiang Lan[2]

Abstract: A physically based quadratic rheological model for hyperconcentrated flows is tested with experimental data sets. The model includes components describing: (1) Cohesion between particles; (2) viscous friction between fluid and sediment particles; (3) impact of particles; and (4) turbulence. The resulting quadratic formulation of the shear stress is shown to be in excellent agreement with the experimental data sets of Bagnold, Savage and McKeown, and Govier et al. When the quadratic model is written in a linearized dimensionless form, the ratio D_v^* of dispersive to viscous stresses is shown to play a dominant role in the rheology of hyperconcentrations. The quadratic model is best suited when ($30 < D_v^* < 400$). At low values of D_v^*, the quadratic model reduces to the simple Bingham plastic model ($D_v^* < 30$), and at large values of D_v^*, a turbulent-dispersive model is indicated ($D_v^* > 400$).

Introduction

The rheology of highly concentrated sediment mixtures has been studied by various researchers including Bagnold (1954), Jeffrey and Acrivos (1976), Takahashi (1980), and Savage and McKeown (1983). Under high rates of shear, Bagnold proposed that the dominant shear stress can be attributed to interparticle friction and collisions. In this grain inertia region, both the normal and shear stresses depend on the second power of the shear rate. These results contrast with observations under low rates of shear (O'Brien and Julien 1988) because in the viscous region, the shear stress in excess of the yield stress increases linearly with the shear rate.

This study describes the rheological properties of hyperconcentrated sediment mixtures at shear rates ranging from the viscous region to the inertial region. It is proposed to test the quadratic rheological model suggested by O'Brien and Julien (1985) with existing data sets from Govier et al. (1957), Savage and McKeown (1983), and Bagnold (1954). This analysis points at the similarities and differences between these three data sets, which give quite different results when analyzed separately. As a second objective, the relative magnitude of the terms in the quadratic model is examined to define the conditions under which simplified rheological formulations can be applied.

Rheological Model Formulation

The shear stress encountered in fluids with large concentrations of sediments should include components to describe: (1) Cohesion between particles; (2) viscous interaction between sediment particles and the surrounding fluid; (3) impact of sediment particles; and (4) turbulence. After considering

[1]Assoc. Prof. of Civ. Engrg., Engrg. Res. Ctr., Colorado State Univ., Fort Collins, CO 80523.

[2]Res. Asst., Dept. of Civ. Engrg., Colorado State Univ., Fort Collins, CO.

Note. Discussion open until August 1, 1991. To extend the closing date one month, a written request must be filed with the ASCE Manager of Journals. The manuscript for this paper was submitted for review and possible publication on November 20, 1987. This paper is part of the ***Journal of Hydraulic Engineering***, Vol. 117, No. 3, March, 1991. ©ASCE, ISSN 0733-9429/91/0003-0346/$1.00 + $.15 per page. Paper No. 25612.

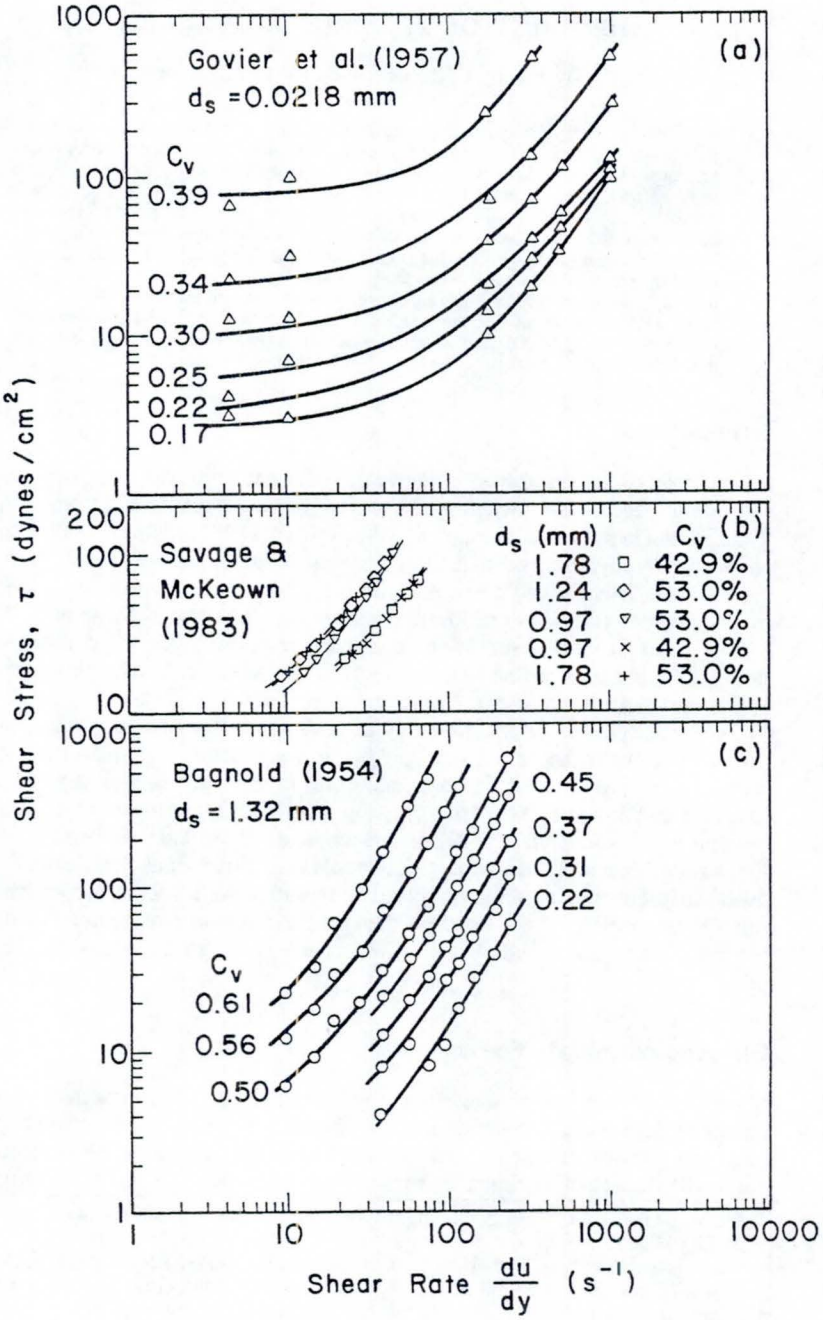

FIG. 1. Rheograms for Three Data Sets: Govier et al. (1957); Savage and McKeown (1983); and Bagnold (1954)

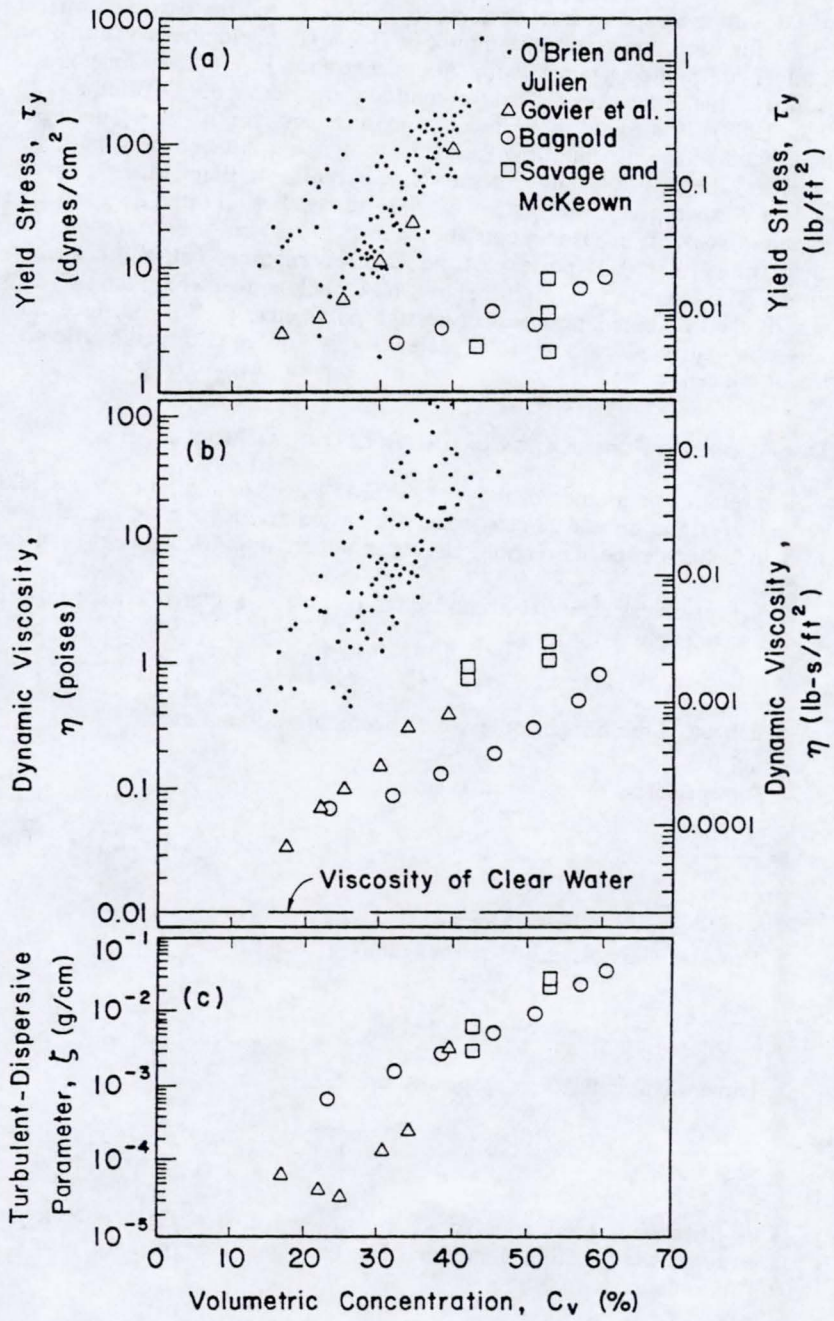

FIG. 2. Yield Stress τ_y, Dynamic Viscosity η, and Turbulent-Dispersive Parameter ζ for Hyperconcentrations

pared with the experimental data points in Fig. 1, and the parameters τ_y, η, and ζ for each data set are compiled in Table 1. Yield stress values from Table 1 are plotted against sediment concentration in Fig. 2(*a*) for comparison with measurements for natural mudflow matrices from O'Brien and Julien (1988). It is found that Govier's measurements for silt size galena particles compare with mudflow matrices comprising silt and clay particles, whereas, the neutrally buoyant sand size particles of Bagnold, and Savage and McKeown give lower values of yield stress. For all three data sets, the dynamic viscosity measurements shown in Fig. 2(*b*) range between those of clear water (η = 0.01 poise) and the mudflow matrices (silt and clay mixtures). The interesting Fig. 2(*c*) shows reasonable agreement among all values of the combined turbulent-dispersive parameter, ζ. For the three data sets, the values of ζ are found to increase very rapidly with volumetric sediment concentration.

Dimensionless Formulation of the Rheological Model

The relative magnitude of the terms in Eq. 1 is examined to seek possible reduction of the three data sets into a dimensionless rheological model, and also to better define the conditions under which simplified models can be applied.

A dimensionless rheological model can be obtained after rewriting Eqs. 1 and 2 in the following form:

$$\tau^* = 1 + (1 + T_d^*)a_1 D_v^* \quad (5)$$

in which the three dimensionless parameters are defined as:

1. Dimensionless excess shear stress

$$\tau^* = \frac{\tau - \tau_y}{\eta \dfrac{du}{dy}} \quad (6)$$

2. Dimensionless dispersive-viscous ratio

$$D_v^* = \frac{\rho_s \lambda^2 d_s^2}{\eta} \left(\frac{du}{dy}\right) \quad (7)$$

3. Dimensionless turbulent-dispersive ratio

$$T_d^* = \frac{\rho_m l_m^2}{a_1 \rho_s \lambda^2 d_s^2} \quad (8)$$

This linearized formulation of the rheological model (Eq. 5) for hyperconcentrated water-sediment mixtures has three major advantages over previous formulations:

1. It involves three dimensionless parameters τ^*, D_v^*, and T_d^*.
2. The second term on the right-hand side of Eq. 5 reflects the deviation from the Bingham plastic model.

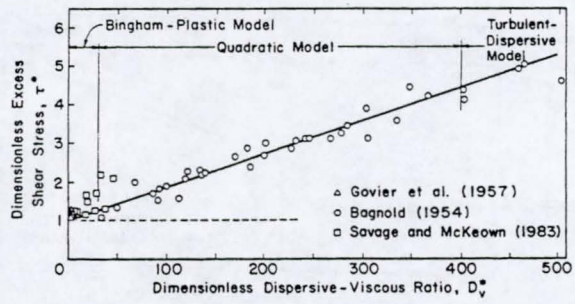

FIG. 3. Comparison of Dimensionless Model with Experimental Data

3. Newtonian and non-Newtonian fluids can be modeled depending on the relative magnitude of the parameters D_v^*, T_d^*, and τ_y.

The usefulness of the dimensionless rheological model is demonstrated in Fig. 3 where τ^* is plotted versus D_v^*. When Eq. 5 is fitted to the experimental data sets of Govier et al. (1957), Savage and McKeown (1983), and Bagnold (1954), it is found that $a_1(1 + T_d^*) = 0.0087$. It has not been possible to evaluate the parameter T_d^* because the mixing length l_m from existing experiments is not available. It is interesting to notice, however, that the value $a_1 = 0.01$ suggested by Bagnold is comparable to the value $a_1 (1 + T_d^*) = 0.0087$ obtained from Eq. 5 when assuming that the turbulent stress is negligible compared to the dispersive stress ($T_d^* << 1$).

It is found in this analysis that not only the linearized dimensionless model (Eq. 5) is applicable to all three data sets, but the parameter D_v^* can be used to delineate particular cases of the quadratic model. The results shown in Fig. 3 indicate that τ^* is sufficiently close to unity when $D_v^* < 30$ to justify the use of a Bingham plastic model. On the other hand, τ^* exceeds 4 when D_v^* is roughly larger than 400, which indicates that in this region the turbulent-dispersive stress is dominant.

Summary and Conclusion

We concur with Savage and McKeown's (1983) conclusion that the rheology of hyperconcentrations is somewhat more complex than originally pictured by Bagnold (1954). The quadratic model describing the rheology of hyperconcentrated sediment flows is well suited to the experimental data sets of Govier et al. (1957), Savage and McKeown (1983), and Bagnold (1954). This analysis illustrates the benefits of combining the turbulent stress with the dispersive stress. When the quadratic model is written in a linearized dimensionless form (Eq. 5), the ratio of dispersive to viscous stresses D_v^* becomes of foremost importance in selecting appropriate rheological models.

It can be concluded that the quadratic model is valid for all values of the parameter D_v^*, and reduces to the Bingham plastic model when $D_v^* < 30$. Turbulent-dispersive formulations may be useful in the inertial region when $D_v^* > 400$.

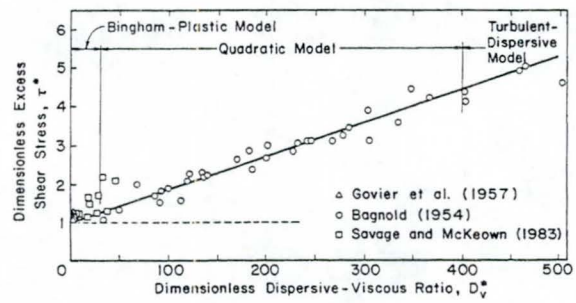

FIG. 3. Comparison of Dimensionless Model with Experimental Data

3. Newtonian and non-Newtonian fluids can be modeled depending on the relative magnitude of the parameters D_v^*, T_d^*, and τ_y.

The usefulness of the dimensionless rheological model is demonstrated in Fig. 3 where τ^* is plotted versus D_v^*. When Eq. 5 is fitted to the experimental data sets of Govier et al. (1957), Savage and McKeown (1983), and Bagnold (1954), it is found that $a_1(1 + T_d^*) = 0.0087$. It has not been possible to evaluate the parameter T_d^* because the mixing length l_m from existing experiments is not available. It is interesting to notice, however, that the value $a_1 = 0.01$ suggested by Bagnold is comparable to the value $a_1\ (1 + T_d^*) = 0.0087$ obtained from Eq. 5 when assuming that the turbulent stress is negligible compared to the dispersive stress ($T_d^* << 1$).

It is found in this analysis that not only the linearized dimensionless model (Eq. 5) is applicable to all three data sets, but the parameter D_v^* can be used to delineate particular cases of the quadratic model. The results shown in Fig. 3 indicate that τ^* is sufficiently close to unity when $D_v^* < 30$ to justify the use of a Bingham plastic model. On the other hand, τ^* exceeds 4 when D_v^* is roughly larger than 400, which indicates that in this region the turbulent-dispersive stress is dominant.

Summary and Conclusion

We concur with Savage and McKeown's (1983) conclusion that the rheology of hyperconcentrations is somewhat more complex than originally pictured by Bagnold (1954). The quadratic model describing the rheology of hyperconcentrated sediment flows is well suited to the experimental data sets of Govier et al. (1957), Savage and McKeown (1983), and Bagnold (1954). This analysis illustrates the benefits of combining the turbulent stress with the dispersive stress. When the quadratic model is written in a linearized dimensionless form (Eq. 5), the ratio of dispersive to viscous stresses D_v^* becomes of foremost importance in selecting appropriate rheological models.

It can be concluded that the quadratic model is valid for all values of the parameter D_v^*, and reduces to the Bingham plastic model when $D_v^* < 30$. Turbulent-dispersive formulations may be useful in the inertial region when $D_v^* > 400$.

Formation of roll waves in laminar sheet flow

Formation d'un train d'ondes dans les écoulements superficiels laminaires

P. Y. JULIEN
Faculty Affiliate, Colorado State University, Fort Collins, CO, U.S.A.

D. M. HARTLEY
Research Hydraulic Engineer, USDA-Agricultural Research Service, Fort Collins, CO, U.S.A.

SUMMARY
The formation of a series of roll waves in laminar sheet flows in a smooth channel is examined both theoretically and experimentally. Roll waves were observed in subcritical flows at a Froude number as low as 0.74. The recommended theoretical relationship for the celerity of roll waves is a function of the momentum correction factor. This relationship is in good agreement with measured celerities of roll waves. The period of roll waves remained fairly constant throughout these experiments. Previous derivations of the length required for the formation of roll wave were modified because experimental evidence demonstrates that the simplified relationship for the celerity of roll waves does not hold true for laminar sheet flows. Using the modified relationship, the dimensionless distance displays an hyperbolic variation with the Froude number and good agreement is obtained with experimental data. This analysis also demonstrates that for supercritical flows the distance is proportional to the ratio of flow depth and slope. Alternatively an equivalent function of Reynolds number and slope can be used.

RÉSUMÉ
La formation d'un train d'ondes dans les écoulements superficiels sur surface lisse est étudiée analytiquement et expérimentalement. Des trains d'ondes ont été observés dans des écoulements fluviaux à des nombre de Froude aussi faibles que 0,74. Une expression analytique fonction du coefficient de Boussinesq est recommandée pour décrire la vitesse de propagation des ondes. La période des ondes demeure constante sous les diverses conditions hydrauliques de cette étude. Les équations existantes décrivant la distance de développement des ondes ont dû être modifiées puisque cette étude expérimentale démontre que certaines hypothèses relatives à la vitesse de propagation des ondes ne sont pas valables pour les écoulements laminaires. Les modifications apportées aux équations donnent des résultats en accord avec les résultats expérimentaux. De plus, l'analyse démontre que pour les écoulements torrentiels, la distance est proportionelle au rapport de la profondeur d'écoulement sur la pente. Une expression équivalente en termes de pente et du nombre de Reynolds peut également être utilisée.

1 Introduction

Sheet flows in steep channels often exhibit surface instabilities which grow until a series of breaking or roll waves are formed. In this study the formation of roll waves under laminar conditions is discussed. Previous treatments of the laminar case have neglected the minimum channel length necessary for roll wave development. Theoretical derivations for turbulent flow [Montuori, 1963 and Liggett, 1975] indicate that simple criteria based on the Froude number are necessary though insufficient since the length required for the formation of roll waves is not considered. In the first part of this study, previous theories on the formation of roll waves are

Revised version received July 11, 1985. Open for discussion July 1, 1986.

3 Theory on the stability of laminar sheet flow

In deriving a fundamental stability criteria for the water surface, several approaches were used by different researchers. Early investigations by Thomas (1939) and Stoker (1957) suggested that the flow is unstable when $S > 4g/C^2$ in which C is the Chézy coefficient. The foremost criterion for instability published in the Russian literature was derived by Vedernikov (1945, 1946). For laminar flows, the Vedernikov number Ve can be written as:

$$Ve = 2F\left(1 - R_h \frac{\partial P}{\partial A}\right) \tag{6}$$

in which

R_h = the hydraulic radius
P = the wetted perimeter
A = the cross-sectional area

The Froude number F defined as $\bar{u}/\sqrt{gh}$ represents the ratio of inertia to gravity forces. For an infinitely wide channel, the Vedernikov number is equal to twice the Froude number and the flow becomes unstable ($Ve > 1$) when the Froude number exceeds 0.5 for laminar flow as compared to 2.0 for turbulent flow. This critical Froude number was also reported by Robertson and Rouse (1941) and Powell (1948). Mayer (1961) observed roll waves in subcritical laminar sheet flows but mistakenly concluded that roll waves can form only when the slope is larger than 3%. Yih (1954, 1963, 1977) and Benjamin (1975) solved the problem of stability of sheet flows down an inclined plane using the Orr-Sommerfeld equation. For very long waves the flow is unstable when:

$$Re \geq \frac{5}{6S} \tag{7}$$

in which Re = the Reynolds number

This criterion was also suggested by Taylor and Kennedy (1961). If equation (2) is substituted into equation (7), uniform flow ($S = S_f$) and a K value of 24 are assumed, a critical Froude number of $F_c = 0.53$ results which is close to the Vedernikov criteria for wide rectangular channels. Ishihara et al. (1961) also suggested the critical value $F_c = 0.577$.

Unfortunately, these criteria based on the Froude number ignore the distance along the channel required for the formation of roll waves. This factor becomes particularly important for subcritical sheet flows since previous studies for turbulent flows [Montuori, 1963] demonstrate that the distance at which the waves are fully developed increases to infinity as the Froude number approaches the critical value.

3.1 *Formation and celerity of roll waves*

When the flow is unstable ($Ve > 1$) a minor perturbation of the water surface induces the formation of small waves. The amplitude of these waves increases gradually as they move downstream until a bore is formed and the wave breaks. The distance travelled between the point at which the perturbation is initiated and the breaking point of the wave defines the distance required for the formation of roll waves. This distance, ξ_c, is determined theoretically from the following procedure using the celerity of roll waves.

$$h' = h + \frac{\partial h'}{\partial \eta}\eta + \frac{1}{2}\frac{\partial^2 h'}{\partial \eta^2}\eta^2 + 0(\eta^3) \tag{15}$$

$$\bar{u}' = \bar{u} + \frac{\partial \bar{u}'}{\partial \eta}\eta + \frac{1}{2}\frac{\partial^2 \bar{u}'}{\partial \eta^2}\eta^2 + 0(\eta^3) \tag{16}$$

$$B' = B + \frac{\partial B'}{\partial h'}\frac{\partial h'}{\partial \eta}\eta + 0(\eta^2) \tag{17}$$

$$A' = A + \frac{\partial A'}{\partial h'}\frac{\partial h'}{\partial \eta}\eta + 0(\eta^2) \tag{18}$$

$$S_f' = S + S\eta\left(\frac{1}{\bar{u}}\frac{\partial \bar{u}'}{\partial \eta} - \frac{2}{h}\frac{\partial h'}{\partial \eta}\right) + 0(\eta^2) \tag{19}$$

The truncated series are valid for small values of η and the solution is examined in the neighborhood of $\eta = 0$. An analysis of equations (13) and (14) using the perturbation defined by equations (15) through (19) as presented in Julien and Hartley (1985) results in the following relationship

$$\frac{\partial^2 h'}{\partial \xi \partial \eta} - \beta\left(\frac{\partial h'}{\partial \eta}\right)^2 + \gamma\frac{\partial h'}{\partial \eta} = 0 \tag{20}$$

in which for rectangular channels ($B = B'$ and $\partial B'/\partial h' = 0$), the coefficients β and γ are respectively:

$$\beta = \frac{3g}{c_0^2 + 2\bar{u}c_0 + gh} \tag{21}$$

and,

$$\gamma = \frac{gS}{\bar{u}^2}\left(1 - \frac{2c_0F^2}{\bar{u}}\right)\left[\frac{1}{2 + \frac{c_0}{\bar{u}} + \frac{\bar{u}}{c_0F^2}}\right] \tag{22}$$

This derivation improves the one given by Liggett (1975) since the wave celerity defined by equation (9) accounts for the velocity distribution present in laminar sheet flow. If a uniform velocity distribution is assumed (i.e. $c_0 = \sqrt{gh}$), equations (21) and (22) reduce to the relationship proposed by Liggett.

The solution of equation (20) is:

$$\frac{\partial h'}{\partial \eta} = \frac{\varepsilon}{\frac{\beta\varepsilon}{\gamma} + e^{\gamma\xi}} \tag{23}$$

in which ε is a constant of integration along the longitudinal distance ξ.

3.3 *Distance for the formation of roll waves*

The critical distance ξ_c at which the wave breaks is assumed to occur when the water surface is vertical. Mathematically, this condition is obtained when the denominator of equation (23) is set equal to zero, or when:

(27) are dimensionless and unique functions of the Froude number as plotted in Fig. 1. For supercritical flows, Ψ has a nearly constant value of 2.0 while Φ increases gradually with the Froude number. It can also be demonstrated that over a fairly wide range of slopes the expression $\ln(S/3\varepsilon)$ will be substantially constant. If Φ is small compared to $\ln(S/3\varepsilon)$ then the following approximate relationship for ξ_c can be written:

$$\xi_c \cong D\frac{h}{S} \tag{28}$$

in which D is equivalent to the factor in braces in equation (25) and is approximately constant. Equations (24) is general while equation (28) represents a simplified expression applicable only to supercritical flows. The ability of equations (24) and (28) to predict the distance ξ_c is evaluated with laboratory data described in the following section.

Table 1. Data summary

S (1)	Re (2)	c m/s (3)	T s (4)	ξ_c m (5)	F (6)	$\frac{gS\xi_c}{\bar{u}^2}$ (7)	D (8)	E mm (9)
0.040	335	0.46	1.33	0.91	2.11	6.03	26.6	1.80
0.040	400	0.50	1.61	0.91	2.31	4.74	25.4	1.71
0.040	500	0.57	1.96	0.91	2.58	3.53	23.5	1.59
0.035	68	0.22	1.27	2.74	0.89	147.30	-	-
0.035	95	0.26	1.28	1.52	1.05	51.20	56.6	3.81
0.035	141	0.34	1.45	1.52	1.28	30.50	49.7	3.35
0.035	188	0.34	1.32	2.13	1.48	28.70	62.6	4.26
0.035	265	0.42	1.37	2.13	1.76	18.40	56.9	3.81
0.035	380	0.43	1.19	2.74	2.11	14.40	64.4	4.33
0.030	90	0.24	1.35	2.13	0.95	72.70	-	-
0.030	122	0.25	1.43	2.13	1.10	49.60	59.7	4.02
0.030	200	0.36	1.47	2.74	1.41	33.10	65.8	4.36
0.030	260	0.41	1.25	2.13	1.61	23.10	46.6	3.99
0.030	340	0.42	1.37	2.13	1.84	16.30	42.9	3.66
0.030	360	0.48	1.35	1.52	2.15	5.90	27.1	1.83
0.030	550	-	-	1.52	2.35	4.68	25.8	1.74
0.025	65	-	-	7.62	0.74	380.00	-	-
0.025	71	-	-	7.62	0.77	340.00	-	-
0.025	85	0.22	1.52	3.35	0.84	118.00	-	-
0.025	104	0.24	1.52	3.35	0.93	91.00	-	-
0.025	130	0.33	1.54	2.74	1.04	54.70	59.1	3.96
0.025	200	0.34	1.61	2.74	1.29	30.70	51.1	3.44
0.025	246	0.38	1.75	2.13	1.43	18.20	37.2	2.50
0.025	320	0.44	1.52	1.52	1.63	9.20	24.5	1.62
0.025	420	0.47	1.19	0.91	1.87	3.83	13.3	0.88
0.025	530	0.50	1.15	1.52	2.10	4.65	20.4	1.37
0.015	140	0.26	1.72	2.74	0.84	41.60	-	-
0.015	173	0.27	1.33	2.13	0.93	24.30	-	-
0.015	260	0.33	1.43	2.13	1.14	14.20	18.4	1.25
0.015	320	0.40	1.23	2.13	1.26	10.80	17.2	1.16
0.015	450	0.43	1.08	1.52	1.50	5.90	11.0	0.88
mean			1.41				38.5	2.67
standard deviation			0.20				18.5	1.28

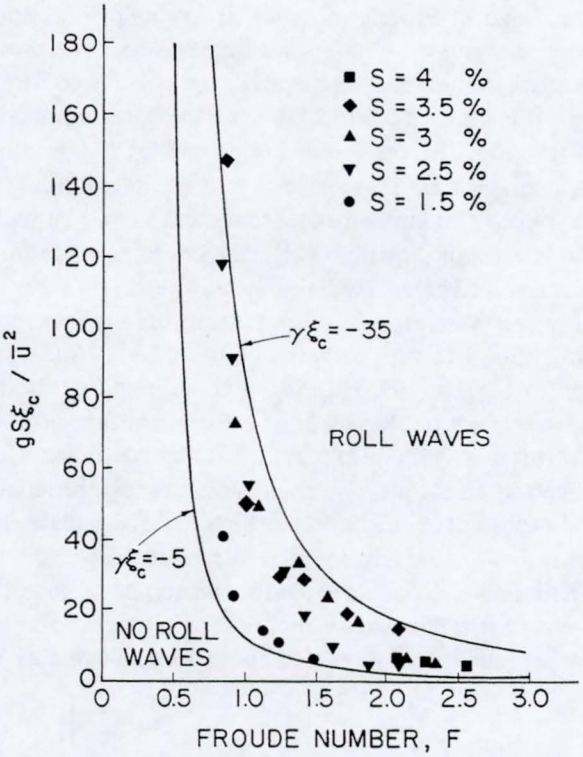

Fig. 3. Dimensionless critical distance as a function of Froude number.
Distance critique adimensionnelle en fonction du nombre de Froude.

4.1 *Analysis of wavelength, period and celerity*

The wavelength can be evaluated from the wave celerity and the period. The observed values of the ratio $c/\sqrt{gh}$ have been plotted against the Froude number on Fig. 2a along with solid and dashed lines representing equation (11) with $\beta_m = 1.2$ and equation (8) for which $\beta_m = 1.0$. The superiority of equation (11) is well supported by the data. Equation (11) can also be written as the ratio of the wave celerity to the mean flow velocity $\bar{u}$ as follows:

$$\frac{c}{\bar{u}} = \beta_m + \sqrt{\frac{1}{F^2} + \beta_m(\beta_m - 1)} \tag{29}$$

For unstable flows ($F > 0.5$), the ratio $c/\bar{u}$ calculated from equation (29) ($\beta_m = 1.2$) decreases from 3.26 to a minimum of 1.69 as shown in Fig. 2b.

The measured wave periods T shown in Table 1 (Col. 4) were fairly constant with a mean value of $\bar{T} = 1.41$ seconds and a standard deviation of 0.20 seconds.

The wavelength L can be obtained from equation (29) in which c is replaced by L/T:

$$\frac{L}{\bar{u}T} = 1.20 + \sqrt{\frac{1}{F^2} + 0.24} \tag{30}$$

For a given mean velocity, the wavelength increases with decreasing Froude number and a first approximation of the wavelength is obtained from the mean value of wave period $\bar{T} = 1.41s$.

possible in laminar sheet flows at Froude numbers as low as 0.50 as compared with 2.0 in turbulent flow. The existence of roll waves at Froude numbers near the lower limit is difficult to verify experimentally because of the extreme channel lengths required. However, in this study, roll waves were observed in laminar, subcritical flow at a Froude number as low as 0.74.

The parabolic velocity distribution in laminar sheet flows implies that the momentum correction factor is larger than unity ($\beta_m = 1.2$). This suggests that the relationship $c = \bar{u} + \sqrt{gh}$ used in previous studies is not applicable to laminar sheet flows and should be replaced by one which uses β_m. The proposed relationship (equation (11)) reduces to $c_0 = \sqrt{gh}$ when $\beta_m = 1$ and is in good agreement with the measured celerities of roll waves when $\beta_m = 1.2$ as shown in Fig. 2. The measured periods of roll waves remained fairly constant in the experimental study at $\bar{T} = 1.41$ second. The wavelength is shown to vary between $1.69\overline{uT} < L < 3.26\overline{uT}$.

The linearized derivation by Liggett (1975) of the length, ξ_c, required for the formation of roll waves has been modified to account for the parabolic velocity distribution of laminar sheet flows. The modified derivation gives more general expressions for the coefficients β and γ which reduce to those proposed by Liggett when $\beta_m = 1$. The results indicate that the length ξ_c is a function of several flow variables and a constant of integration ε which could be calculated from experiments. Though the parameter $\ln \varepsilon$ varies widely ($-61 < \ln \varepsilon < -9.4$), the dimensionless distance shown in Fig. 3 displays a similar relationship to the Froude number as found by Montuori (1963) for turbulent flows. For supercritical flows, ξ_c is proportional to the ratio of flow depth and slope. Alternatively, an equivalent function of Reynolds number and slope may be used.

Acknowledgement

This study has been completed at the Engineering Research Center at Colorado State University. The support of a NATO post-doctoral fellowship to the first author provided by the Natural Sciences and Engineering Research Council of Canada is gratefully acknowledged. The authors would also like to thank the U.S. Department of Agriculture, Agricultural Research Service for providing additional resources for this study.

Notations

A	cross-sectional area for uniform flow
A'	cross-sectional area for flow with a small perturbation
B	top channel width for uniform flow
B'	top channel width for flow with a small perturbation
c	wave celerity
c_0	velocity of the wave relative to the mean velocity $\bar{u}$
C	Chézy coefficient
D, E	empirical constants in equations (28) and (32)
F	Froude number
F_c	critical Froude number
g	gravitational acceleration
h	uniform flow depth
h'	flow depth for flow with a small perturbation
K	friction parameter
L	wavelength

Modeling Circulation in Depth-Averaged Flow

By Victor M. Ponce,[1] M. ASCE, and Steven B. Yabusaki[2]

Introduction

There exists a class of open channel flow problems which can be adequately described in the context of depth-averaged, two-dimensional mathematical models. Essentially, these models are capable of resolving flow currents in two horizontal directions with the fluid and flow properties assumed to be invariant along the vertical. Such simplified representations of a three-dimensional phenomena are justified where turbulent mixing, due to bottom roughness, effectively generates a uniform velocity distribution over the flow depth.

Thermal effluents from cooling facilities, contaminant discharges from chemical processing plants, and sediment movement by local scouring are all evidence of a progressive industrialization which has the potential to tax the natural cleansing action of waterways to the point where serious environmental consequences may result. Knowledge of the effect of proposed modifications is vital to the safe development and utilization of waterways.

In this study, a fundamental investigation of the circulation phenomena in open channels is performed using a depth-averaged mathematical model. Circulation has been observed to have a primary influence on erosion and accretion processes, heat diffusion, and contaminant dispersion. Therefore, the clarification of the physical mechanisms leading to the generation of circulation in free surface flow is a much needed research endeavor.

Literature Review

Prior to the development of efficient, high-speed computer hardware, two alternatives were available to the researcher interested in modeling free-surface flow: (1) analytical solutions; and (2) physical hydraulic models. Despite providing the most accurate results, analytical solutions are extremely rare and apply only in highly simplified situations. Conversely, physical hydraulic models are used widely and quite successfully. Most of the drawbacks associated with

[1] Assoc. Prof. of Civ. Engrg., San Diego State Univ., San Diego, Calif. 92182.

[2] Civ. Engr., Water and Land Resources Dept., Batelle, Pacific Northwest Laboratories, Richland, Wash.

Note.—Discussion open until April 1, 1982. To extend the closing date one month, a written request must be filed with the Manager of Technical and Professional Publications, ASCE. Manuscript was submitted for review for possible publication on August 20, 1980. This paper is part of the Journal of the Hydraulics Division, Proceedings of the American Society of Civil Engineers, ©ASCE, Vol. 107, No. HY11, November, 1981. ISSN 0044-796X/81/0011-1501/$01.00.

physical models are of an economic nature owing to the high cost of construction and the time required to adequately simulate the prototype conditions. Lack of flexibility, however, is probably the largest deterrent to selecting a physical model since a change in configuration usually involves expensive modifications.

The increased efficiency of digital computers has triggered a strong research effort in the refinement of mathematical models. While offering almost unlimited flexibility in the simulation of various alternatives, these models have the additional appeal of smaller development and operating costs. Certain specialized problems still remain within the realm of physical modeling, but the use of mathematical models continues to grow.

Mathematical models of open channel flow exist at various levels of sophistication. The detailed description of flow phenomena is best accomplished in a three-dimensional spatial framework; however, the complexity of a formulation in three dimensions often requires tremendous amounts of computational effort. Where valid, the simplification to a two-dimensional representation can offer a considerable reduction in complexity and expense. This involves an integration of the three-dimensional equations of fluid dynamics over the flow depth. The two-dimensional depth-integrated system of equations is not without its pitfalls: there is a closure problem associated with the effective shear stresses which act tangentially on vertical sides of a fluid element. No rigorous relation between these stresses and the depth-averaged variables is currently available.

Hansen (6) is credited for being the first to outline the depth-averaged two-dimensional formulation. Later, several other researchers, most notably Leendertse (10,11), followed Hansen in applying two-dimensional modeling concepts to the study of estuarine and coastal hydrodynamics. In a detailed analysis of free-surface flow, Leendertse developed a computational model for long period wave propagation in well-mixed estuaries and coastal seas (10). Particular emphasis was given in Leendertse's work to the numerical properties of the two-dimensional model in the form of a linear stability and convergence analysis following the von Neumann approach.

Kuipers and Vreugdenhil (7) extended Leendertse's 1967 model to the realm of secondary flows. By imposing a steady condition at the open boundaries, they were able to use the unsteady character of Leendertse's model as an iterative technique to approach steady circulating flow under certain specified boundary conditions. A theoretical analysis of the vorticity-generating mechanisms was performed in order to throw additional light onto the causes of circulating flow in depth-averaged two-dimensional models. According to Kuipers and Vreugdenhil, if wind stresses are neglected, vorticity can be created either by the convective terms interacting with converging or diverging flow or through the effective shear stresses. Numerical experiments showed the necessity of including the convective inertia terms in order to model two-dimensional circulating flow. The observed circulation in the model is attributed to the combined effect of the convective inertia terms and the artificial viscosity, since no explicit account of the effective stresses was made.

In a companion report to that of Kuipers and Vreugdenhil, Flokstra (3) has directed attention to the importance of correctly modeling the effective shear stresses. Without actually resolving the closure problem associated with the modeling of these stresses, Flokstra made a detailed analysis of the relevant physical mechanisms contributing to the generation of circulation. According

to Flokstra's vorticity balance, it is theoretically impossible to generate circulating flow without modeling the effective shear stresses. In addition, Flokstra's analysis leads to the conclusion that a no-slip velocity condition at closed boundaries is essential to the generation of eddy flow patterns.

Abbott and Rasmussen (1) verified Kuipers and Vreugdenhil's conclusion that the convective inertia terms are necessary for the generation of circulation. Using physical reasoning, they attributed the circulating patterns to a direct consequence of the resistance effects dominating the inertial effects. Abbott and Rasmussen also concluded that "pseudo-circulations," occurring strictly due to the truncation errors of first order difference schemes, were possible in depth-averaged two-dimensional models.

The occurrence of nonlinear instability in two-dimensional numerical models was also studied by Flokstra (4). Three approaches were cited to handle this problem: (1) A spatial smoothing process similar to that used by Kuipers and Vreugdenhil; (2) the explicit introduction of an eddy viscosity term in the equations of motion; and (3) the use of a difference scheme affected with numerical viscosity.

McGuirk and Rodi (12) developed a depth-averaged velocity and contaminant distribution model of open channel flow which described the recirculation region immediately downstream of a side discharge into a flowing river. Considering the constant turbulent diffusion coefficient and nonexplicit representations of the turbulent structure too crude for the side jet phenomena, McGuirk and Rodi utilized an extension of Launder and Spalding's (8) two-dimensional turbulence model.

Lean and Weare (9) tested Flokstrua's theoretically-based conclusions using a depth-averaged circulation model of flows past a breakwater. The effective stresses were shown to have contributions from shear layer turbulence and turbulence generated at the bed. Criteria is presented to delimit the conditions under which the shear layer turbulence will predominate. An observation of numerical circulation (5) similar to that experienced by Abbott and Rasmussen but caused by a coarse computational grid is reported.

At present, many uncertainties exist in the mathematical modeling of depth-averaged two-dimensional open channel flow. Several models which exhibit circulation and numerous theoretical reviews on the factors causing circulation are present in the literature. However, no comprehensive analysis of the various mechanisms leading to circulation has been attempted in conjunction with a numerical model. The objectives of this study are, thus, twofold: (1) The clarification of the physical processes which contribute to the generation of circulation; and (2) the identification of significant factors in the numerical specification of circulating flow problems.

Governing Equations

The derivation of the equations governing depth-averaged free-surface flow is accomplished by the successive simplification of the general three-dimensional fluid flow equations, i.e., the Navier-Stokes equations. Four assumptions are basic to the equation set used in this study: (1) Water is incompressible; (2) vertical velocities and accelerations are negligible; (3) wind stresses and geostrophic effects are negligible; and (4) average values are sufficient to describe

properties which vary over the flow depth.

Fluid density effects are not considered in this study; thus, incompressibility is a limitation to the applicability of the model. The second assumption is a consequence of the relatively large magnitude of the gravitational body force which, in flows of shallow depth, simplifies the z-component of the motion equation to a statement of hydrostatic pressure distribution in the vertical. For the type of flow under consideration, i.e., open channel flow, the magnitude of the wind and geostrophic effects is insignificant compared to the driving forces found in the mean flow currents. These two terms can be easily incorporated into the model if desired, and their absence does not detract from the generality of the conclusions of this study. The most significant assumption is that an average value is capable of representing a property which normally varies over the flow depth. Until this assumption is made, the analysis is fundamentally three-dimensional. Due to the depth-averaging of the equation set, information on the vertical distribution of velocity is partially lost. Fortunately, the shallow waters found in rivers and well-mixed estuaries usually do not require such detailed information.

The resulting depth-averaged equations are:

Conservation of mass
$$\frac{\partial \eta}{\partial t} + \frac{\partial (h\bar{u})}{\partial x} + \frac{\partial (h\bar{v})}{\partial y} = 0 \quad (1)$$

Conservation of momentum
$$\frac{\partial \bar{u}}{\partial t} + \bar{u}\frac{\partial \bar{u}}{\partial x} + \bar{v}\frac{\partial \bar{u}}{\partial y} + g\frac{\partial \eta}{\partial x} + \frac{1}{\rho h}\tau_{bx} - \frac{1}{\rho h}\frac{\partial}{\partial x}(hT_{xx}) - \frac{1}{\rho h}\frac{\partial}{\partial y}(hT_{xy}) = 0 \quad (2)$$

$$\frac{\partial \bar{v}}{\partial t} + \bar{u}\frac{\partial \bar{v}}{\partial x} + \bar{v}\frac{\partial \bar{v}}{\partial y} + g\frac{\partial \eta}{\partial y} + \frac{1}{\rho h}\tau_{by} - \frac{1}{\rho h}\frac{\partial}{\partial x}(hT_{xy}) - \frac{1}{\rho h}\frac{\partial}{\partial y}(hT_{yy}) = 0 \quad (3)$$

in which $\bar{u}$, $\bar{v}$ = depth-averaged velocities; t = time; x, y = coordinate directions; g = gravitational acceleration; η = water elevation ($\eta = h + z_b$); ρ = fluid density; τ_{bx}, τ_{by} = bottom shear stresses; and T_{xx}, T_{xy}, T_{yy} = effective shear stresses defined as follows:

$$T_{xx} = \frac{1}{h}\int_{z_b}^{\eta}\left[2\rho\nu\frac{\partial u}{\partial x} - \rho\overline{u'^2} - \rho(u-\bar{u})^2\right]dz \quad (4)$$

$$T_{xy} = T_{yx} = \frac{1}{h}\int_{z_b}^{\eta}\left[\rho\nu\left(\frac{\partial u}{\partial y} + \frac{\partial v}{\partial x}\right) - \rho\overline{u'v'} - \rho(u-\bar{u})(v-\bar{v})\right]dz \quad (5)$$

$$T_{yy} = \frac{1}{h}\int_{z_b}^{\eta}\left[2\rho\nu\frac{\partial v}{\partial y} - \rho\overline{v'^2} - \rho(v-\bar{v})^2\right]dz \quad (6)$$

in which ν = kinematic viscosity; and u' and v' = turbulent velocity fluctuations.

The foregoing equation set, although containing many approximations and

simplifications, is not closed. Historically, turbulent flow theory has suffered from an incomplete physical representation of the turbulent momentum transfer (Reynolds stresses), i.e., those stresses due to the correlations of turbulent velocity fluctuations. Depth-averaging the formulation further complicates the problem by creating an additional stress due to the nonuniform velocity distribution in the vertical. These two stresses and the viscous shear stress combine into the terms previously identified as the effective shear stresses.

Representing the effective shear stresses in terms of the mean flow variables is by far the largest impediment to the proper depth-averaged modeling of circulating flow. Since this problem remains to be solved, the use of empirical parameters and calibration techniques is indicated. In this study, the procedure developed by Kuipers and Vreugdenhil (7) is adopted. This particular technique does not explicitly include the effective shear stresses in the equation set, but introduces them in a velocity-averaging routine which effectively simulates the contribution of the effective stresses. In this routine, an averaging procedure occurs after each set of new dependent variables has been generated, as follows:

$$\bar{u}^*_{j,k} = \bar{u}_{j,k}(1-\alpha) + \frac{\alpha}{4}(\bar{u}_{j-1,k} + \bar{u}_{j,k-1} + \bar{u}_{j,k+1} + \bar{u}_{j+1,k}) \quad (7)$$

$$\bar{v}^*_{j,k} = \bar{v}_{j,k}(1-\alpha) + \frac{\alpha}{4}(\bar{v}_{j-1,k} + \bar{v}_{j,k-1} + \bar{v}_{j,k+1} + \bar{v}_{j+1,k}) \quad (8)$$

in which $\bar{u}^*_{j,k}$ = spatially averaged $\bar{u}_{j,k}$; $\bar{v}^*_{j,k}$ = spatially averaged $\bar{v}_{j,k}$; α = weighting factor; and j, k = spatial indices. When these substitutions are made in the governing equations, closure terms appear such that

$$\frac{1}{\rho h}\left[\frac{\partial}{\partial x}(hT_{xx}) + \frac{\partial}{\partial y}(hT_{xy})\right] = \epsilon\left(\frac{\partial^2 \bar{u}}{\partial x^2} + \frac{\partial^2 \bar{u}}{\partial y^2}\right) \quad (9)$$

$$\frac{1}{\rho h}\left[\frac{\partial}{\partial x}(hT_{xy}) + \frac{\partial}{\partial y}(hT_{yy})\right] = \epsilon\left(\frac{\partial^2 \bar{v}}{\partial x^2} + \frac{\partial^2 \bar{v}}{\partial y^2}\right) \quad (10)$$

in which $\epsilon = \alpha\,(\Delta x)^2/2\Delta t$; Δx = spatial increment; and Δt = temporal increment.

The bottom shear stress, like the effective shear stress, has not been rigorously related to flow properties. However, years of experimentation has resulted in the development of several satisfactory empirical resistance equations. Any of the applicable resistance equations can be used to relate the bottom shear stress to the flow velocity, assuming the validity of a steady uniform flow roughness. The Chézy expression is preferred here for simplicity, due to the dimensionless friction factor f_r associated with it, as follows:

$$\tau_{bx} = \rho f_r\, \bar{u}\,(\bar{u}^2 + \bar{v}^2)^{1/2} \quad (11)$$

$$\tau_{by} = \rho f_r\, \bar{v}\,(\bar{u}^2 + \bar{v}^2)^{1/2} \quad (12)$$

in which $f_r = g/C^2$; and C = Chézy coefficient.

Mathematical Model

A finite difference approximation is used to represent the partial differential equation set in the numerical model. In order to visualize the computational

structure, the reader must imagine levels of horizontal x-y grids layered in the vertical time dimension. Conceptually, the four variables, u, v, η, and z_b, should all be defined at every node location. However practical limitations in the computational procedure make it more convenient to define a separate grid system for each of these variables. These four grid systems are staggered in space in a form originally due to Platzman (13), as shown in Fig. 1. Normally, it is not necessary for Δx to be equal to Δy; however, the representation of the effective shear stresses used in this model does hinge on this assumption.

Among the several types of finite difference schemes available, the central

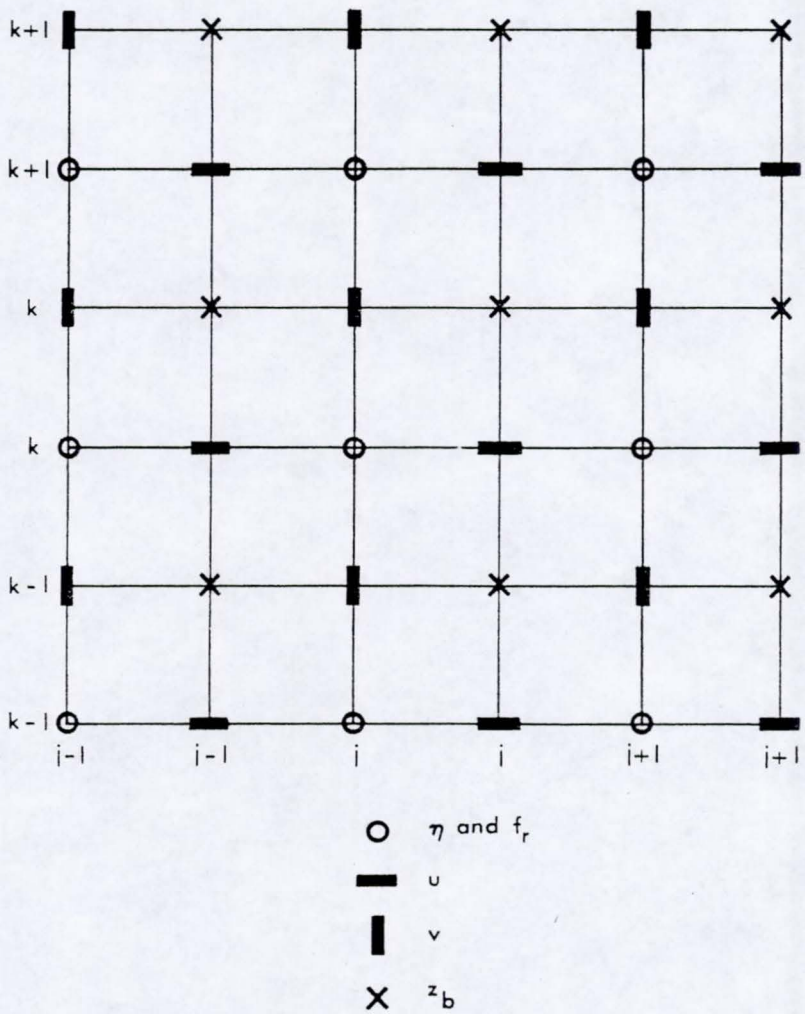

FIG. 1.—Typical Spatial Grid Configuration at Time Level n

difference approximations provide second order accuracy. Generally speaking, spatial derivatives can always be expressed in a central difference format. However, unless iterations are performed, temporal derivatives cannot be represented by central difference schemes because two entire time levels of unknowns would be present. The additional computational effort required by an iterative formulation is normally not warranted. Consequently, a less accurate but more expedient first order difference scheme is preferred for the temporal derivatives.

Equations which are nonlinear with respect to the unknown variables present

formidable difficulties for an efficient numerical solution. Although the governing equations contain nonlinear terms, a judicious specification of known and unknown values in the finite difference equations results in a linear representation of the unknown variables. This equation set is then solved by an efficient matrix inversion algorithm.

The computational procedure used in this model is a multioperational solution mode based on the division of each time step Δt into two stages of half-time step each. Leendertse (10) modified the well-known "alternating-direction implicit" or ADI method, by including two explicit schemes in such a way that each stage comtained an implicit scheme followed by an explicit scheme. The advantage of the ADI method, in addition to those attributable to implicit schemes, lies in the solution procedure which solves the x-momentum equation separately from the y-momentum equation, permitting the two-dimensional problem to be solved as a sequence of two one-dimensional problems. After each implicit step, a single dependent variable remains unknown and can be directly solved for by an explicit method. The numerical model is based on the set of governing equations derived earlier. Each of the three equations has a difference scheme centered about a unique location on the grid system. The x-momentum equation is referenced to the node occupied by $\bar{u}_{j,k}$ while the y-momentum equation is centered about node location $\bar{v}_{j,k}$; $\eta_{j,k}$ is the reference location for the continuity equation (for simplicity, overbars are omitted hereafter).

In the mathematical model used in this study, the finite difference analogs of the various equations are, for the first stage:

x-Momentum (Implicit)
$$\left.\frac{\partial u}{\partial t}\right|_{u_{j,k}^{n+1/2}} = \frac{u_{j,k}^{n+1/2} - u_{j,k}^{n}}{\frac{1}{2}\Delta t} \qquad (13)$$

$$u\left.\frac{\partial u}{\partial x}\right|_{u_{j,k}^{n+1/2}} = u_{j,k}^{n+1/2}\left[\frac{u_{j+1,k}^{n} - u_{j-1,k}^{n}}{2\Delta x}\right] \qquad (14)$$

$$v\left.\frac{\partial u}{\partial y}\right|_{u_{j,k}^{n+1/2}} = \left[\frac{v_{j,k-1}^{n} + v_{j+1,k-1}^{n} + v_{j,k}^{n} + v_{j+1,k}^{n}}{4}\right]\left[\frac{u_{j,k+1}^{n} - u_{j,k-1}^{n}}{2\Delta y}\right] \qquad (15)$$

$$g\left.\frac{\partial \eta}{\partial x}\right|_{u_{j,k}^{n+1/2}} = g\left[\frac{\eta_{j+1,k}^{n+1/2} - \eta_{j,k}^{n+1/2}}{\Delta x}\right] \qquad (16)$$

$$f_r u \left.\frac{(u^2 + v^2)^{1/2}}{(\eta - z)}\right|_{u_{j,k}^{n+1/2}}$$
$$= \left[\frac{f_{r_{j,k}} + f_{r_{j+1,k}}}{2}\right]\left[\frac{u_{j,k}^{n+1/2}\left[(u_{j,k}^{n})^2 + \left(\frac{v_{j,k-1}^{n} + v_{j+1,k-1}^{n} + v_{j,k}^{n} + v_{j+1,k}^{n}}{4}\right)^2\right]^{1/2}}{\left[\frac{\eta_{j+1,k}^{n} + \eta_{j,k}^{n}}{2} - \frac{z_{b_{j,k}} + z_{b_{j,k-1}}}{2}\right]}\right] \qquad (17)$$

Continuity (Implicit)
$$\left.\frac{\partial \eta}{\partial t}\right|_{\eta_{j,k}^{n+1/2}} = \frac{\eta_{j,k}^{n+1/2} - \eta_{j,k}^{n}}{\frac{1}{2}\Delta t} \qquad (18)$$

$$\frac{\partial}{\partial x}\left[(\eta - z_b)u\right]\Bigg|_{\eta_{j,k}^{n+1/2}} = \frac{\left[\dfrac{\eta_{j+1,k}^n + \eta_{j,k}^n}{2} - \dfrac{z_{b_{j,k}} + z_{b_{j,k-1}}}{2}\right] u_{j,k}^{n+1/2}}{\Delta x} - \frac{\left[\dfrac{\eta_{j,k}^n + \eta_{j-1,k}^n}{2} - \dfrac{z_{b_{j-1,k}} + z_{b_{j-1,k-1}}}{2}\right] u_{j-1,k}^{n+1/2}}{\Delta x} \quad (19)$$

$$\frac{\partial}{\partial y}\left[(\eta - z_b)v\right]\Bigg|_{\eta_{j,k}^{n+1/2}} = \frac{\left[\dfrac{\eta_{j,k+1}^n + \eta_{j,k}^n}{2} - \dfrac{z_{b_{j,k}} + z_{b_{j-1,k}}}{2}\right] v_{j,k}^n}{\Delta y} - \frac{\left[\dfrac{\eta_{j,k}^n + \eta_{j,k-1}^n}{2} - \dfrac{z_{b_{j,k-1}} + z_{b_{j-1,k-1}}}{2}\right] v_{j,k-1}^n}{\Delta y} \quad (20)$$

y-Momentum (Explicit) $$\frac{\partial v}{\partial t}\Bigg|_{v_{j,k}^{n+1/2}} = \frac{v_{j,k}^{n+1/2} - v_{j,k}^n}{\frac{1}{2}\Delta t} \quad (21)$$

$$u\frac{\partial v}{\partial x}\Bigg|_{v_{j,k}^{n+1/2}} = \left(\frac{u_{j,k}^{n+1/2} + u_{j,k+1}^{n+1/2} + u_{j-1,k+1}^{n+1/2} + u_{j-1,k}^{n+1/2}}{4}\right)\left(\frac{v_{j+1,k}^n - v_{j-1,k}^n}{2\Delta x}\right) \quad (22)$$

$$v\frac{\partial v}{\partial y}\Bigg|_{v_{j,k}^{n+1/2}} = v_{j,k}^{n+1/2}\left[\frac{v_{j,k+1}^n - v_{j,k-1}^n}{2\Delta y}\right] \quad (23)$$

$$g\frac{\partial \eta}{\partial y}\Bigg|_{v_{j,k}^{n+1/2}} = g\left[\frac{\eta_{j,k+1}^{n+1/2} - \eta_{j,k}^{n+1/2}}{\Delta y}\right] \quad (24)$$

$$f_r\, v\frac{(u^2 + v^2)^{1/2}}{(\eta - z_b)}\Bigg|_{v_{j,k}^{n+1/2}} = \left(\frac{f_{j,k} + f_{j,k+1}}{2}\right)\left[\frac{v_{j,k}^{n+1/2}\left[(v_{j,k}^n)^2 + \left(\dfrac{u_{j,k}^n + u_{j,k+1}^n + u_{j-1,k}^n + u_{j-1,k+1}^n}{4}\right)^2\right]^{1/2}}{\left(\dfrac{\eta_{j,k+1}^{n+1} + \eta_{j,k}^{n+1/2}}{2} - \dfrac{z_{b_{j,k}} + z_{b_{j-1,k}}}{2}\right)}\right] \quad (25)$$

Similar discretization techniques are applicable for the second stage: (1) y-momentum and continuity (implicit); and (2) x-momentum (explicit). See Ref. 14 for additional details.

Two boundary types can be specified in the numerical model: closed and open boundaries. At closed boundaries, the most convenient specification is the condition of zero mass flux (i.e., zero velocity) in a direction perpendicular to the boundary. At open boundaries, either mean velocity or water surface elevation may be specified, depending on the modeling needs.

Spatial central finite differences such as those used on this model require

information which lies outside the boundaries of the computational model. Although a zero velocity tangential to the wall is a realistic assumption (the no-slip velocity condition), a zero water level at the boundary can be grossly inaccurate and may lead to numerical stability problems. A satisfactory alternative appears to be the relocation of interior values. A simple relocation technique was chosen in which exterior values were defined to be equal to those interior values adjacent to the boundaries. This is tantamount to a perfect slip condition, a reasonable assumption in turbulent flows in which the viscous effects have little influence on the horizontal velocity distribution.

A pervasive problem in two-dimensional mathematical modeling is the lack of adequate theoretical numerical stability criteria. Linear stability theory classifies the multi-operational procedure as unconditionally stable. However, experience (15) has shown that it is only weakly stable.

Results

The objective of the numerical experimentation is the clarification of the circulation phenomena found in free surface flow. Two hypothetical configura-

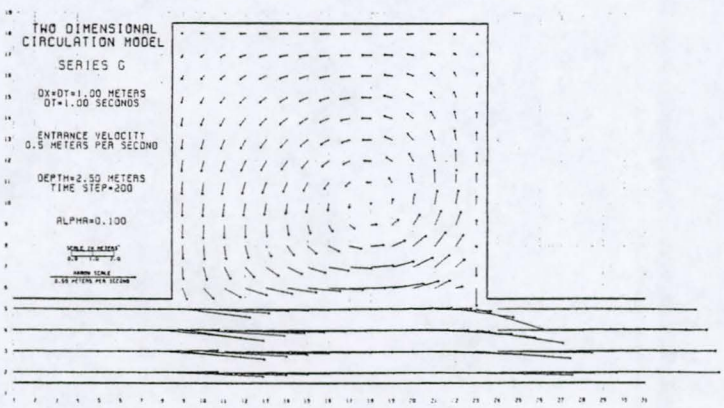

FIG. 2.—Channel-Pool Baseline Flow Pattern, Time Step 200

tions are tested under a gamut of initial and boundary conditions. In addition to a sensitivity analysis, experiments are performed in which more than one element is varied from the baseline in order to determine the interaction between several components of the problem.

The bulk of the testing program consists of experiments performed on a channel-pool configuration; channel dimensions are 4 m in width by 30 m in length, while the pool is a rectangle 14 m wide and 15 m long.

The first series of tests are performed with a 0.5 m/s velocity specified in the channel as an initial condition and at the upstream end as a steady boundary condition. A water depth of 2.5 m serves as both the initial condition and the steady downstream boundary condition., There is no velocity in the pool initially. Closed boundaries are represented by zero velocities perpendicular to walls. Without a bed slope, the water in the system is driven solely by the upstream entrance velocity. Numerical parameters used in the baseline run are: weighting factor $\alpha = 0.1$, friction factor $f_r = 0.0045$, spatial increment $\Delta x = \Delta y = 1.0$ m, and temporal increment $\Delta t = 1.0$ sec. Fig. 2 is a plot

of the baseline velocity vectors after 200 sec of simulation. A well-developed circulation appears in the pool area with little or no divergence from the mainstream flow. Water levels in the pool range from 2.50 m–2.52 m. Entrance levels, however, fall continuously from 2.50 m–2.44 m.

The necessity of modeling the effective shear stresses where physical circulation is present has been explained theoretically by Flokstra (3). In the present model, the representation of the effective shear stresses is not explicit in the discretized equation set; rather, the action of the effective shear stresses is simulated by a velocity averaging interphase which employs a weighting factor α to control the magnitude of the effect. The first experiment performed on the channel-pool configuration omits the effective stress modeling by setting α to zero. Transfer of turbulent momentum from the mainstream to the pool is insignificant in this case. With no flow divergence into the pool, the initial conditions are virtually preserved.

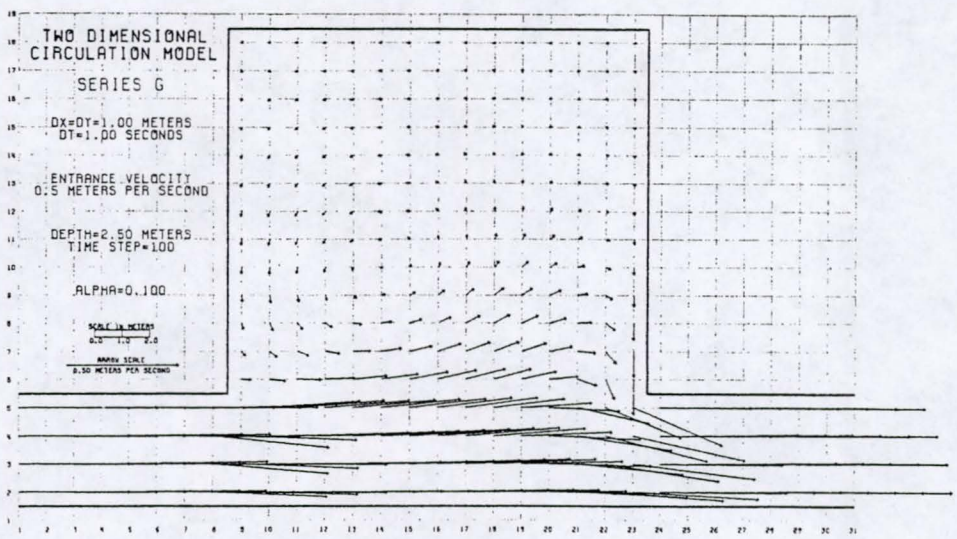

FIG. 3.—Flow Pattern Neglecting Convective Inertia, Time Step 100

The convective inertia terms, $u\ \partial u/\partial x$, $v\ \partial u/\partial y$, $u\ \partial v/\partial x$, and $v\ \partial v/\partial y$, are often neglected in numerical modeling because the nonlinearity of these terms introduces additional difficulties. Several authors have commented on the necessary presence of the convective inertia terms in the equation set when secondary flow is to be resolved. To test this conclusion, all four convective inertia terms were set to zero. The plot at 100 sec of simulation time is presented in Fig. 3. Divergence of the flow from the channel into the pool is strong; however, no circulation sets up. As water in the channel reaches the upstream end of the pool, flow immediately is directed into the pool along the boundaries, preventing circulation from occurring.

In the literature, the role of friction in circulation is not clearly defined. To shed more light on this subject, an experiment is performed wherein the friction terms, $f_r\, u \sqrt{u^2 + v^2}/\eta - z_b$ and $f_r\, v \sqrt{u^2 + v^2}/\eta - z_b$, are eliminated from the computation. The results from this experiment, including detailed quantitative results are virtually indistinguishable from the baseline results, Fig. 2.

The effect of an increase in flow depth has been documented by Bengtsson

(2) following experiments performed on a lake model. His conclusion was that the influence of the horizontal turbulence terms was reduced with increasing depth. In this study, the horizontal dispersion of momentum is simulated by the effective stress closure terms, $\epsilon\ (\partial^2 u/\partial x^2 + \partial^2 u/\partial y^2)$ and $\epsilon(\partial^2 v/\partial x^2 + \partial^2 v/\partial y 2)$. It is therefore, not obvious how depth should affect these terms. To investigate the effect of flow depth, depths ranging from 0.04 m–50 m were tested, with instability occurring only in the 0.04 m run. Results displayed the following trends: shallower depths show more divergence of flow from the channel, larger velocities in the shear layer, and faster set-up of circulation. In the extreme, however, the shallow depth is also subject to instability. Larger depths have less energy transfer to the pool and consequently little or no circulation.

The earlier experiments with friction appear to dismiss the importance attached to it by some authors. However, these tests were all performed on problems of relatively small scale. To test the effect of friction in a large scale problem, the size of the configuration was increased by setting $\Delta x = \Delta y = 100$ m. Experience from the stability analysis testing led to the use of a time increment of 100 sec to accompany the length scale increase. In this test, the baseline friction value, $f_r = 0.0045$, was used. Flow diverged immediately into the pool near the upstream wall, penetrating to the center, before leaving the pool along the downstream wall. No circulation developed in this experiment. The flow pattern was very similar to that seen in the test in which convective inertia was neglected (Fig. 3).

In earlier tests, a perfect-slip velocity condition had been implemented at all closed boundaries with satisfactory results. To test the validity of this assumption, an experiment is performed in which the flow is subject to a no-slip velocity condition as closed physical boundaries. This condition can be approximated by setting all velocities located outside of the physical boundaries to zero. For this experiment, a bed slope $S_0 = 0.0005$ is introduced into the channel-pool configuration. Open boundary conditions at the channel end points are water levels which correspond to the initial bed slope condition. Closed boundaries remain to be defined by zero perpendicular velocities. All other parameters are the same as in the velocity-specified baseline testing, i.e., $\alpha = 0.1$, $\Delta x, = \Delta y = 1.0$ m, $\Delta t = 1.0$ sec, and $f_r = 0.0045$. The no-slip model experiences strong damping of velocity although the development of circulation is apparent after 190 sec of simulation.

Secondary flow in sudden expansions is of a slightly different nature than the channel-pool system treated earlier. This is due in part to the bending of currents into the expansion and the increased exposure of secondary currents to mainstream effects. Abbott and Rasmussen (1) developed a channel expansion model from which results and conclusions were presented. An attempt is made here to verify these conclusions using a similar geometry.

In this testing series, the configuration consists of an entrance channel 9 m wide and 7.5 m long while the expanded channel is 17 m wide and 22.5 m long. A fixed bed slope of $S_0 = 0.0005$ in the direction of the entrance channel flow is specified for the entire configuration. The initial condition is a water surface slope parallel to the bed at a depth of 2.5 m. All velocities are set to zero at the beginning of the simulation. Open boundary conditions at both upstream and downstream ends are water levels which match the initial

conditions. Closed boundaries are zero velocities perpendicular to the walls. Friction in this model is governed by a dimensionless friction factor $f_r = 0.0045$. The weighting factor is set to 0.1 while the space increment is 1.0 m and the time increment is 1.0 sec.

Fig. 4 is a plot of the channel expansion basline results after 100 sec of simulation. A well-developed circulation forms a zone of separation in the corner

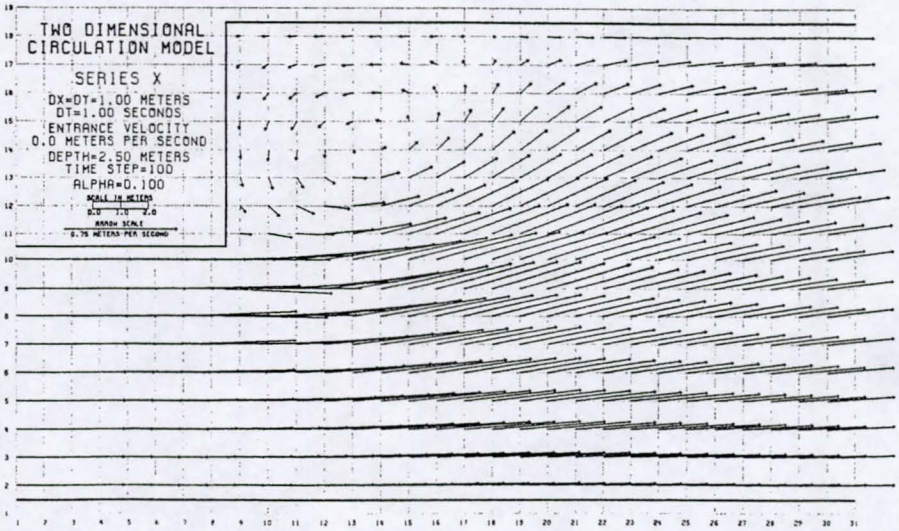

FIG. 4.—Channel Expansion Baseline Flow Pattern, Time Step 100

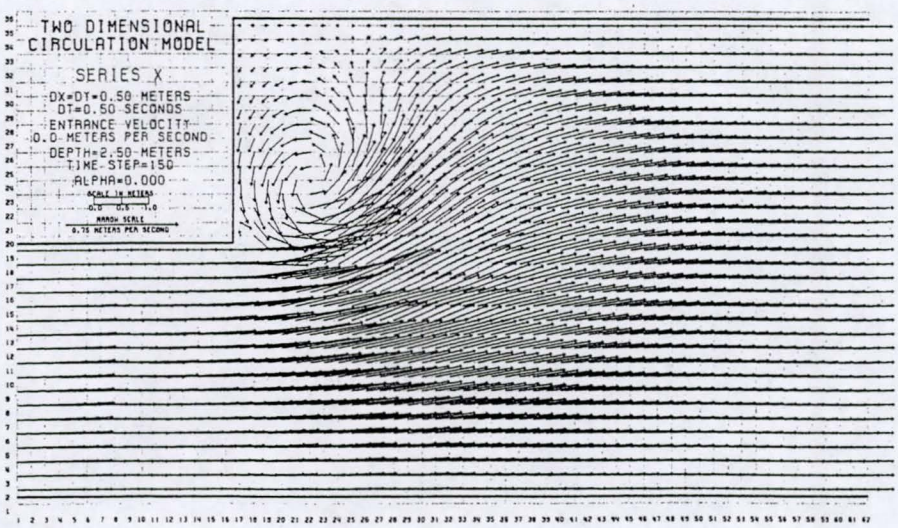

FIG. 5.—Channel Expansion Flow Pattern with Increased Spatial Resolution, Time Step 150

of the expansion. Entrance velocities range from 0.72 m/s at the bottom wall to 0.77 m/s at the top wall while exit velocities vary from 0.44 m/s–0.30 m/s, bottom to top. Water levels throughout the simulation are continuous and stable. Slightly lower elevations are found within the circulation pattern.

For the most part, the testing of the channel expansion produced results consistent with those of the channel-pool configuration. A discrepancy was found, however, when the slope-specified models were tested without modeling

the effective stresses. In the velocity-specified channel-pool model, the absence of the effective stresses resulted in no circulation being produced. Contrary to this result, both configurations, i.e., the channel expansion and the channel-pool system, are able to generate a spiraling secondary flow without the presence of the effective stresses if a bed slope is the driving force.

The question arose that the secondary currents which appear without the benefit of effective stress modeling may be of a strictly numerical nature. Theoretically, numerical effects should be minimized as the discretization of the problem domain is made exceedingly small. To this end, both space and time increments in the expansion model were reduced although the problem size remained constant. The values of these parameters for this test are $\Delta x = \Delta y = 0.5$ m and $\Delta t = 0.5$ sec.

A horizontal water surface without velocity is specified as the initial condition. As the simulation begins, the downstream water level is lowered in 40 time steps to a depth of 2.5 m, the same depth as the upstream boundary condition. Thus a line drawn through the end point water levels will be parallel to the bed slope. The weighting factor for this experiment is zero while the nondimensional friction factor is 0.0045. Fig. 5 is a plot of the velocity vectors after 150 sec of simulation. A strong spiraling "circulation," with a character similar to those observed in earlier slope-specified experiments, sets up in the expansion corner.

Evaluation

The testing program for this study is fairly extensive; therefore, only a limited discussion can be presented here. However, the analysis and evaluation of the numerical experiments is based on all the tests performed. For a more detailed description, the reader is referred to (14).

The use of specified water levels at the open boundaries proved to be a better boundary condition than the velocity specified in the early testing series. When a difference in water levels is the driving force for flow through the configuration, both velocity and water surface are steady and continuous, with few, if any, anomalies. This is in contrast to the velocity-specified model which requires a special initial condition before simulation can begin. In addition, oscillating water levels and velocities plague many of the velocity-specified simulations.

Specific differences in model behavior due to a change in boundary conditions are found only in the testing of α, the weighting factor used in the velocity-averaging routine. In the velocity-specified model, circulation did not occur without the presence of the closure terms, $\epsilon(\partial^2 u/\partial x^2 + \partial^2 u/\partial y^2)$ and $\epsilon(\partial^2 v/\partial x^2 + \partial^2 v/\partial y^2)$, in the computations. However, a spiraling secondary flow did appear in all sloping models when tested without the effective stresses being represented. It does not appear that this result is numerically-produced, as evidenced by the undiminished presence of this "circulation" in spite of increased grid resolution.

While acknowledging the "no-slip" velocity condition in nature, the testing of this model has been performed primarily with a "perfect slip" boundary specification. This is a reasonable assumption in models where the spatial resolution across a channel width is not very fine. In the experiment involving

the specification of zero velocities outside the boundary geometry, overwhelming resistance effects resulted. Obviously, any consideration of a no-slip boundary condition must be coordinated with an accompanying reduction in the bed resistance effects.

Results from the testing program are reasonable and encouraging, despite the presence of two flaws traceable to the representation of the effective stresses. First, there is yet to be found a physical basis by which to choose the appropriate weighting factor, α, on the velocity averaging routine. There are instances in the literature where physical processes have been successfully replaced by numerical techniques in a general manner. Although the selection of the weighting factor is presently a manageable calibration task, a physical link to the turbulence process has yet to be advanced.

The second drawback in the effective stress representation is somewhat more serious than the first. Much of the success is fulfilling the required profile of traits by the closure terms is due to the effect of numerical viscosity. As the weighting factor is increased, the model reacts as if the fluid is becoming more viscous, thus increasing the exchange of lateral momentum and increasing viscous damping. Essentially, viscosity is used to model a turbulence effect. Therefore, care must be exercised when using the velocity averaging routine; a balance must be struck between the simulation of the effective stresses and the associated change in fluid properties.

This study has experimentally verified Flokstra's conclusion that true circulation, i.e., a flow pattern possessing a separation zone with closed circular streamlines, requires the modeling of the effective shear stresses. An order of magnitude analysis performed on the various terms in the equation of motion verifies the significance of the effective stresses in all instances where circulation occurs. Circulation requires a continuous exchange of turbulent energy across the shear layer to be maintained. Withdrawal of the effective stresses after a steady flow pattern has set up dissolves the circulation and ultimately leads to instability.

The order-of-magnitude analysis of terms found in the momentum equation shows that convective inertia is significant in the channel and shear layer for all instances where circulation occurs. The presence of inertia allows the flow to retain a uniform structure for a distance beyond the location of a configuration change, enabling the development of a separation zone adjacent to the free extension of uniform flow. Ultimately, this separation of flow develops into a local zone of circulating flow.

Merely including the convective inertia in the mathematical model will not ensure the generation of secondary flow. Even with the additional stipulation that the effective stresses and all other quantities be precisely described, circulation may yet be inhibited by frictional effects. In every case where secondary currents do not occur, the resistance term is significant and larger than the convective inertia terms.

This study has found that bottom friction is the largest deterrent to the existence of circulating flow. A competition seems to exist between convective inertia and bed resistance forces. The fact that convective inertia terms contain spatial gradients of velocity makes them particularly sensitive to scale effects. In small scale problems, lateral differences in velocity occur over relatively small distances, creating large velocity gradients. The large magnitudes of the convective inertia

terms render the bed resistance effects negligible. No reasonable friction factor can affect this mechanism. Conversely, large scale problems reduce the magnitude of both convective inertia and effective stresses to such a degree that the friction terms are promoted to the point where resistance effects totally inhibit the generation of secondary flow.

This model displays at least two different instability mechanisms: nonlinear and Courant. Nonlinear instability is theoretically described as the inability to resolve energy at scales smaller than twice the spatial grid increment. Physically, energy is "cascaded" to smaller and smaller scales by the action of the nonlinear terms in the governing equations. At the smallest scales, energy is dissipated by viscous effects. the discrete formulation of the numerical model interrupts the energy cascade at the resolution of the grid. Thus, energy accumulates at this scale and eventually spoils the computations.

Nonlinear instability is characterized by gradually developing water surface discontinuities accompanied by a similar behavior in the computed velocities. The process is usually slow, and can take as many as 100 time steps to develop. In this numerical model, nonlinear instability requires the velocity averaging technique to be present in all simulations although the weighting factor need not be large. Most runs were stable with $\alpha = 0.1$. Physically speaking, the use of the velocity averaging routine introduces a stronger viscous dissipation mechanism into the fluid. Energy no longer must be transferred to scales smaller than the grid resolution for viscous effects to act.

Courant instability occurs when the ratio of physical celerity to numerical celerity (defined as the Courant number) exceeds a characteristic value. The physical celerity for this model is the maximum channel velocity, U_{max}, while the numerical celerity is defined as $\Delta x/\Delta t = \Delta y/\Delta t$. Thus, the criterion is of the form $U_{max}\ \Delta t/\Delta x \leq \xi$, in which ξ is the characteristic limit. The two explicit stages contained in the multioperational procedure are presumably responsible for the Courant stability condition found in this model.

Courant instability is characteristically a very rapid process. The simulation proceeds without noticeable difficulty until a sudden discontinuity appears in one of the dependent variables. Within a few time steps the entire calculation is spoiled. In this study the limiting value of the Courant number is dependent upon the weighting factor used in the velocity averaging routine. This is to be expected since large weighting factors can smooth instabilities that would otherwise occur if smaller weighting factors were used. For $\alpha = 0.1$, the Courant number in this model must be less than or equal to 0.5.

Conclusions and Recommendations

Major conclusions from this study are as follows:

1. Effective shear stress modeling is a necessary condition for the resolution of steady, closed-streamline circulation in depth-averaged mathematical models.
2. Convective inertia must be included in an analysis where secondary currents are being considered.
3. A competition seems to exist between convective inertia and the resistance effects at the bed. Circulating flow-barring wind forces is possible only where bed resistance is of minor influence, e.g., at small length scales.

4. The no-slip velocity condition at the physical boundaries is not absolutely necessary. However, if the no-slip condition is specified, the increased resistance effects may have to be corrected for by reducing the friction factor used in the modeling of bed resistance.

5. The type of boundary conditions has a significant effect on the resulting flow patterns for a given problem.

The following recommendations are offered for future research:

1. The greatest source of uncertainty is the modeling of the effective stresses. Although simplified methods of representing the effective stresses have yielded reasonable results, it is surmised that a higher level of sophistication is necessary in order to handle complex flow patterns. In such cases, a separate account of the three components of the effective stresses may be warranted. At present, individual closure assumptions are not available.

2. Additional studies are needed in order to identify the numerical effects of various discretization schemes and techniques used to represent the physical boundaries.

3. Although not directly benefiting the formulation of mathematical models, the compilation of physical data on various circulating flows would certainly be instrumental in the development and testing of management models capable of high accuracy simulation.

Acknowledgments

This study was made possible by a National Science Foundation Grant No. CME-7805458. The support of this institution is gratefully acknowledged.

Appendix I.—References

1. Abbott, M. B., and Rasmussen, C. H., "On the Numerical Modeling of Rapid Expansions and Contractions in Models that are Two-Dimensional in Plan," *Paper A 104,* 17th Congress of the International Association for Hydraulic Research, Baden-Baden, Germany, Vol. 2, 1977, pp. 229–237.
2. Bengtsson, L., "Wind Induced Circulation in Lakes," *Nordic Hydrology,* Vol. 9, No. 2, Stockholm, Sweden, 1978, pp. 75–94.
3. Flokstra, C., "Generation of Two-Dimensional Horizontal Secondary Currents," *Reports S 163-II,* Delft Hydraulics Laboratory, Delft, The Netherlands, July, 1976.
4. Flokstra, C., "The Closure Problem for Depth-Averaged Two-Dimensional Flow," *Paper A 106,* 17th Congress of the International Association for Hydraulic Research, Baden-Baden, Germany, Vol. 2, 1977, pp. 247–256.
5. Forester, C. K., "Higher Order Monotonic Convective Difference Schemes," *Journal of Computational Physics,* Vol. 23, 1977, pp. 1–22.
6. Hansen, W., "Hydrodynamic Methods Applied to Oceanographic Problems," *Proceedings of the Symposium on Mathematical-Hydrodynamical Methods of Physical Oceanography,* Institute für Meereskunde der Universität Hamburg, Hamburg, West Germany, 1962, pp. 25–34.
7. Kuipers, J., and Vreugdenhil, C. B., "Calculations of Two-Dimensional Horizontal Flows," *Report S 163-I,* Delft Hydraulics Laboratory, Delft, The Netherlands, Oct., 1973.
8. Launder, B. E., and Spalding, D. B., "The Numerical Computation of Turbulent Flows," Computational Methods in Applied Mechanical Engineering, Vol. 3, 1974, pp. 269–289.

9. Lean, G. H., and Weare, T. J., "Modeling Two-Dimensional Circulating Flow," *Journal of the Hydraulics Division,* ASCE, Vol. 105, No. HY1, Proc. Paper 14312, Jan., 1979, pp. 17–26.
10. Leendertse, J. J., "Aspects of a Computational Model for Long-Period Water Wave Propagation," *RM-5294-PR,* The Rand Corporation, Santa Monica, Calif., May, 1967.
11. Leendertse, J. J., "A Water-Quality Simulation Model for Well-Mixed Estuaries and Coastal Seas, Vol. I, Principles of Computation," *RM-6230-RC,* The Rand Corp., Santa Monica, Calif., Feb., 1970.
12. McGuirk, J. J., and Rodi, W., "A Depth-Averaged Mathematical Model for the Near Field of Side Discharges into Open Channel Flow," *Journal of Fluid Mechanics,* Vol. 86, Part 4, London, England, 1978, pp. 761–781.
13. Platzman, G. W., "A Numerical Computation of the Surge of 26 June 1954 on Lake Michigan," *Geophysics,* Vol. 6, No. 3–4, 1959. pp. 407–438.
14. Ponce, V. M., and Yabusaki, S. B., "Mathematical Modeling of Circulation in Two-dimensional Plane Flow," *Report CER79-80VMP-SBY59,* Civil Engineering Department, Engineering Research Center, Colorado State University, Fort Collins, Colo., June, 1980.
15. Weare, T. J., "Instability in Tidal Flow Computational Schemes," *Journal of the Hydraulics Division,* ASCE, Vol. 102, No. HY5, Proc. Paper 12100, May, 1976, pp. 569–580.

Appendix II.—Notation

The following symbols are used in this paper:

C = Chézy resistance coefficient;
f_r = dimensionless friction factor;
g = gravitational acceleration;
h = flow depth;
j = x-coordinate nodal index;
k = y-coordinate nodal index;
n = t-coordinate nodal index;
T = effective stress;
t = time;
Δt = time increment;
U = channel velocity;
u = velocity component in x-direction;
u' = temporal velocity fluctuation in x-direction;
$\bar{u}$ = depth-averaged velocity;
$\bar{u}^*$ = spatially-averaged velocity;
v = velocity component in y-direction;
$\bar{v}$ = depth-averaged velocity;
$\bar{v}^*$ = spatially-averaged velocity;
x = coordinate direction;
Δx = space increment in x-direction;
y = coordinate direction;
Δy = space increment in y-direction;
z = coordinate direction;
z_b = bottom elevation;
α = weighting factor;
ϵ = eddy diffusivity;
η = water surface elevation;

ν = kinematic viscosity;
ξ = Courant number criterion;
ρ = fluid density; and
τ = surface stress.

Modeling Circulation in Depth-Averaged Flow[a]

Errata

The following correction should be made to the original paper:

Page 1510, Fig. 3 should be as shown

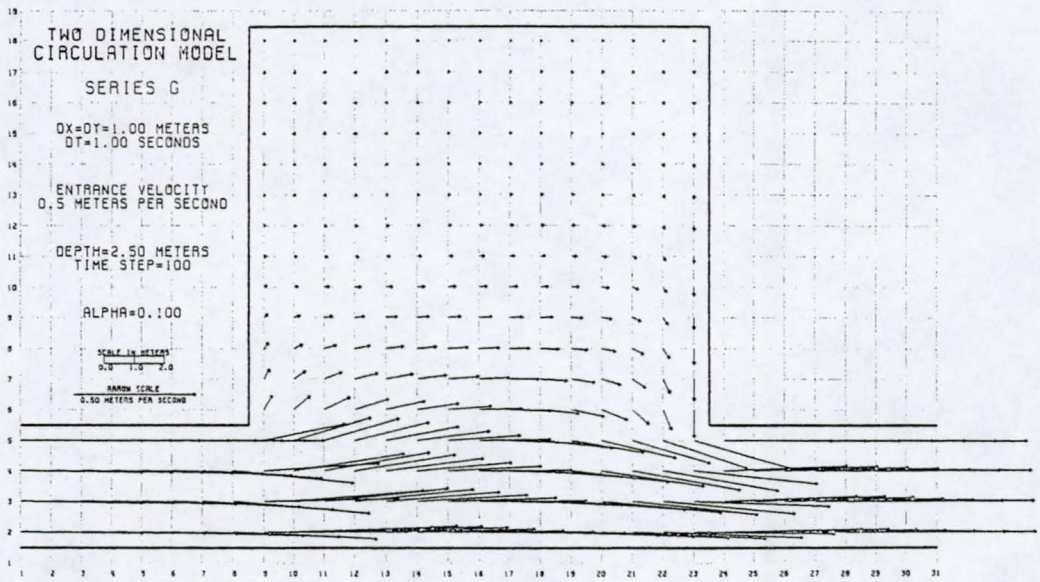

FIG. 3.—Flow Pattern Neglecting Convective Inertia, Time Step 100

[a]November, 1981, by Victor M. Ponce and Steven B. Yabusaki (Proc. Paper 16640)

JOURNAL OF THE
HYDRAULICS DIVISION

Shallow Wave Propagation in Open Channel Flow

By Victor Miguel Ponce,[1] M. ASCE and Daryl B. Simons,[2] F. ASCE

Introduction

Over the years, several investigators have attempted to clarify the phenomenon of propagation of shallow waves in open channel flow. Perhaps the most illuminating of these studies is that reported in the classical paper by Lighthill and Whitham (5), which analyzed in detail the concept of kinematic wave and contrasted it to the dynamic wave. The Lagrange formula (3) for the celerity of shallow gravity waves has also been a subject of considerable attention in the literature. Despite the progress made in the understanding of the physical phenomenon, a coherent theory that accounts for celerity as well as attenuation characteristics has yet to be formulated. In this respect, the theory of linear stability (6) can be used as an effective tool not only to furnish a first approximation analysis but also to provide valuable insight into the underlying physics of the problem.

The analysis presented herein endeavors to apply the theory of linear stability to the set of equations governing the motion in open channel flow. The equations are the so-called Saint Venant equations (1), which are analytical expressions of the principle of mass and momentum conservation. The conclusions relate to the magnitude of celerity and attenuation of various types of shallow water waves, expressed as a function of the Froude number of the steady uniform flow and a dimensionless wave number of the unsteady component of the motion.

Governing Equations

The governing equations for the one-dimensional unsteady flow in broad

Note.—Discussion open until May 1, 1978. To extend the closing date one month, a written request must be filed with the Editor of Technical Publications, ASCE. This paper is part of the copyrighted Journal of the Hydraulics Division, Proceedings of the American Society of Civil Engineers, Vol. 103, No. HY12, December, 1977. Manuscript was submitted for review for possible publication on February 7, 1977.

[1] Asst. Prof. of Civ. Engrg., Colorado State Univ., Fort Collins, Colo.

[2] Prof. of Civ. Engrg., and Assoc. Dean of Research, Colorado State Univ., Fort Collins, Colo.

channels of rectangular cross section, expressed per unit of channel width, are (4) equation of continuity

$$u\frac{\partial d}{\partial x} + d\frac{\partial u}{\partial x} + \frac{\partial d}{\partial t} = 0 \quad (1)$$

and equation of motion

$$\frac{1}{g}\frac{\partial u}{\partial t} + \frac{u}{g}\frac{\partial u}{\partial x} + \frac{\partial d}{\partial x} + (S_f - S_o) = 0 \quad (2)$$

in which u = velocity averaged in a vertical section; d = depth of flow; g = acceleration of gravity; S_f = friction slope; and S_o = bed slope.

The friction slope S_f is directly related to the bottom shear stress τ by the expression (2):

$$S_f = \frac{\tau}{\gamma d} \quad (3)$$

in which γ is the unit weight of water.

In the usual manner of stability calculations (7), Eqs. 1 and 2 must satisfy the unperturbed flow for which $u = u_o$; $d = d_o$; and $\tau = \tau_o$, as well as the perturbed flow for which $u = u_o + u'$; $d = d_o + d'$; and $\tau = \tau_o + \tau'$. The superscript in the flow variables represents a small perturbation to the steady uniform flow. Thus, all quadratic terms in the fluctuating components may be neglected due to an order of magnitude reasoning.

Substitution of the perturbed variables in Eqs. 1, 2, and 3 yields, after linearization (5):

$$u_o\frac{\partial d'}{\partial x} + d_o\frac{\partial u'}{\partial x} + \frac{\partial d'}{\partial t} = 0 \quad (4)$$

$$\frac{1}{g}\frac{\partial u'}{\partial t} + \frac{u_o}{g}\frac{\partial u'}{\partial x} + \frac{\partial d'}{\partial x} + S_o\left(\frac{\tau'}{\tau_o} - \frac{d'}{d_o}\right) = 0 \quad (5)$$

in which $S_o = \dfrac{\tau_o}{\gamma d_o}$ (6)

The boundary shear stress τ can be related to the mean velocity by

$$\tau = f\rho u^2 \quad (7)$$

in which $f = \dfrac{g}{C_f^2}$ (8)

where C_f is the Chezy coefficient; and ρ = the density of water. Considering Eq. 7, Eq. 5 can be rewritten as

$$\frac{1}{g}\frac{\partial u'}{\partial t} + \frac{u_o}{g}\frac{\partial u'}{\partial x} + \frac{\partial d'}{\partial x} + S_o\left(2\frac{u'}{u_o} - \frac{d'}{d_o}\right) = 0 \quad (9)$$

For most practical applications, the Manning equation is preferred over the Chezy equation. The latter, however, has the advantage of nondimensionality,

and it is for this reason that it is used here. Furthermore, the constant C_f is consistent with the small perturbation assumption.

Wave Models

The propagation of shallow water waves is controlled by the balance of the various forces included in the equation of motion. In Eq. 2, the first term represents the local inertia term, the second term represents the convective inertia term, the third term represents the pressure differential term, and the fourth accounts for the friction and bed slopes. Various wave models can be construed, depending on which of these four terms is assumed negligible when compared with the remaining terms.

The following chart provides a ready reference to the various wave models that are recognized.

Term	I	II	III	IV	
Equation of motion	$\frac{1}{g}\frac{\partial u}{\partial t}$	$+\ \frac{u}{g}\frac{\partial u}{\partial x}$	$+\ \frac{\partial d}{\partial x}$	$+\ (S_f - S_o) = 0$	(2)

Wave model and terms used to describe it are: (1) Kinematic wave IV; (2) diffusion wave III + IV; (3) steady dynamic wave II + III + IV; (4) dynamic wave I + II + III + IV; and (5) gravity wave I + II + III.

Small Perturbation Analysis

In order to provide for a convenient way to take explicit account of the various wave models, Eq. 9 is recast as

$$\frac{l}{g}\frac{\partial u'}{\partial t} + \frac{au_o}{g}\frac{\partial u'}{\partial x} + p\frac{\partial d'}{\partial x} + kS_o\left(2\frac{u'}{u_o} - \frac{d'}{d_o}\right) = 0 \quad (10)$$

in which l, a, p, and k are integers that can take values of 0 and 1 only, depending on which terms of Eq. 9 are used to describe the motion.

The solution for a small perturbation in the depth of flow is postulated in the following exponential form:

$$\frac{d'}{d_o} = \hat{d}\exp\left[i(\hat{\sigma}\hat{x} - \hat{\beta}\hat{t})\right] \quad (11)$$

in which d' is a small perturbation to d_o; $\hat{d}$ is a dimensionless depth amplitude function; $\hat{\sigma}$ is a dimensionless wave number; $\hat{\beta}$ is a dimensionless complex propagation factor; and $\hat{x}$ and $\hat{t}$ are dimensionless space and time coordinates such that

$$\hat{\sigma} = \left(\frac{2\pi}{L}\right)L_o \quad (12)$$

$$\hat{\beta}_R = \left(\frac{2\pi}{T}\right)\frac{L_o}{u_o} \quad (13)$$

$$\hat{\beta}_I = \text{amplitude propagation factor} \quad (14)$$

$$\hat{x} = \frac{x}{L_o} \quad (15)$$

$$\hat{t} = t\frac{u_o}{L_o} \quad (16)$$

L = the wavelength of the disturbance; and T = the period. The value L_o = the horizontal length in which the steady uniform flow drops a head equal to its depth, and it is defined as $L_o = d_o/S_o$. The dimensionless celerity of the disturbance is given by

$$\hat{c} = \frac{\frac{L}{T}}{u_o} = \frac{\hat{\beta}_R}{\hat{\sigma}} \quad (17)$$

The wave attenuation follows an exponential law in which the amplitude at a given time t = the initial amplitude at time t_o multiplied by $(e^{\hat{\beta}_I \hat{t}})$, in which $\hat{t} = (t - t_o)u_o/L_o$. When comparing wave amplitudes after one propagation period, the value of $\hat{t}$ is $\hat{t} = T\,u_o/L_o$, or likewise, $\hat{t} = \frac{2\pi}{|\hat{\beta}_R|}$. The logarithmic decrement (10) δ is defined as $\delta = \hat{\beta}_I T\,u_o/L_o$, or $\delta = 2\pi\frac{\hat{\beta}_I}{|\hat{\beta}_R|}$. The value of δ is a measure of the rate at which the unsteady component of the motion changes upon propagation. For δ positive, amplification sets in; for δ negative, the motion attenuates and dies away.

The depth disturbance is associated with a velocity disturbance of the form

$$\frac{u'}{u_o} = \hat{u}\exp\,[i(\hat{\sigma}\,\hat{x} - \hat{\beta}\,\hat{t})] \quad (18)$$

in which $\hat{u}$ is a dimensionless velocity amplitude function. The substitution of Eqs. 11 and 18 into Eqs. 4 and 10 yields, respectively:

$$\hat{\sigma}\hat{u} + (\hat{\sigma} - \hat{\beta})\hat{d} = 0 \quad (19)$$

$$[2k + i\mathsf{F}_o^2(a\hat{\sigma} - l\hat{\beta})]\,\hat{u} + (ip\hat{\sigma} - k)\,\hat{d} = 0 \quad (20)$$

$$\text{in which} \quad \mathsf{F}_o^2 = \frac{u_o^2}{gd_o} \quad (21)$$

Eqs. 19 and 20 constitute a homogeneous system of linear equations in the unknowns $\hat{u}$ and $\hat{d}$. For the solution to be nontrivial, the determinant of the coefficient matrix must vanish. Accordingly,

$$il\hat{\beta}^2\mathsf{F}_o^2 - i\hat{\sigma}^2(p - a\mathsf{F}_o^2) + 3k\hat{\sigma} - 2k\hat{\beta} - i\hat{\sigma}\hat{\beta}\,(l + a)\mathsf{F}_o^2 = 0 \quad (22)$$

Eq. 22 is the characteristic equation governing the propagation of small amplitude water waves. In the treatment that follows, successive simplifications will be made to conform to the various types of wave models considered in the previous section.

Kinematic Wave Model

In the kinematic wave model, the inertia and pressure terms are negligible as compared to the friction-bed slope term.

Accordingly, in Eq. 22, $l = a = p = 0$; and $k = 1$, resulting in

$$3\hat{\sigma} - 2\hat{\beta} = 0 \quad (23)$$

Since all the imaginary terms have dropped out in Eq. 23, $\hat{\beta}_I = 0$; and $\hat{\beta}_R = \hat{\beta}$. The logarithmic decrement δ_k is then

$$\delta_k = 2\pi \frac{\hat{\beta}_I}{\hat{\beta}_R} = 0 \quad (24)$$

and the dimensionless celerity of the kinematic wave is

$$\hat{c}_k = \frac{\hat{\beta}_R}{\hat{\sigma}} = \frac{3}{2} \quad (25)$$

Equations 23–25 warrant the following conclusions regarding kinematic wave propagation: (1) Since Eq. 23 is of the first order, kinematic waves propagate only in the downstream direction; (2) the celerity of a kinematic wave is independent of F_o and $\hat{\sigma}$, and equal to 1.5 times the mean flow velocity; and (3) the attenuation of a kinematic wave is zero, i.e., a kinematic wave propagates downstream without dissipation.

Diffusion Wave Model

In the diffusion wave model, the inertia terms are considered negligible, but the pressure term is taken into account in the calculations. Accordingly, in Eq. 22, $l = a = 0$; $p = k = 1$, resulting in

$$-i\hat{\sigma}^2 + 3\hat{\sigma} - 2\hat{\beta} = 0 \quad (26)$$

and $$\hat{\beta} = \frac{3\hat{\sigma} - i\hat{\sigma}^2}{2} \quad (27)$$

and the celerity of the diffusion wave is

$$\hat{c}_d = \frac{\hat{\beta}_R}{\hat{\sigma}} = \frac{3}{2} \quad (28)$$

The logarithmic decrement of the diffusion wave is

$$\delta_d = 2\pi \frac{\hat{\beta}_I}{\hat{\beta}_R} = -2\pi \left(\frac{\hat{\sigma}}{3}\right) \quad (29)$$

The following conclusions are derived for diffusion waves: (1) Because Eq. 26 is of first order in $\hat{\beta}$, diffusion waves propagate downstream only, and their celerity is independent of F_o and $\hat{\sigma}$ and equal to 1.5 the mean flow velocity; and (2) diffusion waves attenuate as they propagate downstream, and the rate of attenuation is controlled by the dimensionless wave number $\hat{\sigma}$. The larger the dimensionless wave number, the larger the attenuation.

Steady Dynamic Wave Model

In the steady dynamic wave model, the convective inertia term is brought into the problem, and the local inertia term is neglected. Accordingly, in Eq. 22, $l = 0$; and $a = p = k = 1$, resulting in

$$-i\hat{\sigma}^2(1 - F_o^2) + 3\hat{\sigma} - 2\hat{\beta} - i\hat{\sigma}\hat{\beta}F_o^2 = 0 \quad (30)$$

$$\text{and} \quad \hat{\beta} = \frac{3\hat{\sigma} - i\hat{\sigma}^2(1 - F_o^2)}{2 + i\hat{\sigma}F_o^2} \quad (31)$$

$$\text{or} \quad \hat{\beta} = \frac{\hat{\sigma}\,[6 - \hat{\sigma}^2F_o^2(1 - F_o^2)] - i\hat{\sigma}^2(2 + F_o^2)}{4 + \hat{\sigma}^2F_o^4} \quad (32)$$

From Eq. 32, the celerity of the steady dynamic model is

$$\hat{c}_s = 1 + \frac{2 - \hat{\sigma}^2F_o^2}{4 + \hat{\sigma}^2F_o^4} \quad (33)$$

The logarithmic decrement of the steady dynamic model is

$$\delta_s = \left| -2\pi \frac{\hat{\sigma}(2 + F_o^2)}{6 - \hat{\sigma}^2F_o^2(1 - F_o^2)} \right| \quad (34)$$

The following conclusions are derived regarding the steady dynamic model: (1) The propagation of the steady dynamic wave is in one direction, since Eq. 30 is of first order in $\hat{\beta}$; and (2) the celerity and attenuation characteristics are functions of the Froude number of the steady uniform flow F_o and the dimensionless wave number $\hat{\sigma}$.

Dynamic Wave Model

In the dynamic wave model, all terms in the equation of motion are considered. Thus, in Eq. 22, $l = a = p = k = 1$. It follows that

$$(F_o^2)\hat{\beta}^2 - 2(\hat{\sigma}F_o^2 - i)\hat{\beta} - [\hat{\sigma}^2(1 - F_o^2) + 3\hat{\sigma}i] = 0 \quad (35)$$

Equation 35 is of the second order, resulting in two roots. Physically speaking, dynamic waves propagate along two characteristic paths, which can face either: (1) One upstream and another downstream; or (2) both downstream. In the case of propagation in different directions, it is expedient to define as "primary wave" the wave that travels downstream, and identify its celerity and logarithmic decrement by $\hat{c}_1$ and δ_1, respectively. The "secondary wave" is defined as the wave traveling upstream with celerity $\hat{c}_2$ and logarithmic decrement δ_2. In the case of both waves traveling downstream, "primary wave" is the faster wave, and "secondary wave" is the slower wave.

The solution of Eq. 35 is

$$\hat{\beta} = \hat{\sigma}(1 - i\zeta) + \hat{\sigma}\left[\left(\frac{1}{F_o^2} - \zeta^2\right) + i\zeta\right]^{1/2} \quad (36)$$

$$\text{in which} \quad \zeta = \frac{1}{\hat{\sigma}F_o^2} \quad (37)$$

An expression of the same type as Eq. 37 is referred to in the literature as kinematic flow number (9).

The complex square root argument can be expressed in polar form as

$$A + iB = C(\cos\theta + i\sin\theta) \quad (38)$$

in which $$A = \frac{1}{F_o^2} - \zeta^2 \quad (39)$$

$$B = \zeta \quad (40)$$

$$C = \left[\left(\frac{1}{F_o^2} - \zeta^2\right)^2 + \zeta^2\right]^{1/2} \quad (41)$$

$$\theta = \arctan\frac{B}{A} \quad (42)$$

and the root of the complex argument is

$$(A + iB)^{1/2} = C^{1/2}\left(\cos\frac{\theta + 2k\pi}{2} + i\sin\frac{\theta + 2k\pi}{2}\right); \quad \text{for } k = 0, 1 \quad (43)$$

and by use of the half-angle relations

$$(A + iB)^{1/2} = \pm C^{1/2}\left[\left(\frac{1 + \cos\theta}{2}\right)^{1/2} + i\left(\frac{1 - \cos\theta}{2}\right)^{1/2}\right] \quad (44)$$

in which use has been made of the fact that because $\zeta \geq 0$, $\theta/2$ falls in the first quadrant.

Since $$\cos\theta = \frac{A}{C} \quad (45)$$

it follows that

$$(A + iB)^{1/2} = \pm\left[\left(\frac{C + A}{2}\right)^{1/2} + i\left(\frac{C - A}{2}\right)^{1/2}\right] \quad (46)$$

or $$\hat{\beta} = \hat{\sigma}(1 - i\zeta) \pm \hat{\sigma}\left[\left(\frac{C + A}{2}\right)^{1/2} + i\left(\frac{C - A}{2}\right)^{1/2}\right] \quad (47)$$

From Eq. 47, the following two roots are obtained:

$$\hat{\beta}_1 = \hat{\sigma}\left[1 + \left(\frac{C + A}{2}\right)^{1/2}\right] - i\hat{\sigma}\left[\zeta - \left(\frac{C - A}{2}\right)^{1/2}\right] \quad (48)$$

$$\hat{\beta}_2 = \hat{\sigma}\left[1 - \left(\frac{C + A}{2}\right)^{1/2}\right] - i\hat{\sigma}\left[\zeta + \left(\frac{C - A}{2}\right)^{1/2}\right] \quad (49)$$

Now call $$D = \left(\frac{C + A}{2}\right)^{1/2} \quad (50)$$

and $$E = \left(\frac{C - A}{2}\right)^{1/2} \quad (51)$$

and the celerity and attenuation functions are given by

$$\text{primary wave} \quad \hat{c}_1 = 1 + \left(\frac{C + A}{2}\right)^{1/2} \quad \ldots \quad (52)$$

TABLE 1.—Propagation Characteristics of Shallow Water Waves in Open Channel Flow

Type of wave (1)	Relative celerity $\hat{c}_r$ (2)	Logarithmic decrement δ (3)
Kinematic	$1/2$	0
Diffusion	$1/2$	$-2\pi(\hat{\sigma}/3)$
Steady dynamic	$(2 - \hat{\sigma}^2 F_o^2)/(4 + \hat{\sigma}^2 F_o^4)$	$-2\pi\,\hat{\sigma}(2 + F_o^2)/[6 - \hat{\sigma}^2 F_o^2(1 - F_o^2)]$
(*a*) Dynamic		
Primary wave	$+[(C + A)/2]^{1/2}$	$-2\pi(\zeta - E)/\lvert 1 + D\rvert$
Secondary wave	$-[(C + A)/2]^{1/2}$	$-2\pi(\zeta + E)/\lvert 1 - D\rvert$
(*b*) Gravity		
Primary wave	$+1/F_o$	0
Secondary wave	$-1/F_o$	0

Note: $\zeta = 1/(\hat{\sigma} F_o^2)$; $A = (1/F_o^2) - \zeta^2$; $C = \{[(1/F_o^2) - \zeta^2]^2 + \zeta^2\}^{1/2}$; $D = [(C + A)/2]^{1/2}$; $E = [(C - A)/2]^{1/2}$.

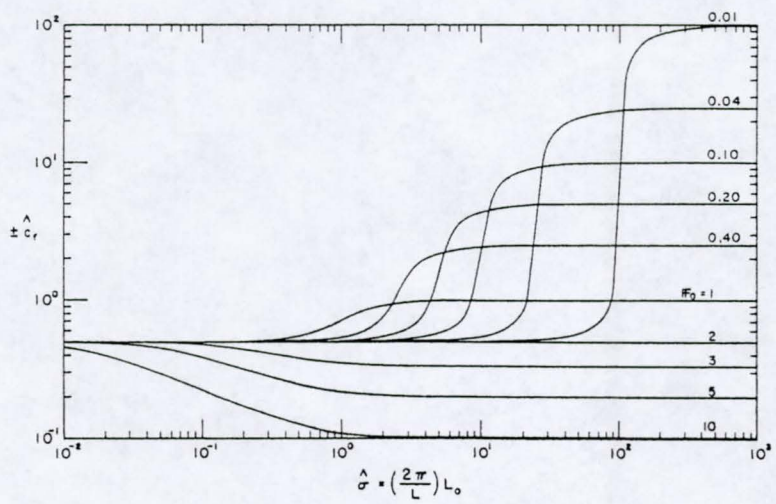

FIG. 1.—Dimensionless Relative Celerity $\hat{c}_r$ versus Dimensionless Wave Number $\hat{\sigma}$; Curve Parameter = Froude Number F_o ($0.01 \leq F_o \leq 10$)

$$\delta_1 = -2\pi \frac{\zeta - E}{|1 + D|} \quad \ldots \quad (53)$$

$$\text{and secondary wave} \quad \hat{c}_2 = 1 - \left(\frac{C + A}{2}\right)^{1/2} \quad \ldots \quad (54)$$

$$\delta_2 = -2\pi \frac{\zeta + E}{|1 - D|} \quad (55)$$

Gravity Wave Model

In the gravity wave model, the friction and bed slope terms are excluded from the momentum equation. It follows that, in Eq. 22, $l = a = p = 1$; and $k = 0$, resulting in

$$\hat{\beta}^2 F_o^2 - 2\hat{\sigma}\hat{\beta} F_o^2 - \hat{\sigma}^2(1 - F_o^2) = 0 \quad (56)$$

Since Eq. 56 is of the second order in $\hat{\beta}$ and contains no imaginary terms, gravity waves have two characteristic directions and are not subject to attenuation.

Solving for $\hat{\beta}_R$ in Eq. 56

$$\hat{\beta}_R = \hat{\sigma}\left(\frac{F_o^2 \pm F_o}{F_o^2}\right) \quad (57)$$

and the celerity of a gravity wave is given as

$$\hat{c}_g = \frac{\hat{\beta}_R}{\hat{\sigma}} = 1 \pm \frac{1}{F_o} \quad (58)$$

or in the more usual way of expressing it (Lagrange formula)

$$c_g = u_o \pm \sqrt{gd_o} \quad (59)$$

Gravity waves propagate along two characteristic directions. In subcritical flow, one direction is downstream, with celerity $c_1 = u_o + \sqrt{gd_o}$, and another is upstream, with celerity $c_2 = u_o - \sqrt{gd_o}$. In critical flow, $c_1 = 2u_o$; and $c_2 = 0$. In supercritical flow, both waves travel downstream, with celerities $c_1 = u_o + \sqrt{gd_o}$; and $c_2 = u_o - \sqrt{gd_o}$.

A summary of the propagation characteristics of the various waves described is given in Table 1. The celerity shown in Table 1 is the relative celerity $\hat{c}_r$, in which

$$\hat{c}_r = \hat{c} - 1 \quad (60)$$

Analysis of Dynamic Model

Eqs. 52–55 enable the calculation of the propagation characteristics of the dynamic wave model, as a function of the Froude number F_o of the steady uniform flow and the dimensionless wave number $\hat{\sigma}$ of the sinusoidal perturbation superimposed on the steady uniform flow.

Fig. 1 shows the calculated values of the dimensionless relative celerity $\hat{c}_r$ versus the dimensionless wave number $\hat{\sigma}$, for Froude numbers between 0.01–10. The following conclusions are derived from this figure:

1. There are three well-defined bands in the wave number spectrum: (a) A kinematic band corresponding to small values of the wave number $\hat{\sigma}$, in which the relative celerity $\hat{c}_r$ is independent of both $\hat{\sigma}$ and the Froude number F_o; (b) a gravity band corresponding to large values of $\hat{\sigma}$, in which $\hat{c}_r$ is independent

of $\hat{\sigma}$ and dependent only on F_o; and (c) a dynamic band, in which $\hat{c}_r$ is a function of both $\hat{\sigma}$ and F_o.

In the kinematic band, $\hat{c}_r$ approaches asymptotically a constant value of 0.5,

TABLE 2.—Celerity[a] and Attenuation[b] Characteristics of the Dynamic Wave

Froude number (1)	Primary Wave $\hat{c}_1$ (2)	Primary Wave δ_1 (3)	Secondary Wave $\hat{c}_2$ (4)	Secondary Wave δ_2 (5)
$F_o < 1$	+	−	−	−
			+	−
$F_o = 1$	+	−	0	−
			+	−
$1 < F_o < 2$	+	−	+	−
$F_o = 2$	+	0	+	−
$F_o > 2$	+	+	+	−

[a] Downstream celerity +; upstream celerity −.
[b] Attenuation −; amplification +.

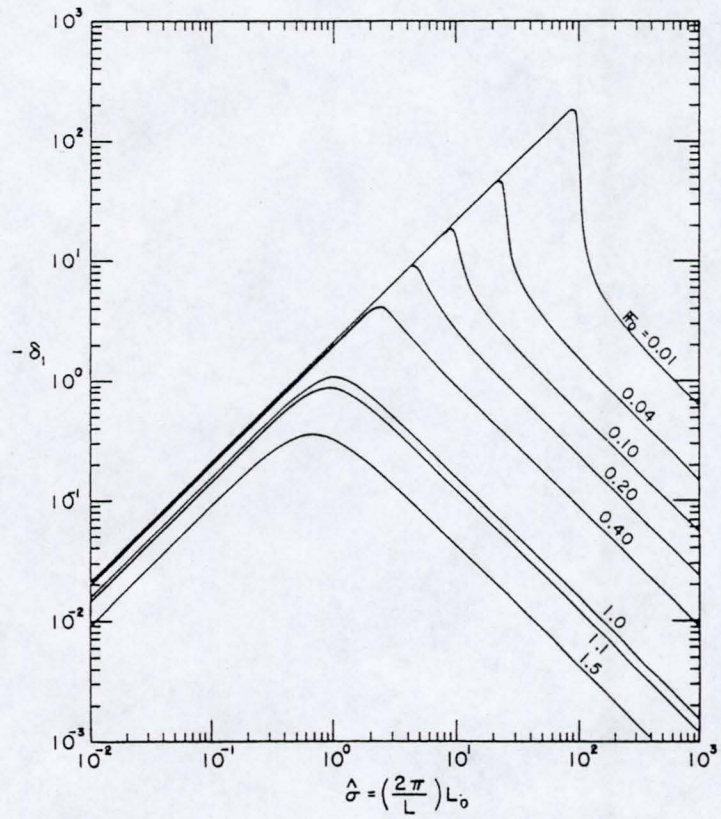

FIG. 2.—Primary Wave Logarithmic Decrement $-\delta_1$ versus Dimensionless Wave Number $\hat{\sigma}$; Curve Parameter = Froude Number F_o ($F_o < 2$)

which corresponds to that of a kinematic wave. In the gravity band, $\hat{c}_r$ approaches asymptotically the value $1/F_o$, which corresponds to that of a gravity wave. In the dynamic band, $\hat{c}_r$ lies between the kinematic and gravity wave celerity values.

2. The location of the dynamic band in the $\hat{\sigma}$ spectrum is a function of F_o.

A corollary resulting from Fig. 1 is that for $F_o = 2$, $\hat{c}_r = 0.5$ for all values of $\hat{\sigma}$. Thus, at $F_o = 2$, all waves, kinematic, dynamic, and gravity, have celerities equal to the kinematic value. The conclusions of Fig. 1 regarding the limiting value of $\hat{c}_r$ in the kinematic and gravity bands can be obtained analytically based on limit theory. It can be shown that as $\hat{\sigma} \rightarrow \infty$, $\hat{c}_r \rightarrow 1/F_o$, and as $\hat{\sigma} \rightarrow 0$, $\hat{c}_r \rightarrow 0.5$ (for F_o constant).

The calculation of the logarithmic decrements δ_1 and δ_2 as a function of $\hat{\sigma}$ and F_o, by means of Eqs. 53 and 55 enable the following general conclusions:

1. For $F_o < 2$, primary waves propagate downstream and attenuate; for $F_o = 2$, primary waves propagate downstream and neither amplify nor attenuate throughout the $\hat{\sigma}$ spectrum; for $F_o > 2$, primary waves propagate downstream and amplify.

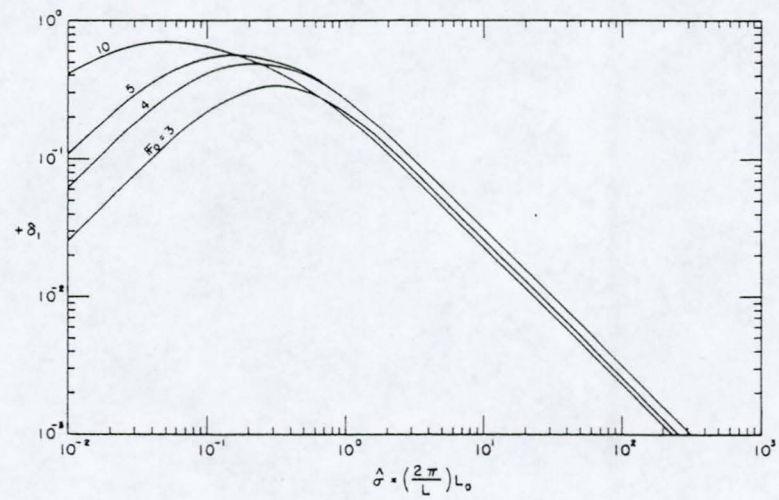

FIG. 3.—Primary Wave Logarithmic Decrement $+\delta_1$ versus Dimensionless Wave Number $\hat{\sigma}$; Curve Parameter = Froude Number F_o ($F_o > 2$)

2. For $F_o < 1$, secondary waves propagate upstream ($\hat{c}_r > 1$), or downstream ($\hat{c}_r < 1$). For $F = 1$, secondary waves remain stationary ($\hat{c}_r = 1$), or propagate downstream ($\hat{c}_r < 1$). For $F_o > 1$, secondary waves propagate downstream. Secondary waves attenuate for all F_o and $\hat{\sigma}$.

Table 2 summarizes the conclusions of the foregoing paragraph.

Primary Wave Attenuation Analysis, $F_o < 2$.—Fig. 2 depicts the variation of the logarithmic decrement δ_1 for $F_o < 2$, as a function of $\hat{\sigma}$. The following conclusions are drawn: (1) The logarithmic decrement δ_1 is maximum (in absolute value) at a value of $\hat{\sigma}$ corresponding to the point of inflexion of the $\hat{c}_r$ versus $\hat{\sigma}$ curve (Fig. 1). The value of $\hat{\sigma}$ for which δ_1 is a maximum (in absolute value) decreases with increasing F_o; and (2) the logarithmic decrement δ_1 is minimized (in absolute value) at both ends of the $\hat{\sigma}$ spectrum. As $\hat{\sigma} \rightarrow 0$, $\delta_1 \rightarrow 0$, corresponding

to the kinematic wave case; as $\hat{\sigma} \rightarrow \infty$, $\delta_1 \rightarrow 0$, corresponding to the gravity wave case.

A general conclusion derived from Fig. 2 relates to the fact that for $F_o < 2$, primary waves will be subject to very strong attenuation in the dynamic band, and to very weak attenuation in the gravity and kinematic bands.

Primary Wave Amplification Analysis, $F_o > 2$.—Fig. 3 depicts the variation of the logarithmic decrement δ_1 for $F_o > 2$, as a function of $\hat{\sigma}$. The following conclusions are drawn: (1) The logarithmic decrement δ_1 has a maximum positive value at a value of $\hat{\sigma}$ corresponding to the point of inflexion of the $\hat{c}_r$ versus $\hat{\sigma}$ curve (Fig. 1). The value of $\hat{\sigma}$ for which δ_1 is a maximum decreases with increasing F_o; and (2) the logarithmic decrement δ_1 is minimized at both ends of the $\hat{\sigma}$ spectrum. As $\hat{\sigma} \rightarrow 0$, $\delta_1 \rightarrow 0$, corresponding to the kinematic wave case; as $\hat{\sigma} \rightarrow \infty$, $\delta_1 \rightarrow 0$, corresponding to the gravity wave case.

A general conclusion derived from Fig. 3 relates to the fact that for $F_o >$

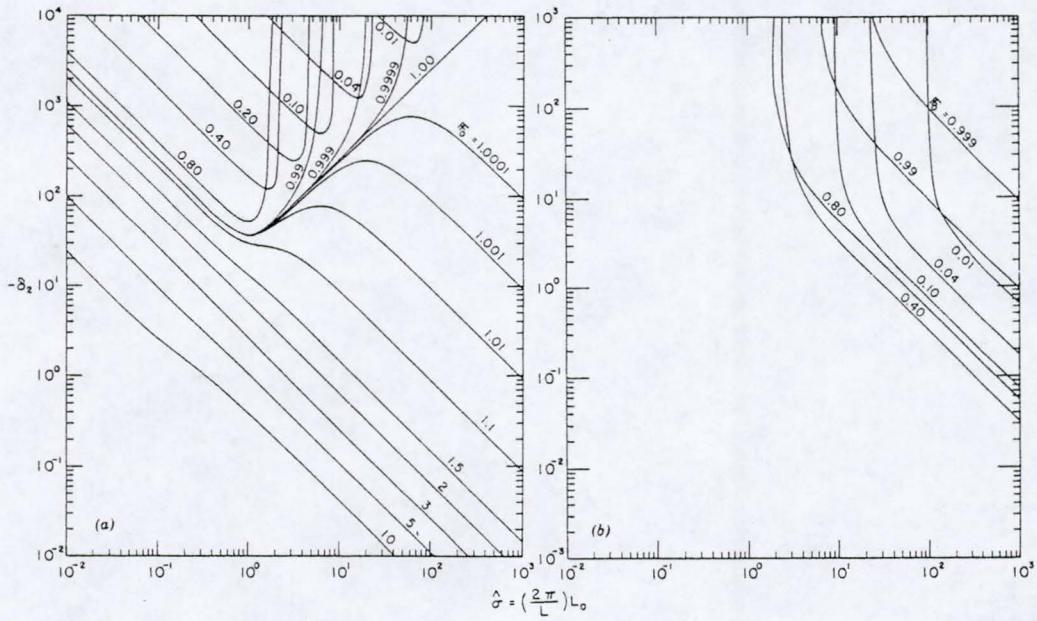

FIG. 4.—Secondary Wave Logarithmic Decrement $-\delta_2$ versus Dimensionless Wave Number $\hat{\sigma}$; Curve Parameter = Froude Number F_o: (*a*) $0.01 \leq F_o \leq 10$; (*b*) $0.01 \leq F_o \leq 0.999$

2, primary waves will be subject to very strong amplification in the dynamic band, and to very weak amplification in the gravity and kinematic bands.

Secondary Wave Attenuation Analysis.—Figs. 4(*a*) and 4(*b*) depict the variation of the logarithmic decrement δ_2 for $0.01 \leq F_o \leq 10$ as a function of $\hat{\sigma}$. The following conclusions are drawn: (1) In subcritical flow, $F_o < 1$, the attenuation of the secondary wave is very strong, and the strength decreases as $\hat{\sigma}$ increases in the gravity band (large $\hat{\sigma}$); (2) at critical flow, $F_o = 1$, the attenuation of the secondary wave is very strong, with a minimum around the center of the dynamic band (intermediate $\hat{\sigma}$); and (3) in supercritical flow, $F_o > 1$ the attenuation of the secondary wave has the pattern shown. For $F_o \geq 2$, δ_2 decreases as $\hat{\sigma}$ increases.

Dynamic Wave Propagation

The propagation of a dynamic wave has been shown to be a function of

two dimensionless parameters, the wave number $\hat{\sigma}$, and the Froude number F_o. The wave number $\hat{\sigma}$ can be interpreted as a ratio of two lengths L_o and L, in which L is the wavelength and L_o is the horizontal length in which the steady uniform flow drops a head equal to its depth. The square of the Froude number F_o is the ratio of twice the velocity head to the flow depth, where the velocity head h_{u_o} is given by

$$h_{u_o} = \frac{u_o^2}{2g} \quad \text{(61)}$$

For $F_o < 2$, the celerity of a dynamic wave that propagates downstream is larger than the kinematic wave celerity, and smaller than the gravity wave celerity. In fact, the kinematic wave celerity constitutes a lower bound to which the dynamic value tends as the wave number $\hat{\sigma}$ decreases. Conversely, the gravity wave celerity is an upper bound to the dynamic wave celerity as the wave number $\hat{\sigma}$ increases. To place this conclusion in the proper perspective it is perhaps of interest to quote here from Stoker's work [(8), p. 486], regarding the celerities of small disturbances and progressive waves:

> . . . What seems to happen is the following: small forerunners of a disturbance travel with the speed $\sqrt{gd}$ relative to the flowing stream, but the resistance forces act in such a way as to decrease the speed of the main portion of the disturbance far below the values given by $\sqrt{gd}$; i.e., to a value corresponding closely to the speed of a steady progressive wave that travels unchanged in form . . .

In reviewing Stoker's work, it is apparent that his reference to a small disturbance is to a wave with a large $\hat{\sigma}$ (gravity wave) and to progressive wave to that with a small $\hat{\sigma}$ (kinematic wave). He proceeds to further elaborate on the limitations of methods of water routing based solely on the kinematic approach, for the cases in which the dynamic effects cannot be disregarded.

For $F_o \geq 2$, the celerity of a dynamic wave that propagates downstream is smaller than the kinematic wave celerity and larger than the gravity wave celerity. In fact, the kinematic wave celerity is an upper bound to the dynamic value, whereas the gravity wave celerity is a lower bound to the dynamic value.

A significant conclusion regarding dynamic wave propagation can be obtained from the summary presented in Table 2. For primary waves, $F_o = 2$ is the threshold dividing the attenuation ($F_o < 2$) and amplification ($F_o > 2$) tendencies. For secondary waves, however, $F_o = 1$ is the threshold dividing the propagation upstream ($F_o < 1$) or downstream ($F_o > 1$) for gravity waves. Thus, $F_o = 2$ is verified to be as important a threshold value as $F_o = 1$ in describing the dynamics of open channel flow phenomena.

Summary and Conclusions

The propagation characteristics of various types of shallow water waves in open channel flow are calculated on the basis of linear stability theory. The celerity and attenuation functions of kinematic, diffusion, steady dynamic, dynamic, and gravity waves are derived. For the most general case, i.e., the dynamic wave model, the propagation characteristics are expressed as a function

of the steady uniform flow Froude number and the dimensionless wave number of the unsteady component of the motion.

For the dynamic model, the wave number spectrum is divided into three bands: (1) A gravity band corresponding to large wave number, in which the wave celerity is the gravity wave celerity; (2) a kinematic band corresponding to a small wave number in which the wave celerity is the kinematic wave celerity; and (3) a dynamic band corresponding to midspectrum values of the wave number, in which the wave celerity falls between the gravity and kinematic celerity values.

Primary dynamic waves propagate downstream, and they attenuate for $F_o < 2$ and amplify for $F_o > 2$. At the $F_o = 2$ threshold, primary dynamic waves neither attenuate nor amplify.

For $F_o \leq 1$, secondary dynamic waves either propagate upstream or downstream, depending on the wave number. At $F_o = 1$, secondary dynamic waves remain stationary or propagate downstream, depending on the wave number. For $F_o > 1$, secondary waves propagate downstream. Secondary waves attenuate throughout the entire wave number spectrum.

Applications

The analysis of the foregoing sections provides an appropriate framework for the systematic study of shallow water waves in open channel flow. Numerous applications are envisioned, among which some of the most important are:

1. The assessment of the accuracy of kinematic and diffusion wave models, and the determination of the criteria for their applicability.
2. The study of the formation of roll waves in open channel flow. The present theory validates the observed fact that roll waves are formed for $F_o > 2$, since there can be no wave amplification for $F_o \leq 2$ (using Chèzy friction).
3. The theory enables a comparison of the various approximate wave models, and an assessment of their capabilities and limitations.
4. Lastly, the theory provides a coherent treatment of the subject of wave propagation in open channel flow. The conclusions may prove of interest to engineers dealing with unsteady open channel flow phenomena.

Appendix I.—References

1. DeSaint-Venant, B., "Theorie du Mouvement Non-permanent des Eaux avec Application aux Crues des Rivierès et l' Introduction des Varées dans leur Lit," *Competes Rendus Hebdomadaires des Seances de l'Academie des Science,* Paris, France, Vol. 73, 1871, pp. 148–154.
2. Henderson, F. M., *Open Channel Flow,* The MacMillan Co., New York, N.Y., 1966.
3. Lagrange, I. L., "Mémoire sur la Théorie du Mouvement des Fluides," *Bulletin de la Classe des Sciences Academie Royal de Belique,* No. 1783, pp. 151–198.
4. Liggett, J. A., "Basic Equations of Unsteady Flow," *Unsteady Flow in Open Channels,* K. Mahmood and V. Yevjevich, ed., Vol. 1, Water Resources Publications, Fort Collins, Colo., 1975.
5. Lighthill, M. J., and Whitham, G. B., "On Kinematic Waves I, Flood Movement in Long Rivers," *Proceedings of the Royal Society of London,* Vol. A229, May, 1955, pp. 281–316.

6. Lin, C. C., *The Theory of Hydrodynamic Stability,* 1st ed., The Cambridge University Press, London, England, 1966.
7. Ponce, V. M., and Mahmood, K., "Meandering Thalwegs in Straight Alluvial Channels," *Proceedings of the 3rd Annual Symposium,* ASCE, Waterways, Harbors, and Coastal Engineering Division, Vol. 2, Aug., 1976, pp. 1418–1441.
8. Stoker, J. J., *Water Waves, the Mathematical Theory with Applications,* Wiley Interscience Publishers, Inc., New York, N.Y., 1957.
9. Woolhiser, D. A., and Liggett, J. A., "Unsteady One-Dimensional Flow over a Plane—The Rising Hydrograph," *Water Resources Research,* Vol. 3, No. 3, Third Quarter, pp. 753–771, 1967.
10. Wylie, C. R., *Advanced Engineering Mathematics,* 3rd ed., McGraw-Hill Book Co., New York, N.Y., 1966.

Appendix II.—Notation

The following symbols are used in this paper:

A = parameter, defined by Eq. 39;
a = integer;
B = parameter, defined by Eq. 40;
C = parameter, defined by Eq. 41;
C_f = Chezy coefficient;
D = parameter, defined by Eq. 50;
d = depth of flow;
E = parameter, defined by Eq. 51;
F_o = Froude number of steady uniform flow;
f = friction factor, defined by Eq. 7;
g = acceleration of gravity;
h_u = velocity head;
k = integer;
L = wavelength;
L_o = length in which the steady uniform flow drops a head equal to its depth;
l = integer;
p = integer;
S_f = friction slope;
S_o = bed slope;
T = wave period;
u = mean velocity;
$\hat{\beta}_I$ = amplitude propagation factor;
$\hat{\beta}_R$ = dimensionless frequency;
γ = unit weight of water;
δ = logarithmic decrement;
ζ = a type of kinematic flow number, as defined by Eq. 37;
θ = parameter, defined by Eq. 43;
$\hat{\sigma}$ = dimensionless wave number;
τ = bottom shear stress; and
∞ = infinity.

Subscripts

d = diffusive wave;

g = gravity wave;
I = imaginary;
k = kinematic wave;
o = steady uniform flow;
R = real;
r = relative to the main flow;
s = steady dynamic wave;
1 = primary dynamic wave; and
2 = secondary dynamic wave.

Superscripts

$'$ = perturbed variable; and
$\hat{}$ = dimensionless function.

13392 SHALLOW WAVE PROPAGATION IN OPEN CHANNELS

KEY WORDS: Attenuation; **Canals;** Celerity; Dynamic characteristics; Kinematics; Propagation; **Rivers; Water flow; Waves**

ABSTRACT: The propagation characteristics of various types of shallow water waves in open channel flow are calculated on the basis of linear stability theory. The celerity and attenuation functions of kinematic, diffusion, convective dynamic, dynamic and gravity waves, are derived. For the most general case, i.e., the dynamic wave model, the propagation characteristics are expressed as a function of the steady uniform flow Froude number and the dimensionless wave number of the unsteady component of the motion. For the dynamic model, the wave number spectrum is divided into three bands: 1)A gravity band corresponding to large wave number, where the wave celerity is the gravity wave celerity; 2)a kinematic band corresponding to a small wave number where the wave celerity is the kinematic wave celerity; and 3)a dynamic band corresponding to mid-spectrum values of the wave number, where the wave celerity falls between the gravity and kinematic celerity values.

REFERENCE: Ponce, Victor Miguel, and Simons, Daryl B., "Shallow Wave Propagation in Open Channel Flow," *Journal of the Hydraulics Division,* ASCE, Vol. 103, No. HY12, **Proc. Paper 13392**, December, 1977, pp. 1461-1476

JOURNAL OF THE
HYDRAULICS DIVISION

Applicability of Kinematic and Diffusion Models

By Victor Miguel Ponce,[1] Ruh-Ming Li,[2] Members, ASCE, and Daryl B. Simons,[3] F. ASCE

Introduction

The kinematic and diffusion wave models have found wide application in engineering practice. Both are approximations to the unsteady open channel flow phenomenon described by the complete Saint Venant equations. The diffusion model assumes that the inertia terms in the equation of motion are negligible as compared with the pressure, friction, and gravity terms. The kinematic model assumes that inertia and pressure terms are negligible as compared with the friction and gravity terms. Although approximate, both the kinematic and diffusion models have been shown to be fairly good descriptions of the physical phenomenon in a variety of cases. The kinematic model has been successfully applied to overland flow, as well as to the description of the travel of slow-rising flood waves. The subsidence of the flood wave, however, is better described by the diffusion model since the kinematic model, by definition, does not allow for subsidence. What do overland flow and slow-rising flood waves have in common that they lend themselves to description by these approximate models? The answer to this question is the subject of this paper.

Wave Propagation in Open Channel Flow

Recently, two of the writers (4) have developed an analytical solution for wave propagation in open channel flow, based on a linearized form of the Saint Venant equations as presented by Lighthill and Whitham (3). They took the linearized equations and sought a solution in sinusoidal form which led to a system of homogeneous linear equations. The nontrivial condition for the

Note.—Discussion open until August 1, 1978. To extend the closing date one month, a written request must be filed with the Editor of Technical Publications, ASCE. This paper is part of the copyrighted Journal of the Hydraulics Division, Proceedings of the American Society of Civil Engineers, Vol. 104, No. HY3, March, 1978. Manuscript was submitted for review for possible publication on August 18, 1977.

[1]Asst. Prof. of Civ. Engrg., Colorado State Univ., Fort Collins, Colo.
[2]Assoc. Prof. of Civ. Engrg., Colorado State Univ., Fort Collins, Colo.
[3]Assoc. Dean for Research and Prof. of Civ. Engrg., Colorado State Univ., Fort Collins, Colo.

determinant of the coefficient matrix yielded the propagation celerity and logarithmic decrement (5) of small sinusoidal perturbations to the equilibrium flow, in terms of the steady equilibrium flow Froude number and a dimensionless wave number of the unsteady component of the motion. In addition, Ponce and Simons calculated the propagation celerity and logarithmic decrement corresponding to the kinematic and diffusion wave models. As it will be shown here, the findings of the theory can be used to determine limits for the applicability of these approximate models, by comparing their propagation celerity and logarithmic decrement with those of the complete Saint Venant equations. At the outset, it is recognized that the validity of the theory is only as good as the assumptions used in its formulation. For instance, the linearized equations have been derived by neglecting second-order terms. Nevertheless, the findings of the theory provide a good insight into the underlying physical mechanism, and their validity as a first approximation appears beyond doubt.

Definitions

The following definitions are advanced: u_o = steady uniform flow mean velocity; d_o = steady uniform flow depth; S_0 = bed slope; L = wavelength of sinusoidal perturbation to steady equilibrium flow; T = wave period of sinusoidal perturbation to steady equilibrium flow; c = wave celerity; L_0 = reference channel length; F_0 = steady uniform flow Foude number; $\hat{\sigma}$ = dimensionless wave number of the unsteady component of the motion; and $\hat{\tau}$ = dimensionless wave period of the unsteady component of the motion, such that

$$c = \frac{L}{T} \quad (1)$$

$$L_0 = \frac{d_0}{S_0} \quad (2)$$

$$\mathsf{F}_0 = \frac{u_0}{\sqrt{gd_0}} \quad (3)$$

$$\hat{\sigma} = \left(\frac{2\pi}{L}\right) L_0 \quad (4)$$

$$\hat{\tau} = T\left(\frac{u_0}{L_0}\right) \quad (5)$$

in which g = the acceleration of gravity.

The propagation celerity c can be expressed in dimensionless form by dividing it by u_0. The dimensionless propagation celerity $\hat{c}$ is

$$\hat{c} = \frac{c}{u_0} \quad (6)$$

The logarithmic decrement δ (5) is defined as

$$\delta = \ln(a_1) - \ln(a_0) \quad (7)$$

in which a_0 and a_1 = the wave amplitudes at the beginning and end of one wave period, respectively.

Two of the writers (4) have shown that for the dynamic model (that based on the complete Saint Venant equations), the dimensionless propagation celerity $\hat{c}$ and logarithmic decrement δ are functions of F_0 and $\hat{\sigma}$ (see Appendix I). In practice, however, it is desirable to express the space parameter $\hat{\sigma}$ as a function of the time parameter $\hat{\tau}$. Combining Eqs. 1, 4, 5, and 6

$$\hat{\tau} = \frac{2\pi}{\hat{c}\,\hat{\sigma}} \qquad (8)$$

Thus, $\hat{c}$ and δ can be expressed as a function of F_0 and $\hat{\tau}$ by use of Eq. 8. Furthermore, the results of the theory suggest that for the comparison of diffusion and full dynamic models, a more appropriate parameter is $\hat{\tau}/F_0$. Making use of Eqs. 2, 3, and 5, $\hat{\tau}/F_0$ is expressed as

$$\frac{\hat{\tau}}{F_0} = T\left(\frac{S_0 u_0}{d_0 F_0}\right) \qquad (9)$$

$$\text{or} \quad \frac{\hat{\tau}}{F_0} = TS_0\left(\frac{g}{d_0}\right)^{1/2} \qquad (10)$$

Kinematic Wave Versus Diffusion Wave

The kinematic model breaks down when the neglect of the pressure term is not justified. Accordingly, it is of interest to compare the kinematic and diffusion models. Both models have a propagation celerity equal to 1.5 times the equilibrium flow velocity. They differ, however, in the attenuation. The logarithmic decrement of the kinematic model is 0, i.e., the kinematic model does not allow for physical attenuation. The attenuation often observed in numerical schemes based on the kinematic model is of an artificial nature (numerical damping due to truncation errors) (1). The logarithmic decrement of the diffusion model is (4)

$$\delta_d = -\frac{2\pi}{3}\hat{\sigma} \qquad (11)$$

Substituting Eq. 8 into Eq. 11

$$\delta_d = -\frac{4}{3}\left(\frac{\pi^2}{\hat{c}\,\hat{\tau}}\right) \qquad (12)$$

$$\text{Since} \quad \hat{c} = \hat{c}_d = \frac{3}{2} \qquad (13)$$

$$\text{it follows that} \quad \delta_d = -\frac{8\pi^2}{9\hat{\tau}} \qquad (14)$$

The kinematic model will be valid when the attenuation factor of the diffusion model, e^{δ_d}, is close to 1. Table 1 shows the values of e^{δ_d} for various $\hat{\tau}$. Thus, for at least 95% accuracy of the kinematic wave solution after one propagation

period, the dimensionless period $\hat{\tau}$ has to be greater than 171.

For example, for a channel with $S_0 = 0.0001$, $d_0 = 10$ ft (3.05 m) and $u_0 = 3$ fps (0.91 m/s), an accuracy of at least 95% in the wave amplitude after one propagation period, requires that the period T be:

$$T \geq \frac{\hat{\tau}\, d_0}{S_0 u_0} = \frac{171 \times 10}{0.0001 \times 3} \cong 66 \text{ days} \quad (15)$$

If water discharge and channel friction are given, u_0 and d_0 can be calculated by the use of the appropriate uniform flow formula (Manning or Chezy).

As another example, assume a value of slope S_0 corresponding to overland flow. If $S_0 = 0.01$, $d_0 = 1$ ft (0.305 m) and $u_0 = 4$ fps (1.22 m/s), for this case

$$T \geq 1.2 \text{ hr} \quad (16)$$

Thus, for mild channel slopes, the period has to be very long for the kinematic model to apply (periods such as those of slow-rising flood waves). For steep slopes such as those prevalent in overland flow, the period does not need to be long. The steeper the slope, the shorter the period required to satisfy the kinematic flow assumption. The conclusion is that most overland flow problems

TABLE 1.—Dimensionless Period $\hat{\tau}$ Versus Attenuation Factor e^{δ_d}

e^{δ_d} (1)	$\hat{\tau}$ (2)
0.99	873
0.95	171
0.90	83

can be modeled as kinematic flow. Likewise, slow-rising flood waves that travel unchanged in form can also be modeled as kinematic flow.

An explanatory note is necessary here. The criteria of Table 1 are based on a comparison of the attenuation (described by the logarithmic decrement δ) of the analytical solutions for the kinematic and diffusion models. In a numerical solution, however, often the truncation errors may mask the nondiffusive character of the analytical solution of the kinematic wave, with the result that the numerical solution of the kinematic wave may resemble the analytical solution of the diffusion wave (1), further complicating the modeling.

Diffusion Wave Versus Dynamic Wave

The next step in the analysis is to compare the propagation celerity $\hat{c}_d$ and logarithmic decrement δ_d of the diffusion model with those of the full dynamic model. For $F_0 < 2$, the propagation celerity of the diffusion wave, $\hat{c}_d = 1.5$, is a lower bound for the dynamic celerity. Since only the primary dynamic wave (that which travels downstream) is of interest here, the dynamic wave celerity will be referred to as $\hat{c}_1$.

Fig. 1 shows the variation of $\hat{c}_1$ as a function of $\hat{\tau}/F_0$. It can be seen from this figure that $\hat{c}_1$ tends to $\hat{c}_d$ as $\hat{\tau}/F_0$ increases, for all F_0. Fig. 2 is an arithmetic

plot of $\hat{c}_1/\hat{c}_d$ versus $\hat{\tau}/F_0$ for $5 \leq \hat{\tau}/F_0 \leq 30$. From this figure, for $\hat{\tau}/F_0 \geq 8$, the celerity error of the diffusion model is within 5%. The curve shown for $F_0 = 0.01$ is an error bound.

Keeping the celerity error to within 5% does not guarantee that the amplitude error will remain within the same tolerance. Fig. 3 is a plot of $e^{\delta_1 - \delta_d}$ versus $\hat{\tau}/F_0$, in which δ_1 and δ_d = the logarithmic decrements of the dynamic and diffusion models, respectively. Fig. 3 shows that for $0.1 \leq F_0 \leq 0.4$, $\hat{\tau}/F_0 > 16$, for the attenuation error of the diffusion model to be within 5%. For a wider range of F_0, say, $0.01 \leq F_0 \leq 1.0$, $\hat{\tau}/F_0 \geq 45$. An exact value of

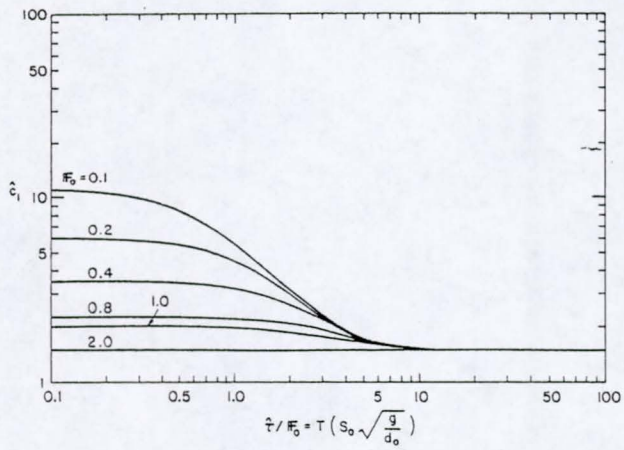

FIG. 1.—Dimensionless Celerity of Dynamic Model $\hat{c}_1$ Versus $\hat{\tau}/F_0$

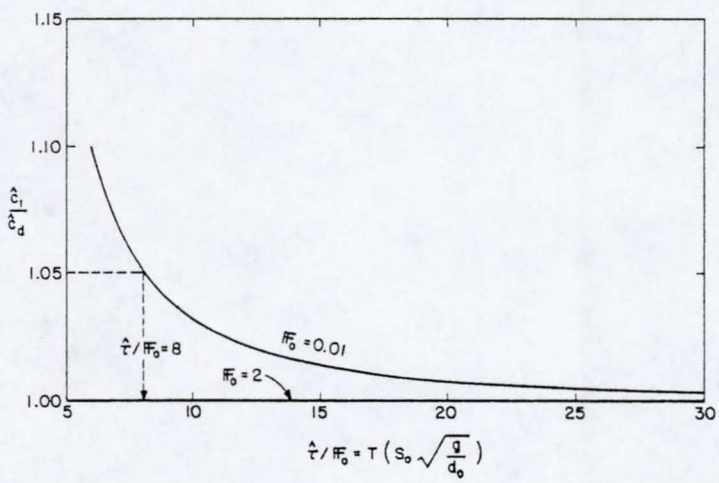

FIG. 2.—Ratio of Celerities $\hat{c}_1/\hat{c}_d$ Versus $\hat{\tau}/F_0$

the parameter $\hat{\tau}/F_0$ for a given error defies generalization, being as it is a function of F_0. Nevertheless, from a practical standpoint, a value of $\hat{\tau}/F_0 > 30$ is postulated (specific values of $\hat{\tau}/F_0$ for a given F_0 can be taken directly from Fig. 3).

Applying this criterion to the same example used before, for $S_0 = 0.0001$ and $d_0 = 10$ ft (3.05 m)

$$TS_0\left(\frac{g}{d_0}\right)^{1/2} \geq 30 \quad (17)$$

from which $T \geq 1.9$ days . . . . . (18)

In the second example shown, for $S_0 = 0.01$ and $d_0 = 1$ ft (0.305 m)

$T \geq 8.8$ min . . . . . (19)

On the basis of the examples shown, it is concluded that the diffusion model applies for a wider range of slopes and periods than the kinematic model, with the added advantage that the diffusion model does allow for physical attenuation. However, if inequality (Eq. 17) is not satisfied, the diffusion model breaks

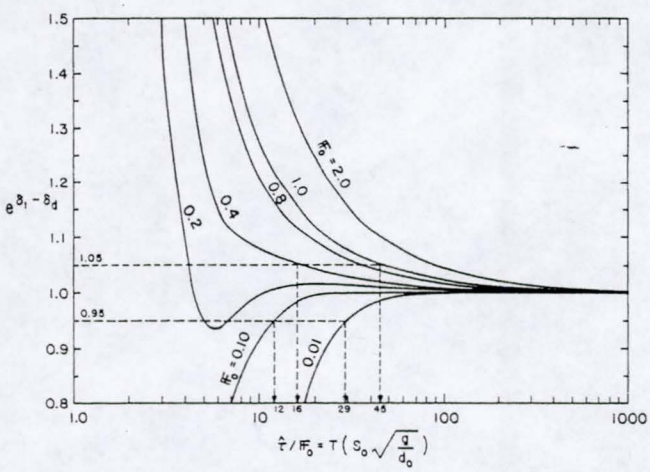

FIG. 3.—Ratio of Attenuation Factors $e^{\delta_1 - \delta_d}$ Versus $\hat{\tau}/F_0$

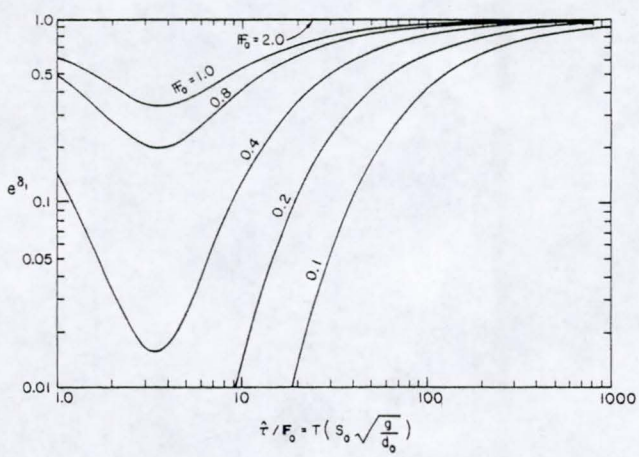

FIG. 4.—Attenuation Factor of Dynamic Model e^{δ_1} Versus $\hat{\tau}/F_0$

down and only the full dynamic model can properly account for the rate of travel and amount of attenuation of the wave.

Full Dynamic Model

Fig. 1 and 4 show $\hat{c}_1$ and e^{δ_1} as a function of F_0 and $\hat{\tau}/F_0$. For $\hat{\tau}/F_0 \leq 30$, i.e., the range where only the full dynamic model would apply, very strong attenuation is shown. For instance, for $\hat{\tau}/F_0 = 30$, and $F_0 = 0.2$, $e^{\delta_1} = 0.23$. This explains the nonpermanent characteristics of the dynamic wave: once formed, it will attenuate quickly. In this regard, it is of interest to point

out here the observations of Hayami (2) regarding the nonpermanent nature of dynamic disturbances in open channel flow. He reasoned that given all the irregularities present in natural river channels, it is striking that the general pattern of the flow closely resembles that of uniform flow. The reason for this lies in the strong dissipative tendencies of dynamic disturbances, its nonpermanency being manifested in the appearance of uniform flow. Kinematic and diffusion waves, however, do not share the strong dissipative tendencies of dynamic waves due precisely to their long duration, or relatively large bed slopes, or both.

Conclusions

The applicability of the kinematic and diffusion models is assessed by comparing the propagation characteristics of sinusoidal perturbations to the steady uniform flow for the kinematic, diffusion, and dynamic models (the dynamic model is that based on the complete Saint Venant equations). The comparison allows the determination of inequality criteria that need to be satisfied if the kinematic or diffusion models are to simulate the physical phenomena within a prescribed accuracy.

It is shown that bed slope and wave period (akin to wave duration in waves of shape other than sinusoidal) are the important physical characteristics in determining the applicability of the approximate models. Larger bed slopes or long wave periods will satisfy the inequality criteria. In practice, larger bed slopes are those of overland flow, and long wave periods are those corresponding to slow-rising flood waves.

The diffusion model is shown to be applicable for a wider range of bed slopes and wave periods than the kinematic model. Where the two models break down, only the dynamic model will simulate the physical phenomena. The dynamic model, however, is shown to have markedly strong dissipative tendencies. This conclusion has had ample corroboration in the literature.

Acknowledgments

The writers wish to acknowledge the United States Environmental Protection Agency, Environmental Research Laboratory, Athens, Ga., and the United States Department of Agriculture Forest Service, Rocky Mountain Forest and Range Experiment Station, Flagstaff, Ariz., for sponsoring this study.

Appendix I.—Equations for Propagation Celerity $\hat{c}$ and Logarithmic Decrement δ

The equations for $\hat{c}$ and δ of the complete dynamic model are $\hat{c}_{1,2} = 1 \pm D$

$$\delta_{1,2} = -2\pi \frac{B \mp E}{|1 \pm D|}$$

in which $A = (1/F_0^2) - B^2$; $B = 1/(\hat{\sigma} F_0^2)$; $C = (A^2 + B^2)^{1/2}$; $D = [(C + A)/2]^{1/2}$; and $E = [(C - A)/2]^{1/2}$.

Appendix II.—References

1. Cunge, J., "On the Subject of a Flood Propagation Computation Method (Muskingum Method)," *Journal of Hydraulic Research*, Vol. 7, No. 2, 1969, pp. 205–230.
2. Hayami, S., "On the Propagation of Flood Waves," *Bulletin of the Disaster Prevention Research Institute*, Kyoto, Japan, Vol. 1, No. 1, Dec., 1951.
3. Lighthill, M. J., and Whitham, G. B., "On Kinematic Waves I Flood Movement in Long Rivers," *Proceedings*, Royal Society of London, London, England, Series A, Vol. 229, 1955, pp. 281–316.
4. Ponce, V. M., and Simons, D. B., "Shallow Wave Propagation in Open Channel Flow," *Journal of the Hydraulics Division*, ASCE, Vol. 103, HY12, Proc. Paper 13392, Dec., 1977, pp. 1461–1476.
5. Wylie, C. R., *Advanced Engineerings Mathematics*, 3rd ed., McGraw-Hill Book Co. Inc., New York, N.Y., 1966.

Appendix III.—Notation

The following symbols are used in this paper:

a_0 = wave amplitude at beginning of period;
a_1 = wave amplitude at end of period;
c = wave celerity, Eq. 1;
$\hat{c}$ = dimensionless wave celerity, Eq. 6;
d_0 = steady uniform flow depth;
F_0 = steady uniform flow Froude number;
g = acceleration of gravity;
L = wavelength;
L_0 = reference channel length, Eq. 2;
S_0 = bed slope;
u_0 = steady uniform flow mean velocity;
T = wave period;
δ = logarithmic decrement, Eq. 7;
$\hat{\tau}$ = dimensionless period, Eq. 5; and
$\hat{\sigma}$ = dimensionless wave number, Eq. 4.

Subscripts

1 = pertaining to primary dynamic wave (traveling downstream);
d = pertaining to diffusion model; and
k = pertaining to kinematic model.

The Kinematic Wave Controversy

By Victor M. Ponce,[1] Member, ASCE

Abstract: Kinematic and diffusion waves are reviewed prompted by the continuing controversy regarding their nature and applicability. Kinematic waves are shown to be nondiffusive, but to undergo change in shape due to nonlinearity. This latter feature gives kinematic waves the capability of steepening, eventually leading to the formation of the kinematic shock. Kinematic wave solutions using finite differences are shown to possess intrinsic amounts of numerical diffusion and dispersion. These numerical effects are artificial and tend to disappear as the grid size is refined, making the solution dependent on the choice of grid size. Kinematic wave theory can be improved by extending it to the realm of diffusion waves. In this way, the diffusion inherent in many practical runoff computations can be accounted for directly in the modeling, rather than as an afterthought. The use of a kinematic wave method is indicated for small catchments, in cases where it is possible to resolve the physical detail without compromising the deterministic nature of the model. Conversely, the unit hydrograph is advocated for midsize catchments, where the kinematic wave method may prove difficult to implement. The dynamic extension to kinematic and diffusion models shows promise, particularly for modeling channel and flow conditions in which the Vedernikov number is substantially different from zero.

Introduction

There is a continuing controversy regarding the nature and applicability of the kinematic wave model. Researchers and practitioners alike have reported successes and failures of the model, with papers continuing to appear in the literature describing what the model can and cannot do (Hromadka and DeVries 1988). Current areas of concern focus on the following issues: (1) Whether the kinematic wave can describe physical diffusion, and if so, under what circumstances. (2) whether the kinematic wave can eventually replace other well-established methods of surface runoff generation such as the unit hydrograph; and (3) whether the kinematic shock is as common in practice as calculations would seem to indicate.

While answers to these questions can be found in the literature, they are dispersed among various sources and not readily accessible. This difficulty appears to be fueling the current controversy (Dawdy 1990; Goldman 1990; Hromadka and DeVries 1990; Merkel 1990; Unkrich and Woolhiser 1990; Woolhiser and Goodrich 1990). Therefore, the aim of the present paper is to review the concept of kinematic wave, delineate its range of applicability, and critically examine its overall modeling philosophy. It is hoped that this review will help focus the attention of researchers and practitioners so that the controversy may be brought to a timely end.

Background

The concept of kinematic wave is well established among the existing methods to solve unsteady, one-dimensional, gradually varied open-channel

[1]Prof. and Chair, Dept. of Civ. Engrg., San Diego State Univ., San Diego, Calif. 92182.

Note. Discussion open until September 1, 1991. To extend the closing date one month, a written request must be filed with the ASCE Manager of Journals. The manuscript for this paper was submitted for review and possible publication on February 23, 1990. This paper is part of the ***Journal of Hydraulic Engineering***, Vol. 117, No. 4, April, 1991. ©ASCE, ISSN 0733-9429/91/0004-0511/$1.00 + $.15 per page. Paper No. 25673.

flow problems. In contrast to the dynamic wave, which features a significant inertial component, a kinematic wave is one in which the inertial component is too small to be of any practical importance. In unsteady open-channel flow modeling, a first type of kinematic wave arises when the governing equations are simplified by neglecting the local inertia, convective inertia, pressure-gradient, and momentum-source terms (Lighthill and Whitham 1955). A second, less restrictive type can be formulated by neglecting the local inertia, convective inertia, and momentum-source terms, but keeping the pressure-gradient term (Hayami 1951). To avoid confusion between these two types of kinematic waves, it is common practice to refer to the first type as kinematic wave proper, and to the second as diffusion wave (Ponce and Simons 1977).

From the physical standpoint, the kinematic wave assumption amounts to substituting a uniform flow formula (such as Manning's or Chezy's) for the equation of motion. In essence, it says that as far as momentum is concerned, the flow can be considered steady. The unsteadiness of the phenomenon, however, is preserved through the rate-of-rise term in the continuity equation (Liggett 1975). The implication of the kinematic wave assumption is that unsteady open-channel flow can be visualized as a succession of steady uniform flows, with the water surface slope remaining constant at all times. This, of course, can be reconciled with reality only if the flow unsteadiness is very mild, i.e., if the changes in momentum are indeed negligible compared to the forces driving the steady component of the motion (gravity and friction).

From the mathematical standpoint, the kinematic wave assumption results in a considerable simplification of the equation of motion, reducing it to a statement of uniform flow (such as, for instance, the Manning equation). Combining this latter equation with the equation of continuity gives rise to a first-order partial differential equation, referred to as the kinematic wave equation

$$\frac{\partial Q}{\partial t} + c\frac{\partial Q}{\partial x} = cq_L \qquad (1)$$

in which Q = discharge; c = kinematic wave celerity; q_L = lateral inflow; x = spatial variable; and t = temporal variable. This equation is applicable to streamflow modeling as well as to channel and gutter flow. For overland flow applications, the kinematic wave equation is expressed in terms of unit-width discharge as follows:

$$\frac{\partial q}{\partial t} + c\frac{\partial q}{\partial x} = ci \qquad (2)$$

in which q = unit-width discharge; i = effective rainfall intensity; and the other terms are as defined previously.

The kinematic wave celerity is defined as the slope of the rating curve, either discharge-flow area ($Q = \alpha A^{\beta}$) in the case of streamflow, or unit-width discharge-flow depth ($q = ad^m$) for overland flow. Accordingly, $c = dQ/dA = \beta(Q/A) = \beta u$ in the case of streamflow; and likewise, $c = m(q/d) = mu$ for overland flow, in which u = mean velocity. In natural channels, the kinematic wave celerity is alternatively expressed as $c = (1/T)(dQ/dy)$, in which T = channel top width, and y = stage.

Eq. 1 (and by extension, Eq. 2) is a differential equation of first order; therefore, it can describe convection but not diffusion, which is a second-order process. In practice, this means that the kinematic wave equation can describe the travel of a flood wave, but not its attenuation as it propagates downstream. Although Eq. 1 cannot describe diffusion, it is a quasi-linear equation because the kinematic wave celerity is a function of discharge. This gives kinematic waves the tendency to change in shape as they propagate. If the celerity increases with discharge, the leading face of the wave will steepen; conversely, if the celerity decreases with discharge, the leading face of the wave will flatten out. In overland flow and inbank streamflow, the tendency is for the wave to steepen; in shallow-overbank streamflow, the tendency is for the wave to flatten out.

Kinematic Wave Solutions

Solutions to Eq. 1 (or Eq. 2) can be attempted in a variety of ways. Analytical solutions are possible for linearized analogs of the governing equations [see for instance Lighthill and Whitham (1955) and Ponce and Simons (1977)]. These solutions describe the convection of a flow quantity (either Q or q) with the celerity c in the absence of diffusion. Numerical solutions are possible using the method of characteristics or the finite difference method. Early work on the kinematic wave used the method of characteristics. In overland flow applications, the nonlinearity (or rather the quasi-linearity) of the phenomena usually led to wave steepening and the eventual development of a kinematic shock. A kinematic shock is a kinematic wave that has steepened to the point where its rising limb has an almost vertical face, wherein the flow develops a singularity and loses its gradually varied property.

Numerical Diffusion and Dispersion

Although kinematic wave solutions using the method of characteristics are prone to shock development, ostensibly because of their lack of diffusion, solutions using the finite difference method exhibit a somewhat different behavior. Finite difference solutions, by virtue of their discrete nature, introduce appreciable amounts of numerical diffusion and numerical dispersion. These numerical effects interfere with the physical effects, modifying them (Abbott 1976). For instance, in overland flow applications, the numerical diffusion has the effect of counteracting the tendency of the wave to steepen, thereby arresting shock development and allowing the unsteady gradually varied flow computation to continue.

The presence of numerical diffusion and dispersion in a numerical solution using the finite difference method is at the crux of the controversy surrounding the kinematic wave model. A numerical scheme is characterized by its amplitude and phase-error portraits (Leendertse 1967). The amplitude portrait describes the way in which the numerical wave amplitude approaches the physical wave amplitude, with the deviation being interpreted as numerical diffusion. The phase portrait describes the way in which the numerical wave phase approaches the physical wave phase, with the deviation being interpreted as numerical dispersion. Examples of amplitude and phase portraits for convection problems are given by Cunge (1969) and Ponce et al. (1979).

Finite difference solutions of the kinematic wave equation exhibit varying amounts of numerical diffusion and dispersion depending on the type of scheme used to discretize Eq. 1 (or Eq. 2). Fully centered schemes are of second order, exhibiting no numerical diffusion. However, these schemes may exhibit numerical dispersion for Courant numbers other than 1. (In kinematic wave theory, the Courant number is defined as the ratio of the physical celerity, i.e. the kinematic wave celerity c, to the "grid celerity" $\Delta x/\Delta t$, with Δx = the spatial increment, or space step, and Δt = the temporal increment, or time step.) Off-centered schemes are of first order, exhibiting varying amounts of numerical diffusion, depending on the size of Δx and Δt. Smaller increments result in smaller amounts of numerical diffusion, with the numerical diffusion vanishing as the increments are driven to zero. These schemes also exhibit variable amounts of numerical dispersion for Courant numbers other than 1.

Numerical diffusion arises due to the neglect of the second-order term of the corresponding Taylor series expansion of the related discrete analog. Numerical dispersion arises due to the neglect of the third-order term of the Taylor series expansion (Cunge 1969; Ponce et al. 1979). Therefore, in a typical application, numerical diffusion is usually about an order of magnitude greater than numerical dispersion. In practice, this means that as a rule, most of the error of numerical solutions can be attributed to numerical diffusion rather than numerical dispersion. Exceptions are the cases in which the Courant number is significantly less than 1, in which case the numerical dispersion may grow to the point where it compares in size with the numerical diffusion.

Numerical diffusion manifests itself as the diffusion or attenuation of the calculated runoff hydrograph. Since the kinematic wave equation has no built-in physical diffusion, it follows that a finite difference solution is actually simulating physical diffusion through numerical diffusion. The fact that the latter is artificial and intrinsically related to the grid size can be readily demonstrated by solving the same problem several times, each time halving the spatial and temporal increments [see for instance Ponce (1986)]. Carried to a practical limit, this test leads to the eventual disappearance of the numerical diffusion in question, with the result approaching the analytical solution of the kinematic wave. The recognition of this fact prompted the USDA Soil Conservation Service to retire its convex method of flood routing in the early 1980s. The convex method showed considerable sensitivity to the grid size, with the numerical diffusion vanishing as the grid size was gradually reduced.

Numerical dispersion manifests itself as dispersion; that is, as the steepening or flattening of the rising limb of the calculated runoff hydrograph. In certain extreme cases, the numerical dispersion is responsible for the wiggles, or the (usually small) negative outflows observed at the beginning or end of the calculated runoff hydrograph (Hjelmfelt 1985). In practice, these negative outflows are small, and disappear (together with all traces of numerical dispersion) as the space and time steps are chosen such that the Courant number is close to 1.

Since numerical diffusion and dispersion are inherent in the choice of space and time steps (and their ratio relative to the wave celerity), the result of a finite difference solution of Eqs. 1 or 2 is per force grid dependent; i.e., the calculated runoff hydrograph varies with the choice of grid size. Therefore,

it seems pointless to try to "calibrate" a kinematic wave model by varying a physical parameter such as Manning's n in order to match calculated results and observed data. This practice amounts to curve-fitting; at best it is good conceptual modeling, but it should not be interpreted as deterministic modeling.

Diffusion-Wave Modeling

In practice, actual runoff hydrographs do exhibit a certain amount of diffusion. To properly simulate this diffusion it is necessary to extend kinematic wave theory to encompass the related diffusion wave theory. Following Hayami (1951) and Lighthill and Whitham (1955), the diffusion wave equation is derived by neglecting the local inertia, convective inertia, and momentum-source terms in the equation of motion, leading to the following equation for streamflow and channel flow:

$$\frac{\partial Q}{\partial t} + c\frac{\partial Q}{\partial x} = \nu\frac{\partial^2 Q}{\partial x^2} + cq_L \qquad (3)$$

and a similar equation for overland flow

$$\frac{\partial q}{\partial t} + c\frac{\partial q}{\partial x} = \nu\frac{\partial^2 q}{\partial x^2} + ci \qquad (4)$$

with ν = hydraulic diffusivity, defined as

$$\nu = \frac{Q}{2TS_0} = \frac{q}{2S_0} \qquad (5)$$

and S_0 = bottom slope; and other terms are as previously defined. Eqs. 3 and 4 describe the movement of kinematic waves with a diffusion component, for short diffusion waves. Unlike their counterparts Eqs. 1 and 2, Eqs. 3 and 4 are second-order parabolic differential equations and are, therefore, able to describe physical diffusion with the diffusion coefficient defined by Eq. 5.

The diffusion wave equation can be solved either analytically, leading to Hayami's diffusion-analogy solution for flood waves, or numerically, with the aid of a numerical scheme for parabolic equations, such as the Crank-Nicolson scheme (Crandall 1956). A third alternative is to extend the finite difference solution of the kinematic wave to the realm of diffusion waves by matching physical and numerical diffusivities (Cunge 1969; Dooge 1973). The physical diffusivity is the hydraulic diffusivity given by Eq. 5. The numerical diffusivity is the numerical diffusion coefficient of the discretized kinematic wave model, i.e., the coefficient of the leading (second-order) error term. When the Muskingum scheme is used to model the kinematic wave, this method is referred to as Muskingum-Cunge model (*Flood* 1975; Ponce and Yevjevich 1979).

The Muskingum-Cunge method has the significant advantage over conventional kinematic wave models of being essentially grid independent (Ponce and Theurer 1982; Ponce 1986). Therefore, calibration requires only a fine tuning of the frictional and cross-sectional parameters such as Manning's n and flow rating exponent (either β for channel flow or m for overland flow).

Then, the choice of spatial and temporal increments is based solely on considerations of problem scale.

Applicability of Kinematic Waves

The question of the applicability of kinematic waves has interested researchers and practitioners alike. Although kinematic waves were originally used for describing river flows (Seddon 1900), it is in the field of overland flow that questions first arose with respect to its applicability and accuracy. Notable among these contributions is that of Woolhiser and Liggett (1967), who identified a parameter k defined as

$$k = \frac{S_0 L_0}{d_0 \mathsf{F}_0^2} \qquad (6)$$

to characterize the applicability of the kinematic wave to overland flow situations. In Eq. 6, S_0 = bottom slope; L_0 = length of the overland flow plane; d_0 = normal depth; and F_0 = Froude number based on normal flow. The parameter k has been referred to in the literature as kinematic flow number (Liggett 1975). This parameter can be used as a criterion to aid in determining whether the kinematic wave solution is sufficiently accurate when used to solve overland flow problems. According to Woolhiser and Liggett (1967), a value of $k \geq 20$ indicates that the flow is strongly kinematic, and therefore suited to solution using the kinematic wave equation. More recently, however, Morris and Woolhiser (1980) have stated that for low-Froude-number flows, it is also necessary that $k\mathsf{F}_0^2 \geq 5$, a condition compatible with the Woolhiser and Liggett criterion ($k \geq 20$) for the case of $\mathsf{F}_0 \geq 0.5$.

Ponce et al. (1978) used an analytical solution of the linearized equation set (Lighthill and Whitham 1955) to develop criteria for the applicability of kinematic and diffusion waves to open channel flow. They used sinusoidal perturbations to the mean flow, with L = wavelength; and T = wave period. For kinematic waves, the Ponce et al. criterion states that for the solution to be within 95% accuracy after one period of propagation, the dimensionless wave period has to be greater than 171. The dimensionless wave period τ is defined

$$\tau = \frac{T S_0 u_0}{d_0} \qquad (7)$$

in which u_0 = reference flow mean velocity; d_0 = reference flow depth; and S_0 = bottom slope. For practical applications, the wave period T can be taken as twice the time-of-rise of the flood wave.

For diffusion waves, a parameter τ/F_0, in which F_0 = reference flow Froude number, is shown to be a better descriptor of the overall accuracy, accounting for both amplitude and phase errors. A practical applicability criterion for diffusion waves is the following (Ponce et al. 1978):

$$\frac{\tau}{\mathsf{F}_0} = T S_0 \left(\frac{\mathsf{g}}{d_0}\right)^{1/2} \geq 30 \qquad (8)$$

in which g = gravitational acceleration; and the other terms are as previously defined.

Ponce et al. (1978) confirmed the conclusions of Lighthill and Whitham (1955), as well as those of many others, that most overland flow situations would satisfy the kinematic wave criterion, and that most flood wave propagation cases in stream channels (excluding those with significant downstream control) would satisfy the diffusion wave criterion. Only in situations with markedly strong dissipative tendencies (for instance, a dam-break flood wave), flow into large reservoirs (with substantial backwater effects), or flow reversals would it be necessary to resort to the dynamic wave to properly describe the propagation of shallow-water waves.

Overland Flow versus Unit Hydrograph

The issue of whether an overland flow kinematic wave solution can replace (and perhaps eventually retire) the unit hydrograph as a practical method of runoff generation remains clouded in controversy. Due to the fundamental differences between these two methods, a resolution of this conflict does not appear to be forthcoming in the near future. The overland flow kinematic wave solution is a deterministic, distributed-parameter, hydraulic-data-intensive method (requiring geometric and frictional parameters), which is primarily applicable to small catchments [i.e. those less than 1 sq mi (2.5 km^2)], for which the idealizations inherent in mathematical modeling can be justified on practical grounds. In other words, for the kinematic wave solution to be useful, the discretization must reflect what is actually occurring in the field. When used indiscriminately, without due regard for problem scale, there is a risk that the amount of lumping introduced may interfere with the deterministic character of the method and its ability to simulate overland flows in a distributed context.

In contrast to the overland flow kinematic wave solution, the unit hydrograph is a conceptual model of runoff generation, spatially lumped, and based exclusively on hydrologic data (streamflow measurements). Although originally derived for large catchments (Sherman 1932), the method has been found to have primary applicability to midsize catchments, i.e., those in excess of 1 sq mi (2.5 km^2) but less than 400 sq mi (1,000 km^2). While these limits are somewhat arbitrary, they tend to reflect current hydrologic engineering practice. Furthermore, in the proper modeling context (i.e. with catchment subdivision), the applicability of the unit hydrograph can be extended to large catchments.

Since the overland flow kinematic wave solution is primarily applicable to small catchments, and the unit hydrograph is primarily applicable to midsize (and, by extension, to large) catchments, it seems that there should be little overlap between these two methods. In practice, however, existing computer models [for instance, the U.S. Army Corps of Engineers HEC-1 (*HEC-1* 1985)] provide users with a choice between these two methods to solve any given runoff problem, regardless of scale. This raises the question of which method is better, or more accurate, for a given problem, a question that has no easy answer. The methods are of such different nature and have such different data needs that they are not readily comparable. Perhaps the only defensible argument in this regard is that the kinematic wave solution should increase in accuracy as the catchment size decreases; and the unit hydrograph should increase in practicality as the catchment scale increases. Specific comparisons between the two methods are likely to lead to heated

arguments, but the central issue of accuracy is not likely to be settled soon. For one thing, the overland flow kinematic wave solution is based on our currently imperfect knowledge of friction mechanisms, including the estimation of Manning's n and of the rating exponent m describing the mixed laminar-turbulent regime characterizing most overland flow situations. Likewise, the unit hydrograph would have to be verified with concurrent rainfall-runoff data, which are not readily available for the typical midsize catchment application.

Keeping in mind the question of scale, the kinematic wave solution does have the significant advantage that it can describe spatial and/or temporal rainfall and roughness variations, which the unit hydrograph method, by virtue of its being lumped, cannot do. Therefore, in situations where the scale question can be reasonably compromised, the overland flow solution should provide better detail in the simulation of flood flows, including the description of runoff concentration and diffusion. Therein lies the promise of kinematic waves and the expectation of significant improvements in the accuracy of runoff prediction.

As kinematic wave solutions continue to mature, particularly with the advent of a physically meaningful description of runoff diffusion, the way will be paved for the two methods of runoff generation to complement rather than compete with each other. There is an urgent need to develop synthetic unit hydrographs that reach beyond established practice [the Snyder unit hydrograph, to follow Corps of Engineers' practice; or the SCS dimensionless, to follow the Soil Conservation Service, (USDA: *SCS* 1985)]. Acting on this perceived need, the U.S. Bureau of Reclamation has developed a set of regional synthetic unit hydrographs for use within its jurisdiction (11 western United States) (USBR: *Design* 1987). In an attempt to overcome the shortcomings of conventional synthetic unit hydrographs, local agencies are engaged in developing synthetic unit hydrographs of the S-graph type (Sabol 1987, 1990). It is envisioned that under the proper modeling context, the overland flow kinematic wave model can be used as a tool to develop synthetic unit hydrographs without the burden of an extensive (and expensive) network of streamflow data collection [see Overton (1970)].

A precedent for the use of models to synthesize peak flows already exists in U.S. hydrologic practice: the TR-55 method (USDA: "Urban" 1986). This SCS method of peak flow generation was developed using the hydrologic catchment model TR-20 (USDA: "Computer" 1983) to generate synthetic peak flows that take into account the catchment's concentration properties, regional temporal rainfall distribution, and event-abstraction mechanisms of infiltration and depression storage. The TR-55 method improves on the rational method, substituting modeling for empiricism and leading to better and more consistent runoff predictions.

Kinematic Shock

The kinematic shock was discussed in detail by Lighthill and Whitham (1955); and since then, numerous studies have endeavored to analyze its causes and effects. But the subject continues to mystify researchers and practitioners alike (Cunge 1969; Kibler and Woolhiser 1970). The shock arises due to the nonlinear feature of kinematic waves, which under the right set of circumstances can result in the kinematic wave steepening to the point

where it becomes for all practical purposes a wall of water. (In overland flow situations, the "wall of water" would be a small discontinuity in the water surface profile.) The shock is a direct consequence of the nonlinear steepening tendency, which is abetted when the following conditions occur (Ponce and Windingland 1985).

First, the wave is kinematic as opposed to diffusion (or dynamic). Diffusion is a mechanism acting to oppose the nonlinear steepening tendency. The more diffusive (or dynamic) a wave is, the less kinematic, and therefore, the less the steepening tendency.

Second, there is a low base-to-peak flow ratio. The steepening tendency is promoted when the flow is subject to large relative changes, with baseflow being only a small fraction of peak flow. In the limit, as the baseflow approaches zero, i.e., in the case of an ephemeral stream, the steepening tendency (due to this condition) is greatest. This explains the fact that the shock is a relatively more frequent occurrence in the case of flash floods in arid and semiarid regions, which are caused by intense thunderstorms concentrating large flows into ephemeral streambeds.

Third, there is a hydraulically wide and sufficiently long channel. Since the wave steepening is gradual, a sufficiently long channel is needed to give the shock a chance to develop. Strong steepening tendencies may require a shorter reach; a weak tendency may never develop the shock, given the complicating spatial effect of lateral inflows. A necessary condition for shock development is that the channel be hydraulically wide, that is, one in which the wetted perimeter is nearly constant. In practice, this hydraulic condition is reflected in a canyon-type situation, with essentially vertical walls in which as the flow increases, the wetted perimeter increases very little in comparison with the increase in flow depth and area. Mathematically, this condition is represented by a rating exponent β much greater than 1 (approaching $\beta = 3/2$ for Chezy friction; or $\beta = 5/3$ for Manning friction). Conversely, in shallow-overbank flow situations (with channels rapidly expanding their top width, such that the wetted perimeter increases in the same proportion as the flow area, and consequently, the hydraulic radius remains nearly constant), the steepening tendency is counteracted and shock development is arrested. Mathematically, this condition is represented by a value of the rating exponent $\beta \cong 1$.

Fourth, there is a high-Froude-number flow. In hydraulically wide channels, high-Froude-number flows lack sufficient diffusion to effectively counteract the steepening tendency (Ponce and Simons 1977). Therefore, at high Froude numbers, at or above critical, the steepening tendency may be promoted to the point where the shock may develop because of this condition. Theoretically, as the Froude number for turbulent flow approaches the condition of neutral stability ($F_n = 1.5$ for Manning friction; $F_n = 2$ for Chezy friction), the shock becomes unstable and the theory ceases to apply. In practice, however, such high-Froude-number flows are rare in natural streams and rivers, and the instability is seldom, if ever, observed. However, in artificial and other channels of relatively smooth boundary, free-surface instability of the type discussed here leads to the well-known roll waves (Dressler 1949; Chow 1959; Jolly and Yevjevich 1971). These roll waves are often seen in steep city streets and similar situations where prevailing laminar (or mixed laminar-turbulent) flow conditions may reduce the neutral-stability Froude number to values well below that corresponding to turbulent flow

(to $F_n \cong 1$ for mixed laminar-turbulent flow; and to $F_n = 0.5$ for laminar flow).

The preceding four physical conditions contribute to shock development. When all of them occur at the same time, the shock is very likely to develop. If only one or two of them are present, the shock may not develop. While the kinematic shock has been interpreted differently by many authors [see for instance Cunge (1969) and Kibler and Woolhiser (1970)], there is no doubt that the shock is physical, and that it occurs under the proper set of highly selective circumstances. Unfortunately, adequate documentation of the occurrence of kinematic shocks in stream channels is lacking in the literature. Measurements are next to impossible, with sightings being all that diligent observers can settle for. The shock appears to be present in flash floods, with the related killer flood being a nefarious manifestation of the kinematic shock [see for instance Hjalmarson's account of the flood of July 26, 1982, in Tanque Verde Creek, east of Tucson, Arizona, in which the lives of eight unsuspecting bathers were claimed by what was in all likelihood a kinematic shock (Hjalmarson 1985)].

The conditions for kinematic shock development having been identified, the question remains as to whether the kinematic shock is as common in practice as calculations using an overland flow kinematic wave model would seem to indicate. For instance, the shock is a common occurrence in kinematic wave solutions using the method of characteristics. This is understandable, since this method solves the kinematic wave equation without introducing any numerical diffusion. A case in point: Kibler and Woolhiser (1970) used the method of characteristics to study the cascade of planes as a possible hydrologic model, and were able to derive a kinematic shock parameter as a function of geometric and frictional characteristics of two adjacent planes. However, in summarizing their findings, Kibler and Woolhiser stated: "While the kinematic shock may arise under certain highly selective physical circumstances, it is looked upon in this study as a property of the mathematical equations used to explore the overland flow problem rather than an observable feature of this hydrodynamic process."

The shock is a much less common occurrence in finite difference solutions, particularly when these feature a large numerical diffusion component. For instance, the shock is conspicuously absent from the convex method, which by fully offsetting its derivatives features a substantial amount of numerical diffusion (Ponce et al. 1979). Characteristic solutions intrinsically satisfy the aforementioned first condition; finite difference solutions usually do not. However, as shown by Ponce and Windingland (1985), the shock can indeed develop in finite difference solutions, particularly when the four conditions are met concurrently.

In practice, the shock is an uncommon occurrence in natural channels. In overland flow situations, the presence of shocks has been documented under highly selective circumstances, usually in connection with overland flow in long rectangular planes of constant slope (such as intense runoff on steep city streets and parking lots). Spatial rainfall nonuniformities and small topographic irregularities usually generate enough diffusion-like effects to counteract shock development. Therefore, the presence of the shock in a kinematic wave solution, more often than warranted (as in a characteristic solution), must be interpreted as the method's inability to properly account for flow and catchment irregularities. Moreover, the practitioners' preference

for kinematic wave finite difference solutions, where the shock is an uncommon occurrence (Alley and Smith 1982), does not come as a great surprise.

The resolution of this conflict appears to be in the proper description of runoff diffusion within the context of a kinematic wave solution sensu lato. Diffusion will effectively counteract the nonlinear steepening tendency which is at the root of shock development. Such an improved kinematic wave formulation should lead only to isolated instances of the shock's presence, and therefore be much more in agreement with physical reality.

Dynamic Extension to Kinematic Waves

Under the proper set of linearizing assumptions, kinematic wave theory can be extended to the realm of dynamic waves (Ponce 1990). Early work on this subject was done by Dooge (1973), who derived the expression for a dynamic hydraulic diffusivity ν_d for the case of a wide channel with Chezy friction

$$\nu_d = \frac{q}{2S_0}\left[1 - \frac{\mathsf{F}_0^2}{4}\right] \quad (9)$$

For overland flow, a general expression for the dynamic hydraulic diffusivity is

$$\nu_d = \frac{q}{2S_0}[1 - (m - 1)^2\mathsf{F}_0^2] \quad (10)$$

which reduces to Eq. 9 for $m = 3/2$.

For streamflow and channel flow, an expression for the dynamic hydraulic diffusivity is (Ponce 1986)

$$\nu_d = \frac{Q}{2TS_0}[1 - (\beta - 1)^2\mathsf{F}_0^2] \quad (11)$$

Since the hydraulic diffusivity vanishes at the condition of neutral stability, Eqs. 9–11 do account for dynamic wave behavior (Ponce and Simons 1977). This condition is characterized by the Vedernikov number $V = 1$. The Vedernikov number (Vedernikov 1945; Craya 1952; Chow 1959) is defined

$$V = (m - 1)\mathsf{F}_0 = (\beta - 1)\mathsf{F}_0 \quad (12)$$

Given Eqs. 10–12, the dynamic hydraulic diffusivity can be expressed in terms of the Vedernikov number as follows:

$$\nu_d = \frac{q}{2S_0}[1 - V^2] = \frac{Q}{2TS_0}[1 - V^2] \quad (13)$$

For $\beta = 1$ [i.e., a channel of rapidly expanding top width such that the wetted perimeter increases in the same proportion as the flow area (a channel of constant hydraulic radius)], Eq. 12 predicts that $V = 0$, and the dynamic hydraulic diffusivity (Eq. 13) reduces to the hydraulic diffusivity of Eq. 5. This confirms the practical observation that a kinematic shock does not occur

in a channel with a rating exponent $\beta \cong 1$.

Given Eq. 13, it is possible to extend kinematic wave theory to the realm of dynamic waves. A dynamic component can then be effectively incorporated into overland flow solutions while remaining within the same computational framework of kinematic wave solutions. The use of a dynamic (i.e., a Vedernikov-number-dependent) hydraulic diffusivity is bound to be more general than either kinematic or diffusion wave solutions, particularly in situations in which the Vedernikov number is substantially different from zero (for instance, for near-critical and supercritical inbank flows). However, its practicality when applied to overland flow problems remains to be determined by further work.

Summary and Conclusions

Kinematic and diffusion wave theories are reviewed prompted by the continuing controversy regarding their nature and applicability. Kinematic waves are shown to be nondiffusive but undergo change in shape during propagation due to nonlinearity. In overland flow and inbank streamflow this feature gives kinematic waves the capability of steepening, eventually leading to the formation of the kinematic shock. The kinematic shock is shown to be rare, and to occur only under a set of highly selective circumstances, including: (1) A kinematic wave proper; (2) a low base-to-peak flow ratio; (3) a hydraulically wide and sufficiently long channel; and (4) a high-Froude-number flow. The common occurrence of the kinematic shock in overland flow kinematic wave solutions, particularly when using the method of characteristics, is attributed to the total absence of runoff diffusion in these solutions. In practice, small flow and catchment irregularities usually produce enough diffusion-like effects to counteract the development of the shock.

Kinematic wave solutions using finite differences are shown to possess intrinsic amounts of numerical diffusion and dispersion, as a consequence of the finite grid size. These numerical effects are artificial, tending to disappear as the grid size is refined. In the limit, as the grid size approaches zero, the numerical effects vanish altogether. In practice, this means that overland flow kinematic wave solutions are grid dependent; that is, the results are a function of grid size, with a typical solution featuring appreciable amounts of numerical diffusion and dispersion.

Kinematic wave modeling can be improved by extending kinematic wave theory to the realm of diffusion waves. In this way, the diffusion inherent in many practical runoff computations can be accounted for directly in the modeling, rather than as an afterthought. In this regard, the Muskingum-Cunge method is particularly attractive, because while remaining within the computational framework of kinematic wave models, it has enough physical information to compare favorably with implicit numerical solutions of the diffusion wave equation. Unlike conventional finite difference kinematic wave models, the Muskingum-Cunge method is shown to be grid independent, further underscoring its usefulness as a practical model of diffusion waves.

The applicability of kinematic and diffusion waves is reviewed. It is concluded, echoing many past authors, that most overland flow situations would satisfy the kinematic wave criterion, and that most flood wave propagation cases in stream channels would satisfy the diffusion wave criterion. Only in situations with markedly strong dissipative tendencies or substantial down-

stream control would it be necessary to resort to the dynamic wave to properly describe the propagation of shallow water waves.

The issue of the choice between kinematic wave and unit hydrograph methods for practical runoff computations is examined with the aid of the concept of catchment scale. The use of the kinematic wave method is indicated primarily for small catchments [those less than 1 sq mi (2.5 km^2)], particularly in the cases in which it is possible to resolve the physical detail without compromising the deterministic nature of the model. The use of the unit hydrograph method is advocated for midsize catchments; i.e. those greater than 1 sq mi (2.5 km^2) but less than 400 sq mi (1,000 km^2), in which the kinematic wave method may prove difficult to implement. A case is made for the use of the kinematic wave as a tool for the development of synthetic unit hydrographs.

The dynamic extension to kinematic and diffusion wave theory is reviewed with a view to the future. The dynamic extension is shown to properly account for the dependence of the hydraulic diffusivity on the Vedernikov number, allowing the simulation to be responsive to the dynamic effect. This type of modeling would be particularly applicable to channel and flow conditions such that the Vedernikov number is substantially different from zero, for instance, for near-critical and supercritical inbank flows.

Appendix I. References

Abbott, M. B. (1976). "Computational hydraulics: A short pathology." *J. Hydr. Res.*, 14(4), 271–285.

Alley, W. M., and Smith, P. E. (1982). "Distributed routing rainfall-runoff model—version II: User's manual." *Open-File Report 82-344,* U.S. Geological Survey Water Resources Division, Gulf Coast Hydroscience Center, NSTL Station, Miss.

Chow, V. T. (1959). *Open-channel hydraulics.* McGraw Hill Book Co., Inc., New York, N.Y.

"Computer program for project formulation-hydrology." (1983). USDA Soil Conservation Service, *Tech. Release No. 20 (TR-20),* Washington, D.C.

Cunge, J. A. (1969). "On the subject of a flood propagation computation method (Muskingum method)." *J. Hydr. Res.*, 7(2), 205–230.

Crandall, S. H. (1956). *Engineering analysis: A survey of numerical procedures.* McGraw-Hill Book Co., New York, N.Y.

Craya, A. (1952). "The criterion for the possibility of roll wave formation." *Proc., Gravity Waves Symp., Circular 521,* U.S. National Bureau of Standards, Washington, D.C., 294–332.

Dawdy, D. R. (1990). Discussion of "Kinematic wave routing and computational error." *J. Hydr. Engrg.*, ASCE, 116(2), 278–280.

Design of small dams, 3rd ed. (1987). U.S. Bureau of Reclamation, Denver, Colo.

Dooge, J. C. I. (1973). "Linear theory of hydrologic systems." *Tech. Bulletin No. 1468,* USDA Agricultural Research Service, Washington, D.C.

Dressler, R. F. (1949). "Mathematical solution of the problem of roll waves in inclined open channels." *Communications in Pure and Appl. Mathematics,* 2, 149–194.

Flood studies report. (1975). Natural Environment Research Council, London, England, Vol. III.

Goldman, D. (1990). Discussion of "Kinematic wave routing and computational error." *J. Hydr. Engrg.*, ASCE, 116(2), 280–282.

Hayami, S. (1951). "On the propagation of flood waves." *Bulletin of the Disaster Prevention Research Institute,* Disaster Prevention Research Institute, Kyoto, Japan, 1(1), 1–16.

HEC-1, flood hydrograph package: Users' manual. (1985). U.S. Army Corps of Engineers, Hydrologic Engineering Center, Davis, Calif.

Hjalmarson, H. W. (1984). "Flash flood in Tanque Verde Creek, Tucson, Arizona," *J. Hydr. Engrg.*, 110(12), 1841–1852.

Hjelmfelt, A. T. (1984). "Negative outflows from Muskingum flood routing." *J. Hydr. Engrg.*, ASCE, 111(6), 1010–1014.

Hromadka, T. V., and DeVries, J. J. (1988). "Kinematic wave and computational error." *J. Hydr. Engrg.*, ASCE, 114(2), 207–217.

Hromadka, T. V., and DeVries, J. J. (1990). Closure of "Kinematic wave and computational error." *J. Hydr. Engrg.*, ASCE, 116(2), 288–289.

Jolly, P. J., and Yevjevich, V. (1971). "Amplification criterion of gradually varied, single peaked waves." *Hydrol. Paper No. 51,* Colorado State University, Fort Collins, Colo.

Kibler, D. F., and Woolhiser, D. A. (1970). "The kinematic cascade as a hydrologic model." *Hydrol. Paper No. 39,* Colorado State University, Fort Collins, Colo.

Leendertse, J. J. (1967). "Aspects of a computational model for long-period water wave propagation." *RM-5294-PR,* The Rand Corporation, Santa Monica, Calif.

Liggett, J. A. (1975). "Basic equations of unsteady flow." *Unsteady flow in open channels,* K. Mahmood and V. Yevjevich, eds., Water Resources Publications, Fort Collins, Colo., Vol. 1.

Lighthill, M. J., and Whitham, G. B. (1955). "On kinematic waves. I: Flood movement in long rivers." *Proc., Royal Society,* London, England, A229, 281–316.

Merkel, W. H. (1990). Discussion of "Kinematic wave routing and computational error." *J. Hydr. Engrg.*, ASCE, 116(2), 282–284.

Morris, E. M., and Woolhiser, D. A. (1980). "Unsteady one-dimensional flow over a plane: Partial equilibrium and recession hydrographs." *Water Resour. Res.*, 16(2), 355–360.

Overton, D. E. (1970). "Route or Convolute?" *Water Resour. Res.*, 6(1), 43–52.

Ponce, V. M., and Simons, D. B. (1977). "Shallow wave propagation in open channel flow." *J. Hydr. Div.*, ASCE, 103(12), 1461–1476.

Ponce, V. M., Li, R. M., and Simons, D. B. (1978). "Applicability of kinematic and diffusion models." *J. Hydr. Div.*, ASCE, 104(3), 353–360.

Ponce, V. M., and Yevjevich, V. (1978). "Muskingum-Cunge method with variable parameters." *J. Hydr. Div.*, ASCE, 104(12), 1663–1667.

Ponce, V. M., Chen, Y. H., and Simons, D. B. (1979). "Unconditional stability in convection computations." *J. Hydr. Div.*, ASCE, 105(9), 1079–1086.

Ponce, V. M., and Theurer, F. D. (1982). "Accuracy criteria in diffusion routing." *J. Hydr. Div.*, ASCE, 108(6), 747–757.

Ponce, V. M., and Windingland, D. (1985). "Kinematic shock: Sensitivity analysis." *J. Hydr. Engrg.*, ASCE, 111(4), 600–611.

Ponce, V. M. (1986). "Diffusion wave modeling of catchment dynamics." *J. Hydr. Engrg.*, ASCE, 112(8), 716–727.

Ponce, V. M. (1990). "Generalized diffusion wave model with inertial effects." *Water Resour. Res.*, 26(5), 1099–1101.

Sabol, G. V. (1987). "Development, use, and synthesis of S-graphs." *Proc., Engrg. Hydrol. Symp.*, ASCE, New York, N.Y., 627–632.

Sabol, G. V. (1990). "Maricopa County hydrology procedure." *Proc., Watershed Management Symp.*, ASCE, New York, N.Y., 423–431.

SCS national engineering handbook, section 4: Hydrology. (1985). USDA Soil Conservation Service, Washington, D.C.

Seddon, J. A. (1900). "River hydraulics." *Trans.*, ASCE, 43, 179–229.

Sherman, L. K. (1932). "Streamflow from rainfall by unit-graph method." *Engrg. News Record,* 108, April 7, 501–505.

Unkrich, C. L., and Woolhiser, D. A. (1990). Discussion of "Kinematic wave routing and computational error." *J. Hydr. Engrg.*, ASCE, 116(2), 284–286.

"Urban hydrology for Small Watersheds." (1986). *Tech. Release No. 55 (TR-55),* USDA Soil Conservation Service, Washington, D.C.

Vedernikov, V. V. (1945). "Conditions at the front of a translation wave distributing a steady motion of a real fluid." *Comptes Rendus (Doklady) de l'Academie des Sciences de l' U.R.S.S.*, (in French), 48(4).

Woolhiser, D. A., and Liggett, J. A. (1967). "Unsteady one-dimensional flow over

a plane—the rising hydrograph." *Water Resour. Res.*, 3(3), 753–771.
Woolhiser, D. A., and Goodrich, D. C. (1990). Discussion of "Kinematic wave routing and computational error." *J. Hydr. Engrg.*, ASCE, 116(2), 278–288.

Appendix II. Notation

The following symbols are used in this paper:

A = flow area;
a = coefficient of the unit-width-discharge-flow depth rating;
c = kinematic wave celerity;
d_0 = normal depth, Eq. 6; reference flow depth, Eq. 7;
F_0 = Froude number based on normal flow, Eq. 6; reference flow Froude number, Eq. 8;
F_n = neutral-stability Froude number;
g = gravitational acceleration;
i = effective rainfall intensity;
k = kinematic flow number, Eq. 6;
L = physical wavelength;
L_0 = length of the (overland flow) plane or channel;
m = exponent of the unit-width-discharge-flow depth rating;
Q = discharge;
q = unit-width discharge;
q_L = lateral inflow;
S_0 = bottom slope;
T = wave period in Eqs. 7 and 8, also, channel top width;
t = temporal variable;
u = mean velocity;
u_0 = reference flow mean velocity, Eq. 7;
V = Vedernikov number, Eq. 12;
x = spatial variable;
y = stage;
α = coefficient of the discharge-flow area rating;
β = exponent of the discharge-flow area rating;
Δt = temporal increment, or time step;
Δx = spatial increment, or space step;
ν = hydraulic diffusivity;
ν_d = dynamic hydraulic diffusivity, Eqs. 9, 10, 11, and 13; and
τ = dimensionless wave period, Eq. 7.

International Symposium on
Hydrology of Mountainous Areas
Shimla (INDIA) May 28-30, 1992

KINEMATIC WAVE MODELLING: WHERE DO WE GO FROM HERE?

VICTOR M. PONCE

Department of Civil Engineering, San Diego State University

San Diego, California 92182 USA

The kinematic wave model of surface water hydrology is reviewed with a look towards the future. The paper focuses on three areas of concern: (1) the applicability of kinematic waves, (2) the role of numerical diffusion in kinematic wave modelling, and (3) the nature of kinematic shock. A brief discussion on the role of the Vedernikov number in flood wave diffusion is included. The paper closes with an attempt to answer the question: Where do we go from here in kinematic wave modelling?

INTRODUCTION

The hydrology of surface waters in mountainous areas is characterized by steep slopes. Flow in steep channels is governed primarily by the gravitational and frictional forces (i.e., those associated with the channel bed slope S_o and friction slope S_f, respectively), and to a much lesser extent by the force originating in the flow depth gradient (i.e., the water surface slope minus the channel bed slope), or by the inertial force. The kinematic wave is a shallow water wave model that considers only the gravitational and frictional forces.

The theory of kinematic waves dates back to the middle 1950's (Lighthill and Whitham, 1955). In the last three decades, its application to overland flow and streamflow has gained considerable momentum (Wooding, 1965; Woolhiser and Liggett, 1967; Ponce and Simons, 1977; Hydrologic Engineering Center, 1990). There is a substantial body of knowledge on the kinematic wave, and papers continue to appear in the literature describing what the model can and cannot do (Hromadka and DeVries, 1988; Ponce, 1990a). There is, however, still some misunderstanding about the precise role that kinematic waves play in surface water hydrology.

Current areas of concern focus on the following issues: (1) Are kinematic waves applicable to mountain streams and well as to alluvial rivers? (2) Can the kinematic wave describe physical diffusion? If so, under what circumstances? (3) Under what conditions will the kinematic wave steepen to the point where it becomes a kinematic shock? This paper answers these as well as the following question: Given the current status of kinematic wave modelling, where do we go from here?

KINEMATIC WAVES

The kinematic wave can be defined in more than one way. First and foremost, a kinematic wave is a wave that transports mass, in contrast to the inertial or "gravity" wave of classical mechanics, which

transports energy. In flood hydrology, a kinematic wave is characterized by the existence of a *one-to-one* relationship between discharge and stage. In surface water hydrology, a kinematic wave is a shallow water wave that considers only the gravitational and frictional forces and neglects the forces arising from the flow depth gradient and inertia.

These definitions are all related. To put them in the proper perspective, we turn to Lighthill and Whitham (1955), who, in introducing the concept of kinematic wave, saw fit to subtitle their paper *Flood Movement in Long Rivers*. Flood waves transport mass; kinematic waves also transport mass. However, while flood waves are kinematic in nature, not all kinematic waves are flood waves. To clearly distinguish between flood waves and kinematic waves, we explore Lighthill and Whitham's subtitle a little further. What is a long river? Surely, they did not mean to imply that the kinematic wave could be used only for long rivers. If that is the case, the kinematic wave could not be applied to mountain streams, which are short compared to most alluvial rivers. We now know that kinematic waves apply to both "short" mountain streams as well as to "long" alluvial rivers.

The resolution of this conflict was made possible by the work of Ponce and Simons (1977), who identified the length parameter describing the applicability of kinematic waves. In fact, the latter is controlled, not by the "length" of the river, or by the length L of the shallow wave, by rather, by the dimensionless ratio L_o/L, where L_o is a reference channel length (a function of channel bed slope and frictional characteristics), defined as the length of channel in which the reference flow drops a head equal to its depth: $L_o = d_o/S_o$, with d_o= reference flow depth, and S_o= channel bed slope. According to Ponce and Simons (1977), a wave is kinematic if the dimensionless wave number $\sigma = (2\pi/L)L_o$ is sufficiently small. For a given Froude number F_o [$F_o = u_o/(gd_o)^{1/2}$, in which u_o= mean flow velocity and g= gravitational acceleration], the smaller the value of σ, the more kinematic the wave is. Therefore, it is neither L_o nor L that determines whether a wave is kinematic, but rather their ratio L_o/L.

The concept of reference channel length L_o is clear, provided a value of reference flow depth can be established, which is usually the case. The same cannot be said for the wavelength L, which needs to be converted to the temporal domain if it is going to be of any practical use in hydrology. (Understandably, hydrologists are reluctant to relate to the concept of flood wavelength, and prefer instead to describe flood waves in terms of flood and/or stage hydrographs). Since $L = cT$, where c is the wave celerity and T is the wave period, the ratio L_o/L can be expressed as: $L_o/L = d_o/(S_o cT)$. We use Seddon's law (Seddon, 1900; Chow, 1959) to express the kinematic wave celerity c in terms of the mean flow velocity: $c = (3/2)u_o$, applicable to Chezy friction in wide channels. Therefore, the ratio L_o/L can be expressed as: $L_o/L = (2/3)d_o/(TS_o u_o)$. Furthermore, assuming that the flood wave period T (a concept foreign to flood hydrologists) can be expressed in terms of the more familiar flood wave time-of-rise t_r, say $T = 2t_r$, then: $L_o/L = (1/3)d_o/(t_r S_o u_o)$.

While t_r and S_o tend to vary within a broad range in nature, d_o and u_o are usually restricted within a narrow range. In fact, the flood wave time-of-rise t_r can be as short as 5 to 15 minutes in small steep catchments, and as long as 3 to 6 months in large mild-relief catchments. (To give an extreme example, the time-of-rise of the Upper Paraguay river at Porto Murtinho, Brazil, is approximately 6 months). The channel bed slope S_o typically varies between S_o= 0.1 (or steeper) in mountain stream situations, and S_o= 0.00001 in some deltaic and tidal settings. Thus, in general, the ratio L_o/L is inversely related to the product $t_r S_o$. It is this latter product that determines whether a kinematic wave is applicable: For a given Froude number, the larger the product $t_r S_o$ (and therefore, the smaller the ratio L_o/L), the more kinematic the wave is.

In light of the preceding considerations, the meaning of Lighthill and Whitham's subtitle *Flood Movement in Long Rivers* is now fully elucidated: The adjective "long" should be construed as referring to a large $t_r S_o$ product. This implies that either t_r or S_o, or both, should be large. Experience reveals that Mother Nature has contrived not to make these two parameters large simultaneously. Either the time-of-rise t_r is long (as in the case of a large mild-relief catchment), or the channel bed slope S_o is steep (as in the case of a mountain stream, or alternatively, steep overland flow), but usually not at the same time. This behavior confirms the wide range of field situations in which the kinematic wave is applicable: for *both* steep and mild catchments, and *both* fast-rising and slow-rising hydrographs, provided the product $t_r S_o$ is sufficiently large.

Ponce et al (1978) developed a criterion for the applicability of kinematic waves, and subsequently modified it for practical applications (Ponce, 1989). The criterion states that for a shallow water wave (whether flood wave or overland flow wave) to be kinematic, it should satisfy the following dimensionless inequality: $N = t_r S_o (u_o/d_o) > 85$. The larger the value of N, the more kinematic the wave is. For instance, if $t_r = 6$ h, $S_o = 0.01$, mean velocity $u_o = 2$ ms^{-1}, and flow depth $d_o = 1$ m, it follows that $N = 432 > 85$, confirming that this wave is kinematic. According to our definitions, this wave will have the following properties: (a) it will transport mass, (b) it will not diffuse appreciably, (c) it will describe a one-to-one relationship between discharge and stage at any cross-section, and (d) the forces arising from the flow depth gradient and inertia will be so small so as to be negligible compared to the gravitational and frictional forces.

DIFFUSION WAVES

The specification of a one-to-one relationship between discharge and stage, a key trait of the kinematic wave, imposes a significant physical and mathematical constraint: The wave cannot diffuse; i.e., it can travel downstream and transport mass in the process, but it cannot dissipate (i.e., spread in space and time) its discharge or stage. This limitation of the kinematic wave is grounded in the mathematics: The neglect of the flow depth gradient and inertia terms results in a first-order partial differential equation governing the motion. This equation cannot describe diffusion, since diffusion is a second-order process. From a physical perspective, the one-to-one stage-discharge relationship implies that wave diffusion is clearly out of the picture, since wave diffusion is caused by the presence of a loop (however small!) in the stage-discharge rating.

Since in nature there exist shallow water waves which do diffuse--although in small amounts--the theory of kinematic waves is incomplete without a means of incorporating this important diffusion mechanism. Lighthill and Whitham (1955) clearly saw this when they suggested the extension of kinematic waves to the realm of *diffusion waves*, i.e. of kinematic waves that incorporate a small amount of diffusion. To accomplish this, the mathematics of kinematic waves is modified to include the flow-depth gradient term, while still excluding the inertia terms. This significant extension allows the description of looped stage-discharge ratings, and consequently, of the diffusion of kinematic waves, properly now, *diffusion waves*. To put it in a nutshell: diffusion waves are still kinematic in nature; they still transport mass; however, unlike kinematic waves, diffusion waves have the capability to undergo small amounts of *physical* diffusion.

This physical diffusion is confirmed by theory and experience: As long as the flow depth gradient is not negligible, it will produce a looped stage-discharge rating for every shallow wave, which will in turn cause the wave in question to dissipate as it travels downstream. In practice, as the channel bed

slope S_o decreases (as the flow moves from mountain streams to alluvial rivers), the friction slope S_f decreases accordingly (as channel roughness typically decreases in a downstream direction), and the flow depth gradient becomes increasingly too important to be disregarded. Intuitively, while kinematic waves are seen to apply to mountain streams, diffusion waves are seen to apply to valley streams and alluvial rivers. A rule of thumb, validated by experience, says that if the channel bed slope is greater than 1 percent ($S_o > 0.01$), the wave is most likely to be kinematic (and to feature a one-to-one relationship between discharge and stage, and not diffuse appreciably). If the channel bed slope is less than 1 percent, the wave may not be kinematic; it may be a diffusion wave. If so, it will feature a looped stage-discharge rating and show a small but appreciable amount of diffusion.

Ponce (1989) has presented a practical criterion for the applicability of diffusion waves. The criterion states that for a shallow wave (whether flood wave or overland flow wave) to be a diffusion wave, the following dimensionless inequality should be satisfied: $M = t_r S_o (g/d_o)^{1/2} > 15$. For instance, if $t_r = 6$ h, $S_o = 0.001$, and flow depth $d_o = 1$ m, it follows that $M = 67.6 > 15$, confirming that this wave is a diffusion wave. According to our definitions, this wave will have the following properties: (a) it will transport mass, like the kinematic wave; (b) it will diffuse appreciably, unlike the kinematic wave; (c) it will describe a looped stage-discharge relationship at any cross-section, and (d) the force arising from the flow depth gradient can no longer be neglected.

It should be noted that in the example of the previous section, had the channel bed slope been $S_o = 0.001$, then $N = 43.2$, and the wave would not have qualified as a kinematic wave. However, in the example of this section, if the slope is $S_o = 0.01$ instead, then $M = 676$, and the wave would still qualify as a diffusion wave. It is concluded that while the kinematic wave model *does not apply* to diffusion waves, the diffusion wave model *does apply* to kinematic waves. In other words, the theory of diffusion waves (represented by the diffusion wave equation) can properly describe *both* kinematic and diffusion waves. The converse does not hold true: The theory of kinematic waves (represented by the kinematic wave equation) is limited only to kinematic waves and cannot describe diffusion waves.

DYNAMIC WAVES

At this point, we leave Lighthill and Whitham and their concept of kinematic/diffusion waves and approach the problem of shallow water wave propagation in its most general form, i.e., by considering the "dynamic" wave, that which, in addition to gravitational, frictional and flow-depth gradient forces, also includes the inertial force. This leads us to a set of two partial differential equations of continuity and motion, also referred to as the "Saint Venant equations."

Before we give up on theory and resort to our computer models, branding the often-repeated dictum "There is no known analytical solution of the Saint Venant equations," it is worthwhile to reckon the existence of a number of incomplete yet illuminating analytical solutions which are scattered throughout the literature (Lighthill and Whitham, 1955; Dooge, 1973; Ponce and Simons, 1977). In particular, the linear solution of Ponce and Simons is significant because it gives us great insight into the behavior of shallow water waves, including kinematic, diffusion, dynamic, and inertial waves.

The work of Ponce and Simons (1977) can be summarized in the following statements:

1. The dynamic wave lies towards the middle of the dimensionless wave number spectrum ($10^0 < \sigma < 10^2$), while kinematic/diffusion waves lie to the left ($10^{-2} < \sigma < 10^0$), and inertial waves to the right ($10^1 < \sigma < 10^4$).

2. In the stable flow regime (Vedernikov number $V < 1$, Chow, 1959; Ponce, 1990), the dynamic wave shows very strong diffusive tendencies.
3. At the threshold of flow instability ($V = 1$), the Seddon and Lagrange speeds (Chow, 1959) are the same, and kinematic, dynamic, and inertial waves have the same celerity and lack diffusion.
4. In the unstable flow regime ($V > 1$), kinematic, dynamic, and inertial waves have a tendency to amplify during propagation.

The findings of Ponce and Simons (1977) pose an interesting theoretical question which helps place the nature of shallow water waves in the proper perspective. Granted that kinematic waves (and by extension, diffusion waves), lying to the left of the σ spectrum, transport mass. This is an intuitive conclusion which cannot be challenged. On the other hand, the inertial wave, the so-called "gravity" wave of classical mechanics, lying to the right of the σ spectrum, transports energy. What, then, do dynamic waves transport, since they lie towards the middle of the wave number spectrum? Mass, or energy? It stands to logic that the answer is: both. Therein lies the reason for the markedly strong dissipative tendencies of the dynamic wave: Shallow water waves can transport mass and energy simultaneously *only* at the expense of wave diffusion. In the stable flow regime ($V < 1$), the more dynamic a wave is, the more strongly dissipative it is (Ponce et al, 1978). At the threshold of flow instability ($V = 1$), dynamic waves lose their ability to dissipate, and their properties coalesce with those of kinematic and inertial waves.

The preceding discussion raises a practical question which has been in the minds of many researchers and practitioners who have dealt with the dynamic wave. If the dynamic wave is so strongly dissipative in most cases of practical interest, is it worth attempting to compute it? Would it not dissipate shortly after it is generated, with its mass going to join the underlying larger, kinematic/diffusion, wave? Or, can it be tracked downstream as it propagates? If so, what is its characteristic speed? A more practical question is: If the dynamic wave is so strongly dissipative, could it be properly construed as a flood wave? These questions continue to trouble those who use the dynamic wave. Lighthill and Whitham (1955) put it in a nutshell when they stated (op. cit., p. 293): "Under the conditions appropriate for flood waves... the dynamic waves rapidly become negligible, and it is the kinematic waves, following at lower speed, which assume the dominant role."

In summary, dynamic waves *do not apply* to floods in mountain streams. Attempts to do this will be futile, given the accumulated body of theoretical and practical experience pointing otherwise. There is still the unresolved question of whether dynamic waves apply to the routing of flood waves in any physically realistic setting. Dam-break flood waves notwithstanding, perhaps the only clear statement that can be made today is that the dynamic wave applies to tidal flow and similar such situations where there is a significant downstream control of the flow.

PHYSICAL VS NUMERICAL DIFFUSION

If kinematic waves cannot diffuse, why is it that numerical models of kinematic waves are able to show some wave diffusion? The resolution of this paradox lies in the conversion of a partial differential equation into a finite difference equation. This conversion can only be done at the expense of introducing an error. This error is a function of the grid size (Δx and Δt) and tends to disappear as the grid size is progressively refined. In flood routing, the error that creeps into a typical computation using finite differences manifests itself as *numerical diffusion* and *numerical dispersion* effects.

These effects are the direct result of specifying a discrete space-time domain, and are not necessarily related to the physical diffusion and dispersion which are inherent in the nature of flood waves.

Numerical diffusion arises because the calculated wave amplitude is smaller than the physical wave amplitude. Numerical dispersion arises when the calculated wave celerity is different from the physical wave celerity. In conventional finite difference (F.D.) shallow water wave models, the aim is to minimize numerical diffusion and dispersion by choosing a grid size sufficiently small to drive these errors to inconsequential amounts. Then, the convection and diffusion of the shallow water wave can be properly described by the numerical model.

Unfortunately, not all F.D. kinematic wave models have sought to minimize numerical diffusion and dispersion. Often, a F.D. kinematic wave model has inadvertedly used the numerical diffusion as a way of showing a certain amount of "physically realistic" diffusion in the calculated results (Li et al, 1975; Curtis et al, 1978). A detailed treatment of this subject is out of the scope of this paper. The interested reader is referred to the paper by Ponce et al (1979), which treats the various numerical schemes of the convection-diffusion equation (of which the kinematic wave equation is a special type), and their numerical diffusion/dispersion effects (amplitude and phase portraits). For our present purpose, we quote Cunge (1969) in stating that finite difference schemes of the kinematic wave equation introduce varying amounts of numerical diffusion and dispersion. The latter interfere with the physical effects, modifying them (Abbott, 1976; Ponce, 1990a). Thus, a finite difference kinematic wave model may be able to show some diffusion, the actual amount being a function of the grid size and weighting factors (used in discretizing the terms of the kinematic wave equation). The fact that this diffusion is artificial and intrinsically related to the grid size can be readily demonstrated by solving the same problem several times, each time halving the spatial increment Δx and temporal increment Δt. Carried to the practical limit, this test leads to the eventual disappearance of the numerical diffusion in question, with the result approaching the analytical solution of the kinematic wave, which is nondiffusive.

We are now in a quandary! If we solve the kinematic wave *properly*, achieving the complete elimination of numerical diffusion and dispersion, we can only hope to describe kinematic waves, but not diffusion waves; if the problem does have some physical diffusion, the latter would be entirely missing from this approach. Conversely, if we solve the kinematic wave *improperly*, introducing numerical diffusion and dispersion by our choice of grid size, there is no guarantee that these will be related to the diffusion and dispersion, if any, of the physical problem. Any arbitrary choice of grid size will cause some numerical diffusion and/or dispersion, and since the latter are unrelated to the physical problem, the solution degrades accordingly, from deterministic to *conceptual*. It would be hit and miss, as far as the accurate reproduction of wave properties is concerned.

Fortunately, there is a way out of this difficulty. As shown by Cunge (1969), and subsequently by others (Natural Environment Research Council, 1975; Ponce and Yevjevich, 1979; Ponce, 1989), the numerical diffusion and dispersion of F.D. kinematic wave models *can* be managed! There is a way to optimize the numerical diffusion while minimizing the numerical dispersion, to make the method--and its inherent errors--work for us instead of against us! By a careful match of the numerical diffusion with the physical diffusion, the F.D. kinematic wave model can reproduce *both* kinematic and diffusion waves, in a methodology that has been referred to as the Muskingum-Cunge (M-C) method.

In a nutshell, the M-C method is a variant of the Muskingum method of flood routing in which the parameters K and X are calculated directly, based on hydraulic data (channel friction, bed slope, and

cross-sectional characteristics), instead of indirectly, based on the conventional hydrologic data (storage-weighted flow relations). The M-C method was first applied to open channel flow, and later to overland flow (Ponce, 1986). Extensive tests have shown that the method holds promise for overland flow, since unlike conventional finite difference kinematic wave models, the M-C model is essentially grid independent. In other words, the solution does not depend on the choice of grid size (Ponce, 1986).

In summary, a conventional F. D. kinematic wave model will diffuse numerically, with the diffusion being dependent on the choice of grid size. If the grid size is refined to eliminate the numerical diffusion, no physical diffusion (if present) can be simulated. If the grid size is not refined, the amount of numerical diffusion is arbitrary and not related to the physical diffusion (if any), and the model degrades into a conceptual status. If the M-C method is used, the numerical diffusion is matched with the physical diffusion; consequently, the result is independent of the grid size, and thus, the deterministic character of the method is preserved.

KINEMATIC SHOCK

Kinematic waves lack physical diffusion. However, kinematic waves are nonlinear (or rather, quasilinear), a property which gives them the inherent tendency to change their shape upon propagation: either steepen or flatten, depending on the stage relative to the channel cross-section (flow inbank or out-of-bank). Under the right set of circumstances, a kinematic flood wave can steepen to the point where it becomes for all practical purposes a "wall of water." (In overland flow situations, the "wall of water" would be a small discontinuity in the water surface profile). This is the *kinematic shock,* i.e., a kinematic wave that has steepened upon propagation to the point of being nearly discontinuous.

Contrary to conventional wisdom (Kibler and Woolhiser, 1970; Cunge, 1969), there is no physical unreality about the kinematic shock. If the steepening tendency is allowed to continue unchecked, the kinematic shock *will form* in due time. Diffusion, however, acts to counteract the steepening tendency. Therefore, in cases where diffusion, either physical or numerical, is present, the development of the kinematic shock is likely to be arrested. This explains the pervasive presence of kinematic shocks in analytical solutions of the kinematic wave, which have no diffusion, numerical or otherwise. On the other hand, kinematic shocks are shown to be conspicuously absent from finite difference kinematic wave models, particularly from those that have appreciable amounts of built-in numerical diffusion.

Ponce and Windingland (1985) have clarified the conditions under which the kinematic shock is likely to develop. Based on theoretical considerations supported by extensive numerical experiments, they established the following conditions for kinematic shock development:

1. The wave must be kinematic, i.e., it must have negligible physical diffusion. Diffusion tends to counteract the development of the shock.
2. The ratio of base-to-peak flow Q_b/Q_p must be small, with zero as the lower limit, such as in the case of an ephemeral stream (recall the flash floods occurring on dry beds).
3. The channel is (a) hydraulically wide, i.e., of nearly constant wetted perimeter, to allow the wave steepening to progress unchecked by the cross-sectional shape; and (b) sufficiently long to allow enough time for the shock to develop.

4. The flow is at high Froude number, within the stable flow regime ($V < 1$). The higher the Froude number within the stable flow regime, the smaller the physical diffusion, and the more likely the shock can continue to develop unchecked. In the limit, as the Vedernikov number approaches 1 (and the Froude number approaches 2, for hydraulically wide channels with Chezy friction), diffusion vanishes as the flow reaches the threshold of instability.

In practice, all four conditions may prevail at the same time in a given situation. Whether a kinematic shock will form will depend on the strength of any one condition, or, if more than one is present, on their combined strength. For instance, an analytical solution of the kinematic wave in an overland flow plane satisfies conditions 1 and 3 (a), and maybe even 3 (b) if the plane is long enough. The case of a flash flood in an ephemeral stream in an arid or semiarid region satisfies condition 2, and probably even 3 (a), 3 (b), and 4. The fact that kinematic shocks are not a common sight in nature points to the practical difficulty of satisfying all of these conditions.

Condition 1 is satisfied in channels where the product $t_r S_o$ is large. Condition 2 is satisfied in ephemeral streams. Condition 3 (a) is satisfied in inbank flow in wide rectangular channels, but not if the flow goes overbank, since in this case the wetted perimeter would cease to be nearly constant. Condition 3 (b) is dependent of the catchment's physiography, geology, and drainage density. The longer a stream, uninterrupted by lateral inflow at tributary confluences, the better the chances for the shock to develop. Condition 4 is dependent on the channel aspect ratio, boundary friction, and presence or absence of riparian vegetation. In this regard, we echo Jarrett (1984) in reminding the reader that Mother Nature does not like high-Froude-number flows! So condition 4 is more likely to be the exception rather than the rule.

In closing, it should be noted that kinematic shocks, particularly those associated with flash floods, are very difficult to document precisely, given the obvious likelihood of bodily harm and possibly even death for those daring enough to attempt it. For the conditions prevalent in mountainous areas, kinematic shocks (and flash floods) would be associated with one or more of the following: (1) intense cloud bursts, (2) an arid or semiarid region, (3) a steep ephemeral stream, (4) a low-friction channel (in both bed and banks), and (5) a catchment of low drainage density.

ROLE OF THE VEDERNIKOV NUMBER IN FLOOD WAVE DIFFUSION

As pointed out by Hayami (1951) in his classical paper on diffusion waves, the hydraulic diffusivity is the physical parameter controlling the diffusion of diffusion waves. The hydraulic diffusivity is: $\nu = q_o/(2S_o)$, in which q_o= reference unit-width discharge, and S_o= channel bed slope. Therefore, the amount of diffusion that a flood wave undergoes during propagation is directly proportional to the unit-width discharge and inversely proportional to the channel bed slope. In other words, the steeper the channel bed slope, the lesser the amount of flood wave diffusion. In the limit, as the channel bed slope increases, the diffusion disappears and the flood wave becomes a kinematic wave.

Hayami's hydraulic diffusivity is properly a *kinematic* hydraulic diffusivity [$\nu_k = q_o/(2S_o)$], because it lacks inertia altogether. It is strictly applicable to flow well within the stable regime, i.e., for small Vedernikov numbers, in the range $0 < V < 0.25$ ($0 < F_o < 0.5$, for hydraulically wide channels with Chezy friction). By including inertia in the formulation, Dooge (1973) and Dooge et al (1982) have extended the concept of hydraulic diffusivity to the realm of dynamic waves. This leads to the concept of *dynamic* hydraulic diffusivity: $\nu_d = (1 - V^2)\, q_o/(2S_o)$ (Ponce, 1990a; 1990b).

It is seen that unlike its kinematic counterpart, the dynamic hydraulic diffusivity is also a function of the Vedernikov number. As the Vedernikov number approaches 0 (in the case of low-Froude-number flows), ν_d reduces to ν_k. Conversely, as the Vedernikov number approaches 1 ($V = 1$ is the threshold of flow instability), ν_d reduces to 0, and wave diffusion vanishes (obviously, a process which could not be simulated with ν_k). It is seen that ν_d applies through a wider range of flow conditions than ν_k (in the range $0 < V < 1$) . Since ν_d does not significantly complicate the expression for hydraulic diffusivity, it should be the preferred way of modelling flood wave diffusion. In practice, since wave diffusion is usually small (most flood waves are diffusion waves!), the dynamic contribution to wave diffusion turns out to be also small.

The inclusion of the Vedernikov number in the expression for hydraulic diffusivity has the advantage that it can also account for channels of arbitrary cross-sectional shape, i.e., those other than hydraulically wide. Taken to the limit, i.e., for the inherently stable channel (Ponce, 1990b), $V = 0$, regardless of Froude number, and the kinematic and dynamic hydraulic diffusivities are one and the same. It is seen that in this case, the flood wave attenuation is governed by the kinematic hydraulic diffusivity, for all values of discharge or stage.

WHERE DO WE GO FROM HERE?

Having reviewed the status of kinematic waves, it is only fitting that we now take a stab at the question: Where do we go from here? We know very well that kinematic waves are useful tools in applied hydrology. They describe the flow in steep streams (recall the theme of this symposium: *The Hydrology of Mountainous Areas*), and they do it very well. With the applicability issue now clearly settled, there is no doubt that kinematic waves will continue to be used in the future. In fact, when the extension is made to diffusion waves, the applicability issue is no longer a serious roadblock. In this the last decade of the century, the burden of proof is seen to be slowly shifting to the dynamic wave. The dynamic wave has yet to show, beyond reasonable doubt, that in most cases of practical interest, *it is there* for us to calculate it.

Caution should be exercised when applying the kinematic wave to overland flow and streamflow in the context of a numerical computer model, now that we know that numerical diffusion is likely to creep in and degrade the accuracy of the computation. In this regard, the method of matched diffusivities (M-C method) holds particular promise, given its demonstrated grid independent for a wide range of grid sizes. The M-C method is an analog of the diffusion wave model, and therefore, can be used to solve for *both* kinematic and diffusion waves. Furthermore, when the dynamic hydraulic diffusivity is used in lieu of its kinematic counterpart, the method can account for most of the wave dynamics, including the Vedernikov number and its effect on cross-sectional shape and boundary friction.

More research is needed into the nature of kinematic shock and its relevance to the modelling of flash floods. Given that the conditions under which these shocks develop have now been clearly identified, the following question is posed: Can a hazard rating be established for flash floods, in terms of regional climate, catchment geology, physiography, and drainage density, and channel slope, friction, and cross-sectional shape? This question is in need of immediate attention if we are going to apply the theory of kinematic waves to guarantee the safety of the populations that are currently at risk all over the world.

REFERENCES

1. Abbott, M. B., (1976), "Computational hydraulics: A short pathology," *J. Hydr. Res.*, Vol. 14, No. 4, pp. 271-285.
2. Chow, V. T., (1959), *Open-Channel Hydraulics*, McGraw-Hill, New York.
3. Cunge, J. A., (1969), "On the subject of a flood propagation computation method (Muskingum method)," *J. Hydr. Res.*, Vol. 7, No. 2, pp. 205-230.
4. Curtis, D. C., R. L. Mitchell, and J. C. Schaake, Jr., (1978), "A deterministic runoff model for use in flash flood planning," *Conf. of Flash Floods: Hydrometeorological Aspects, American Meteorological Society*, May 2-3, Los Angeles, Calif.
5. Dooge, J. C. I., (1973), "Linear theory of hydrologic systems," *Tech. Bull. 1468,* 327 pp., U.S. Dept. of Agric., Washington, D. C..
6. Dooge, J. C. I., W. B. Strupczewski, and J. J. Napiorkowski, (1982), "Hydrodynamic derivation of storage parameters in the Muskingum model," *J. Hydrol.,* Vol. 54, pp. 371-387.
7. Hayami, S., (1951), "On the propagation of flood waves," *Bull. Disaster Prev. Res. Inst. Kyoto Univ.,* Vol. 1, pp. 1-16.
8. Hromadka, T. V., and J. J. DeVries, (1988), "Kinematic wave and computational error," *J. Hydraul. Eng.*, Vol. 116, No. 2, pp. 207-217.
9. Hydrologic Engineering Center, U.S. Army Corps of Engineers, (1990), HEC-1, *Flood Hydrograph Package, User's Manual,* Version 4.0, Sept.
10. Jarrett, R. D., (1984), "Hydraulics of high-gradient streams," *J. Hydraul. Eng.,* Vol. 110, No. 11, pp. 1519-1539.
11. Kibler, D. F., and D. A. Woolhiser, (1970), "The kinematic cascade as a hydrologic model," *Hydrol. Paper No. 39*, Colorado State Univ., Ft. Collins, 1970.
12. Li, R. M., D. B. Simons, and M. A. Stevens, (1975), "Nonlinear kinematic wave approximation for water routing," *Water Resourc. Res.*, Vol. 11, No. 2, pp. 245-252.
13. Lighthill, M. J., and G. B. Whitham, (1955), "On kinematic waves. I. Flood movement in long rivers," *Proc. R. Soc. London, Ser. A.,* Vol. 229, pp. 281-316.
14. Natural Environment Research Council, (1975), *Flood Studies Report, Vol. III: Flood Routing Studies*, London, England.
15. Ponce, V. M., (1986), "Diffusion wave modelling of catchment dynamics," *J. Hydraul. Eng.,* Vol. 112, No. 8, pp. 716-727.
16. Ponce, V. M., (1989), *Engineering Hydrology: Principles and Practices*, Prentice Hall, Englewood Cliffs, New Jersey.
17. Ponce, V. M., (1990a), "The kinematic wave controversy," *J. Hydraul. Eng.,* Vol. 117, No. 4, pp. 511-525.
18. Ponce, V. M., (1990b), "New perspective on the Vedernikov number," *Water Resour. Res.,* Vol. 27, No. 7, pp. 1777-1779.

19. Ponce, V. M., and D. B. Simons, (1977), "Shallow wave propagation in open channel flow," *J. Hydraul. Div. Am. Soc. Civ. Eng.*, Vol. 103, No. HY12, pp. 1461-1476.

20. Ponce, V. M., and D. Windingland, (1985), "Kinematic shock: Sensitivity analysis," *J. Hydraul. Eng.*, Vol. 111, No. 4, pp. 600-611.

21. Ponce, V. M., and V. Yevjevich, (1978), "Muskingum-Cunge method with variable parameters," *J. Hydraul. Div. Am. Soc. Civ. Eng.*, Vol. 104, No. HY12, pp. 1663-1667.

22. Ponce, V. M., Y. H. Chen, and D. B. Simons, (1979), "Unconditional stability in convection computations," *J. Hydraul. Div. Am. Soc. Civ. Eng.*, Vol. 105, No. HY9, pp. 1079-1086.

23. Ponce, V. M., R. M. Li, and D. B. Simons, (1978), "Applicability of kinematic and diffusion models," *J. Hydraul. Div. Am. Soc. Civ. Eng.*, Vol. 104, No. HY3, pp. 353-360.

24. Seddon, J. A., (1900), "River Hydraulics," *Trans., Am. Soc. Civ. Eng.*, Vol. 43, pp. 179-229.

25. Wooding, R. A., (1965), "A hydraulic model for the catchment-stream problem, " *J. Hydrol.*, Vol. 3, pp. 254-267.

26. Woolhiser, D. A., and J. A. Liggett, (1967), "Unsteady one-dimensional flow over a plane--the rising hydrograph," *Water Resour. Res.*, Vol. 3, No. 3, pp. 753-771.

Two-Dimensional Water Flood and Mudflow Simulation

By J. S. O'Brien,[1] P. Y. Julien,[2] and W. T. Fullerton,[3] Members, ASCE

Abstract: FLO-2D is a two-dimensional finite difference model that simulates clear-water flood hazards, mudflows, and debris flows on alluvial fans and urban floodplains. Interactive flood or mudflow routing between channel, street, and floodplain flow is performed using a uniform grid system to describe complex floodplain topography. A quadratic rheological model, developed from field and laboratory mudflow data, enables appropriate simulations of flooding conditions ranging from clear water to hyperconcentrated sediment flows. Computer-aided design (CAD) graphics of predicted time-sequenced flood depths automates the delineation of flood hazards. Replication of the 1983 Rudd Creek mudflow in Utah demonstrates the capability of the model.

Introduction

Most flood hazard studies, and particularly those on alluvial fans, are conducted in urban development areas. The extent of urban flooding is generally defined by considering a variety of flow conditions, including flow through subdivisions, street flow, and culvert or flood channel discharge. Conventional one-dimensional hydraulic models, such as the U.S. Army Corps of Engineers HEC-2 model, require the interpretation of overbank flood boundaries between cross sections that may extend through urban areas. Flood elevations and areas of inundation are difficult to interpret for locations where floodplain storage, flood attenuation, flow around buildings, or flow in streets is significant.

Flood hazards on alluvial fans are presently delineated with a simplistic probabilistic model adopted by the Federal Emergency Management Agency (FEMA) (*FAN*, 1990). Since the FEMA method doesn't simulate flood hydrographs, it is inappropriate for the design of flood mitigation structures such as levees, flood containment walls and flood channels. It is also inappropriate for flooding in urban areas, as well as for analyzing mud and debris flow hazards.

Previous attempts to simulate debris flows were accomplished with one-dimensional flow-routing models. DeLeon and Jeppson (1982) modeled laminar water flows with enhanced friction factors. Spatially varied and steady-state Newtonian flow was assumed, and flow stoppage could not be simulated. Schamber and MacArthur (1985) designed a one-dimensional finite element model for mudflows using the Bingham rheological model to evaluate the shear stresses of a nonNewtonian fluid. O'Brien (1986) designed a one-dimensional mudflow model for watershed channels that also utilized the Bingham model.

In 1986, MacArthur and Schamber presented two-dimensional finite element model for application to simplified overland topography. The fluid properties were considered to be those of a Bingham fluid, whose static

[1]Prin., FLO Engrg., Inc., P.O. Box 1659, Breckenridge, CO 80424.
[2]Assoc. Prof., Dept. of Civ. Engrg., Colorado State Univ., Fort Collins, CO 80523.
[3]Pres., FLO Engrg., Inc., P.O. Box 1659, Breckenridge, CO 80424.

Note. Discussion open until July 1, 1993. To extend the closing date one month, a written request must be filed with the ASCE Manager of Journals. The manuscript for this paper was submitted for review and possible publication on August 27, 1992. This paper is part of the ***Journal of Hydraulic Engineering***, Vol. 119, No. 2, February, 1993. ©ASCE, ISSN 0733-9429/93/0002-0244/$1.00 + $.15 per page. Paper No. 1965.

Two-Dimensional Water Flood and Mudflow Simulation

By J. S. O'Brien,[1] P. Y. Julien,[2] and W. T. Fullerton,[3] Members, ASCE

Abstract: FLO-2D is a two-dimensional finite difference model that simulates clear-water flood hazards, mudflows, and debris flows on alluvial fans and urban floodplains. Interactive flood or mudflow routing between channel, street, and floodplain flow is performed using a uniform grid system to describe complex floodplain topography. A quadratic rheological model, developed from field and laboratory mudflow data, enables appropriate simulations of flooding conditions ranging from clear water to hyperconcentrated sediment flows. Computer-aided design (CAD) graphics of predicted time-sequenced flood depths automates the delineation of flood hazards. Replication of the 1983 Rudd Creek mudflow in Utah demonstrates the capability of the model.

Introduction

Most flood hazard studies, and particularly those on alluvial fans, are conducted in urban development areas. The extent of urban flooding is generally defined by considering a variety of flow conditions, including flow through subdivisions, street flow, and culvert or flood channel discharge. Conventional one-dimensional hydraulic models, such as the U.S. Army Corps of Engineers HEC-2 model, require the interpretation of overbank flood boundaries between cross sections that may extend through urban areas. Flood elevations and areas of inundation are difficult to interpret for locations where floodplain storage, flood attenuation, flow around buildings, or flow in streets is significant.

Flood hazards on alluvial fans are presently delineated with a simplistic probabilistic model adopted by the Federal Emergency Management Agency (FEMA) (*FAN*, 1990). Since the FEMA method doesn't simulate flood hydrographs, it is inappropriate for the design of flood mitigation structures such as levees, flood containment walls and flood channels. It is also inappropriate for flooding in urban areas, as well as for analyzing mud and debris flow hazards.

Previous attempts to simulate debris flows were accomplished with one-dimensional flow-routing models. DeLeon and Jeppson (1982) modeled laminar water flows with enhanced friction factors. Spatially varied and steady-state Newtonian flow was assumed, and flow stoppage could not be simulated. Schamber and MacArthur (1985) designed a one-dimensional finite element model for mudflows using the Bingham rheological model to evaluate the shear stresses of a nonNewtonian fluid. O'Brien (1986) designed a one-dimensional mudflow model for watershed channels that also utilized the Bingham model.

In 1986, MacArthur and Schamber presented two-dimensional finite element model for application to simplified overland topography. The fluid properties were considered to be those of a Bingham fluid, whose static

[1]Prin., FLO Engrg., Inc., P.O. Box 1659, Breckenridge, CO 80424.
[2]Assoc. Prof., Dept. of Civ. Engrg., Colorado State Univ., Fort Collins, CO 80523.
[3]Pres., FLO Engrg., Inc., P.O. Box 1659, Breckenridge, CO 80424.

Note. Discussion open until July 1, 1993. To extend the closing date one month, a written request must be filed with the ASCE Manager of Journals. The manuscript for this paper was submitted for review and possible publication on August 27, 1992. This paper is part of the ***Journal of Hydraulic Engineering***, Vol. 119, No. 2, February, 1993. ©ASCE, ISSN 0733-9429/93/0002-0244/$1.00 + $.15 per page. Paper No. 1965.

glecting the last three acceleration terms of (2) and (3). Further, by neglecting the pressure term, a kinematic wave representation is derived. These approximations are valid for steep alluvial fans. The option of using either a kinematic wave or diffusive wave equation is available in FLO-2D.

The diffusive wave aproximation has a broader application than the kinematic wave model (Ponce et al. 1978), and very little accuracy is normally sacrificed compared to the full dynamic model (Akan and Yen 1981). Concomitantly, computation time improves when a diffusive wave approximation is used instead of the full dynamic wave (Hromadka and Yen 1987).

The rheological behavior of hyperconcentrated sediment flows involves the interaction of several complex physical processes. The nonNewtonian behavior of the fluid matrix is controlled in part by the cohesion between fine sediment particles. This cohesion contributes to the yield stress τ_y, which must be exceeded by an applied stress in order to initiate fluid motion. By combining the yield stress and viscous stress components, the well-known Bingham plastic model is prescribed. For large rates of fluid matrix shear (as might occur on steep alluvial fans), turbulent stresses may be generated. An additional shear stress component arises in turbulent flow from the collision of sediment particles under large rates of deformation.

The total shear stress in hyperconcentrated sediment flows, including those described as debris flows, mud flows, and mud floods, can be calculated from the summation of five shear stress components

$$\tau = \tau_c + \tau_{mc} + \tau_v + \tau_t + \tau_d \quad (4)$$

in which the total shear stress τ depends on the cohesive yield stress τ_c, the Mohr-Coulomb shear τ_{mc}, the viscous shear stress τ_v, the turbulent shear stress τ_t, and the dispersive shear stress τ_d. When written in terms of shear rates (dv/dy), the following quadratic rheological model can be developed (O'Brien and Julien 1985):

$$\tau = \tau_y + \eta \left(\frac{dv}{dy}\right) + C \left(\frac{dv}{dy}\right)^2 \quad (5a)$$

where

$$\tau_y = \tau_c + \tau_{mc} \quad (5b)$$

and

$$C = \rho_m l^2 + f(\rho_m, C_v)\, d_s^2 \quad (5c)$$

in which η = dynamic viscosity; τ_c = cohesive yield strength; the Mohr-Coulomb stress $\tau_{mc} = p_s \tan \phi$ depends on the intergranular pressure p_s and the angle of repose ϕ of the material; and C = inertial shear stress coefficient, which depends on the mass density of the mixture ρ_m, the Prandtl mixing length l, the sediment size d_s, and a function of the volumetric sediment concentration C_v. Bagnold (1954) defined $f(\rho_m, C_v)$ as

$$f(\rho_m, C_v) = a_i \rho_m \left[\left(\frac{C_*}{C_v}\right)^{1/3} - 1 \right] \quad (5d)$$

in which the empirical coefficient $a_i = 0.01$ and C_* = maximum static volume concentration for the sediment particles. Egashira et al. (1989) challenged this relationship, and posed

glecting the last three acceleration terms of (2) and (3). Further, by neglecting the pressure term, a kinematic wave representation is derived. These approximations are valid for steep alluvial fans. The option of using either a kinematic wave or diffusive wave equation is available in FLO-2D.

The diffusive wave aproximation has a broader application than the kinematic wave model (Ponce et al. 1978), and very little accuracy is normally sacrificed compared to the full dynamic model (Akan and Yen 1981). Concomitantly, computation time improves when a diffusive wave approximation is used instead of the full dynamic wave (Hromadka and Yen 1987).

The rheological behavior of hyperconcentrated sediment flows involves the interaction of several complex physical processes. The nonNewtonian behavior of the fluid matrix is controlled in part by the cohesion between fine sediment particles. This cohesion contributes to the yield stress τ_y, which must be exceeded by an applied stress in order to initiate fluid motion. By combining the yield stress and viscous stress components, the well-known Bingham plastic model is prescribed. For large rates of fluid matrix shear (as might occur on steep alluvial fans), turbulent stresses may be generated. An additional shear stress component arises in turbulent flow from the collision of sediment particles under large rates of deformation.

The total shear stress in hyperconcentrated sediment flows, including those described as debris flows, mud flows, and mud floods, can be calculated from the summation of five shear stress components

$$\tau = \tau_c + \tau_{mc} + \tau_v + \tau_t + \tau_d \quad (4)$$

in which the total shear stress τ depends on the cohesive yield stress τ_c, the Mohr-Coulomb shear τ_{mc}, the viscous shear stress τ_v, the turbulent shear stress τ_t, and the dispersive shear stress τ_d. When written in terms of shear rates (dv/dy), the following quadratic rheological model can be developed (O'Brien and Julien 1985):

$$\tau = \tau_y + \eta \left(\frac{dv}{dy}\right) + C \left(\frac{dv}{dy}\right)^2 \quad (5a)$$

where

$$\tau_y = \tau_c + \tau_{mc} \quad (5b)$$

and

$$C = \rho_m l^2 + f(\rho_m, C_v)\, d_s^2 \quad (5c)$$

in which η = dynamic viscosity; τ_c = cohesive yield strength; the Mohr-Coulomb stress $\tau_{mc} = p_s \tan \phi$ depends on the intergranular pressure p_s and the angle of repose ϕ of the material; and C = inertial shear stress coefficient, which depends on the mass density of the mixture ρ_m, the Prandtl mixing length l, the sediment size d_s, and a function of the volumetric sediment concentration C_v. Bagnold (1954) defined $f(\rho_m, C_v)$ as

$$f(\rho_m, C_v) = a_i \rho_m \left[\left(\frac{C_*}{C_v}\right)^{1/3} - 1\right] \quad (5d)$$

in which the empirical coefficient a_i = 0.01 and C_* = maximum static volume concentration for the sediment particles. Egashira et al. (1989) challenged this relationship, and posed

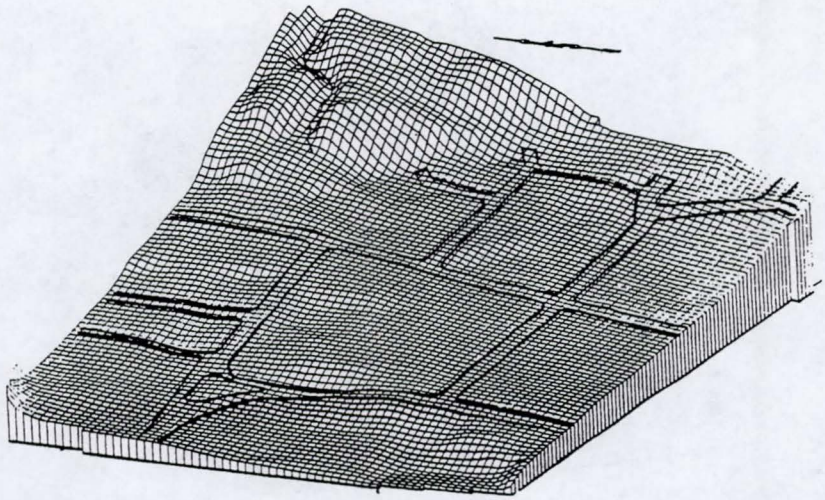

FIG. 2. Rudd Creek Alluvial Fan Topography

and represent the internal resistance stresses of a Bingham fluid. The sum of the yield stress and viscous stress defines the shear stress of a cohesive, hyperconcentrated sediment fluid in a viscous flow regime. The last term represents the sum of the dispersive and turbulent shear stresses, which depends on the square of the vertical velocity gradient. A discussion of these stresses and their role in hyperconcentrated sediment flows can be found in Julien and O'Brien (1987).

A mudflow model that incorporates only the Bingham stresses, and ignores the inertial stresses, assumes that the simulated mudflow is viscous. This assumption is not generally applicable, because all mud floods and some mudflows are turbulent, with velocities as high as 8 m/s (25 fps). Even flows considered as mudflows with concentrations up to 40% by volume can be turbulent (O'Brien 1986). Depending on the fluid matrix properties, viscosity and yield stresses for concentrations up to 40% can still be relatively small compared to the turbulent stresses at high velocities.

To define the terms in (5*a*) for use in the FLO-2D model, the following approach was taken. By analogy with the work of Meyer-Peter and Müller (1948) and Einstein (1950), the shear stress relationship (4) is depth-integrated and rewritten in the following slope form

$$S_f = S_y + S_v + S_{td} \quad (6)$$

in which the total friction slope S_f = sum of the components: the yield slope S_y; the viscous slope S_v; and the turbulent-dispersive slope S_{td}. The viscous and turbulent-dispersive slope terms are written in terms of depth-averaged velocity V. The viscous slope can be written as

$$S_v = \frac{K\eta}{8\gamma_m}\frac{V}{h^2} \quad (7)$$

in which γ_m = specific weight of the sediment mixture. The resistance parameter K for laminar flow equals 24 for smooth, wide, rectangular channels, but increases with roughness and irregular cross section geometry.

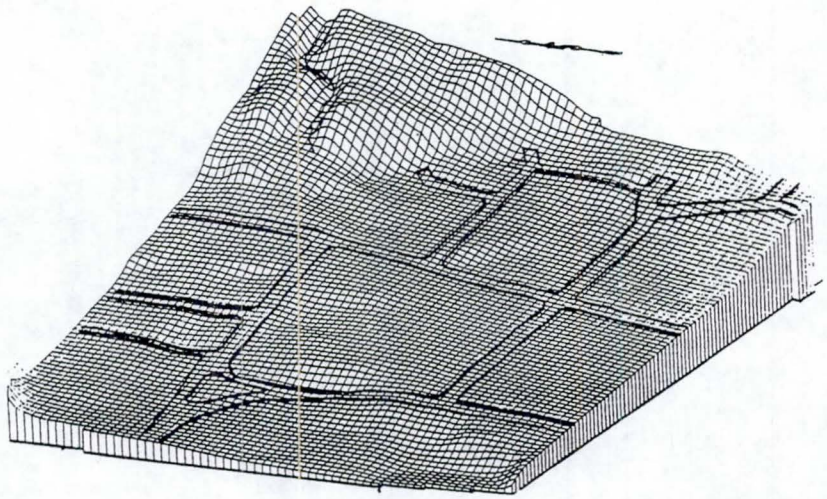

FIG. 2. Rudd Creek Alluvial Fan Topography

and represent the internal resistance stresses of a Bingham fluid. The sum of the yield stress and viscous stress defines the shear stress of a cohesive, hyperconcentrated sediment fluid in a viscous flow regime. The last term represents the sum of the dispersive and turbulent shear stresses, which depends on the square of the vertical velocity gradient. A discussion of these stresses and their role in hyperconcentrated sediment flows can be found in Julien and O'Brien (1987).

A mudflow model that incorporates only the Bingham stresses, and ignores the inertial stresses, assumes that the simulated mudflow is viscous. This assumption is not generally applicable, because all mud floods and some mudflows are turbulent, with velocities as high as 8 m/s (25 fps). Even flows considered as mudflows with concentrations up to 40% by volume can be turbulent (O'Brien 1986). Depending on the fluid matrix properties, viscosity and yield stresses for concentrations up to 40% can still be relatively small compared to the turbulent stresses at high velocities.

To define the terms in (5*a*) for use in the FLO-2D model, the following approach was taken. By analogy with the work of Meyer-Peter and Müller (1948) and Einstein (1950), the shear stress relationship (4) is depth-integrated and rewritten in the following slope form

$$S_f = S_y + S_v + S_{td} \quad \text{(6)}$$

in which the total friction slope S_f = sum of the components: the yield slope S_y; the viscous slope S_v; and the turbulent-dispersive slope S_{td}. The viscous and turbulent-dispersive slope terms are written in terms of depth-averaged velocity V. The viscous slope can be written as

$$S_v = \frac{K\eta}{8\gamma_m}\frac{V}{h^2} \quad \text{(7)}$$

in which γ_m = specific weight of the sediment mixture. The resistance parameter K for laminar flow equals 24 for smooth, wide, rectangular channels, but increases with roughness and irregular cross section geometry.

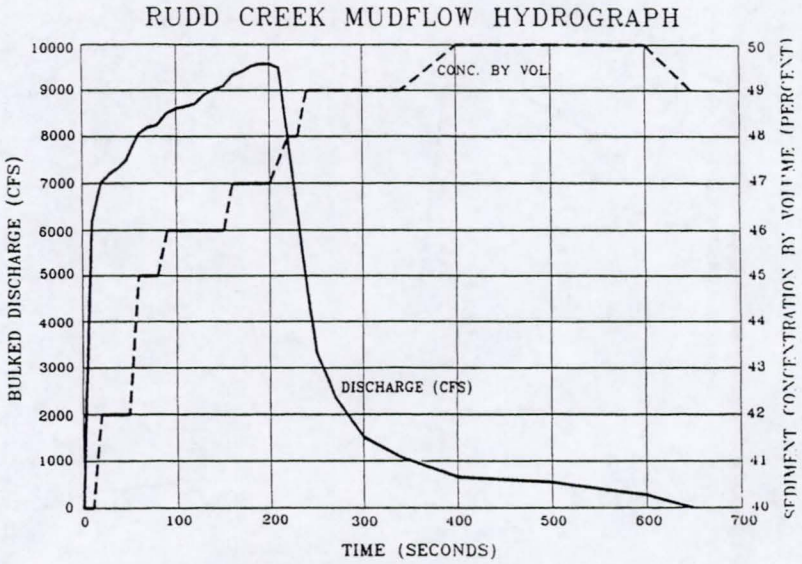

FIG. 4. Rudd Creek Mudflow Hydrograph

FIG. 5. Mudflow Frontal Deposit (Courtesy of USDA Soil Conservation Service, Salt Lake City)

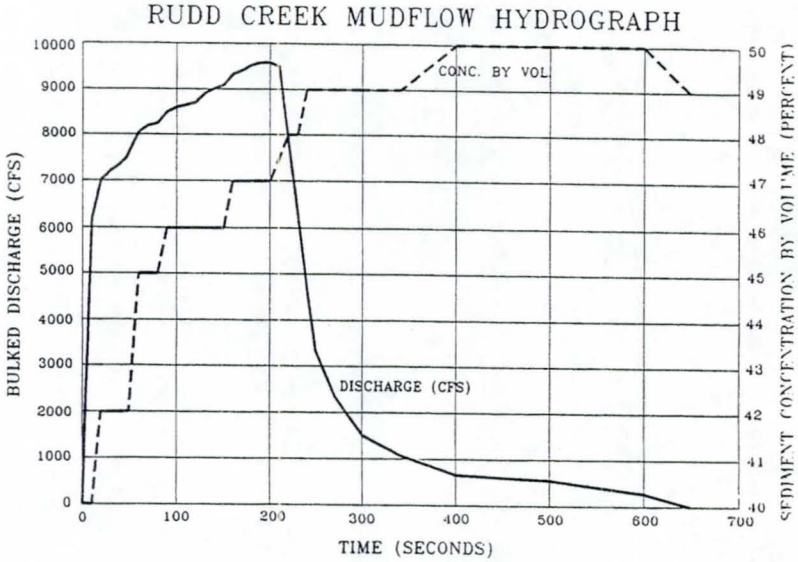

FIG. 4. Rudd Creek Mudflow Hydrograph

FIG. 5. Mudflow Frontal Deposit (Courtesy of USDA Soil Conservation Service, Salt Lake City)

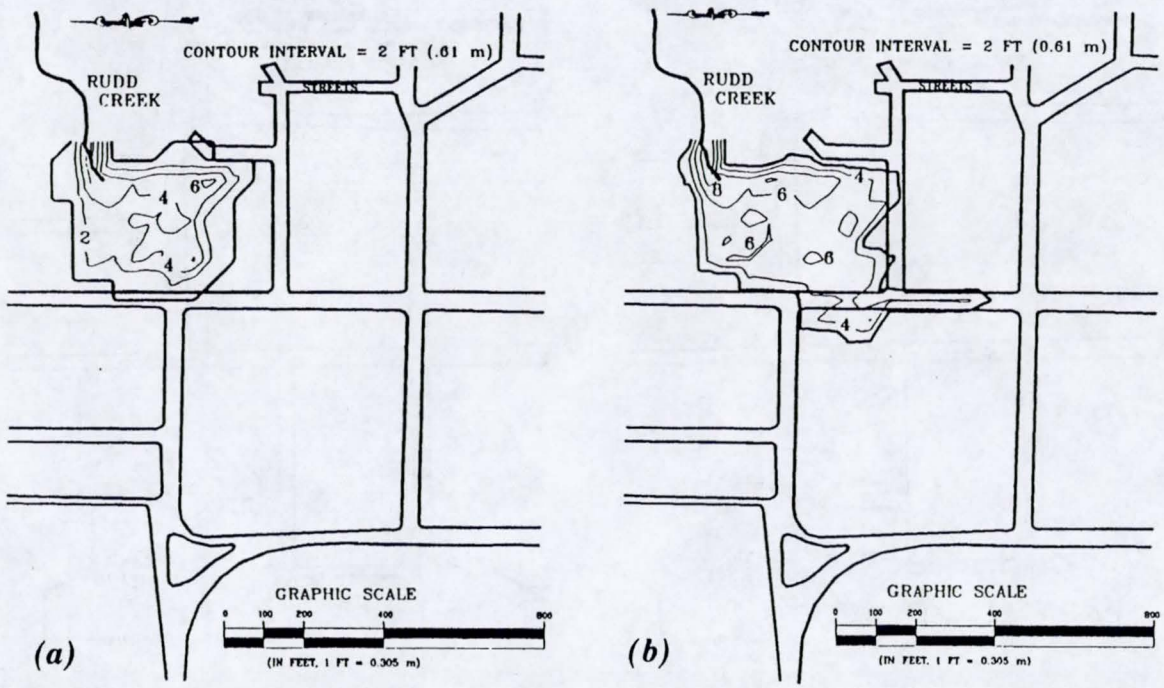

FIG. 7. Time-Lapse Simulation of Rudd Creek Mudflow: (*a*) Flow Depth after 1 Min; (*b*) Flow Depth after 2 Min

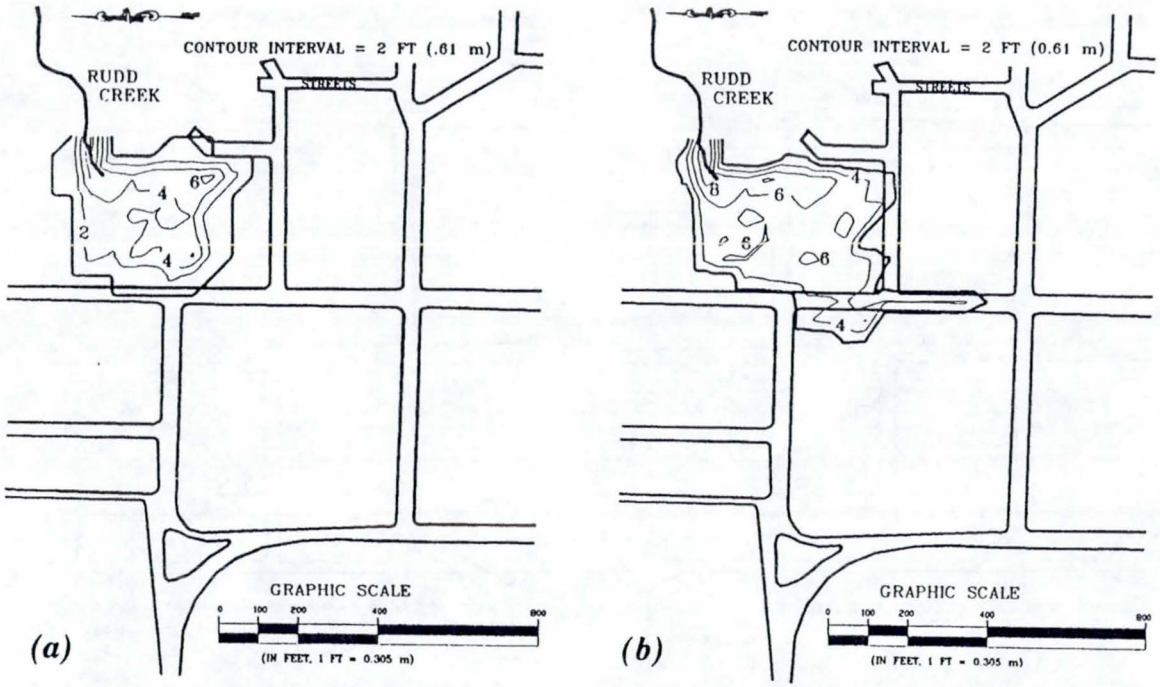

FIG. 7. Time-Lapse Simulation of Rudd Creek Mudflow: (*a*) Flow Depth after 1 Min; (*b*) Flow Depth after 2 Min

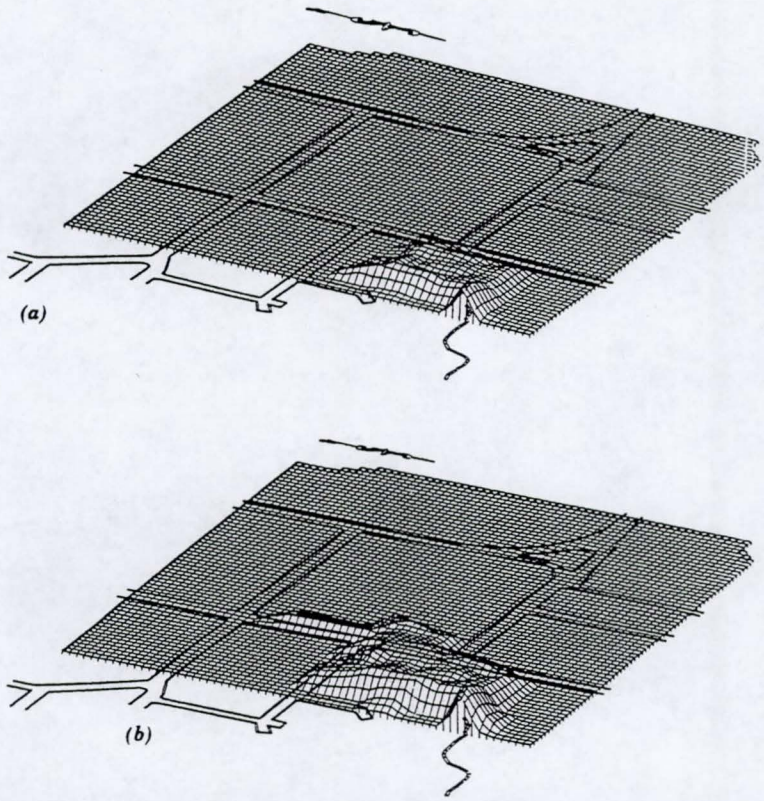

FIG. 8. 3-D Graphic Presentation of Time-Lapse Simulation: (*a*) Flow Depth after 1 Min; (*b*) Flow Depth after 2 Min

FLO-2D Model Description

The FLO-2D model evolved from the diffusive hydrodynamic model (DHM) (Hromadka and Yen 1987). The original DHM routing algorithm was revised and expanded to improve computational stability, decrease computational time, and broaden its application to more diverse flooding conditions. Very little of the original code remains.

The model uses a central finite difference routing scheme (an explicit numerical technique) for the application of the equations of motion. The surface topography is discretized into uniform square-grid elements. Each element is assigned a location on the grid system, an elevation, a roughness factor, and area and flow width reduction factors used to simulate flow blockage.

Flow is routed through the grid system using estimates of the flow depth to compute discharge. For a given element and time step, the discharge across each of the four boundaries is computed and summed. The resultant volume change is uniformly distributed over the available flow area in the element. Time steps vary according to the Courant-Friedrich-Lewy stability condition (Liggett and Cunge 1975), resulting in relatively short time steps (e.g., 1–30 s).

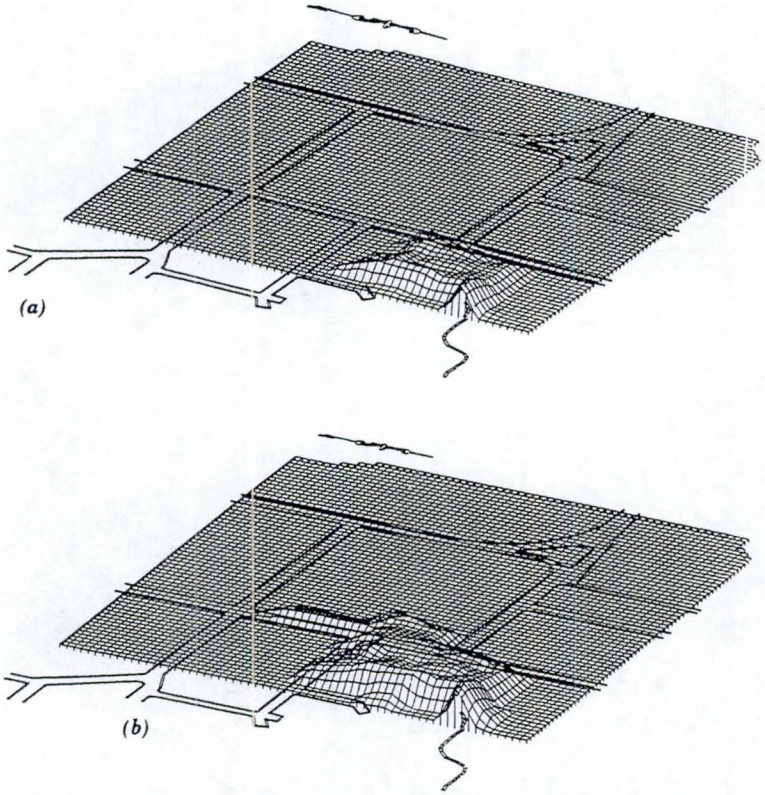

FIG. 8. 3-D Graphic Presentation of Time-Lapse Simulation: (*a*) Flow Depth after 1 Min; (*b*) Flow Depth after 2 Min

FLO-2D Model Description

The FLO-2D model evolved from the diffusive hydrodynamic model (DHM) (Hromadka and Yen 1987). The original DHM routing algorithm was revised and expanded to improve computational stability, decrease computational time, and broaden its application to more diverse flooding conditions. Very little of the original code remains.

The model uses a central finite difference routing scheme (an explicit numerical technique) for the application of the equations of motion. The surface topography is discretized into uniform square-grid elements. Each element is assigned a location on the grid system, an elevation, a roughness factor, and area and flow width reduction factors used to simulate flow blockage.

Flow is routed through the grid system using estimates of the flow depth to compute discharge. For a given element and time step, the discharge across each of the four boundaries is computed and summed. The resultant volume change is uniformly distributed over the available flow area in the element. Time steps vary according to the Courant-Friedrich-Lewy stability condition (Liggett and Cunge 1975), resulting in relatively short time steps (e.g., 1–30 s).

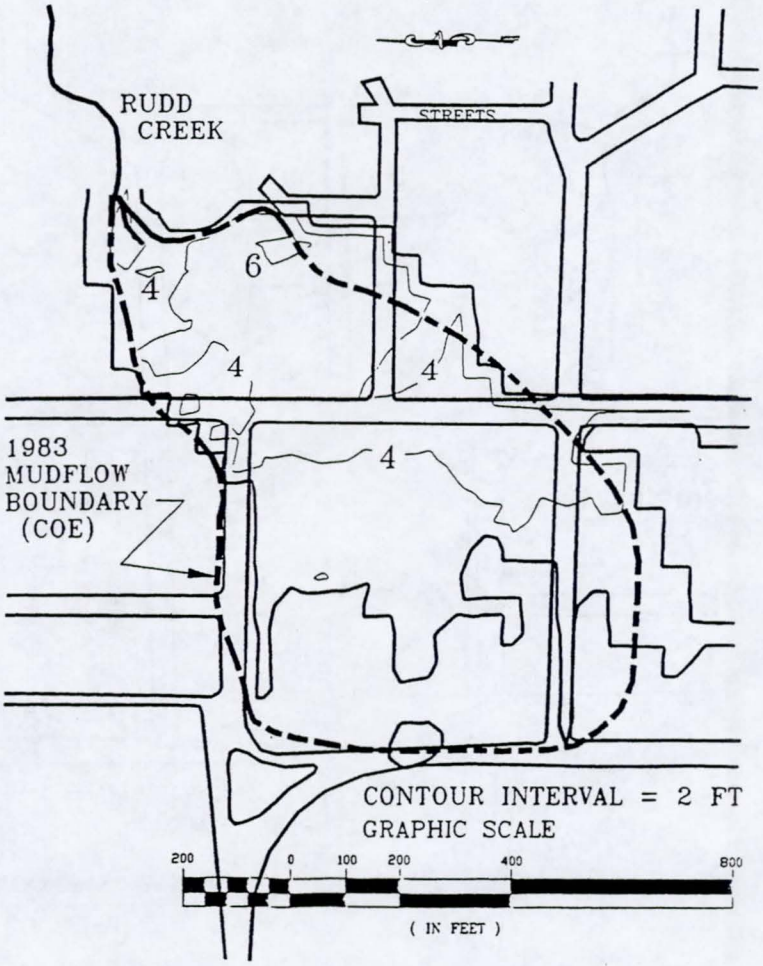

FIG. 9. Rudd Creek Mudflow Simulation after 15 Min

Model Limitations and Assumptions

Wave attenuation in the diffusive model is the result of overbank storage and the interaction of the friction slope and diffusive pressure gradient terms with the bed slope. The present model does not have the ability to simulate shock waves or hydraulic jumps, and tends to smooth out these abrupt changes in the flow profile.

The inherent assumptions in applying the model for flood routing are: (1) Steady flow for the duration of the time step (usually a few seconds); (2) hydrostatic pressure distribution; (3) steady flow resistance equation; (4) sufficiently uniform cross section shape and hydraulic roughness of the channel; and (5) single values of grid-element elevation and roughness.

In addition, FLO-2D is a rigid bed model and does not simulate degradation. This is not a serious limitation for urban floodplain flow (less erodible

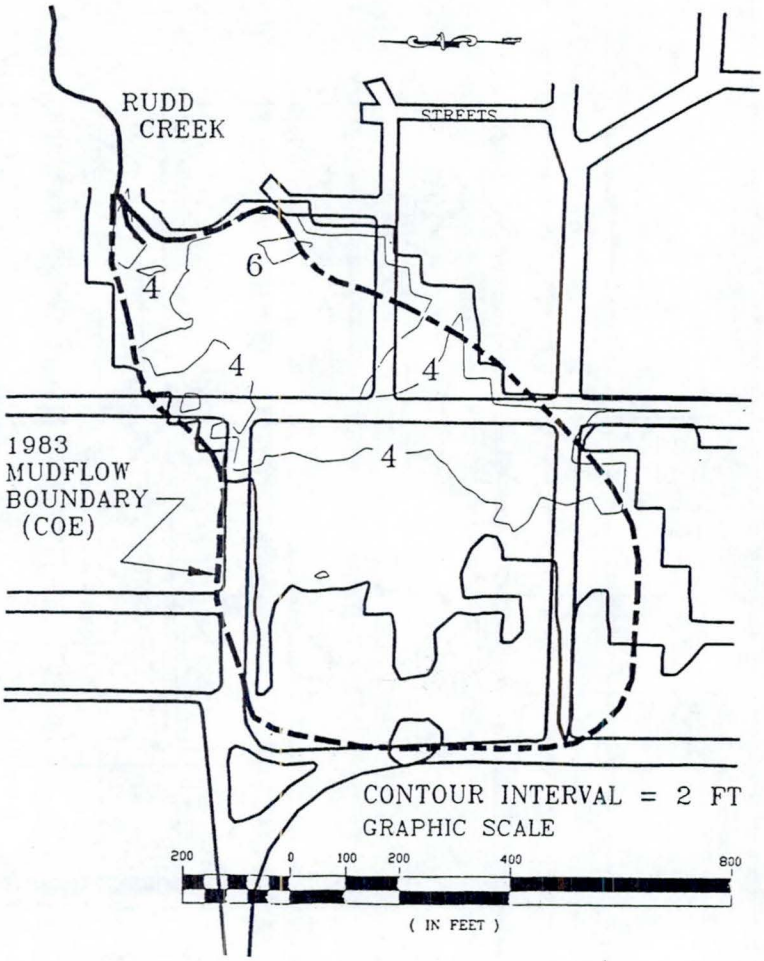

FIG. 9. Rudd Creek Mudflow Simulation after 15 Min

Model Limitations and Assumptions

Wave attenuation in the diffusive model is the result of overbank storage and the interaction of the friction slope and diffusive pressure gradient terms with the bed slope. The present model does not have the ability to simulate shock waves or hydraulic jumps, and tends to smooth out these abrupt changes in the flow profile.

The inherent assumptions in applying the model for flood routing are: (1) Steady flow for the duration of the time step (usually a few seconds); (2) hydrostatic pressure distribution; (3) steady flow resistance equation; (4) sufficiently uniform cross section shape and hydraulic roughness of the channel; and (5) single values of grid-element elevation and roughness.

In addition, FLO-2D is a rigid bed model and does not simulate degradation. This is not a serious limitation for urban floodplain flow (less erodible

the approximate boundary of the mudflow after the flow had ceased, as indicated by the U.S. Army Corps of Engineers (*Incorporating* 1986). Close examination of photos taken after the event shows that the boundaries of the deposit were slightly more irregular than shown in Figs. 2 and 3, but the correlation is reasonable.

The flood hydrograph and other pertinent data used in the simulation were published by the U.S. Army Corps of Engineers (*Incorporating* 1986). The hydrograph is shown in Fig. 4. Available field data from the event included: (1) The area of inundation indicated from photography; (2) a surveyed volume of the mudflow deposit of approximately 64,200 m^3 (84,000 cu yd); (3) mudflow frontal velocity on the alluvial fan of approximately the speed that a man could walk [0.6–1.2 m/s (2–4 fps), eyewitness account]; and (4) observed mudflow depths that ranged from approximately 3.7 m (12 ft) at the apex of the alluvial fan to approximately 0.6–0.9 m (2–3 ft) at the debris front (Fig. 5).

The mudflow was initiated by a landslide, and therefore a relatively uniform sediment concentration was assumed, which increased slightly as the event progressed to simulate dewatering (Fig. 4). Manning n roughness values for each grid element varied from 0.035 to 0.10, depending on vegetation and flow obstruction. Appropriate values from laboratory data were selected for α_i and β_i in (10) and (11) to compute viscous and yield stresses. The buildings that influenced the flow path were modeled, and their location is shown in Fig. 6.

A time-lapse simulation of the progression of the mudflow over the Rudd Creek alluvial fan is illustrated in Fig. 7. Time-sequence flow depths are written to files for a CAD graphics program that plots the depth contours. With the plotting package, the flood hazard delineation is automated. When the viscous flow encounters a street with a favorable slope, it proceeds ahead of the main body of the flow, as shown for the 2 min and 5 min simulation times in Fig. 7. A 3-dimensional graphic display of the time-lapse simulation, as viewed from the upstream direction, is shown in Fig. 8. The 3-D view helps to visualize how the mud piles up near the fan apex. Postevent photos revealed that houses in this vicinity received the most damage.

The hydrograph in Fig. 4 indicates that the flood event was over in less than 7 min. The model predicted that the mudflow continued to creep down the fan for several more minutes before flow cessation. By the end of 15 min, all the flow on the fan had ceased (Fig. 9). There is little difference in the mudflow boundary after 15 min (Fig. 9) and the boundary for the 5 min simulation (Fig. 7).

The maximum computed flow depth of 3.6 m (11.8 ft) downstream of the apex compared well with the 3.7 m (12 ft) observed depth (Fig. 10). Mudflow velocities predicted on the fan ranged from 0.3 to 1.2 m/s (1–4 fps) or approximately walking speed, as was observed. Near the fan apex, maximum predicted velocities were less than 3.0 m/s (10 fps). Just upstream of the apex in the Rudd channel area, predicted velocities exceeded 6.1 m/s (20 fps). Predicted frontal lobe depths ranged from 0.6 to 1.2 m (2–4 ft), depending on the location on the fan, and correlated well with postevent photos.

Conclusions

The two-dimensional model FLO-2D is a flexible tool to augment the capability of the floodplain manager and engineer to predict flood hydraulics, identify areas of inundation, and design options for flood containment.

the approximate boundary of the mudflow after the flow had ceased, as indicated by the U.S. Army Corps of Engineers (*Incorporating* 1986). Close examination of photos taken after the event shows that the boundaries of the deposit were slightly more irregular than shown in Figs. 2 and 3, but the correlation is reasonable.

The flood hydrograph and other pertinent data used in the simulation were published by the U.S. Army Corps of Engineers (*Incorporating* 1986). The hydrograph is shown in Fig. 4. Available field data from the event included: (1) The area of inundation indicated from photography; (2) a surveyed volume of the mudflow deposit of approximately 64,200 m^3 (84,000 cu yd); (3) mudflow frontal velocity on the alluvial fan of approximately the speed that a man could walk [0.6–1.2 m/s (2–4 fps), eyewitness account]; and (4) observed mudflow depths that ranged from approximately 3.7 m (12 ft) at the apex of the alluvial fan to approximately 0.6–0.9 m (2–3 ft) at the debris front (Fig. 5).

The mudflow was initiated by a landslide, and therefore a relatively uniform sediment concentration was assumed, which increased slightly as the event progressed to simulate dewatering (Fig. 4). Manning n roughness values for each grid element varied from 0.035 to 0.10, depending on vegetation and flow obstruction. Appropriate values from laboratory data were selected for α_i and β_i in (10) and (11) to compute viscous and yield stresses. The buildings that influenced the flow path were modeled, and their location is shown in Fig. 6.

A time-lapse simulation of the progression of the mudflow over the Rudd Creek alluvial fan is illustrated in Fig. 7. Time-sequence flow depths are written to files for a CAD graphics program that plots the depth contours. With the plotting package, the flood hazard delineation is automated. When the viscous flow encounters a street with a favorable slope, it proceeds ahead of the main body of the flow, as shown for the 2 min and 5 min simulation times in Fig. 7. A 3-dimensional graphic display of the time-lapse simulation, as viewed from the upstream direction, is shown in Fig. 8. The 3-D view helps to visualize how the mud piles up near the fan apex. Postevent photos revealed that houses in this vicinity received the most damage.

The hydrograph in Fig. 4 indicates that the flood event was over in less than 7 min. The model predicted that the mudflow continued to creep down the fan for several more minutes before flow cessation. By the end of 15 min, all the flow on the fan had ceased (Fig. 9). There is little difference in the mudflow boundary after 15 min (Fig. 9) and the boundary for the 5 min simulation (Fig. 7).

The maximum computed flow depth of 3.6 m (11.8 ft) downstream of the apex compared well with the 3.7 m (12 ft) observed depth (Fig. 10). Mudflow velocities predicted on the fan ranged from 0.3 to 1.2 m/s (1–4 fps) or approximately walking speed, as was observed. Near the fan apex, maximum predicted velocities were less than 3.0 m/s (10 fps). Just upstream of the apex in the Rudd channel area, predicted velocities exceeded 6.1 m/s (20 fps). Predicted frontal lobe depths ranged from 0.6 to 1.2 m (2–4 ft), depending on the location on the fan, and correlated well with postevent photos.

Conclusions

The two-dimensional model FLO-2D is a flexible tool to augment the capability of the floodplain manager and engineer to predict flood hydraulics, identify areas of inundation, and design options for flood containment.

ation of Landslides, Flash Floods and Debris Flow Hazards in Utah, Utah Water Research Lab., Univ. of Utah at Logan, Utah, 260–279.
O'Brien, J. S., and Julien, P. Y. (1988). "Laboratory analysis of mudflow properties." *J. Hydr. Engrg.*, ASCE, 114(8), 877–887.
Ponce, V. M., Li, R. M., and Simons, D. B. (1978). "Applicability of kinematic and diffusion models." *J. of Hydr. Div.*, ASCE, 104(3), 353–360.
Schamber, D. R., and MacArthur, R. C. (1985). "One-dimensional model for mudflows." *Proc., ASCE specialty conference on hydr. and hydro. in the small comp. age.* Vol. 2, ASCE, New York, N.Y., 1334–1339.
Takahashi, T., and Tsujimoto, H. (1985). "Delineation of the debris flow hazardous zone by a numerical simulation method." *Proc., Int. Symp. on Erosion, Debris Flow and Disaster Prevention*, Tsukuba, Japan, 457–462.
Takahashi, T., and Nakagawa, H. (1989). "Debris flow hazard zone mapping." *Proc., Japan-China (Taipei) Joint Seminar on Natural Hazard Mitigation*, Kyoto, Japan, 363–372.

Appendix II. Notation

The following symbols are used in this paper:

a_i = coefficient defined by Bagnold;
C = inertial shear stress coefficient;
C_v = volumetric sediment concentration;
C_* = maximum static volume concentration for sediment particles;
d_s = representative sediment size;
e_n = particle energy restitution coefficient after impact;
f = Darcy-Weisbach friction coefficient;
g = gravitational acceleration;
h = flow depth;
i = rainfall intensity;
K = resistance parameter for viscous flow;
l = Prandtl mixing length;
n = Manning resistance coefficient;
S_f = friction slope;
S_{fx} = friction slope component along x coordinate axis;
S_{fy} = friction slope component along y coordinate axis;
S_{td} = turbulent-dispersive slope;
S_v = viscous slope;
S_y = yield slope;
S_{ox} = bed slope component along x coordinate axis;
S_{oy} = bed slope component along y coordinate axis;
t = time;
V = depth averaged velocity;
V_x = velocity component along x coordinate axis;
V_y = velocity component along y coordinate axis;
v = velocity;
x = coordinate axis;
y = coordinate axis;
α_I = average particle impact angle;
α_i = coefficients of viscosity and yield stress;
β_i = exponents of viscosity and yield stress;
γ_m = specific weight of mixture;
η = dynamic viscosity;

ation of Landslides, Flash Floods and Debris Flow Hazards in Utah, Utah Water Research Lab., Univ. of Utah at Logan, Utah, 260–279.
O'Brien, J. S., and Julien, P. Y. (1988). "Laboratory analysis of mudflow properties." *J. Hydr. Engrg.*, ASCE, 114(8), 877–887.
Ponce, V. M., Li, R. M., and Simons, D. B. (1978). "Applicability of kinematic and diffusion models." *J. of Hydr. Div.*, ASCE, 104(3), 353–360.
Schamber, D. R., and MacArthur, R. C. (1985). "One-dimensional model for mudflows." *Proc., ASCE specialty conference on hydr. and hydro. in the small comp. age.* Vol. 2, ASCE, New York, N.Y., 1334–1339.
Takahashi, T., and Tsujimoto, H. (1985). "Delineation of the debris flow hazardous zone by a numerical simulation method." *Proc., Int. Symp. on Erosion, Debris Flow and Disaster Prevention*, Tsukuba, Japan, 457–462.
Takahashi, T., and Nakagawa, H. (1989). "Debris flow hazard zone mapping." *Proc., Japan-China (Taipei) Joint Seminar on Natural Hazard Mitigation*, Kyoto, Japan, 363–372.

Appendix II. Notation

The following symbols are used in this paper:

a_i = coefficient defined by Bagnold;
C = inertial shear stress coefficient;
C_v = volumetric sediment concentration;
C_* = maximum static volume concentration for sediment particles;
d_s = representative sediment size;
e_n = particle energy restitution coefficient after impact;
f = Darcy-Weisbach friction coefficient;
g = gravitational acceleration;
h = flow depth;
i = rainfall intensity;
K = resistance parameter for viscous flow;
l = Prandtl mixing length;
n = Manning resistance coefficient;
S_f = friction slope;
S_{fx} = friction slope component along x coordinate axis;
S_{fy} = friction slope component along y coordinate axis;
S_{td} = turbulent-dispersive slope;
S_v = viscous slope;
S_y = yield slope;
S_{ox} = bed slope component along x coordinate axis;
S_{oy} = bed slope component along y coordinate axis;
t = time;
V = depth averaged velocity;
V_x = velocity component along x coordinate axis;
V_y = velocity component along y coordinate axis;
v = velocity;
x = coordinate axis;
y = coordinate axis;
α_I = average particle impact angle;
α_i = coefficients of viscosity and yield stress;
β_i = exponents of viscosity and yield stress;
γ_m = specific weight of mixture;
η = dynamic viscosity;

TECHNICAL STANDARDS FOR DELINEATING ALLUVIAL FAN FLOODING

Jim O'Brien[1] and Brian Hyde[2]

ABSTRACT

Communities and transportation corridors have encroached on alluvial fans in most western mountainous states. In Colorado, Telluride, Vail, Aspen and Glenwood Springs are only a few of the communities confronting the challenge of delineating alluvial fan flood hazards and regulating development where lives are threatened and expensive property may be impacted. In addition, transportation corridors which experience alluvial fan flooding including mud and debris flow events are costly to maintain, potentially disruptive to the economy and dangerous for motorists.

Predictions of flood hazard on alluvial fans is being conducted with no technical standards for assessment of the hazard. Administration of delineated hazard areas is based on a non-integrated approach by local and state agencies. The Federal Emergency Management Agency (FEMA) recognizes the special flood hazards on alluvial fans, but the FEMA guidelines do not specifically address the delineation of mud and debris flow hazards. In Colorado, the statutory authority for regulating alluvial fans flood investigations exists without the technical standards for delineation and approval of alluvial fan flood hazard studies. Standards for alluvial fan flood hazard delineation, for administration of flood hazard areas, for evaluation of mitigation measures and for compliance with development regulations are proposed in this paper.

INTRODUCTION

After more than 100 years of community development on alluvial fans, floodplain administrators are now facing the challenge of coping with extensive development where evidence of pre-development large floods and mudflows is apparent. Within the history of the community, several notable floods may have occurred, but the period of record is still so short that the 100-year design flood is still the disaster of the future. Of all the difficult issues facing floodplain administrators in communities with alluvial fans, the lack of technical standards for hazard delineation and the absence of appropriate zoning regulations for the administration of flood-prone fan areas pose the greatest challenges. Approximate delineation methods have resulted in delineating the entire alluvial fan as a potential flood hazard zone. On fans that have experienced urbanization, the issue of flood hazard delineation may be ancillary to mitigation concerns, but a comprehensive mitigation plan still requires accurate technical analysis of the flood hazard potential.

Alluvial fan flooding is characterized by relatively unconfined flows on steep surfaces. Most alluvial fans are evolved through a combination of water flooding and mud/debris flow events. The flow behavior is often subject to surging associated with high concentrations of sediment and debris. Channels relocating (channel avulsion) on undeveloped portions of alluvial fans adds to the complexity of the flood hazard delineation. The general geomorphic evolution of alluvial fans dictates that the fan surface is aggrading over the long term; however, channel incision may occur during the episodic growth of the fan. Deeply incised channels associated with a long period of declining watershed sediment yield may limit the area of inundation. Delineation methodologies and administrative tools need to consider these physical processes.

---

[1] Principal, FLO Engineering, Inc., Breckenridge, CO.

[2] Senior Water Resource Specialist, Colorado Water Conservation Board and Chair of ASFPM Mapping and Engineering Committee

TECHNICAL STANDARDS FOR DELINEATING ALLUVIAL FAN FLOODING

Jim O'Brien[1] and Brian Hyde[2]

ABSTRACT

Communities and transportation corridors have encroached on alluvial fans in most western mountainous states. In Colorado, Telluride, Vail, Aspen and Glenwood Springs are only a few of the communities confronting the challenge of delineating alluvial fan flood hazards and regulating development where lives are threatened and expensive property may be impacted. In addition, transportation corridors which experience alluvial fan flooding including mud and debris flow events are costly to maintain, potentially disruptive to the economy and dangerous for motorists.

Predictions of flood hazard on alluvial fans is being conducted with no technical standards for assessment of the hazard. Administration of delineated hazard areas is based on a non-integrated approach by local and state agencies. The Federal Emergency Management Agency (FEMA) recognizes the special flood hazards on alluvial fans, but the FEMA guidelines do not specifically address the delineation of mud and debris flow hazards. In Colorado, the statutory authority for regulating alluvial fans flood investigations exists without the technical standards for delineation and approval of alluvial fan flood hazard studies. Standards for alluvial fan flood hazard delineation, for administration of flood hazard areas, for evaluation of mitigation measures and for compliance with development regulations are proposed in this paper.

INTRODUCTION

After more than 100 years of community development on alluvial fans, floodplain administrators are now facing the challenge of coping with extensive development where evidence of pre-development large floods and mudflows is apparent. Within the history of the community, several notable floods may have occurred, but the period of record is still so short that the 100-year design flood is still the disaster of the future. Of all the difficult issues facing floodplain administrators in communities with alluvial fans, the lack of technical standards for hazard delineation and the absence of appropriate zoning regulations for the administration of flood-prone fan areas pose the greatest challenges. Approximate delineation methods have resulted in delineating the entire alluvial fan as a potential flood hazard zone. On fans that have experienced urbanization, the issue of flood hazard delineation may be ancillary to mitigation concerns, but a comprehensive mitigation plan still requires accurate technical analysis of the flood hazard potential.

Alluvial fan flooding is characterized by relatively unconfined flows on steep surfaces. Most alluvial fans are evolved through a combination of water flooding and mud/debris flow events. The flow behavior is often subject to surging associated with high concentrations of sediment and debris. Channels relocating (channel avulsion) on undeveloped portions of alluvial fans adds to the complexity of the flood hazard delineation. The general geomorphic evolution of alluvial fans dictates that the fan surface is aggrading over the long term; however, channel incision may occur during the episodic growth of the fan. Deeply incised channels associated with a long period of declining watershed sediment yield may limit the area of inundation. Delineation methodologies and administrative tools need to consider these physical processes.

---

[1] Principal, FLO Engineering, Inc., Breckenridge, CO.

[2] Senior Water Resource Specialist, Colorado Water Conservation Board and Chair of ASFPM Mapping and Engineering Committee

STATUTORY AUTHORITY

Authority and Technical Standards for Designating and Approving Alluvial Fan Flood Hazard Studies

In Colorado, the statutes provide that all floodplain delineations must be approved by the Colorado Water Conservation Board (CWCB) before they are applied by local governments for regulatory purposes. Rules and Regulations for the approval of floodplain studies and the technical criteria for study review were promulgated under the authority granted to the CWCB. These rules were intended to provide uniform technical standards for floodplain studies and to prescribe the process for the designation and approval of floodplain delineations. The Statutes state:

> *"No floodplain shall be designated by any local government until such designation has been first approved by the Colorado Water Conservation Board."*

Colorado communities must, therefore, obtain state designation and approval of floodplain delineations in order to regulate activities in the floodplain zones. The scope of the CWCB statutory authority and of the rules and regulations for delineation studies extends to floodplain information as it related to zoning. It does not cover individual subdivision drainage reports, economic criteria for facilities in the floodplain, or inundation of areas by hydraulic structure failure such as dams. Such detailed studies would be subject to CWCB regulation only inasmuch as they must either show conformity with the existing delineation or justify changes in the flood hazard delineation. State policy might be simply stated as, "The CWCB blesses the floodplain delineation and supporting documentation and the local governments then utilize it."

Definitions

The State's authority to regulate floodplain studies on alluvial fans is provided in the Colorado Revised Statutes which define several floodplain features related to alluvial fans. The pertinent definitions in the Statutes are:

> *(4) "Debris-fan floodplain" means a floodplain which is located at the mouth of a mountain valley tributary stream as such stream enters the valley floor.*
>
> *(5) "Dry wash channel and dry wash floodplain" means a small watershed with a very high percentage of runoff after torrential rainfall.*
>
> *(7) "Floodplain" means an area adjacent to a stream, which area is subject to flooding as the result of the occurrence of an intermediate regional flood and which area thus is so adverse to past, current, or foreseeable construction or land use as to constitute a significant hazard to public health and safety or to property. The term includes but is not limited to:*
>
> > *(a) Mainstream floodplains;*
> > *(b) Debris-fan floodplains; and*
> > *(c) Dry wash channels and dry wash floodplains.*
>
> *(11) "Mainstream floodplain" means an area adjacent to a perennial stream, which area is subject to periodic flooding.*
>
> *(12) "Mudflow" means the downward movement of mud in a mountain watershed because of peculiar characteristics of extremely high sediment yield and occasional high runoff.*

STATUTORY AUTHORITY

Authority and Technical Standards for Designating and Approving Alluvial Fan Flood Hazard Studies

In Colorado, the statutes provide that all floodplain delineations must be approved by the Colorado Water Conservation Board (CWCB) before they are applied by local governments for regulatory purposes. Rules and Regulations for the approval of floodplain studies and the technical criteria for study review were promulgated under the authority granted to the CWCB. These rules were intended to provide uniform technical standards for floodplain studies and to prescribe the process for the designation and approval of floodplain delineations. The Statutes state:

> *"No floodplain shall be designated by any local government until such designation has been first approved by the Colorado Water Conservation Board."*

Colorado communities must, therefore, obtain state designation and approval of floodplain delineations in order to regulate activities in the floodplain zones. The scope of the CWCB statutory authority and of the rules and regulations for delineation studies extends to floodplain information as it related to zoning. It does not cover individual subdivision drainage reports, economic criteria for facilities in the floodplain, or inundation of areas by hydraulic structure failure such as dams. Such detailed studies would be subject to CWCB regulation only inasmuch as they must either show conformity with the existing delineation or justify changes in the flood hazard delineation. State policy might be simply stated as, "The CWCB blesses the floodplain delineation and supporting documentation and the local governments then utilize it."

Definitions

The State's authority to regulate floodplain studies on alluvial fans is provided in the Colorado Revised Statutes which define several floodplain features related to alluvial fans. The pertinent definitions in the Statutes are:

> *(4) "Debris-fan floodplain" means a floodplain which is located at the mouth of a mountain valley tributary stream as such stream enters the valley floor.*
>
> *(5) "Dry wash channel and dry wash floodplain" means a small watershed with a very high percentage of runoff after torrential rainfall.*
>
> *(7) "Floodplain" means an area adjacent to a stream, which area is subject to flooding as the result of the occurrence of an intermediate regional flood and which area thus is so adverse to past, current, or foreseeable construction or land use as to constitute a significant hazard to public health and safety or to property. The term includes but is not limited to:*
>
> > *(a) Mainstream floodplains;*
> > *(b) Debris-fan floodplains; and*
> > *(c) Dry wash channels and dry wash floodplains.*
>
> *(11) "Mainstream floodplain" means an area adjacent to a perennial stream, which area is subject to periodic flooding.*
>
> *(12) "Mudflow" means the downward movement of mud in a mountain watershed because of peculiar characteristics of extremely high sediment yield and occasional high runoff.*

Additional regulations are required for predicting the flow hydraulics (flow depths and velocities) of unconfined flooding and mud/debris flows on alluvial fans. These can be developed within the scope of the existing CWCB Rules and Regulations. A proposed policy for the flood hazard delineation and administration of flood prone areas on alluvial fans in Colorado is described in the next section.

Proposed Policy

Each alluvial fan and watershed has unique geology, topography, soil and hydrologic characteristics and, therefore has unique flooding hazards. The fan topography, mudflow deposits and fluvial features provide clues as to the nature and magnitude of the potential hazard event. Local communities should address their unique flooding problems in preparing general policy, flood hazard delineation studies and zoning regulations. In general the community should adopt a policy and program, subject to State review, which would include the following components:

- Statements regarding the uniqueness of the special flood hazard on their alluvial fans.
- Rules and regulations related to the use of approved hydrologic and hydraulic modeling practices.
- Rules and regulations related to flood hazard mapping for both existing conditions and proposed modifications.
- Statements regarding the need for compliance with the comprehensive master drainage and development plan.
- Special considerations related to the analysis of existing conditions and proposed mitigation measures.
- Detailed instructions for the delineation process for proposed development in mud/debris flow hazard zones.
- Statements regarding policy for Flood Insurance Studies and the removal of properties from flood hazard mapping for insurance purposes.

Detailed hydrologic studies which lead to the creation of a flood hydrograph at the fan apex are recommended. Professionals carrying out the hydraulic analysis and the delineation of alluvial fan flood hazards should consider the inappropriateness of step-backwater methods (i.e. HEC-2) and of approximate methods not applicable for urbanized fans (i.e. FEMA FAN model) and pursue two-dimensional flood routing models that can also simulate mud and debris flows. Alluvial fan flooding may be unconfined and the hazard delineation should be based on predicted 1 ft maximum depth flood contours. These recommendations will be discussed further in subsequent sections.

The Colorado Water Conservation Board, Flood Control and Floodplain Management Section, has published a review report and checklist for the technical review of floodplain information for riverine floodplains. It includes a request form for the designation and approval of the floodplain delineation by the Board as well as a request form for a variance. Such a checklist could be developed for reviewing alluvial fan floodplain information.

Additional regulations are required for predicting the flow hydraulics (flow depths and velocities) of unconfined flooding and mud/debris flows on alluvial fans. These can be developed within the scope of the existing CWCB Rules and Regulations. A proposed policy for the flood hazard delineation and administration of flood prone areas on alluvial fans in Colorado is described in the next section.

Proposed Policy

Each alluvial fan and watershed has unique geology, topography, soil and hydrologic characteristics and, therefore has unique flooding hazards. The fan topography, mudflow deposits and fluvial features provide clues as to the nature and magnitude of the potential hazard event. Local communities should address their unique flooding problems in preparing general policy, flood hazard delineation studies and zoning regulations. In general the community should adopt a policy and program, subject to State review, which would include the following components:

- Statements regarding the uniqueness of the special flood hazard on their alluvial fans.
- Rules and regulations related to the use of approved hydrologic and hydraulic modeling practices.
- Rules and regulations related to flood hazard mapping for both existing conditions and proposed modifications.
- Statements regarding the need for compliance with the comprehensive master drainage and development plan.
- Special considerations related to the analysis of existing conditions and proposed mitigation measures.
- Detailed instructions for the delineation process for proposed development in mud/debris flow hazard zones.
- Statements regarding policy for Flood Insurance Studies and the removal of properties from flood hazard mapping for insurance purposes.

Detailed hydrologic studies which lead to the creation of a flood hydrograph at the fan apex are recommended. Professionals carrying out the hydraulic analysis and the delineation of alluvial fan flood hazards should consider the inappropriateness of step-backwater methods (i.e. HEC-2) and of approximate methods not applicable for urbanized fans (i.e. FEMA FAN model) and pursue two-dimensional flood routing models that can also simulate mud and debris flows. Alluvial fan flooding may be unconfined and the hazard delineation should be based on predicted 1 ft maximum depth flood contours. These recommendations will be discussed further in subsequent sections.

The Colorado Water Conservation Board, Flood Control and Floodplain Management Section, has published a review report and checklist for the technical review of floodplain information for riverine floodplains. It includes a request form for the designation and approval of the floodplain delineation by the Board as well as a request form for a variance. Such a checklist could be developed for reviewing alluvial fan floodplain information.

Deficiencies in the Current Procedures

If the engineer predicts fan flood hydraulics and areas of inundation with alternative methods that are more conservative than those predicted by the FEMA FAN model, then the results may be accepted in the review process. In this manner, the FEMA FAN method becomes the de-facto standard for fan flood hazard delineation. Based on the analyses of other authors regarding the simplified and inappropriate assumptions in the FEMA method (Dawdy, et al., 1989; Fuller, 1990; French and Fuller, 1992, Grindeland, et al., 1990), lack of model verification (O'Brien and Fullerton, 1991) and failure to consider geological and topographical constraints (Baker, et al., 1990); the following conclusions have been reached regarding the FEMA method for delineating alluvial fan flood hazards:

- The FEMA method does not present a realistic analysis of physical processes on alluvial fans. It is not a physically based model.
- There are no published guidelines on the limits of the FAN model applicability.
- There is no verification of the model.
- The FEMA model does not err conservatively.

The FEMA FAN model and step-backwater water surface profile models such as HEC-2 are <u>not</u> recommended. The FEMA method poorly predicts flood hydrologic zones and is not suitable for urbanized alluvial fans. Flood wave attenuation and fan rainfall are important facets of alluvial fan flooding that HEC-2 cannot simulate.

Successful application for a LOMR on alluvial fan flood hazard areas is a hit or miss proposition. Furthermore, FEMA does not have any reasonable, applicable or comprehensible criteria for LOMR's and CLOMR's for mud/debris flow hazard zones. In the seven Colorado communities and counties where FEMA mapping of alluvial fans exist, the current mapping does not support or provide adequate guidance for zoning regulations or mitigation design.

PROPOSED TECHNICAL STANDARDS FOR DELINEATING ALLUVIAL FAN FLOODING

The failure of FEMA to provide adequate technical guidance and the significant limitations of State Rules and Regulations creates a void in the analysis of the unique processes of alluvial fan flooding. As a result, the following technical standards for delineating alluvial fan flooding, including a list of appropriate definitions, are proposed.

Definitions

There are several definitions of physical processes or features specific to alluvial fan flooding as provided in the literature which may deviate from those contained in the Colorado Revised Statutes or in the CWCB Rules and Regulations. In nature, there exists a continuum of flood flow conditions and behavior, and one flood event may consist of several processes. Although the transitions between the different types of flow are difficult to distinguish, mass wasting processes can be divided into four main categories which are described below: water floods, mud floods, mud flows and landslides (NRC, 1982; O'Brien and Julien, 1985). Most of the definitions presented herein are in concert with those promulgated by the National Research Council (1982).

Deficiencies in the Current Procedures

If the engineer predicts fan flood hydraulics and areas of inundation with alternative methods that are more conservative than those predicted by the FEMA FAN model, then the results may be accepted in the review process. In this manner, the FEMA FAN method becomes the de-facto standard for fan flood hazard delineation. Based on the analyses of other authors regarding the simplified and inappropriate assumptions in the FEMA method (Dawdy, et al., 1989; Fuller, 1990; French and Fuller, 1992, Grindeland, et al., 1990), lack of model verification (O'Brien and Fullerton, 1991) and failure to consider geological and topographical constraints (Baker, et al., 1990); the following conclusions have been reached regarding the FEMA method for delineating alluvial fan flood hazards:

- The FEMA method does not present a realistic analysis of physical processes on alluvial fans. It is not a physically based model.
- There are no published guidelines on the limits of the FAN model applicability.
- There is no verification of the model.
- The FEMA model does not err conservatively.

The FEMA FAN model and step-backwater water surface profile models such as HEC-2 are <u>not</u> recommended. The FEMA method poorly predicts flood hydrologic zones and is not suitable for urbanized alluvial fans. Flood wave attenuation and fan rainfall are important facets of alluvial fan flooding that HEC-2 cannot simulate.

Successful application for a LOMR on alluvial fan flood hazard areas is a hit or miss proposition. Furthermore, FEMA does not have any reasonable, applicable or comprehensible criteria for LOMR's and CLOMR's for mud/debris flow hazard zones. In the seven Colorado communities and counties where FEMA mapping of alluvial fans exist, the current mapping does not support or provide adequate guidance for zoning regulations or mitigation design.

PROPOSED TECHNICAL STANDARDS FOR DELINEATING ALLUVIAL FAN FLOODING

The failure of FEMA to provide adequate technical guidance and the significant limitations of State Rules and Regulations creates a void in the analysis of the unique processes of alluvial fan flooding. As a result, the following technical standards for delineating alluvial fan flooding, including a list of appropriate definitions, are proposed.

Definitions

There are several definitions of physical processes or features specific to alluvial fan flooding as provided in the literature which may deviate from those contained in the Colorado Revised Statutes or in the CWCB Rules and Regulations. In nature, there exists a continuum of flood flow conditions and behavior, and one flood event may consist of several processes. Although the transitions between the different types of flow are difficult to distinguish, mass wasting processes can be divided into four main categories which are described below: water floods, mud floods, mud flows and landslides (NRC, 1982; O'Brien and Julien, 1985). Most of the definitions presented herein are in concert with those promulgated by the National Research Council (1982).

Mud Flood: Hyperconcentrated sediment flow with a fluid matrix ranging in concentration from 20 to approximately 45 percent by volume. Sediment transport capacity equations are not applicable because of the higher viscosities of fluid matrix. Water floods and mud floods are classified under the NFIP definition of floods.

Mudflow: Mudflows are hyperconcentrated sediment flows where the viscous stress controls the flow behavior. Mudflows generally have a flow matrix with a sediment concentration by volume exceeding 40 to 45 percent but less than the concentration for a landslide of 50 to 55%.

Risk: The assignment of flood risk is related to the frequency of the storm event; i.e. a 100-yr flood has an annual probability of 0.01. On the average, a 100-yr flood will occur once during a 100-year period. With respect to a mudflow, the 100-yr storm is assumed to produce a 100-yr return period mudflow event even though a mudflow may not occur with a storm of the return frequency of a 100-yr event. Generally, the 100-yr mudflow event is predicted by bulking the 100-yr water flood at the fan apex.

Shallow Flooding: On alluvial fans, shallow flooding refers to water flooding or mud flooding with flow depths less than 0.5 ft. Shallow flooding may be assigned a separate flood hazard delineation zone.

Water Flood: Conventional water flooding is defined as water inundation by overbank discharge. Sediment is transported through the mechanisms of suspension and rolling and saltation along the bed which largely depend on flow velocity and turbulence. Sediment concentrations are relatively low under these conditions and do not significantly affect fluid properties.

Approximate Delineation

The CWCB has standards for approximate flood hazard delineations for riverine floodplain. These standards cover work maps, and hydrologic and hydraulic analyses. The hydrologic analysis requires the calculation of the 100-yr peak discharge and the hydraulic analysis is based on an assumed depth determined from a regression analysis of depth-frequency relations or from a slope-area-conveyance calculation. CWCB standards permit the approximate delineation of the 100-year flood boundary from geomorphic features and/or historic flood data.

Unfortunately approximate flood delineation for alluvial fans is not this straight forward. Unconfined flow does not permit reasonable assumptions of flow depths and flood boundaries and furthermore, mudflows may cease flowing on the fan. There is no simple method for determining the effects of loss of channel conveyance or bridge blockage. An approximate 100-yr peak discharge may be estimated at the fan apex, but 100 ft downfan, the area of inundation or flow depth would be impossible to approximate. Therefore, other than identifying the entire alluvial fan within the flood hazard boundary, approximate flood hazard delineation on alluvial fans is not recommended.

It should be noted that there are reasons for using geologic or other techniques for identifying entire fans as flood hazard areas. States can apply the delineations to prioritize fans for future detailed studies. Local governments can use approximate delineations to determine areas where studies should be completed before permitting development. Applying approximate methods, however, for detailed land use or flood insurance analysis is discouraged.

Mud Flood: Hyperconcentrated sediment flow with a fluid matrix ranging in concentration from 20 to approximately 45 percent by volume. Sediment transport capacity equations are not applicable because of the higher viscosities of fluid matrix. Water floods and mud floods are classified under the NFIP definition of floods.

Mudflow: Mudflows are hyperconcentrated sediment flows where the viscous stress controls the flow behavior. Mudflows generally have a flow matrix with a sediment concentration by volume exceeding 40 to 45 percent but less than the concentration for a landslide of 50 to 55%.

Risk: The assignment of flood risk is related to the frequency of the storm event; i.e. a 100-yr flood has an annual probability of 0.01. On the average, a 100-yr flood will occur once during a 100-year period. With respect to a mudflow, the 100-yr storm is assumed to produce a 100-yr return period mudflow event even though a mudflow may not occur with a storm of the return frequency of a 100-yr event. Generally, the 100-yr mudflow event is predicted by bulking the 100-yr water flood at the fan apex.

Shallow Flooding: On alluvial fans, shallow flooding refers to water flooding or mud flooding with flow depths less than 0.5 ft. Shallow flooding may be assigned a separate flood hazard delineation zone.

Water Flood: Conventional water flooding is defined as water inundation by overbank discharge. Sediment is transported through the mechanisms of suspension and rolling and saltation along the bed which largely depend on flow velocity and turbulence. Sediment concentrations are relatively low under these conditions and do not significantly affect fluid properties.

Approximate Delineation

The CWCB has standards for approximate flood hazard delineations for riverine floodplain. These standards cover work maps, and hydrologic and hydraulic analyses. The hydrologic analysis requires the calculation of the 100-yr peak discharge and the hydraulic analysis is based on an assumed depth determined from a regression analysis of depth-frequency relations or from a slope-area-conveyance calculation. CWCB standards permit the approximate delineation of the 100-year flood boundary from geomorphic features and/or historic flood data.

Unfortunately approximate flood delineation for alluvial fans is not this straight forward. Unconfined flow does not permit reasonable assumptions of flow depths and flood boundaries and furthermore, mudflows may cease flowing on the fan. There is no simple method for determining the effects of loss of channel conveyance or bridge blockage. An approximate 100-yr peak discharge may be estimated at the fan apex, but 100 ft downfan, the area of inundation or flow depth would be impossible to approximate. Therefore, other than identifying the entire alluvial fan within the flood hazard boundary, approximate flood hazard delineation on alluvial fans is not recommended.

It should be noted that there are reasons for using geologic or other techniques for identifying entire fans as flood hazard areas. States can apply the delineations to prioritize fans for future detailed studies. Local governments can use approximate delineations to determine areas where studies should be completed before permitting development. Applying approximate methods, however, for detailed land use or flood insurance analysis is discouraged.

locations of recent and historic channels, debris producing areas, type of expected flooding (mudflow, mud flood, debris flow, etc.), possibility of channel incision, and potential for flood control/debris basins.

In creating a data base, a report should be prepared which identifies the general fan features, existing flood hazard mapping, recent flow deposits, possible and desirable flow directions, streets and buildings and potential development. Survey data should be identified for future reference. The data base should be compared with any data requirements for state and local regulations or for FEMA flood insurance map revisions.

Technical Analysis of Existing Conditions

Geology. Alluvial fan flooding and possibility of mud or debris flow is a direct consequence of the geologic formations regarded as the sediment supply. A geologic assessment of historic flow deposits and fan geomorphology will enhance the hydraulic analysis. The following information is useful:

- Identification of source areas.
- Percentage of silt and clay in undisturbed deposits.
- Depositional features, lobes, rock levees, runout distances, maximum size transported boulders (flow competence), height of scars on trees.
- Estimates of maximum flow depths and velocities as discerned from physical evidence.
- State of the alluvial fan, aggradational or incisional.
- Fan geomorphology, slopes, channels, age of flows.

Hydrology. The magnitude of the flood event on the alluvial fan is controlled by the upstream watershed hydrology. The hydrologic analysis should include the 10-, 50- and 100-year rainfall events. Analysis of stream gaging records is preferred, but few, if any, ephemeral fan channels have been gaged. Furthermore, the gaging records are usually too short to encompass any of the extreme events that usually produce mud and debris flows. The requirement to analyze mud and debris flows as a function of these large discharge events will also preclude regional regression analysis or transposition of gaging records from other watersheds to predict flood magnitudes.

Flood hydrographs for ungaged watersheds should be accomplished with a suitable rainfall/runoff model. A frequency analysis should be performed on appropriate rain gage data to derive the 10-, 50-, and 100-yr precipitation totals. The network of rain gages in the mountains is usually limited and appropriate precipitation data may be unavailable. The NOAA rainfall atlas should be referred to when estimating precipitation totals. Available rainfall records should be closely examined for prescribing storm duration and intensity. Often, local drainage criteria may specify storm characteristics. The State should be specific about which hydrology models are appropriate and should prescribe permissible modifications to storm duration. Calibration of hydrologic model watershed parameters should be attempted whenever practical. This may entail simulation of a rainfall event on a nearby gaged watershed.

The Corps of Engineers HEC-1 rainfall/runoff model is recommended for predicting watershed hydrology. With it, the flood hydrograph can be prepared at the fan apex. The flood hydrograph can be adjusted for mud/debris bulking and average sediment concentration. Consideration should be given to hydrograph timing for mud and debris flow events (frontal wave delay).

Mud and debris flows are not always associated with rainfall and may be initiated by snowmelt or saturated ground conditions. These less frequent modes of mudflow mobilization usually initiate as landslides and may transform into mudflows. Sediment concentrations associated with these types of mudflows are more uniform and may increase on the falling limb of the event hydrograph. Estimating flood hydrograph volumes is valuable to the accuracy of the flood simulation.

locations of recent and historic channels, debris producing areas, type of expected flooding (mudflow, mud flood, debris flow, etc.), possibility of channel incision, and potential for flood control/debris basins.

In creating a data base, a report should be prepared which identifies the general fan features, existing flood hazard mapping, recent flow deposits, possible and desirable flow directions, streets and buildings and potential development. Survey data should be identified for future reference. The data base should be compared with any data requirements for state and local regulations or for FEMA flood insurance map revisions.

Technical Analysis of Existing Conditions

Geology. Alluvial fan flooding and possibility of mud or debris flow is a direct consequence of the geologic formations regarded as the sediment supply. A geologic assessment of historic flow deposits and fan geomorphology will enhance the hydraulic analysis. The following information is useful:

- Identification of source areas.
- Percentage of silt and clay in undisturbed deposits.
- Depositional features, lobes, rock levees, runout distances, maximum size transported boulders (flow competence), height of scars on trees.
- Estimates of maximum flow depths and velocities as discerned from physical evidence.
- State of the alluvial fan, aggradational or incisional.
- Fan geomorphology, slopes, channels, age of flows.

Hydrology. The magnitude of the flood event on the alluvial fan is controlled by the upstream watershed hydrology. The hydrologic analysis should include the 10-, 50- and 100-year rainfall events. Analysis of stream gaging records is preferred, but few, if any, ephemeral fan channels have been gaged. Furthermore, the gaging records are usually too short to encompass any of the extreme events that usually produce mud and debris flows. The requirement to analyze mud and debris flows as a function of these large discharge events will also preclude regional regression analysis or transposition of gaging records from other watersheds to predict flood magnitudes.

Flood hydrographs for ungaged watersheds should be accomplished with a suitable rainfall/runoff model. A frequency analysis should be performed on appropriate rain gage data to derive the 10-, 50-, and 100-yr precipitation totals. The network of rain gages in the mountains is usually limited and appropriate precipitation data may be unavailable. The NOAA rainfall atlas should be referred to when estimating precipitation totals. Available rainfall records should be closely examined for prescribing storm duration and intensity. Often, local drainage criteria may specify storm characteristics. The State should be specific about which hydrology models are appropriate and should prescribe permissible modifications to storm duration. Calibration of hydrologic model watershed parameters should be attempted whenever practical. This may entail simulation of a rainfall event on a nearby gaged watershed.

The Corps of Engineers HEC-1 rainfall/runoff model is recommended for predicting watershed hydrology. With it, the flood hydrograph can be prepared at the fan apex. The flood hydrograph can be adjusted for mud/debris bulking and average sediment concentration. Consideration should be given to hydrograph timing for mud and debris flow events (frontal wave delay).

Mud and debris flows are not always associated with rainfall and may be initiated by snowmelt or saturated ground conditions. These less frequent modes of mudflow mobilization usually initiate as landslides and may transform into mudflows. Sediment concentrations associated with these types of mudflows are more uniform and may increase on the falling limb of the event hydrograph. Estimating flood hydrograph volumes is valuable to the accuracy of the flood simulation.

Other aspects of the design of mitigation measures include: freeboard which accounts for potential deposition, wave height and frontal wave impact; floodwall design which allows for maximum scour depth, maximum deposit depth and impact forces; riprap design for levees and berms; detention basin volume with bulked sediment flows; and the protection of conveyance channels from debris blockage. Several practical mitigation guidelines are presented in Appendix A. For floodplain administrators to assess the effectiveness of mitigation measures and approve of construction, the following information should be submitted to support the proposed mitigation measures.

Proposed Mitigation. A technical description of the proposed mitigation measures should be prepared. This would include such factors as location on the fan, mitigation purpose, design parameters and the potential impact of the mitigation on flood hydraulics and downfan property. The technical description should be supplemented with a description of the proposed project for the general public.

Effect on Hydrology and Hydraulics. The mitigation measure may alter the flood direction or the local drainage on the fan. Fan runoff may be increased through an increase in impervious area, confinement of the flow or channelization and may be decreased through construction of detention basins. The mitigation designs need to be evaluated for possible impact on other development. The report on the mitigation design should include a discussion of the potential impacts with and without the proposed mitigation including a comparison of flow depth, velocity contours and areas of inundations.

Assessment of the Structural Integrity of the Mitigation. The design of the mitigation structure should be assessed based on the effect of the mitigation on the flood hydraulics. The structure design should be evaluated for scour and deposition, boulder impact, static and dynamic pressure, overtopping, overturning and flow abrasion. Two aspects of the structure design and maintenance plan are the structural integrity during successive events and the potential for failure immediately following an event. Colorado has a meteorological history of having several days of successive storms, so this very real possibility must be considered. The maintenance plan should demonstrate access to the mitigation site, prescribe a method of mud and debris removal and identify a disposal site for removed mud and debris.

Report Preparation. The final mitigation design should be submitted in a report documenting flow hydraulics, flood hydrograph, flood routing techniques and comparison of the mitigation design with State criteria. If the mitigation measures and their effects have not been sufficiently demonstrated to the floodplain administrator, then the report should include a computer diskette with the engineering information needed to accurately model the proposed structure. The mitigation project proponent will be responsible for providing information to demonstrate the structural integrity and the hydraulic impact of the mitigation. In this circumstance, the floodplain administrator or local government (or a consultant retained for this purpose) will run the computer model with the proposed changes to verify the effects of the mitigation prior to approval of the mitigation. Mitigation design may permit removal of some areas from flood insurance hazard zones.

Other aspects of the design of mitigation measures include: freeboard which accounts for potential deposition, wave height and frontal wave impact; floodwall design which allows for maximum scour depth, maximum deposit depth and impact forces; riprap design for levees and berms; detention basin volume with bulked sediment flows; and the protection of conveyance channels from debris blockage. Several practical mitigation guidelines are presented in Appendix A. For floodplain administrators to assess the effectiveness of mitigation measures and approve of construction, the following information should be submitted to support the proposed mitigation measures.

Proposed Mitigation. A technical description of the proposed mitigation measures should be prepared. This would include such factors as location on the fan, mitigation purpose, design parameters and the potential impact of the mitigation on flood hydraulics and downfan property. The technical description should be supplemented with a description of the proposed project for the general public.

Effect on Hydrology and Hydraulics. The mitigation measure may alter the flood direction or the local drainage on the fan. Fan runoff may be increased through an increase in impervious area, confinement of the flow or channelization and may be decreased through construction of detention basins. The mitigation designs need to be evaluated for possible impact on other development. The report on the mitigation design should include a discussion of the potential impacts with and without the proposed mitigation including a comparison of flow depth, velocity contours and areas of inundations.

Assessment of the Structural Integrity of the Mitigation. The design of the mitigation structure should be assessed based on the effect of the mitigation on the flood hydraulics. The structure design should be evaluated for scour and deposition, boulder impact, static and dynamic pressure, overtopping, overturning and flow abrasion. Two aspects of the structure design and maintenance plan are the structural integrity during successive events and the potential for failure immediately following an event. Colorado has a meteorological history of having several days of successive storms, so this very real possibility must be considered. The maintenance plan should demonstrate access to the mitigation site, prescribe a method of mud and debris removal and identify a disposal site for removed mud and debris.

Report Preparation. The final mitigation design should be submitted in a report documenting flow hydraulics, flood hydrograph, flood routing techniques and comparison of the mitigation design with State criteria. If the mitigation measures and their effects have not been sufficiently demonstrated to the floodplain administrator, then the report should include a computer diskette with the engineering information needed to accurately model the proposed structure. The mitigation project proponent will be responsible for providing information to demonstrate the structural integrity and the hydraulic impact of the mitigation. In this circumstance, the floodplain administrator or local government (or a consultant retained for this purpose) will run the computer model with the proposed changes to verify the effects of the mitigation prior to approval of the mitigation. Mitigation design may permit removal of some areas from flood insurance hazard zones.

State Approval of Technical Methods. The CWCB, in cooperation with the Colorado Geological Survey, is the authority in Colorado for approving the application of floodplain hazard delineation tools for alluvial fans. Approval of a flood routing model should be based on the following criteria:

- Theoretical and fundamental soundness of the model algorithms.
- Demonstration of conservation of mass in the model application.
- Model capability to replicate basic water hydraulics compared with a standard step-backwater model.
- Ability of the model to be calibrated to replicate an historical flood event.
- Appropriate resolution of the model results for mapping purposes.
- Submittal of a model users manual, a report describing the model, model code and an executable version of the model.
- Submittal of model results depicting the model's capability.

A state policy board should address the limitations of the model during the approval process including: Does the model grossly overestimate or underestimate the potential flood hazard; and Does the model oversimplify the physical processes contributing to the flood hazard? These questions should be resolved by entities like the CWCB to establish rules for conducting alluvial fans studies concerning specific hydraulic models. Examples of acceptable models should be indicated by the approving agency to guide users in the choice of acceptable models. Approval of models for alluvial fan flood hazard delineation by the State will lead to the development of submittal requirements, technical standards and adoption procedures for fan flood studies.

Submittal Requirements. Alluvial fan flood hazard studies are to be submitted first to the local governments and then to the state agency (CWCB) unless the studies are being conducted by a state or federal agency. State submittal requirements should be adopted by the local government as part of their own regulations. The submittal requirements for the flood hazard study should incorporate the following components:

- Identification of the flood hazard.
- Compilation of the data base.
- Technical analysis including: a description of the geology, hydrology, fan hydraulics and flood routing, data base, and flood contour mapping.
- Computer diskette with the hydraulic model and model results.

In the case of proposed mitigation, the CWCB would provide review and comments only until the mitigation construction is completed, at which time the mitigation would be approved along with the changes in the flood hazard delineation. Submittals for mitigation approval would include:

- Description of the mitigation.
- Effect on hydrology, hydraulics, and flood hazard delineation with and without proposed mitigation.
- Revised flood hazard mapping.
- Assessment of the structural integrity of the mitigation measure.
- Computer diskette with the hydraulic model and results.

Technical Standards. Technical standards for alluvial fan flood hazard investigations must be developed by the state. The standards should address the following study components:

- Fan geology and geomorphology.
- Hydrology.
- Data base and base maps.
- Fan hydraulics and flood routing.
- Flood hazard delineation, flood contours and hazard mapping.
- Computer diskette submitted with the appropriate models and results.

State Approval of Technical Methods. The CWCB, in cooperation with the Colorado Geological Survey, is the authority in Colorado for approving the application of floodplain hazard delineation tools for alluvial fans. Approval of a flood routing model should be based on the following criteria:

- Theoretical and fundamental soundness of the model algorithms.
- Demonstration of conservation of mass in the model application.
- Model capability to replicate basic water hydraulics compared with a standard step-backwater model.
- Ability of the model to be calibrated to replicate an historical flood event.
- Appropriate resolution of the model results for mapping purposes.
- Submittal of a model users manual, a report describing the model, model code and an executable version of the model.
- Submittal of model results depicting the model's capability.

A state policy board should address the limitations of the model during the approval process including: Does the model grossly overestimate or underestimate the potential flood hazard; and Does the model oversimplify the physical processes contributing to the flood hazard? These questions should be resolved by entities like the CWCB to establish rules for conducting alluvial fans studies concerning specific hydraulic models. Examples of acceptable models should be indicated by the approving agency to guide users in the choice of acceptable models. Approval of models for alluvial fan flood hazard delineation by the State will lead to the development of submittal requirements, technical standards and adoption procedures for fan flood studies.

Submittal Requirements. Alluvial fan flood hazard studies are to be submitted first to the local governments and then to the state agency (CWCB) unless the studies are being conducted by a state or federal agency. State submittal requirements should be adopted by the local government as part of their own regulations. The submittal requirements for the flood hazard study should incorporate the following components:

- Identification of the flood hazard.
- Compilation of the data base.
- Technical analysis including: a description of the geology, hydrology, fan hydraulics and flood routing, data base, and flood contour mapping.
- Computer diskette with the hydraulic model and model results.

In the case of proposed mitigation, the CWCB would provide review and comments only until the mitigation construction is completed, at which time the mitigation would be approved along with the changes in the flood hazard delineation. Submittals for mitigation approval would include:

- Description of the mitigation.
- Effect on hydrology, hydraulics, and flood hazard delineation with and without proposed mitigation.
- Revised flood hazard mapping.
- Assessment of the structural integrity of the mitigation measure.
- Computer diskette with the hydraulic model and results.

Technical Standards. Technical standards for alluvial fan flood hazard investigations must be developed by the state. The standards should address the following study components:

- Fan geology and geomorphology.
- Hydrology.
- Data base and base maps.
- Fan hydraulics and flood routing.
- Flood hazard delineation, flood contours and hazard mapping.
- Computer diskette submitted with the appropriate models and results.

2-Zone Alluvial Fan Flood Hazard Delineation System

The delineated hazard map would consist of two zones which would invoke different development regulations. A system defining two levels of hazards and two levels of regulations is proposed.

Zones Where Development is Prohibited. In alluvial fan flood hazard zones where the potential flooding is predicted to be a certain depth or higher, for example one foot or greater for mudflows or three feet or greater for water, development should be prohibited unless there is proposed mitigation for hazard avoidance. Such areas would be similar in concept to a floodway, however, the "no rise" principle would be replaced by hazard elimination or removal.

Zones Where Development is Restricted. In fan flood hazard zones where the potential flooding is predicted to be less than a certain depth, (for example, one foot or less for mudflows or three feet or less for water flooding), development is restricted to mitigated flow depths that are less than 0.5 ft for mudflows or 1 ft for water flooding. Mitigation may involve redirection or confinement of the flow or raising the elevation of the development to reduce the level of flood inundation. Buildings and infrastructure constructed in this zone would have to comply with structural and technical requirements to assure safety during a 100-year event. Flood hazard delineation changes would have to be documented and mapped.

Alluvial Fan Floodplain Development Permit

Without a permit no development would be allowed. It is an obligation of the local government to require a floodplain permit for development. Hazard avoidance should be the primary focus of the permitting system. Development in shallow flooding areas may be possible with appropriate floodproofing and mitigation measures. The uniqueness of the alluvial fan flooding requires a special permitting process and special permit conditions may be imposed. Although similar to the conventional floodplain development permitting process, the alluvial fan permit would be functionally separate from a riverine floodplain permit. The components of a permit application would include:

- Description of the flooding problem and the proposed development.
- Description of the proposed mitigation plan, if any.
- Report on hydrologic and hydraulic analysis of flooding.
- Flood model application to replicate existing conditions and demonstrate the effectiveness of the proposed mitigation.
- A verification of the flood simulation by the floodplain administrator or the contractor.
- An assessment of the structural integrity of the proposed mitigation.
- Permit and checklist.

Zoning regulations would direct the project proponent to prepare and submit a permit application which would include a detailed study. The permit would be issued only after all the appropriate reviews had been satisfactorily completed.

Construction Inspection and Post-Construction Certification

As part of local zoning regulations and the alluvial fan floodplain development permit process, regularly scheduled inspections should occur during construction. Final inspection reports and as-built drawings should be submitted to the CWCB staff, to the planning and zoning commissions, and to local officials as specified by the regulations to obtain a certification of occupancy. Procedural and technical compliance with regulations will be a prerequisite for certification of occupancy in mud and debris flow hazard zones.

2-Zone Alluvial Fan Flood Hazard Delineation System

The delineated hazard map would consist of two zones which would invoke different development regulations. A system defining two levels of hazards and two levels of regulations is proposed.

Zones Where Development is Prohibited. In alluvial fan flood hazard zones where the potential flooding is predicted to be a certain depth or higher, for example one foot or greater for mudflows or three feet or greater for water, development should be prohibited unless there is proposed mitigation for hazard avoidance. Such areas would be similar in concept to a floodway, however, the "no rise" principle would be replaced by hazard elimination or removal.

Zones Where Development is Restricted. In fan flood hazard zones where the potential flooding is predicted to be less than a certain depth, (for example, one foot or less for mudflows or three feet or less for water flooding), development is restricted to mitigated flow depths that are less than 0.5 ft for mudflows or 1 ft for water flooding. Mitigation may involve redirection or confinement of the flow or raising the elevation of the development to reduce the level of flood inundation. Buildings and infrastructure constructed in this zone would have to comply with structural and technical requirements to assure safety during a 100-year event. Flood hazard delineation changes would have to be documented and mapped.

Alluvial Fan Floodplain Development Permit

Without a permit no development would be allowed. It is an obligation of the local government to require a floodplain permit for development. Hazard avoidance should be the primary focus of the permitting system. Development in shallow flooding areas may be possible with appropriate floodproofing and mitigation measures. The uniqueness of the alluvial fan flooding requires a special permitting process and special permit conditions may be imposed. Although similar to the conventional floodplain development permitting process, the alluvial fan permit would be functionally separate from a riverine floodplain permit. The components of a permit application would include:

- Description of the flooding problem and the proposed development.
- Description of the proposed mitigation plan, if any.
- Report on hydrologic and hydraulic analysis of flooding.
- Flood model application to replicate existing conditions and demonstrate the effectiveness of the proposed mitigation.
- A verification of the flood simulation by the floodplain administrator or the contractor.
- An assessment of the structural integrity of the proposed mitigation.
- Permit and checklist.

Zoning regulations would direct the project proponent to prepare and submit a permit application which would include a detailed study. The permit would be issued only after all the appropriate reviews had been satisfactorily completed.

Construction Inspection and Post-Construction Certification

As part of local zoning regulations and the alluvial fan floodplain development permit process, regularly scheduled inspections should occur during construction. Final inspection reports and as-built drawings should be submitted to the CWCB staff, to the planning and zoning commissions, and to local officials as specified by the regulations to obtain a certification of occupancy. Procedural and technical compliance with regulations will be a prerequisite for certification of occupancy in mud and debris flow hazard zones.

Maintenance and Monitoring of Mitigation Facilities

Mud and debris flow mitigation facilities should be monitored prior to each flood season. In Colorado, the high hazard season extends from May through October. As a prerequisite for approval of mitigation measures, a maintenance and monitoring schedule should be submitted with the mitigation design. Mitigation structures and facilities should be maintained immediately following an event. This epitomizes the need for on-going care of the hazard delineation and mitigation system.

Maintenance and Operation of Mitigation Facilities

Maintenance and operation of mitigation facilities may include removing sediment and debris from debris basins, clearing trash and debris fences, cleaning conveyance channels and streets, removing debris blockage from all conveyance structures, repairing or restoring freeboard in levees and berms, and repairing any damaged structures. It is possible that a extreme rainfall event may be followed a smaller rainfall event that could be potentially more damaging because the extreme event stored or charged the upstream watershed channel with large quantities of sediment and debris that did not reach the fan apex. Long term and short term maintenance should be scheduled for continued satisfactory operation of the mitigation structures.

The monitoring for potential problems with the mitigation structures should be primary focus of the city or county engineer. Uncertified mitigation measures should be monitored for potential downstream hazard in the event of failure. The mitigation system should be inspected and declared functional after an event and certified that it would not be prone to failure during the next event.

Monitoring and Updating of the Flood Hazard Delineation Model and Data Base

The hazard delineation model should be upgraded and revised as the model is improved and as subsequent flood hazard investigations expand the data base. The floodplain administrator should update the model to incorporate improvements and enhance the model's capability to simulate the physical system. For the model to be effective, it must be updated to provide an accurate portrayal of the alluvial fan physical condition and changes including the degree of urbanization and the construction of flood mitigation. Ongoing research should lead to improved modeling capability in the areas of GIS delineation of streets and buildings, risk assessment and mobile bed analysis. There is a dearth of data related to mud and debris flow events. Monitoring will provide information regarding performance of mitigation measures. Volumes, peak discharge, rainfall totals, timing and duration should all be considered in designing a monitoring program.

Maintenance and Monitoring of Mitigation Facilities

Mud and debris flow mitigation facilities should be monitored prior to each flood season. In Colorado, the high hazard season extends from May through October. As a prerequisite for approval of mitigation measures, a maintenance and monitoring schedule should be submitted with the mitigation design. Mitigation structures and facilities should be maintained immediately following an event. This epitomizes the need for on-going care of the hazard delineation and mitigation system.

Maintenance and Operation of Mitigation Facilities

Maintenance and operation of mitigation facilities may include removing sediment and debris from debris basins, clearing trash and debris fences, cleaning conveyance channels and streets, removing debris blockage from all conveyance structures, repairing or restoring freeboard in levees and berms, and repairing any damaged structures. It is possible that a extreme rainfall event may be followed a smaller rainfall event that could be potentially more damaging because the extreme event stored or charged the upstream watershed channel with large quantities of sediment and debris that did not reach the fan apex. Long term and short term maintenance should be scheduled for continued satisfactory operation of the mitigation structures.

The monitoring for potential problems with the mitigation structures should be primary focus of the city or county engineer. Uncertified mitigation measures should be monitored for potential downstream hazard in the event of failure. The mitigation system should be inspected and declared functional after an event and certified that it would not be prone to failure during the next event.

Monitoring and Updating of the Flood Hazard Delineation Model and Data Base

The hazard delineation model should be upgraded and revised as the model is improved and as subsequent flood hazard investigations expand the data base. The floodplain administrator should update the model to incorporate improvements and enhance the model's capability to simulate the physical system. For the model to be effective, it must be updated to provide an accurate portrayal of the alluvial fan physical condition and changes including the degree of urbanization and the construction of flood mitigation. Ongoing research should lead to improved modeling capability in the areas of GIS delineation of streets and buildings, risk assessment and mobile bed analysis. There is a dearth of data related to mud and debris flow events. Monitoring will provide information regarding performance of mitigation measures. Volumes, peak discharge, rainfall totals, timing and duration should all be considered in designing a monitoring program.

Appendix A. Practical Mitigation Design Guidelines

Some practical guidelines on development and mitigation on alluvial fans.

- Development should not be permitted without a master drainage and development plan.
- Flood conveyance off the fan is preferred over storage above populated areas.
- Redirection of flow near the fan apex should be avoided.
- Basements and mobile homes should be prohibited or subject to strict regulation.
- Streets should be aligned and designed to help convey flows.
- Emergency access routes should be designed and should not convey flows.
- Berms and levees can help direct the flow away from structures and into streets.
- Downfan impacts of redirected flows should be carefully analyzed.
- The use of slope stabilization and drop structures should be encouraged in residential areas.
- Elevation of structures should be regulated according to hazard zone delineation. Structures should be elevated to a prescribed height above the potential depositional flow depth.
- All mitigation measures should be in concert with existing flood control facilities.
- Floodproofing methods should be encouraged.
- Conveyance features should be designed and maintained for stability and permanence.
- Floodwall height should be designed with appropriate freeboard for mudflows.
- Scour depth for mitigation design should be analyzed on the basis of clear water flows and maximum velocity. Floodwalls and pilings should be placed at a prescribed depth below predicted scour depths.
- Riprap on berms or levees should be considered as a potential source for increasing the debris load. Concrete lining is a much better alternative near the fan apex.
- Flood detention should be designed to store the 100-yr event with appropriate bulking for sediment loads. Debris basins should be fitted with debris racks.
- Loss of channel conveyance is the most common cause of flood damage on alluvial fans. Potential blockage may occur at bridges, culverts, channel bends and constrictions, and changes in slope. Texas dips or low flow culverts and over-road capacity are preferred channel crossings. Bridges should be designed without pilings. Important emergency access routes should be kept open during flooding.
- The potential for boulder impact should be considered when designing mitigation structures.
- As a condition of plat or building permit approval, developers should be required to implement mitigation and prepare revisions to the master drainage plan.
- Buildings should be prohibited in areas of predicted high velocities; replacement of existing buildings in such locations should be strongly discouraged or prohibited.
- Slope protection that will not erode during mudflow events should be required for fill, berms and levees.

FEMA METHOD FOR PREDICTING FLOOD HYDRAULIC BOUNDARIES ON ALLUVIAL FANS REQUIRES VERIFICATION

J. S. O'Brien
FLO Engineering, Inc.

W. T. Fullerton
FLO Engineering, Inc.

Introduction

The Federal Emergency Management Agency (FEMA) has published a user's manual for its probabilistic approach to delineating hydraulic boundaries on alluvial fans. The manual describes the application of the computer program FAN, an encoded version of the FEMA method. The FEMA method has been the subject of much scrutiny (Fuller, 1990; Baker, et al., 1990; French, 1987; Grindeland, et al., 1990). The inherent assumptions in the method do not apply to most alluvial fans and it should not be used on urbanized fans. The limited available field data do not support its continued application.

FEMA's Alluvial Fan Method for Predicting Hydraulic Boundaries

Most alluvial fan flood studies are conducted because of underlying interest in flood insurance or flood mitigation for existing or proposed development. FEMA's method for assessing flood hazard zones on alluvial fans combines a single channel method (referred to as the Dawdy method; Dawdy, 1979) and a multiple channel method which is applied downfan of the single channel point of bifurcation (DMA, 1985). The depth and velocity boundaries are determined in 1 foot or 1 fps increments, respectively. Flood insurance rates are based on predicted hydraulic boundaries with a flow depth exceeding 0.5 ft. These boundaries have a risk assessment of one percent corresponding to the 100-year return period flood.

The only data required to apply the FEMA single channel model are several peak discharges from the upstream watershed and their associated return periods. The hydraulic boundaries are expressly dependent on the skew coefficient of the flood frequency curve of ungaged watersheds. For the

multiple channel method an average fan slope and Manning n roughness value are also required. The resulting velocity and depth boundaries when superimposed on a topographic map are intended to define the physical extent of flooding. The data base required by the method is insufficient to adequately address the complex physical processes of unconfined flow over an alluvial fan.

Discussion of the Assumptions and Limitations of the FEMA Method

An in-depth investigation of the FEMA method reveals that it is based on a set of assumptions implicit in the use of channel regime equations (Dawdy, 1979; DMA, 1985; French, 1987). The method also incorporates various assumptions regarding channel avulsion and critical flow. Concern over these assumptions and the effect of the FEMA method results on floodplain management have been expressed by others (Fuller, 1990; Baker, et al., 1990). A brief discussion of several of the assumptions in the FEMA method follows.

* *FEMA's method assumes an equal probability and random distribution of a single channel across a given fan contour. The fan is assumed to have a uniform surface at locations equidistant from the fan apex.*

The application of the method should be limited to undeveloped, uniform topography alluvial fans (fans with an idealized, plane conical surface). When applied to a fan with complex topography, local relief is ignored. Within a predicted FEMA depth boundary, large variation in actual flow depth will occur. FEMA elevation requirements for structures within a given boundary are the same regardless whether the structures are designed for a channel bottom or a higher ridge. The portions of a fan that are steeper or have existing channels have a higher probability of flow occurrence.

* *The flow is assumed to be confined to an identifiable channel which migrates over the fan during the flood event.*

Channel migration is based on an assumed probability of avulsion of 0.5 resulting in a channel avulsion factor of 1.5. This assumes that there is a 50% chance that the channel will avulse upstream of a given hydraulic boundary during the peak flow. The avulsion factor has the consequence of increasing the fan width corresponding to a particular depth or velocity boundary and

extends the boundary further downfan. An 1.5 avulsion factor results in a fifty percent larger boundary width than if no avulsion was considered. Considering the actual process of channel avulsion, avulsion increases neither the physical width of the potential flow surface or the downfan flow hydraulics. Although any value can be assumed, the avulsion factor has not been verified and there is no basis for choosing a specific value.

Channel migration does not occur during every flood event and depends on debris loading, channel incision and potential for channel erosion. Channel avulsion is more likely to occur on small braided channels than on large incised channels. DMA (1985) reports that avulsions occur on a geologic time scale rather than over a "planning horizon." The concept of channel avulsion is less important for large flood events, where flow depths overwhelm small obstructions and tend to follow the steepest route downfan.

* *FEMA's method does not consider development and flood control measures which affect the flow path and discharge.*

The assessment of fan flooding is generally associated with development where the flow paths have been altered by buildings, levees or debris basins. FEMA's method assumes the flow is unobstructed or unconstrained. FEMA addresses this problem, "In portions of alluvial fans in which natural alluvial fan processes may not occur, such as in areas of entrenched channels, areas protected by flood control works and heavily developed areas, the Study Contractor should exercise good engineering judgement in determining the most appropriate methodology..." (FEMA Guidelines, 1985). Nevertheless, FEMA's method is routinely applied to developed fans.

* *Fan hydraulics predicted with the FEMA method are based on empirical channel geometry relationships not representative of self-forming channels on alluvial fans.*

The expressions for channel width W and flow depth d as function of peak discharge Q as based on the Dawdy method are (Dawdy, 1979): $W = 9.5\ Q^{0.4}$ and $d = 0.07\ Q^{0.4}$. These equations result in a <u>constant</u> width to depth ratio $W/d = 136$ regardless of fan slope, channel roughness, and bed and bank material, all of which cause variation in channel geometry in the downfan direction or between different fans.

extends the boundary further downfan. An 1.5 avulsion factor results in a fifty percent larger boundary width than if no avulsion was considered. Considering the actual process of channel avulsion, avulsion increases neither the physical width of the potential flow surface or the downfan flow hydraulics. Although any value can be assumed, the avulsion factor has not been verified and there is no basis for choosing a specific value.

Channel migration does not occur during every flood event and depends on debris loading, channel incision and potential for channel erosion. Channel avulsion is more likely to occur on small braided channels than on large incised channels. DMA (1985) reports that avulsions occur on a geologic time scale rather than over a "planning horizon." The concept of channel avulsion is less important for large flood events, where flow depths overwhelm small obstructions and tend to follow the steepest route downfan.

* *FEMA's method does not consider development and flood control measures which affect the flow path and discharge.*

The assessment of fan flooding is generally associated with development where the flow paths have been altered by buildings, levees or debris basins. FEMA's method assumes the flow is unobstructed or unconstrained. FEMA addresses this problem, "In portions of alluvial fans in which natural alluvial fan processes may not occur, such as in areas of entrenched channels, areas protected by flood control works and heavily developed areas, the Study Contractor should exercise good engineering judgement in determining the most appropriate methodology..." (FEMA Guidelines, 1985). Nevertheless, FEMA's method is routinely applied to developed fans.

* *Fan hydraulics predicted with the FEMA method are based on empirical channel geometry relationships not representative of self-forming channels on alluvial fans.*

The expressions for channel width W and flow depth d as function of peak discharge Q as based on the Dawdy method are (Dawdy, 1979): $W = 9.5\ Q^{0.4}$ and $d = 0.07\ Q^{0.4}$. These equations result in a <u>constant</u> width to depth ratio $W/d = 136$ regardless of fan slope, channel roughness, and bed and bank material, all of which cause variation in channel geometry in the downfan direction or between different fans.

18% average difference for 10 of the 11 fan floods; Apparently, a good correlation. Would the channel width/depth ratios compare as well?

The FEMA predicted width/depth ratio of a single channel is constant 136. From the DMA (1985) report, W/d ratios can be computed from reported discharges, observed widths and using the previously described depth-discharge equation for the 11 alluvial fan floods. The W/d ratio ranged from 19 to 289, a poor comparison with the FEMA value of 136. Nevertheless, these results lead DMA to conclude "(t)he width of a single channel can be reasonably determined by the present FEMA method."

DMA was unable to substantiate avulsion coefficient of 1.5. There was insufficient data to even attempt a statistical correlation. DMA concluded that "(t)he present data base is insufficient to better define the avulsion coefficient. Therefore the present value of the avulsion coefficient should continue to be used." A questionable conclusion! The conclusion should have been drawn that there was no data to justify an avulsion coefficient.

Finally, DMA plotted channel position near the fan apex and concluded that the evidence supported the FEMA method assumption of random channel locations on the fan. The channel direction, however, was not correlated with the fan slope. If the channel path did not correlate with the steepest portion of the fan, then the randomness conclusion would have been justified.

The FEMA method requires verification. The DMA study accomplished nothing towards this goal. There are no published results to verify the method with measured flood depths and velocities.

Conclusions

Application of the FEMA method is often requested on alluvial fans studies by either the floodplain manager or FEMA's technical representative. Although, intended for the purpose of assessing flood insurance rates, the FEMA method has been used to evaluate the design of mitigation measures. Consequently, there is a concern that the FEMA method results may be incorporated into the design of flood containment structures.

Several conclusions can be drawn from this review: 1) The theoretical derivation of the FEMA model is flawed. The FEMA method for the prediction of flood hydraulics on alluvial fans does not present a realistic analysis of the physical processes on alluvial fans. 2) There are technical deficiencies in its application and there are no published guidelines on the limits of its applicability. Highlighted in text was the lack of verification of its assumptions, empirical equations or results. 3) The method does not err on the conservative side and it should not be used for flood mitigation design. 4) Finally, the risk assessment based on the FEMA method does not reflect the potential of the flood hazard.

References

Baker, V. R., Demsey, K. A., Ely, L. L., Fuller, J. E., House, P. K., O'Conner, J. E., Onken, J. A., Pearthree, P. A., and Vincent, K. R. 1990. "Application of Geological Information to Arizona Flood Hazard Assessment." In Proceedings ASCE Symposium on Hydraulics/Hydrology of Arid Lands. San Diego, CA., pp. 621-626.

Dawdy, D. R. 1979 "Flood Frequency Estimates on Alluvial Fans." J. Hydr. Div., ASCE, V. 105, pp. 1407-1413.

Dawdy, D. R., Hill, J. C. and Hanson, K. C. 1989 "Implementation of FEMA Guidelines on Alluvial Fans." In Proceedings of the 1989 ASCE Natl. Conf. on Hydraulic Engineering, New Orleans, LA., pp. 64-69.

DMA 1985 "Alluvial Fan Flooding Methodology and Analysis." Prepared for FEMA by DMA Consulting Engineers, Rey, CA.

Federal Emergency Management Agency 1985 "Guidelines and Specifications for Study Contractors." Federal Insurance Administration, Washington, D.C.

French, R. H. 1987 Hydraulic Process on Alluvial Fans. Elsevier Science Publishing Co., New York.

Fuller, J. E. 1990 "Misapplication of the FEMA Alluvial Fan Model: A Case History." In Proceedings ASCE Symposium on Hydraulics/Hydrology of Arid Lands. San Diego, CA., pp. 367-372.

Grindeland, T. R., J. S. O'Brien, and R. M. Li 1990 "Flood Hazard Delineation on Alluvial Fans." In Proceedings of the ASCE Symposium on Hydraulics/Hydrology of Arid Lands, San Diego, CA., pp. 268-373.

Table 1. Freeboard and Factor of Safety Recommendations[1]		
Type of Flooding	Freeboard (ft)	Impact Factor of Safety
Shallow water flooding <1 ft	1	1.1
Moderate water flooding <3 ft	1	1.2
Moderate water flooding <3 ft; debris and boulders <1 ft	1	1.2
Mud floods, debris flows, 3 ft, surging, debris, sediment deposition, boulders <1 ft	2	1.25
Mudflows, debris flows, <3 ft, surging, debris, sediment deposition, minor waves, boulders > 1ft, mud levees	3	1.4
Mudflows, debris flows, >3 ft, surging, waves, boulders >3 ft, major deposition	3 +	1.5
[1]After FEMA Manual, Chapter 4 (1994 draft), modified.		

Channel lining with concrete, soil cement or riprap grouting can be effective, but very expensive. Two important design considerations with lining channels on steep alluvial fan slopes are abrasion of the lining and excess pore water pressure. The abrasion of concrete lining occurs with frequent or perennial low flows with high bedload. Failure to consider abrasion during design can shorten the life of the structure and could cause failure during a design flood event. Drains pipes and weep holes can reduce pore water pressure buildup, but construction of channel linings with drain pipes and weep holes can be very expensive for long channel reaches.

The most difficult design task for mud flood channels is to design the inlet and outlet transitions of the straightened reach. At the inlet, a smooth transition is required to avoid flow constriction and debris plugging. Scour and sedimentation may induce failure of the inlet structure. Headwalls and aprons are often necessary at both the inlet and outlets. Without an apron or headwall, local outlet scour can initiate headcuts that will migrate upstream through the straight portion of the channel and undermine channel facilities such as riprap bank protection, and channel drop structures.

Mudflows

Mudflows have high fluid viscosity and low velocities compared to mud floods. Mudflows are more commonly associated with higher frequency, smaller magnitude storm events typically with 10-year to 25-year return periods. Larger flood events have too much water for the available sediment loading in the watershed to generate a mudflow. Within a given watershed, the total volume of water and sediment in a mudflow will generally be less that in a mud flood. One exception is volcanically initiated mudflows.

The hydraulic flow properties of mudflows include relatively slow flow velocities and large flow depths which sustain motion on flat slopes. Flood mitigation design must include consideration of flow avulsion, debris and mud plugging of channel and conveyance facilities, and cleanup/maintenance. Effective mitigation measures for mudflows include storage, deflection, spreading and frontal wave dissipation. Mudflow detention basins can be very effective where mudflow volume is relatively small and can be estimated for the design flood event. Steep watershed canyons provide limited storage capacity for detention basins. When storage capacity is insufficient, a preferred mitigation alternative is to spread the flow over non-urban areas such as open space areas, parks and recreation areas where cleanup costs are minimal. Flow deflection to accomplish flow spreading can be complicated and should consider impact pressures, static loading, and flow runup over previously mud deposits which could result in overtopping the structure. Possible flow avulsions near the inlet of storage facilities must also be considered as deposits buildup. Deflection of flow into areas that require disposal of the excavated material can be very expensive to operate and maintain.

Deflection walls can be constructed of concrete or consist of earth berms. Earth berms designed to confine mudflows should have an erosion resistant core or face. Runup and overtopping of berms and walls can be averted by proper orientation of the structure thus deflecting the flow path. Vertical impact faces are also recommended to limit runup. The arrival of a mudflow frontal wave can be very destructive. As part of effective flood hazard mitigation, it is necessary to absorb the momentum of the frontal wave which could be carrying large boulders and debris capable of tremendous impact forces and runup against mitigation structures. Impact surfaces should be designed to withstand the impact of the large boulders found on the fan flowing at design depth and velocities. Freeboard design and factor of safety values for impact structures are given in Table 1.

Effective mitigation measures include levees that confine the mudflow outside the channel on the alluvial fan. A portion of the alluvial fan surface can be dedicated to the overbank storage detention. The levee is constructed parallel to the channel allowing an appropriate distance between the channel and berm for mudflow and debris storage; typically 50 ft to 100 ft can be set aside. The channel conveyance capacity is then designed to permit some overbank flow during the peak discharge. Lowering channel banks to create overbank flooding and grading floodplain areas for overbank storage will enhance mudflow deposition. The levee design will generally only require a height of 3 ft to 5 ft, as long as a major change in flow direction is not anticipated. Trees and other obstacles can be left on the floodplain to enhance flow cessation. Potential for levee erosion and failure must be evaluated. A maintenance plan should be prepared to access and remove mudflow deposits between the levees after the event. This concept for mudflow mitigation is being considered for several alluvial fans in Colorado Springs on Cheyenne Mountain.

Impact loads result from objects entrained in the flow striking a structure surface with a velocity component perpendicular to the flow direction. To compute the impact load, consideration should be given to the evidence of debris and boulders transported on the fan by recent flood events. To be conservative, the largest boulder transported by a flow should be used to determine the impact load. The impact loading P_I is given by:

$$P_I = \frac{wV}{(Ag\Delta t)}$$

where w is the weight of the object, g is the gravitational acceleration, V is the flow velocity, A is the area of impact assumed to be a percentage of the cross sectional area of the object and Δt is the duration of impact. The FEMA Manual (draft, 1994) also presents equations for the computation of the hydrostatic and hydrodynamic loads.

The design of detention basins requires the assessment of the volume of sediment for the design flood event. An acceptable method is to bulk the 100-year hydrograph volume for the potential average concentration of the flow event. Typically, peak sediment concentration by volume for a mudflow event ranges from 45% to 55%, and the average sediment concentration for the flow event is of the order of 25% to 35%. A conservative approach is to use an average concentration of 50% by volume which results in a bulking factor BF of 2 given by:

$$BF = \frac{1}{(1 - Cv)}$$

Debris Flows

Debris flows involve the motion of large clastic material and debris characterized by destructive frontal impact surging and flow cessation on steep slopes. Dispersive stress arising from the collision of clastic particles controls the exchange of flow momentum and energy dissipation. Debris flows are much less fluid than mud floods. The fluid matrix viscosity is comparatively small corresponding to the small concentration of fine sediments. The fluid matrix is essentially non-cohesive. The interstial fluid does not significantly inhibit particle contact, permitting frequent collisions and impact between the solid clasts.

Debris flows generally originate on steep slopes and attain high velocities. The impact forces generated by fast moving course material can be exceedingly destructive. Debris flow flood hazard mitigation should be focused on arresting the large clast and avoiding the destructive impact forces while draining the matrix fluid. A major problem with debris flow mitigation is assessing the volume of the event. Mitigation may be impractical for large events (i.e. 100-year event). Structures such as sabo dams, debris rakes and fences are designed to separate out the debris material. The purpose of sabo dams is to arrest the frontal wave of debris, store as much solid material as possible and allow the debris flow to be drained of the fluid matrix.

Sabo dams are constructed in the steep mountain canyons near the source of debris in the upper watershed. The storage capacity of sabo dams is limited by the steep slope, but its purpose is to remove the largest debris elements from the flow matrix. The concrete walls of sabo dams are extremely thick (up to 10 m) and are constructed with drain pipes or steel frame structures (such as railroad rails) to permit drainage of the pore water. Once the pore water is drained, the mobility of coarse clasts decreases very rapidly. The design of sabo dams requires an assessment of the potential storage volume, maximum impact forces, protection against scour, stability under static loading, and a plan for maintenance access and debris removal. Sabo dams in basins generating frequent debris flows should be periodically inspected for impact damage, foundation stability and scour around the structure. Some sabo dams have early warning systems to monitoring the debris flow arrival or the rates of filling to provide advanced warning for downfan evacuation.

Other recommended measures to mitigate the damage of debris flows are limited to detention basins. Channel conveyance off the alluvial fan is not suggested because a break-in-slope or channel transition can cause the debris flow to abruptly stop and plug the conveyance facility. Debris flows generally will not flow on the mild slopes of alluvial fans and tend to pile up near fan apex. In most cases, debris flow hazard avoidance is the preferred mitigation.

CONCLUSIONS

The rheology of hyperconcentration sediment flow is relatively complex, but the quadratic formulation describes the continuum of flow behavior ranging from mud floods to debris flows. The quadratic rheological combines the effects of yield, viscous, turbulent and dispersive stresses in hyperconcentrated sediment flows. Numerical modeling of mud floods, mudflows and debris flows is possible with the two-dimensional model FLO-2D.

This paper emphasizes the need to design appropriate mitigation structures based on the rheological behavior of hyperconcentrated sediment flows. Straight, uniform flowing channels that convey the water and sediment off alluvial fans are best suited for mud floods. Detention basins, deflection walls, berms and levees are best suited for mudflows. Thick sabo dams in steep mountain canyons are recommended to arrest debris flows.

REFERENCES

Bagnold, R. A. (1954). "Experiments on a gravity-free dispersion of large solid spheres in a Newtonian fluid under shear," *Proc. Royal Soc. of London*, Series A, 225, 49-63.

Sabo dams are constructed in the steep mountain canyons near the source of debris in the upper watershed. The storage capacity of sabo dams is limited by the steep slope, but its purpose is to remove the largest debris elements from the flow matrix. The concrete walls of sabo dams are extremely thick (up to 10 m) and are constructed with drain pipes or steel frame structures (such as railroad rails) to permit drainage of the pore water. Once the pore water is drained, the mobility of coarse clasts decreases very rapidly. The design of sabo dams requires an assessment of the potential storage volume, maximum impact forces, protection against scour, stability under static loading, and a plan for maintenance access and debris removal. Sabo dams in basins generating frequent debris flows should be periodically inspected for impact damage, foundation stability and scour around the structure. Some sabo dams have early warning systems to monitoring the debris flow arrival or the rates of filling to provide advanced warning for downfan evacuation.

Other recommended measures to mitigate the damage of debris flows are limited to detention basins. Channel conveyance off the alluvial fan is not suggested because a break-in-slope or channel transition can cause the debris flow to abruptly stop and plug the conveyance facility. Debris flows generally will not flow on the mild slopes of alluvial fans and tend to pile up near fan apex. In most cases, debris flow hazard avoidance is the preferred mitigation.

CONCLUSIONS

The rheology of hyperconcentration sediment flow is relatively complex, but the quadratic formulation describes the continuum of flow behavior ranging from mud floods to debris flows. The quadratic rheological combines the effects of yield, viscous, turbulent and dispersive stresses in hyperconcentrated sediment flows. Numerical modeling of mud floods, mudflows and debris flows is possible with the two-dimensional model FLO-2D.

This paper emphasizes the need to design appropriate mitigation structures based on the rheological behavior of hyperconcentrated sediment flows. Straight, uniform flowing channels that convey the water and sediment off alluvial fans are best suited for mud floods. Detention basins, deflection walls, berms and levees are best suited for mudflows. Thick sabo dams in steep mountain canyons are recommended to arrest debris flows.

REFERENCES

Bagnold, R. A. (1954). "Experiments on a gravity-free dispersion of large solid spheres in a Newtonian fluid under shear," *Proc. Royal Soc. of London*, Series A, 225, 49-63.

KEYWORDS:

mudflows
mud floods
debris flows
structural design
mud/debris flow countermeasures
mud/debris flow mitigation
mud/debris flow rheology
mud/debris flow shear stresses

ON THE IMPORTANCE OF MUD AND DEBRIS FLOW RHEOLOGY IN STRUCTURAL DESIGN

P. Y. Julien[1] and J. S. O'Brien[2], Members, ASCE

ABSTRACT

Hyperconcentrated sediment flows have been classified as mud floods, mudflows and debris flows. Distinct physical processes characterize each type of sediment laden flow. The design of flood mitigation requires knowledge of the rheological properties of the hyperconcentrated sediment flow expected in a given watershed. Mitigation design strategies are outlined for mud floods, mudflows and debris flows. For mud floods, subcritical turbulent flows are conveyed in straight channels with minimal frictional resistance. For mudflows, flood hazard mitigation should consider detention basins for small volumes or spreading large volumes with the use of deflection walls. High momentum, debris flows require sabo dams. Mitigation measures should be fully operational through the range of hyper-concentrated sediment flows.

INTRODUCTION

Hyperconcentrated sediment flows can be initiated by numerous causes including intense rainfall, rapid snowmelt volcanic and man-made activities. The sediment load may also be increased by hillslope failure and bank collapse during the flood event. Flow hydraulics, flow cessation and runout distances of hyperconcentrated sediment flows are governed by the volume and properties of the fluid matrix which is comprised of the fluid and sediment particles. The fluid matrix

---

[1] Prof. of Civil Engineering, Engineering Research Center, Colorado State University, Ft. Collins, CO 80523 (Phone: 970-491-8450; Fax: 970-491-7008; e-mail: pjulien@engr.colostate.edu).

[2] Hydraulic Engineer, FLO Engineering, Inc., Breckenridge, CO 80424 (Phone and Fax: 520-339-1935; e-mail: jsobflo2d@aol.com).

of historical flood events, and a rheological and particle size analysis of deposits. Rheological analyses involve four different types of shear stresses: 1) yield stress; 2) viscous stress; 3) turbulent stress; and 4) dispersive stress. The non-Newtonian nature of hyperconcentration sediment flows results from several physical processes: the cohesive nature of fine sediment particles τ_c; the Mohr-Coulomb shear τ_{mc}, the sum of which defines yield stress τ_y; the viscous shear stress τ_v which accounts for the fluid-particle viscosity; the turbulent shear stress τ_t, and finally, the dispersive stress τ_d which accounts for the collision of sediment clasts.

The total fluid shear stress τ in hyperconcentrated sediment flows results from the sum of the five shear stress components:

$$\tau = \tau_{mc} + \tau_c + \tau_v + \tau_t + \tau_d \tag{1}$$

A quadratic rheological equation describes the flow continuum through the range of sediment concentration for these shear stresses. When written in term of shear rates, or velocity gradient du/dy; τ_{mc} and τ_c are independent of velocity gradient, τ_v varies linearly with the velocity gradient and both τ_t and τ_d vary with the second power of the velocity gradient. The following quadratic rheological model is obtained:

$$\tau = \tau_y + \eta \frac{du}{dy} + \zeta \left(\frac{du}{dy}\right)^2 \tag{2}$$

where

$$\tau_y = \tau_{mc} + \tau_c$$

and $$\zeta = \rho_m l_m^2 + a_i \rho_s \lambda^2 d_s^2$$

In the above equations η is the dynamic viscosity of the mixture; τ_c is the cohesive yield strength; τ_{mc} is the Mohr-Coulomb shear stress where $\tau_{mc}=p_s \tan \phi$ depending on the intergranular pressure p_s and the angle of repose ϕ of the material; and ζ is the inertial shear stress coefficient depending on the mass density of the mixture ρ_m, the Prandtl mixing length l_m, the sediment size d_s, the volumetric sediment concentration C_v; and ρ_s is the mass density of sediment. The mixing length l_m is usually given as a function of the distance from the boundary y and the von Karman constant κ. As a first approximation in depth-integrated flows, the approximate mixing length can be determined by $l_m \cong \kappa h$, where h is the flow depth h and $\kappa=0.4$. The coefficient a_i has been shown to highly variable and Takahashi (1980) proposed $a_i \cong 0.01$. Bagnold defined the linear sediment concentration λ as

$$\frac{1}{\lambda} = \left(\frac{C_m}{C_v}\right)^{1/3} - 1 \tag{3}$$

in which the maximum concentration of sediment particles $C_m \cong 0.615$.

of historical flood events, and a rheological and particle size analysis of deposits. Rheological analyses involve four different types of shear stresses: 1) yield stress; 2) viscous stress; 3) turbulent stress; and 4) dispersive stress. The non-Newtonian nature of hyperconcentration sediment flows results from several physical processes: the cohesive nature of fine sediment particles τ_c; the Mohr-Coulomb shear τ_{mc}, the sum of which defines yield stress τ_y; the viscous shear stress τ_v which accounts for the fluid-particle viscosity; the turbulent shear stress τ_t, and finally, the dispersive stress τ_d which accounts for the collision of sediment clasts.

The total fluid shear stress τ in hyperconcentrated sediment flows results from the sum of the five shear stress components:

$$\tau = \tau_{mc} + \tau_c + \tau_v + \tau_t + \tau_d \tag{1}$$

A quadratic rheological equation describes the flow continuum through the range of sediment concentration for these shear stresses. When written in term of shear rates, or velocity gradient du/dy; τ_{mc} and τ_c are independent of velocity gradient, τ_v varies linearly with the velocity gradient and both τ_t and τ_d vary with the second power of the velocity gradient. The following quadratic rheological model is obtained:

$$\tau = \tau_y + \eta \frac{du}{dy} + \zeta \left(\frac{du}{dy} \right)^2 \tag{2}$$

where

$$\tau_y = \tau_{mc} + \tau_c$$

and $$\zeta = \rho_m l_m^2 + a_i \rho_s \lambda^2 d_s^2$$

In the above equations η is the dynamic viscosity of the mixture; τ_c is the cohesive yield strength; τ_{mc} is the Mohr-Coulomb shear stress where $\tau_{mc}=p_s \tan \phi$ depending on the intergranular pressure p_s and the angle of repose ϕ of the material; and ζ is the inertial shear stress coefficient depending on the mass density of the mixture ρ_m, the Prandtl mixing length l_m, the sediment size d_s, the volumetric sediment concentration C_v; and ρ_s is the mass density of sediment. The mixing length l_m is usually given as a function of the distance from the boundary y and the von Karman constant κ. As a first approximation in depth-integrated flows, the approximate mixing length can be determined by $l_m \cong \kappa h$, where h is the flow depth h and $\kappa=0.4$. The coefficient a_i has been shown to highly variable and Takahashi (1980) proposed $a_i \cong 0.01$. Bagnold defined the linear sediment concentration λ as

$$\frac{1}{\lambda} = \left(\frac{C_m}{C_v} \right)^{1/3} - 1 \tag{3}$$

in which the maximum concentration of sediment particles $C_m \cong 0.615$.

Julien (1997). A manual is available which further discusses the model attributes and its applications. Over thirty flood hazard delineation projects have been completed using the FLO-2D model. A short course by O'Brien and Julien (1997) is prepared to make the model available to floodplain managers and engineers.

INFLUENCE OF FLOW RHEOLOGY ON STRUCTURAL DESIGN

Flood mitigation design must take into consideration the rheological behavior of the three types of hyperconcentrated sediment flows previously described, i.e. mud floods, mudflows and debris flows. Flood mitigation measures fall into four categories: 1) flood hazard avoidance; 2) regulatory and zoning; 3) storage; or 4) conveyance. The first two categories include such measures as elevating on armored fill, planning open space for flood prone areas and physically removing structures in the flood path. The last two mitigation measures cover storage and conveyance methods which include detention/debris basins, levees and berms, debris fences and deflectors, channelization and channel lining, drop structures, energy dissipation and street alignment. Mitigation measures for each of the three classes of hyper-concentrated sediment flows are discussed.

Mud floods

Mud floods are very fluid flows with high velocities in which the fluid matrix viscosity is comparable to that of water. For large storm events on the order of the 100-year storm the volume of water and sediment may exceed the storage of small detention basins constructed in steep watershed canyons. In this case, flood mitigation should focus on the conveyance of the flood volume off the alluvial fan.

Conveyance design for mud floods should include consideration of sediment bulking, surging (roll waves), supercritical flow, debris plugging, sediment abrasion, superelevation, and potential for sediment scour and deposition. Extra freeboard that commensurate with the velocity head of mud floods should be considered (see Table 1). It is preferable to maintain the channel cross-section as straight and uniform as possible. Straight, steep channels will result in high velocities and high Froude numbers and will prevent the formation of cross waves and local deposition behind channel irregularities.

One of the engineering challenges in the design of straight alluvial channels is the control over the channel path. Streams with high Froude numbers are very erosive and channel migration or avulsion can occur during a flood event. Bed and bank stability are critical concerns. Using large riprap in steep channels for bank stability is not recommended because the riprap material can be launched by the flow, thus adding to the debris loading. Reducing the slope through drop structures can also be effective in controlling the flow.

ON THE IMPORTANCE OF MUDFLOW ROUTING

J. S. O'Brien[1] and P. Y. Julien[2], Members, ASCE

ABSTRACT

Mudflows exhibit highly nonuniform and unsteady flow behavior related to surging, point source sediment loading, dilution, debris blockage and roll waves which are generally short lived phenomena. The key variable which affects the mudflow hydrograph shape is sediment concentration. To predict spatial variation in mudflow hydraulics for flood mitigation design, it is necessary to route the flood hydrograph. Hydrograph routing depends on the accurate assessment of the water volume runoff from the upstream watershed, channel storage (floodwave attenuation), and points of sediment loading. Several practical guidelines to evaluate the accuracy of the flood hydrograph are presented. The FLO-2D model is used to route mudflows for a watershed in Colorado Springs, Colorado which has historically generated debris flows. The mudflow hydrograph peak discharge at the watershed outfall exceeds the peak discharge that would be obtained by bulking the water flood hydrograph by 50%.

INTRODUCTION

The first attempt to develop a mud and debris flow routing model was undertaken by DeLeon and Jeppson (1982) who modeled laminar water flows with enhanced friction factors. Spatially-varied and steady-state Newtonian flow was assumed and flow cessation could not be predicted. Schamber and MacArthur (1985) designed a one-dimensional finite element model for mudflows using a Bingham rheological model to evaluate the shear stresses of a non-Newtonian fluid.

[1]Hydraulic Engineer, FLO Engineering, Inc., Breckenridge, CO 80424. (Phone and Fax: 520-339-1935; e-mail: jsobflo2d@aol.com).

[2]Professor of Civil Engineering, Colorado State University, Fort Collins, CO 80523. (Phone: 970-491-8450; Fax: 970-491-7008; e-mail: pjulien@vines.ColoState.edu.

ON THE IMPORTANCE OF MUDFLOW ROUTING

J. S. O'Brien[1] and P. Y. Julien[2], Members, ASCE

ABSTRACT

Mudflows exhibit highly nonuniform and unsteady flow behavior related to surging, point source sediment loading, dilution, debris blockage and roll waves which are generally short lived phenomena. The key variable which affects the mudflow hydrograph shape is sediment concentration. To predict spatial variation in mudflow hydraulics for flood mitigation design, it is necessary to route the flood hydrograph. Hydrograph routing depends on the accurate assessment of the water volume runoff from the upstream watershed, channel storage (floodwave attenuation), and points of sediment loading. Several practical guidelines to evaluate the accuracy of the flood hydrograph are presented. The FLO-2D model is used to route mudflows for a watershed in Colorado Springs, Colorado which has historically generated debris flows. The mudflow hydrograph peak discharge at the watershed outfall exceeds the peak discharge that would be obtained by bulking the water flood hydrograph by 50%.

INTRODUCTION

The first attempt to develop a mud and debris flow routing model was undertaken by DeLeon and Jeppson (1982) who modeled laminar water flows with enhanced friction factors. Spatially-varied and steady-state Newtonian flow was assumed and flow cessation could not be predicted. Schamber and MacArthur (1985) designed a one-dimensional finite element model for mudflows using a Bingham rheological model to evaluate the shear stresses of a non-Newtonian fluid.

---

[1]Hydraulic Engineer, FLO Engineering, Inc., Breckenridge, CO 80424. (Phone and Fax: 520-339-1935; e-mail: jsobflo2d@aol.com).

[2]Professor of Civil Engineering, Colorado State University, Fort Collins, CO 80523. (Phone: 970-491-8450; Fax: 970-491-7008; e-mail: pjulien@vines.ColoState.edu.

MUDFLOW ROUTING

A two dimensional, flood routing model FLO-2D can simulate mud and debris flows using a finite difference solution of the continuity and momentum equations. An explicit numerical scheme was developed to solve the momentum equation with viscous stress terms of hyperconcentrated sediment flows. The solution domain for the nonlinear partial differential equation momentum equation is discretized into uniform square grid elements. The computation of flow hydraulics using explicit finite difference schemes is limited to small timesteps by strict numerical stability criteria. The algorithm advances the solution in space and time by solving for the unknown variables of depth and velocity one grid element at a time.

The routing algorithm for channel flow in the FLO-2D model was recently expanded to include the full dynamic wave equation solution for the momentum equation and the numerical stability criteria and is now dependent on volume conservation. In FLO-2D, the numerical stability criteria is variable with the grid element. It is expressed as:

$$\Delta t < (\zeta S_o \Delta x^2) / q_o \qquad (1)$$

where q_o is the unit discharge, S_o is the water surface slope, Δx is the spatial increment (channel length within the grid element), and ζ is an empirical coefficient with a range from $0.25 < \zeta < 1.0$ (Ponce and Theurer, 1982). This coefficient is a variable unique to the channel element discharge flux and is evaluated at each timestep based on the accuracy of the volume conservation.

Starting with a specified minimum timestep, the timestep increases until the numerical stability condition is exceeded, then the timestep is decremented. Timesteps generally range from 0.1 to 120 seconds. The timesteps computed by FLO-2D are a function of the discharge flux for a given grid element and its available surface storage area. By selecting weighting factors for the numerical stability criteria, the user makes a tradeoff between volume conservation accuracy and model runtime.

In mudflow routing, the water and sediment is tracked separately. For each timestep, the grid element sediment concentration is recomputed with potential for dilution effects or increased sediment loading. The sediment concentration is used to compute the yield stress and viscosity parameters in the hyperconcentrated sediment flow equation. The relationship between the sediment concentration, water surface slope, and roughness (including flow obstacles) can result in flow cessation. Flow deposits remain as part of the flow depth throughout the flow simulation and can be remobilized by subsequent more dilute flows.

The FLO-2D model represents a progression from single discharge, one-dimensional Newtonian hydraulic models to a complex topography, unconfined, non-

MUDFLOW ROUTING

A two dimensional, flood routing model FLO-2D can simulate mud and debris flows using a finite difference solution of the continuity and momentum equations. An explicit numerical scheme was developed to solve the momentum equation with viscous stress terms of hyperconcentrated sediment flows. The solution domain for the nonlinear partial differential equation momentum equation is discretized into uniform square grid elements. The computation of flow hydraulics using explicit finite difference schemes is limited to small timesteps by strict numerical stability criteria. The algorithm advances the solution in space and time by solving for the unknown variables of depth and velocity one grid element at a time.

The routing algorithm for channel flow in the FLO-2D model was recently expanded to include the full dynamic wave equation solution for the momentum equation and the numerical stability criteria and is now dependent on volume conservation. In FLO-2D, the numerical stability criteria is variable with the grid element. It is expressed as:

$$\Delta t < (\zeta S_o \Delta x^2) / q_o \qquad (1)$$

where q_o is the unit discharge, S_o is the water surface slope, Δx is the spatial increment (channel length within the grid element), and ζ is an empirical coefficient with a range from $0.25 < \zeta < 1.0$ (Ponce and Theurer, 1982). This coefficient is a variable unique to the channel element discharge flux and is evaluated at each timestep based on the accuracy of the volume conservation.

Starting with a specified minimum timestep, the timestep increases until the numerical stability condition is exceeded, then the timestep is decremented. Timesteps generally range from 0.1 to 120 seconds. The timesteps computed by FLO-2D are a function of the discharge flux for a given grid element and its available surface storage area. By selecting weighting factors for the numerical stability criteria, the user makes a tradeoff between volume conservation accuracy and model runtime.

In mudflow routing, the water and sediment is tracked separately. For each timestep, the grid element sediment concentration is recomputed with potential for dilution effects or increased sediment loading. The sediment concentration is used to compute the yield stress and viscosity parameters in the hyperconcentrated sediment flow equation. The relationship between the sediment concentration, water surface slope, and roughness (including flow obstacles) can result in flow cessation. Flow deposits remain as part of the flow depth throughout the flow simulation and can be remobilized by subsequent more dilute flows.

The FLO-2D model represents a progression from single discharge, one-dimensional Newtonian hydraulic models to a complex topography, unconfined, non-

infiltration, channel geometry and other data files to provide the simulation detail.

The model results can be viewed graphically or the flows and velocities output files can imported to the CAD software for plotting contours on the original digitized map. In addition, outflow hydrographs can be created at virtually any location in the channel or on floodplain cross sections. Most engineers are interested in maximum flow depths and velocities and these results can be plotted to view the area of inundation.

PRACTICAL GUIDELINES

In small watersheds (less than 5 square miles) where the alluvial fans have evolved by mudflows over geologic time, the 100-year flood event generally has too much water volume to create a mudflow. Mudflows are usually associated with frequent flood events such as the 10-year or 25 year return period flood. Unless the watershed has unusually erosive geology, there will be insufficient available sediment in the watershed to create a mudflow with the 100-year flood event. Extreme flood events (e.g. 100-year flood) will behave as a dilute mud flood (Table 1).

Table 1. Mudflow Behavior as a Function of Sediment Concentration

Flow Description	Sediment Concentration		Flow Characteristics
	by Volume	by Weight	
Landslide	0.65 - 0.80	0.83 - 0.91	Will not flow; failure by block sliding
	0.55 - 0.65	0.76 - 0.83	Block sliding failure with internal deformation during the slide; slow creep prior to failure
Mudflow	0.48 - 0.55	0.72 - 0.76	Flow evident; slow creep sustained mudflow; plastic deformation under its own weight; cohesive; will not spread on level surface
	0.45 - 0.48	0.69 - 0.72	Flow spreading on level surface; cohesive flow; some mixing
Mud Flood	0.40 - 0.45	0.65 - 0.69	Flow mixes easily; shows fluid properties in deformation; spreads on horizontal surface but maintains an inclined fluid surface; large particle (boulder) setting; waves appear but dissipate rapidly
	0.35 - 0.40	0.59 - 0.65	Marked settling of gravels and cobbles; spreading nearly complete on horizontal surface; liquid surface with two fluid phases appears; waves travel on surface
	0.30 - 0.35	0.54 - 0.59	Separation of water on surface; waves travel easily; most sand and gravel has settled out and moves as bedload
	0.20 - 0.30	0.41 - 0.54	Distinct wave action; fluid surface; all particles resting on bed in quiescent fluid condition
Water Flood	< 0.20	< 0.41	Water flood with conventional suspended load and bedload

There are several simple checks to determine the potential for a watershed to generate a mudflow. The first check is a watershed inspection for loose boulders and debris in the channel, eroding and undercut banks, potential for hillslope failures, and

infiltration, channel geometry and other data files to provide the simulation detail.

The model results can be viewed graphically or the flows and velocities output files can imported to the CAD software for plotting contours on the original digitized map. In addition, outflow hydrographs can be created at virtually any location in the channel or on floodplain cross sections. Most engineers are interested in maximum flow depths and velocities and these results can be plotted to view the area of inundation.

PRACTICAL GUIDELINES

In small watersheds (less than 5 square miles) where the alluvial fans have evolved by mudflows over geologic time, the 100-year flood event generally has too much water volume to create a mudflow. Mudflows are usually associated with frequent flood events such as the 10-year or 25 year return period flood. Unless the watershed has unusually erosive geology, there will be insufficient available sediment in the watershed to create a mudflow with the 100-year flood event. Extreme flood events (e.g. 100-year flood) will behave as a dilute mud flood (Table 1).

Table 1. Mudflow Behavior as a Function of Sediment Concentration

Flow Description	Sediment Concentration		Flow Characteristics
	by Volume	by Weight	
Landslide	0.65 - 0.80	0.83 - 0.91	Will not flow; failure by block sliding
	0.55 - 0.65	0.76 - 0.83	Block sliding failure with internal deformation during the slide; slow creep prior to failure
Mudflow	0.48 - 0.55	0.72 - 0.76	Flow evident; slow creep sustained mudflow; plastic deformation under its own weight; cohesive; will not spread on level surface
	0.45 - 0.48	0.69 - 0.72	Flow spreading on level surface; cohesive flow; some mixing
Mud Flood	0.40 - 0.45	0.65 - 0.69	Flow mixes easily; shows fluid properties in deformation; spreads on horizontal surface but maintains an inclined fluid surface; large particle (boulder) setting; waves appear but dissipate rapidly
	0.35 - 0.40	0.59 - 0.65	Marked settling of gravels and cobbles; spreading nearly complete on horizontal surface; liquid surface with two fluid phases appears; waves travel on surface
	0.30 - 0.35	0.54 - 0.59	Separation of water on surface; waves travel easily; most sand and gravel has settled out and moves as bedload
	0.20 - 0.30	0.41 - 0.54	Distinct wave action; fluid surface; all particles resting on bed in quiescent fluid condition
Water Flood	< 0.20	< 0.41	Water flood with conventional suspended load and bedload

There are several simple checks to determine the potential for a watershed to generate a mudflow. The first check is a watershed inspection for loose boulders and debris in the channel, eroding and undercut banks, potential for hillslope failures, and

watershed, the exposed rock outcrops are near vertical and the channel slope exceeds 45%. Upstream of the Ski Area parking lot, the alluvial fan slope averages 13%. A short distance downstream, the channel winds through the Broadmoor Hotel South Golf Course in a deeply incised ravine. Both channels are charged with boulders and organic debris in the reach upstream of the Ski Area parking lot.

Photo 1. Cheyenne Mountain Ski Basin Watershed

The rainfall frequency and storm distribution were evaluated from the records of five local rain gages. The Corps of Engineers HEC-1 hydrologic model parameters were calibrated using a contiguous gaged basin and were checked against those in other local studies and those in City drainage criteria manual. The 100-year return period storm data for portion of the basin generating the mudflow is:

Watershed Area = 0.34 mi^2
Total Storm Precipitation = 3.10 inches
Excess Rainfall = 0.99 inches
100-year Peak Water Discharge = 372 cfs
Runoff Volume = 19.44 acre-ft
Percent Runoff = 31.9%
Peak Unit Discharge = 1,094 cfs/mi^2

Values of the 100-year peak unit discharge in other studies ranged from 950 cfs/mi^2 to 1,140 cfs/mi^2 for basins less than 2 mi^2 in the Colorado Springs area (RCI, 1989).

watershed, the exposed rock outcrops are near vertical and the channel slope exceeds 45%. Upstream of the Ski Area parking lot, the alluvial fan slope averages 13%. A short distance downstream, the channel winds through the Broadmoor Hotel South Golf Course in a deeply incised ravine. Both channels are charged with boulders and organic debris in the reach upstream of the Ski Area parking lot.

Photo 1. Cheyenne Mountain Ski Basin Watershed

The rainfall frequency and storm distribution were evaluated from the records of five local rain gages. The Corps of Engineers HEC-1 hydrologic model parameters were calibrated using a contiguous gaged basin and were checked against those in other local studies and those in City drainage criteria manual. The 100-year return period storm data for portion of the basin generating the mudflow is:

Watershed Area = 0.34 mi^2
Total Storm Precipitation = 3.10 inches
Excess Rainfall = 0.99 inches
100-year Peak Water Discharge = 372 cfs
Runoff Volume = 19.44 acre-ft
Percent Runoff = 31.9%
Peak Unit Discharge = 1,094 cfs/mi^2

Values of the 100-year peak unit discharge in other studies ranged from 950 cfs/mi^2 to 1,140 cfs/mi^2 for basins less than 2 mi^2 in the Colorado Springs area (RCI, 1989).

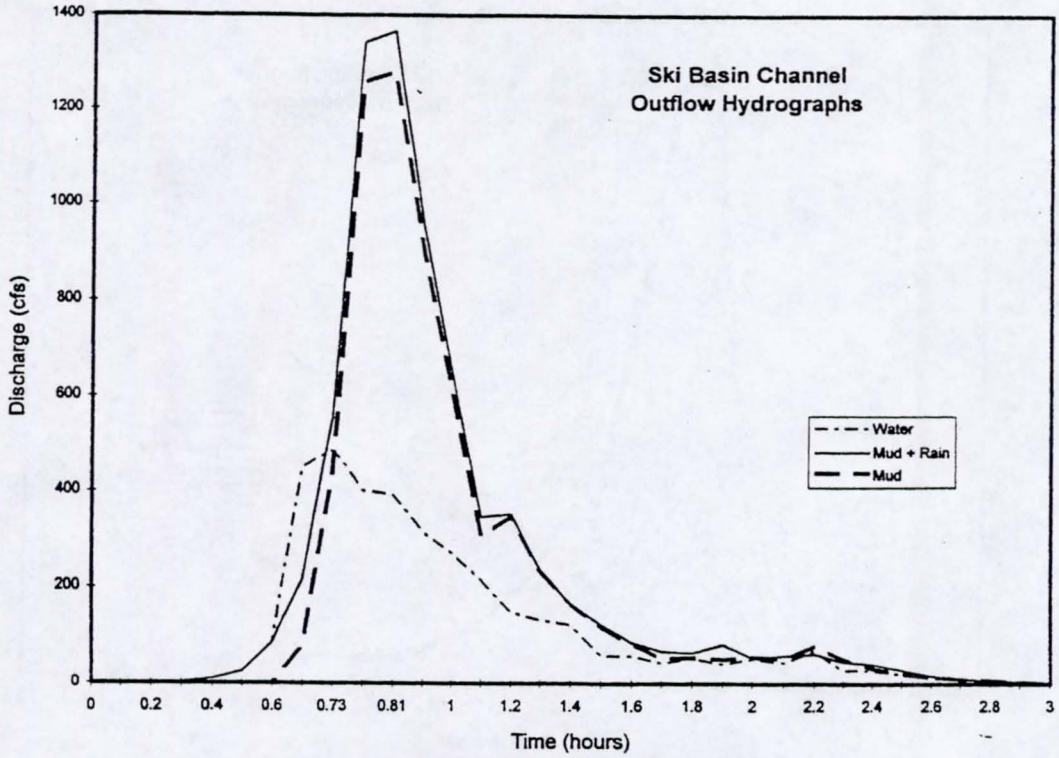

Figure 2. Ski Basin Channel Outflow Hydrographs

There are two important results to be highlighted. First, the mudflow peak discharge (+1,250 cfs) at the basin outfall exceeds the bulked peak water discharge (968 cfs) obtained with a sediment concentration of 50% (a bulking factor of two). This infers that if a conventional water flood analysis were conducted and the peak discharge was conservatively bulked at the outflow point by 50%, the design discharge could be significantly underestimated. Secondly, it is important to note that the hydrograph shape for the mudflows has a steeper rising limb. In the case of the mudflow, the discharge increases from 0 cfs to 1258 cfs in 0.2 hours whereas the water discharge increases from 9 cfs to 446 cfs in 0.3 hours.

Mitigation Measures

Several flood mitigation measures are being considered for the Ski Basin. The upper watershed channels are too steep for detention storage. Mitigation measures must focus on conveyance control. Channelization of the alluvial fan combined with levees are proposed to mitigate the mudflow hazard. Channel capacity will be designed to contain the 100-year mudflow peak discharge without freeboard. Levees will be set back 75 ft from the channel to permit overbank flows and the mudflow deposition. Overbank mudflow storage will be enhanced by grading deposition areas and lowering channel banks to encourage deposition in locations where removal of the deposits can be facilitated. Some trees will be left between the levees to increase floodplain roughness and promote debris deposition. Levee heights will be about five feet.

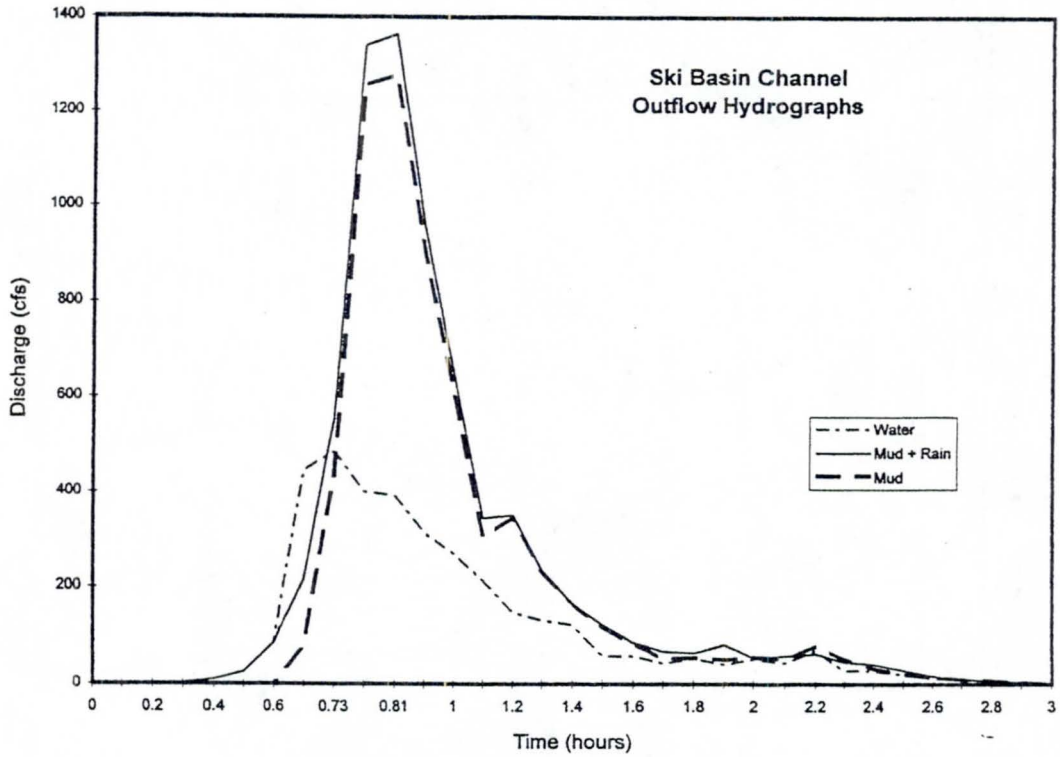

Figure 2. Ski Basin Channel Outflow Hydrographs

There are two important results to be highlighted. First, the mudflow peak discharge (+1,250 cfs) at the basin outfall exceeds the bulked peak water discharge (968 cfs) obtained with a sediment concentration of 50% (a bulking factor of two). This infers that if a conventional water flood analysis were conducted and the peak discharge was conservatively bulked at the outflow point by 50%, the design discharge could be significantly underestimated. Secondly, it is important to note that the hydrograph shape for the mudflows has a steeper rising limb. In the case of the mudflow, the discharge increases from 0 cfs to 1258 cfs in 0.2 hours whereas the water discharge increases from 9 cfs to 446 cfs in 0.3 hours.

Mitigation Measures

Several flood mitigation measures are being considered for the Ski Basin. The upper watershed channels are too steep for detention storage. Mitigation measures must focus on conveyance control. Channelization of the alluvial fan combined with levees are proposed to mitigate the mudflow hazard. Channel capacity will be designed to contain the 100-year mudflow peak discharge without freeboard. Levees will be set back 75 ft from the channel to permit overbank flows and the mudflow deposition. Overbank mudflow storage will be enhanced by grading deposition areas and lowering channel banks to encourage deposition in locations where removal of the deposits can be facilitated. Some trees will be left between the levees to increase floodplain roughness and promote debris deposition. Levee heights will be about five feet.

Appendix Table of Contents

Authors and Papers

1. P.Y. Julien and Y. Lan. "Rheology of Hyperconcentrations."

2. J.S. O'Brien, P.Y. Julien and W.T. Fullerton. "Two-Dimensional Water Flood and Mudflow Simulation."

3. J.S. O'Brien and P.Y. Julien. "Laboratory Analysis of Mudflow Properties."

4. J.S. O'Brien and P.Y. Julien. "On the Importance of Mudflow Routing."

5. P.Y. Julien and J.S. O'Brien. "On the Importance on Mud and Debris Flow Rheology in Structure Design."

6. J.S. O'Brien and P.Y. Julien. "Physical Properties and Mechanics of Hyperconcentrated Sediment Flows."

7. J.S. O'Brien and B. Hyde. "Technical Standards for Delineating Alluvial Fan Flooding."

8. J.S. O'Brien and W.T. Fullerton. "FEMA Method for Predicting Flood Hydraulic Boundaries on Alluvial Fans Requires Verification."

9. J.S. O'Brien and J.E. Fuller. "Preferred Directions of Flow on Alluvial Fans."

10. P.Y. Julien and J.S. O'Brien. "Selected Notes on Debris Flow Dynamics."

11. P.Y. Julien and D.M. Hartley. "Formation of Roll Waves in Laminar Sheet Flow."

FEMA METHOD FOR PREDICTING FLOOD HYDRAULIC BOUNDARIES ON ALLUVIAL FANS REQUIRES VERIFICATION

J. S. O'Brien
FLO Engineering, Inc.

W. T. Fullerton
FLO Engineering, Inc.

Introduction

The Federal Emergency Management Agency (FEMA) has published a user's manual for its probabilistic approach to delineating hydraulic boundaries on alluvial fans. The manual describes the application of the computer program FAN, an encoded version of the FEMA method. The FEMA method has been the subject of much scrutiny (Fuller, 1990; Baker, et al., 1990; French, 1987; Grindeland, et al., 1990). The inherent assumptions in the method do not apply to most alluvial fans and it should not be used on urbanized fans. The limited available field data do not support its continued application.

FEMA's Alluvial Fan Method for Predicting Hydraulic Boundaries

Most alluvial fan flood studies are conducted because of underlying interest in flood insurance or flood mitigation for existing or proposed development. FEMA's method for assessing flood hazard zones on alluvial fans combines a single channel method (referred to as the Dawdy method; Dawdy, 1979) and a multiple channel method which is applied downfan of the single channel point of bifurcation (DMA, 1985). The depth and velocity boundaries are determined in 1 foot or 1 fps increments, respectively. Flood insurance rates are based on predicted hydraulic boundaries with a flow depth exceeding 0.5 ft. These boundaries have a risk assessment of one percent corresponding to the 100-year return period flood.

The only data required to apply the FEMA single channel model are several peak discharges from the upstream watershed and their associated return periods. The hydraulic boundaries are expressly dependent on the skew coefficient of the flood frequency curve of ungaged watersheds. For the

extends the boundary further downfan. An 1.5 avulsion factor results in a fifty percent larger boundary width than if no avulsion was considered. Considering the actual process of channel avulsion, avulsion increases neither the physical width of the potential flow surface or the downfan flow hydraulics. Although any value can be assumed, the avulsion factor has not been verified and there is no basis for choosing a specific value.

Channel migration does not occur during every flood event and depends on debris loading, channel incision and potential for channel erosion. Channel avulsion is more likely to occur on small braided channels than on large incised channels. DMA (1985) reports that avulsions occur on a geologic time scale rather than over a "planning horizon." The concept of channel avulsion is less important for large flood events, where flow depths overwhelm small obstructions and tend to follow the steepest route downfan.

* *FEMA's method does not consider development and flood control measures which affect the flow path and discharge.*

The assessment of fan flooding is generally associated with development where the flow paths have been altered by buildings, levees or debris basins. FEMA's method assumes the flow is unobstructed or unconstrained. FEMA addresses this problem, "In portions of alluvial fans in which natural alluvial fan processes may not occur, such as in areas of entrenched channels, areas protected by flood control works and heavily developed areas, the Study Contractor should exercise good engineering judgement in determining the most appropriate methodology..." (FEMA Guidelines, 1985). Nevertheless, FEMA's method is routinely applied to developed fans.

* *Fan hydraulics predicted with the FEMA method are based on empirical channel geometry relationships not representative of self-forming channels on alluvial fans.*

The expressions for channel width W and flow depth d as function of peak discharge Q as based on the Dawdy method are (Dawdy, 1979): $W = 9.5\ Q^{0.4}$ and $d = 0.07\ Q^{0.4}$. These equations result in a <u>constant</u> width to depth ratio $W/d = 136$ regardless of fan slope, channel roughness, and bed and bank material, all of which cause variation in channel geometry in the downfan direction or between different fans.

18% average difference for 10 of the 11 fan floods; Apparently, a good correlation. Would the channel width/depth ratios compare as well?

The FEMA predicted width/depth ratio of a single channel is constant 136. From the DMA (1985) report, W/d ratios can be computed from reported discharges, observed widths and using the previously described depth-discharge equation for the 11 alluvial fan floods. The W/d ratio ranged from 19 to 289, a poor comparison with the FEMA value of 136. Nevertheless, these results lead DMA to conclude "(t)he width of a single channel can be reasonably determined by the present FEMA method."

DMA was unable to substantiate avulsion coefficient of 1.5. There was insufficient data to even attempt a statistical correlation. DMA concluded that "(t)he present data base is insufficient to better define the avulsion coefficient. Therefore the present value of the avulsion coefficient should continue to be used." A questionable conclusion! The conclusion should have been drawn that there was no data to justify an avulsion coefficient.

Finally, DMA plotted channel position near the fan apex and concluded that the evidence supported the FEMA method assumption of random channel locations on the fan. The channel direction, however, was not correlated with the fan slope. If the channel path did not correlate with the steepest portion of the fan, then the randomness conclusion would have been justified.

The FEMA method requires verification. The DMA study accomplished nothing towards this goal. There are no published results to verify the method with measured flood depths and velocities.

Conclusions

Application of the FEMA method is often requested on alluvial fans studies by either the floodplain manager or FEMA's technical representative. Although, intended for the purpose of assessing flood insurance rates, the FEMA method has been used to evaluate the design of mitigation measures. Consequently, there is a concern that the FEMA method results may be incorporated into the design of flood containment structures.

We appreciate this opportunity to address the limitations of the FEMA model. Although French's statistical formulation represents an enhancement in the FEMA model, the revision of the probability function improves only one of the FEMA model's fundamentally poor assumptions.

Appendix I. References

Baker, V. R., Demsey, D. A., Ely, L. L., Fuller, J. E., House, P. K., O'Conner, J. E., Onken, J. A., Pearthree, P. A., and Vincent, K. R. (1990). "Application of geological information to Arizona flood hazard assessment." Proc. Int. Symp. on Hydr./Hydrol. of Arid Lands, R. H. French, Ed., ASCE, New York, N.Y., 621-626.

Bull, W. B. (1964). "Geomorphology of segmented alluvial fans in western Fresno County, California." U.S. Geological Survey Prof. Paper 352-E, Washington, D.C.

Dawdy, D. R., Hill, J. C. and Hanson, K. C. (1989). "Implementation of FEMA guidelines on alluvial fans." Proc. Natl. Conf. on Hydr. Engineering, M. A. Ports, Ed., ASCE, New York, N.Y., 64-69.

Dawdy, D. R. (1979). "Flood frequency estimates on alluvial fans." J. Hydr. Div., ASCE, 105(11), 1407-1412.

Fan: An alluvial fan flooding computer program. (1990). Federal Emergency Management Agency, Washington, D. C.

"Flood insurance study: Guidelines and specifications for study contractors." (1985). FEMA-37, Federal Emergency Management Agency, Washington, D.C.

French, R. H. and Fuller, J. E. (1992). "Theoretical and Technical Deficiencies in the FEMA alluvial fan model." Proc. 16th Annual Conf., Assoc. of State Floodplain Managers, Inc., Grand Rapids, MI.

French, R. H. (1992a), "Design of flood protection for transportation alignments on alluvial fans." J. Irrig. and Drain. Div., ASCE, 118(2), 320-330.

French, R. H. (1992b), "Preferred directions of flow on alluvial fans." J. Hydr. Div., ASCE, 118(7), 1002-1013.

Fuller, J. E. (1990). "Misapplication of the FEMA alluvial fan model: A case history." Proc. Int. Symp. on Hydr./Hydrol. of

Preferred Directions of Flow on Alluvial Fans[a]

Discussion by J. S. O'Brien,[2] Member, ASCE and

J. E. Fuller,[3] Assoc. Member ASCE

In two recent papers, one in the Journal of Hydraulic Engineering, July, 1992b and the other in the Journal of Irrigation and Drainage Engineering, March/April, 1992a, French has modified the FEMA model (FAN) for delineating flood hazard zones on alluvial fans. The modifications suggested by French are intended as refinements to the model for engineering applications. In the Irrigation and Drainage paper, French (1992a) uses the FAN model to estimate discharge and fan hydraulics to design drainage protection for transportation alignments. Similarly, Mifflin (1988) suggested application of the FEMA model for project design hydraulics. In this discussion, we address French's modifications to the FEMA model, fundamental problems with the model and accuracy of the model's results. Furthermore, we want to discourage the application of the FEMA model for the design of flood structures and mitigation.

---

[a]July, 1992, Vol. 118, No. 7, by Richard H. French (Paper No. 2244).

[2]Princ. Engr, FLO Engineering, Inc., Breckenridge, CO, 80424.

[3]Hydrologist, CH2M Hill, Tempe, AZ , 85285.

The deficiencies in the FEMA model and its results have been detailed in other papers. These deficiencies include simplified and inappropriate assumptions (Fuller, 1990; Grindeland, et al., 1990; French and Fuller, 1992), lack of model verification (O'Brien and Fullerton, 1991) and failure to consider geological and topographical constraints (Baker, et al., 1990). Even Dawdy, who formulated the model in 1979, later adopted by FEMA, recognized some of the model's shortcomings (Dawdy, 1979; Dawdy, et al., 1989). Review of these papers have lead to the following conclusions:

1) The FEMA method does not present a realistic analysis of physical processes on alluvial fans. It is not a physically based model.

2) There are no published guidelines on the limits of the FAN model applicability.

3) There has been no verification of the model.

4) The FEMA method does not err on the conservative side.

The FEMA model predicts average flood hydraulic zones associated with long term fan evolution on undeveloped, uniform fan surfaces. It should not be applied on urbanized fans, fans with incised channels or topographic controls or to analyze mud/debris flow events. In Guidelines for Alluvial Fan Studies (1985), FEMA recognizes some of these limitations of the model by stating:

> "In portions of alluvial fans in which natural alluvial fan processes may not occur, such as in areas of entrenched channels, areas protected by flood control works, and heavily developed areas, the Study Contractor should exercise good engineering judgement in determining the most appropriate methodology or combinations of methodologies."

SELECTED NOTES ON DEBRIS FLOW DYNAMICS

by

P.Y. Julien[1] and J.S. O'Brien[2]

ABSTRACT

Heavily sediment-laden flows have been described and classified as hyperconcentrated sediment flows, including mud floods, mudflows, and debris flows. The authors prescribe definitions based on governing physical processes and limited concentrations of cohesive material. Viscous mudflows contain large concentrations of fine cohesive material. Rocky debris flows contain large concentrations of clastic material. Rheological analyses should recognize four types of shear stresses: 1) yield stress; 2) viscous stress; 3) turbulent stress; and 4) dispersive stress. These shear stresses combine into a quadratic rheological model. Dimensionless parameters from the ratio of shear stress terms identify the predominant physical process.

The two-dimensional model FLO-2D has been developed for the simulation of a wide range of hyperconcentrated sediment flows based on the quadratic rheological model. The simulation of the Pine Creek mudflow during the 1980 eruption of Mount St. Helens is presented as an example of our continuing progress in the physically-based analysis of natural disasters from heavily sediment-laden flows.

---

1 Prof. of Civil Engineering, Engineering Research Center, Colorado State University, Fort Collins, CO 80523, USA.

2 Hydraulic Engineer, FLO Engineering, Inc., P.O. Box 1659, Breckenridge, CO 80424, USA.

occurs almost exclusively through particle collision. The water, which may be present in small quantities does not influence particle collision or lubricate the mass. Our understanding of sediment particle interaction in flowing water evolved from the study of O'Brien and Julien (1985). The definitions involving hyperconcentrated sediment flows should focus on the physical processes of the fluid motion which can be explored through the rheological study of sediment hyperconcentrations. Nomenclature has been formulated on the basis of what constitutes the fluid matrix (mixture of water and fine sediment particles) which govern the flow properties.

RHEOLOGY OF HYPERCONCENTRATED SEDIMENT FLOWS

The non-Newtonian nature of hyperconcentrations results from several physical processes: The cohesion and bonding of fine sediment particles τ_c; the Mohr-Coulomb shear τ_{mc}, which is important when considering the static stability of steep slopes; the yield stress τ_y is defined as the sum of cohesive strength τ_c, plus the Mohr-Coulomb shear τ_{mc} and must be exceeded to initiate motion; the viscous shear stress τ_v which accounts for the increase in Newtonian viscosity; the turbulent shear stress τ_t which describes the turbulent nature of hyperconcentrated sediment flows of fine granular material; finally, the dispersive stress τ_d describes the effects of the collision of sediment clasts. Energy dissipation through turbulence, large eddies trailing major obstacles like trees and boulders, can be accounted for by considering τ_t.

The total shear stress τ in hyperconcentrated sediment flows includes contributions from each of these five shear stress components:

$$\tau = \tau_{mc} + \tau_c + \tau_v + \tau_t + \mathrm{tau}_d \tag{1}$$

When written in terms of shear rates, or velocity gradient $\left(\frac{du}{dy}\right)$, the following quadratic rheological model is obtained:

$$\tau = \tau_y + \eta \frac{du}{dy} + \zeta \left(\frac{du}{dy}\right)^2 \tag{2}$$

in which the three dimensionless parameters τ^*, D_v^* and T_d^* are defined as:

1. dimensionless excess shear stress τ^*

$$\tau^* = \frac{\tau - \tau_y}{\eta \frac{du}{dy}}$$

2. dimensionless dispersive-viscous ratio D_v^*

$$D_v^* = \frac{\rho_s \lambda^2 d_s^2}{\eta} \left(\frac{du}{dy}\right)$$

3. dimensionless turbulent-dispersive ratio T_d^*

$$T_d^* = \frac{\rho_m l_m^2}{a_i \rho_s \lambda^2 d_s^2}$$

It is suggested to relate the following parametric delineations to the classification of hyperconcentrations: 1) mudflows when yield and viscous stresses are dominant at $D_v^* < 30$; 2) debris flows or granular flows for which the dispersive stress is dominant at $D_v^* > 400$ and $T_d^* < 1$; and 3) mud floods when the turbulent shear stress is dominant at $D_v^* > 400$ and $T_d^* > 1$. A transition regime may be expected when $30 < D_v^* < 400$ for which all the terms of the quadratic equation are not negligible.

TWO-DIMENSIONAL SIMULATION MODEL FLO-2D

Based on the quadratic rheological model, O'Brien et al. (1993) developed the two-dimensional flow routing model FLO-2D for the simulation of the continuum from water floods to mudflows. The momentum equation is solved after considering three components of the total friction slope S_f, namely: the yield slope S_y, the viscous slope S_v, and the turbulent-dispersive slope S_{td}. The total friction slope can therefore be rewritten as:

$$S_f = \frac{\tau_y}{\gamma_m h} + \frac{K \eta V}{8 \gamma_m h^2} + \frac{n^2 V^2}{h^{4/3}} \qquad \textbf{(5)}$$

4) the channel geometry data for 12 cross-sections were reduced and prepared in a data input file. Selected Manning n values ranged from 0.03 to 0.1. The distances between cross-sections for the FLO-2D simulation were approximated from the mapping provided by the USGS; and 5) the inflow hydrograph was estimated at the first cross-section to reproduce the estimated peak discharge at cross-section 2 and the inflow volume to the reservoir. The first grid element was located several thousand feet upstream of the first cross-section.

The computed mudflow viscosity and yield stress from Major and Pierson (1992) revealed that the equivalent sediment concentration ranged from 60-65%. FLO-2D was run several times to replicate the known flow conditions:

1) an estimated peak discharge at cross-section 2 equal to 28,600 $\frac{m^3}{s}$;
2) an estimated peak discharge at the reservoir of 7,500 $\frac{m^3}{s}$;
3) timing of the peak discharge arrival at the reservoir; and
4) estimated volumetric inflow to the reservoir.

When these conditions were satisfactorily met, the computed flow parameters were compared with those estimated by Pierson (1985) at 12 cross-sections. During the Pine Creek FLO-2D simulations, it was noted that an increase of 2% in sediment concentration would result in flow cessation on the falling limb of the hydrograph. This model response assisted in defining the limits in sediment concentration. There was still a question, however, whether the mudflow rheologic parameters used in the FLO-2D simulation would result in high velocity estimates for Pine Creek and would replicate the Swift Reservoir inflow hydrograph. The following FLO-2D results were obtained:

Hydrograph Timing - Arrival of the Peak discharge in Swift Reservoir

Pierson estimate: 20±3 min. FLO-2D simulated: 20.4 min.

Volume - Total inflow volume into Swift Reservoir

Pierson estimate: 13,431,000 m^3 FLO-2D simulated: 13,490,000 m^3

Peak discharge - Peak discharge into Swift Reservoir

Pierson estimate: 7,500 m^3 FLO-2D simulated: 11,750 m^3

The hydrograph timing and volume from the FLO-2D simulations were the most accurate of the three flow conditions based on the response of the Swift Reservoir recording gage. The

REFERENCES

Bagnold, R.A., 1954. Experiments on a Gravity-free Dispersion of Large Solid Spheres in a Newtonian Fluid under Shear, Proc. Royal Soc. of London, Ser. A, 225, 49-63.

Julien, P.Y. and Y.Q. Lan, 1991. On the Rheology of Hyperconcentrations, J. Hyd. Eng., ASCE, 117(3), 346-353.

Major, J.M. and T.C. Pierson, 1992. Debris Flow Rheology: Experimental Analysis of Fine-grained Slurries, Water Res. Res. 28(3), 841-857.

O'Brien, J.S., and P.Y. Julien, 1985. Physical Properties and Mechanics of Hyperconcentrated Sediment Flows, Proc. ASCE Hyd. Div. Spec. Conf on Delineation of Landslides, Flash Flood and Debris Flow Hazards, Logan Utah, June 1984, 260-279.

O'Brien, J.S., and P.Y. Julien, 1988. Laboratory Analysis of Mudflow Properties, J. Hyd. Eng., ASCE, 114(8), 877-887.

O'Brien, J.S., P.Y. Julien and W.T. Fullerton, 1993. Two-dimensional Water Flood and Mudflow Simulation, J. Hyd. Eng., ASCE, 119(2), 244-261.

Pierson, T.C., 1985. Initiation and Flow Behavior of the 1980 Pine Creek and Muddy River Lahars, Mount St. Helens, Washington, Geol. Soc. of America, Bull. V. 96, 1056-1069.

Takahashi, T., 1978. Mechanical Characteristics of Debris Flow, J. Hyd. Div., ASCE, 104, 1153-1169.

Woo, H.S., P.Y. Julien, and E.V. Richardson, 1988. Suspension of large concentrations of sands, J. Hyd. Eng., ASCE, 114(8), 888-898.

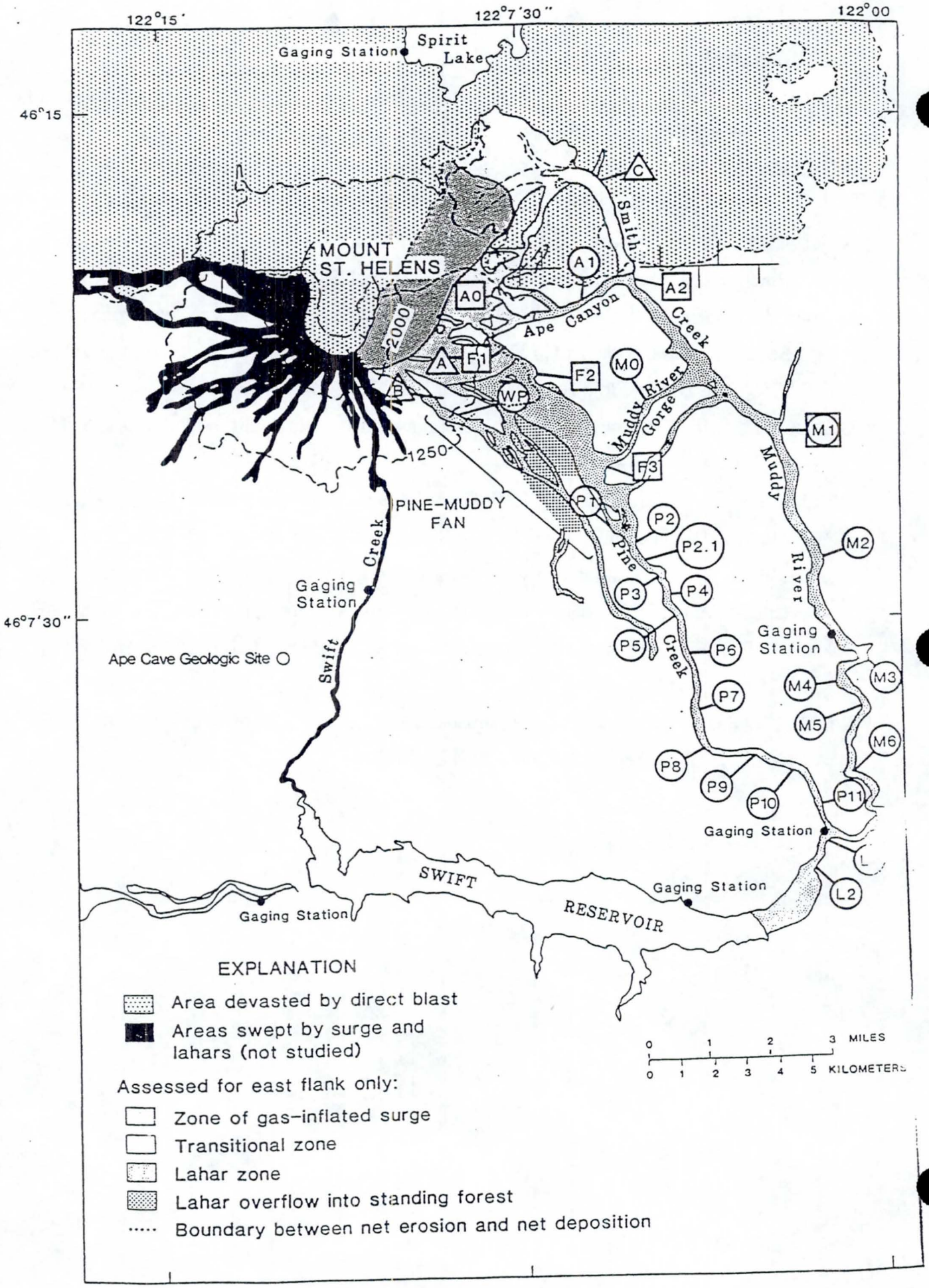
122°15'
122°7'30"
122°00
46°15
46°7'30"
Gaging Station
Spirit Lake
MOUNT ST. HELENS
2000
1250
C
A1
A2
A0
A
F1
F2
M0
WP
B
F3
M1
P1
P2
P2.1
P3
P4
P5
P6
P7
P8
P9
P10
P11
M2
M3
M4
M5
M6
L
L2
Smith Creek
Ape Canyon
Muddy River Gorge
Muddy River
Pine Creek
PINE-MUDDY FAN
Swift Creek
Ape Cave Geologic Site
SWIFT RESERVOIR
EXPLANATION
Area devasted by direct blast
Areas swept by surge and lahars (not studied)
Assessed for east flank only:
Zone of gas-inflated surge
Transitional zone
Lahar zone
Lahar overflow into standing forest
Boundary between net erosion and net deposition
0 1 2 3 MILES
0 1 2 3 4 5 KILOMETERS

Formation of roll waves in laminar sheet flow

Formation d'un train d'ondes dans les écoulements superficiels laminaires

P. Y. JULIEN
Faculty Affiliate, Colorado State University, Fort Collins, CO, U.S.A.

D. M. HARTLEY
Research Hydraulic Engineer, USDA-Agricultural Research Service, Fort Collins, CO, U.S.A.

SUMMARY
The formation of a series of roll waves in laminar sheet flows in a smooth channel is examined both theoretically and experimentally. Roll waves were observed in subcritical flows at a Froude number as low as 0.74. The recommended theoretical relationship for the celerity of roll waves is a function of the momentum correction factor. This relationship is in good agreement with measured celerities of roll waves. The period of roll waves remained fairly constant throughout these experiments. Previous derivations of the length required for the formation of roll wave were modified because experimental evidence demonstrates that the simplified relationship for the celerity of roll waves does not hold true for laminar sheet flows. Using the modified relationship, the dimensionless distance displays an hyperbolic variation with the Froude number and good agreement is obtained with experimental data. This analysis also demonstrates that for supercritical flows the distance is proportional to the ratio of flow depth and slope. Alternatively an equivalent function of Reynolds number and slope can be used.

RÉSUMÉ
La formation d'un train d'ondes dans les écoulements superficiels sur surface lisse est étudiée analytiquement et expérimentalement. Des trains d'ondes ont été observés dans des écoulements fluviaux à des nombre de Froude aussi faibles que 0,74. Une expression analytique fonction du coefficient de Boussinesq est recommandée pour décrire la vitesse de propagation des ondes. La période des ondes demeure constante sous les diverses conditions hydrauliques de cette étude. Les équations existantes décrivant la distance de développement des ondes ont dû être modifiées puisque cette étude expérimentale démontre que certaines hypothèses relatives à la vitesse de propagation des ondes ne sont pas valables pour les écoulements laminaires. Les modifications apportées aux équations donnent des résultats en accord avec les résultats expérimentaux. De plus, l'analyse démontre que pour les écoulements torrentiels, la distance est proportionelle au rapport de la profondeur d'écoulement sur la pente. Une expression équivalente en termes de pente et du nombre de Reynolds peut également être utilisée.

1 Introduction

Sheet flows in steep channels often exhibit surface instabilities which grow until a series of breaking or roll waves are formed. In this study the formation of roll waves under laminar conditions is discussed. Previous treatments of the laminar case have neglected the minimum channel length necessary for roll wave development. Theoretical derivations for turbulent flow [Montuori, 1963 and Liggett, 1975] indicate that simple criteria based on the Froude number are necessary though insufficient since the length required for the formation of roll waves is not considered. In the first part of this study, previous theories on the formation of roll waves are

Revised version received July 11, 1985. Open for discussion July 1, 1986.

3 Theory on the stability of laminar sheet flow

In deriving a fundamental stability criteria for the water surface, several approaches were used by different researchers. Early investigations by Thomas (1939) and Stoker (1957) suggested that the flow is unstable when $S > 4g/C^2$ in which C is the Chézy coefficient. The foremost criterion for instability published in the Russian literature was derived by Vedernikov (1945, 1946). For laminar flows, the Vedernikov number Ve can be written as:

$$Ve = 2F\left(1 - R_h \frac{\partial P}{\partial A}\right) \tag{6}$$

in which

R_h = the hydraulic radius
P = the wetted perimeter
A = the cross-sectional area

The Froude number F defined as $\bar{u}/\sqrt{gh}$ represents the ratio of inertia to gravity forces. For an infinitely wide channel, the Vedernikov number is equal to twice the Froude number and the flow becomes unstable ($Ve > 1$) when the Froude number exceeds 0.5 for laminar flow as compared to 2.0 for turbulent flow. This critical Froude number was also reported by Robertson and Rouse (1941) and Powell (1948). Mayer (1961) observed roll waves in subcritical laminar sheet flows but mistakenly concluded that roll waves can form only when the slope is larger than 3%. Yih (1954, 1963, 1977) and Benjamin (1975) solved the problem of stability of sheet flows down an inclined plane using the Orr-Sommerfeld equation. For very long waves the flow is unstable when:

$$Re \geq \frac{5}{6S} \tag{7}$$

in which Re = the Reynolds number

This criterion was also suggested by Taylor and Kennedy (1961). If equation (2) is substituted into equation (7), uniform flow ($S = S_f$) and a K value of 24 are assumed, a critical Froude number of $F_c = 0.53$ results which is close to the Vedernikov criteria for wide rectangular channels. Ishihara et al. (1961) also suggested the critical value $F_c = 0.577$.

Unfortunately, these criteria based on the Froude number ignore the distance along the channel required for the formation of roll waves. This factor becomes particularly important for subcritical sheet flows since previous studies for turbulent flows [Montuori, 1963] demonstrate that the distance at which the waves are fully developed increases to infinity as the Froude number approaches the critical value.

3.1 *Formation and celerity of roll waves*

When the flow is unstable ($Ve > 1$) a minor perturbation of the water surface induces the formation of small waves. The amplitude of these waves increases gradually as they move downstream until a bore is formed and the wave breaks. The distance travelled between the point at which the perturbation is initiated and the breaking point of the wave defines the distance required for the formation of roll waves. This distance, ξ_c, is determined theoretically from the following procedure using the celerity of roll waves.

$$h' = h + \frac{\partial h'}{\partial \eta}\eta + \frac{1}{2}\frac{\partial^2 h'}{\partial \eta^2}\eta^2 + 0(\eta^3) \tag{15}$$

$$\bar{u}' = \bar{u} + \frac{\partial \bar{u}'}{\partial \eta}\eta + \frac{1}{2}\frac{\partial^2 \bar{u}'}{\partial \eta^2}\eta^2 + 0(\eta^3) \tag{16}$$

$$B' = B + \frac{\partial B'}{\partial h'}\frac{\partial h'}{\partial \eta}\eta + 0(\eta^2) \tag{17}$$

$$A' = A + \frac{\partial A'}{\partial h'}\frac{\partial h'}{\partial \eta}\eta + 0(\eta^2) \tag{18}$$

$$S_f' = S + S\eta\left(\frac{1}{\bar{u}}\frac{\partial \bar{u}'}{\partial \eta} - \frac{2}{h}\frac{\partial h'}{\partial \eta}\right) + 0(\eta^2) \tag{19}$$

The truncated series are valid for small values of η and the solution is examined in the neighborhood of $\eta = 0$. An analysis of equations (13) and (14) using the perturbation defined by equations (15) through (19) as presented in Julien and Hartley (1985) results in the following relationship

$$\frac{\partial^2 h'}{\partial \xi \partial \eta} - \beta\left(\frac{\partial h'}{\partial \eta}\right)^2 + \gamma\frac{\partial h'}{\partial \eta} = 0 \tag{20}$$

in which for rectangular channels ($B = B'$ and $\partial B'/\partial h' = 0$), the coefficients β and γ are respectively:

$$\beta = \frac{3g}{c_0^2 + 2\bar{u}c_0 + gh} \tag{21}$$

and,

$$\gamma = \frac{gS}{\bar{u}^2}\left(1 - \frac{2c_0F^2}{\bar{u}}\right)\left[\frac{1}{2 + \frac{c_0}{\bar{u}} + \frac{\bar{u}}{c_0F^2}}\right] \tag{22}$$

This derivation improves the one given by Liggett (1975) since the wave celerity defined by equation (9) accounts for the velocity distribution present in laminar sheet flow. If a uniform velocity distribution is assumed (i.e. $c_0 = \sqrt{gh}$), equations (21) and (22) reduce to the relationship proposed by Liggett.

The solution of equation (20) is:

$$\frac{\partial h'}{\partial \eta} = \frac{\varepsilon}{\frac{\beta\varepsilon}{\gamma} + e^{\gamma\xi}} \tag{23}$$

in which ε is a constant of integration along the longitudinal distance ξ.

3.3 *Distance for the formation of roll waves*

The critical distance ξ_c at which the wave breaks is assumed to occur when the water surface is vertical. Mathematically, this condition is obtained when the denominator of equation (23) is set equal to zero, or when:

(27) are dimensionless and unique functions of the Froude number as plotted in Fig. 1. For supercritical flows, Ψ has a nearly constant value of 2.0 while Φ increases gradually with the Froude number. It can also be demonstrated that over a fairly wide range of slopes the expression $\ln(S/3\varepsilon)$ will be substantially constant. If Φ is small compared to $\ln(S/3\varepsilon)$ then the following approximate relationship for ξ_c can be written:

$$\xi_c \cong D\frac{h}{S} \tag{28}$$

in which D is equivalent to the factor in braces in equation (25) and is approximately constant. Equations (24) is general while equation (28) represents a simplified expression applicable only to supercritical flows. The ability of equations (24) and (28) to predict the distance ξ_c is evaluated with laboratory data described in the following section.

Table 1. Data summary

S (1)	Re (2)	c m/s (3)	T s (4)	ξ_c m (5)	F (6)	$\frac{gS\xi_c}{\bar{u}^2}$ (7)	D (8)	E mm (9)
0.040	335	0.46	1.33	0.91	2.11	6.03	26.6	1.80
0.040	400	0.50	1.61	0.91	2.31	4.74	25.4	1.71
0.040	500	0.57	1.96	0.91	2.58	3.53	23.5	1.59
0.035	68	0.22	1.27	2.74	0.89	147.30	–	–
0.035	95	0.26	1.28	1.52	1.05	51.20	56.6	3.81
0.035	141	0.34	1.45	1.52	1.28	30.50	49.7	3.35
0.035	188	0.34	1.32	2.13	1.48	28.70	62.6	4.26
0.035	265	0.42	1.37	2.13	1.76	18.40	56.9	3.81
0.035	380	0.43	1.19	2.74	2.11	14.40	64.4	4.33
0.030	90	0.24	1.35	2.13	0.95	72.70	–	–
0.030	122	0.25	1.43	2.13	1.10	49.60	59.7	4.02
0.030	200	0.36	1.47	2.74	1.41	33.10	65.8	4.36
0.030	260	0.41	1.25	2.13	1.61	23.10	46.6	3.99
0.030	340	0.42	1.37	2.13	1.84	16.30	42.9	3.66
0.030	360	0.48	1.35	1.52	2.15	5.90	27.1	1.83
0.030	550	–	–	1.52	2.35	4.68	25.8	1.74
0.025	65	–	–	7.62	0.74	380.00	–	–
0.025	71	–	–	7.62	0.77	340.00	–	–
0.025	85	0.22	1.52	3.35	0.84	118.00	–	–
0.025	104	0.24	1.52	3.35	0.93	91.00	–	–
0.025	130	0.33	1.54	2.74	1.04	54.70	59.1	3.96
0.025	200	0.34	1.61	2.74	1.29	30.70	51.1	3.44
0.025	246	0.38	1.75	2.13	1.43	18.20	37.2	2.50
0.025	320	0.44	1.52	1.52	1.63	9.20	24.5	1.62
0.025	420	0.47	1.19	0.91	1.87	3.83	13.3	0.88
0.025	530	0.50	1.15	1.52	2.10	4.65	20.4	1.37
0.015	140	0.26	1.72	2.74	0.84	41.60	–	–
0.015	173	0.27	1.33	2.13	0.93	24.30	–	–
0.015	260	0.33	1.43	2.13	1.14	14.20	18.4	1.25
0.015	320	0.40	1.23	2.13	1.26	10.80	17.2	1.16
0.015	450	0.43	1.08	1.52	1.50	5.90	11.0	0.88
mean			1.41				38.5	2.67
standard deviation			0.20				18.5	1.28

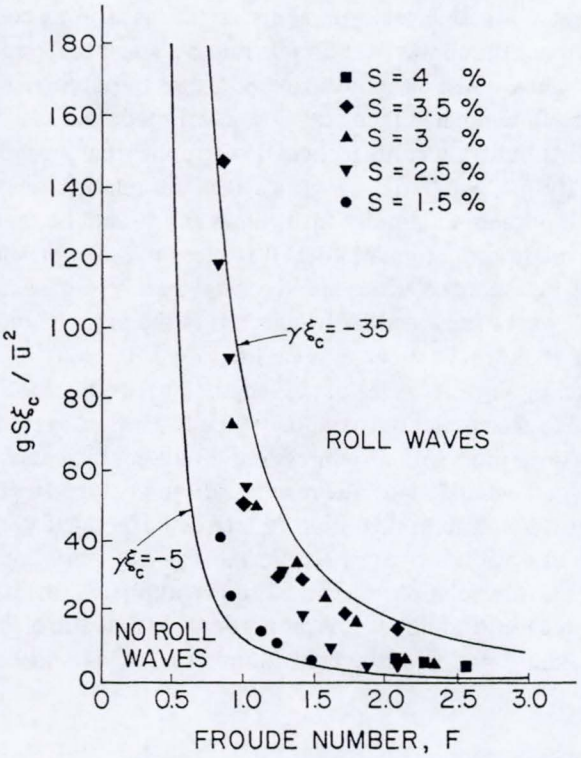

Fig. 3. Dimensionless critical distance as a function of Froude number.
Distance critique adimensionnelle en fonction du nombre de Froude.

4.1 *Analysis of wavelength, period and celerity*

The wavelength can be evaluated from the wave celerity and the period. The observed values of the ratio $c/\sqrt{gh}$ have been plotted against the Froude number on Fig. 2a along with solid and dashed lines representing equation (11) with $\beta_m = 1.2$ and equation (8) for which $\beta_m = 1.0$. The superiority of equation (11) is well supported by the data. Equation (11) can also be written as the ratio of the wave celerity to the mean flow velocity $\bar{u}$ as follows:

$$\frac{c}{\bar{u}} = \beta_m + \sqrt{\frac{1}{F^2} + \beta_m(\beta_m - 1)} \tag{29}$$

For unstable flows ($F > 0.5$), the ratio $c/\bar{u}$ calculated from equation (29) ($\beta_m = 1.2$) decreases from 3.26 to a minimum of 1.69 as shown in Fig. 2b.

The measured wave periods T shown in Table 1 (Col. 4) were fairly constant with a mean value of $\bar{T} = 1.41$ seconds and a standard deviation of 0.20 seconds.

The wavelength L can be obtained from equation (29) in which c is replaced by L/T:

$$\frac{L}{\bar{u}T} = 1.20 + \sqrt{\frac{1}{F^2} + 0.24} \tag{30}$$

For a given mean velocity, the wavelength increases with decreasing Froude number and a first approximation of the wavelength is obtained from the mean value of wave period $\bar{T} = 1.41s$.

possible in laminar sheet flows at Froude numbers as low as 0.50 as compared with 2.0 in turbulent flow. The existence of roll waves at Froude numbers near the lower limit is difficult to verify experimentally because of the extreme channel lengths required. However, in this study, roll waves were observed in laminar, subcritical flow at a Froude number as low as 0.74.

The parabolic velocity distribution in laminar sheet flows implies that the momentum correction factor is larger than unity ($\beta_m = 1.2$). This suggests that the relationship $c = \bar{u} + \sqrt{gh}$ used in previous studies is not applicable to laminar sheet flows and should be replaced by one which uses β_m. The proposed relationship (equation (11)) reduces to $c_0 = \sqrt{gh}$ when $\beta_m = 1$ and is in good agreement with the measured celerities of roll waves when $\beta_m = 1.2$ as shown in Fig. 2. The measured periods of roll waves remained fairly constant in the experimental study at $\bar{T} = 1.41$ second. The wavelength is shown to vary between $1.69\overline{uT} < L < 3.26\overline{uT}$.

The linearized derivation by Liggett (1975) of the length, ξ_c, required for the formation of roll waves has been modified to account for the parabolic velocity distribution of laminar sheet flows. The modified derivation gives more general expressions for the coefficients β and γ which reduce to those proposed by Liggett when $\beta_m = 1$. The results indicate that the length ξ_c is a function of several flow variables and a constant of integration ε which could be calculated from experiments. Though the parameter $\ln \varepsilon$ varies widely ($-61 < \ln \varepsilon < -9.4$), the dimensionless distance shown in Fig. 3 displays a similar relationship to the Froude number as found by Montuori (1963) for turbulent flows. For supercritical flows, ξ_c is proportional to the ratio of flow depth and slope. Alternatively, an equivalent function of Reynolds number and slope may be used.

Acknowledgement

This study has been completed at the Engineering Research Center at Colorado State University. The support of a NATO post-doctoral fellowship to the first author provided by the Natural Sciences and Engineering Research Council of Canada is gratefully acknowledged. The authors would also like to thank the U.S. Department of Agriculture, Agricultural Research Service for providing additional resources for this study.

Notations

A	cross-sectional area for uniform flow
A'	cross-sectional area for flow with a small perturbation
B	top channel width for uniform flow
B'	top channel width for flow with a small perturbation
c	wave celerity
c_0	velocity of the wave relative to the mean velocity $\bar{u}$
C	Chézy coefficient
D, E	empirical constants in equations (28) and (32)
F	Froude number
F_c	critical Froude number
g	gravitational acceleration
h	uniform flow depth
h'	flow depth for flow with a small perturbation
K	friction parameter
L	wavelength

Rheology of Hyperconcentrations

By Pierre Y. Julien[1] and Yongqiang Lan[2]

Abstract: A physically based quadratic rheological model for hyperconcentrated flows is tested with experimental data sets. The model includes components describing: (1) Cohesion between particles; (2) viscous friction between fluid and sediment particles; (3) impact of particles; and (4) turbulence. The resulting quadratic formulation of the shear stress is shown to be in excellent agreement with the experimental data sets of Bagnold, Savage and McKeown, and Govier et al. When the quadratic model is written in a linearized dimensionless form, the ratio D_v^* of dispersive to viscous stresses is shown to play a dominant role in the rheology of hyperconcentrations. The quadratic model is best suited when ($30 < D_v^* < 400$). At low values of D_v^*, the quadratic model reduces to the simple Bingham plastic model ($D_v^* < 30$), and at large values of D_v^*, a turbulent-dispersive model is indicated ($D_v^* > 400$).

Introduction

The rheology of highly concentrated sediment mixtures has been studied by various researchers including Bagnold (1954), Jeffrey and Acrivos (1976), Takahashi (1980), and Savage and McKeown (1983). Under high rates of shear, Bagnold proposed that the dominant shear stress can be attributed to interparticle friction and collisions. In this grain inertia region, both the normal and shear stresses depend on the second power of the shear rate. These results contrast with observations under low rates of shear (O'Brien and Julien 1988) because in the viscous region, the shear stress in excess of the yield stress increases linearly with the shear rate.

This study describes the rheological properties of hyperconcentrated sediment mixtures at shear rates ranging from the viscous region to the inertial region. It is proposed to test the quadratic rheological model suggested by O'Brien and Julien (1985) with existing data sets from Govier et al. (1957), Savage and McKeown (1983), and Bagnold (1954). This analysis points at the similarities and differences between these three data sets, which give quite different results when analyzed separately. As a second objective, the relative magnitude of the terms in the quadratic model is examined to define the conditions under which simplified rheological formulations can be applied.

Rheological Model Formulation

The shear stress encountered in fluids with large concentrations of sediments should include components to describe: (1) Cohesion between particles; (2) viscous interaction between sediment particles and the surrounding fluid; (3) impact of sediment particles; and (4) turbulence. After considering

[1]Assoc. Prof. of Civ. Engrg., Engrg. Res. Ctr., Colorado State Univ., Fort Collins, CO 80523.

[2]Res. Asst., Dept. of Civ. Engrg., Colorado State Univ., Fort Collins, CO.

Note. Discussion open until August 1, 1991. To extend the closing date one month, a written request must be filed with the ASCE Manager of Journals. The manuscript for this paper was submitted for review and possible publication on November 20, 1987. This paper is part of the ***Journal of Hydraulic Engineering***, Vol. 117, No. 3, March, 1991. ©ASCE, ISSN 0733-9429/91/0003-0346/$1.00 + $.15 per page. Paper No. 25612.

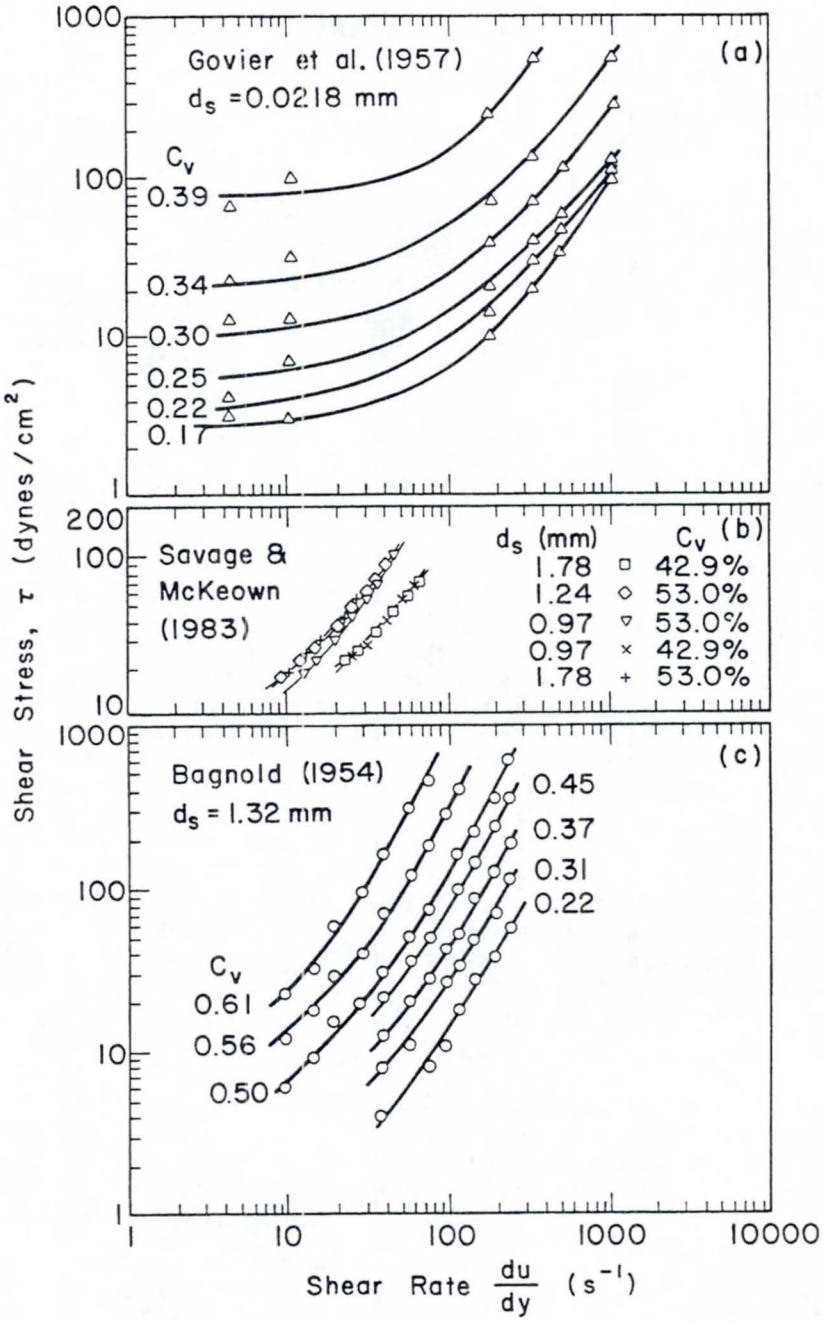

FIG. 1. Rheograms for Three Data Sets: Govier et al. (1957); Savage and McKeown (1983); and Bagnold (1954)

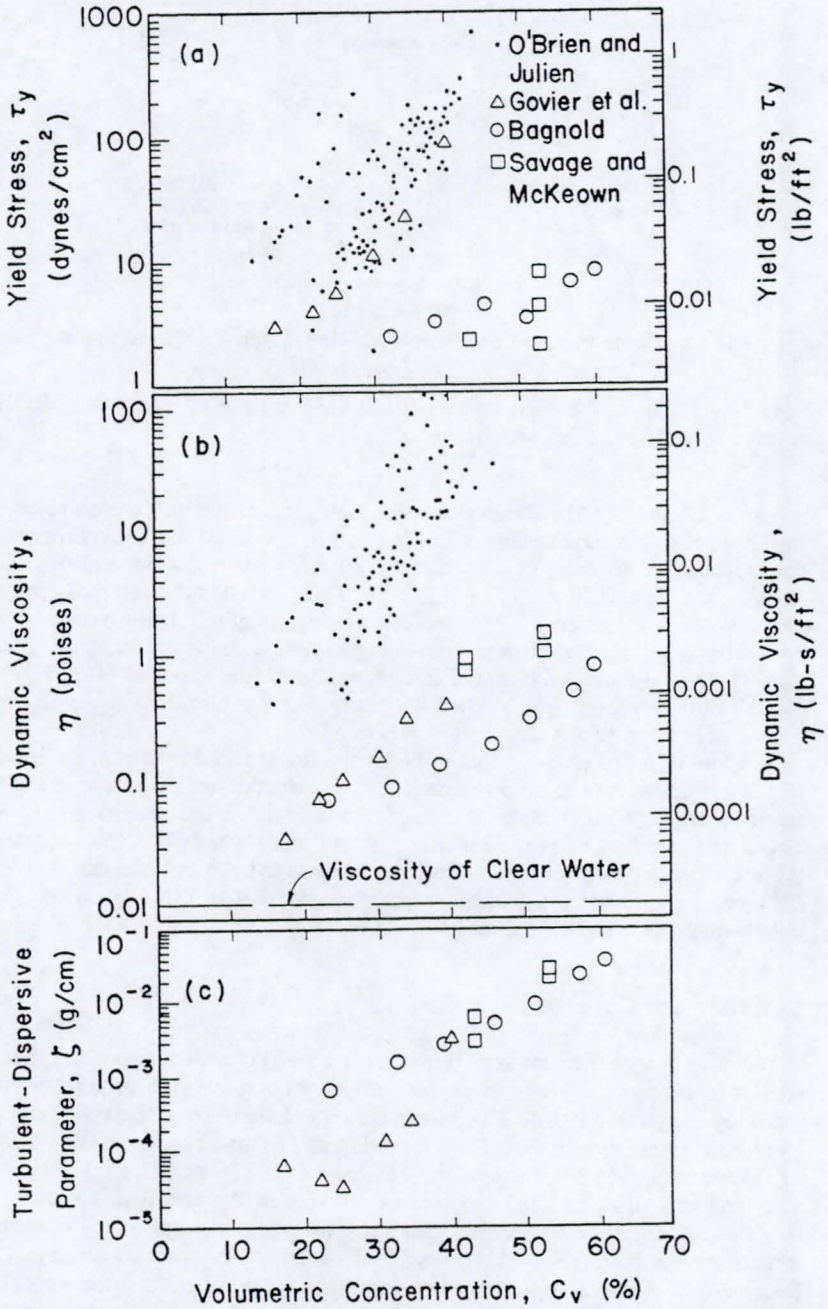

FIG. 2. Yield Stress τ_y, Dynamic Viscosity η, and Turbulent-Dispersive Parameter ζ for Hyperconcentrations

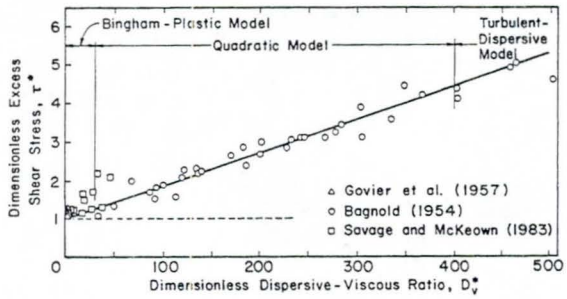

FIG. 3. Comparison of Dimensionless Model with Experimental Data

3. Newtonian and non-Newtonian fluids can be modeled depending on the relative magnitude of the parameters D_v^*, T_d^*, and τ_y.

The usefulness of the dimensionless rheological model is demonstrated in Fig. 3 where τ^* is plotted versus D_v^*. When Eq. 5 is fitted to the experimental data sets of Govier et al. (1957), Savage and McKeown (1983), and Bagnold (1954), it is found that $a_1(1 + T_d^*) = 0.0087$. It has not been possible to evaluate the parameter T_d^* because the mixing length l_m from existing experiments is not available. It is interesting to notice, however, that the value $a_1 = 0.01$ suggested by Bagnold is comparable to the value $a_1\ (1 + T_d^*) = 0.0087$ obtained from Eq. 5 when assuming that the turbulent stress is negligible compared to the dispersive stress ($T_d^* << 1$).

It is found in this analysis that not only the linearized dimensionless model (Eq. 5) is applicable to all three data sets, but the parameter D_v^* can be used to delineate particular cases of the quadratic model. The results shown in Fig. 3 indicate that τ^* is sufficiently close to unity when $D_v^* < 30$ to justify the use of a Bingham plastic model. On the other hand, τ^* exceeds 4 when D_v^* is roughly larger than 400, which indicates that in this region the turbulent-dispersive stress is dominant.

Summary and Conclusion

We concur with Savage and McKeown's (1983) conclusion that the rheology of hyperconcentrations is somewhat more complex than originally pictured by Bagnold (1954). The quadratic model describing the rheology of hyperconcentrated sediment flows is well suited to the experimental data sets of Govier et al. (1957), Savage and McKeown (1983), and Bagnold (1954). This analysis illustrates the benefits of combining the turbulent stress with the dispersive stress. When the quadratic model is written in a linearized dimensionless form (Eq. 5), the ratio of dispersive to viscous stresses D_v^* becomes of foremost importance in selecting appropriate rheological models.

It can be concluded that the quadratic model is valid for all values of the parameter D_v^*, and reduces to the Bingham plastic model when $D_v^* < 30$. Turbulent-dispersive formulations may be useful in the inertial region when $D_v^* > 400$.

Two-Dimensional Water Flood and Mudflow Simulation

By J. S. O'Brien,[1] P. Y. Julien,[2] and W. T. Fullerton,[3] Members, ASCE

Abstract: FLO-2D is a two-dimensional finite difference model that simulates clear-water flood hazards, mudflows, and debris flows on alluvial fans and urban floodplains. Interactive flood or mudflow routing between channel, street, and floodplain flow is performed using a uniform grid system to describe complex floodplain topography. A quadratic rheological model, developed from field and laboratory mudflow data, enables appropriate simulations of flooding conditions ranging from clear water to hyperconcentrated sediment flows. Computer-aided design (CAD) graphics of predicted time-sequenced flood depths automates the delineation of flood hazards. Replication of the 1983 Rudd Creek mudflow in Utah demonstrates the capability of the model.

Introduction

Most flood hazard studies, and particularly those on alluvial fans, are conducted in urban development areas. The extent of urban flooding is generally defined by considering a variety of flow conditions, including flow through subdivisions, street flow, and culvert or flood channel discharge. Conventional one-dimensional hydraulic models, such as the U.S. Army Corps of Engineers HEC-2 model, require the interpretation of overbank flood boundaries between cross sections that may extend through urban areas. Flood elevations and areas of inundation are difficult to interpret for locations where floodplain storage, flood attenuation, flow around buildings, or flow in streets is significant.

Flood hazards on alluvial fans are presently delineated with a simplistic probabilistic model adopted by the Federal Emergency Management Agency (FEMA) (*FAN*, 1990). Since the FEMA method doesn't simulate flood hydrographs, it is inappropriate for the design of flood mitigation structures such as levees, flood containment walls and flood channels. It is also inappropriate for flooding in urban areas, as well as for analyzing mud and debris flow hazards.

Previous attempts to simulate debris flows were accomplished with one-dimensional flow-routing models. DeLeon and Jeppson (1982) modeled laminar water flows with enhanced friction factors. Spatially varied and steady-state Newtonian flow was assumed, and flow stoppage could not be simulated. Schamber and MacArthur (1985) designed a one-dimensional finite element model for mudflows using the Bingham rheological model to evaluate the shear stresses of a nonNewtonian fluid. O'Brien (1986) designed a one-dimensional mudflow model for watershed channels that also utilized the Bingham model.

In 1986, MacArthur and Schamber presented two-dimensional finite element model for application to simplified overland topography. The fluid properties were considered to be those of a Bingham fluid, whose static

[1]Prin., FLO Engrg., Inc., P.O. Box 1659, Breckenridge, CO 80424.
[2]Assoc. Prof., Dept. of Civ. Engrg., Colorado State Univ., Fort Collins, CO 80523.
[3]Pres., FLO Engrg., Inc., P.O. Box 1659, Breckenridge, CO 80424.

Note. Discussion open until July 1, 1993. To extend the closing date one month, a written request must be filed with the ASCE Manager of Journals. The manuscript for this paper was submitted for review and possible publication on August 27, 1992. This paper is part of the ***Journal of Hydraulic Engineering***, Vol. 119, No. 2, February, 1993. ©ASCE, ISSN 0733-9429/93/0002-0244/$1.00 + $.15 per page. Paper No. 1965.

glecting the last three acceleration terms of (2) and (3). Further, by neglecting the pressure term, a kinematic wave representation is derived. These approximations are valid for steep alluvial fans. The option of using either a kinematic wave or diffusive wave equation is available in FLO-2D.

The diffusive wave aproximation has a broader application than the kinematic wave model (Ponce et al. 1978), and very little accuracy is normally sacrificed compared to the full dynamic model (Akan and Yen 1981). Concomitantly, computation time improves when a diffusive wave approximation is used instead of the full dynamic wave (Hromadka and Yen 1987).

The rheological behavior of hyperconcentrated sediment flows involves the interaction of several complex physical processes. The nonNewtonian behavior of the fluid matrix is controlled in part by the cohesion between fine sediment particles. This cohesion contributes to the yield stress τ_y, which must be exceeded by an applied stress in order to initiate fluid motion. By combining the yield stress and viscous stress components, the well-known Bingham plastic model is prescribed. For large rates of fluid matrix shear (as might occur on steep alluvial fans), turbulent stresses may be generated. An additional shear stress component arises in turbulent flow from the collision of sediment particles under large rates of deformation.

The total shear stress in hyperconcentrated sediment flows, including those described as debris flows, mud flows, and mud floods, can be calculated from the summation of five shear stress components

$$\tau = \tau_c + \tau_{mc} + \tau_v + \tau_t + \tau_d \quad (4)$$

in which the total shear stress τ depends on the cohesive yield stress τ_c, the Mohr-Coulomb shear τ_{mc}, the viscous shear stress τ_v, the turbulent shear stress τ_t, and the dispersive shear stress τ_d. When written in terms of shear rates (dv/dy), the following quadratic rheological model can be developed (O'Brien and Julien 1985):

$$\tau = \tau_y + \eta \left(\frac{dv}{dy}\right) + C \left(\frac{dv}{dy}\right)^2 \quad (5a)$$

where

$$\tau_y = \tau_c + \tau_{mc} \quad (5b)$$

and

$$C = \rho_m l^2 + f(\rho_m, C_v)\, d_s^2 \quad (5c)$$

in which η = dynamic viscosity; τ_c = cohesive yield strength; the Mohr-Coulomb stress $\tau_{mc} = p_s \tan \phi$ depends on the intergranular pressure p_s and the angle of repose ϕ of the material; and C = inertial shear stress coefficient, which depends on the mass density of the mixture ρ_m, the Prandtl mixing length l, the sediment size d_s, and a function of the volumetric sediment concentration C_v. Bagnold (1954) defined $f(\rho_m, C_v)$ as

$$f(\rho_m, C_v) = a_i \rho_m \left[\left(\frac{C_*}{C_v}\right)^{1/3} - 1\right] \quad (5d)$$

in which the empirical coefficient a_i = 0.01 and C_* = maximum static volume concentration for the sediment particles. Egashira et al. (1989) challenged this relationship, and posed

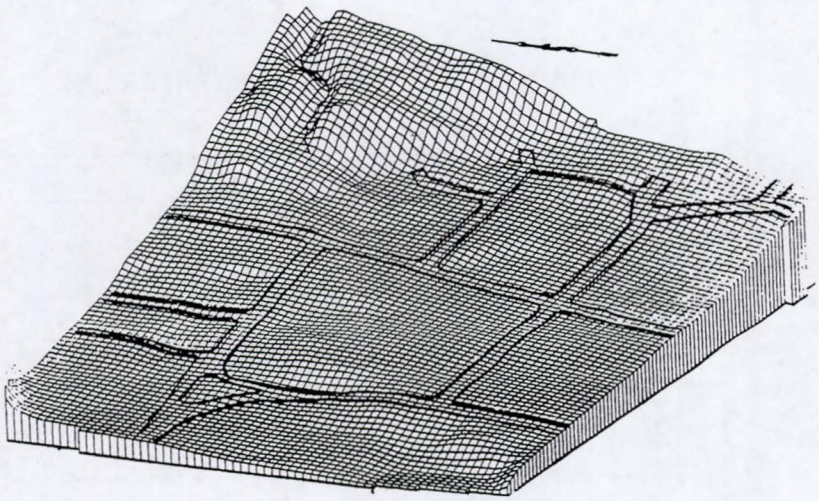

FIG. 2. Rudd Creek Alluvial Fan Topography

and represent the internal resistance stresses of a Bingham fluid. The sum of the yield stress and viscous stress defines the shear stress of a cohesive, hyperconcentrated sediment fluid in a viscous flow regime. The last term represents the sum of the dispersive and turbulent shear stresses, which depends on the square of the vertical velocity gradient. A discussion of these stresses and their role in hyperconcentrated sediment flows can be found in Julien and O'Brien (1987).

A mudflow model that incorporates only the Bingham stresses, and ignores the inertial stresses, assumes that the simulated mudflow is viscous. This assumption is not generally applicable, because all mud floods and some mudflows are turbulent, with velocities as high as 8 m/s (25 fps). Even flows considered as mudflows with concentrations up to 40% by volume can be turbulent (O'Brien 1986). Depending on the fluid matrix properties, viscosity and yield stresses for concentrations up to 40% can still be relatively small compared to the turbulent stresses at high velocities.

To define the terms in (5*a*) for use in the FLO-2D model, the following approach was taken. By analogy with the work of Meyer-Peter and Müller (1948) and Einstein (1950), the shear stress relationship (4) is depth-integrated and rewritten in the following slope form

$$S_f = S_y + S_v + S_{td} \quad \text{(6)}$$

in which the total friction slope S_f = sum of the components: the yield slope S_y; the viscous slope S_v; and the turbulent-dispersive slope S_{td}. The viscous and turbulent-dispersive slope terms are written in terms of depth-averaged velocity V. The viscous slope can be written as

$$S_v = \frac{K\eta}{8\gamma_m}\frac{V}{h^2} \quad \text{(7)}$$

in which γ_m = specific weight of the sediment mixture. The resistance parameter K for laminar flow equals 24 for smooth, wide, rectangular channels, but increases with roughness and irregular cross section geometry.

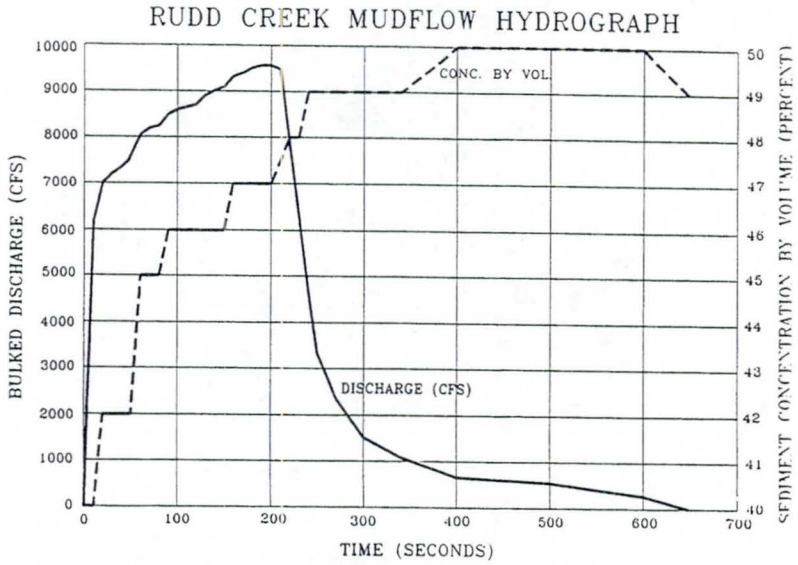

FIG. 4. Rudd Creek Mudflow Hydrograph

FIG. 5. Mudflow Frontal Deposit (Courtesy of USDA Soil Conservation Service, Salt Lake City)

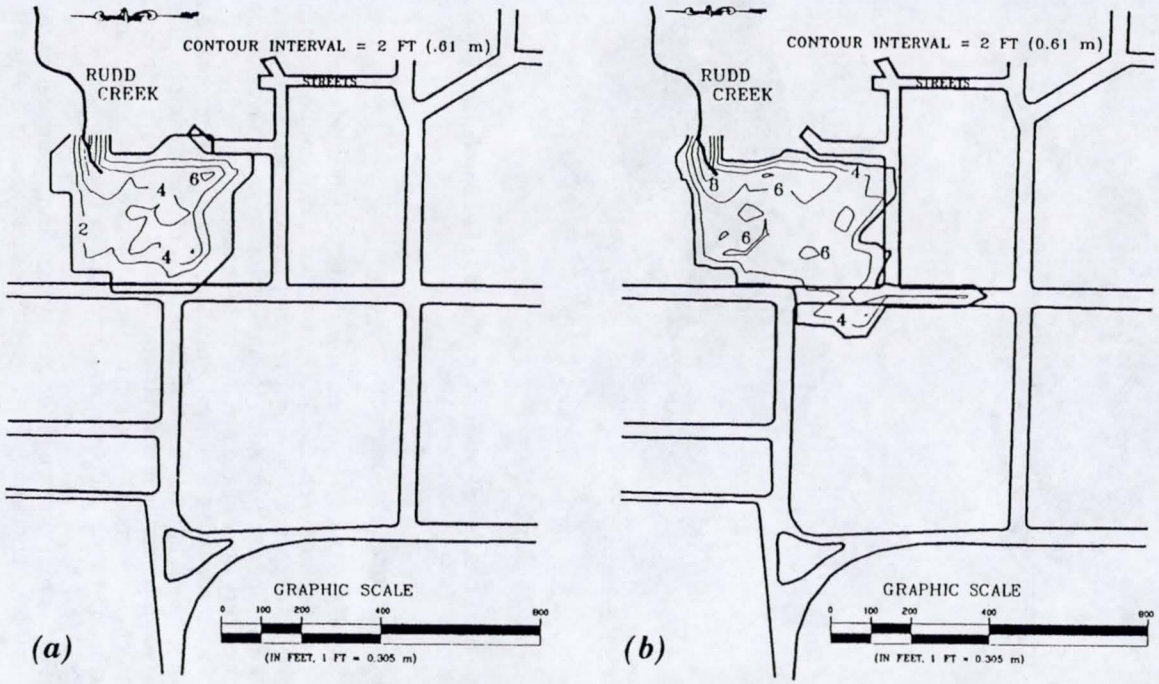

FIG. 7. Time-Lapse Simulation of Rudd Creek Mudflow: (*a*) Flow Depth after 1 Min; (*b*) Flow Depth after 2 Min

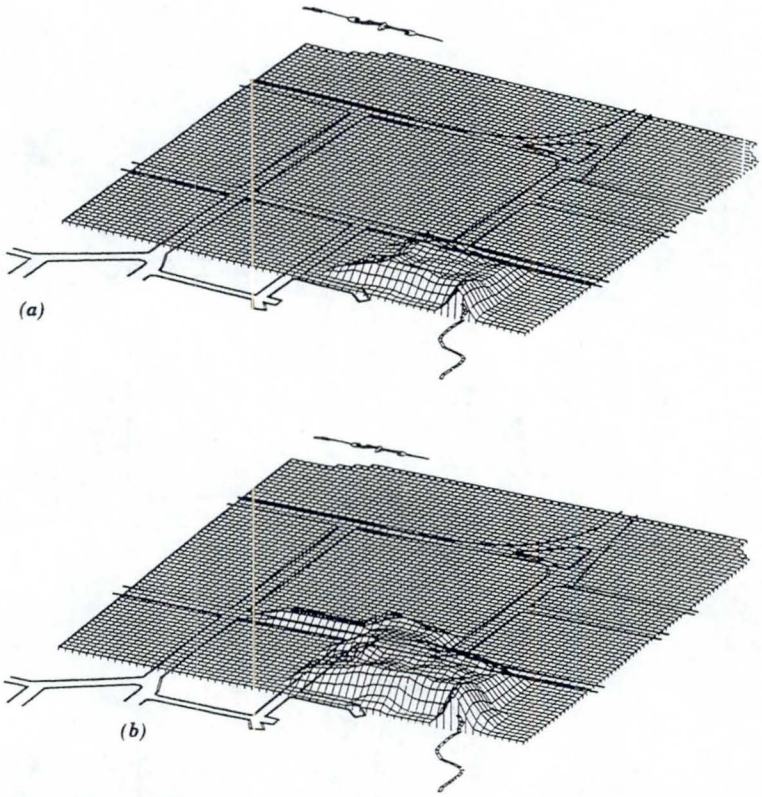

FIG. 8. 3-D Graphic Presentation of Time-Lapse Simulation: (*a*) Flow Depth after 1 Min; (*b*) Flow Depth after 2 Min

FLO-2D Model Description

The FLO-2D model evolved from the diffusive hydrodynamic model (DHM) (Hromadka and Yen 1987). The original DHM routing algorithm was revised and expanded to improve computational stability, decrease computational time, and broaden its application to more diverse flooding conditions. Very little of the original code remains.

The model uses a central finite difference routing scheme (an explicit numerical technique) for the application of the equations of motion. The surface topography is discretized into uniform square-grid elements. Each element is assigned a location on the grid system, an elevation, a roughness factor, and area and flow width reduction factors used to simulate flow blockage.

Flow is routed through the grid system using estimates of the flow depth to compute discharge. For a given element and time step, the discharge across each of the four boundaries is computed and summed. The resultant volume change is uniformly distributed over the available flow area in the element. Time steps vary according to the Courant-Friedrich-Lewy stability condition (Liggett and Cunge 1975), resulting in relatively short time steps (e.g., 1–30 s).

the approximate boundary of the mudflow after the flow had ceased, as indicated by the U.S. Army Corps of Engineers (*Incorporating* 1986). Close examination of photos taken after the event shows that the boundaries of the deposit were slightly more irregular than shown in Figs. 2 and 3, but the correlation is reasonable.

The flood hydrograph and other pertinent data used in the simulation were published by the U.S. Army Corps of Engineers (*Incorporating* 1986). The hydrograph is shown in Fig. 4. Available field data from the event included: (1) The area of inundation indicated from photography; (2) a surveyed volume of the mudflow deposit of approximately 64,200 m^3 (84,000 cu yd); (3) mudflow frontal velocity on the alluvial fan of approximately the speed that a man could walk [0.6–1.2 m/s (2–4 fps), eyewitness account]; and (4) observed mudflow depths that ranged from approximately 3.7 m (12 ft) at the apex of the alluvial fan to approximately 0.6–0.9 m (2–3 ft) at the debris front (Fig. 5).

The mudflow was initiated by a landslide, and therefore a relatively uniform sediment concentration was assumed, which increased slightly as the event progressed to simulate dewatering (Fig. 4). Manning n roughness values for each grid element varied from 0.035 to 0.10, depending on vegetation and flow obstruction. Appropriate values from laboratory data were selected for α_i and β_i in (10) and (11) to compute viscous and yield stresses. The buildings that influenced the flow path were modeled, and their location is shown in Fig. 6.

A time-lapse simulation of the progression of the mudflow over the Rudd Creek alluvial fan is illustrated in Fig. 7. Time-sequence flow depths are written to files for a CAD graphics program that plots the depth contours. With the plotting package, the flood hazard delineation is automated. When the viscous flow encounters a street with a favorable slope, it proceeds ahead of the main body of the flow, as shown for the 2 min and 5 min simulation times in Fig. 7. A 3-dimensional graphic display of the time-lapse simulation, as viewed from the upstream direction, is shown in Fig. 8. The 3-D view helps to visualize how the mud piles up near the fan apex. Postevent photos revealed that houses in this vicinity received the most damage.

The hydrograph in Fig. 4 indicates that the flood event was over in less than 7 min. The model predicted that the mudflow continued to creep down the fan for several more minutes before flow cessation. By the end of 15 min, all the flow on the fan had ceased (Fig. 9). There is little difference in the mudflow boundary after 15 min (Fig. 9) and the boundary for the 5 min simulation (Fig. 7).

The maximum computed flow depth of 3.6 m (11.8 ft) downstream of the apex compared well with the 3.7 m (12 ft) observed depth (Fig. 10). Mudflow velocities predicted on the fan ranged from 0.3 to 1.2 m/s (1–4 fps) or approximately walking speed, as was observed. Near the fan apex, maximum predicted velocities were less than 3.0 m/s (10 fps). Just upstream of the apex in the Rudd channel area, predicted velocities exceeded 6.1 m/s (20 fps). Predicted frontal lobe depths ranged from 0.6 to 1.2 m (2–4 ft), depending on the location on the fan, and correlated well with postevent photos.

Conclusions

The two-dimensional model FLO-2D is a flexible tool to augment the capability of the floodplain manager and engineer to predict flood hydraulics, identify areas of inundation, and design options for flood containment.

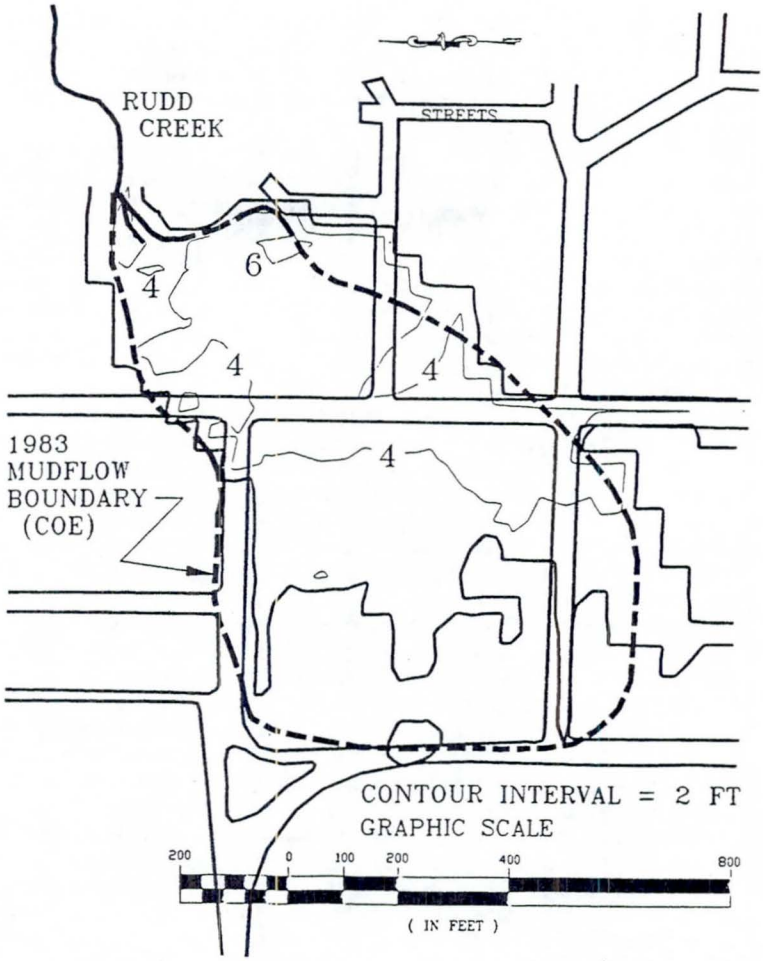

FIG. 9. Rudd Creek Mudflow Simulation after 15 Min

Model Limitations and Assumptions

Wave attenuation in the diffusive model is the result of overbank storage and the interaction of the friction slope and diffusive pressure gradient terms with the bed slope. The present model does not have the ability to simulate shock waves or hydraulic jumps, and tends to smooth out these abrupt changes in the flow profile.

The inherent assumptions in applying the model for flood routing are: (1) Steady flow for the duration of the time step (usually a few seconds); (2) hydrostatic pressure distribution; (3) steady flow resistance equation; (4) sufficiently uniform cross section shape and hydraulic roughness of the channel; and (5) single values of grid-element elevation and roughness.

In addition, FLO-2D is a rigid bed model and does not simulate degradation. This is not a serious limitation for urban floodplain flow (less erodible

ation of Landslides, Flash Floods and Debris Flow Hazards in Utah, Utah Water Research Lab., Univ. of Utah at Logan, Utah, 260–279.
O'Brien, J. S., and Julien, P. Y. (1988). "Laboratory analysis of mudflow properties." *J. Hydr. Engrg.*, ASCE, 114(8), 877–887.
Ponce, V. M., Li, R. M., and Simons, D. B. (1978). "Applicability of kinematic and diffusion models." *J. of Hydr. Div.*, ASCE, 104(3), 353–360.
Schamber, D. R., and MacArthur, R. C. (1985). "One-dimensional model for mudflows." *Proc., ASCE specialty conference on hydr. and hydro. in the small comp. age.* Vol. 2, ASCE, New York, N.Y., 1334–1339.
Takahashi, T., and Tsujimoto, H. (1985). "Delineation of the debris flow hazardous zone by a numerical simulation method." *Proc., Int. Symp. on Erosion, Debris Flow and Disaster Prevention*, Tsukuba, Japan, 457–462.
Takahashi, T., and Nakagawa, H. (1989). "Debris flow hazard zone mapping." *Proc., Japan-China (Taipei) Joint Seminar on Natural Hazard Mitigation*, Kyoto, Japan, 363–372.

Appendix II. Notation

The following symbols are used in this paper:

a_i = coefficient defined by Bagnold;
C = inertial shear stress coefficient;
C_v = volumetric sediment concentration;
C_* = maximum static volume concentration for sediment particles;
d_s = representative sediment size;
e_n = particle energy restitution coefficient after impact;
f = Darcy-Weisbach friction coefficient;
g = gravitational acceleration;
h = flow depth;
i = rainfall intensity;
K = resistance parameter for viscous flow;
l = Prandtl mixing length;
n = Manning resistance coefficient;
S_f = friction slope;
S_{fx} = friction slope component along x coordinate axis;
S_{fy} = friction slope component along y coordinate axis;
S_{td} = turbulent-dispersive slope;
S_v = viscous slope;
S_y = yield slope;
S_{ox} = bed slope component along x coordinate axis;
S_{oy} = bed slope component along y coordinate axis;
t = time;
V = depth averaged velocity;
V_x = velocity component along x coordinate axis;
V_y = velocity component along y coordinate axis;
v = velocity;
x = coordinate axis;
y = coordinate axis;
α_I = average particle impact angle;
α_i = coefficients of viscosity and yield stress;
β_i = exponents of viscosity and yield stress;
γ_m = specific weight of mixture;
η = dynamic viscosity;

Laboratory Analysis of Mudflow Properties

By Jim S. O'Brien[1] and Pierre Y. Julien,[2] Member, ASCE

Abstract: A rotational viscometer has been designed for laboratory measurements of the rheological properties of natural mudflow deposits in Colorado. The mudflow matrices comprised of silt and clay particles are sheared under temperature-controlled conditions at volumetric sediment concentrations ranging from 0.10–0.45. This study stresses the importance of conducting rheological measurements at low rates of shear because: 1) Those are the conditions found in natural channels; and 2) they avoid the slippage problems observed at large sediment concentrations. At low rates of shear, the Bingham model is fitted to the measured rheograms, and both the viscosity and yield stress increase exponentially with the sediment concentration of the fluid matrix. Both the yield stress and the viscosity increase by three orders of magnitude as the volumetric concentration of sediments in the fluid matrix changes from 0.10 to 0.40. The addition of sand particles does not significantly alter the rheological properties of the matrix unless the volumetric concentration of sands exceeds 0.20.

Introduction

In the United States, losses from landslides, subsidence, and other ground failures exceed the losses from all other natural hazards combined. Indeed, the Committee on Ground Failure Hazards (NRC 1982) reported that landsliding in the U.S. causes $1–$2 billion in economic losses and 25–50 deaths each year. Individual landslides can be widely scattered in space and time, but a substantial portion of the annual landslide loss is associated with a few major catastrophic events such as the mudflows in the San Francisco Bay area and along the Wasatch Front in Utah. Semiarid alpine mudflows and debris flows are triggered by the slumping or slipping of unconsolidated material on steep slopes (Higgins et al. 1983). Such movement usually occurs following soil saturation due to fairly intense and short-duration rainfall events, or as a consequence of rapid snowmelt. Mud and debris flows originate on steep slopes or landslide areas. The zone of sediment transport typically has a steep channel system, at the end of which a sudden break in slope on the valley floor induces deposition to form a conical debris fan.

Several investigations have promulgated various classifications of mudflows and hyperconcentrated flows [e.g., Blackwelder (1928), Sharp and Nobles (1953), Johnson (1965), and O'Brien and Julien (1985)]. An attempt to delineate hyperconcentrated flows and mass wasting processes was initiated by the National Research Council Committee on Methodologies for Predicting Mud Flows (NRC 1982). The committee proposed four main categories: water floods, mud floods, mudflows, and landslides. The

[1]Res. Assoc., Dept. of Civ. Engrg., Colorado State Univ., Ft. Collins, CO 80523.
[2]Asst. Prof., Dept. of Civ. Engrg., Colorado State Univ., Ft. Collins, CO 80523.

Note. Discussion open until January 1, 1989. To extend the closing date one month, a written request must be filed with the ASCE Manager of Journals. The manuscript for this paper was submitted for review and possible publication on May 6, 1987. This paper is part of the *Journal of Hydraulic Engineering*, Vol. 114, No. 8, August, 1988. ©ASCE, ISSN 0733-9420/88/0008-0877/$1.00 + $.15 per page. Paper No. 22680.

shows convexity to the shear stress, and this behavior is referred to as yield-pseudoplastic. There is no theoretically based equation for yield-pseudoplastics, but any empirical equation such as the power-law equation can be used:

$$\tau = \tau_y + a\left(\frac{du}{dy}\right)^n \quad \text{(2)}$$

in which a and n = empirical parameters. This model, first proposed by Herschel and Bulkley (1926), describes the behavior of clay-water suspensions reasonably well at high rates of shear (Govier and Aziz 1982).

Although several investigators have applied the Bingham model to water-sediment mixtures, most available data were collected for dilute mixtures of bentonite and kaolin clays under very high shear rates, well in excess of 100 s^{-1} (Thomas 1963; Plessis and Ansley 1967; Valentik and Whitmore 1965; Mills et al. 1983). When compared to measurements under low rates of shear, these analyses led to larger values of yield stress and lower values of viscosity. It must be considered that typical shear rates for hyperconcentrated sediment flows in the field are on the order of 5–50 s^{-1}. Data from Johnson (1970) show this value to be of a magnitude of 10 s^{-1} or less. Yano and Daido (1965) report shear rates less than 10 s^{-1} for open-channel mudflows with concentrations up to 35% by weight. Therefore, rates of shear in excess of 50 s^{-1} appear to be uncommon in open-channel mudflows. This corroborates the findings of Qian and Wan (1986) in that the rate of shear in hyperconcentrated flows rarely exceeds 100 s^{-1}. Thus, not only must the viscometer experiments be conducted at low shear rates, but the fluid properties must be evaluated at lower shear rates as well.

Measurement of Mudflow Properties

The measurement and interpretation of the physical properties of mudflow mixtures is more complex than the viscosity measurements of Newtonian fluids. Three different types of apparatus are in common use for measuring the rheological properties of non-Newtonian fluids; (1) The capillary viscometer; (2) the rotational viscometer; and (3) the cone-and-plate viscometer.

A capillary viscometer measures the rate of flow of a fluid in a capillary tube under a given pressure gradient. The rate of shear varies across the capillary section; this viscometer is not suitable for time-dependent fluids. Due to its simplicity, this viscometer can be invaluable at large rates of shear.

In rotational viscometers, the fluid is sheared at a nearly constant rate between a stationary and a rotating cylinder. The shear stress is obtained from the torque measured on the stationary cylinder. Precautions must be taken to ensure laminar flow and constant temperature; end-effect corrections may also be required. Its suitability to a wide range of shear stresses makes it a versatile and useful instrument to analyze non-Newtonian fluids.

The cone-and-plate viscometer shears the fluid in the narrow space between the flat circular rotating plate and an inverted cone. This viscometer is ideal to study the properties of non-Newtonian fluids at low and

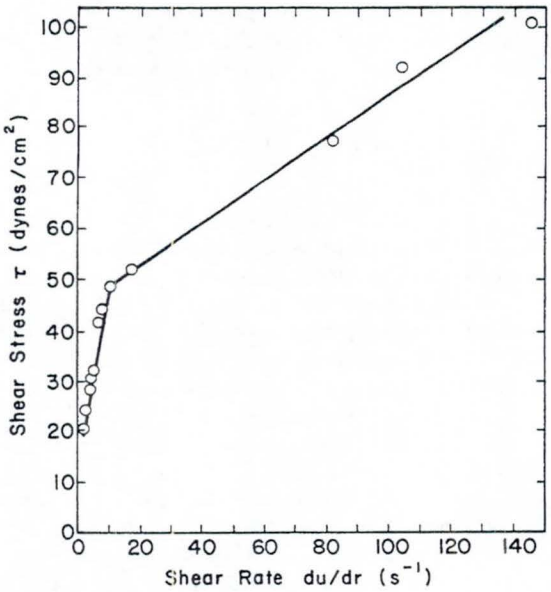

FIG. 1. Aspen Natural Soil Rheogram (C_v = 34.2%; Silts and Clays)

$10\ s^{-1}$, as shown in Fig.1. For this reason, the evaluation of viscosity and yield stress from the Bingham plastic model was based on the measurements taken at lower shear rates. Of course, when compared to measurements at high rates of shear, this analysis gives slightly lower values of yield stress and larger viscosity measurements.

In hyperconcentrated flows, the Bingham plastic model (Eq. 1) has been used by many researchers, e.g., Cao et al. (1983), Hou and Yang (1983), Higgins et al. (1983), Street (1958), Thomas (1963), Qian et al. (1980), Govier and Aziz (1982), and Dai et al. (1980). It has been generally accepted that both the viscosity η and the yield stress τ_y increase exponentially with the volumetric concentration of fine sediments C_v:

$$\eta = \alpha_1 e^{\beta_1 C_v} \quad (3)$$

and

$$\tau_y = \alpha_2 e^{\beta_2 C_v} \quad (4)$$

The values of the four empirical coefficients α_1, α_2, β_1, and β_2 obtained by regression analysis for each mudflow sample are presented in Table 2; the results are in reasonable agreement with those found in the literature. Particularly, the experimental values of the yield stress fall within the range of values defined by Fei (1981). The dispersion of the points at a given concentration certainly calls for more fundamental research to examine possible effects of thixotropy and clay mineralogy. Nevertheless, the open points (Glenwood) indicating lower percentages of clay in Fig. 2 have lower values of yield stress when compared with the samples with larger clay contents (Aspen). This trend is not quite apparent when

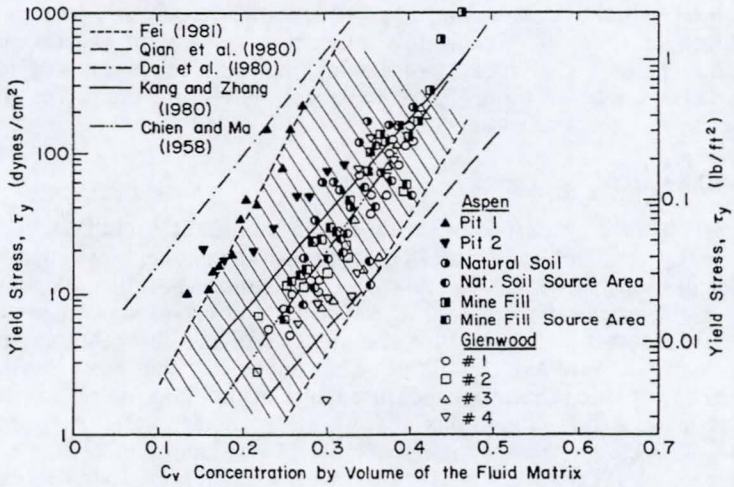

FIG. 2. Yield Stress of Mudflow Samples versus Volumetric Concentration

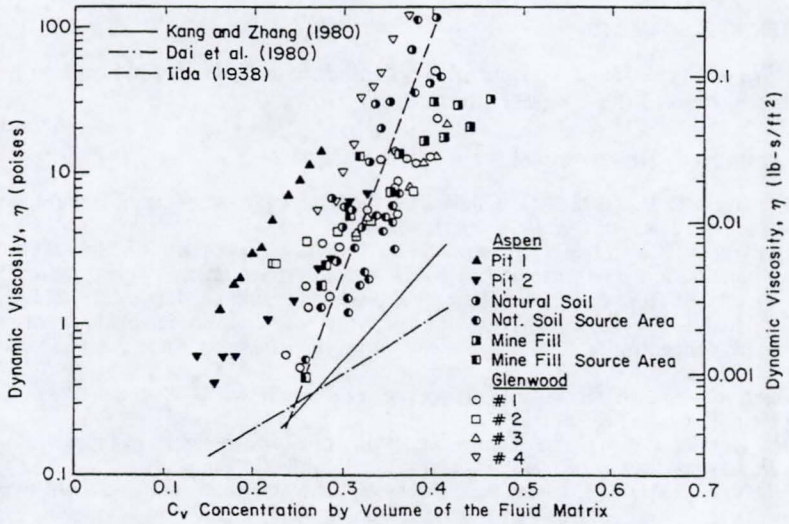

FIG. 3. Dynamic Viscosity of Mudflow Samples versus Volumetric Concentration

obtained, which indicates that large concentrations of sand particles are required in order to significantly alter the physical properties of the mudflow matrix. The viscosity of the fluid matrix increases very rapidly at volumetric concentrations of sand in excess of 20%. Further investigation is needed with coarser grained slurries.

Summary and Conclusion

Two physical properties of the fluid matrix of natural mudflow deposits in the central Colorado Rocky Mountains have been investigated at concentrations ranging from 10–45% by volume. The fluid matrix comprised of particles finer than 0.07 mm (silts and clays) was sheared in a special viscometer designed for the analysis of mudflow samples under temperature-controlled conditions. The viscometer gap size was determined to provide laboratory measurements of the fluid matrix properties under laminar flow conditions at low rates of shear without secondary flows. This study stresses the importance of conducting measurements at low rates of shear because: (1) those are the conditions found in natural channels; and (2) they avoid the slippage problems observed at large sediment concentrations. The Bingham rheological model was applied to the measured rheograms at low rates of shear. Both the yield stress and viscosity are shown in Figs. 2 and 3 to increase by three orders of magnitude as the volumetric concentration of sediments in the fluid matrix changes from 10–40%. The effect of adding sand particles to either a bentonite clay suspension or natural mudflow matrix of silts and clays is negligible, provided that the sand concentration remains less than 20% by volume. The viscosity of mudflow material with volumetric sand concentrations less than 20% simply corresponds to the viscosity of the silt-clay mixture. The viscosity of the mixture, however, increases rapidly with volumetric sand concentrations beyond 20%.

Acknowledgments

We are grateful to Y. Lan, Ph.D. candidate at CSU, for his comprehensive review of the Chinese literature.

Appendix I. References

Blackwelder, E. (1928). "Mudflow as a geologic agent in semiarid mountains." *Geologic Soc. Am., Bulletin* 39(1), 465–484.

Bradley, J. B., and McCutcheon, S. C. (1985). "The effects of high sediment concentration on transport processes and flow phenomena." *Proc., Conf. on Erosion, Debris Flow, and Disaster Prevention*, Tsukuba, Japan, 219–225.

Cao, R., et al. (1983). "The Law of hydraulic resistance in density current with hyperconcentration." *Proc., Second Int. Symposium on River Sedimentation*, 65–79.

Chien, N., and Ma, H. (1958). "Properties of slurry flow." *J. Sediment Res.*, 3(3), Beijing, China (in Chinese).

Dai, J., et al. (1980). "An experimental study of slurry transport in pipes." *Proc., Int. Symposium on River Sedimentation*, 195–204 (in Chinese).

Fei, X. J. (1981). "Bingham yield stress of sediment water mixtures with hyperconcentration." *J. Sediment Res.*, 3, Beijing, China, 19–28 (in Chinese).

Govier, G. W., and Aziz, K. (1982). *The flow of complex mixtures in pipes*. Krieger Publishing Co., Melbourne, Fla.

Disaster Prevention Research Institute, Kyoto University, Kyoto, Japan, 7, 340–347.

Appendix II. Notation

The following symbols are used in this paper:

a, n = empirical parameters for pseudo-plastic fluids;
C_v = volumetric concentration of fluid matrix;
D = sediment size;
du/dy = velocity gradient;
$\alpha_1, \alpha_2, \beta_1, \beta_2$ = coefficients;
η = dynamic viscosity of fluid matrix;
τ = total shear stress; and
τ_y = yield stress.

ON THE IMPORTANCE OF MUDFLOW ROUTING

J. S. O'Brien[1] and P. Y. Julien[2], Members, ASCE

ABSTRACT

Mudflows exhibit highly nonuniform and unsteady flow behavior related to surging, point source sediment loading, dilution, debris blockage and roll waves which are generally short lived phenomena. The key variable which affects the mudflow hydrograph shape is sediment concentration. To predict spatial variation in mudflow hydraulics for flood mitigation design, it is necessary to route the flood hydrograph. Hydrograph routing depends on the accurate assessment of the water volume runoff from the upstream watershed, channel storage (floodwave attenuation), and points of sediment loading. Several practical guidelines to evaluate the accuracy of the flood hydrograph are presented. The FLO-2D model is used to route mudflows for a watershed in Colorado Springs, Colorado which has historically generated debris flows. The mudflow hydrograph peak discharge at the watershed outfall exceeds the peak discharge that would be obtained by bulking the water flood hydrograph by 50%.

INTRODUCTION

The first attempt to develop a mud and debris flow routing model was undertaken by DeLeon and Jeppson (1982) who modeled laminar water flows with enhanced friction factors. Spatially-varied and steady-state Newtonian flow was assumed and flow cessation could not be predicted. Schamber and MacArthur (1985) designed a one-dimensional finite element model for mudflows using a Bingham rheological model to evaluate the shear stresses of a non-Newtonian fluid.

---

[1]Hydraulic Engineer, FLO Engineering, Inc., Breckenridge, CO 80424. (Phone and Fax: 520-339-1935; e-mail: jsobflo2d@aol.com).

[2]Professor of Civil Engineering, Colorado State University, Fort Collins, CO 80523. (Phone: 970-491-8450; Fax: 970-491-7008; e-mail: pjulien@vines.ColoState.edu.

MUDFLOW ROUTING

A two dimensional, flood routing model FLO-2D can simulate mud and debris flows using a finite difference solution of the continuity and momentum equations. An explicit numerical scheme was developed to solve the momentum equation with viscous stress terms of hyperconcentrated sediment flows. The solution domain for the nonlinear partial differential equation momentum equation is discretized into uniform square grid elements. The computation of flow hydraulics using explicit finite difference schemes is limited to small timesteps by strict numerical stability criteria. The algorithm advances the solution in space and time by solving for the unknown variables of depth and velocity one grid element at a time.

The routing algorithm for channel flow in the FLO-2D model was recently expanded to include the full dynamic wave equation solution for the momentum equation and the numerical stability criteria and is now dependent on volume conservation. In FLO-2D, the numerical stability criteria is variable with the grid element. It is expressed as:

$$\Delta t < (\zeta S_o \Delta x^2)/ q_o \qquad (1)$$

where q_o is the unit discharge, S_o is the water surface slope, Δx is the spatial increment (channel length within the grid element), and ζ is an empirical coefficient with a range from $0.25 < \zeta < 1.0$ (Ponce and Theurer, 1982). This coefficient is a variable unique to the channel element discharge flux and is evaluated at each timestep based on the accuracy of the volume conservation.

Starting with a specified minimum timestep, the timestep increases until the numerical stability condition is exceeded, then the timestep is decremented. Timesteps generally range from 0.1 to 120 seconds. The timesteps computed by FLO-2D are a function of the discharge flux for a given grid element and its available surface storage area. By selecting weighting factors for the numerical stability criteria, the user makes a tradeoff between volume conservation accuracy and model runtime.

In mudflow routing, the water and sediment is tracked separately. For each timestep, the grid element sediment concentration is recomputed with potential for dilution effects or increased sediment loading. The sediment concentration is used to compute the yield stress and viscosity parameters in the hyperconcentrated sediment flow equation. The relationship between the sediment concentration, water surface slope, and roughness (including flow obstacles) can result in flow cessation. Flow deposits remain as part of the flow depth throughout the flow simulation and can be remobilized by subsequent more dilute flows.

The FLO-2D model represents a progression from single discharge, one-dimensional Newtonian hydraulic models to a complex topography, unconfined, non-

infiltration, channel geometry and other data files to provide the simulation detail.

The model results can be viewed graphically or the flows and velocities output files can imported to the CAD software for plotting contours on the original digitized map. In addition, outflow hydrographs can be created at virtually any location in the channel or on floodplain cross sections. Most engineers are interested in maximum flow depths and velocities and these results can be plotted to view the area of inundation.

PRACTICAL GUIDELINES

In small watersheds (less than 5 square miles) where the alluvial fans have evolved by mudflows over geologic time, the 100-year flood event generally has too much water volume to create a mudflow. Mudflows are usually associated with frequent flood events such as the 10-year or 25 year return period flood. Unless the watershed has unusually erosive geology, there will be insufficient available sediment in the watershed to create a mudflow with the 100-year flood event. Extreme flood events (e.g. 100-year flood) will behave as a dilute mud flood (Table 1).

Table 1. Mudflow Behavior as a Function of Sediment Concentration

Flow Description	Sediment Concentration		Flow Characteristics
	by Volume	by Weight	
Landslide	0.65 - 0.80	0.83 - 0.91	Will not flow; failure by block sliding
	0.55 - 0.65	0.76 - 0.83	Block sliding failure with internal deformation during the slide; slow creep prior to failure
Mudflow	0.48 - 0.55	0.72 - 0.76	Flow evident; slow creep sustained mudflow; plastic deformation under its own weight; cohesive; will not spread on level surface
	0.45 - 0.48	0.69 - 0.72	Flow spreading on level surface; cohesive flow; some mixing
Mud Flood	0.40 - 0.45	0.65 - 0.69	Flow mixes easily; shows fluid properties in deformation; spreads on horizontal surface but maintains an inclined fluid surface; large particle (boulder) setting; waves appear but dissipate rapidly
	0.35 - 0.40	0.59 - 0.65	Marked settling of gravels and cobbles; spreading nearly complete on horizontal surface; liquid surface with two fluid phases appears; waves travel on surface
	0.30 - 0.35	0.54 - 0.59	Separation of water on surface; waves travel easily; most sand and gravel has settled out and moves as bedload
	0.20 - 0.30	0.41 - 0.54	Distinct wave action; fluid surface; all particles resting on bed in quiescent fluid condition
Water Flood	< 0.20	< 0.41	Water flood with conventional suspended load and bedload

There are several simple checks to determine the potential for a watershed to generate a mudflow. The first check is a watershed inspection for loose boulders and debris in the channel, eroding and undercut banks, potential for hillslope failures, and

watershed, the exposed rock outcrops are near vertical and the channel slope exceeds 45%. Upstream of the Ski Area parking lot, the alluvial fan slope averages 13%. A short distance downstream, the channel winds through the Broadmoor Hotel South Golf Course in a deeply incised ravine. Both channels are charged with boulders and organic debris in the reach upstream of the Ski Area parking lot.

Photo 1. Cheyenne Mountain Ski Basin Watershed

The rainfall frequency and storm distribution were evaluated from the records of five local rain gages. The Corps of Engineers HEC-1 hydrologic model parameters were calibrated using a contiguous gaged basin and were checked against those in other local studies and those in City drainage criteria manual. The 100-year return period storm data for portion of the basin generating the mudflow is:

Watershed Area = 0.34 mi^2
Total Storm Precipitation = 3.10 inches
Excess Rainfall = 0.99 inches
100-year Peak Water Discharge = 372 cfs
Runoff Volume = 19.44 acre-ft
Percent Runoff = 31.9%
Peak Unit Discharge = 1,094 cfs/mi^2

Values of the 100-year peak unit discharge in other studies ranged from 950 cfs/mi^2 to 1,140 cfs/mi^2 for basins less than 2 mi^2 in the Colorado Springs area (RCI, 1989).

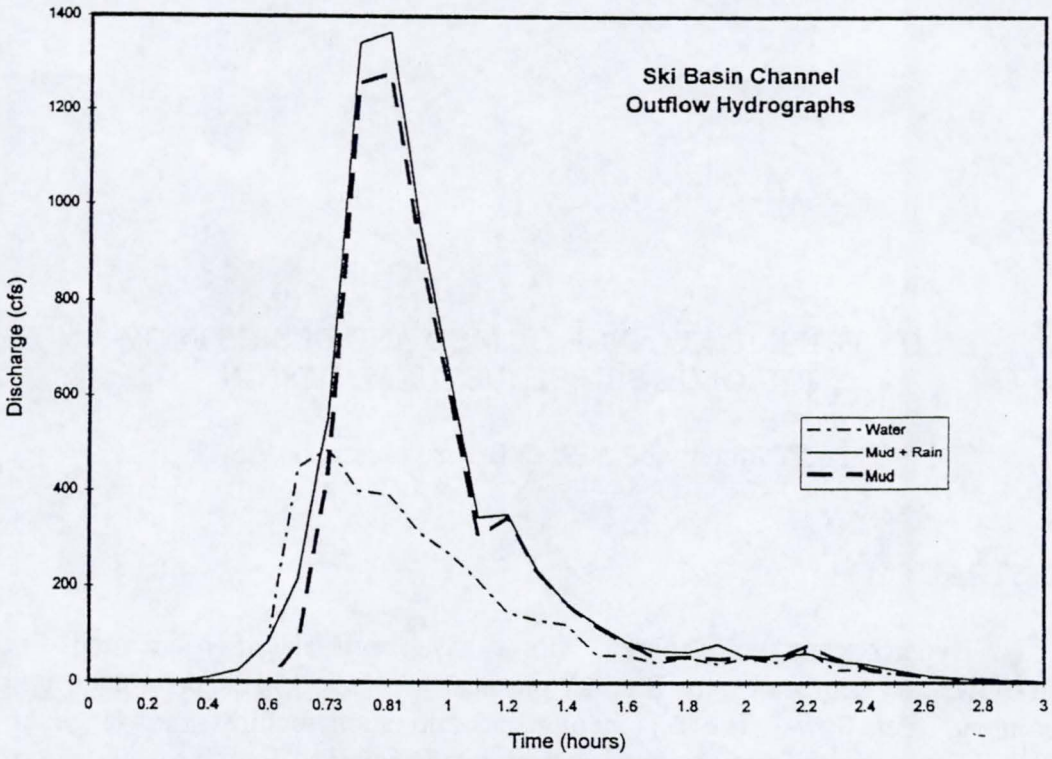

Figure 2. Ski Basin Channel Outflow Hydrographs

There are two important results to be highlighted. First, the mudflow peak discharge (+1,250 cfs) at the basin outfall exceeds the bulked peak water discharge (968 cfs) obtained with a sediment concentration of 50% (a bulking factor of two). This infers that if a conventional water flood analysis were conducted and the peak discharge was conservatively bulked at the outflow point by 50%, the design discharge could be significantly underestimated. Secondly, it is important to note that the hydrograph shape for the mudflows has a steeper rising limb. In the case of the mudflow, the discharge increases from 0 cfs to 1258 cfs in 0.2 hours whereas the water discharge increases from 9 cfs to 446 cfs in 0.3 hours.

Mitigation Measures

Several flood mitigation measures are being considered for the Ski Basin. The upper watershed channels are too steep for detention storage. Mitigation measures must focus on conveyance control. Channelization of the alluvial fan combined with levees are proposed to mitigate the mudflow hazard. Channel capacity will be designed to contain the 100-year mudflow peak discharge without freeboard. Levees will be set back 75 ft from the channel to permit overbank flows and the mudflow deposition. Overbank mudflow storage will be enhanced by grading deposition areas and lowering channel banks to encourage deposition in locations where removal of the deposits can be facilitated. Some trees will be left between the levees to increase floodplain roughness and promote debris deposition. Levee heights will be about five feet.

ON THE IMPORTANCE OF MUD AND DEBRIS FLOW RHEOLOGY IN STRUCTURAL DESIGN

P. Y. Julien[1] and J. S. O'Brien[2], Members, ASCE

ABSTRACT

Hyperconcentrated sediment flows have been classified as mud floods, mudflows and debris flows. Distinct physical processes characterize each type of sediment laden flow. The design of flood mitigation requires knowledge of the rheological properties of the hyperconcentrated sediment flow expected in a given watershed. Mitigation design strategies are outlined for mud floods, mudflows and debris flows. For mud floods, subcritical turbulent flows are conveyed in straight channels with minimal frictional resistance. For mudflows, flood hazard mitigation should consider detention basins for small volumes or spreading large volumes with the use of deflection walls. High momentum, debris flows require sabo dams. Mitigation measures should be fully operational through the range of hyper-concentrated sediment flows.

INTRODUCTION

Hyperconcentrated sediment flows can be initiated by numerous causes including intense rainfall, rapid snowmelt volcanic and man-made activities. The sediment load may also be increased by hillslope failure and bank collapse during the flood event. Flow hydraulics, flow cessation and runout distances of hyperconcentrated sediment flows are governed by the volume and properties of the fluid matrix which is comprised of the fluid and sediment particles. The fluid matrix

---

[1] Prof. of Civil Engineering, Engineering Research Center, Colorado State University, Ft. Collins, CO 80523 (Phone: 970-491-8450; Fax: 970-491-7008; e-mail: pjulien@engr.colostate.edu).

[2] Hydraulic Engineer, FLO Engineering, Inc., Breckenridge, CO 80424 (Phone and Fax: 520-339-1935; e-mail: jsobflo2d@aol.com).

of historical flood events, and a rheological and particle size analysis of deposits. Rheological analyses involve four different types of shear stresses: 1) yield stress; 2) viscous stress; 3) turbulent stress; and 4) dispersive stress. The non-Newtonian nature of hyperconcentration sediment flows results from several physical processes: the cohesive nature of fine sediment particles τ_c; the Mohr-Coulomb shear τ_{mc}, the sum of which defines yield stress τ_y; the viscous shear stress τ_v which accounts for the fluid-particle viscosity; the turbulent shear stress τ_t, and finally, the dispersive stress τ_d which accounts for the collision of sediment clasts.

The total fluid shear stress τ in hyperconcentrated sediment flows results from the sum of the five shear stress components:

$$\tau = \tau_{mc} + \tau_c + \tau_v + \tau_t + \tau_d \tag{1}$$

A quadratic rheological equation describes the flow continuum through the range of sediment concentration for these shear stresses. When written in term of shear rates, or velocity gradient du/dy; τ_{mc} and τ_c are independent of velocity gradient, τ_v varies linearly with the velocity gradient and both τ_t and τ_d vary with the second power of the velocity gradient. The following quadratic rheological model is obtained:

$$\tau = \tau_y + \eta \frac{du}{dy} + \zeta \left(\frac{du}{dy} \right)^2 \tag{2}$$

where

$$\tau_y = \tau_{mc} + \tau_c$$

and $$\zeta = \rho_m l_m^2 + a_i \rho_s \lambda^2 d_s^2$$

In the above equations η is the dynamic viscosity of the mixture; τ_c is the cohesive yield strength; τ_{mc} is the Mohr-Coulomb shear stress where $\tau_{mc} = p_s \tan \phi$ depending on the intergranular pressure p_s and the angle of repose ϕ of the material; and ζ is the inertial shear stress coefficient depending on the mass density of the mixture ρ_m, the Prandtl mixing length l_m, the sediment size d_s, the volumetric sediment concentration C_v; and ρ_s is the mass density of sediment. The mixing length l_m is usually given as a function of the distance from the boundary y and the von Karman constant κ. As a first approximation in depth-integrated flows, the approximate mixing length can be determined by $l_m \cong \kappa h$, where h is the flow depth h and $\kappa = 0.4$. The coefficient a_i has been shown to highly variable and Takahashi (1980) proposed $a_i \cong 0.01$. Bagnold defined the linear sediment concentration λ as

$$\frac{1}{\lambda} = \left(\frac{C_m}{C_v} \right)^{1/3} - 1 \tag{3}$$

in which the maximum concentration of sediment particles $C_m \cong 0.615$.

Julien (1997). A manual is available which further discusses the model attributes and its applications. Over thirty flood hazard delineation projects have been completed using the FLO-2D model. A short course by O'Brien and Julien (1997) is prepared to make the model available to floodplain managers and engineers.

INFLUENCE OF FLOW RHEOLOGY ON STRUCTURAL DESIGN

Flood mitigation design must take into consideration the rheological behavior of the three types of hyperconcentrated sediment flows previously described, i.e. mud floods, mudflows and debris flows. Flood mitigation measures fall into four categories: 1) flood hazard avoidance; 2) regulatory and zoning; 3) storage; or 4) conveyance. The first two categories include such measures as elevating on armored fill, planning open space for flood prone areas and physically removing structures in the flood path. The last two mitigation measures cover storage and conveyance methods which include detention/debris basins, levees and berms, debris fences and deflectors, channelization and channel lining, drop structures, energy dissipation and street alignment. Mitigation measures for each of the three classes of hyper-concentrated sediment flows are discussed.

Mud floods

Mud floods are very fluid flows with high velocities in which the fluid matrix viscosity is comparable to that of water. For large storm events on the order of the 100-year storm the volume of water and sediment may exceed the storage of small detention basins constructed in steep watershed canyons. In this case, flood mitigation should focus on the conveyance of the flood volume off the alluvial fan.

Conveyance design for mud floods should include consideration of sediment bulking, surging (roll waves), supercritical flow, debris plugging, sediment abrasion, superelevation, and potential for sediment scour and deposition. Extra freeboard that commensurate with the velocity head of mud floods should be considered (see Table 1). It is preferable to maintain the channel cross-section as straight and uniform as possible. Straight, steep channels will result in high velocities and high Froude numbers and will prevent the formation of cross waves and local deposition behind channel irregularities.

One of the engineering challenges in the design of straight alluvial channels is the control over the channel path. Streams with high Froude numbers are very erosive and channel migration or avulsion can occur during a flood event. Bed and bank stability are critical concerns. Using large riprap in steep channels for bank stability is not recommended because the riprap material can be launched by the flow, thus adding to the debris loading. Reducing the slope through drop structures can also be effective in controlling the flow.

The hydraulic flow properties of mudflows include relatively slow flow velocities and large flow depths which sustain motion on flat slopes. Flood mitigation design must include consideration of flow avulsion, debris and mud plugging of channel and conveyance facilities, and cleanup/maintenance. Effective mitigation measures for mudflows include storage, deflection, spreading and frontal wave dissipation. Mudflow detention basins can be very effective where mudflow volume is relatively small and can be estimated for the design flood event. Steep watershed canyons provide limited storage capacity for detention basins. When storage capacity is insufficient, a preferred mitigation alternative is to spread the flow over non-urban areas such as open space areas, parks and recreation areas where cleanup costs are minimal. Flow deflection to accomplish flow spreading can be complicated and should consider impact pressures, static loading, and flow runup over previously mud deposits which could result in overtopping the structure. Possible flow avulsions near the inlet of storage facilities must also be considered as deposits buildup. Deflection of flow into areas that require disposal of the excavated material can be very expensive to operate and maintain.

Deflection walls can be constructed of concrete or consist of earth berms. Earth berms designed to confine mudflows should have an erosion resistant core or face. Runup and overtopping of berms and walls can be averted by proper orientation of the structure thus deflecting the flow path. Vertical impact faces are also recommended to limit runup. The arrival of a mudflow frontal wave can be very destructive. As part of effective flood hazard mitigation, it is necessary to absorb the momentum of the frontal wave which could be carrying large boulders and debris capable of tremendous impact forces and runup against mitigation structures. Impact surfaces should be designed to withstand the impact of the large boulders found on the fan flowing at design depth and velocities. Freeboard design and factor of safety values for impact structures are given in Table 1.

Effective mitigation measures include levees that confine the mudflow outside the channel on the alluvial fan. A portion of the alluvial fan surface can be dedicated to the overbank storage detention. The levee is constructed parallel to the channel allowing an appropriate distance between the channel and berm for mudflow and debris storage; typically 50 ft to 100 ft can be set aside. The channel conveyance capacity is then designed to permit some overbank flow during the peak discharge. Lowering channel banks to create overbank flooding and grading floodplain areas for overbank storage will enhance mudflow deposition. The levee design will generally only require a height of 3 ft to 5 ft, as long as a major change in flow direction is not anticipated. Trees and other obstacles can be left on the floodplain to enhance flow cessation. Potential for levee erosion and failure must be evaluated. A maintenance plan should be prepared to access and remove mudflow deposits between the levees after the event. This concept for mudflow mitigation is being considered for several alluvial fans in Colorado Springs on Cheyenne Mountain.

Sabo dams are constructed in the steep mountain canyons near the source of debris in the upper watershed. The storage capacity of sabo dams is limited by the steep slope, but its purpose is to remove the largest debris elements from the flow matrix. The concrete walls of sabo dams are extremely thick (up to 10 m) and are constructed with drain pipes or steel frame structures (such as railroad rails) to permit drainage of the pore water. Once the pore water is drained, the mobility of coarse clasts decreases very rapidly. The design of sabo dams requires an assessment of the potential storage volume, maximum impact forces, protection against scour, stability under static loading, and a plan for maintenance access and debris removal. Sabo dams in basins generating frequent debris flows should be periodically inspected for impact damage, foundation stability and scour around the structure. Some sabo dams have early warning systems to monitoring the debris flow arrival or the rates of filling to provide advanced warning for downfan evacuation.

Other recommended measures to mitigate the damage of debris flows are limited to detention basins. Channel conveyance off the alluvial fan is not suggested because a break-in-slope or channel transition can cause the debris flow to abruptly stop and plug the conveyance facility. Debris flows generally will not flow on the mild slopes of alluvial fans and tend to pile up near fan apex. In most cases, debris flow hazard avoidance is the preferred mitigation.

CONCLUSIONS

The rheology of hyperconcentration sediment flow is relatively complex, but the quadratic formulation describes the continuum of flow behavior ranging from mud floods to debris flows. The quadratic rheological combines the effects of yield, viscous, turbulent and dispersive stresses in hyperconcentrated sediment flows. Numerical modeling of mud floods, mudflows and debris flows is possible with the two-dimensional model FLO-2D.

This paper emphasizes the need to design appropriate mitigation structures based on the rheological behavior of hyperconcentrated sediment flows. Straight, uniform flowing channels that convey the water and sediment off alluvial fans are best suited for mud floods. Detention basins, deflection walls, berms and levees are best suited for mudflows. Thick sabo dams in steep mountain canyons are recommended to arrest debris flows.

REFERENCES

Bagnold, R. A. (1954). "Experiments on a gravity-free dispersion of large solid spheres in a Newtonian fluid under shear," *Proc. Royal Soc. of London*, Series A, 225, 49-63.

KEYWORDS:

mudflows
mud floods
debris flows
structural design
mud/debris flow countermeasures
mud/debris flow mitigation
mud/debris flow rheology
mud/debris flow shear stresses

PHYSICAL PROPERTIES AND MECHANICS OF HYPERCONCENTRATED SEDIMENT FLOWS

by J. S. O'Brien and P. Y. Julien

ABSTRACT

The authors advance a better understanding of hyperconcentrated sediment flows, commonly referred to as debris flows or mudflows, with a fundamental investigation of the nature of fluid motion. In these flows of large concentrations of sediment, the predominant processes of energy dissipation are related to the viscous, turbulent, dispersive and yield stresses. The relative magnitude of these components largely depend on the fluid properties and whether the flow matrix consists of cohesive or noncohesive sediment. Based on experimental data, the following relationships are provided: 1) stress versus rate of strain, 2) viscosity versus sediment concentration, and 3) yield strength versus sediment concentration. These results expand our knowledge of the physical properties of hyperconcentrated flows.

The authors also review the application of fluid principles to these flows. The fundamentals of fluid mechanics are outlined for the case of hyperconcentrated flows on steep slopes with emphasis on the physical properties of non-Newtonian fluids. A theoretically sound and simplified methodology prescribe the engineering analysis for these hazard flows.

INTRODUCTION

Hyperconcentrated sediment flows are commonly referred to as mud flows or debris flows. The term hyperconcentrated, however, depicts a broader spectrum of sediment transport ranging from large concentrations of suspended sediment in streams to landslides. Sharp and Nobles (1953) refer to hyperconcentrated flows as debris flows instead of mud flows when fifty percent or more of the sediment in the flow matrix is coarser than sand. Debris flows have also been described as granular flows which are identified by the absence of fine material (silts and clays).

Hyperconcentrated flows originate in basins which can be delineated into three zones. The sediment source area is located in the uppermost region of the watershed and may be in a landslide area. The zone of sediment transport is a steep channel system in which erosion and deposition are generally in equilibrium. Finally, the alluvial fan is a depositional zone often identified by a break in the bed slope of the main channel.

Jim S. O'Brien, P.E., is Research Associate at the Civil Engineering Department, Colorado State University, Fort Collins, Colorado.
Pierre Y. Julien, Ph.D., is faculty Affiliate at the Civil Engineering Department, Colorado State University, Fort Collins, Colorado.

analyzed for size fraction and silt and clay content, and the properties of the mixture were described for various water and sediment concentrations. The results were incorporated into the definitions promulgated by the NRC committee and are shown in Table 1.

In nature, there exist a continuum of flow conditions and one hydrologic event may consist of several flow processes. Flow deposits, scour characteristics, and fan patterns are helpful tools in identifying the flow regimes and processes. Although the transition between the different types of flow are difficult to distinguish, mass wasting processes can be divided in four main categories: water floods, mud floods, mud flows, and landslides.

Conventional water flooding is defined as water inundation by overbank discharge. Sediment is transported through the mechanisms of suspension and rolling and saltation along the bed which depend largely on water velocity and turbulence. For water floods, standard hydrologic and sediment transport capacity methods and formulas are applicable. Water floods are not a phenomena analyzed in this paper.

Mud floods define a range of concentration from 20 to 45 percent by volume (Table 1). This concentration refers to the fluid matrix and should be assumed to consist of silts, clays and fine sands only. Water floods and mud floods display inherent fluid properties, both are unable to resist shear stress without motion or exhibit any appreciable yield strength. Conventional analysis using momentum, energy and continuity equations are applicable. Sediment transport capacity equations such as Einstein and Meyer-Peter and Müller are inappropriate because higher viscosities of the mixture and lower fall velocities of solid particles invalidate the empirical constants which are based on clear water as the fluid medium. Water floods and mud floods are classified under the National Flood Insurance Program (NFIP) definition of floods by the NCR (see Figure 1).

In mud flows the sediment concentration is sufficient to support large clastic material in a quiescent condition without settling. The flow matrix exhibits a distinct resistance to motion (high yield strength). This resistance to shear stress is a pseudo-plastic flow property corresponding to high viscosities. The National Research Council (NRC, 1982) report states, "The key characteristic in differentiating between mud floods and mud flows is that a mud flow displays a combination of density and strength that will support inclusions of higher density than water, such as boulders, both during transport and when the mass comes to rest". Throughout the flow process the combination of fluid matrix density and small settling velocities keep the boulders near the surface in the absence of turbulence. In steep basins, mud flows are generated under certain conditions of rainfall and sediment availability. When unlimited supplies of sediment become available, the probability of producing a mud flow is very high for intense rainfall events. Debris flows are acknowledged as having more than fifty percent of the sediment sizes coarser than sand. Debris flows without fine materials (silts and clays) are referred to as granular flows.

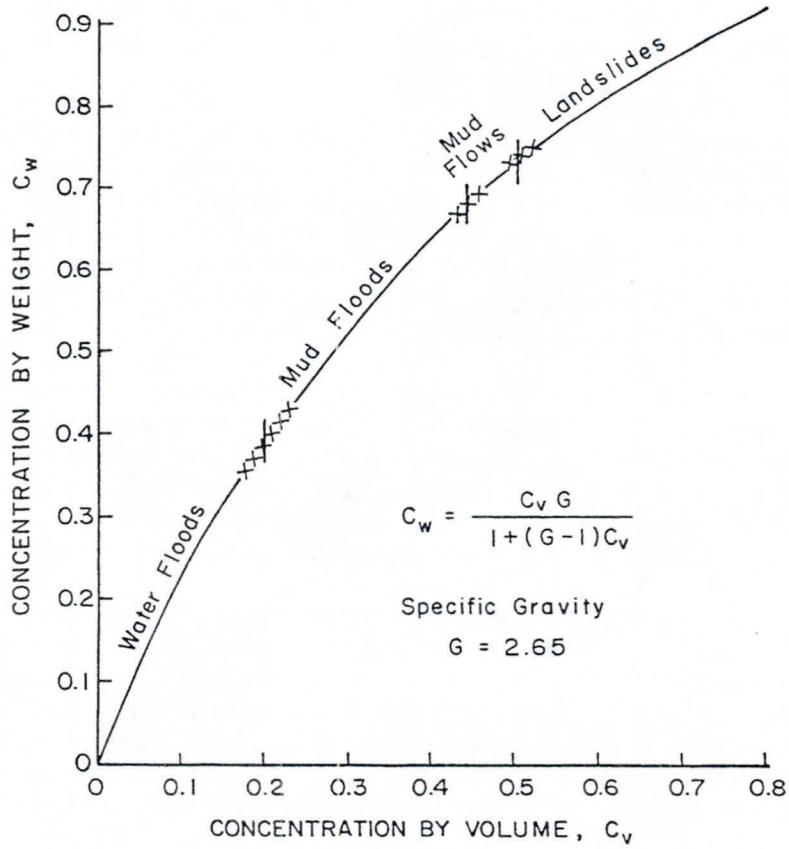

FIGURE 1. HYPERCONCENTRATED SEDIMENT FLOWS CLASSIFICATION

Landslides consist of downslope movement of earth by mechanisms of falling, toppling, sliding and spreading. Such earth movements may be either wet or dry. Landslides and bank slumps are an integral part of generating mud flows and mud floods in steep basins. This mechanism delivers source material to channel in brief singular events that often perturbate the channel flow hydraulics.

PHYSICAL PROPERTIES OF THE FLUID MATRIX

The presence of large concentrations of sediment induces complex processes of energy dissipation in the fluid matrix. Besides the viscous and turbulent stresses existing in clear water flows, the interaction of water and sediment, the exchange of sediment particles with the channel boundary, and the collisions of suspended particles (dispersive stress) all contribute to the dissipation of energy from the fluid matrix. Moreover, the presence of clay particles whose cohesive forces arise from hydrophilic bonding, modifies the physical processes governing the fluid flows. Hyperconcentrated sediment flows, therefore, are a function of complex interrelationships between water and sediments which require further investigation.

properties of viscosity and density and, therefore, the lift, drag and buoyancy forces acting on the particle exceed that which would have been exerted by water alone. The fluid matrix consists of the fluid plus the sediment particles which will have a negligible fall velocity in a quiescent condition.

Consider the case of granular flows in which the fluid matrix is water and the sediment is virtually all noncohesive clastic material. Granular flows may be either wet or dry (Passman et al., 1980, Nunziato and Passman, 1980 and Savage, 1979). The fluid medium is water and the fall velocity of the particle is large due to the absence of fines and the corresponding small viscosity of the fluid matrix.

Concentration and flow properties should be expected to change with larger concentrations of silt and clay. Graf (1971) reported that the fall velocity of particles decreases with the addition of fine sediment to water. A small percent concentration by weight of sediment in flowing water dampens turbulent eddies (Vanoni, 1941). Bagnold (1956) further indicated that at high concentrations of sediment, the turbulence may disappear altogether. Increasing the concentration of fines has the effect of increasing both the viscosity and density of the flow. Viscosities of actual debris flow deposits have been measured in the laboratory in excess of 1000 poises (the viscosity of water is about 0.01 poises).

The sediment concentration determines the physical characteristics of hyperconcentrated sediment flows. Concentration can be measured either by weight C_w or by volume C_v with a conversion of

$$C_w = \frac{C_v G}{1 + (G-1)C_v} \qquad (1)$$

where G is the specific gravity of dry sediment. A concentration of 50% by volume corresponds to 73% concentration by weight using 2.65 as the specific gravity for the sediment. Referring to Table 1, 50% concentration by volume represents a perceived limit to a mud flow with some fluid properties as determined through laboratory experiments.

It is noteworthy that Bagnold (1954), in his paper on dispersive stress theory, described flows of uniform grains with a concentration by volume of 57% as a granular paste and 52% concentration by volume as the Newtonian fluid limit. In his calculations he correctly reported that the maximum concentration for spheres is 74% by volume with a lower value of 65% for natural, reasonably rounded uniform grains. Using some data from Lamb and Whitman (1969) and Das (1983) the concentrations in Table 2 were computed. The loosest stable arrangement for uniform spheres is a simple cubic structure with a concentration of 53% by volume. The average minimum volumetric concentration of several soil types shown in this table is 54%. For impending fluid motion of the sediment, the concentrations must decrease from these minimum values given in Table 2; otherwise the sediment would move as a block. This evidence supports the delineation of flow definitions indicated in Table 1.

In the field, higher concentrations may be possible with larger quantities of silt and clay in the flow matrix. Written accounts of mud flows describe a wide range of concentrations with maximum concentrations by weight as high as 79 to 85% (Sharp and Nobles, 1953), 60 to 78% (Pierson, 1981) 59 to 86% (Pierson, 1980), 60 to 90% (Johnson, 1970) and 91% (Curry, 1966). Any loss of water during the sampling process, however, could result in significantly higher concentrations than actually occurred during the flow events. Surges and nonuniformity in the flow concentrations also distort the measured estimates of the flow properties. It is suggested that attempts at reporting mud and debris flow events should focus on a description of the mean flow properties which will assist in developing future predictive methods.

MECHANICS OF HYPERCONCENTRATED SEDIMENT FLOWS

The predominant processes of energy dissipation and resistance to motion are a function of the viscous, turbulent, dispersive and yield shear stresses. The relative magnitude of these stresses largely depend on the fluid properties, the concentration of sediment and whether the flow matrix includes cohesive sediment. Although the initiation of motion through landslides and creeping soil failures are more properly examined through a soil mechanics approach, the hyperconcentrated flows should be analyzed in a continuum approach to describe a wide range of concentrations ranging from clear water to very viscous mud flows.

Newton's second law is applied to describe the one-dimensional motion of an incompressible water-sediment mixture. The force equilibrium per unit mass may be written as

$$\frac{\partial u}{\partial t} + u \frac{\partial u}{\partial x} = g \sin\theta - \frac{1}{\rho_m} \frac{\partial p}{\partial x} + \frac{1}{\rho_m} \frac{\partial \tau}{\partial y} \qquad (2)$$

where ρ_m is the density of the fluid mixture, u is the velocity in the downstream x-direction, p is the internal pressure, τ is the shear stress, g is the gravitational acceleration, $\sin\theta$ is the channel slope and y is the upward distance above the channel bed perpendicular to the flow. The left side of the equation represents the local and convective acceleration of the fluid. These terms depict the unsteadiness and nonuniformity of the flow. The right side of the equation represents the gravity, pressure, and resistive shear stress terms. In the original Navier-Stokes equation valid for Newtonian fluids, the pressure distribution can be assumed to be hydrostatic and the shear stress is a function of the viscosity μ and of the rate of deformation

$$\tau = \mu \frac{\partial u}{\partial y} \qquad (3)$$

In mud flows, however, the shear stress is a complex function of the water and sediment properties comprising the fluid matrix which limits its direct application for predictive modeling. A general equation postulated for the resistive shear stress in a water sediment mixture is

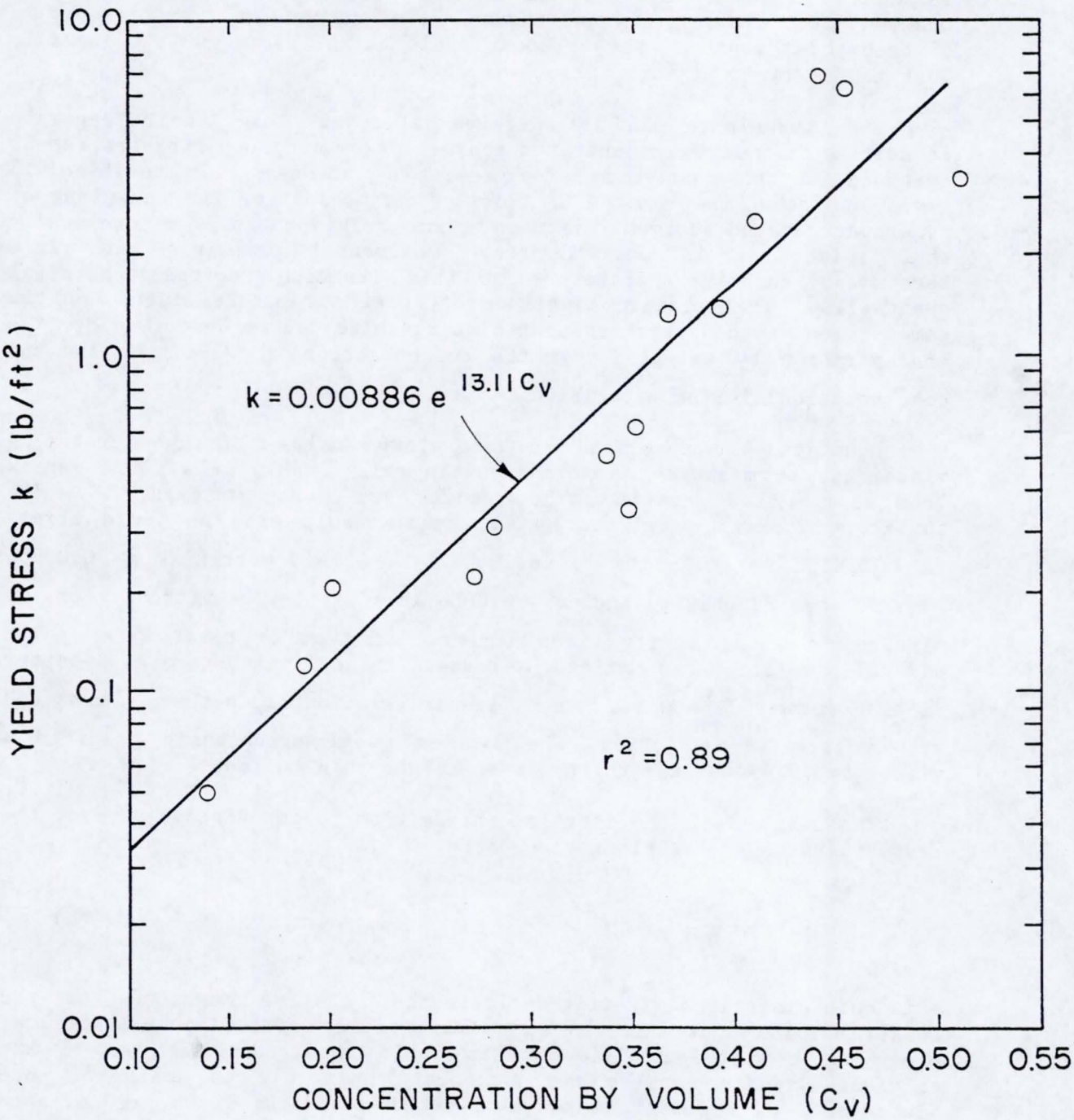

FIGURE 3. YIELD STRESS vs. CONCENTRATION BY VOLUME

the eddies in a cumulative manner dissipating the smaller eddies first or hampering their formation altogether. Sharp and Nobles (1953) noted this phenomena in their descriptive paper. In this fashion, the energy is sapped from the main body of the flow and expended to increase the sediment particle velocity and the height of suspension. This energy is distributed throughout the various levels of the flow and is eventually lost in the fluid mixture through viscous heat.

The turbulence and dispersive stresses lose their separate identities in a hyperconcentrated sediment flow and both stresses can be combined in the last term of Eq. 4. The stress-strain relationship given by Eq. 4 is promoted as correctly representing the behaviour of hyperconcentrated sediment mixtures. This relationship is theoretically sound since it is derived from fundamental principles in fluid mechanics, and the parameters of this function represent physical quantities. The relative magnitude of these parameters depends on the composition of the water-sediment mixture which can be described by (the concentration by weight C_w or the concentration by volume C_v and the concentration of fine material C_f.

Equation 4 was tested in laboratory analysis using a rotating viscometer to measure the stress-strain relationship of a fluid matrix from a mud flow deposit. The results are shown in Figure 5. The physical properties defined by the relationship are the yield stress ($k = 0.0108$ lb/ft^2), the viscosity of the fluid matrix ($\mu_m = 0.00065$ lb-s/ft^2 = 0.31 poises) and $C_1 = 0.0065$ lb-s^2/ft^2. The viscosity of the mixture is about thirty times larger than that of clear water. The parabolic relationship defined by regression analysis generates a better fitting curve ($r^2 = 0.98$) than a linear relationship between stress and strain rate ($r^2 = 0.95$). The Bingham model erroneously predicts a viscosity (9.43 poises) thirty times larger than the Eq. 4.

The ratio R of the inertial stress term to the viscous stress, the last two terms on the right side of Eq. 4, is

$$R = \frac{C_1}{\mu_m} \frac{\partial u}{\partial y} \tag{8}$$

This non-dimensional ratio defines the relative magnitude of the inertial to viscous stresses in a form similar to the Rouse number for clear water turbulent flows. This ratio supercedes the use of any critical Reynolds number which is not applicable to delineate non-Newtonian flow regimes. A small value of R indicates the predominance of viscous stresses and suggest the use of a Bingham model rather than the complete solution of Eq. 4. The value of C_1 is determined through laboratory analysis from Figure 3 and is a function of the sediment concentration, particle diameter, flow depth and clay concentration.

Similarly the Bingham number can be written as the ratio of the yield stress to the viscous stress

$$B = \frac{k}{\mu_m} \frac{\partial y}{\partial u} \tag{9}$$

This ratio indicates the relative magnitude of the yield and viscous terms. As R becomes small and B reduces to zero, the fluid will behave as a Newtonian fluid. These two ratios R and B are valid at every point along a velocity profile since they are both a function of $\frac{\partial u}{\partial y}$. In order to describe the mean flow characteristics, however, the partial derivative $\frac{\partial u}{\partial y}$ can be replaced by the ratio of average velocity $\bar{u}$ to the flow depth d in Eqs. 8 and 9. Both ratios must be defined by laboratory investigation.

APPLICATIONS

The physical processes encountered in mud flows are extremely complex. Valuable insight into the real nature of these non-Newtonian flows was gained through theoretical work, laboratory analysis and field investigations. Simplified methodologies based on the dominant physical processes have been applied to 16 small steep watersheds generating mud flows near Glenwood Springs, Colorado. One objective was to determine the relative magnitude of the losses attributed to internal viscous dissipation as compared to the losses due to channel boundary roughness. This analysis is based on the force balance equation (Eq. 2). The pressure term is written as a function of flow depth d and the shear stress τ in the channel is subdivided in two components. The first component τ_b is due to the large boundary roughness elements written as a function of the boundary energy loss gradient S_b and the second accounts for the internal stress τ_i. Assuming an hydrostatic pressure distribution in a one-dimensional flow over rough boundaries, Eq. 2 can be rewritten as

$$\frac{\partial u}{\partial t} + u \frac{\partial u}{\partial x} + g \frac{\partial d}{\partial x} - g \sin\theta + g S_b + \frac{1}{\mu_m} \frac{\partial \tau_i}{\partial y} = 0 \tag{10}$$

The solution to this equation when combined with the continuity equation gives a complete one-dimensional dynamic description of the motion of hyperconcentrated sediment flows. Steady uniform flow conditions can be assumed which eliminates the first three terms of Eq. 10, the internal energy gradient S_i is then defined as

$$S_i = \frac{1}{\rho_m g} \frac{\partial \tau_i}{\partial y} = S_o - S_b \tag{11}$$

where the bed slope ($\sin\theta$) is written as S_o. The boundary friction slope term S_b is important because the large boundary roughness elements force the fluid mixture to flow around boulders, trees and other channel obstacles, thus creating additional losses which enhance the C_1 term in Eq. 4. In this manner, energy is first transformed into turbulence and

TABLE 3. RATIO OF INTERNAL TO BOUNDARY ROUGHNESS STRESSES R_s

	Flood Event Return Period in Years		
C_v	100	25	10
.36	2.2*	2.3	2.7
.38	3.3	4.0	4.9
.40	5.3	6.6	8.2
.42	9.5	11.9	14.6
.44	17.0	20.8	24.9
.46	30.0	36.4	42.3
.49	48.2	57.0	63.5
.51	71.5	78.1	82.7
.54	88.3	92.3	94.2

*R_s values in percent, Standard Error ranged from 0.3 to 3.9%

This simplified analysis reveals the importance of the physical properties of the fluid matrix and prescribes the need for more fundamental research on mud flows. Ignoring either the viscous or friction slope term in the analysis would result in the overprediction of the velocity of the flow. There are inaccuracies in this analysis. First, the Manning's equation is only applicable for fully developed rough turbulent flows. Second, the Bingham model is not applicable for high velocity, rough turbulent flow. Mud flows and debris are inherently unsteady, nonuniform flows. On steep slopes, using the kinematic wave analogy, equation (15) should be solved using the three terms of Eq. 4 and this requires the use of C_1. More experimental analysis is required for the evaluation of C_1 and its variability with concentration, sediment size and boundary roughness. A stainless steel viscometer has been designed for this purpose.

CONCLUSION

The devastating effects of hyperconcentrated sediment flows in the past demonstrate an urgent need for a predictive methodology to define the hazard levels and to aid in the design of adequate mitigations measures and structures. Such a methodology would rely on an accurate knowledge of the physical properties of the water-sediment mixture. Research efforts must be focused on fundamental investigations involving both theoretical and experimental analysis.

This paper emphasizes the physical properties of hyperconcentrated sediment flows. Flow descriptions have been classified as a function of the concentration of sediments. Various experimental, theoretical and field data show that the maximum concentration by volume for mud flows is unlikely to be in excess of 0.50.

Basic fluid mechanics principles are recommended to describe the broad continuum of hyperconcentrated flows. A simple quadratic model (Eq. 4) is postulated, in which each term represents a well-defined physical property of the fluid. The last term of this equation

G specific gravity of sediments

k yield stress

p internal pressure

r^2 coefficient of determination

R ratio of inertial stress to viscous stress

R_s ratio of internal stress to boundary roughness stress

S_b boundary energy gradient

S_i internal energy gradient

S_o bed slope

t time

u velocity

$\bar{u}$ mean velocity

x longitudinal coordinate (positive downstream)

y upward distance above the channel bed

κ von Karman constant

θ angle of the channel with the horizontal

λ linear concentration

μ_m dynamic viscosity of the mixture

ρ density of clear water

ρ_m density of the fluid mixture

τ shear stress

τ_b shear stress from the boundary roughness

τ_D dispersive stress

τ_i internal stress

τ_R turbulence stress

REFERENCES

Bagnold, R. A. 1954. Experiments on a gravity-free dispersion of large solid spheres in a Newtonian fluid under shear. Proceedings Royal Society of London, Series A, V. 225, pp. 49-63.

Bagnold, R. A. 1956. Flow of cohension grains in fluids. Philosophical Transactions of the Royal Society of London, Series A, V. 249, pp. 234-297.

Curry, R. R. 1966. Observations of alpine mudflows in the Ten Mile Range, central Colorado. Geol. Soc. Am. Bull., V. 77, pp. 771-776.

Das, B. M. 1983. Advanced Soil Mechanics, McGraw-Hill, New York, 511 p.

TECHNICAL STANDARDS FOR DELINEATING ALLUVIAL FAN FLOODING

Jim O'Brien[1] and Brian Hyde[2]

ABSTRACT

Communities and transportation corridors have encroached on alluvial fans in most western mountainous states. In Colorado, Telluride, Vail, Aspen and Glenwood Springs are only a few of the communities confronting the challenge of delineating alluvial fan flood hazards and regulating development where lives are threatened and expensive property may be impacted. In addition, transportation corridors which experience alluvial fan flooding including mud and debris flow events are costly to maintain, potentially disruptive to the economy and dangerous for motorists.

Predictions of flood hazard on alluvial fans is being conducted with no technical standards for assessment of the hazard. Administration of delineated hazard areas is based on a non-integrated approach by local and state agencies. The Federal Emergency Management Agency (FEMA) recognizes the special flood hazards on alluvial fans, but the FEMA guidelines do not specifically address the delineation of mud and debris flow hazards. In Colorado, the statutory authority for regulating alluvial fans flood investigations exists without the technical standards for delineation and approval of alluvial fan flood hazard studies. Standards for alluvial fan flood hazard delineation, for administration of flood hazard areas, for evaluation of mitigation measures and for compliance with development regulations are proposed in this paper.

INTRODUCTION

After more than 100 years of community development on alluvial fans, floodplain administrators are now facing the challenge of coping with extensive development where evidence of pre-development large floods and mudflows is apparent. Within the history of the community, several notable floods may have occurred, but the period of record is still so short that the 100-year design flood is still the disaster of the future. Of all the difficult issues facing floodplain administrators in communities with alluvial fans, the lack of technical standards for hazard delineation and the absence of appropriate zoning regulations for the administration of flood-prone fan areas pose the greatest challenges. Approximate delineation methods have resulted in delineating the entire alluvial fan as a potential flood hazard zone. On fans that have experienced urbanization, the issue of flood hazard delineation may be ancillary to mitigation concerns, but a comprehensive mitigation plan still requires accurate technical analysis of the flood hazard potential.

Alluvial fan flooding is characterized by relatively unconfined flows on steep surfaces. Most alluvial fans are evolved through a combination of water flooding and mud/debris flow events. The flow behavior is often subject to surging associated with high concentrations of sediment and debris. Channels relocating (channel avulsion) on undeveloped portions of alluvial fans adds to the complexity of the flood hazard delineation. The general geomorphic evolution of alluvial fans dictates that the fan surface is aggrading over the long term; however, channel incision may occur during the episodic growth of the fan. Deeply incised channels associated with a long period of declining watershed sediment yield may limit the area of inundation. Delineation methodologies and administrative tools need to consider these physical processes.

---

[1] Principal, FLO Engineering, Inc., Breckenridge, CO.

[2] Senior Water Resource Specialist, Colorado Water Conservation Board and Chair of ASFPM Mapping and Engineering Committee

STATUTORY AUTHORITY

Authority and Technical Standards for Designating and Approving Alluvial Fan Flood Hazard Studies

In Colorado, the statutes provide that all floodplain delineations must be approved by the Colorado Water Conservation Board (CWCB) before they are applied by local governments for regulatory purposes. Rules and Regulations for the approval of floodplain studies and the technical criteria for study review were promulgated under the authority granted to the CWCB. These rules were intended to provide uniform technical standards for floodplain studies and to prescribe the process for the designation and approval of floodplain delineations. The Statutes state:

> *"No floodplain shall be designated by any local government until such designation has been first approved by the Colorado Water Conservation Board."*

Colorado communities must, therefore, obtain state designation and approval of floodplain delineations in order to regulate activities in the floodplain zones. The scope of the CWCB statutory authority and of the rules and regulations for delineation studies extends to floodplain information as it related to zoning. It does not cover individual subdivision drainage reports, economic criteria for facilities in the floodplain, or inundation of areas by hydraulic structure failure such as dams. Such detailed studies would be subject to CWCB regulation only inasmuch as they must either show conformity with the existing delineation or justify changes in the flood hazard delineation. State policy might be simply stated as, "The CWCB blesses the floodplain delineation and supporting documentation and the local governments then utilize it."

Definitions

The State's authority to regulate floodplain studies on alluvial fans is provided in the Colorado Revised Statutes which define several floodplain features related to alluvial fans. The pertinent definitions in the Statutes are:

> *(4) "Debris-fan floodplain" means a floodplain which is located at the mouth of a mountain valley tributary stream as such stream enters the valley floor.*
>
> *(5) "Dry wash channel and dry wash floodplain" means a small watershed with a very high percentage of runoff after torrential rainfall.*
>
> *(7) "Floodplain" means an area adjacent to a stream, which area is subject to flooding as the result of the occurrence of an intermediate regional flood and which area thus is so adverse to past, current, or foreseeable construction or land use as to constitute a significant hazard to public health and safety or to property. The term includes but is not limited to:*
>
> > *(a) Mainstream floodplains;*
> > *(b) Debris-fan floodplains; and*
> > *(c) Dry wash channels and dry wash floodplains.*
>
> *(11) "Mainstream floodplain" means an area adjacent to a perennial stream, which area is subject to periodic flooding.*
>
> *(12) "Mudflow" means the downward movement of mud in a mountain watershed because of peculiar characteristics of extremely high sediment yield and occasional high runoff.*

Additional regulations are required for predicting the flow hydraulics (flow depths and velocities) of unconfined flooding and mud/debris flows on alluvial fans. These can be developed within the scope of the existing CWCB Rules and Regulations. A proposed policy for the flood hazard delineation and administration of flood prone areas on alluvial fans in Colorado is described in the next section.

Proposed Policy

Each alluvial fan and watershed has unique geology, topography, soil and hydrologic characteristics and, therefore has unique flooding hazards. The fan topography, mudflow deposits and fluvial features provide clues as to the nature and magnitude of the potential hazard event. Local communities should address their unique flooding problems in preparing general policy, flood hazard delineation studies and zoning regulations. In general the community should adopt a policy and program, subject to State review, which would include the following components:

- Statements regarding the uniqueness of the special flood hazard on their alluvial fans.
- Rules and regulations related to the use of approved hydrologic and hydraulic modeling practices.
- Rules and regulations related to flood hazard mapping for both existing conditions and proposed modifications.
- Statements regarding the need for compliance with the comprehensive master drainage and development plan.
- Special considerations related to the analysis of existing conditions and proposed mitigation measures.
- Detailed instructions for the delineation process for proposed development in mud/debris flow hazard zones.
- Statements regarding policy for Flood Insurance Studies and the removal of properties from flood hazard mapping for insurance purposes.

Detailed hydrologic studies which lead to the creation of a flood hydrograph at the fan apex are recommended. Professionals carrying out the hydraulic analysis and the delineation of alluvial fan flood hazards should consider the inappropriateness of step-backwater methods (i.e. HEC-2) and of approximate methods not applicable for urbanized fans (i.e. FEMA FAN model) and pursue two-dimensional flood routing models that can also simulate mud and debris flows. Alluvial fan flooding may be unconfined and the hazard delineation should be based on predicted 1 ft maximum depth flood contours. These recommendations will be discussed further in subsequent sections.

The Colorado Water Conservation Board, Flood Control and Floodplain Management Section, has published a review report and checklist for the technical review of floodplain information for riverine floodplains. It includes a request form for the designation and approval of the floodplain delineation by the Board as well as a request form for a variance. Such a checklist could be developed for reviewing alluvial fan floodplain information.

Deficiencies in the Current Procedures

If the engineer predicts fan flood hydraulics and areas of inundation with alternative methods that are more conservative than those predicted by the FEMA FAN model, then the results may be accepted in the review process. In this manner, the FEMA FAN method becomes the de-facto standard for fan flood hazard delineation. Based on the analyses of other authors regarding the simplified and inappropriate assumptions in the FEMA method (Dawdy, et al., 1989; Fuller, 1990; French and Fuller, 1992, Grindeland, et al., 1990), lack of model verification (O'Brien and Fullerton, 1991) and failure to consider geological and topographical constraints (Baker, et al., 1990); the following conclusions have been reached regarding the FEMA method for delineating alluvial fan flood hazards:

- The FEMA method does not present a realistic analysis of physical processes on alluvial fans. It is not a physically based model.
- There are no published guidelines on the limits of the FAN model applicability.
- There is no verification of the model.
- The FEMA model does not err conservatively.

The FEMA FAN model and step-backwater water surface profile models such as HEC-2 are <u>not</u> recommended. The FEMA method poorly predicts flood hydrologic zones and is not suitable for urbanized alluvial fans. Flood wave attenuation and fan rainfall are important facets of alluvial fan flooding that HEC-2 cannot simulate.

Successful application for a LOMR on alluvial fan flood hazard areas is a hit or miss proposition. Furthermore, FEMA does not have any reasonable, applicable or comprehensible criteria for LOMR's and CLOMR's for mud/debris flow hazard zones. In the seven Colorado communities and counties where FEMA mapping of alluvial fans exist, the current mapping does not support or provide adequate guidance for zoning regulations or mitigation design.

PROPOSED TECHNICAL STANDARDS FOR DELINEATING ALLUVIAL FAN FLOODING

The failure of FEMA to provide adequate technical guidance and the significant limitations of State Rules and Regulations creates a void in the analysis of the unique processes of alluvial fan flooding. As a result, the following technical standards for delineating alluvial fan flooding, including a list of appropriate definitions, are proposed.

Definitions

There are several definitions of physical processes or features specific to alluvial fan flooding as provided in the literature which may deviate from those contained in the Colorado Revised Statutes or in the CWCB Rules and Regulations. In nature, there exists a continuum of flood flow conditions and behavior, and one flood event may consist of several processes. Although the transitions between the different types of flow are difficult to distinguish, mass wasting processes can be divided into four main categories which are described below: water floods, mud floods, mud flows and landslides (NRC, 1982; O'Brien and Julien, 1985). Most of the definitions presented herein are in concert with those promulgated by the National Research Council (1982).

Mud Flood: Hyperconcentrated sediment flow with a fluid matrix ranging in concentration from 20 to approximately 45 percent by volume. Sediment transport capacity equations are not applicable because of the higher viscosities of fluid matrix. Water floods and mud floods are classified under the NFIP definition of floods.

Mudflow: Mudflows are hyperconcentrated sediment flows where the viscous stress controls the flow behavior. Mudflows generally have a flow matrix with a sediment concentration by volume exceeding 40 to 45 percent but less than the concentration for a landslide of 50 to 55%.

Risk: The assignment of flood risk is related to the frequency of the storm event; i.e. a 100-yr flood has an annual probability of 0.01. On the average, a 100-yr flood will occur once during a 100-year period. With respect to a mudflow, the 100-yr storm is assumed to produce a 100-yr return period mudflow event even though a mudflow may not occur with a storm of the return frequency of a 100-yr event. Generally, the 100-yr mudflow event is predicted by bulking the 100-yr water flood at the fan apex.

Shallow Flooding: On alluvial fans, shallow flooding refers to water flooding or mud flooding with flow depths less than 0.5 ft. Shallow flooding may be assigned a separate flood hazard delineation zone.

Water Flood: Conventional water flooding is defined as water inundation by overbank discharge. Sediment is transported through the mechanisms of suspension and rolling and saltation along the bed which largely depend on flow velocity and turbulence. Sediment concentrations are relatively low under these conditions and do not significantly affect fluid properties.

Approximate Delineation

The CWCB has standards for approximate flood hazard delineations for riverine floodplain. These standards cover work maps, and hydrologic and hydraulic analyses. The hydrologic analysis requires the calculation of the 100-yr peak discharge and the hydraulic analysis is based on an assumed depth determined from a regression analysis of depth-frequency relations or from a slope-area-conveyance calculation. CWCB standards permit the approximate delineation of the 100-year flood boundary from geomorphic features and/or historic flood data.

Unfortunately approximate flood delineation for alluvial fans is not this straight forward. Unconfined flow does not permit reasonable assumptions of flow depths and flood boundaries and furthermore, mudflows may cease flowing on the fan. There is no simple method for determining the effects of loss of channel conveyance or bridge blockage. An approximate 100-yr peak discharge may be estimated at the fan apex, but 100 ft downfan, the area of inundation or flow depth would be impossible to approximate. Therefore, other than identifying the entire alluvial fan within the flood hazard boundary, approximate flood hazard delineation on alluvial fans is not recommended.

It should be noted that there are reasons for using geologic or other techniques for identifying entire fans as flood hazard areas. States can apply the delineations to prioritize fans for future detailed studies. Local governments can use approximate delineations to determine areas where studies should be completed before permitting development. Applying approximate methods, however, for detailed land use or flood insurance analysis is discouraged.

locations of recent and historic channels, debris producing areas, type of expected flooding (mudflow, mud flood, debris flow, etc.), possibility of channel incision, and potential for flood control/debris basins.

In creating a data base, a report should be prepared which identifies the general fan features, existing flood hazard mapping, recent flow deposits, possible and desirable flow directions, streets and buildings and potential development. Survey data should be identified for future reference. The data base should be compared with any data requirements for state and local regulations or for FEMA flood insurance map revisions.

Technical Analysis of Existing Conditions

Geology. Alluvial fan flooding and possibility of mud or debris flow is a direct consequence of the geologic formations regarded as the sediment supply. A geologic assessment of historic flow deposits and fan geomorphology will enhance the hydraulic analysis. The following information is useful:

- Identification of source areas.
- Percentage of silt and clay in undisturbed deposits.
- Depositional features, lobes, rock levees, runout distances, maximum size transported boulders (flow competence), height of scars on trees.
- Estimates of maximum flow depths and velocities as discerned from physical evidence.
- State of the alluvial fan, aggradational or incisional.
- Fan geomorphology, slopes, channels, age of flows.

Hydrology. The magnitude of the flood event on the alluvial fan is controlled by the upstream watershed hydrology. The hydrologic analysis should include the 10-, 50- and 100-year rainfall events. Analysis of stream gaging records is preferred, but few, if any, ephemeral fan channels have been gaged. Furthermore, the gaging records are usually too short to encompass any of the extreme events that usually produce mud and debris flows. The requirement to analyze mud and debris flows as a function of these large discharge events will also preclude regional regression analysis or transposition of gaging records from other watersheds to predict flood magnitudes.

Flood hydrographs for ungaged watersheds should be accomplished with a suitable rainfall/runoff model. A frequency analysis should be performed on appropriate rain gage data to derive the 10-, 50-, and 100-yr precipitation totals. The network of rain gages in the mountains is usually limited and appropriate precipitation data may be unavailable. The NOAA rainfall atlas should be referred to when estimating precipitation totals. Available rainfall records should be closely examined for prescribing storm duration and intensity. Often, local drainage criteria may specify storm characteristics. The State should be specific about which hydrology models are appropriate and should prescribe permissible modifications to storm duration. Calibration of hydrologic model watershed parameters should be attempted whenever practical. This may entail simulation of a rainfall event on a nearby gaged watershed.

The Corps of Engineers HEC-1 rainfall/runoff model is recommended for predicting watershed hydrology. With it, the flood hydrograph can be prepared at the fan apex. The flood hydrograph can be adjusted for mud/debris bulking and average sediment concentration. Consideration should be given to hydrograph timing for mud and debris flow events (frontal wave delay).

Mud and debris flows are not always associated with rainfall and may be initiated by snowmelt or saturated ground conditions. These less frequent modes of mudflow mobilization usually initiate as landslides and may transform into mudflows. Sediment concentrations associated with these types of mudflows are more uniform and may increase on the falling limb of the event hydrograph. Estimating flood hydrograph volumes is valuable to the accuracy of the flood simulation.

Other aspects of the design of mitigation measures include: freeboard which accounts for potential deposition, wave height and frontal wave impact; floodwall design which allows for maximum scour depth, maximum deposit depth and impact forces; riprap design for levees and berms; detention basin volume with bulked sediment flows; and the protection of conveyance channels from debris blockage. Several practical mitigation guidelines are presented in Appendix A. For floodplain administrators to assess the effectiveness of mitigation measures and approve of construction, the following information should be submitted to support the proposed mitigation measures.

Proposed Mitigation. A technical description of the proposed mitigation measures should be prepared. This would include such factors as location on the fan, mitigation purpose, design parameters and the potential impact of the mitigation on flood hydraulics and downfan property. The technical description should be supplemented with a description of the proposed project for the general public.

Effect on Hydrology and Hydraulics. The mitigation measure may alter the flood direction or the local drainage on the fan. Fan runoff may be increased through an increase in impervious area, confinement of the flow or channelization and may be decreased through construction of detention basins. The mitigation designs need to be evaluated for possible impact on other development. The report on the mitigation design should include a discussion of the potential impacts with and without the proposed mitigation including a comparison of flow depth, velocity contours and areas of inundations.

Assessment of the Structural Integrity of the Mitigation. The design of the mitigation structure should be assessed based on the effect of the mitigation on the flood hydraulics. The structure design should be evaluated for scour and deposition, boulder impact, static and dynamic pressure, overtopping, overturning and flow abrasion. Two aspects of the structure design and maintenance plan are the structural integrity during successive events and the potential for failure immediately following an event. Colorado has a meteorological history of having several days of successive storms, so this very real possibility must be considered. The maintenance plan should demonstrate access to the mitigation site, prescribe a method of mud and debris removal and identify a disposal site for removed mud and debris.

Report Preparation. The final mitigation design should be submitted in a report documenting flow hydraulics, flood hydrograph, flood routing techniques and comparison of the mitigation design with State criteria. If the mitigation measures and their effects have not been sufficiently demonstrated to the floodplain administrator, then the report should include a computer diskette with the engineering information needed to accurately model the proposed structure. The mitigation project proponent will be responsible for providing information to demonstrate the structural integrity and the hydraulic impact of the mitigation. In this circumstance, the floodplain administrator or local government (or a consultant retained for this purpose) will run the computer model with the proposed changes to verify the effects of the mitigation prior to approval of the mitigation. Mitigation design may permit removal of some areas from flood insurance hazard zones.

State Approval of Technical Methods. The CWCB, in cooperation with the Colorado Geological Survey, is the authority in Colorado for approving the application of floodplain hazard delineation tools for alluvial fans. Approval of a flood routing model should be based on the following criteria:

- Theoretical and fundamental soundness of the model algorithms.
- Demonstration of conservation of mass in the model application.
- Model capability to replicate basic water hydraulics compared with a standard step-backwater model.
- Ability of the model to be calibrated to replicate an historical flood event.
- Appropriate resolution of the model results for mapping purposes.
- Submittal of a model users manual, a report describing the model, model code and an executable version of the model.
- Submittal of model results depicting the model's capability.

A state policy board should address the limitations of the model during the approval process including: Does the model grossly overestimate or underestimate the potential flood hazard; and Does the model oversimplify the physical processes contributing to the flood hazard? These questions should be resolved by entities like the CWCB to establish rules for conducting alluvial fans studies concerning specific hydraulic models. Examples of acceptable models should be indicated by the approving agency to guide users in the choice of acceptable models. Approval of models for alluvial fan flood hazard delineation by the State will lead to the development of submittal requirements, technical standards and adoption procedures for fan flood studies.

Submittal Requirements. Alluvial fan flood hazard studies are to be submitted first to the local governments and then to the state agency (CWCB) unless the studies are being conducted by a state or federal agency. State submittal requirements should be adopted by the local government as part of their own regulations. The submittal requirements for the flood hazard study should incorporate the following components:

- Identification of the flood hazard.
- Compilation of the data base.
- Technical analysis including: a description of the geology, hydrology, fan hydraulics and flood routing, data base, and flood contour mapping.
- Computer diskette with the hydraulic model and model results.

In the case of proposed mitigation, the CWCB would provide review and comments only until the mitigation construction is completed, at which time the mitigation would be approved along with the changes in the flood hazard delineation. Submittals for mitigation approval would include:

- Description of the mitigation.
- Effect on hydrology, hydraulics, and flood hazard delineation with and without proposed mitigation.
- Revised flood hazard mapping.
- Assessment of the structural integrity of the mitigation measure.
- Computer diskette with the hydraulic model and results.

Technical Standards. Technical standards for alluvial fan flood hazard investigations must be developed by the state. The standards should address the following study components:

- Fan geology and geomorphology.
- Hydrology.
- Data base and base maps.
- Fan hydraulics and flood routing.
- Flood hazard delineation, flood contours and hazard mapping.
- Computer diskette submitted with the appropriate models and results.

2-Zone Alluvial Fan Flood Hazard Delineation System

The delineated hazard map would consist of two zones which would invoke different development regulations. A system defining two levels of hazards and two levels of regulations is proposed.

Zones Where Development is Prohibited. In alluvial fan flood hazard zones where the potential flooding is predicted to be a certain depth or higher, for example one foot or greater for mudflows or three feet or greater for water, development should be prohibited unless there is proposed mitigation for hazard avoidance. Such areas would be similar in concept to a floodway, however, the "no rise" principle would be replaced by hazard elimination or removal.

Zones Where Development is Restricted. In fan flood hazard zones where the potential flooding is predicted to be less than a certain depth, (for example, one foot or less for mudflows or three feet or less for water flooding), development is restricted to mitigated flow depths that are less than 0.5 ft for mudflows or 1 ft for water flooding. Mitigation may involve redirection or confinement of the flow or raising the elevation of the development to reduce the level of flood inundation. Buildings and infrastructure constructed in this zone would have to comply with structural and technical requirements to assure safety during a 100-year event. Flood hazard delineation changes would have to be documented and mapped.

Alluvial Fan Floodplain Development Permit

Without a permit no development would be allowed. It is an obligation of the local government to require a floodplain permit for development. Hazard avoidance should be the primary focus of the permitting system. Development in shallow flooding areas may be possible with appropriate floodproofing and mitigation measures. The uniqueness of the alluvial fan flooding requires a special permitting process and special permit conditions may be imposed. Although similar to the conventional floodplain development permitting process, the alluvial fan permit would be functionally separate from a riverine floodplain permit. The components of a permit application would include:

- Description of the flooding problem and the proposed development.
- Description of the proposed mitigation plan, if any.
- Report on hydrologic and hydraulic analysis of flooding.
- Flood model application to replicate existing conditions and demonstrate the effectiveness of the proposed mitigation.
- A verification of the flood simulation by the floodplain administrator or the contractor.
- An assessment of the structural integrity of the proposed mitigation.
- Permit and checklist.

Zoning regulations would direct the project proponent to prepare and submit a permit application which would include a detailed study. The permit would be issued only after all the appropriate reviews had been satisfactorily completed.

Construction Inspection and Post-Construction Certification

As part of local zoning regulations and the alluvial fan floodplain development permit process, regularly scheduled inspections should occur during construction. Final inspection reports and as-built drawings should be submitted to the CWCB staff, to the planning and zoning commissions, and to local officials as specified by the regulations to obtain a certification of occupancy. Procedural and technical compliance with regulations will be a prerequisite for certification of occupancy in mud and debris flow hazard zones.

Maintenance and Monitoring of Mitigation Facilities

Mud and debris flow mitigation facilities should be monitored prior to each flood season. In Colorado, the high hazard season extends from May through October. As a prerequisite for approval of mitigation measures, a maintenance and monitoring schedule should be submitted with the mitigation design. Mitigation structures and facilities should be maintained immediately following an event. This epitomizes the need for on-going care of the hazard delineation and mitigation system.

Maintenance and Operation of Mitigation Facilities

Maintenance and operation of mitigation facilities may include removing sediment and debris from debris basins, clearing trash and debris fences, cleaning conveyance channels and streets, removing debris blockage from all conveyance structures, repairing or restoring freeboard in levees and berms, and repairing any damaged structures. It is possible that a extreme rainfall event may be followed a smaller rainfall event that could be potentially more damaging because the extreme event stored or charged the upstream watershed channel with large quantities of sediment and debris that did not reach the fan apex. Long term and short term maintenance should be scheduled for continued satisfactory operation of the mitigation structures.

The monitoring for potential problems with the mitigation structures should be primary focus of the city or county engineer. Uncertified mitigation measures should be monitored for potential downstream hazard in the event of failure. The mitigation system should be inspected and declared functional after an event and certified that it would not be prone to failure during the next event.

Monitoring and Updating of the Flood Hazard Delineation Model and Data Base

The hazard delineation model should be upgraded and revised as the model is improved and as subsequent flood hazard investigations expand the data base. The floodplain administrator should update the model to incorporate improvements and enhance the model's capability to simulate the physical system. For the model to be effective, it must be updated to provide an accurate portrayal of the alluvial fan physical condition and changes including the degree of urbanization and the construction of flood mitigation. Ongoing research should lead to improved modeling capability in the areas of GIS delineation of streets and buildings, risk assessment and mobile bed analysis. There is a dearth of data related to mud and debris flow events. Monitoring will provide information regarding performance of mitigation measures. Volumes, peak discharge, rainfall totals, timing and duration should all be considered in designing a monitoring program.

Appendix A. Practical Mitigation Design Guidelines

Some practical guidelines on development and mitigation on alluvial fans.

- Development should not be permitted without a master drainage and development plan.
- Flood conveyance off the fan is preferred over storage above populated areas.
- Redirection of flow near the fan apex should be avoided.
- Basements and mobile homes should be prohibited or subject to strict regulation.
- Streets should be aligned and designed to help convey flows.
- Emergency access routes should be designed and should not convey flows.
- Berms and levees can help direct the flow away from structures and into streets.
- Downfan impacts of redirected flows should be carefully analyzed.
- The use of slope stabilization and drop structures should be encouraged in residential areas.
- Elevation of structures should be regulated according to hazard zone delineation. Structures should be elevated to a prescribed height above the potential depositional flow depth.
- All mitigation measures should be in concert with existing flood control facilities.
- Floodproofing methods should be encouraged.
- Conveyance features should be designed and maintained for stability and permanence.
- Floodwall height should be designed with appropriate freeboard for mudflows.
- Scour depth for mitigation design should be analyzed on the basis of clear water flows and maximum velocity. Floodwalls and pilings should be placed at a prescribed depth below predicted scour depths.
- Riprap on berms or levees should be considered as a potential source for increasing the debris load. Concrete lining is a much better alternative near the fan apex.
- Flood detention should be designed to store the 100-yr event with appropriate bulking for sediment loads. Debris basins should be fitted with debris racks.
- Loss of channel conveyance is the most common cause of flood damage on alluvial fans. Potential blockage may occur at bridges, culverts, channel bends and constrictions, and changes in slope. Texas dips or low flow culverts and over-road capacity are preferred channel crossings. Bridges should be designed without pilings. Important emergency access routes should be kept open during flooding.
- The potential for boulder impact should be considered when designing mitigation structures.
- As a condition of plat or building permit approval, developers should be required to implement mitigation and prepare revisions to the master drainage plan.
- Buildings should be prohibited in areas of predicted high velocities; replacement of existing buildings in such locations should be strongly discouraged or prohibited.
- Slope protection that will not erode during mudflow events should be required for fill, berms and levees.

TAYLOR, R. H. and KENNEDY, J. F., Discussion on roll waves and slug flows in inclined open channels by P. G. Mayer, Transactions of the ASCE, 1961, pp. 541–548.
THOMAS, H. A., The propagation of waves in steep prismatic conduits, Proc. Hydraulic Conference, Univ. of Iowa, 1939, pp. 214–229.
VEDERNIKOV, V. V., Conditions at the front of a translation wave disturbing a steady motion of a real fluid, USSR Academy of Sciences, Vol. 48, No. 4, 1945, pp. 239–242.
VEDERNIKOV, V. V., Characteristic features of a liquid flow in an open channel, USSR Academy of Sciences, Vol. 52, 1946, pp. 207–210.
YIH, C. S., Stability of parallel laminar flow with a free surface, Proc. 2nd U.S. Congress in Applied Mechanics, 1954, pp. 623–628.
YIH, C. S., Stability of liquid flow down an inclined plane, Physics Fluids, Vol. 6, 1963, pp. 321–334.
YIH, C. S., *Fluid mechanics,* West River Press, 1977, pp. 502–507.